Small Antennas: Miniaturization Techniques and Applications

Guest Editors: Wenhua Yu, Wenxing Li, Dau-chyrh Chang, and Yingsong Li

Small Antennas: Miniaturization Techniques and Applications

Small Antennas: Miniaturization Techniques and Applications

Guest Editors: Wenhua Yu, Wenxing Li, Dau-chyrh Chang, and Yingsong Li

Editorial Board

Contents

Contents

Editorial

Small Antennas: Miniaturization Techniques and Applications

Wenhua Yu,[1] Wenxing Li,[2] Dau-Chyrh Chang,[3] and Yingsong Li[2]

[1] *2COMU, Inc., Fairfax, VA 22030, USA*
[2] *College of Information and Communications Engineering, Harbin Engineering University, Harbin 150001, China*
[3] *Communication Research Center, Oriental Institute of Technology, Taipei 22061, Taiwan*

Correspondence should be addressed to Wenhua Yu; wenyu@2comu.com

Although small antenna designs and miniaturization techniques have been widely studied in recent years, there are still many challenging issues in small antenna applications and research. In this special issue, several small antennas have been proposed and discussed for wireless local area networks (WLANs), UHF band, multiple-input-multiple-output (MIMO), long-term-evolution (LTE), and other wireless communication applications. These designed antennas are not only small in size but also able to provide high performance to meet the practical engineering requirements with respect to the impedance bandwidth and the radiation patterns. On the other hand, two horn antennas with enhanced performance were developed for modern wireless communication applications. One of the horn antennas was designed to obtain high gain, which was realized by the integration of a horn antenna into a microstrip antenna. The other horn antenna was presented for ultra-wideband (UWB) applications by the combination of a TEM horn antenna with a Vivaldi antenna together. Both of the proposed improved horn antennas have been verified that they have low profile and good performance.

In addition, several compact antennas have been proposed and investigated to provide high efficiency antenna and low SAR, which are suitable for on-body and mobile communications. Motivated by the rapid developments of the microwave imaging, a right angle-bent monopole antenna has been built to obtain small size and low profile for microwave tomographic imaging application. In addition, a compact frequency selective surface (FSS) has been proposed based on the square loop aperture element. The designed FSS can give high polarization stability, angle stability, and smaller size in comparison with the previously proposed FSS structures.

Beyond that, frequency reconfigurable antennas have also been proposed in this special issue for multifunction communication applications. Since each narrowband system should be provided a different antenna, a reconfigurable antenna can be operated in several narrowband by controlling its reconfigurable states, which is flexible and can reduce the cost for practical engineering applications. A reconfigurable antenna has been investigated by using MEMS to realize multiband antenna. Furthermore, the MEMS technique has been also exploited for minimizing the antenna by means of tunable capacitors.

As for the optimization method and measurement techniques, an orthogonal design method was proposed to optimize roughly designed antennas. Additionally, a wideband differential-mode current injection testing technique was also presented based on directional coupling device.

In this special issue, two adaptive signal processing algorithms have been developed for sparse channel estimation and virtual array antenna applications. Both of the proposed adaptive algorithms can provide higher performance compared with previous classical algorithm and can be further developed for applying in the antenna arrays.

Acknowledgments

Research Article

An Effective Technique for Enhancing Direction Finding Performance of Virtual Arrays

Wenxing Li, Xiaojun Mao, Wenhua Yu, and Chongyi Yue

College of Information and Communication Engineering, Harbin Engineering University, Harbin 150001, China

Correspondence should be addressed to Xiaojun Mao; wwwmaoxiaojun@126.com

The array interpolation technology that is used to establish a virtual array from a real antenna array is widely used in direction finding. The traditional interpolation transformation technology causes significant bias in the directional-of-arrival (DOA) estimation due to its transform errors. In this paper, we proposed a modified interpolation method that significantly reduces bias in the DOA estimation of a virtual antenna array and improves the resolution capability. Using the projection concept, this paper projects the transformation matrix into the real array data covariance matrix; the operation not only enhances the signal subspace but also improves the orthogonality between the signal and noise subspace. Numerical results demonstrate the effectiveness of the proposed method. The proposed method can achieve better DOA estimation accuracy of virtual arrays and has a high resolution performance compared to the traditional interpolation method.

1. Introduction

Array signal processing has a wide range of applications in radar, communications, sonar, and acoustics. Interpolation or mapping technique from a real antenna array to a virtual antenna array is a popular topic in array signal processing [1]. Virtual array interpolation (mapping) technique was introduced in 1980s [2–5]. Virtual array transformation can map an arbitrary planar structure antenna array to be a uniform linear array- (ULA-) type array and can increase the degrees of freedom (DOF) of an antenna array, which is widely used in the DOA estimation and adaptive beamforming [6, 7].

There exist some efficient DOA estimation algorithms such as "root-MUSIC" and "root-WSF," which are normally restricted to the ULA geometry. These algorithms cannot be used for the conformal arrays or uniform circular array (UCA) directly; however, the interpolation transform technique can solve this problem efficiently [8]. In Friedlander's virtual array transformation (VAT) method [9], an arbitrary shaped antenna array can be transformed into a desired virtual antenna array by interpolating the interested scanning sector. The basic idea of Friedlander's VAT is to divide the spatial region into several subregions, and then by taking interpolation in the array scanning sector of interest,

the manifold of the virtual array can be obtained by the linear interpolation of the manifold of the real array. The transform matrix is computed as the least squares solution.

The performance of array interpolation in the DOA estimation has been reported in the literature [10–12]. Although the array interpolation approach has some attractive properties [13, 14], an essential shortcoming of the method is that it often introduces mapping errors that cause bias in the DOA estimation. Hence, the DOA estimations are not statistically optimal.

Pesavento et al. developed a robust interpolation method in [15]. The method ensures that the interpolation transform error of the selected sectors is minimal, while the conversion outside region sets up multiple "stop bands" to make the conversion error less than a criterion.

Hyberg et al. proposed a geometrical interpretation method of a Taylor series expansion of the DOA estimator criterion function to derive an alternative design of the mapping matrix [16, 17]. The proposed design considers the orthogonality between the manifold mapping errors and certain gradients of the estimator criterion function. This bias-minimizing theory was extended to not only minimize bias but also consider finite sample effects due to noise reducing the DOA mean-square error (MSE). DOA MSE is
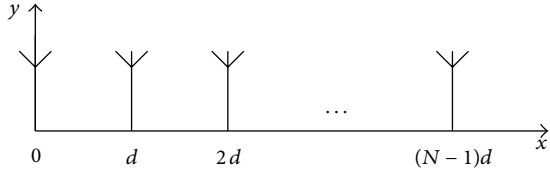
FIGURE 1: The structure of ULA.

Real antenna unit

Virtual antenna unit

FIGURE 2: Real antenna and interpolated arrays.

not reduced by minimizing the size of the mapping errors, but instead by rotating the errors and the associated noise subspace into the optimal directions related to a certain gradient of the DOA estimator criterion function in [17]. The two methods show the superior performance on the DOA MSE reduction of array interpolation but its derivation computed procedure is complex.

This paper proposed a novel method to reduce the DOA bias of virtual interpolation. Using the projection concept, project the transformation matrix onto the real array covariance matrix to enhance the signal subspace, which improves the orthogonality between the signal and noise subspace. The proposed method is efficient and easy to realize. Numerical simulations verify that this method can get better estimation accuracy and has a high resolution performance compared to the traditional interpolation method.

2. Signal Model

Considering an omnidirectional array with N elements illuminated by M narrow band signals, the distance of the array elements is d, as shown in Figure 1.

The signal $s_k(t)$ is incident in the direction θ_k; the received signal $\mathbf{X}$ can be expressed as follows:

$$\mathbf{X}(t) = \mathbf{A}\mathbf{S}(t) + \mathbf{N}(t), \tag{1}$$

where $\mathbf{X}(t) = [x_1(t), x_2(t), \ldots, x_N(t)]^T$ is a $N \times 1$ snap data vector. $\mathbf{S}(t) = [s_1(t), s_2(t), \ldots, s_M(t)]^T$ is a vector containing the complex signal envelops of M narrow-band signal sources. $\mathbf{N}(t) = [n_1(t), n_2(t), \ldots, n_N(t)]^T$ is a vector of zero-mean spatial white sensor noise of variance σ_n^2; $\mathbf{A}$ is an array manifold matrix; namely, $\mathbf{A} = [\mathbf{a}(\theta_1), \mathbf{a}(\theta_2), \ldots, \mathbf{a}(\theta_M)]$, where $\mathbf{a}(\theta_1) = [1, e^{j\beta_k}, \ldots, e^{j(N-1)\beta_k}]^T$, $k = 1, 2, \ldots, M$ represents a steering vector in the θ_k direction, and β_k is the phase difference that can be represented as

$$\beta_k = \frac{2\pi}{\lambda} d \sin(\theta_k). \tag{2}$$

Assume that the signal and noise are linearly independent, and then the data covariance is written in the format below:

$$\mathbf{R} = E\left\{\mathbf{X}(t)\mathbf{X}^H(t)\right\} = \mathbf{A}\mathbf{R}_s\mathbf{A}^H + \sigma_n^2\mathbf{I}, \tag{3}$$

where $E\{\}$ denotes the expectation operator; $\mathbf{R}_s = E\{S(t)S^H(t)\}$ represents the autocorrelation matrix of signal complex envelops. σ_n^2 is the noise power; $\mathbf{I}$ is the unit matrix; and $(\cdot)^H$ denotes the matrix conjugate transposition.
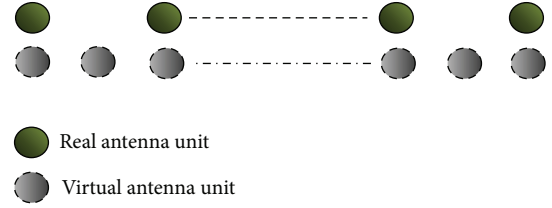
In practice, the desired signal is often present in the snapshots. The sample array covariance matrix can be expressed as follows:

$$\widehat{\mathbf{R}} = \frac{1}{K}\sum_{i=1}^{K}\mathbf{X}(i)\mathbf{X}^H(i), \tag{4}$$

where K is number of snapshots. VAT is based on interpolation technique [8] in which the entire antenna array scanning vector is divided into several subregions, and the subregion of interest will be segmented through a certain transformation to realize the mapping from the original array to the corresponding virtual array.

3. Conventional Interpolated Array

Consider a real ULA transformed into a virtual ULA via array interpolation, as illustrated in Figure 2.

Assume that there is a signal located in the region Θ; we equally divide Θ into

$$\Theta = [\theta_l, \theta_l + \Delta\theta, \theta_l + 2\Delta\theta, \ldots, \theta_r - \Delta\theta, \theta_r], \tag{5}$$

where θ_l and θ_r are the left and right boundary of region Θ, respectively. $\Delta\theta$ is size of the interpolation step, which is determined by the specified accuracy.

The real array manifold matrix in the chosen area can be expressed as follows:

$$\mathbf{A} = [\mathbf{a}(\theta_l), \mathbf{a}(\theta_l + \Delta\theta), \mathbf{a}(\theta_l + 2\Delta\theta), \ldots,$$
$$\mathbf{a}(\theta_r - \Delta\theta), \mathbf{a}(\theta_r)], \tag{6}$$

where $\mathbf{a}(\theta_l)$ represents the steering vector of a real array in the θ_l direction. The array manifold matrix of virtual array in the same area Θ is expressed as follows:

$$\overline{\mathbf{A}} = [\overline{\mathbf{a}}(\theta_l), \overline{\mathbf{a}}(\theta_l + \Delta\theta), \overline{\mathbf{a}}(\theta_l + 2\Delta\theta), \ldots,$$
$$\overline{\mathbf{a}}(\theta_r - \Delta\theta), \overline{\mathbf{a}}(\theta_r)], \tag{7}$$

where $\overline{\mathbf{a}}(\theta_l)$ represents the steering vector of a virtual array in the θ_l direction. There must exist a mapping relationship between the real and the virtual array vectors. Then an interpolation matrix $\mathbf{B}$ is designed to satisfy the least square; that is,

$$\min_{\mathbf{B}} \left\|\mathbf{B}^H\mathbf{A} - \overline{\mathbf{A}}\right\|_F^2, \tag{8}$$

where $\| \cdot \|_F$ denotes the Frobenius norm for a matrix. The real and the virtual array manifold vectors satisfy the following relationship:

$$\mathbf{B}^H \mathbf{A}(\theta) = \overline{\mathbf{A}}(\theta) \quad \theta \in \Theta. \tag{9}$$

And their steering vectors satisfy the following equation:

$$\mathbf{B}^H \mathbf{a}(\theta) = \overline{\mathbf{a}}(\theta) \quad \theta \in \Theta. \tag{10}$$

When the number of a transformed array is greater than the actual number of antenna elements and the matrix $\overline{\mathbf{A}}$ has a nonzero condition value, by solving (8) the virtual transformation matrix $\mathbf{B}$ is

$$\mathbf{B} = \left(\mathbf{A}\mathbf{A}^H\right)^{-1} \mathbf{A}\overline{\mathbf{A}}^H. \tag{11}$$

Define the transformation error

$$E(\mathbf{B}) = \frac{\min_{\mathbf{B}} \left\| \mathbf{B}^H \mathbf{A} - \overline{\mathbf{A}} \right\|_F}{\left\| \overline{\mathbf{A}} \right\|_F}. \tag{12}$$

In an ideal case, there is no error in the virtual transformation; $E(\mathbf{B})$ should be zero. However, in practice, since interpolation points in the transformation area infinities are limited, the interpolation operation often introduces mapping errors. These preprocessing techniques often introduce mapping bias and excess variance in the DOA estimations. Hence, the estimations are not statistically optimal [6].

4. Modified Interpolated Method

In this section, we describe a modified interpolation algorithm. We set the data covariance matrix of the real array $\widehat{\mathbf{R}}$ as a projection matrix. After obtaining the transform matrix $\mathbf{B}$, according to (11), we reconstruct the transformation matrix $\overline{\mathbf{B}}$ by projecting it to the sample array covariance matrix

$$\overline{\mathbf{B}} = \widehat{\mathbf{R}}\mathbf{B}. \tag{13}$$

For a given transformation matrix $\overline{\mathbf{B}}$, we can compute the covariance matrix of a virtual antenna array

$$\begin{aligned}
\overline{\mathbf{R}} &= \overline{\mathbf{B}}\mathbf{A}\mathbf{R}_s\mathbf{A}^H\overline{\mathbf{B}}^H + \overline{\mathbf{B}}\left(\sigma_n^2\mathbf{I}\right)\overline{\mathbf{B}}^H \\
&= \widehat{\mathbf{R}}\mathbf{B}\mathbf{A}\mathbf{R}_s\mathbf{A}^H\mathbf{B}^H\widehat{\mathbf{R}}^H + \sigma_n^2\widehat{\mathbf{R}}\mathbf{B}\mathbf{B}^H\widehat{\mathbf{R}}^H.
\end{aligned} \tag{14}$$

The above procedure can enhance the signal components in the virtual covariance matrix $\overline{\mathbf{R}}$ and improve the orthogonality between the signal and the noise subspace.

We can clearly see that $\overline{\mathbf{B}}\overline{\mathbf{B}}^H \neq \mathbf{I}$, which implies that the original white noise turns into the colored noise after the virtual transformation. For most DOA estimation algorithms can only work when the background noise is Gaussian white noise, and the colored noise must be prewhitened. Define the transformation matrix as

$$\mathbf{T} = \left(\overline{\mathbf{B}}^H\overline{\mathbf{B}}\right)^{-1/2}\overline{\mathbf{B}}^H. \tag{15}$$

Real antenna array data $\mathbf{X}$

Virtual subarray interpolator $\mathbf{B}$

$\overline{\mathbf{X}}$

Projection process $\overline{\mathbf{B}} = \widehat{\mathbf{R}}\mathbf{B}$

$\widetilde{\overline{\mathbf{X}}}$

Prewhiten noise

$\widehat{\overline{\mathbf{R}}}$

Virtual array output
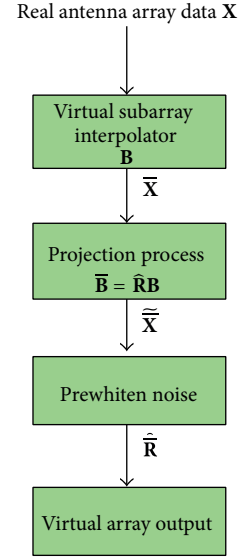
FIGURE 3: Construction of modified interpolated approach.

The real antenna array steering vector $\mathbf{a}(\theta)$ and the virtual array steering vector $\overline{\mathbf{a}}(\theta)$ have the following relationship:

$$\mathbf{T}\mathbf{a}(\theta) = \left(\overline{\mathbf{B}}^H\overline{\mathbf{B}}\right)^{-1/2}\overline{\mathbf{a}}(\theta) = \widehat{\overline{\mathbf{a}}}(\theta) \quad \theta \in \Theta. \tag{16}$$

After the noise prewhitening above, the covariance matrix of the virtual antenna can be computed by using the transformation matrix $\mathbf{T}$.

Consider

$$\widehat{\overline{\mathbf{R}}} = \mathbf{T}\mathbf{R}\mathbf{T}^H = \widehat{\overline{\mathbf{A}}}\,\mathbf{R}_s\widehat{\overline{\mathbf{A}}}^H + \sigma_n^2\mathbf{I}. \tag{17}$$

Therefore, the covariance matrix of the virtual antenna is obtained, and the application of a direction finding estimator to (17) is straightforward [6].

To summarize the modified interpolation transformation technique, the transformation procedure is shown in Figure 3.

In this paper, the multiple signal classification (MUSIC) algorithm is used to estimate the DOA. MUSIC algorithm is a high resolution technique based on exploiting the eigenstructure of an input covariance matrix. We decompose the autocorrelation matrix into signal and noise subspaces. The covariance matrix $\widehat{\overline{\mathbf{R}}}$ can be written as

$$\widehat{\overline{\mathbf{R}}} = \mathbf{U}_S\Sigma_S\mathbf{U}_S^H + \mathbf{U}_N\Sigma_N\mathbf{U}_N^H, \tag{18}$$

where $\mathbf{U}_S$ represents the signal subspace; $\mathbf{U}_N$ represents the noise subspace; $\Sigma_S = \mathrm{diag}\{\lambda_1, \lambda_2, \ldots, \lambda_M\}$ is the signal eigenvalue; $\Sigma_N = \mathrm{diag}\{\lambda_{M+1}, \lambda_{M+2}, \ldots, \lambda_N\}$ is the noise eigenvalue. The noise subspace $\mathbf{U}_N$ is orthogonal to all M signal steering vectors. The spectrum of the MUSIC algorithm is given by

$$P_{\mathrm{MUSIC}} = \frac{1}{\mathbf{a}^H(\theta)\,\mathbf{U}_N\mathbf{U}_N^H\mathbf{a}^H(\theta)} = \frac{1}{\left\|\mathbf{U}_N^H\mathbf{a}(\theta)\right\|}. \tag{19}$$

TABLE 1: Comparison of the two methods.

	Notion of DOA RMSE reduction	Computational complexity of mapping matrix $\mathbf{T}$	Additional prior information compared to [8]
Array interpolation of [17]	Rotate the mapping errors and noise subspace into optimal directions relative to a certain gradient of the DOA estimator criterion function	$O\left(2\left(2\overline{N}+1\right)^2 N_{\text{cal}}^2 \overline{N}N\right)$	Complex gradient of criterion of the used estimator
Proposed method	Project the transformation matrix on the real array covariance matrix to strengthen thesignal subspace	$O\left(\overline{N}N^3\right)$	None

If θ is equal to DOA, the noise subspace $\mathbf{U}_N$ is orthogonal to the signal steering vectors and $\|\mathbf{U}_N^H \mathbf{a}(\theta)\|$ becomes zero when θ is a signal direction and the denominator is identical to zero. It is obvious that in practice $\mathbf{U}_N^H \mathbf{a}(\theta) \neq 0$ due to finite samples. If this happens the performance of MUSIC algorithm will not be optimal.

Now, we can summarize the modified VAT procedure as follows.

Step 1. Compute the real array covariance matrix $\widehat{\mathbf{R}}$.

Step 2. Compute the real array manifold $\mathbf{A}(\theta)$ and virtual array manifold $\overline{\mathbf{A}}(\theta)$ and then compute the transformation matrix $\mathbf{B}$ using (11).

Step 3. Take the projection operation to get the new transformation matrix $\overline{\mathbf{B}}$ using $\overline{\mathbf{B}} = \widehat{\mathbf{R}}\mathbf{B}$.

Step 4. Compute the covariance matrix $\widehat{\overline{\mathbf{R}}}$ of the virtual array from the covariance matrix $\widehat{\mathbf{R}}$ of the real array.

Step 5. Apply the MUSIC algorithm to the covariance $\widehat{\overline{\mathbf{R}}}$ in (19).

We compare the proposed method with Hyberg's method in [17], which is selected for comparison because of its superior performance on DOA mean-square error (MSE) reduction of array interpolation. In [17], the authors proposed a design algorithm for the mapping matrix that minimized the DOA estimate bias. The MSE-minimizing mapping matrix T is designed as

$$
\begin{aligned}
\mathbf{T}_{\text{opt}} = \ \text{arg}\ \min_{\mathbf{T}} &\left\{ \sum_{i=1}^{N_{\text{cal}}} (1-\mu) \left\| \Delta e_v^{(i)} \right\|^2 \right. \\
&+ \frac{\mu}{\ddot{V}^2\left(\theta^{(i)}, e_v^{(i)}\right)} \\
&\times \left[4\left(\text{Re}\left\{g_v^{(i)} \Delta e_v^{(i)}\right\}\right)^2 \right. \\
&\left.\left. + \sum_{k=2}^{m} 2\alpha^{(i)} \left| g_v^{(i)} \mathbf{T}^H e_k^{(i)} \right|^2 \right] \right\},
\end{aligned}
\tag{20}
$$

where μ is a weighting factor ($0 \le \mu < 1$) and $g_v^{(i)} \triangleq g_v(\theta^{(i)})$ are the gradient vectors. N_{cal} is the number of calibration directions. In general, the superscript (i) means that the corresponding quantity should be computed as if there were a single source in the ith calibration direction (see [17] for details). DOA MSE is not reduced by minimizing the size of the mapping errors but instead by rotating these errors and the associated noise subspace into optimal directions relative to a certain gradient of the DOA estimator criterion function. We can clearly see that criterion in (20) is a quadratic function of the elements of $\mathbf{T}$. The characteristics of the method of [17] and the proposed method are listed in Table 1.

The comparisons of the two methods are given in Table 1 where we can see that method in [17] is much more complex than our method, which need to calculate the complex gradient of criterion of the used estimator at first compared to [8]. The calculation of references [17] is more than eight times higher than the proposed method. Simulation is conducted to evaluate the performance of the different methods.

5. Numerical Examples

In this section, the estimation accuracy of the proposed interpolation method and the conventional approach [3, 8, 9] is evaluated through numerical simulations.

Numerical Experiment 1. The real array is uniform and linear with 4 elements and the element space is λ. The nondirectional noise is spatial white Gaussian with a unit variance. The virtual antenna array is uniform and linear array with 8 elements and element space $\lambda/2$. There are four independent signals arriving from the directions $-55.0°$, $-50.0°$, $10.0°$, and $15.0°$. The signal-to-noise ratio (SNR) of the six signals is 10 dB and the virtual transform sector is $[-60°, -40°] \cup [0°, 20°]$. The step size is 0.1°. The number of snapshots is 128. 200 Monte Carlo runs are used to obtain each point.

The simulation results of conventional method and the proposed method are shown in Figure 4. It can be seen from the Figure 4 that the real array has 3 DOFs, which can process 3 signals at most, while the virtual antenna array has 8 elements with 7 DOFs and can process more than 3 signals. But the conventional interpolation method fails to distinguish the two close signals ($-55.0°, -50.0°$) and ($10.0°, 15.0°$) for its large transform errors. The modified
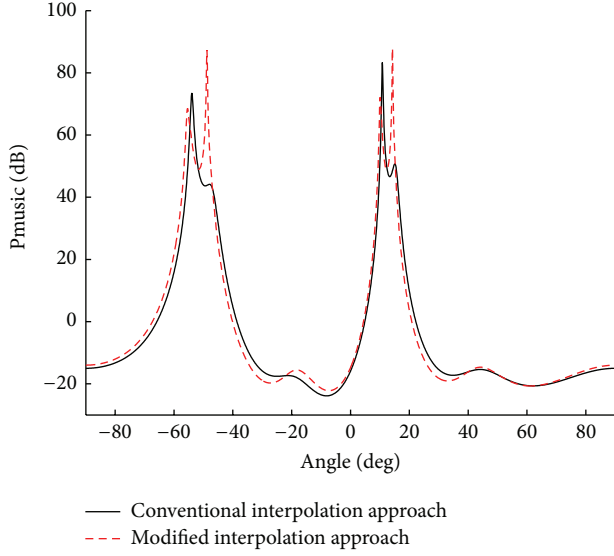
FIGURE 4: Spatial spectrum of MUSIC algorithm for two methods comparison.

FIGURE 5: Spatial spectrum of MUSIC algorithm for two methods comparison.

interpolation method can distinguish the two very close signals. The DOA finding results is ($-55.4°$, $-49.2°$, $10.1°$, and $14.4°$), and the result is accurate. We also can see that the modified interpolation method can still work in the case of the number of signals exceeding the DOFs of actual array and the resolution is improved compared to the conventional interpolation method.

Numerical Experiment 2. We consider a uniform and linear array with 4 elements and the element space λ. The nondirectional noise is spatial white Gaussian with a unit variance. The virtual antenna array is also uniform and linear array with 8 elements and element space $\lambda/2$. Two independent signals arrive from the directions $0.0°$ and $5.0°$ and the virtual transformation area is $[-5°, 10°]$, and the step size is $0.1°$. The SNR of the two signals is 10 dB. All SNR values are referred as per antenna element, and the number of snapshots is 128 and, once again, 200 Monte Carlo runs are used to obtain each point.

Figure 5 shows the performance of conventional method and the proposed method; we can clearly see that the proposed method can distinguish the two signals while the conventional VAT fails for the SNR = 10 dB. The DOA finding results of proposed method is ($0.1°$, $5.2°$). The resolution and accuracy has been greatly improved compared conventional interpolated method. This is because the proposed method enhanced the signal subspace and improved the orthogonality between the signal and noise subspace by projection process. The proposed method is considerably more accurate than the conventional methods (also see Figure 4).

Figure 6 shows the root-mean-square errors (RMSEs) for the MUSIC-based DOA estimators versus SNR by using the conventional interpolation approach, the modified interpolation approach, and the real eight-antenna array. The Cramer-Rao bounds (CRB) [18] of a real four-element array (CRB1) and eight-element array (CRB2) are plotted as a benchmark.
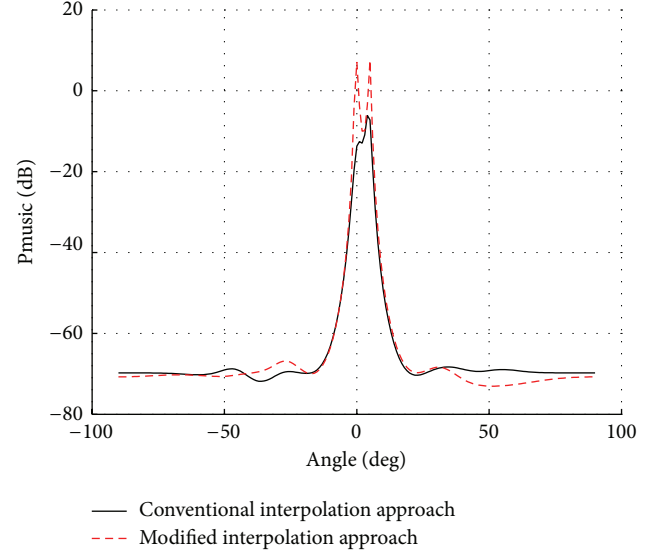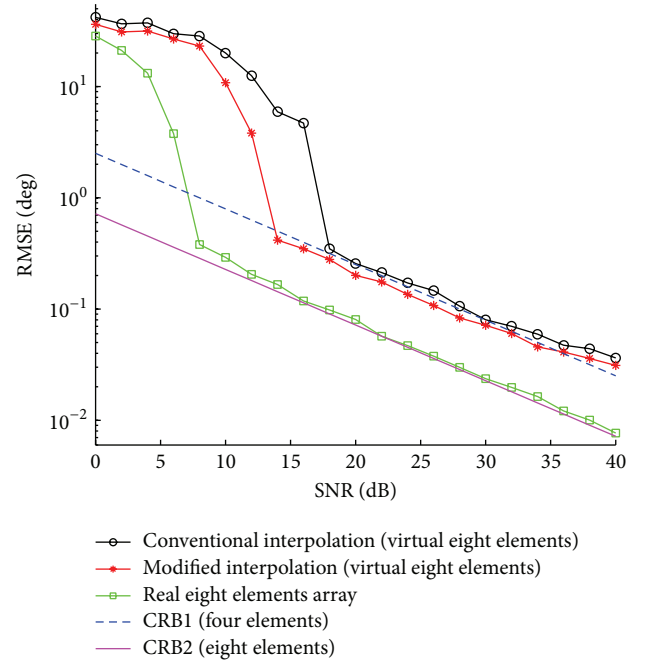
FIGURE 6: RMSE versus SNR for MUSIC-based DOA.

It can be observed from this figure that the proposed method has better RMSE performance than the conventional method for the entire range of SNR values. Since the interpolation transformation can increase the DOF of an antenna array, the DOF of the four-antenna array increases to seven in this example. When SNR > 15 dB, the RMSE of modified interpolation is lower than CRB1 but is still larger than CRB2. The RMSE of the conventional interpolation approach is larger than CRB1.

The probabilities of source resolution versus SNR are shown in Figure 7 for different methods. It can be observed
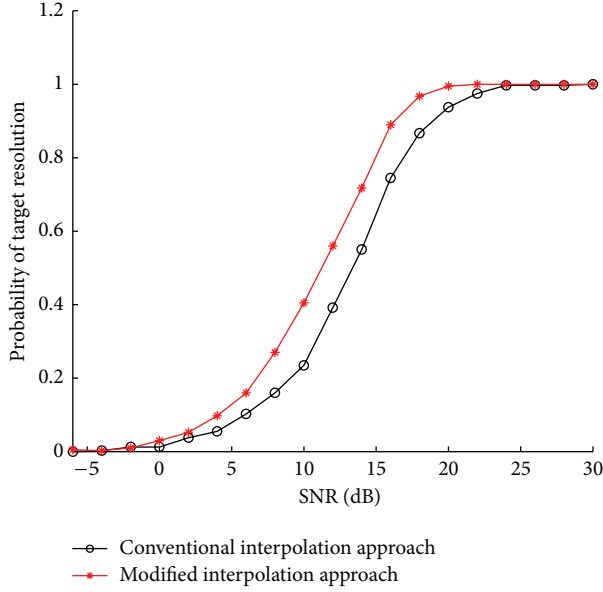
FIGURE 7: Probability of target resolution versus SNR.

FIGURE 8: RMSE versus SNR.

from Figure 7 that, with the SNR increase, the probabilities of source resolution of the methods increase, but the proposed method has better source resolution capabilities than the traditional method.

Numerical Experiment 3. We consider that an eight-element UCA with element space is one wave length. The mapping is from the UCA onto an eight-element half-wavelength-spaced ULA. Virtual transformation area is $[0°, 60°]$. One signal arrives from the direction $30.0°$. The number of snapshots is 100, and 200 Monte Carlo runs are used to obtain each point. All SNR values are referenced per antenna element, which are modeled as isotropic, unity gain, and nonpolarized.

The RMSE values as well as the CRB for the unmapped UCA data were plotted versus the SNR in Figure 8. It can be seen that the method in [17] has the highest RMSE performance which is slightly larger than the CRB. It also can be seen that the proposed technique outperforms the traditional interpolated method, though it is still worse than the method in [17] but it has low complexity and is easy to realize. The lower complexity makes our proposed algorithm suitable for real-time implementation.

6. Conclusion

The array interpolation technique is widely used in array signal processing. The interpolation preprocessing techniques introduce mapping errors that cause large bias in DOA estimation. This paper proposed a modified interpolation method based on the covariance matrix projection; the transformation matrix is reconstructed by using the covariance matrix projection. The modified interpolation method enhances the signal subspace and improves the orthogonality between the signal and the noise subspaces. Simulation
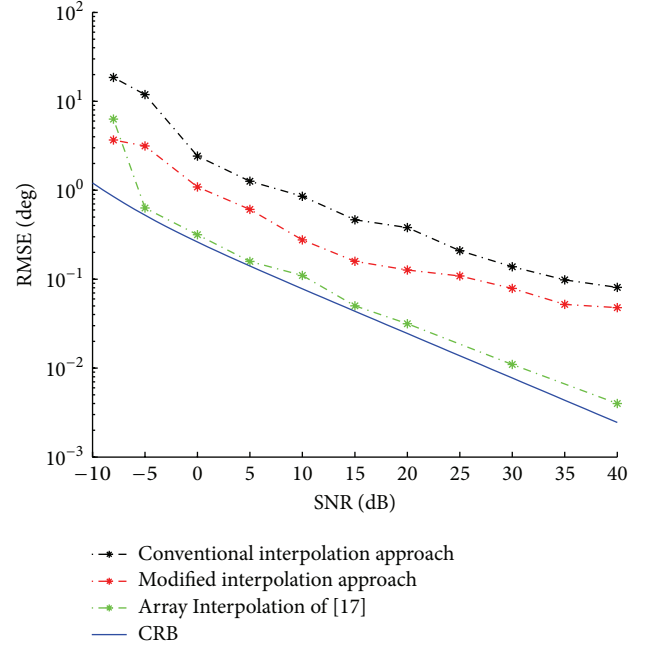
results show that the proposed approach offers better estimation accuracy and has a high resolution performance compared to the tradition interpolation method.

Conflict of Interests

The authors declare that there is no conflict of interests regarding the publication of this paper.

Acknowledgments

References

[1] K. M. Reddy and V. Reddy, "Analysis of interpolated arrays with spatial smoothing," *Signal Processing*, vol. 54, no. 3, pp. 261–272, 1996.

[2] T. P. Bronez, "Sector interpolation of nonuniform arrays for efficient high resolution bearing estimation," in *Proceedings of the IEEE International Conference on Acoustics, Speech and Signal Processing*, vol. 5, pp. 2885–2888, April 1988.

[3] A. J. Weiss and M. Gavish, "Direction finding using ESPRIT with interpolated arrays," *IEEE Transactions on Signal Processing*, vol. 39, no. 6, pp. 1473–1478, 1991.

[4] A. J. Weiss, "Performance analysis of spatial smoothing with interpolated arrays," *EEE Transactions on Signal Processing*, vol. 41, no. 5, pp. 1881–1892, 1993.

[5] D. N. Swingler and R. S. Walker, "Line-array beamforming using linear prediction for aperture interpolation and extrapolation," *IEEE Transactions on Acoustics, Speech, and Signal Processing*, vol. 37, no. 1, pp. 16–30, 1989.

[6] F. Belloni, A. Richter, and V. Koivunen, "DoA estimation via manifold separation for arbitrary array structures," *IEEE Transactions on Signal Processing*, vol. 55, no. 10, pp. 4800–4810, 2007.

[7] W. Li, Y. Li, and W. Yu, "On adaptive beamforming for coherent interference suppression via virtual antenna array," *Progress in Electromagnetics Research*, vol. 125, pp. 165–184, 2012.

[8] B. Friedlander, "Direction finding using an interpolated array," in *Proceedings of the International Conference on Acoustics, Speech, and Signal Processing (ICASSP '90)*, vol. 5, pp. 2951–2954, Albuquerque, NM, USA, April 1990.

[9] B. Friedlander, "The root-MUSIC algorithm for direction finding with interpolated arrays," *Signal Processing*, vol. 30, no. 1, pp. 15–29, 1993.

[10] Y. S. Kim and Y. S. Kim, "Modified resolution capability via virtual expansion of array," *Electronics Letters*, vol. 35, no. 19, pp. 1596–1597, 1999.

[11] Y. Wang, H. Chen, and S. Wan, "An effective DOA method via virtual array transformation," *Science in China Series E: Technological Sciences*, vol. 44, no. 1, pp. 75–82, 2001.

[12] B. Friedlander and A. J. Weiss, "Direction finding using spatial smoothing with interpolated arrays," *IEEE Transactions on Aerospace and Electronic Systems*, vol. 28, no. 2, pp. 574–587, 1992.

[13] B. K. Lau, G. Cook, and Y. H. Leung, "A modified array interpolation approach to DOA estimation in correlated signal environments," in *Proceedings of the IEEE International Conference on Acoustics, Speech, and Signal Processing*, vol. 2, no. 2, pp. 237–240, 2004.

[14] P. Yang, F. Yang, and Z. P. Nie, "DOA estimation with sub-array divided technique and interporlated esprit algorithm on a cylindrical conformal array antenna," *Progress in Electromagnetics Research*, vol. 103, pp. 201–216, 2010.

[15] M. Pesavento, A. B. Gershman, and Z. Q. Luo, "Robust array interpolation using second-order cone programming," *Signal Processing Letters*, vol. 9, no. 1, pp. 8–11, 2002.

[16] P. Hyberg, M. Jansson, and B. Ottersten, "Array interpolation and bias reduction," *IEEE Transactions on Signal Processing*, vol. 52, no. 10, pp. 2711–2720, 2004.

[17] P. Hyberg, M. Jansson, and B. Ottersten, "Array interpolation and DOA MSE reduction," *IEEE Transactions on Signal Processing*, vol. 53, no. 12, pp. 4464–4471, 2005.

[18] P. Stoica and A. Nehorai, "MUSIC, maximum likelihood, and Cramer-Rao bound: further results and comparisons," *IEEE Transactions on Acoustics, Speech and Signal Processing*, vol. 38, no. 12, pp. 2140–2150, 1990.

Research Article

A Compact Vivaldi Shaped Partially Dielectric Loaded TEM Horn Antenna for UWB Communication

**Mustafa İlarslan,[1] A. Serdar Türk,[1] Salih Demirel,[1]
M. Emre Aydemir,[2] and A. Kenan Keskin[1]**

[1] *Electronics & Communication Engineering Department, Yildiz Technical University, Esenler, 34220 Istanbul, Turkey*
[2] *Aeronautics & Space Technologies Institute, Turkish Air Force Academy, Yesilyurt, 34149 Istanbul, Turkey*

Correspondence should be addressed to A. Serdar Türk; asturk@yildiz.edu.tr

Ultrawideband (UWB) antennas are of huge demand and Vivaldi antennas as well as the TEM horn antennas are good candidates for UWB applications as they both have relatively simple geometry and high gain over a wide bandwidth. The aim of this study is to design a compact antenna that achieves maximum gain over a bandwidth between 1.5 and 10.6 GHz while minimizing its size. The idea is to make use of combined respective advantages of Vivaldi and TEM horn antennas to achieve the desired goals by shaping the TEM horn antenna to look like a Vivaldi antenna. The antenna structure is modified by a dielectric load in the center to increase the gain bandwidth. It is placed in a surrounding box made of PEC material to reduce the undesired side lobes and to obtain more directive radiation pattern. The simulations are performed by using the CST STUDIO SUITE electromagnetic (EM) simulation software and they are later verified by the actual measurements. The Vivaldi shaped partially dielectric loaded (VS-PDL) TEM horn antenna is proposed as a compact UWB antenna for systems using the newly established UWB band and also for the communication systems of popular bands like ISM, Wi-Fi, and GSM.

1. Introduction

Even though the idea was older, UWB technology has become popular starting from the late 1960s because of its use in the form of impulse radar in military area. Its development even accelerated after FCC had approved the UWB technology for commercial use in 2002 [1].

UWB technologies have been used increasingly for high-speed RF wireless communication, high power RF jamming, and high-resolution impulse radar systems as they have a number of advantages over traditional narrowband systems like low complexity, low cost, and improved detection, ranging, and target resolution performances [1, 2].

UWB antennas are obviously a vital part of these systems as they are closely linked to the system performance. They are basically needed to have maximum gain over a specified wide bandwidth. Other antenna features can be considered as application specific.

In this study, our purpose is to design a compact UWB antenna with a gain level close to 10 dBi over the bandwidth starting from 1.5 GHz up to 10.6 GHz. In the analog RF frontend, a high relative bandwidth and not necessarily a high absolute bandwidth poses new challenges to the RF system design. We therefore concentrate on this band where a large variety of system concepts are under investigation worldwide [1].

This paper is composed of four sections in total; following the introduction, antenna design is described in Section 2, simulation and measurement results are given in Section 3, and finally Section 4 is for the conclusions.

2. Antenna Design

This paper is all about the design and development of a compact UWB antenna based upon Vivaldi and TEM horn antennas both of which have respective advantages for the
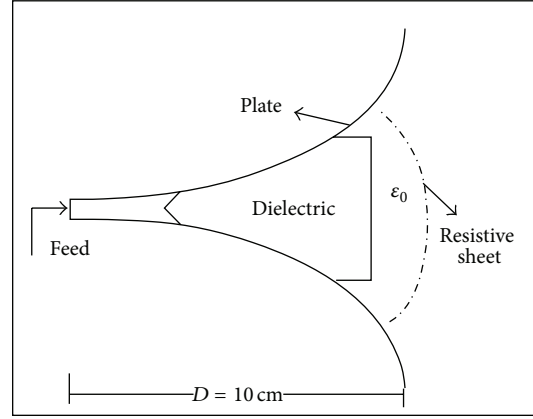
FIGURE 1: Vivaldi Shaped TEM horn antenna (PDVA10) [7].

possible UWB applications as mentioned above. The idea is to make use of these combined respective advantages of Vivaldi antennas and TEM horn antennas to achieve the desired goals by shaping the TEM horn antenna to look like a Vivaldi antenna.

The antenna structure is modified by partially loading it in the center with a dielectric Teflon material of $\varepsilon r = 2.1$ in order to decrease the lower frequency limit and by doing so increasing the frequency range of the antenna [3]. The dielectric filling or partial dielectric loading techniques are employed commonly as mentioned in the literature [4–6] to broaden the operational band up to twice and improve the directivity (gain) performance. It is noted that the partial dielectric loading operation should not result in altering the physical dimensions of the antenna (including its weight) in a negative manner [6].

The partially dielectric loaded TEM (PDTEM) horn, its Vivaldi shaped version (PDVA), and array combinations have been introduced by Turk as efficient UWB impulse radiators for GPR (Ground Penetrating Radar) operation to obtain UWB characteristics from 150 MHz to 10 GHz [4, 7, 8].

As a specific example, the partially dielectric-loaded Vivaldi antenna (PDVA) which yields ultrawide band antenna characteristics from 400 MHz to 10 GHz was introduced and referred to as PDVA10 (meaning an aperture depth length of 10 cm) in [7] as given in Figure 1. It had a positive gain over the specified bandwidth which came close to 10 dBi at higher frequencies. It was designed for multisensor adaptive-impulse GPR operation and its performance was promising when compared to the regular (no dielectric loading) TEM horn and Vivaldi antennas.

However, it has the disadvantage of having a large size. Our purpose herein is to improve that design to make it smaller (compact) for some possible applications in UWB communication systems as it covers whole popular wireless frequency bands. To make it compact, the height of the antenna is reduced up to 8 cm to cancel the lower bands of the spectrum which were needed for GPR operations and the depth of the E-plane (flared vertically) horn antenna aperture has been changed from 8 cm down to 3 cm as the primary
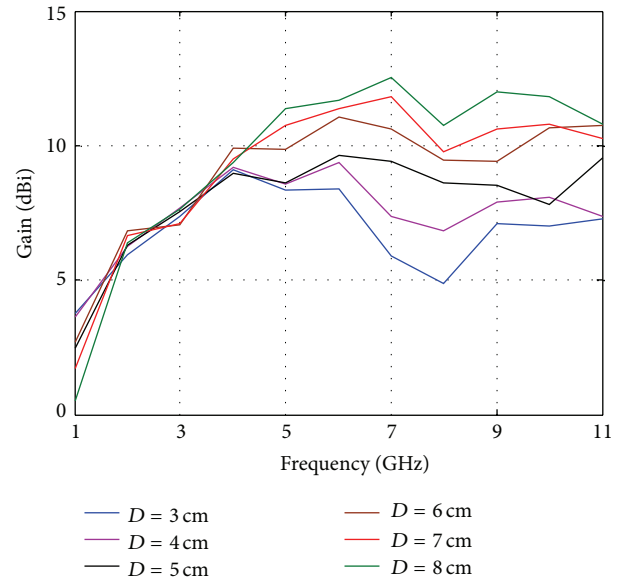
FIGURE 2: The variation of gain with respect to frequency for various aperture depth (D) values (simulation only).

parameter affecting the antenna gain. The gain values have been examined by using CST STUDIO SUITE EM simulation software. The simulation results (Figure 2) showed that the antenna gain was decreasing especially for the band above 4.0 GHz and the radiation pattern was deforming as the antenna aperture depth shortened. As a result, an antenna structure with aperture depth $D = 5$ cm is decided as optimal by taking into consideration the fact that it was aimed to be constructed as compact as possible.

It is placed in a surrounding box made of PEC material to reduce the undesired side lobes and to obtain a more directive radiation pattern. It would also help to obtain physical protection and EM shielding in a possible application like wireless communication system to overcome the coupling affects between the transmit/receive antennas [8]. The final design of the VS-PDL TEM horn antenna with its dimensions

TABLE 1: Frequency bands of some of the popular wireless communication systems.

806–960 MHz, 1,710–2,025 MHz, 2,110–2,200 MHz, and 2,500–2,690 MHz. (ITU-R approved bands)	1.227–1.575 GHz	2.3 GHz	2.4 GHz	868 MHz, 915 MHz, and 2.4 GHz	3.1–10.6 GHz	900 MHz, 1.8 GHz, 2.4 GHz, and 5.8 GHz
Cellular Phone Operations (GSM 3G and 4G (WiMax/LTE))	Global positioning system—GPS	Satellite radio	WiFi/802.11 b/g and Bluetooth	Zigbee/802.15.4	UWB	ISM (Industrial, scientific, medical)
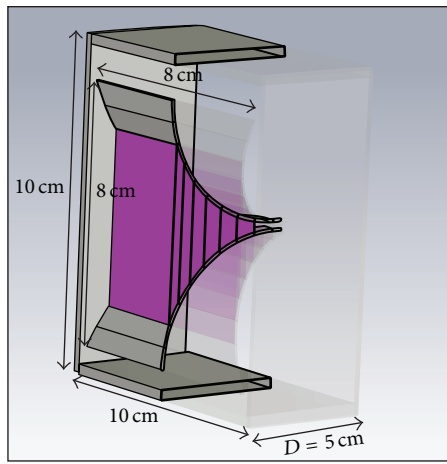
(a)

(b)

FIGURE 3: (a) VS-PDL TEM horn antenna design with its dimensions given on the figure. (b) The manufactured antenna.

is given in Figure 3(a) as vertically divided right-hand-side made transparent for the purpose of clarity while the manufactured antenna is shown in the Figure 3(b).

3. The Simulation and Actual Measurement Results

The simulation results show that the Vivaldi shaped partially dielectric loaded (VS-PDL) TEM horn antenna with 5 cm aperture depth as given in Figure 3(a) achieves an optimum performance over the desired bandwidth while it is practically possible to implement it physically as a compact structure.

The simulated radiation patterns of the VS-PDL TEM horn antenna at selected frequencies within the 1.5–10.6 GHz band for "boxed" and "unboxed" configurations are given in Figure 4 where the bolder line is for the "boxed" configuration.

It can easily be noticed from this figure that, with the metallic box, the radiation pattern becomes more directive especially at the higher frequencies. It offers superior gain performance starting from lower frequencies. The measured radiation patterns of the manufactured antenna verify the simulation results as shown in Figure 5.

The simulated and measured gain values for the antenna are given in Figure 6 while the simulated and measured VSWR plots are given in Figure 7. The measured gain of the antenna remains above 7 dBi over the practical band which is considered as a satisfactory gain performance.

Regarding the VSWR measurements, it remains below 2.0 throughout the operational band until 9.8 GHz but it exceeds that value for the rest of the band which can be considered as not satisfactory. On the other hand, as it does not impact the gain and radiation performance in a negative manner, it can still be considered as practically acceptable. It is also noteworthy to state that for "boxed" configuration, the box itself has a negative effect on VSWR performance at lower part of the bandwidth (1.5 to 2.5 GHz) resulting a higher VSWR values when compared to "unboxed" case but still the
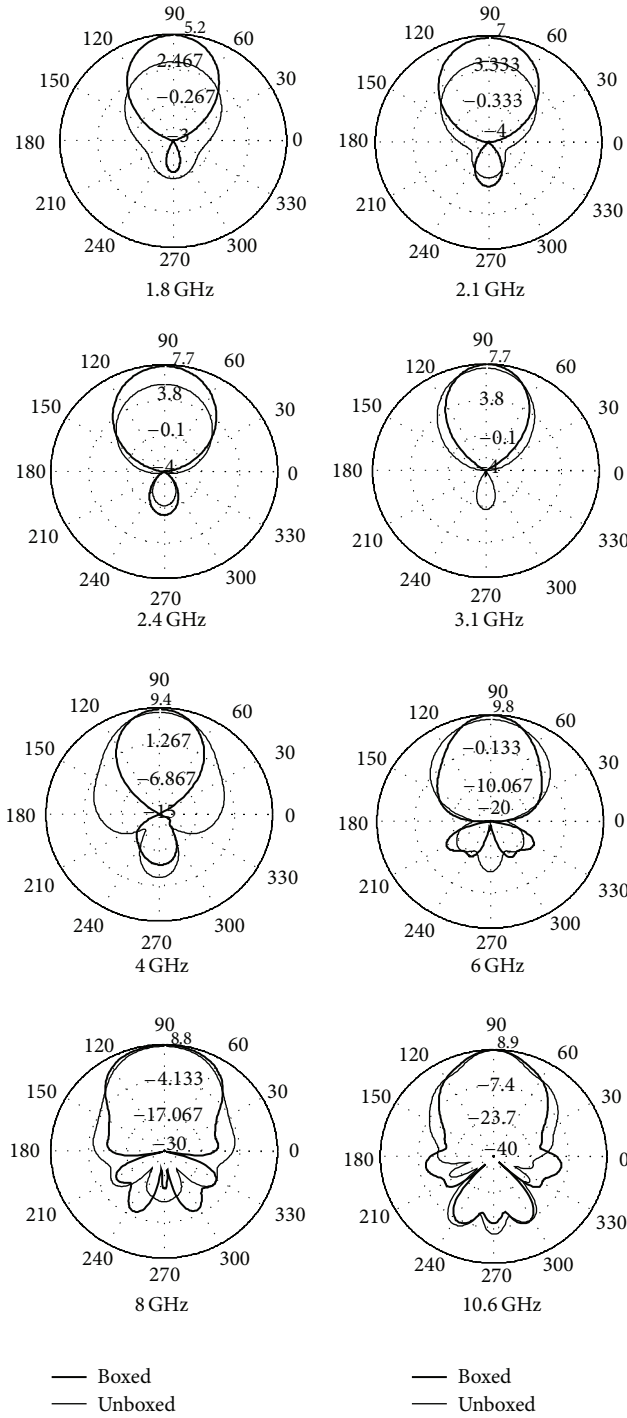
Figure 4: The simulated radiation patterns of the VS-PDL TEM horn antenna for "boxed" and "unboxed" configurations at various frequencies.

"boxed" antenna has a satisfactory performance with VSWR values below 2.

Figure 8 gives the time-domain characteristic of the proposed antenna for the measured received pulse case at various angles for 1.5–11.0 GHz. It denotes a smooth pulse
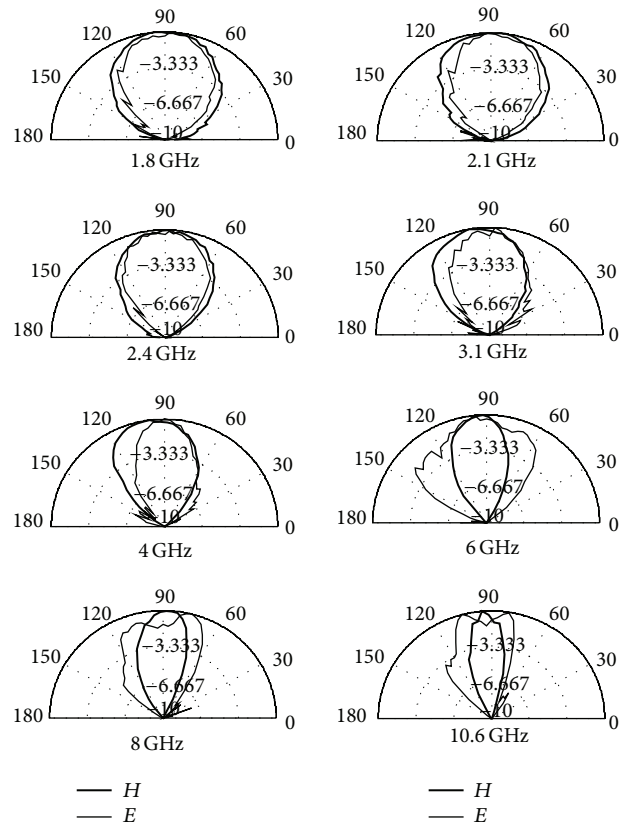
Figure 5: Measured E-plane and H-Plane (normalized) radiation patterns of the proposed antenna.

shape with minimal ringing effects. The excitation pulse also is plotted within the Figure 8.

If one evaluates the overall measured performance of the proposed antenna, one can easily conclude that it satisfies the requirements of a multitude of applications ranging from UWB communication to electromagnetic compatibility (EMC) measurement systems in terms of gain, VSWR, and radiation performance due to its reduced size and shielded metallic box structure. Hence it can be considered as a good candidate for popular communication systems like cellular phone, SATCOM, Wi-Fi, Wi-Max/LTE, and other systems using ISM and UWB (Table 1).

4. Conclusion

In this paper, a novel compact Vivaldi shaped partially dielectric loaded (VS-PDL) TEM horn antenna has been designed and developed for UWB communication systems of 1.5–10.6 GHz frequency band. We have shown that a new panel type quasiplanar design obtained by more bending the tapered Vivaldi shaped wings (shortened aperture depth) of the TEM horn antenna leads to a significant size reduction of the device. Furthermore, simulation and measurement results that were in coincidence showed that, when installed
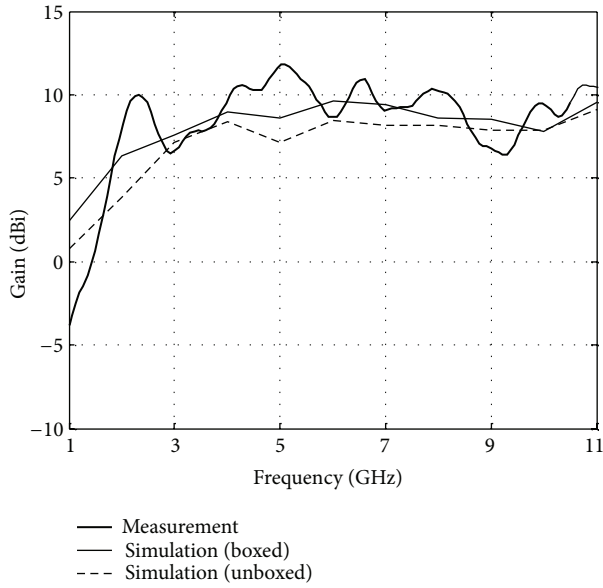
FIGURE 6: Gain performance of the antenna for simulation (both boxed and unboxed) and actual measurement cases.
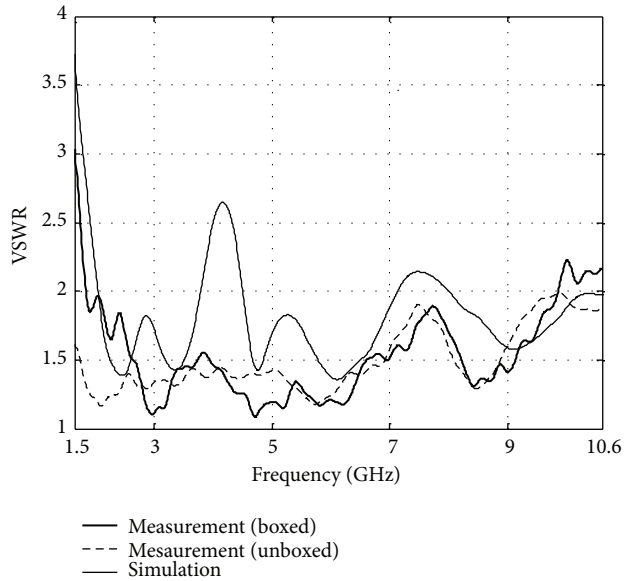
FIGURE 7: Simulated and measured (for both boxed and unboxed cases) VSWR plot of the antenna.

FIGURE 8: Time-domain characteristic of the proposed antenna measured on received pulse for various angles and for 1.5–11.0 GHz. The excitation pulse is given within the figure as well.

Conflict of Interests

The authors declare that there is no conflict of interests regarding the publication of this paper.

References

[1] T. Zwick, W. Wiesbeck, J. Timmermann, and G. Adamiuk, Eds., *Ultra-Wideband RF System Engineering*, EuMA High Frequency Technologies Series, Cambridge University Press, 2013.

[2] A. S. Turk and A. K. Keskin, "Vivaldi shaped TEM horn fed ridged horn antenna design for UWB GPR systems," in *Proceedings of the 6th International Workshop on Advanced Ground Penetrating Radar (IWAGPR '11)*, pp. 1–4, June 2011.

[3] A. Teggatz, A. Jöstingmeier, and A. S. Omar, A New TEM Double-ridged Horn Antenna for Ground Penetrating Radar Applications. Presented at unknown, 2004, http://duepublico .uni-duisburg-essen.de/servlets/DerivateServlet/Derivate-14694/ Final_Papers/GM0023-F.pdf.

[4] A. S. Turk and D. A. Sahinkaya, "Partial dielectric loaded TEM horn design for ultra-wideband ground penetrating impulse radar systems," in *Ultra-Wideband, Short-Pulse Electromagnetics 7*, chapter 34, pp. 306–315, Springer, Berlin, Germany, 2007.

[5] M. Scheers and A. Acheroy, "Time-domain simulation and characterisation of TEM horns using a normalised impulse response," *IEE Proceedings: Microwaves, Antennas and Propagation*, vol. 147, no. 6, pp. 463–468, 2000.

[6] A. G. Yarovoy, A. D. Schukin, I. V. Kaploun, and L. P. Ligthart, "The dielectric wedge antenna," *IEEE Transactions on Antennas and Propagation*, vol. 50, no. 10, pp. 1460–1472, 2002.

within a metallic box, VS-PDL TEM horn antenna with a 5 cm aperture depth has satisfactory far-field radiation characteristics and high gain/lower VSWR over the practical bandwidth. That means such a panel type quasiplanar antenna would be a good candidate for UWB applications like popular communication systems of GSM, GPS, ISM, Wi-Fi, and SATCOM bands requiring satisfactory antenna performance.

[7] A. S. Turk, "Ultra-wideband vivaldi antenna design for multi-sensor adaptive ground-penetrating impulse radar," *Microwave and Optical Technology Letters*, vol. 48, no. 5, pp. 834–839, 2006.

[8] A. S. Turk, D. A. Sahinkaya, M. Sezgin, and H. Nazli, "Investigation of convenient antenna designs for ultra-wide band GPR systems," in *Proceedings of the 4th International Workshop on Advanced Ground Penetrating Radar (IWAGPR '07)*, pp. 192–196, June 2007.

Research Article

Triple Band Parasitic Array Antenna for C-X-Ku-Band Application Using Out-of-Phase Coupling Approach

Anubhuti Khare and Rajesh Nema

University Institute of Technology Rajiv Gandhi Proudyogiki Vishwavidyalay, Bhopal, India

Correspondence should be addressed to Rajesh Nema; rajeshnema20018@gmail.com

Triple band parasitic array antenna for C-X-Ku-band application is presented. The proposed antenna is designed using the concept of parasitic array and out-of-phase coupling approach. The objects of research are to optimize total inductance of geometry by using out-of-phase inductance approach. The out of phase inductance of geometry consists of using two U-patches novel director on the left side of geometry, appropriate dimension of ground plan, and gap coupling between parasitic and active patches. The dimension of the ground plan geometry is 0.5λ mil $\times$ 0.5154λ mil. The usable impedance bandwidth of design antenna is "5.8 GHz to 18 GHz" (102% impedance bandwidth) and gain enhancement is up to 11.8 dBi. The proposed antenna can be used for X-Ku band and C-band applications. Both simulated and measured results are presented, which are in good agreement. The proposed antenna was fabricated with a thin copper layer printed on a thin lossy FR4 substrate for low-cost production.

1. Introduction

An explosive growth of the wireless radio a communication system is currently observed in the microwave band. In [1], a dual-frequency antenna based on the Sierpinski fractal with two parasitic patches to enhance the impedance bandwidth was presented. An electrical circuit model is formed by RLC resonators to learn about the antenna physical behaviour and to achieve the dual band operation minimizing a trial-and-error numerical/measurement proofs. The antenna designed, using a method of moment, obtained two bands with a broad bandwidth and similar radiation patterns. In [2], a triple-frequency antenna is designed having a dual-band and monoband antenna with broadside radiation patterns. The dual-band antenna is inspired in the Sierpinski fractal. Such a dual-band antenna is stacked over a monoband antenna. The antenna presented a broadband behavior at each band using parasitic patches. The antenna is designed using a MoM commercial code, obtaining three bands with a broad bandwidth, high efficiency, and similar radiation patterns. Huang et al. [3] presented a microstrip antenna design that effectively circular polarized (CP) and suppressed harmonics. By modifying the size and position of two peripheral cuts,

two orthogonal modes that have equal amplitude and are 90 out of phase were simultaneously excited. The four right-angle slits embedded in the antenna can block the second- and third-order harmonic signals. The adopted CP antenna built on a low-cost FR4 substrate measured bandwidth of 137 MHz (10-dB return loss) and a 30-MHz CP bandwidth (3-dB axial ratio). This work is further extended in [4] where a triband dual-polarization (TBDP) shared aperture microstrip array antenna is designed for synthetic aperture radar (SAR) application. It operates in L-S-X Bands with a frequency ratio of $1 : 2.8 : 8$. This TBDP shared aperture array is assembled by two L/S and L/X DBDP shared-aperture sub arrays with one L-band dual-polarized sub array, which exhibits wide impedance bandwidth of 13.4%, 14.8%, and 16.8% in L-S band and X-bands. Usable bandwidth of design antenna is further modified in [5], a printed wide-slot antenna with a parasitic patch for bandwidth enhancement, which is 80% for $|S11| \leq -10$ dB ranging from "2.23 GHz to 5.35 GHz." Work further carried in [5–8], in [8] presented a novel compact ultra wideband (UWB) printed slot antenna with three extra bands for various wireless applications. The low-profile antenna consists of an octagonal-shaped slot fed by a beveled and stepped rectangular patch for covering the UWB band

("3.1 GHz–10.6 GHz"). In [7], a new design of a compact ultra wideband (UWB) antenna with multiple bands notched characteristic utilized a C-shape ground to realize miniaturization and two mushroom-type electromagnetic band gap (EBG) structures to create notched bands. The antenna achieved an operation frequency band from "3 GHz to 13 GHz" (10 GHz Bandwidth slot). Modification of paper [7] done in [8], where a compact planar ultra wideband (UWB) antenna is designed for wireless universal serial bus (USB) dongle application. Cutting 7 notches and embedding types of slots into a rectangular patch, multiple resonances with effective bandwidth enhancement is achieved. This prototype antenna is constructed and measured to show an ultra wide operating band with 10-dB return-less bandwidth of about 10.42 GHz ranging from "2.86 GHz to 13.38 GHz," highest bandwidth modification done in [9]. The gain enhancement technique is displayed, which loosely configured grooved ground plan able to significantly enhance the gain of a standard patch antenna with a flat, electrically large ground plan. Simulation and measurement results show the enhancement of the gain up to 10.2 dBi at 10.45 GHz and the proposed antenna is designed to achieve usable bandwidth 12.2 GHz from "5.8 GHz to 18.15 GHz." The proposed design of antenna in this paper is modification of [6–9] to achieve more −10 dB impedance bandwidth slot and directivity.

2. Proposed Geometry Design

The Proposed Geometry consists of

(i) Δ = 3 mil air gap between top and bottom layer,

(ii) geometry which consists of glass epoxy PCB and air gap (FR-4 – air-FR-4) material,

(iii) total height of geometry which is 3.07 mm (from a ground plan to top layer),

(iv) middle layer driven element which has patch dimension $L \times W$ = 10.44 mm × 11.32 mm (0.1808λ mm × 0.1962λ mm),

(v) top parasitic patches which have dimension of $L_1 \times W_1$ = 2.54 mm × 3.81 mm (0.044λ mm × 0.066λ mm) used as director,

(vi) the dimensions of ground plan which is 28.87 mm × 29.76 mm (0.05λ mm × 0.05154λ mm) used as a reflector.

The geometry consists of two U-type patches on the left side of the top layer shown in Figure 2. The proposed geometry is simulated using IE3D simulator.

3. Mutual Coupling Approach for Designing of Proposed Antenna

The proposed antenna is design to reduce the total mutual inductance of geometry, in geometry U-type patch directors is configured in out-of-phase mutual coupling through vertical arms of U-patch is shown in Figure 3. Two sections of U-patch carrying currents in the same direction have

positive mutual inductance here as the inductance is negative for a current flowing in opposite directions is shown in Figure 4. The lengthening of the effective patch's surface current paths is due to the additional downward paths in the added rims, which is different from that of the meandered designs; a relatively very small perturbation on the excited surface current distribution in the radiating patch is expected. This implies that it is possible for the radiation characteristics of this compact design to be as good as those of a corresponding conventional patch antenna with a planar radiating patch. Adjacent resonant modes with similar radiation characteristics can be excited at frequencies close to each other, resulting in a wide bandwidth microstrip antenna. Furthermore by properly adjusting the parameters of slots, both of the adjacent resonant modes could achieve good impedance matching, which makes the antenna broadband and compact:

$$L_{\text{Total}} = \Sigma L + \Sigma M_+ - \Sigma M_-, \tag{1}$$

$$\Sigma M_- = 2\Sigma M_{13} + \Sigma L_{mg} + 2\Sigma M_{34} + 2\Sigma M_{46} + 2\Sigma M_{16}, \tag{2}$$

$$M_{13} = 2 \times 10^{-4} l_e \left[\text{In} \left\{ \frac{l_e}{d} + \sqrt{1 + \left(\frac{l_e}{d}\right)^2} \right\} \right.$$
$$\left. + \frac{d}{2l} - \sqrt{1 + \left(\frac{d}{l_e}\right)^2} + \frac{d}{l_e} \right], \tag{3}$$

$$M_{34} = 2 \times 10^{-4} l_{e1} \left[\text{In} \left\{ \frac{l_{e1}}{d_{34}} + \sqrt{1 + \left(\frac{l_{e1}}{d_{34}}\right)^2} \right\} \right.$$
$$\left. + \frac{d_{34}}{2l_{e1}} - \sqrt{1 + \left(\frac{d_{34}}{l_{e1}}\right)^2} + \frac{d_{34}}{l_{e1}} \right],$$

$$M_{16} = 2 \times 10^{-4} l_{e2} \left[\text{In} \left\{ \frac{l_{e2}}{d_{16}} + \sqrt{1 + \left(\frac{l_{e2}}{d_{16}}\right)^2} \right\} \right.$$
$$\left. + \frac{d_{16}}{2l_{e2}} - \sqrt{1 + \left(\frac{d_{34}}{l_{e2}}\right)^2} + \frac{d_{16}}{l_{e2}} \right], \tag{4}$$

where l_e is the effective length of the arms between 1 and 3, which calculated the mutual inductance M_{13}. Dimensions of l_e and d are in microns and M_{13} is in nanohenries. As an approximation, l_e can be considered an average length for three sections $l_e = l_1 + l_2 + l_3$, l_{e1} is an effective length of the sections 3 and 4, and l_{e2} is the effective length of sections 1 and 6. d_{16} and d_{34} are distance between 1 and 6, 3 and 4, respectively. M_{16} and M_{34} are mutual inductance between 1 and 6, 3 and 4, respectively.

So total inductance of U-patch is

$$L = L_1 + L_2 + L_3 + X_P. \tag{5}$$

The free-space inductance L (in nanohenries) of a width of U-patch is d and l length, (in microns) given by [10, 11].
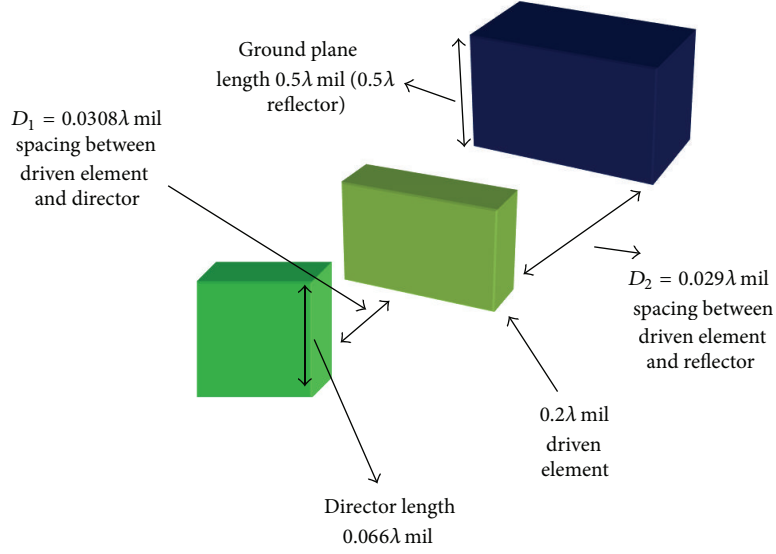
FIGURE 1: Proposed model.

For $l \ll d$

l = length of U-patch,

d = width of U-patch:

$$L_1 = L_3 = 2 \times 10^{-4} l \left[\text{In} \left\{ \frac{2l}{d} + \sqrt{1 + \left(\frac{2l}{d}\right)^2} \right\} \right.$$
$$\left. + \frac{d}{2l} - \sqrt{1 + \left(\frac{d}{2l}\right)^2} + C \right], \quad (6)$$

$$L_2 = 2 \times 10^{-4} l_2 \left[\text{In} \left\{ \frac{2l_2}{d} + \sqrt{1 + \left(\frac{2l_2}{d}\right)^2} \right\} \right.$$
$$\left. + \frac{d}{2l_2} - \sqrt{1 + \left(\frac{d}{2l_2}\right)^2} + C \right],$$

where $l_1 = l_2 = l$

$$C = 0.25 \tanh\left(\frac{4\delta}{d}\right),$$
$$\delta = \frac{1}{\sqrt{\pi \sigma f \mu}}. \quad (7)$$

The inductor X_P produced by the probe is given by

$$X_P = \frac{\eta}{\pi} \tan\left(0.5 k_o h\right) \text{In}\left(\frac{2.25}{k_o d}\right). \quad (8)$$
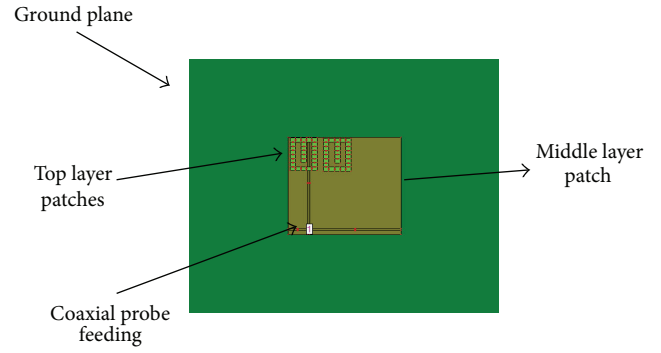
FIGURE 2: Optimization model for geometry.

$l \gg d$ where σ is the conductivity of the wire material. For gold wires, $\delta = 2.486 f - 0.5$, where frequency f is expressed in gigahertz. When δ/d are small, $C = \delta/d$.

When $1 \gg d$, (4), (5) reduces to

$$L_1 = L_3 = 2 \times 10^{-4} l \left(\text{In} \frac{4l}{d} + 0.5 \frac{d}{l} - 1 + C \right),$$
$$L_2 = 2 \times 10^{-4} l_2 \left(\text{In} \frac{4l_2}{d} + 0.5 \frac{d}{l_2} - 1 + C \right), \quad (9)$$
$$L = L_1 + L_2 + L_3 + X_P.$$

3.1. Ground Plan Effect. The effect of the ground plan on the inductance value of an antenna has also been considered [12]. If the radiating patch is at a distance h above the ground plan as shown in Figure 1, it sees its image at 2 h from it. The U-Slot patches and its image consists mutual inductance L_{mg}. Because the image of antenna carries a current opposite to the current flow in the patch, the mutual inductance of
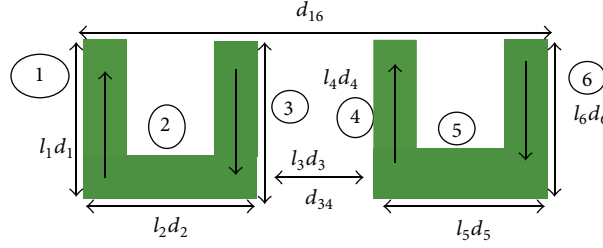
FIGURE 3: U-patch model for mutual coupling approach.

(a)   (b)
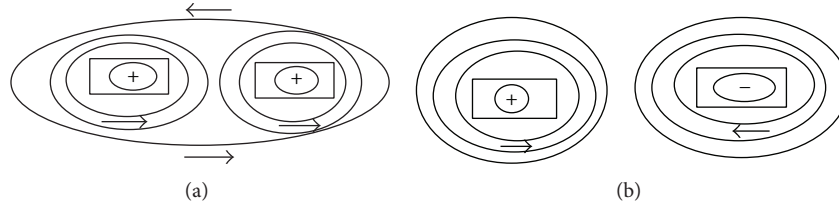
FIGURE 4: (a) Positive mutual coupling and (b) out-of-phase coupling.

the antenna L_{mg} is calculated from (6) by mutual coupling approach

$$L_{mg} = 2 \times 10^{-4} l \left[\ln \left\{ \frac{l}{2h} + \sqrt{1 + \left(\frac{l}{2h}\right)^2} \right\} \right.$$
$$+ \sqrt{1 + \left(\frac{l}{2h}\right)^2} + \frac{2h}{l} \qquad (10)$$
$$\left. - \sqrt{1 + \left(\frac{2h}{l}\right)^2} + C \right].$$

4. Optimization Using Ground Plan

In this optimization section, proposed antenna is optimized using only change in dimension of ground plan. The dimension of ground plan severely has an effect on reflected signal; according to (10), L_{mg} is mutual inductance of ground plan and depends on the dimensions length of ground plan, width of ground plan, total height of antenna, loss tangent of dielectric material, and conductivity of ground plan. When the dimensions of ground plan increase the mutual inductance of the ground plan (L_{mg}) also increases so that overall out-of-phase inductance increases as per (2) and total dominate inductance of proposed design is reduced and achieved reduction in reflected signal; this optimization approach provides impedance matching over a wide band of frequency and this approach is more feasible and easy. When the dimension of ground plan changes from $11.43 \times 13.97\,mm^2$ to $28.87 \times 29.76\,mm^2$, simultaneously the useful -10 dB impedance matching bandwidth slot improves from 8 GHz to 12.2 GHz. After $28.87 \times 29.76\,mm^2$ ground dimension, the increment in dimension of ground plan is not feasible because size of antenna is not compatible over a useful bandwidth slot and therefore optimization is done up to 28.87 $\times$ 29.76 mm^2 only.

4.1. Optimization Using Ground Plan Dimensions 11.43 × 13.97 mm^2. In this optimization section, the dimensions of ground plan are changed; the dimension of ground plan is $11.43 \times 13.97\,mm^2$ and achieved -10 dB impedance bandwidth 8 GHz is shown in Figure 5(a).

4.2. Optimization Using Ground Plan of Dimensions 12.7 × 12.7 mm^2. In this optimization section, the dimension of ground plan is $12.7 \times 12.7\,mm^2$ and obtained -10 dB impedance bandwidth 8.9 GHz is shown in Figure 5(b).

4.3. Optimization Using Ground Plan of Dimensions Is 12.7 × 13.97 mm^2. In this optimization section, the dimension of ground plan is $12.7 \times 13.97\,mm^2$ and obtained -10 dB impedance bandwidth 9 GHz is shown in Figure 5(c).

4.4. Optimization Using Ground Plan of Dimensions Is 28.87 × 29.76 mm^2. From the validation of proposed geometry in IE3D simulator, obtained -10 dB impedance bandwidth is 12.2 GHz and return losses of -20 dB as shown in Figure 5(d). Simulation results obtained for 5.8 to 18 GHz frequency slots and at 12 GHz achieved -20 dB return loss.

The results of all optimization section using ground plan are shown in Table 2.

5. Results and Discussion

The proposed structure consists of one reflector of dimension 0.5λ mm $\times$ 0.5154λ mm. The dimensions of reflector give 180 deg phase shift so that all the reflected waves will be reflected from the reflector and move towards the director and achieved elimination of reflected waves over wide range of frequency. The dimension of the driven element is 0.1808λ mm $\times$ 0.1962λ mm giving 70 deg phase shift for forward wave with the intention that wave is coupled more towards the director. In antenna theory gain, bandwidth does not increase simultaneously if gain of the antenna is more than bandwidth of antenna which is less but in our

(a)

(b)

(c)

(d)
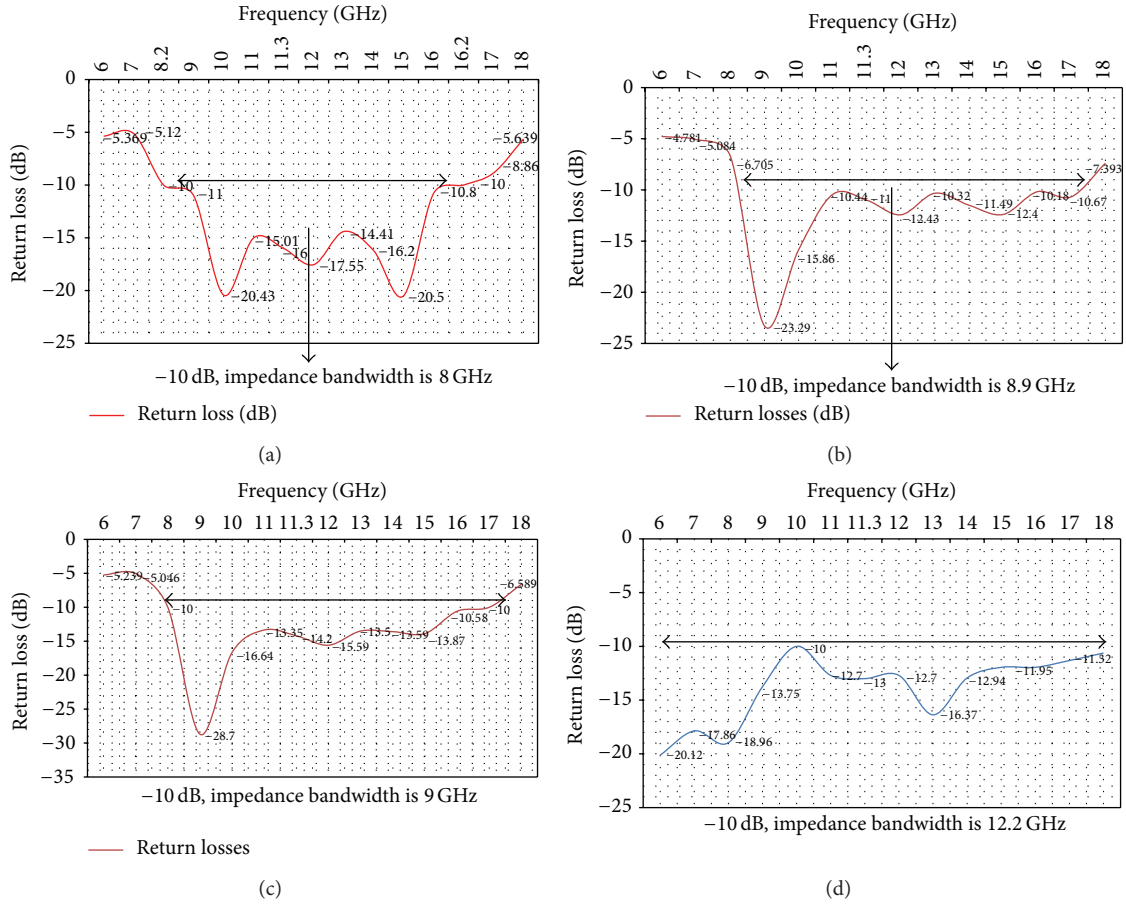
FIGURE 5: (a) Return losses versus frequency for dimension of ground plan 11.43×13.97 mm^2. (b) Return losses versus frequency for dimension of ground plan 12.7×12.7 mm^2. (c) Return losses versus frequency for dimension of ground plan 12.7×13.97 mm^2. (d) Return losses versus frequency.

design required optimal gain over a broad bandwidth therefore considered an appropriate dimension, 0.1808λ mm $\times$ 0.1962λ mm dimensions for driving element; the spacing between elements is $D_1 = 0.038\lambda$ mm and $D_2 = 0.02\lambda$ mm; the spacing between elements gives 10 deg phase shift so that the signal cannot losses between elements and maximum signal coupled to director. The dimension of U-type novel director is 0.044λ mil $\times 0.066\lambda$ mil; director exists in 13 deg phase shift and consequently all forward wave has received and again has been amplified by the director so that it achieved optimum gain from 5.8 GHz to 18 GHz.

The wide band operation is obtained from proposed structures. The 0.5λ mm $\times 0.5154\lambda$ mm ground plan is inductive in nature in order to provided impedance matching for lower frequency. The middle layer patch 0.1808λ mm $\times$ 0.1962λ mm is resistive in nature and provided impedance matching for middle frequency. The top layer patch 0.044λ mm $\times 0.066\lambda$ mm, is capacitive in nature and provided impedance matching for high frequency. Appropriate U-type patches and appropriate dimensions of ground plan reduced total inductance of geometry by increasing out-of-phase inductance of geometry and providing impedance matching over broad bandwidth, the range of broad band decided by the length, width of U-type patch, spacing between U Type patches, and dimension of ground plan.
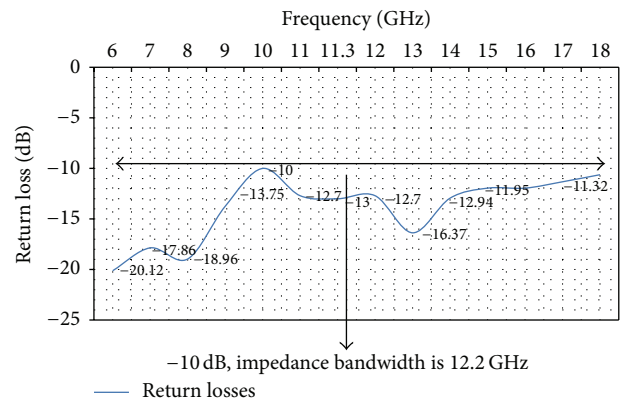
FIGURE 6: Return losses versus frequency.

5.1. Return Losses versus Frequency. From the validation of proposed geometry in IE3D simulator, -10 dB impedance bandwidth is 12.2 GHz as is shown in **Figure 6** and return losses of -20 dB. Simulation results obtained for 5.8 to 18 GHz frequency slots.

5.2. Gain versus Frequency. The simulation result in **Figure 7** concluded that out-of-phase coupling severely reduced
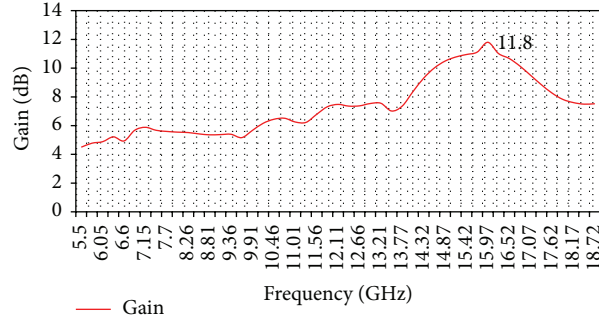
FIGURE 7: Gain versus frequency.

$f = 5.5$ GHz	$f = 6.32$ GHz	$f = 7.15$ GHz	$f = 7.979$ GHz	$f = 9.08$ GHz
(a)	(b)	(c)	(d)	(e)

$f = 10.18$ GHz	$f = 11$ GHz	$f = 12$ GHz	$f = 13$ GHz	$f = 14$ GHz	$f = 15$ GHz
(f)	(g)	(h)	(i)	(j)	(k)

$f = 16$ GHz	$f = 17$ GHz	$f = 18$ GHz
(l)	(m)	(n)
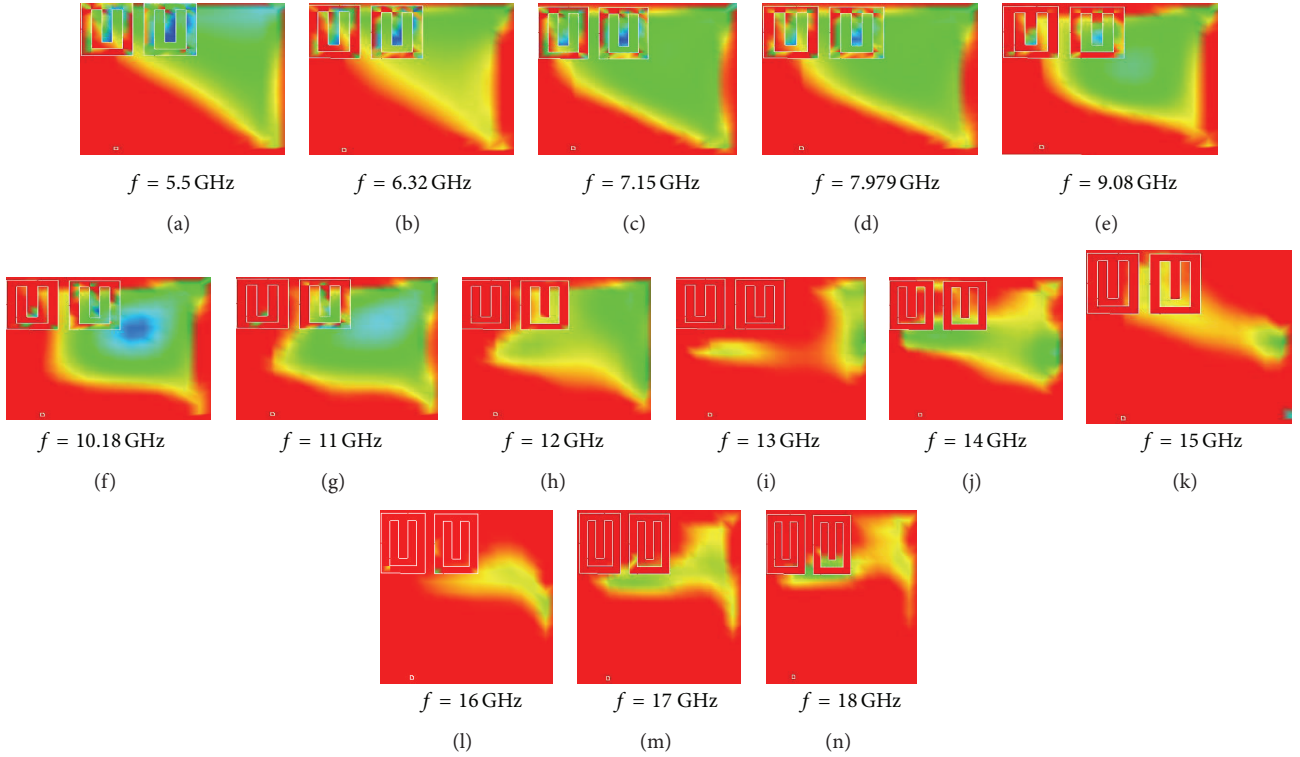
FIGURE 8: Current density of geometry at different frequency.

the inductance of design and improved gain, achieved gain 4 dBi to 11.8 dBi; the maximum value of gain 11.8 dBi is at 15.97 GHz.

5.3. Current Density at Different Frequency for Geometry-I.
Using IE3D simulator observed current density, the current density analysis is shown in **Figure 8** and found higher current density towards a higher range of frequency and obtained higher radiating and antenna efficiency towards the higher edge of frequency.

All comparison results for geometry are shown in **Table 1** which shows comparable results in terms of VSWR, return losses (S11 ≤ −10 dB), and impedance bandwidth, analyzed geometry, and got impedance bandwidth VSWR ≤ 2 and −10 dB and impedance bandwidth up to 12.2 GHz (**Table 3**). The gain of geometry in **Figure 8** varies from 5 dBi to 11.8 dBi.

The proposed geometry is appropriate for C-band, X-band and Ku-band application. Fabricated and validation is done for the proposed geometry.

5.4. Radiation Pattern

5.4.1. Elevation Radiation Pattern at $f = 18.17$ GHz, phi(ϕ) = 70 deg.
See **Figure 9(a)**.

5.4.2. Elevation Radiation Pattern at $f = 10.4592$ GHz, phi(ϕ) = 50 deg.
See **Figure 9(b)**.

Current distribution simulation shows what areas of the antenna are excited (**Figure 8**). It is interesting to note that the current distribution does not follow any regular pattern as in the case of regular shapes. At 10.45 GHz, 12.11 GHz, 15.97 GHz, 16.24 GHz, 17.07 GHz, and 18.17 GHz the gain

(a)

(b)

(c)

(d)

(e)

(f)
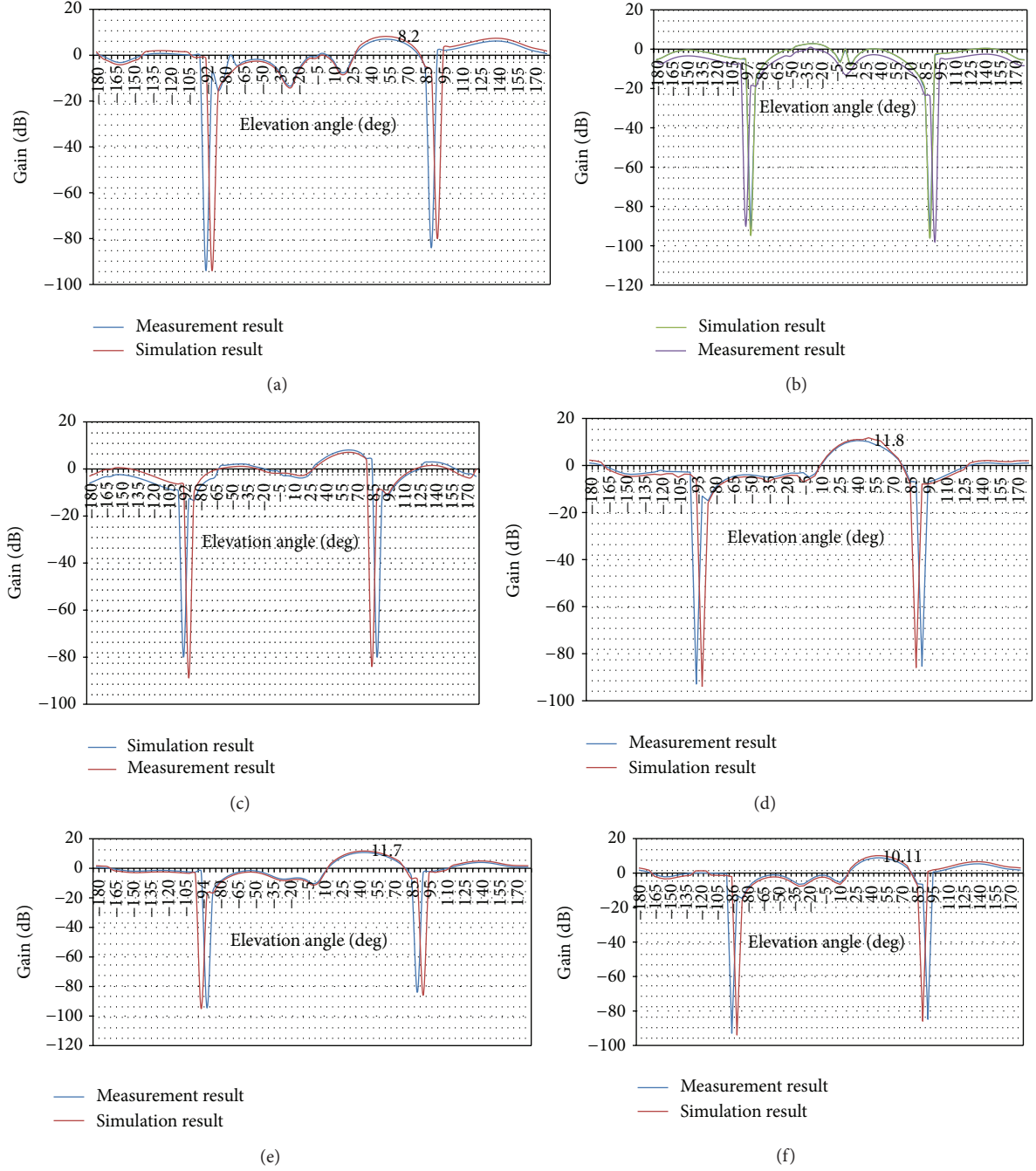
Figure 9: (a) Elevation radiation pattern at f = 18.17 GHz, phi(ϕ) = 70 deg. (b) Elevation radiation pattern at f = 10.4592 GHz, phi(ϕ) = 50 deg. (c) Elevation radiation pattern at f = 12.1122 GHz, phi(ϕ) = 50 deg. (d) Elevation radiation pattern at f = 15.97 GHz, phi(ϕ) = 50 deg. (e) Elevation radiation pattern at f = 16.2449 GHz, phi(ϕ) = 60 deg. (f) Elevation radiation pattern at f = 17.0714 GHz, phi(ϕ) = 70 deg.

Table 1: Dimension of proposed design.

Dimension of top layer			
Length of U-slot L_1	2.54 mm	Width of U-slot W_1	3.81 mm
Dimension of middle layer			
Length of middle patch L	10.4394 mm	Width of middle patch W	11.33 mm
Dimension of ground plan			
Length of ground plan L_g	28.87 mm	Width of ground plan W_g	29.76 mm

(a)   (b)
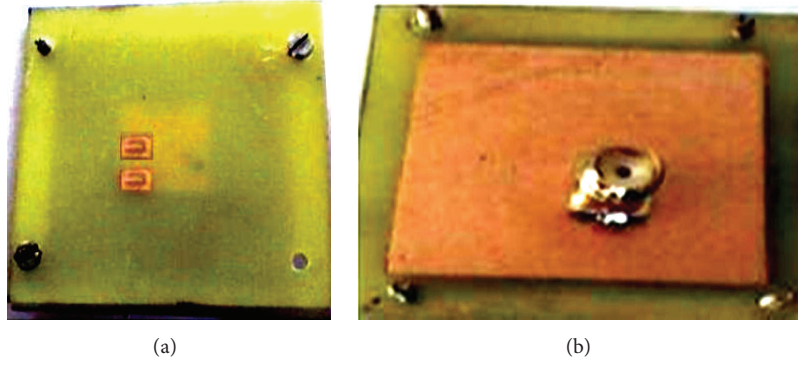
FIGURE 10: (a) Front view of fabricated antenna. (b) Bottom view of fabricated antenna.

TABLE 2: Optimization of bandwidth using different ground plan dimensions.

Ground plan dimension	11.43×13.97 mm^2	12.7×12.7 mm^2	12.7×13.97 mm^2	28.87×29.76 mm^2
Useful bandwidth	8 GHz	8.9 GHz	9 GHz	12.2 GHz

TABLE 3: Validation of antenna parameters of different geometry with reference paper.

Antenna parameters	Proposed work	Reference [6]	Reference [7]
−10 dB, Impedance bandwidth	12.2 GHz	10.42 GHz (2.86 GHz to 13.38 GHz)	10 GHz (3 GHz to 13 GHz)
VSWR ≤ 2, Impedance bandwidth	12.2 GHz	10.42 GHz (2.86 GHz to 13.38 GHz)	10 GHz (3 GHz to 13 GHz)

Proposed geometry reported impedance bandwidth greater than 12 GHz.

values are 4 dBi, 8 dBi, 11.8 dBi, 11.7 dBi, 10.11 dBi, and 8.2 dBi, respectively. In conclusion, it can be seen from the simulation results that the antenna performs well at the operating frequency 5.8 GHz to 18 GHz. There is also some deviation from the theoretically expected operating frequency; the main reason for this is the discretization applied during simulation.

5.4.3. Elevation Radiation Pattern at f = 12.1122 GHz, phi(ϕ) = 50 deg. See Figure 9(c).

5.4.4. Elevation Radiation Pattern at f = 15.97 GHz, phi(ϕ) = 50 deg. See Figure 9(d).

5.4.5. Elevation Radiation Pattern at f = 16.2449 GHz, phi(ϕ) = 60 deg. See Figure 9(e).

5.4.6. Elevation Radiation Pattern at f = 17.0714 GHz, phi(ϕ) = 70 deg. See Figure 9(f).

6. Fabrication of Proposed Structure

The fabricate antenna used FR-4 and air, the layout of the antenna is designed in AUTO CAD software, its etching is done using ferric-chloride acid. For feeding SMA connector is used (Figure 10).

7. Hardware Validation of Fabricated Antenna

There are some deviation 0.108 values from the theoretically expected; the main reason for this is the discretization applied
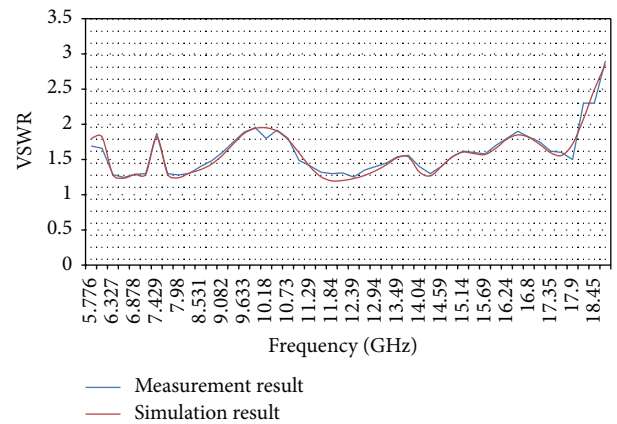
FIGURE 11: VSWR measurement of fabricated antenna.

during simulation. Figure 11 shows hardware validation of fabricated antenna.

8. Conclusion

In this paper, the out-of-phase inductance coupling approach is used for designing of proposed geometry; the out-of-phase inductance consists of two U-type patches and ground plan. This is justified in mutual coupling approach; after the analysis of the results of the proposed antenna, it is concluded that the total inductance is optimized, reflection is reduced and enhanced surface current over wide bandwidth

(12.2 GHz); achieved impedance bandwidth S11 (≤ -10 dB impedance bandwidth) from 5.8 GHz to 18 GHz is 102%, VSWR ≤ 2 over 12.2 GHz bandwidth slot. Utilized impedance bandwidth, 38% of X-band, 19% of C-band and 45% of Ku-band, achieved gain "4 dBi to 11.8 dBi" over 12.2 GHz impedance bandwidth slot. This proposed antenna geometry can be used for X-band, Ku-band, and C-band application. The hardware validation and simulation results are matched to this design. In this research we observed that ground dimension 0.5λ mm $\times$ 0.5154λ mm has improved the efficiency and useful bandwidth of antenna.

Conflict of Interests

The authors declare that there is no conflict of interests regarding the publication of this paper.

References

[1] J. Anguera, E. Martínez, C. Puente, C. Borja, and J. Soler, "Broad-band dual-frequency microstrip patch antenna with modified Sierpinski fractal geometry," *IEEE Transactions on Antennas and Propagation*, vol. 52, no. 1, pp. 66–73, 2004.

[2] J. Anguera, E. Martínez-Ortigosa, C. Puente, C. Borja, and J. Soler, "Broadband triple-frequency microstrip patch radiator combining a dual-band modified Sierpinski fractal and a monoband antenna," *IEEE Transactions on Antennas and Propagation*, vol. 54, no. 11, pp. 3367–3373, 2006.

[3] F.-J. Huang, T.-C. Yo, C.-M. Lee, and C.-H. Luo, "Design of circular polarization antenna with harmonic suppression for rectenna application," *IEEE Antennas and Wireless Propagation Letters*, vol. 11, pp. 592–595, 2012.

[4] S.-S. Zhong, Z. Sun, L.-B. Kong, C. Gao, W. Wang, and M.-P. Jin, "Tri-band dual-polarization shared-aperture microstrip array for SAR applications," *IEEE Transactions on Antennas and Propagation*, vol. 60, no. 9, pp. 4157–4165, 2012.

[5] Y. Sung, "Bandwidth enhancement of a microstrip line-fed printed wide-slot antenna with a parasitic center patch," *IEEE Transactions on Antennas and Propagation*, vol. 60, no. 4, pp. 1712–1716, 2012.

[6] C.-M. Wu, Y.-L. Chen, and W.-C. Liu, "A compact ultrawideband slotted patch antenna for wireless USB dongle application," *IEEE Antennas and Wireless Propagation Letters*, vol. 11, pp. 596–599, 2012.

[7] T. Li, H.-Q. Zhai, G.-H. Li, and C.-H. Liang, "Design of compact UWB band-notched antenna by means of electromagnetic-bandgap structures," *Electronics Letters*, vol. 48, no. 11, pp. 608–609, 2012.

[8] M. Bod, H. R. Hassani, and M. M. S. Taheri, "Compact UWB printed slot antenna with extra bluetooth, GSM, and GPS bands," *IEEE Antennas and Wireless Propagation Letters*, vol. 11, pp. 531–534, 2012.

[9] B. Lv, X. Wang, C. Zheng, J. Huangfu, C. Li, and L. Ran, "Radiation enhancement for standard patch antennas using a loosely grooved ground plane ," *IEEE Antennas and Wireless Propagation Letters*, vol. 11, pp. 604–607, 2012.

[10] G. Kumar and K. C. Gupta, "Non radiating edges and four edges gap-coupled multiple resonator, broadband microstrip antennas," *IEEE Transactions on Antennas and Propagation*, vol. AP-33, no. 2, pp. 173–178, 1985.

[11] K. Siakavara and T. Ganatsos, "Modification of the radiation patterns of higher order modes of triangular printed antennas by EBG ground planes," *IEEE Antennas and Wireless Propagation Letters*, vol. 8, pp. 124–128, 2009.

[12] F. E. Terman, *Radio Engineer Handbook*, McGraw-Hill, New York, NY, USA, 1943.

Research Article

Ultrasubwavelength Ferroelectric Leaky Wave Antenna in a Planar Substrate-Superstrate Configuration

G. Lovat,[1] P. Burghignoli,[2] R. Araneo,[1] and S. Celozzi[1]

[1] *Department of Astronautical, Electrical and Energetic Engineering (DIAEE), Sapienza University of Rome,*
 Via Eudossiana 18, 00148 Roma, Italy
[2] *Department of Information Engineering, Electronics and Telecommunications, Sapienza University of Rome,*
 Via Eudossiana 18, 00148 Roma, Italy

Correspondence should be addressed to G. Lovat; giampiero.lovat@uniroma1.it

The possibility of achieving directive fan-beam radiation with planar Fabry-Pérot cavity antennas constituted by an upper ferroelectric thin film and a lower ground plane having ultrasubwavelength thickness is studied by means of a simple transverse-equivalent-network approach and a cylindrical leakywave analysis, deriving simple design formulas. The performance of the proposed antenna is investigated in terms of power density radiated at broadside and directivity in the principal planes, pointing out the main limitations and tradeoffs associated with the reduced thickness.

1. Introduction

Planar antennas based on partially reflecting surfaces (PRSs) have been receiving increasing interest during the last decade, thanks to their attractive features of low profile, high directivity, and simple feeding. Since the first design proposed and realized by von Trentini in 1956 [1], in which the directivity of truncated waveguides opening in an infinite conducting ground plane was increased by means of periodic metal screens, a number of different PRS realizations have been proposed, based, for example, on dielectric substrate-superstrate configurations [2] or on two-dimensional periodic array of metal patches [3, 4] or slots cut in a top plate [5].

The typical thickness of PRS-based planar antennas is of the order of one-half of the free-space wavelength. In fact, the directivity enhancement afforded by the PRS can be attributed to the resonant behavior of the partially open planar cavity formed by the ground plane and the PRS; the antenna can thus be viewed as a sort of *Fabry-Pérot* resonator (hence the name Fabry-Pérot cavity (FPC) antennas) [2, 6]. Alternatively, the antenna can be viewed as a two-dimensional leaky wave antenna, in which the primary source excites a pair of *cylindrical* TM^z and TE^z leaky modes; these

propagate along the structure and give the main contribution to the antenna aperture field, thus establishing the main features of the antenna radiation pattern [7, 8]. A leaky wave analysis of FPC antennas showed that the power density radiated at broadside is maximum when the thickness of the cavity is optimum, that is, close to half of the wavelength inside the substrate above which the PRS is placed; when such an optimum thickness is used to create a broadside beam, the leaky modes supported by the structure have nearly the same wavenumber with nearly equal low values of the phase and attenuations constants [9–11] thus producing a highly directive broadside beam.

In this paper we study PRS-based planar antennas in which the total thickness is *considerably smaller* than the values typical of the usual FPC antennas [2, 7] and which has been the subject of many investigations [12–14]. A preliminary investigation on this kind of structure has been presented in [15]. Here we consider a planar substrate constituted by a conventional dielectric covered by a thin ferroelectric film. The structure is similar to that presented in [16] where the ferroelectric film was used to allow for an electrical tuning of the main parameters characterizing the radiation pattern of the antenna. Here the ferroelectric film

is used to obtain an equivalent capacitive PRS which allows for dramatically reducing the total thickness of the antenna capable of obtaining a directive beam. The performance of the proposed antenna is investigated in terms of power density radiated at broadside and directivity in the principal planes, pointing out the main limitations and tradeoffs associated with the reduced thickness.

2. Structure Description

The reference structure, shown in Figure 1, is a dielectric slab (the substrate) of thickness b and relative permittivity ε_{r1}, bounded below by a perfectly conducting (PEC) ground plane and covered by a ferroelectric film of thickness t with permittivity $\varepsilon_{r2} = \varepsilon'_{r2} - j\varepsilon''_{r2}$. The materials are assumed to be nonmagnetic (i.e., $\mu_{r1} = \mu_{r2} = 1$). The structure is assumed to be excited by a unit-amplitude (1 V·m) horizontal magnetic dipole (HMD) directed along the x-axis and placed over the ground plane, thus modeling a thin slot etched on the ground plane and excited by a suitable waveguide structure (e.g., a microstrip line). This kind of source is chosen instead of the more conventional horizontal electric dipole (HED) since in an ultrasubwavelength configuration the latter would radiate poorly due to the electrical closeness to the PEC ground plane. A time-harmonic dependence $\exp(j\omega t)$ of sources and fields will be assumed and suppressed throughout.

3. Antenna Radiation

3.1. Far-Field Pattern via Reciprocity. The far-field pattern radiated by the HMD in the presence of the planar structure described above can be calculated through a standard application of reciprocity theorem, by letting a plane wave impinge on the structure from the observation direction (θ, ϕ) and calculating the reaction between the resulting total field and the HMD source [2, 6]. The field produced by the incident plane wave can in turn be readily calculated using the transverse equivalent network (TEN) representation of the structure shown in Figure 2(a), where the substrate and superstrate layers are modeled with lengths of transmission lines (TLs).

Assuming that the relative permittivity of the ferroelectric film is very large ($|\varepsilon_{r2}| \gg 1$), $k_{z2} = k_0\sqrt{\varepsilon_{r2} - \sin^2\theta} \cong k_{z2} = k_0\sqrt{\varepsilon_{r2}}$ results and hence $Y_2 \cong \sqrt{\varepsilon_{r2}}/\eta_0$ for both TM and TE polarizations (here $k_0 = 2\pi/\lambda_0$ and η_0 are the free-space wavenumber and characteristic impedance, resp.). Assuming further that the electrical thickness of the ferroelectric film is small, the relevant length of TL can be replaced by a shunt admittance $Y_f = G_f + jB_f = k_0 t\varepsilon_{r2}/\eta_0$ for both TM and TE polarizations [16, 17], thereby obtaining the TEN in Figure 2(b). Using the latter TEN, the expressions of the far-field pattern are obtained as

$$E_\theta(r, \theta, \phi)$$

$$= E_0 \sin\phi \frac{-2jY_1^{\text{TM}}}{\left(Y_0^{\text{TM}} + Y_f\right)\sin(k_{z1}b) - jY_1^{\text{TM}}\cos(k_{z1}b)},$$

$$E_\phi(r, \theta, \phi)$$

$$= -E_0 \cos\phi\cos\theta \frac{-2jY_1^{\text{TE}}}{\left(Y_0^{\text{TE}} + Y_f\right)\sin(k_{z1}b) - jY_1^{\text{TE}}\cos(k_{z1}b)},$$

(1)

where

$$E_0 = -jk_0 \frac{e^{-jk_0 r}}{4\pi r}$$

(2)

and the TL parameters are

$$Y_0^{\text{TM}} = \frac{k_0}{\eta_0 k_{z0}},$$

$$Y_0^{\text{TE}} = \frac{k_{z0}}{\eta_0 k_0}$$

$$Y_1^{\text{TM}} = \frac{\varepsilon_{r1} k_0}{\eta_0 k_{z1}},$$

$$Y_1^{\text{TE}} = \frac{k_{z1}}{\eta_0 k_0}$$

$$k_{z0} = k_0 \cos\theta,$$

$$k_{z1} = \sqrt{\varepsilon_{r1} k_0^2 - \sin^2\theta}.$$

(3)

3.2. Design Equations for Maximum Broadside Radiation. From (1), at broadside we have

$$E_\phi(\theta = 0)\big|_H = E_\theta(\theta = 0)\big|_E$$

$$= E$$

$$= E_0 \frac{-2jn_1}{\left(1 + \overline{Y}_f\right)\sin\left(2\pi n_1\widehat{b}\right) - jn_1\cos\left(2\pi n_1\widehat{b}\right)},$$

(4)

where $n_1 = \sqrt{\varepsilon_{r1}}$, $\widehat{b} = b/\lambda_0$, and $\overline{Y}_f = \eta_0 Y_f$. For very thin substrates (i.e., $n_1\widehat{b} \ll 1$), (4) can be approximated using a Taylor expansion of the trigonometric functions as

$$E \simeq E_0 \frac{-2jn_1}{\left(1 + \overline{Y}_f\right)\left(2\pi n_1\widehat{b}\right) - jn_1\left[1 - \left(\left(2\pi n_1\widehat{b}\right)^2/2\right)\right]}$$

$$\simeq \frac{-2jE_0}{\left(1 + \overline{G}_f\right)2\pi\widehat{b} + j\left(2\pi\widehat{b}\overline{B}_f - 1\right)}.$$

(5)

Then, for a high-permittivity low-loss ferroelectric medium [18–20], $\overline{B}_f \gg \max\{1, \overline{G}_f\}$ results and the absolute value of the expression in (5) is maximized when $2\pi\widehat{b}\overline{B}_f - 1 = 0$; that is,

$$\overline{B}_f = \frac{1}{2\pi\widehat{b}}$$

(6)
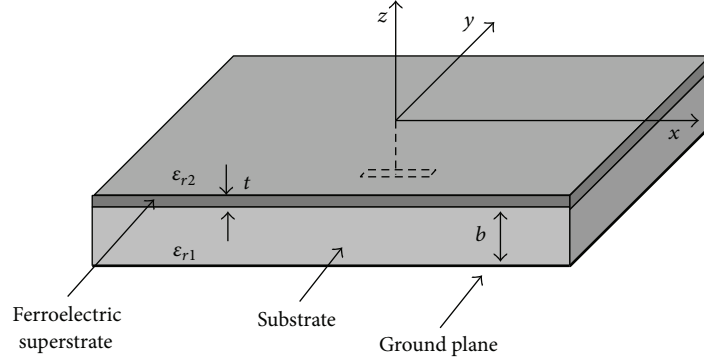
FIGURE 1: Planar substrate-superstrate configuration excited by a magnetic dipole over the ground plane with the relevant geometric and physical parameters.
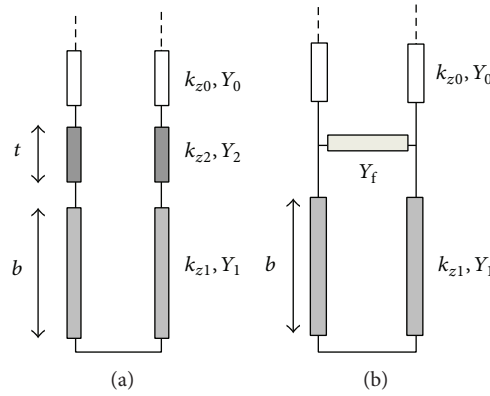
FIGURE 2: Transverse equivalent network of the structure in Figure 1. Exact representation (a) and approximate representation (b) valid for a high-permittivity thin-film superstrate.

or

$$\widehat{b} = \frac{1}{2\pi \overline{B}_f}. \tag{7}$$

Therefore, very thin substrates require large values of the normalized (capacitive) susceptance $\overline{B}_f$. In such a case, the power density at broadside is given by

$$P(0) = \frac{|E|^2}{2\eta_0} \simeq \frac{k_0^2}{8\pi^2\eta_0} \frac{\overline{B}_f^2}{\left(1 + G_f\right)^2} \simeq \frac{k_0^2}{8\pi^2\eta_0} \overline{B}_f^2. \tag{8}$$

Therefore, the power density radiated at broadside is enhanced of a factor $\overline{B}_f^2$ with respect to the case of a magnetic dipole radiating on a PEC ground plane with free space above. (This may be contrasted with the case of a HED excitation [15], in which no such enhancement is found because the short-circuiting effect of the PEC ground plane compensates the resonant effect of the PRS.) To establish whether the enhancement of power density is accompanied with an enhancement of directivity as well, we have to determine if the structure can support leaky waves with small values of the phase and attenuation constants.

4. Leaky Wave Analysis

The dispersion equation coincides with the denominator in (1); that is, (neglecting $\overline{G}_f \ll \overline{B}_f$, [18–20])

$$\overline{Y}_0^{\text{TE/TM}} + j\overline{B}_f - j\overline{Y}_1^{\text{TE/TM}} \cot\left(2\pi\widehat{k}_{z1}\widehat{b}\right) = 0. \tag{9}$$

We assume a solution for the normalized longitudinal propagation constant $\widehat{k}_x$ of the form

$$\widehat{k}_x = \delta = \delta_R - j\delta_J, \tag{10}$$

where δ_R and δ_J are "small" ($|\delta_R| \ll 1$ and $|\delta_J| \ll 1$), so that the normalized transverse propagation constants $\widehat{k}_{z0}$ and $\widehat{k}_{z1}$ in air and inside the slab, respectively, are approximated as

$$\widehat{k}_{z0} = \sqrt{1 - \widehat{k}_x^2} = \sqrt{1 - \delta^2} \simeq 1 - \frac{\delta^2}{2},$$

$$\widehat{k}_{z1} = \sqrt{\varepsilon_{r1} - \widehat{k}_x^2} = \sqrt{\varepsilon_{r1} - \delta^2} \simeq n_1 - \frac{\delta^2}{2n_1} \tag{11}$$

while the cotangent function in (9) can be approximated as

$$\cot\left(2\pi\widehat{k}_{z1}\widehat{b}\right) \simeq \frac{\left(1/2\pi n_1\widehat{b}\right)\left(-\left(n_1/\pi\widehat{h}\delta^2\right)\right) - 1}{\left(1/2\pi n_1\widehat{b}\right) + \left(-\left(n_1/\pi\widehat{b}\delta^2\right)\right)}$$
$$= \frac{n_1\left(1 + 2\pi^2\widehat{b}^2\delta^2\right)}{\pi\widehat{b}\left(2n_1^2 - \delta^2\right)}. \tag{12}$$

Now we have to consider separately the two cases of TE and TM modes.

4.1. TE Leaky Waves. For TE modes the transverse characteristic impedances are

$$\overline{Y}_0^{\text{TE}} = \widehat{k}_{z0} \qquad \overline{Y}_1^{\text{TE}} = \widehat{k}_{z1}. \tag{13}$$

Based on the above approximations, (9) can be written as

$$1 - \frac{\delta^2}{2} + j\overline{B}_f - j\left(n_1 - \frac{\delta^2}{2n_1}\right)\frac{n_1\left(1 + 2\pi^2\widehat{b}^2\delta^2\right)}{\pi\widehat{b}\left(2n_1^2 - \delta^2\right)} = 0. \tag{14}$$

That is,

$$\pi\widehat{b}\left(2n_1^2 - \delta^2\right) - \pi\widehat{b}\left(2n_1^2 - \delta^2\right)\frac{\delta^2}{2}$$
$$+ j\pi\widehat{b}\left(2n_1^2 - \delta^2\right)\overline{B}_f - j\left(n_1 - \frac{\delta^2}{2n_1}\right) \tag{15}$$
$$\times n_1\left(1 + 2\pi^2\widehat{b}^2\delta^2\right) = 0.$$

By neglecting all the terms $o(\delta^4)$, (15) is written as

$$\left(4n_1^2\pi\widehat{b} + j4n_1^2\pi\widehat{h}\overline{B}_f - j2n_1^2\right)$$
$$+ \left(j - \pi\widehat{b} - 2n_1^2\pi\widehat{b} - j2\pi\widehat{h}\overline{B}_f - j4n_1^2\pi^2\widehat{b}^2\right)\delta^2 \tag{16}$$
$$= 0.$$

Under the optimum condition (4) (or (5)), (16) becomes

$$\left(2n_1^2\frac{1}{\overline{B}_f}\right) + \left(-\frac{1}{2\overline{B}_f} - n_1^2\frac{1}{\overline{B}_f} - jn_1^2\frac{1}{\overline{B}_f^2}\right)\delta^2 = 0. \tag{17}$$

That is,

$$\delta^2 = \frac{4n_1^2}{\left(2n_1^2 + 1\right)} - j\frac{8n_1^4}{\left(2n_1^2 + 1\right)^2\overline{B}_f}. \tag{18}$$

By equating the real and the imaginary parts of (18) we obtain

$$\delta_R^2 - \delta_J^2 \simeq \frac{4n_1^2}{\left(2n_1^2 + 1\right)}$$
$$2\delta_R\delta_J \simeq \frac{8n_1^4}{\left(2n_1^2 + 1\right)^2\overline{B}_f}. \tag{19}$$

Equations (19) contradict the assumption of "small" δ_R and δ_J, so that no TE leaky waves exist in this case with $\widehat{\beta} = \widehat{\alpha}$ and $\widehat{\alpha} \ll 1$.

4.2. TM Leaky Waves. For TM modes the transverse characteristic impedances are

$$\overline{Y}_0^{\text{TM}} = \frac{1}{\widehat{k}_{z0}} \qquad \overline{Y}_1^{\text{TM}} = \frac{\varepsilon_{r1}}{\widehat{k}_{z1}} \tag{20}$$

and (9) can be approximated as

$$2\pi\widehat{b}\left(2n_1^2 - \delta^2\right)^2 + j\overline{B}_f\pi\widehat{b}\left(2n_1^2 - \delta^2\right)^2\left(2 - \delta^2\right)$$
$$- j2\varepsilon_{r1}n_1^2\left(2 - \delta^2\right)\left(1 + 2\pi^2\widehat{b}^2\delta^2\right) = 0. \tag{21}$$

By neglecting all the terms $o(\delta^4)$, (21) is rewritten as

$$\left(4n_1^2\pi\widehat{b} + j4n_1^2\overline{B}_f\pi\widehat{b} - j2\varepsilon_{r1}\right)$$
$$+ \left(j\varepsilon_{r1} - 4\pi\widehat{b} - j4\overline{B}_f\pi\widehat{b} - j2n_1^2\overline{B}_f\pi\widehat{b} - j4\varepsilon_{r1}\pi^2\widehat{b}^2\right)\delta^2 = 0. \tag{22}$$

Under the optimum condition (4) (or (5)), (22) becomes

$$\left(\frac{2n_1^2}{\overline{B}_f}\right) - \left(\frac{2}{\overline{B}_f} + 2j + j\frac{n_1^2}{\overline{B}_f^2}\right)\delta^2 = 0, \tag{23}$$

from which

$$\delta^2 = \left(\frac{2n_1^2}{\overline{B}_f}\right)\frac{1}{\left(\left(2/\overline{B}_f\right) + 2j + j\left(n_1^2/\overline{B}_f^2\right)\right)}$$
$$= \frac{2n_1^2\overline{B}_f}{2\overline{B}_f + j\left(2\overline{B}_f^2 + n_1^2\right)}. \tag{24}$$

For thin substrates the susceptance $\overline{B}_f$ is large (see (6)) so that (24) can be approximated as

$$\delta^2 \simeq \frac{2n_1^2\overline{B}_f}{2\overline{B}_f + j2\overline{B}_f^2} = \frac{n_1^2}{1 + j\overline{B}_f} = \frac{n_1^2\left(1 - j\overline{B}_f\right)}{1 + \overline{B}_f^2}$$
$$\simeq \frac{n_1^2}{\overline{B}_f^2} - j\frac{n_1^2}{\overline{B}_f}. \tag{25}$$

By equating the real and the imaginary parts of (25) we obtain

$$\delta_R^2 - \delta_J^2 \simeq \frac{n_1^2}{\overline{B}_f^2},$$
$$2\delta_R\delta_J \simeq \frac{n_1^2}{\overline{B}_f}. \tag{26}$$

In the limit of large $\overline{B}_f$, the RHS of the first of (26) can be neglected with respect to the RHS of the second. Finally, from the second we obtain

$$\delta_R \simeq \delta_J \simeq \sqrt{\frac{\varepsilon_{r1}}{2\overline{B}_f}}. \tag{27}$$

Since the radiation pattern in the E plane is mainly determined by radiation from TM leaky modes, a directive broadside beam is expected in the E plane for sufficiently large values of the normalized shunt susceptance $\overline{B}_f$. Alternatively, (27) can be written in terms of the normalized thickness as

$$\widehat{\beta}^{TM} \simeq \widehat{\alpha}^{TM} \simeq \sqrt{\pi \varepsilon_{r1} \widehat{b}}, \qquad (28)$$

which shows that a directive broadside beam in the E plane requires very thin substrates.

5. Pencil-Beam Radiation

Based on the above analysis a *fan* shape of the radiation pattern can be expected, directive in the E plane and nondirective in the H plane. In fact, as it will be shown in Section 6, when the antenna is designed for maximum broadside power density the pattern in the H plane is almost constant. Since the pattern in (1) is of BOR$_1$ type [21], that is,

$$\mathbf{E}(r, \theta, \phi) = E_0 \left[\sin\phi C_E(\theta) \boldsymbol{\theta}_0 + \cos\phi C_H(\theta) \boldsymbol{\phi}_0 \right], \quad (29)$$

this is equivalent to saying that $C_E(\theta)$ is peaked and $C_H(\theta)$ is almost constant. Under this condition, it is easy to show that the maximum directivity of the pattern cannot be larger than 2:

$$D_{max} = \frac{2\pi r^2 |\mathbf{E}(r, 0, \phi)|^2}{\int_0^{2\pi} \int_0^{\pi/2} |\mathbf{E}(r, 0, \phi)|^2 r^2 \sin\theta \, d\theta \, d\phi}$$

$$= \frac{2}{\int_0^{\pi/2} \left[1 + |C_E(\theta)/C_E(0)|^2 \right] \sin\theta \, d\theta} \leq 2 \qquad (30)$$

(e.g., for a HMD in free space, it is equal to 3/2, as is well known).

If a *pencil beam* is desired, with narrow patterns in *both* principal planes, a linear array of HMD sources may be employed. Since the element pattern is directive in the E plane (orthogonal to the HMD direction) and nondirective in the H plane (parallel to the HMD direction), the elements of the array should be aligned along the HMD direction (i.e., in the cases considered so far, along the x-axis). Assuming for simplicity a uniform equispaced array with interelement spacing d and $2n+1$ elements, placed symmetrically with respect to the origin, the resulting array factor is $F(\theta, \phi) = \sin[(2n+1)\xi/2]/\sin[\xi/2]$, with $\xi = k_0 d \sin\theta \cos\phi$ [22]. In this way the E plane array pattern is determined by the element pattern, whereas the H plane array pattern is determined by the array factor. In particular, for small H plane beam widths $\theta_{3\,dB}^H$ and a small array spacing (i.e., $k_0 d \ll 1$),

$$\theta_{3\,dB}^H \simeq \frac{1.391}{n k_0 d} \qquad (31)$$

approximately results [21]. On the other hand, since the E plane element pattern is due to radiation from a TM leaky wave, using (7) the E plane array beam width $\theta_{3\,dB}^E$ can approximately be evaluated as [9]

$$\theta_{3\,dB}^E \simeq \sqrt{\frac{2\varepsilon_{r1}}{\overline{B}_f}} \qquad (32)$$

with the approximation being more accurate for small beam widths (i.e., large normalized PRS susceptances). The array parameters, that is, the number n and the spacing d, can then be determined through (31) and (32), for example, by requiring that the 3 dB beam width of the array factor in the H plane be equal to that of the element pattern in the E plane. Finally, for narrow beams the resulting broadside directivity can be estimated as [22]

$$D_{max} \simeq \frac{9.9}{(2\theta_{3\,dB}^E)(2\theta_{3\,dB}^H)} \simeq 1.8 n k_0 d \sqrt{\frac{\overline{B}_f}{2\varepsilon_{r1}}}. \qquad (33)$$

It is worth noting that, remaining within the class of directive planar antennas, a similar performance in terms of directivity could be achieved also with ordinary phased arrays of, for example, metal patch antennas. As already mentioned, these structures would require a significant larger overall thickness; moreover, by considering truncated structures, whereas the transverse dimensions would be comparable, for these conventional classes of antennas, a 2D instead of a 1D array would be required, with a considerably larger number of radiating elements and hence a higher cost.

6. Results and Discussion

In order to check the accuracy of the asymptotic expressions derived in the above sections, a grounded dielectric slab covered with a capacitive PRS consisting of a low-loss ferroelectric thin film is considered with $\varepsilon_{r1} = 2.2$ at the operating frequency $f = 1$ GHz. The values of the phase and attenuation constants have been numerically calculated as a function of the normalized shunt susceptance $\overline{B}_f$ representing the ferroelectric thin film in the transverse equivalent network. For each value of $\overline{B}_f$, the thickness b of the slab has been calculated according to the optimization condition in (6). In particular, in Figure 3, the exact results are compared with the approximate asymptotic ones for the TM leaky mode. The asymptotic approximate expression (28) is seen to be very accurate in a wide range of values of $\overline{B}_f$, starting approximately from $\overline{B}_f = 10$. As expected, no TE leaky waves are found. In Figure 4, the optimum subwavelength thickness is reported as a function of $\overline{B}_f$.

We then consider the same substrate with a fixed thickness b equal to $\lambda_0/70$ at the frequency $f = 1$ GHz (i.e., $b = 4.28$ mm); according to (5), in order to have maximum broadside radiation at $f = 1$ GHz a normalized susceptance $\overline{B}_f = 11.14$ is required, which can be obtained, for example, with a ferroelectric film having $t = 2$ mil and $\varepsilon_{r2} = 6.68 \cdot 10^3$ [20]. In Figure 5, the dispersion curve of the TM leaky mode is reported as a function of frequency, together with the power density radiated at broadside by a horizontal magnetic dipole on the ground plane. It can be seen that, at $f = 1$ GHz, $\widehat{\beta}^{TM} \simeq \widehat{\alpha}^{TM} \simeq 0.31$ results which is the value predicted by the approximate formula (28). It can also be observed that the broadside power density is maximum at $f = 1$ GHz.

In order to investigate the radiation properties, radiation patterns in the E and H planes are reported in Figure 6 at the
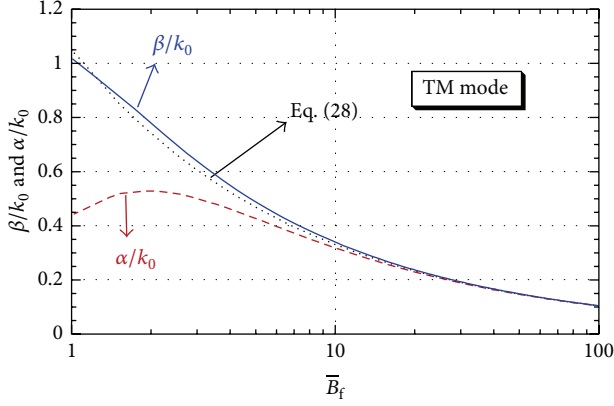
FIGURE 3: TM leaky wave normalized phase β/k_0 and attenuation α/k_0 constants as a function of the normalized susceptance $\overline{B}_f$ representing the ferroelectric thin film for the proposed antenna. Parameters: $\varepsilon_{r1} = 2.2$; $f = 1$ GHz; for each value of $\overline{B}_f$, the thickness b of the slab has been calculated according to the optimization condition in (6).
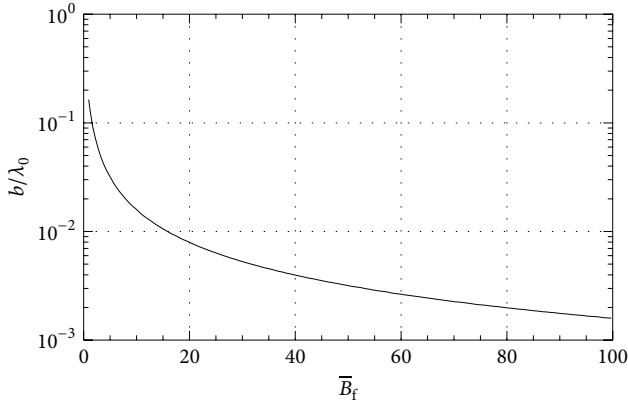
FIGURE 4: Optimum subwavelength thickness for directive TM radiation as a function of $\overline{B}_f$.
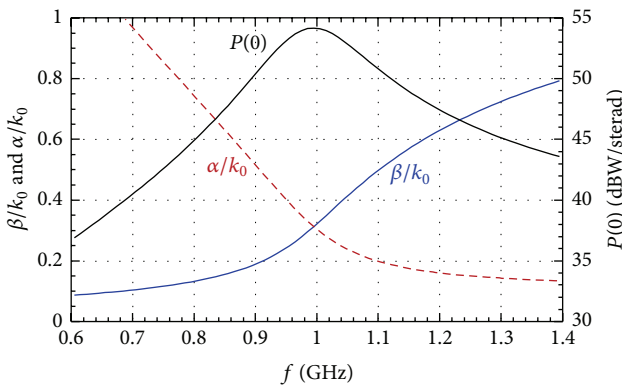
FIGURE 5: Dispersion curve of the supported TM leaky wave and power density radiated at broadside by a horizontal magnetic dipole on the ground plane as functions of frequency when the antenna thickness is $b = \lambda_0/70$ at $f = 1$ GHz. Other parameters: $\overline{B}_f = 11.14$.
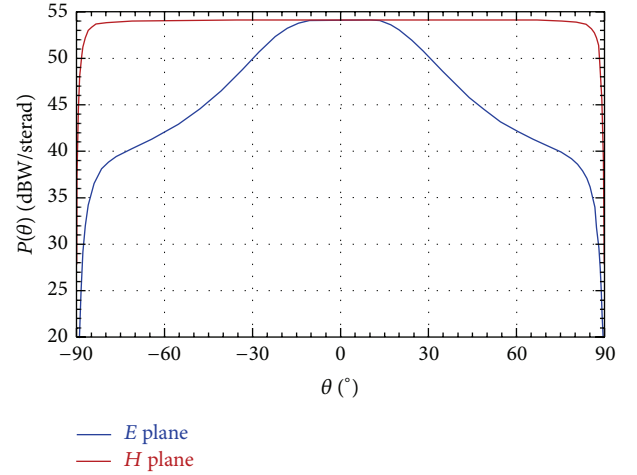
    —— E plane
    —— H plane

FIGURE 6: Radiation patterns in the E and H planes at $f = 1$ GHz for a structure with $b = \lambda_0/70$ and $\overline{B}_f = 11.41$.

frequency $f = 1$ GHz. It can be seen that the pattern is flat in the H plane (no TE leaky wave is excited), while it is quite directive (at broadside) in the E plane (due to the excitation of a TM leaky wave).

More directive beams can be obtained with thinner substrates (and, accordingly, larger values of the normalized susceptance). An example is shown in Figures 7 and 8, where the same structure of Figures 5 and 6 has been considered but with a thickness $b = \lambda_0/300$ at the frequency $f = 1$ GHz, for example, $b = 1$ mm (according to (5), a normalized susceptance $\overline{B}_f = 47.75$ is required).

In Figure 7, the dispersion curve of the TM leaky mode is reported as a function of frequency, together with the power density radiated at broadside by a horizontal magnetic dipole over the ground plane. It can be seen that, at $f = 1$ GHz, $\widehat{\beta}^{TM} \simeq \widehat{\alpha}^{TM} \simeq 0.15$ results which is the value predicted by the approximate formula (28). It can also be observed that the broadside power density is maximum at $f = 1$ GHz and, with respect to the structure of Figure 5, the broadside bandwidth has been reduced.

The radiation patterns in the E and H planes are reported in Figures 8(a) and 8(b) at the frequency $f = 1$ GHz. Again a flat pattern is radiated in the H plane, whereas a highly directive beam at broadside is radiated in the E plane.

In Figure 9 the patterns at different frequencies are reported in order to verify the scanning features typical of a leaky wave antenna. The radiation patterns in the principal planes are so different because in the E plane the pattern is mainly determined by a weakly attenuated TM leaky wave; hence it is directive; on the other hand, as shown in Section 4, no weakly attenuated TE leaky waves exist in the considered structure at the same frequencies; hence the pattern in the H plane is not directive. Please note that the radial scale in the plot of Figure 9(a) is linear (not in dB); hence both the E plane and the H plane patterns are very broad at 0.8 GHz. (The pattern in the H plane is however narrower than at 1 GHz; this may be due to the excitation at 0.8 GHz of a TE leaky wave
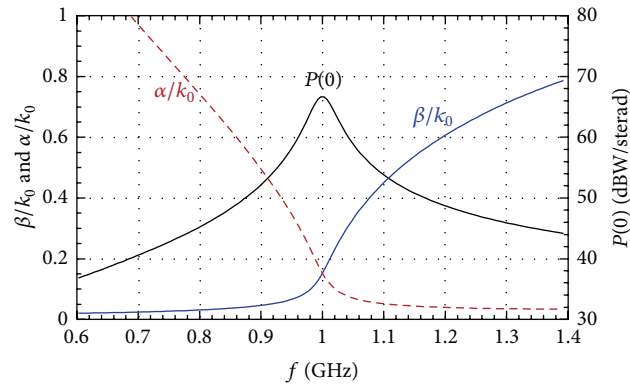
FIGURE 7: Same as in Figure 5 for a structure with $b = \lambda_0/300$ at $f = 1$ GHz. Other parameters: $\overline{B}_f = 47.75$.

(a)

(b)
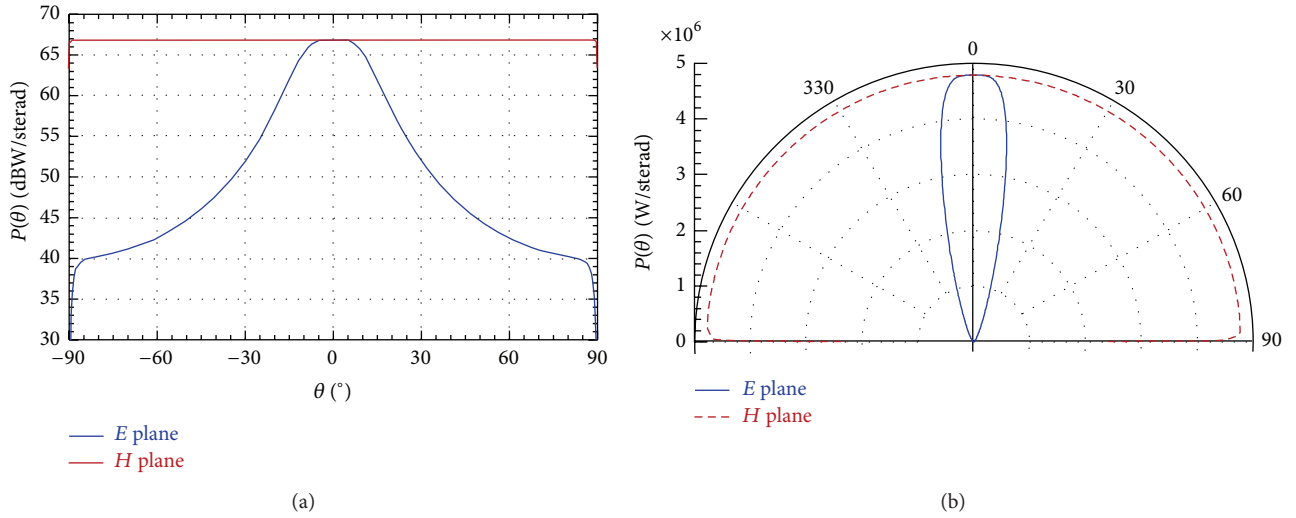
FIGURE 8: Radiation patterns in the E and H planes at $f = 1$ GHz for a structure with $b = \lambda_0/300$ and $\overline{B}_f = 47.75$. Log-log plot (a) and polar linear plot (b).

(a)

(b)
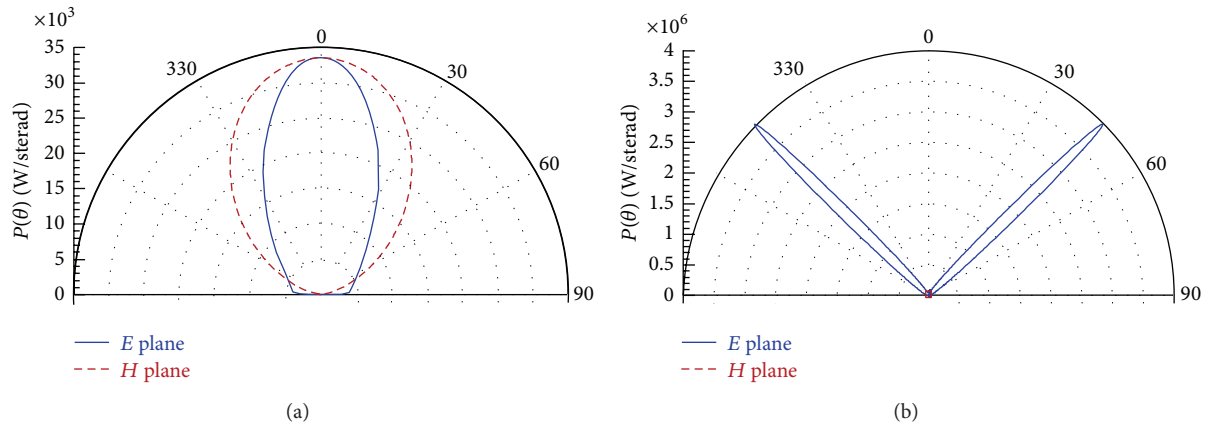
FIGURE 9: Radiation patterns in the E and H planes at different frequencies to show the scanning features of the proposed antenna. Parameters: $b = \lambda_0/300$ at $f = 1$ GHz and $\overline{B}_f = 47.75$. (a) $f = 0.8$ GHz and (b) $f = 1.3$ GHz.
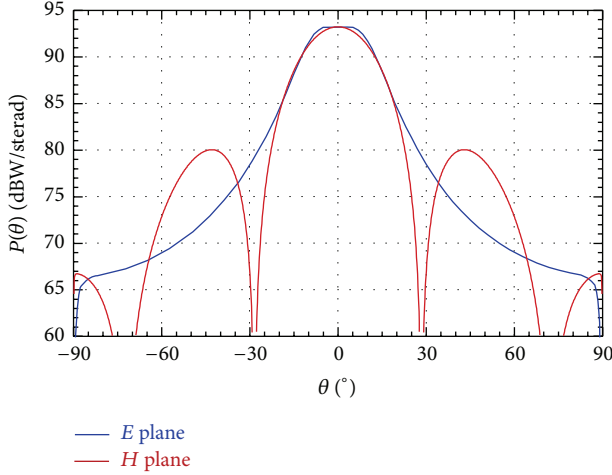
FIGURE 10: Radiation patterns in the E and H planes at $f = 1$ GHz for a structure with $b = \lambda_0/300$ and $\overline{B}_f = 47.75$ excited by a linear array of 21 equiamplitude HMDs placed along the x-axis with spacing $d = \lambda_0/10$.

with a large attenuation constant, which is not significant at 1 GHz and whose existence cannot be excluded from the analysis presented in this study.) Note that in the scanned case the maximum power density in the H plane is much lower than the maximum in the E plane; hence the nondirective H plane pattern is not visible in Figure 9(b).

The presence of losses in the ferroelectric film negligibly affects the performance of the antenna since it has been shown that doped relaxor ferroelectric materials may have very low values of the loss tangent [20].

Finally, the case of a linear array of HMD sources is considered, in order to obtain broadside *pencil-beam* radiation. As explained in Section 5, by aligning the sources along the HMD direction the almost isotropic pattern in the H plane can be made directive; in particular, the same structure as in Figure 9 has been excited by an array of 21 HMD elements with interelement spacing $d = \lambda_0/10$, in order to obtain the same 3 dB beam widths in both principal planes. The relevant radiation patterns are shown in Figure 10; it can be seen that the principal-plane beam widths are indeed equal (while the secondary lobes are higher in the H plane due to the uniform-amplitude excitation of the array).

7. Conclusion

The possibility of achieving directive fan-beam radiation with planar antennas having ultrasubwavelength thickness has been demonstrated. The proposed antenna consists of high-permittivity superstrate (e.g., a low-loss ferroelectric thin film) above a ground plane; the primary source is a thin slot etched in the ground plane. In particular, it has been shown analytically that this kind of structure supports a weakly attenuated TM leaky wave which is responsible of a highly directive beam in the E plane of the structure. By using a uniform array of slot sources aligned along the H plane the radiation pattern can be made directive in the H plane as well,

thus obtaining a pencil broadside beam. Numerical results are provided which confirm the conclusion theoretically derived. Future work will concern the issues related to the practical excitation of these structures, that is, the feed design and the relevant analysis of the antenna input impedance.

Conflict of Interests

The authors declare that there is no conflict of interests regarding the publication of this paper.

References

[1] G. von Trentini, "Partially reflecting sheet arrays," *IRE Transactions on Antennas and Propagation*, vol. AP-4, pp. 666–671, 1956.

[2] D. R. Jackson and N. G. Alexópoulos, "Gain enhancement methods for printed circuit antennas," *IEEE Transactions on Antennas and Propagation*, vol. AP-33, no. 9, pp. 976–987, 1985.

[3] A. P. Feresidis and J. C. Vardaxoglou, "High gain planar antenna using optimised partially reflective surfaces," *IEE Proceedings: Microwaves, Antennas and Propagation*, vol. 148, no. 6, pp. 345–350, 2001.

[4] T. Zhao, D. R. Jackson, J. T. Williams, H.-Y. D. Yang, and A. A. Oliner, "2-D periodic leaky-wave antennas—part I: metal patch design," *IEEE Transactions on Antennas and Propagation*, vol. 53, no. 11, pp. 3505–3514, 2005.

[5] T. Zhao, D. R. Jackson, and J. T. Williams, "2-D periodic leaky-wave antennas—part II: slot design," *IEEE Transactions on Antennas and Propagation*, vol. 53, no. 11, pp. 3515–3524, 2005.

[6] P. Burghignoli, G. Lovat, F. Capolino, D. R. Jackson, and D. R. Wilton, "Highly polarized, directive radiation from a fabry-prot cavity leaky-wave antenna based on a metal strip grating," *IEEE Transactions on Antennas and Propagation*, vol. 58, no. 12, pp. 3873–3883, 2010.

[7] D. R. Jackson and A. A. Oliner, "Leaky-wave analysis of the high-gain printed antenna configuration," *IEEE Transactions on Antennas and Propagation*, vol. 36, no. 7, pp. 905–910, 1988.

[8] A. Ip and D. R. Jackson, "Radiation from cylindrical leaky waves," *IEEE Transactions on Antennas and Propagation*, vol. 38, no. 4, pp. 482–488, 1990.

[9] G. Lovat, P. Burghignoli, and D. R. Jackson, "Fundamental properties and optimization of broadside radiation from uniform leaky-wave antennas," *IEEE Transactions on Antennas and Propagation*, vol. 54, no. 5, pp. 1442–1452, 2006.

[10] P. Burghignoli, G. Lovat, and D. R. Jackson, "Analysis and optimization of leaky-wave radiation at broadside from a class of 1-D periodic structures," *IEEE Transactions on Antennas and Propagation*, vol. 54, no. 9, pp. 2593–2604, 2006.

[11] D. R. Jackson, P. Burghignoli, G. Lovat et al., "The fundamental physics of directive beaming at microwave and optical frequencies and the role of leaky waves," *Proceedings of the IEEE*, vol. 99, no. 10, pp. 1780–1805, 2011.

[12] H. Ostner, J. Detlefsen, and D. R. Jackson, "Radiation from one-dimensional dielectric leaky-wave antennas," *IEEE Transactions on Antennas and Propagation*, vol. 43, no. 4, pp. 331–339, 1995.

[13] P. Baccarelli, P. Burghignoli, F. Frezza, A. Galli, G. Lovat, and D. R. Jackson, "Approximate analytical evaluation of the continuous spectrum in a substrate-superstrate dielectric waveguide," *IEEE Transactions on Microwave Theory and Techniques*, vol. 50, no. 12, pp. 2690–2701, 2002.

[14] P. Baccarelli, P. Burghignoli, F. Frezza, A. Galli, G. Lovat, and D. R. Jackson, "Uniform analytical representation of the continuous spectrum excited by dipole sources in a multilayer dielectric structure through weighted cylindrical leaky waves," *IEEE Transactions on Antennas and Propagation*, vol. 52, no. 3, pp. 653–665, 2004.

[15] G. Lovat, P. Burghignoli, and D. R. Jackson, "An investigation of directive radiation from ultra subwavelength-thick planar antennas with partially-reflecting surfaces," in *Proceedings of the IEEE International Symposium on Antennas and Propagation and USNC/URSI National Radio Science Meeting (APSURSI '08)*, San Diego, Calif, USA, July 2008.

[16] G. Lovat, P. Burghignoli, and S. Celozzi, "A tunable ferroelectric antenna for fixed-frequency scanning applications," *IEEE Antennas and Wireless Propagation Letters*, vol. 5, no. 1, pp. 353–356, 2006.

[17] T. Zhao, D. R. Jackson, J. T. Williams, and A. A. Oliner, "Simple CAD model for a dielectric leaky-wave antenna," *IEEE Antennas and Wireless Propagation Letters*, vol. 3, no. 1, pp. 243–245, 2004.

[18] F. de Flaviis, N. G. Alexopoulos, and O. M. Stafsudd, "Planar microwave integrated phase-shifter design with high purity ferroelectric material," *IEEE Transactions on Microwave Theory and Techniques*, vol. 45, no. 6, pp. 963–969, 1997.

[19] E. A. Nenasheva, N. F. Kartenko, I. M. Gaidamaka et al., "Low loss microwave ferroelectric ceramics for high power tunable devices," *Journal of the European Ceramic Society*, vol. 30, no. 2, pp. 395–400, 2010.

[20] Q. Zhang, J. Zhai, and L. B. Kong, "Relaxor ferroelectric materials for microwave tunable applications," *Journal of Advanced Dielectrics*, vol. 2, 2012.

[21] P.-S. Kildal, Foundations of Antennas, Lund, Sweden, Studentlitteratur AB, 2000.

[22] C. A. Balanis, *Antenna Theory*, Wiley, Hoboken, NJ, USA, 3rd edition, 2005.

Research Article

Low SAR, Simple Printed Compact Multiband Antenna for Mobile and Wireless Communication Applications

K. S. Sultan, H. H. Abdullah, and E. A. Abdallah

Microstrip and Microwave Engineering Departments, Electronics Research Institute, 33 El Bohouth St., Dokki, Giza 12622, Egypt

Correspondence should be addressed to H. H. Abdullah; haythm_eri@yahoo.com

Simple multiband planar antenna for wireless communication applications is presented. The proposed antenna performs four resonant modes covering multibands of wireless standards, including LTE 700, GSM, DCS, PCS, UMTS, and LTE 2300/2500. Furthermore, it covers the ISM, WiMAX, and the WLAN bands. The geometry of the proposed antenna consists of a single FR4 substrate where an open cavity fed by a coplanar U-shaped monopole is etched on one side and a short-circuited meander line in the opposite side. The cavity by its nature supports a wide range of higher frequencies, while its boundary that consists of a thin monopole resonates at 900 MHz. The meander line in the opposite side supports the LTE 700 band. The operating bands ranges are (680–748 MHz), (870–960 MHZ), (1.36–1.59 GHz), and (1.71–2.56 GHz). The antenna size is $30 \times 18 \times 0.8 \, mm^3$. The antenna not only has a compact size but also supports a low SAR radiation at all the operating frequencies. The proposed antenna is tested using the four recommended test positions of the CTIA association where the proposed antenna reveals good performance in all test cases in the presence of handset (keypad, battery, speaker camera, RF circuit, and LCD) in talking position, and in standby position.

1. Introduction

With the vast increase of mobile services and with the introduction of compact electronics, there is a great demand for developing new low specific absorption rate (SAR) antenna with compact size that is compatible with the compact electronic components sizes. Also, the future development of the personal communication devices will aim to provide image, voice, and data communication at any time. This indicates that mobile devices are required to support different technologies and operate in different frequency bands. So, the LTE (long term evolution) is a new high-performance air interface standard for cellular mobile communication systems. It is the 4th generation (4G) of radio technologies to increase the capacity and speed of mobile telephone networks [1, 2].

Several studies have been performed to produce an antenna structure able to satisfy the demands of low SAR compact multiband antenna for use in hand-held devices [2–7]. Miniaturisation techniques with control circuits were introduced [3–6]; however, they had problems such as low antenna efficiency because of insertion loss in lumped elements, as well as an increased cost. Multilayer has been used for the multiband antenna method; however, they have certain disadvantages that cause high loss as well as high cost.

In order to include LTE bands, Guo et al. [5] introduced a new compact multiband antenna to cover GSM 900, DCS 1800, PCS 1900, UMTS 2100, and some LTE bands (FDD-LTE bands 1–6 and 8–10 and TDD-LTE bands 19, 20, and 33–37) with dimensions of $50 \times 15 \times 4 \, mm^3$. Also, Chen and Jhang [6] introduced a compact multiband antenna that consists of a direct-fed monopole with a chip inductor, a grounded strip, and a coupled-fed monopole with a distributed inductor and dimensions of $75 \times 10 \times 0.8 \, mm^3$. Recently, Elsheakh and Abdallah [8] introduced a new compact multiband printed inverted-F antenna (IFAs) with dimensions $35 \times 45 \, mm^2$ which covers GSM, LTE, UMTS, Bluetooth, and WLAN (at −6 dB).

In this paper, a new compact size, single layer planar antenna, is proposed. The new antenna has dimensions of

(a) Front view

(b) Back view

FIGURE 1: Geometry of the proposed antenna: (a) front view and (b) back view.
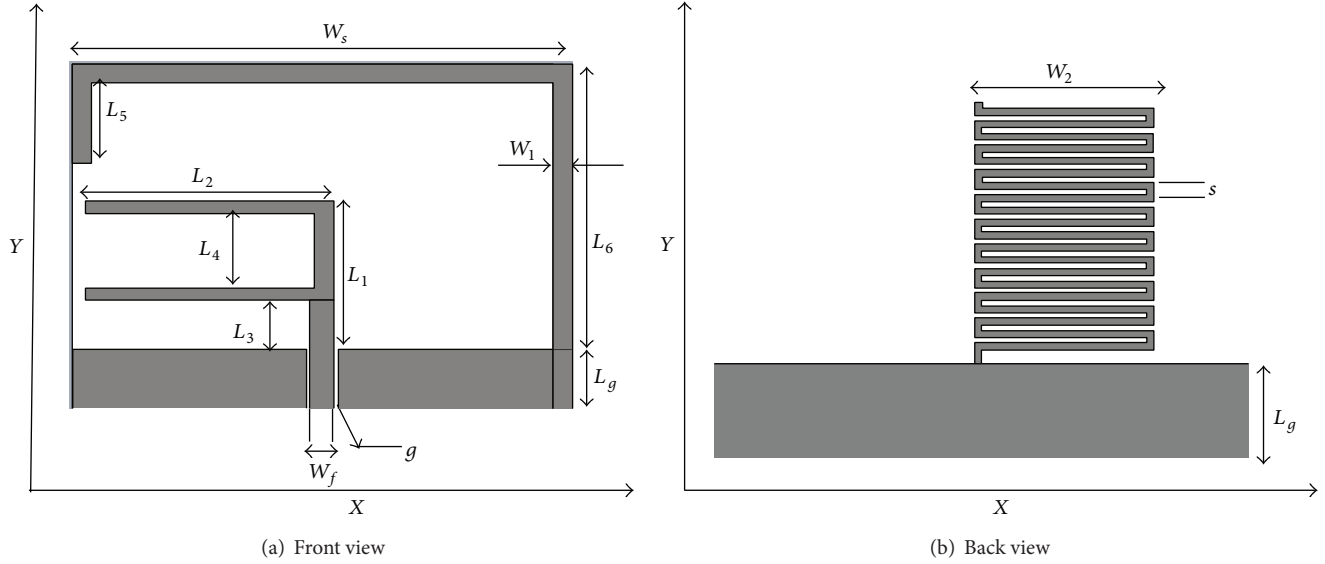
(a) Front view
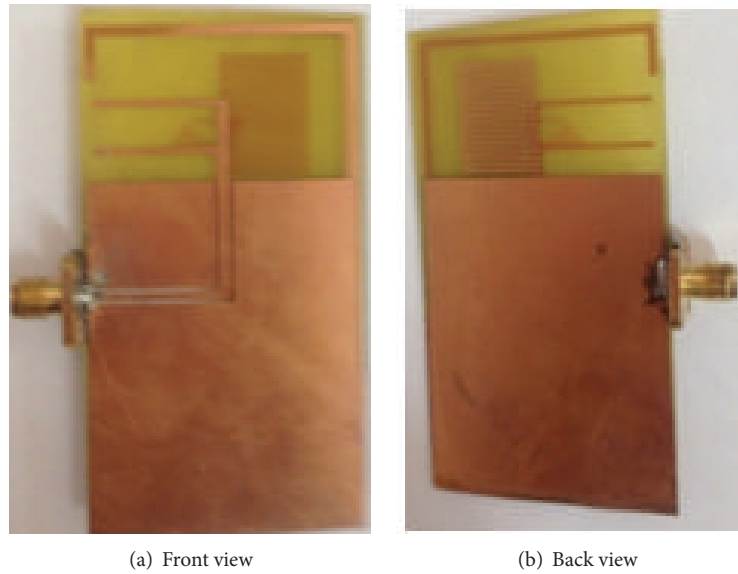
(b) Back view

FIGURE 2: Prototype of the proposed antenna: (a) front view and (b) back view.

$30 \times 18 \times 0.8 \, \text{mm}^3$. It covers the following operating bands; GSM 900, DCS 1800, PCS 1900, UMTS 2100, ISM 2450, almost LTE bands (FDD-LTE bands 1–4, 7–12, 15–17, and 23–25 and TDD-LTE bands 33–38), WiMAX (2.3-2.4 GHz, 2.5-2.56 GHz), and WLAN (2.4-2.5 GHz).

2. Antenna Design

The proposed antenna is a planar microstrip antenna with compact dimensions of $(30 \times 18 \times 0.8) \, \text{mm}^3$. So, the antenna can be easily integrated in small and sleek mobile device. Figure 1 shows the geometry of the proposed antenna. All the labeled dimensions are tabulated in Table 1. The proposed

antenna is designed over FR4 substrate ($\varepsilon_r = 4.5$) with 0.8 mm thickness and loss tangent of 0.025.

The antenna is composed of an open cavity excited by a U-shaped monopole fed in a coplanar way. The electrical length of the monopole is a quarter-wavelength at 2.1 GHz. The cavity radiates in the range from 1.71 GHz to 2.5 GHz. In order to support the GSM 900 application, the arm length of the cavity is designed to resonate at 900 MHz. The most challenging resonance is the LTE 700 which necessitates a long branch that consumes more area of the antenna. In order to overcome this problem a meander line is etched on the opposite side of the antenna where it is fed by aperture coupling. The meander line has the advantage of having long length in a very small area but at the expense

Table 1: Geometrical parameters of the proposed antenna.

Parameter	Value (mm)	Parameter	Value (mm)	Parameter	Value (mm)
L_1	10	L_5	6	W_f	1.5
L_2	17	L_6	18	W_s	30
L_3	3	W_1	1.5	g	0.25
L_4	5	W_2	9	s	0.9
L_g	5				

Figure 3: Measured and simulated reflection coefficient of the proposed antenna.

Figure 4: The effect of ground plane length against frequency.

Table 2: Gain and the radiation efficiency of the proposed antenna.

F (GHz)		0.7	0.9	1.8	2.1
Gain dBi	Simulated	2.1	1.8	2.3	2.7
	Measured	—	1.55	1.8	2.5
Radiation efficiency %	Simulated	69	74	78.2	79.6
	Measured	—	69	72.5	77.4

Table 3: Characteristics of the mobile parts.

Mobile parts	Material type	ε_r
LCD	LCD film	4.78
Battery	PEC	—
Rf circuit	PEC	—
Side key, function keys	Rubber	3.5
Camera	PEC	—
Speaker	PEC	—
Casing (housing)	PVC	2.8
PCB	FR4	4.5

of its high impedance which complicates the matching. This problem is solved by ending the meander line by a rectangular conducting slab connected to the ground.

Compared to the 3D structure of the PIFA antennas, the proposed antenna is via free antenna and has a simple structure that effectively reduces the manufacturing costs and complexity. A prototype of the antenna is fabricated as shown in Figure 2.

The proposed antenna was simulated using the CST Microwave Studio 2012. Figure 3 shows a comparison between the simulated and measured results of the reflection coefficient. The simulated and the experimental results ensure that the antenna covers all the aforementioned mobile and wireless applications bands. Taking the 6 dB return loss as a reference, the antenna operates in the four bands (680–748 MHz), (870–960 MHZ), (1.36–1.59 GHz), and (1.71–2.56 GHz) to cover GSM 900, DCS 1800, PCS 1900, UMTS 2100, ISM 2450, most LTE bands, WLAN, Bluetooth, and Wi-Fi. The ground plane on the lower part of PCB has an area of 30×50 mm^2, representing a typical system board of mobile terminals. The ground plane below the radiator is removed for coupling between the radiator and the meander line. The effect of ground plane is taken into consideration as shown in Figure 4. It is noticed that the length of ground plane affects the matching slightly. Figure 5 shows the measured and simulated radiation patterns at frequencies 0.9, 1.8, and 2.1 GHz in free space. Radiation pattern measurements were carried out using SATIMO Anechoic antenna chamber where the available frequency range starts from 0.8 GHz.

Table 2 shows the values of gain and radiation efficiency of the proposed antenna.

It is worth illustrating the degradation of the radiation pattern in presence of the human body model. As shown in Figure 6, the simulated radiation in the presence of the human body is directed away from the human body due to the high reflection of the head materials. Thus, the nature of the human body itself contributes to lowering the SAR within the human body.

3. Handset Modeling

The smart phone has a number of components besides the system circuit board and the antenna. Figure 7 shows mobile Samsung Galaxy SIII with standard dimensions ($136.6 \times 70.6 \times 8.6$ mm^3). The antenna is assembled with battery, camera, speaker, RF circuit, and touch screen LCD. The
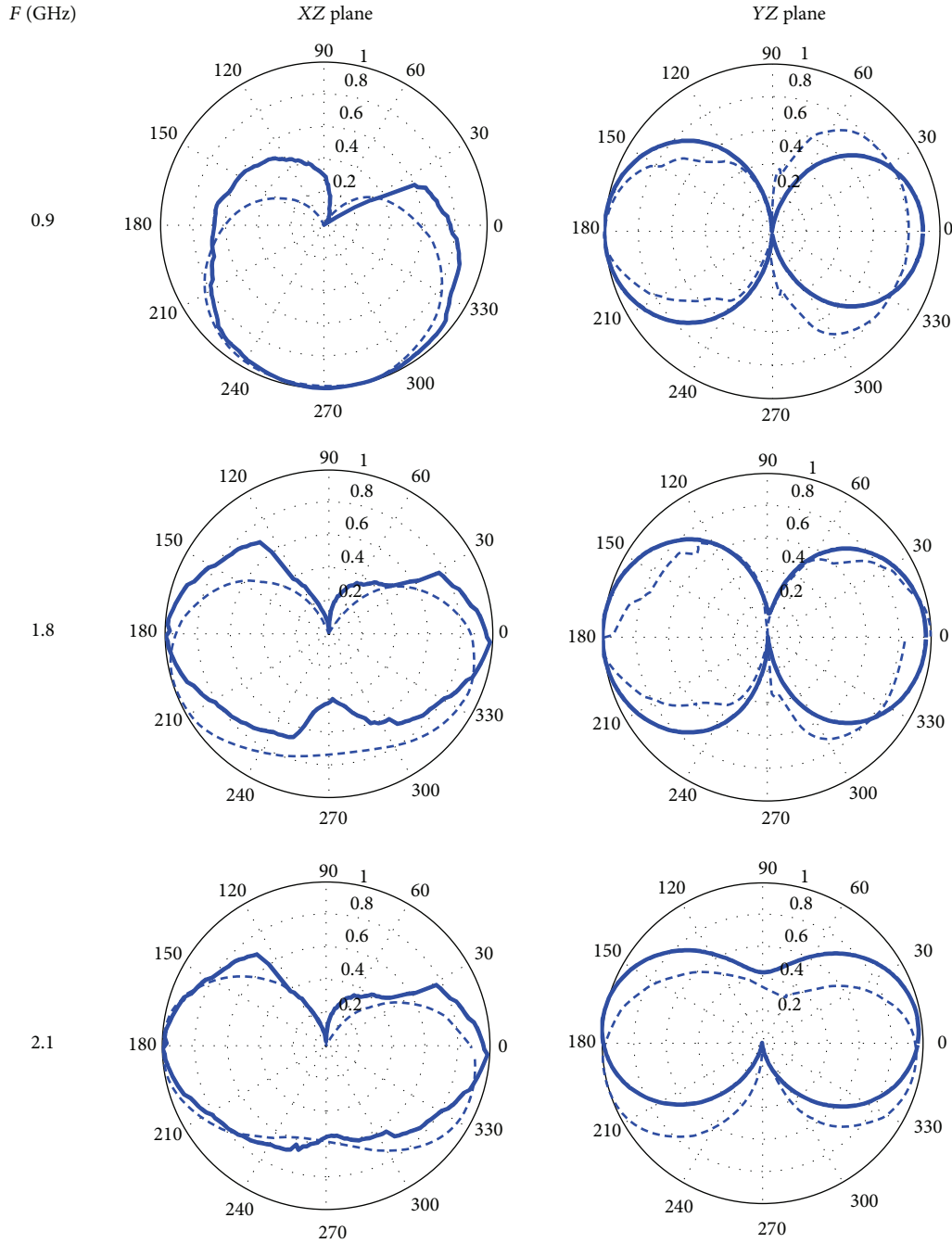
Figure 5: The radiation pattern in the *XZ* and *YZ* planes. The antenna is in the *XY* plane: simulated (solid line); measured (dash line).

housing of the mobile is a polyvinyl chloride material (PVC) with permittivity of 2.8 and loss tangent of 0.019 where the total dimensions of the mobile are $136.6 \times 70.6 \times 8.6$ mm^3 and its wall thickness is 1 mm. The camera has a diameter of 5 mm, and 4 mm thickness. Opposite to the camera is a speaker with the dimensions of 15 mm length and 6 mm width; a battery with volume $70 \times 50 \times 3$ mm^3 and a large touch LCD with size $110 \times 60 \times 2$ mm^3 are connected to the main circuit board

via connectors. Table 3 shows the characteristics of the mobile parts.

CTIA has proposed several body test cases for a mobile phone as shown in Figure 8, namely, mobile handset in free space, browsing mode, talking position, and talking position with hand [9]. Figure 9 shows the return loss of the antenna in the 4 different cases. The primary effect of the hand and head has little shift and degradation in the impedance matching.
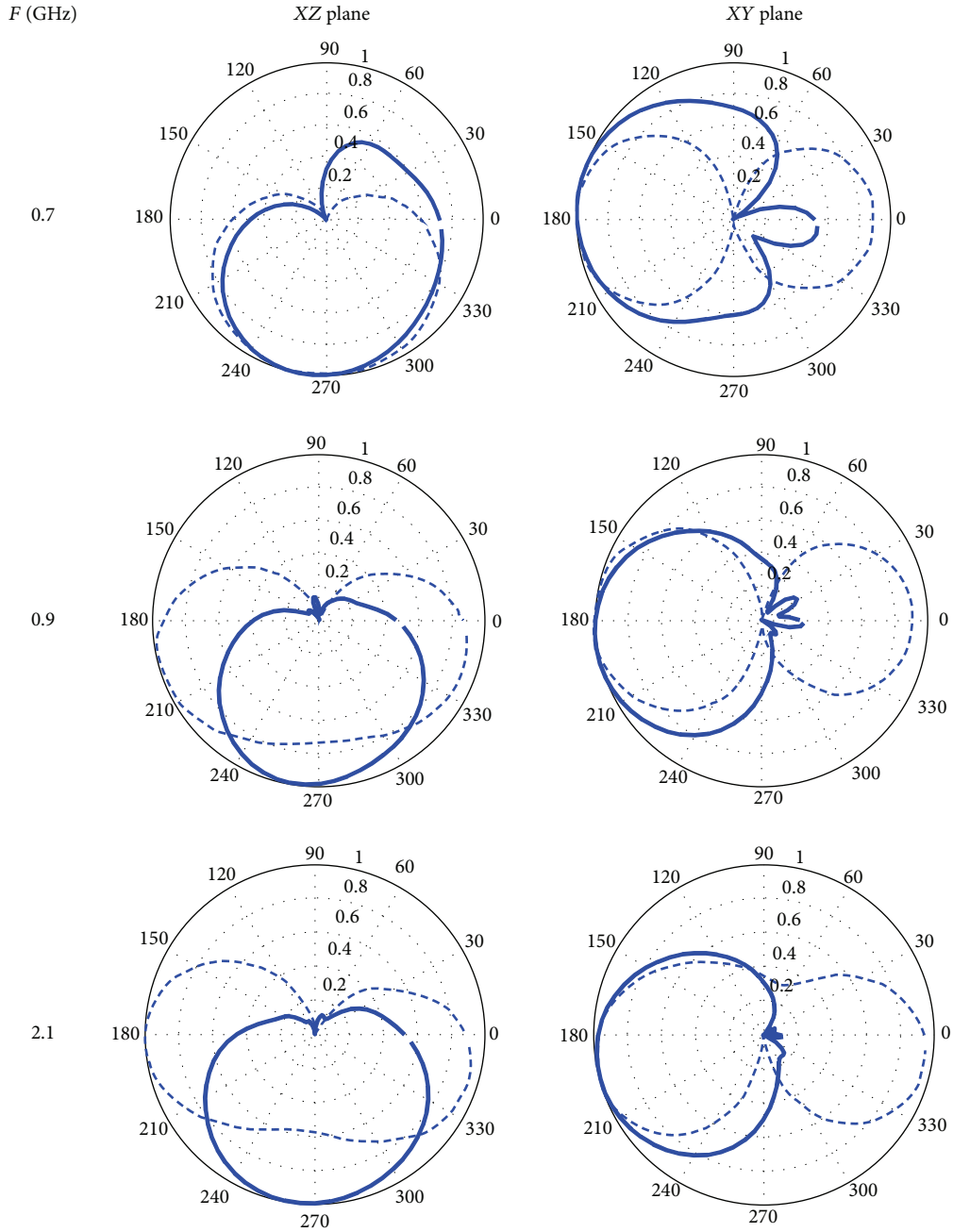
FIGURE 6: The simulated radiation pattern in the *XZ* and *XZ* planes. The antenna is in the *YZ* plane: without human body (Dash line); with human body (Solid line).

However, the impedance matching over the operating bands is still acceptable for practical applications of the mobile phone.

4. SAR Calculation

As the use of the mobile phone is increased, the research on the health risk due to the electromagnetic (EM) fields generated from wireless terminals is widely in progress. Many factors may affect the EM interaction while using cellular handset in close proximity to head and hand. One of the most widely used parameters for the evaluation of exposure is SAR, specific absorption rate. Therefore, some regulations and standards have been issued to limit the radiation exposure from the mobile handsets not only to decrease the SAR but also to increase the antenna systems efficiency. The SAR limit specified in IEEE C95.1-2005 has been updated to 2 W/kg over any 10 g of tissue [10], which is comparable to the limit specified in the International Commission on Non-Ionizing Radiation Protection (ICNIRP) guidelines [11].

(a) Front view   (b) Back view   (c) Side view
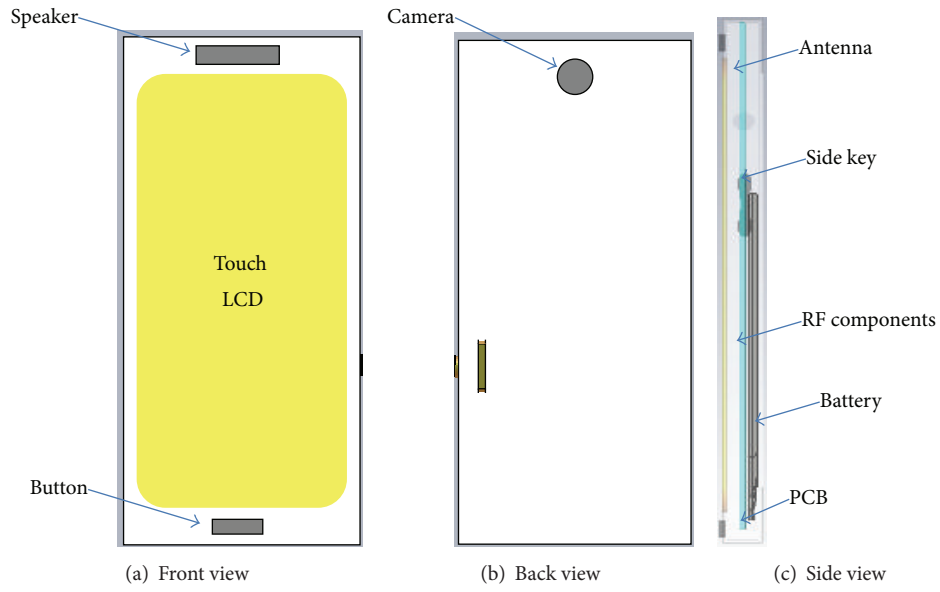
Figure 7: Structure of mobile handset: (a) front, (b) back, and (c) side view.

(a)   (b)

(c)   (d)
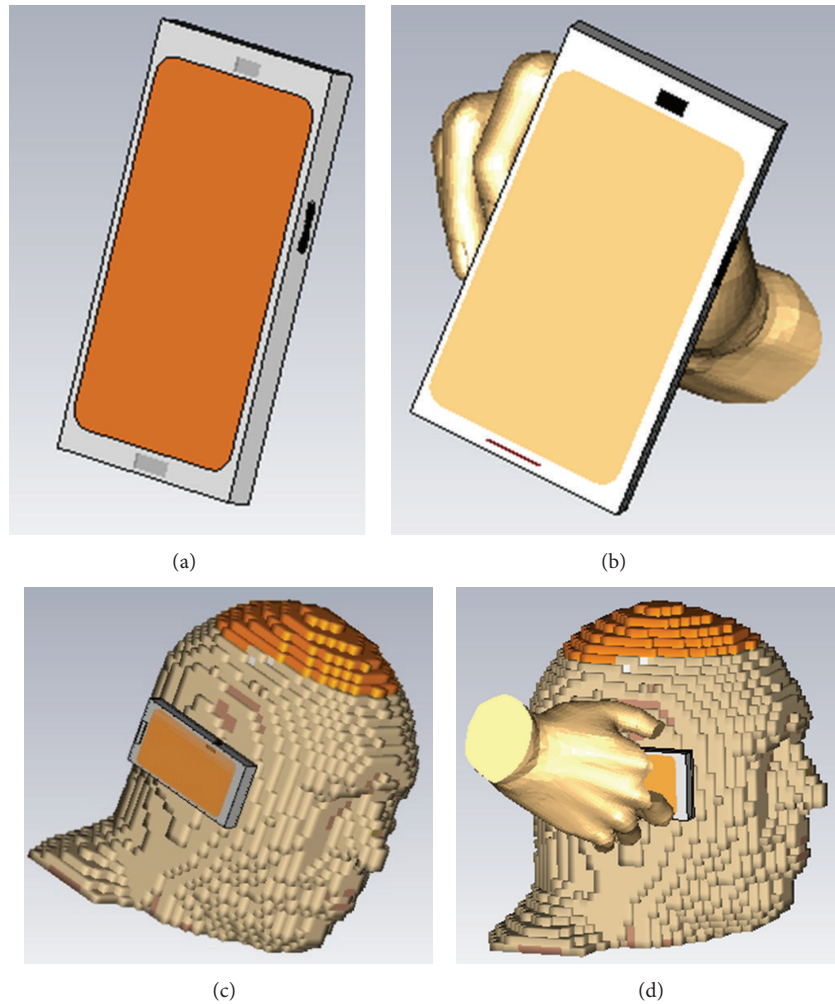
Figure 8: CTIA-defined four different test positions: (a) free space, (b) browsing mode, (c) talking position, and (d) talking position with hand.

TABLE 4: SAR values and the effects of human model on antenna properties.

F (GHz)	SAR (W/kg) (10 g)	In free space		With human model	
		$|S_{11}|$ (dB)	Radiation efficiency (%)	$|S_{11}|$ (dB)	Radiation efficiency (%)
0.7	0.98	−17	69	−15.5	66.5
0.9	0.93	−29.5	74	−29	70.6
1.8	0.80	−8	78.2	−7.2	72.8
2.1	1.2	−10	79.6	−9.4	73.3
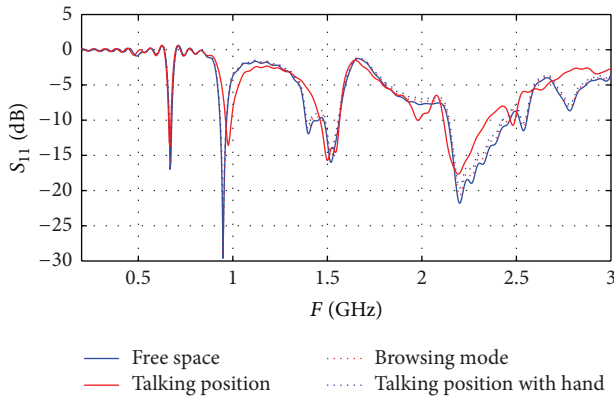
FIGURE 9: The simulated return loss of antenna in mobile handset in four different test positions.
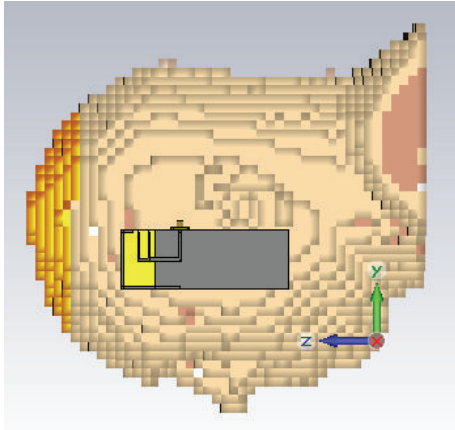
FIGURE 10: Antenna structure with the human head model (Hugo voxel model).

In this paper, The SAR calculations on human head model are done in the presence of the antenna in the ZY plane as shown in Figure 10. The SAR is tested at 0.7, 0.9, 1.8, and 2.1 GHz when the antenna is close to the human head and the output power of the cellular phone is set to 500 mW. The SAR calculations are done using the CST 2012 commercial package with Hugo model CST Microwave Studio [12]; the tissues that are contained have relative permittivities and conductivities, according to [13]. The tissues frequency dispersive properties are taken into consideration.

Table 4 shows the maximum SAR at the aforementioned operating frequencies when the antenna is close to the body;

the radiation efficiency and S_{11} are also shown in Table 3 in free space and with human model.

5. Conclusion

A new compact planar antenna design that supports all of the operating mobile services, ISM applications, and wireless communication services is introduced. The SAR values of the antenna satisfy the standard safety guidelines. The antenna has more compact size when compared to other published antennas. The antenna was simulated using the CST simulator and fabricated using the photolithographic technique. Very good agreement is obtained between the simulated and the experimental results.

Conflict of Interests

The authors declare that there is no conflict of interests regarding the publication of this paper.

Acknowledgment

References

[1] S. Sesia, I. Toufik, and M. Baker, *LTE—The UMTS Long Term Evolution: From Theory to Practice*, Wiley, Chichester, UK, 2009.

[2] R. A. Bhatti, S. Yi, and S. Park, "Compact antenna array with port decoupling for LTE-standardized mobile phones," *IEEE Antennas and Wireless Propagation Letters*, vol. 8, pp. 1430–1433, 2009.

[3] K.-L. Wong, Y. C. Lin, and B. Chen, "Internal patch antenna with a thin air-layer substrate for GSM/DCS operation in a PDA phone," *IEEE Transactions on Antennas and Propagation*, vol. 55, no. 4, pp. 1165–1172, 2007.

[4] M. Martínez-Vázquez, O. Litschke, M. Geissler, D. Heberling, A. M. Martínez-González, and D. Sánchez-Hernández, "Integrated planar multiband antennas for personal communication handsets," *IEEE Transactions on Antennas and Propagation*, vol. 54, no. 2, pp. 384–391, 2006.

[5] Q. Guo, R. Mittra, F. Lei, Z. Li, J. Ju, and J. Byun, "Interaction between internal antenna and external antenna of mobile phone and hand effect," *IEEE Transactions on Antennas and Propagation*, vol. 61, no. 2, pp. 862–870, 2013.

[6] W. S. Chen and W. C. Jhang, "A planar WWAN/LTE antenna for portable devices," *IEEE Antennas and Wireless Propagation Letters*, vol. 12, pp. 19–22, 2013.

[7] K. S. Sultan, H. H. Abdullah, E. A. Abdallah, and E. A. Hashish, "Low SAR, miniaturized printed antenna for mobile, ISM, and WLAN service," *Antennas and Wireless Propagation Letters*, vol. 12, pp. 1106–1109, 2013.

[8] D. Elsheakh and E. Abdallah, "Compact multiband printed IFA on electromagnetic band-gap structures ground plane for wireless applications," *International Journal of Microwave Science and Technology*, vol. 2013, Article ID 248501, 9 pages, 2013.

[9] CTIA Certification Department Program, Test Plan for Mobile Station over the Air Performance Method of Measurement for Radiated RF Power and Receiver Performance, http://www.ctia.org/.

[10] IEEE C95.1-2005, *IEEE Standards for Safety Levels with Respect to Human Exposure to Radio Frequency Electromagnetic Fields, 3 kHz to 300 GHz*, Institute of Electrical and Electronics Engineers, New York, NY, USA, 2005.

[11] International Non-Ionizing Radiation Committee of the International Radiation Protection Association, "Guidelines on limits on exposure to radio frequency electromagnetic fields in the frequency range from 100 kHz to 300 GHz," *Health Physics*, vol. 54, no. 1, pp. 115–123, 1988.

[12] "CST Microwave Studio Suite 2011 User's Manual," http://www.cst.com.

[13] S. Gabriel, R. W. Lau, and C. Gabriel, "The dielectric properties of biological tissues: II. Measurements in the frequency range 10 Hz to 20 GHz," *Physics in Medicine and Biology*, vol. 41, no. 11, pp. 2251–2269, 1996.

Research Article

Antenna Miniaturization with MEMS Tunable Capacitors: Techniques and Trade-Offs

Samantha Caporal Del Barrio,[1,2] Art Morris,[2] and Gert F. Pedersen[1]

[1] *Section of Antennas, Propagation and Radio Networking (APNet), Department of Electronic Systems,*
  Faculty of Engineering and Science, Aalborg University, Denmark
[2] *WiSpry Inc., 20 Fairbanks, Suite 198, Irvine, CA 92618, USA*

Correspondence should be addressed to Samantha Caporal Del Barrio; scdb@es.aau.dk

In today's mobile device market, there is a strong need for efficient antenna miniaturization. Tunable antennas are a very promising way to reduce antenna volume while enlarging its operating bandwidth. MEMS tunable capacitors are state-of-the-art in terms of insertion loss. Their characteristics are used in this investigation. This paper uses field simulations to highlight the trade-offs between the design of the tuner and the design of the antenna, especially the impact of the location of the tuner and the degree of miniaturization. Codesigning the tuner and the antenna is essential to optimize radiated performance.

1. Introduction

With their increasing functionality, mobile phones are embedding better screens, better cameras, larger batteries, and more antennas, among others. In order to keep the portability of such device, a very high degree of integration is required. Chipset miniaturization has seen a large success over the last years [1]; however, antenna volume is ruled by fundamental laws [2] that relate size, efficiency, and bandwidth. To support the latest mobile communication standards, long-term evolution (LTE), and LTE-advanced (LTE-A), the antennas need to operate in frequency bands ranging from 698 MHz to 2.690 GHz. In order to maintain good performance throughout such a large bandwidth with a conventional design, the antenna volume must be increased.

Nowadays, the most common types of antenna designs for mobile phones are classified into two categories: self-resonating elements and nonresonating elements (also known as capacitive coupling elements). Self-resonating multiband antennas can cover several bands simultaneously. Literature reports a coverage up to 9 simultaneous bands. These antennas are space consuming as the antenna volume increases nearly linearly with the number of bands supported.

For example, [3] occupies a volume of 4.6 cc to cover all GSM bands, the antenna presented in [4] covers the GSM, DCS, PCS, and UMTS bands in a volume of 1.9 cc, and [5] needs about 7 cc to also include GPS, Bluetooth, WLAN, AMPS, and DVB-H bands. Nonresonating antennas exhibit a lower profile and exploit the ground plane modes to obtain a large bandwidth. Hence, covering the lowest LTE band is possible. However, this type of antennas typically uses several matching components at the feed, which affects the total efficiency. For example, [6] covers down to 700 MHz in 2.5 cc, but with a total efficiency dropping to 55%. Additionally, nonresonating antennas fully utilize the ground plane, which complicates decoupling, required for the multiple-input multiple-output (MIMO) technique in LTE and LTE-A.

Modern phones have antennas that exhibit a very low profile, at the cost of their performance. The investigation in [7] shows total radiated power (TRP) and total isotropic sensitivity (TIS) values in the presence of hand and head phantoms, for popular smart-phones in 2012. For example, TRP ranges from 16.6 dBm to 20.1 dBm in the GSM-900 band. Before 2000, handsets with a patch antenna performed with TRP values of about 26 dBm [8], in the presence of a user for GSM-900. Today's phones exhibit poor antenna efficiency, it

can be as low as −7.7 dB [9] in free space. This phenomenon is due to the ever increasing number of bands to cover the constrained space available for the antenna. It has led to antenna designs exhibiting a wide but mismatched antenna impedance [9]. Efficient miniaturization has not happened yet in commercial devices.

To address the bandwidth-size challenge of modern antennas, tunable antennas are investigated. They use a tunable component in order to reconfigure their resonance frequency. These antennas exhibit an instantaneous narrow bandwidth, that can be reconfigured to a wide range of frequencies, thus resulting in an effectively wide bandwidth. As the antenna is designed for a narrow bandwidth, it can have a very low profile. In the architecture proposed in [10], the antenna only needs to cover a channel (maximum 20 MHz in LTE and LTE-A). Exploiting the narrow-band property of tunable antennas, very compact designs can be made. In [10], the radiators only occupy 1.0 cc and cover operating bands between 600 MHz and 2.1 GHz. Tunable antennas have a tremendous potential for miniaturization.

The performance of tunable antennas is tested over-the-air [11] and relies on an efficient codesign of the radiator and the tuner. The objective of this paper is to investigate the trade-offs and the requirements between the antenna designers and the tuner designers. Codesigning the antenna and the tuner is essential to manufacture small and efficient tunable antennas. Section 2 compares the different tuning technologies. Section 3 describes the impacts of the location of the tuner on the antenna design. Section 4 investigates the requirements on the tuner for different levels of miniaturization. Finally, Section 5 discloses the conclusions.

2. Tuning Elements

Because reconfiguring the resonance frequency of an antenna allows to extend its operating bandwidth without modifying its physical size, tunable antennas are very promising to address the antenna miniaturization challenge. There are several components that can be used to tune the resonance frequency of an antenna. To name the most common ones, there are switched capacitors, tunable substrates, and micro-electromechanical Systems (MEMS).

The switching approach combines a single-pole-multiple-throw (SPnT) switch and a bank of capacitors to choose from. It uses most commonly field effect transistors (FET) which leads to an intrinsically low breakdown voltage and power handling, limiting its application to mobile communication standards [12]. PIN diodes can handle more power; however, they exhibit a higher insertion loss, a smaller tuning range, and a higher power consumption [13].

Tunable substrates (also known as paraelectric solutions) provide variable capacitance without the need for a FET switch, thus increasing the quality factor (Q) of the component. It uses barium strontium titanate (BST) which causes the design to have issues with linearity.

In the mechanism of MEMS tunable capacitors, an electrostatic force actuates a beam. When the beam is down, only dielectric separates it from the metal trace below it and
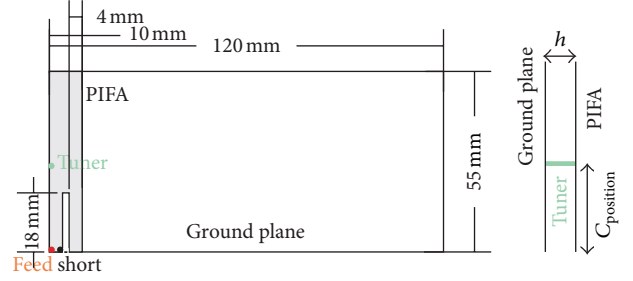
FIGURE 1: Antenna design used to investigate the impact of C_{position}.

the capacitor is *on*. When the beam is up, an additional air gap separates the beam from the metal trace and the capacitor is *off* [12]. With this architecture, the RF path is a metal trace. Therefore, MEMS capacitors offer significantly higher Q and linearity than the previous solutions. Additionally, the structure of the component allows for the handling of higher voltages. Tunability can also be realized using varactors, as in [14–17]. However, the limit on maximum achievable capacitance and the high bias voltage requirements reduce the flexibility of such tuning technique.

MEMS tunable solutions are state-of-the-art in terms of insertion loss and power consumption. The following investigations are made considering that the tuner is a MEMS tunable capacitor. More specifically, a commercially available tuner is used [18] that exhibits a tuning range from 1 pF to 4.875 pF with steps of 125 fF.

3. Tuner Location Trade-Offs

In order to reconfigure the resonance frequency of an antenna, one can choose to place a tuner at different locations. These locations depend on the antenna type and the tuning objectives. In the case of antennas based on wideband coupling elements, the tuner is typically placed at the feed to match the antenna to different operating frequencies simultaneously [6, 19–21] or instantaneously [22–25]. Frequency reconfigurability can also be achieved by loading the antenna structure itself [26–28] or by placing the tuner between the antenna element and the ground plane [29–35]. The latter is the most common use of tunable MEMS capacitors; therefore, this placement will be used for the following investigation. The following is illustrated with a low-band design.

3.1. Simulation Results. The antenna design described in Figure 1 is chosen for this investigation. Simulations are conducted with the transient solver, based on finite-element method (FEM), of the CST software [36]. It is a typical planar-inverted-F antenna (PIFA) for mobile phone application and addresses the low-bands of LTE, 698 MHz to 960 MHz. The position of the tuner (C_{position}) is given in mm away from the feed, at the edge of the antenna and the ground plane. The instantaneous bandwidth of the antenna is determined by the height of the PIFA above the ground plane (h). When $h = 2$ mm, the bandwidth of the antenna, at −6 dB return loss, equals 34 MHz, centered in 960 MHz. The initial resonance

FIGURE 2: Antenna tuning, with tuner placed in $C_{position}$ = 20 mm.

TABLE 1: Trade-offs due to location of the tuner.

$C_{position}$ [mm]	5	10	15	30	55
f_r [MHz]	700	700	700	700	700
L_{ins} [dB]	3	3	3	3	3
ESR_{max} [Ω]	0.41	0.58	0.80	1.13	1.48
V_{tuner} [V]	30	41	53	80	97
C_{step} [pF]	0.9	0.6	0.4	0.2	0.1
C_{max} [pF]	11.4	7.2	4.8	2.7	1.9

FIGURE 3: Low-band demonstrator, tuner placed in $C_{position}$ = 10 mm. The tuner has a minimum capacitance of 1 pF and a maximum capacitance of 4.875 pF.

frequency of the proposed design is 960 MHz, as it is the high bound of the low bands of 4 G. Tuning enables it to cover the 261 MHz required for LTE, as shown with the simulations of Figure 2. This design uses a tunable capacitor placed at the position $C_{position}$ = 20 mm, providing varying capacitance from 1 pF to 4.875 pF.

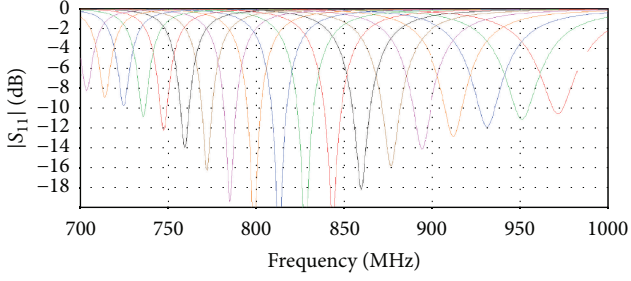The location of the tuner on the antenna structure has an impact on the specifications required for the MEMS tunable capacitor, that is, insertion loss (L_{ins}), voltage across the tuner (V_{tuner}), tuning step (C_{step}), and maximum capacitance (C_{max}). The insertion loss of the tuner depends on its maximum equivalent series resistance (ESR_{max}) and the current that flows to it.

In this investigation, it has been set that the efficiency should be better or equal to 50% throughout the operable bandwidth. This means that L_{ins} = 3 dB at 700 MHz, low bound of 4 G bands. Indeed, the antenna radiation efficiency degrades as it is tuned further away from its original resonance frequency. That is because higher fields concentrate around the antenna structure, inducing larger currents to the capacitor. Therefore, larger currents to the ESR of the capacitor cause higher loss. Hence, the lowest efficiency is observed at the lowest operating frequency of the tunable antenna. With L_{ins} = 3 dB at 700 MHz, L_{ins} will be equal to 2 dB at 800 MHz and 1 dB at 900 MHz.

In order to demonstrate the trade-offs linked to the position of the tuner on the antenna, different locations of the tuner are simulated and compared. The position of the tuner varies in arbitrary steps from 5 mm away from the feed (high current location) to 55 mm away from the feed (high voltage location). The antenna is continuously tuned from 960 MHz to 700 MHz. The requirements on the tuner, depending on its location, are summarized in Table 1, for 700 MHz, where the requirements are the toughest, since the fields are the highest. It is observed that the requirements on V_{tuner} and C_{step} are toughened as the tuner is placed further away from the feed. Similarly, the requirements on the C_{max} and ESR_{max} are toughened as the tuner is placed closer to the feed. Indeed, as $C_{position}$ decreases, the current flowing to the capacitor increases and the ESR of the tuner dissipates more power. Thus, it needs to be smaller to keep the efficiency at 50%. One can notice that the impact of the tuner location on the tuner design is significant, as its requirements on V_{tuner} and ESR_{max} are nearly quadrupled, and its requirements on C_{step} are nearly ten times toughened. Moreover, if

the V_{tuner} allows it, the most efficient location for a tuner is the furthest from the feed, as the power dissipation due to the ESR will be minimized. Therefore, this location is used for the investigation of Section 4. The achievable bandwidth only varies by 1 MHz, depending on the different locations of the tuner.

3.2. Measurement Results. A demonstrator of the presented antenna is built and shown in Figure 3. The tuner was placed at $C_{position}$ = 10 mm due to schematic limitations on the demonstrator board. This position only allows for the tuning of the antenna to 800 MHz, with a tuner exhibiting 4.875 pF tuning range. Continuous tuning is shown in Figure 4. The demonstrator was measured in Satimo StarLab and exhibited a total efficiency (η_T) of −2.0 dB at 900 MHz and −3.2 dB at 800 MHz. The η_T includes mismatch loss and 0.8 dB of trace loss. Improvements in the ESR will directly improve the measured η_T.

4. Antenna Miniaturization Trade-Offs

4.1. Theory. The antenna quality factor (Q_{ant}) is a measure that can be translated into antenna volume, stored energy, or bandwidth. These relations are detailed in [37]. In order to understand the trade-offs of miniaturization, one needs to understand the consequences of decreasing antenna volume on the Q_{ant}.

Q_{ant} relates to volume as follows [38]:

$$Q_{ant}(\omega) = \left(\frac{1}{(ka)^3} + \frac{1}{ka} \right), \tag{1}$$

--- No MEMS

..... MEMS connected

— MEMS tuning
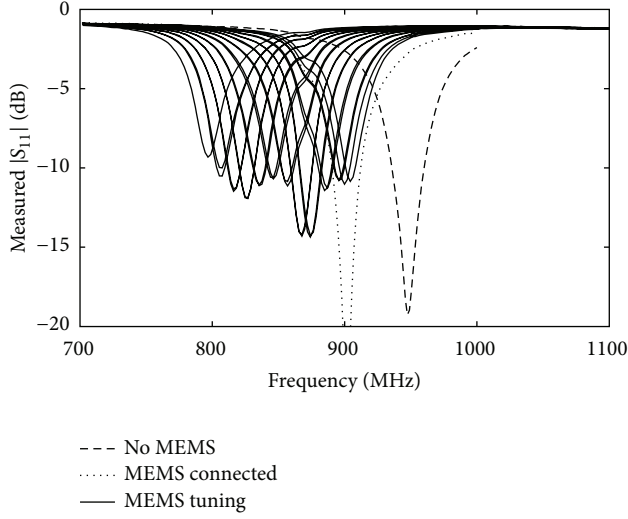
FIGURE 4: Measured frequency response of the demonstrator shown in Figure 3, with C_{max} = 4.875 pF and C_{step} = 125 fF.

where a is the radius of an imaginary sphere circumscribing the maximum dimension of the antenna and k is the wave number. As the volume occupied by the antenna decreases the Q_{ant} increases, at a given angular frequency (ω). The Q_{ant} is also related to the instantaneous bandwidth of the antenna, for single resonance antennas. The relationship between Q_{ant} and fractional bandwidth (FBW) is [37]

$$Q_{ant}(\omega) = \frac{2\sqrt{\beta}}{\text{FBW}_{\text{VSWR}}(\omega)}, \qquad \sqrt{\beta} = \frac{s-1}{2\sqrt{s}}, \qquad (2)$$

where FBW_{VSWR} is the FBW matched to a voltage standing wave ratio (VSWR) and s is the specific value of the VSWR. The antenna bandwidth is inversely proportional to Q_{ant}. Thus, the volume is proportional to the antenna bandwidth. That is to say, when the antenna volume decreases, the bandwidth does as well. Finally, the Q_{ant} is also a measure of the stored energy (W) in the antenna structure versus the accepted power (P_A) [37]

$$Q_{ant}(\omega) = \frac{\omega |W(\omega)|}{P_A(\omega)}. \qquad (3)$$

Therefore, the larger the Q_{ant}, the larger the stored energy. Thus, larger fields are confined in the antenna structure. Consequently, larger currents and voltages flow to the tuner, impacting insertion loss and voltage handling. To sum up, as the antenna becomes smaller, its bandwidth decreases and the tuning capacitor needs to have better characteristics in order to cope with the increased fields.

*4.2. Example.* The above is illustrated using a high-band design to emphasize how small an antenna can get. In the following, a design addressing band 41 [2.496 GHz–2.690 GHz] will be presented and used for the miniaturization investigation. The antenna is placed on a 120 mm × 55 mm ground plane and its geometry is described in

TABLE 2: Antenna geometry.

Parameters [mm]	D0	D1	D2	D3	D4
L	10	3.8	3.8	4.8	7.5
H	2.0	5.0	4.0	3.0	1.0
W	5.0	5.0	5.0	2.0	1.0
w	5.0	2.0	2.0	2.0	1.0
h	1.0	1.0	1.0	1.0	1.0
d	4.0	1.5	1.0	1.0	0.6
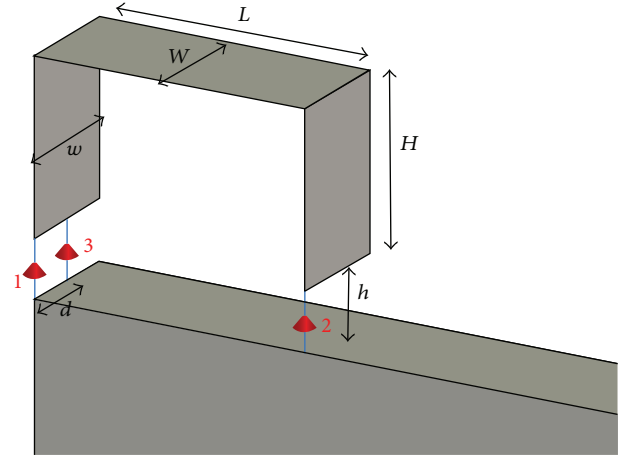
FIGURE 5: High-band antenna design.

Figure 5. Simulations are conducted using the transient solver of CST [36]. Three ports are placed on the antenna, where port 1 represents the feed, port 2 presents the tuner, and port 3 presesnts the short. The tuner is placed the furthest form the feed, given the results of Section 3. The design is modified in order to have four different models with four different initial bandwidths. The width of the top plate (W) and its height (H) are the main parameters controlling the bandwidth of the antenna, that is, Q_{ant}. The length parameter (L) varies accordingly, in order to adjust the initial resonance to 2.690 GHz. Five antenna designs are simulated (D0–D4), with initial bandwidths varying from 168 MHz to 32 MHz. The geometry required for each of these cases is described in Table 2. The characteristics of the five designs are summarized in Table 3, especially the volume, the bandwidth at the high bound of band 41 ($\text{BW}_{2.7\text{GHz}}$), and the bandwidth at 2.400 GHz ($\text{BW}_{2.4\text{GHz}}$). Implementing tuning allows to have tremendously small antenna designs; for example, D4 is ten times smaller than D1 and still cover the required band with tuning.

All four designs are tuned to 2.400 GHz. As the antenna becomes narrow-band, that is, smaller, it will store higher fields and impact the L_{ins} and V_{tuner}. In order to maintain 50% total efficiency at 2.400 GHz, the ESR_{max} needs to decrease as the bandwidth decreases. D4 occupies 1/10 of the volume of D1 and needs an ESR_{max} four times smaller. Simultaneously, the V_{tuner} needs to increase as the antenna becomes smaller. D4 requires a V_{tuner} three times larger. The results are summarized in Table 4. Both the antenna volume and the ESR

Table 3: Design characteristics.

	D0	D1	D2	D3	D4
Volume [cc]	0.15	0.11	0.09	0.04	0.01
$BW_{2.7GHz}$ [MHz]	168	118	78	62	32
$BW_{2.4GHz}$ [MHz]	119	84	61	46	23

Table 4: Tuner requirements.

	D0	D1	D2	D3	D4
f_r [GHz]	2.400	2.400	2.400	2.400	2.400
L_{ins} [dB]	3	3	3	3	3
ESR_{max} [Ω]	4.5	3.2	2.5	1.5	0.8
V_{tuner} [V]	10	10	10	17	31

Table 5: Q comparisons at 2.400 GHz.

	D0	D1	D2	D3	D4
Q_{ant}	16	23	25	47	97
Q_{MEMS}	35	35	45	75	142

of the tuner can be expressed in terms of Q values. Q_{ant} is calculated using (2). It is the unloaded Q_{ant}, meaning that it is calculated based on a lossless simulation. Table 5 compares the Q values between the antenna design and the MEMS capacitor design leading to 3 dB L_{ins}. The Q_{MEMS} is calculated as detailed in (4), where C is the capacitance. It is observed that the ratio between Q_{MEMS} and Q_{ant} leading to 50% total efficiency is nearly constant and equals 1.5

$$Q_{MEMS}(\omega) = \frac{1}{\omega \times C \times ESR}. \tag{4}$$

4.3. Measurements

(1) High-Band Tuning. A demonstrator is built for the design D0, as it is shown in Figure 6. The dimensions of the board are 120 mm × 55 mm. In practice, the antenna is soldered directly on the feeding pad of the board; therefore, $h = 0$ mm. The tuner is a MEMS tunable capacitor [18] and it is connected to the antenna from the other side of the board. In order to deal with the small minimum capacitance (C_{min}) required for the proposed designed, a series capacitor is placed between the antenna and the tuner according to the schematics depicted in Figure 7. The series capacitor has a value of 0.6 pF, which decreases the C_{min} from 1 pF (original value for the commercial tuner) to 0.375 pF. Moreover, the addition of the series capacitor decreases V_{tuner}.

Continuous tuning from 2.7 GHz (high bound of 4 G) to 2.4 GHz (WiFi) is shown in Figure 8. On can see that, as the antenna is tuned further away from its natural resonance frequency, the tuning steps are reduced. This is due to the insertion of the series capacitor. The η_T of the demonstrator was measured with 3D-pattern integration tehnique using Satimo StarLab. The results are shown for three tuning stages in Figure 9. Due to the low Q_{ant} (wide bandwidth) and the position of the tuner (furthest from the feed), fields strength
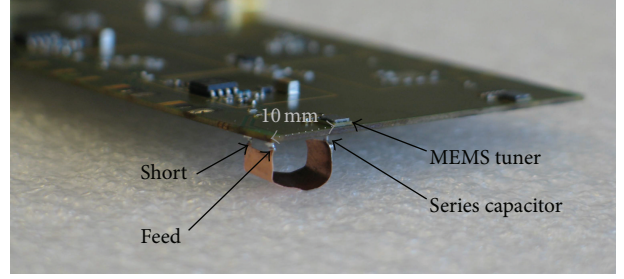
Figure 6: High-band demonstrator.
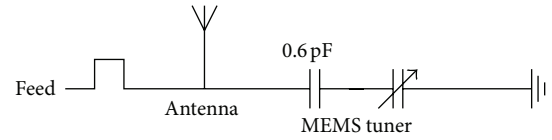
Figure 7: Schematic of the high-band demonstrator.

is kept low and the demonstrator is efficient. Moreover, the efficiency remains quasiconstant throughout tuning: −2.0 dB to −2.5 dB. It includes mismatch loss and trace loss on the board (0.8 dB).

(2) Miniaturization. Using the design techniques of the above-presented antennas, a new design is built to address the low bands of 4 G. This design is identical to D0, except for H that is equal to 10 mm instead of 5 mm. The electrical dimensions of the antenna are electrically small. At 700 MHz, the maximum antenna dimension (10 mm) represents 1/42th of the wavelength. This experiment tests the limitations of miniaturization.

Given the tuner properties (tuning range from 1 pF to 4.875 pF [18]), an additional fixed capacitor is placed in series with the tuner, in order to have enough capacitance to reach 700 MHz. The schematic is shown in Figure 10.

The demonstrator is shown in Figures 11 and 12. The antenna volume is 0.5 cc for operation in the low LTE bands. The frequency reconfigurability of the antenna is plotted in Figure 13 and shows continuous tuning from 940 MHz to 700 MHz. With the operating frequencies being very far from the natural resonance frequency of the antenna design, the unloaded Q_{ant} is very large. It is simulated to be larger than 300, which means that the antenna is very sensitive to the insertion loss of the tuner. The demonstrator is measured in the Satimo StarLab and η_T is computed with 3D-pattern integration technique. The results are shown in Figure 14 for three different tuning stages. The η_T includes the mismatch loss (less than 0.5 dB) and the loss of the traces in the board (0.8 dB). Efficiency degradation is observed as the antenna is tuned towards lower frequencies. For the lowest operating frequencies, the η_T reaches −11 dB. The limitation of miniaturization with tuners is the achievable efficiency of the system. The cause of loss is twofold: the metal loss due to nonperfect conductor (copper) and the ESR loss due to increasing Q_{ant} and field strength around the tuner, thus currents in the ESR. The net ESR of the tuner and interconnects used on the board
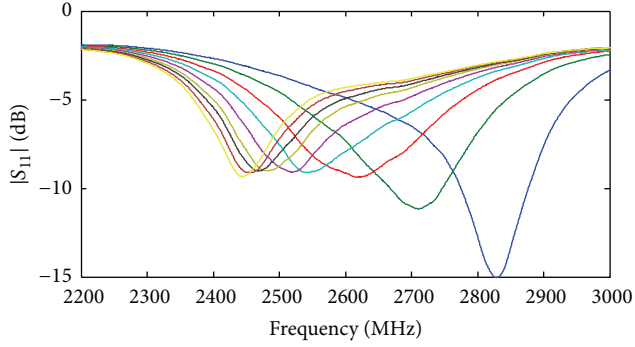
Figure 8: Measured tuning range of the demonstrator in Figure 6.

— $C = 1.5\,\text{pF}$
— $C = 2.5\,\text{pF}$
— $C = 4\,\text{pF}$
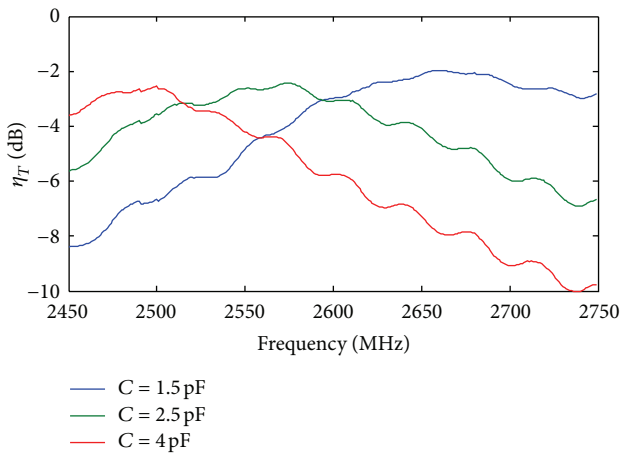
Figure 9: Measured total efficiency of the demonstrator in Figure 6.
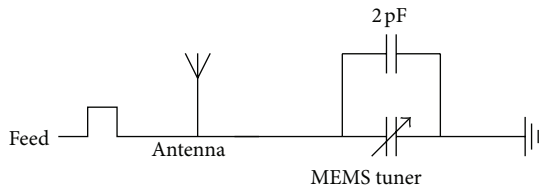
Figure 10: Schematic of the miniaturization demonstrator.
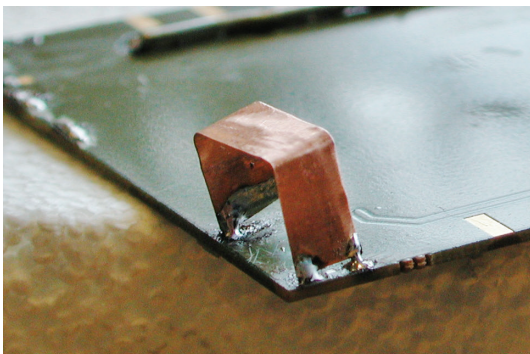
Figure 11: Antenna miniaturization demonstrator, top view.
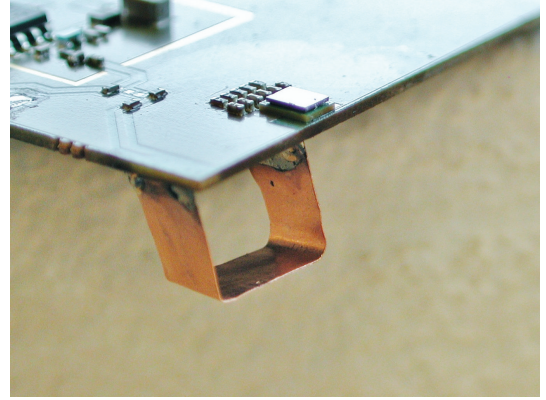
Figure 12: Antenna miniaturization demonstrator, bottom view.
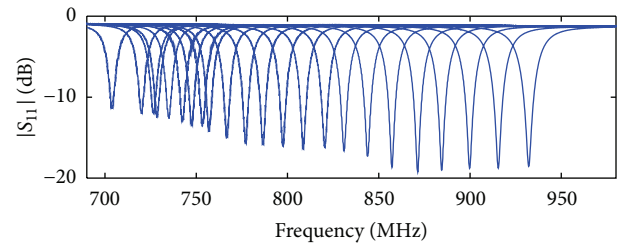
Figure 13: Measured tuning range of the demonstrator in Figure 11.

is equal to $2\,\Omega$ and causes most of the loss for this very high Q antenna. Thus, the efficiency will significantly improve by using a newer generation of tuners that exhibits a lower ESR along with improvements in the interconnects. In order to get a loss of 3 dB at 700 MHz for the proposed design, the effective ESR should be reduced to $0.2\,\Omega$.

5. Conclusion

This work has detailed the interdependency of the antenna design and the tuner design. The presented investigations have highlighted the importance of codesigning the tuner and the antenna. Examples have been given for a low-band antenna design as well as for a high-band antenna design. The design trade-offs come from two sources. On one hand, the required characteristics of the tunable capacitor relate to its location on the antenna. On the other hand, they relate to the antenna initial bandwidth, in other words the Q_{ant}. Depending on its application, the tunable antenna will require a certain volume and, together with the location of the tuner, they will determine a set of tuner parameters (ESR, voltage handling and maximum capacitance) to realize an optimized design. The required characteristics of the tuner are strongly dependent on its location; for example, the required capacitance steps can be up to 10 times smaller, if placed far from the feed.

Using tunable components, the antenna volume can be dramatically decreased and the efficiency can remain above 50% as long as the ratio between Q_{MEMS} and the unloaded Q_{ant} is about 1.5. Demonstrators have been built supporting
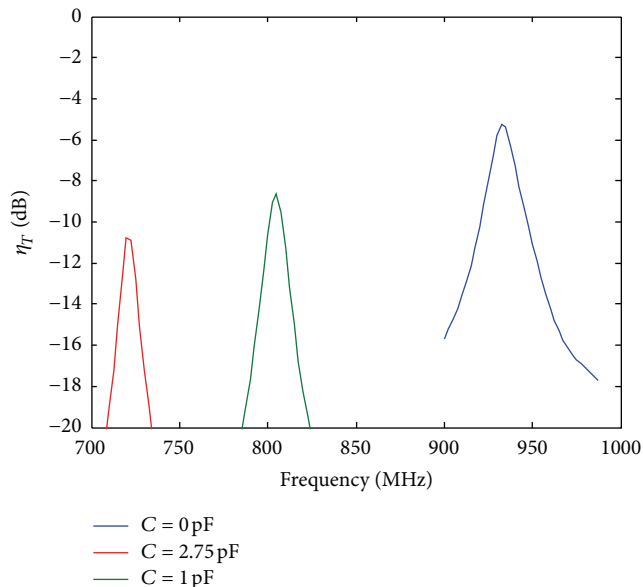
FIGURE 14: Measured total efficiency of the demonstrator in Figure 11.

the investigation on codesigning trade-offs. Efficiency of tunable antennas can be optimized. The limits of miniaturization lie in the achievable antenna efficiency, which determines the feasibility of the system. Improvements in tuner insertion loss will directly improve the total efficiency of tunable antennas and highlight their tremendous potential for miniaturization.

Conflict of Interests

The authors declare that there is no conflict of interests regarding the publication of this paper.

References

[1] D. Vye, "The economics of handset RF front-end integration," *Microwave Journal*, vol. 53, pp. 22–67, 2010.

[2] R. F. Harrington, "Effect of antenna size on gain, bandwidth, and efficiency," *Journal of Research of the National Bureau of Standards D: Radio Propagation*, vol. 64, no. 1, pp. 1–12, 1960.

[3] Y. Guo, M. Y. W. Chia, and Z. N. Chen, "Miniature built-in quad-band antennas for mobile handsets," *IEEE Antennas and Wireless Propagation Letters*, vol. 2, no. 10, pp. 30–32, 2003.

[4] H. Rhyu, J. Byun, F. J. Harackiewicz et al., "Multi-band hybrid antenna for ultra-thin mobile phone applications," *Electronics Letters*, vol. 45, no. 15, pp. 773–774, 2009.

[5] K. R. Boyle and P. J. Massey, "Nine-band antenna system for mobile phones," *Electronics Letters*, vol. 42, no. 5, pp. 265–266, 2006.

[6] J. Ilvonen, P. Vainikainen, R. Valkonen, and C. Icheln, "Inherently non-resonant multi-band mobile terminal antenna," *Electronics Letters*, vol. 49, no. 1, pp. 11–13, 2013.

[7] A. Tatomirescu and G. F. Pedersen, "Body-loss for popular thin smart phones," in *Proceedings of the 7th European Conference on Antennas and Propagation (EuCAP '13)*, pp. 3754–3757, April 2013.

[8] G. F. Pedersen and J. Ø. Nielsen, "Radiation pattern measurements of mobile phones next to different head phantoms," in *Proceedings of the 13th IEEE International Symposium on Personal, Indoor and Mobile Radio Communications (PIMRC '02)*, vol. 4, pp. 1888–1892, September 2002.

[9] S. Caporal Del Barrio and G. F. Pedersen, "Correlation evaluation on small LTE handsets," in *Proceedings of the 76th IEEE Vehicular Technology Conference (VTC '12)*, pp. 1–4, September 2012.

[10] S. C. del Barrio, A. Tatomirescu, G. F. Pedersen, and A. Morris, "Novel architecture for LTE world-phones," *IEEE Antennas and Wireless ropagation Letters*, vol. 12, no. 1, pp. 1676–1679, 2013.

[11] W. Fan, X. C. B. de Lisbona, F. Sun, J. O. Nielsen, M. B. Knudsen, and G. F. Pedersen, "Emulating spatial characteristics of MIMO channels for OTA testing," *IEEE Transactions on Antennas and Propagation*, vol. 61, no. 8, pp. 4306–4314, 2013.

[12] V. Steel and A. Morris, "Tunable RF Technology Overview," 2012.

[13] R. Cory and D. Fryklund, "Solid State RF/Microwave Switch Technology: Part 2," 2009.

[14] S. K. Oh, H. S. Yoon, and S. O. Park, "A PIFA-type varactor-tunable slim antenna with a PIL patch feed for multiband applications," *IEEE Antennas and Wireless Propagation Letters*, vol. 6, no. 11, pp. 103–105, 2007.

[15] N. Behdad and K. Sarabandi, "A varactor-tuned dual-band slot antenna," *IEEE Transactions on Antennas and Propagation*, vol. 54, no. 2, pp. 401–408, 2006.

[16] N. Behdad and K. Sarabandi, "Dual-band reconfigurable antenna with a very wide tunability range," *IEEE Transactions on Antennas and Propagation*, vol. 54, no. 2, pp. 409–416, 2006.

[17] L. M. Feldner, C. T. Rodenbeck, C. G. Christodoulou, and N. Kinzie, "Electrically small frequency-agile PIFA-as-a-package for portable wireless devices," *IEEE Transactions on Antennas and Propagation*, vol. 55, no. 11, pp. 3310–3319, 2007.

[18] WiSpry Tunable Digital Capacitor Arrays (TDCA), http://www.wispry.com/products-capacitors.php.

[19] A. Cihangir, F. Sonnerat, F. Ferrero et al., "Neutralisation technique applied to two coupling element antennas to cover low LTE and GSM communication standards," *Electronics Letters*, vol. 49, no. 13, pp. 781–782, 2013.

[20] A. Cihangir, F. Ferrero, C. Luxey, G. Jacquemod, and P. Brachat, "A bandwidth-enhanced antenna in LDS technology for LTE700 and GSM850/900 standards," in *Proceedings of the 7th European Conference on Antennas and Propagation (EuCAP '13)*, pp. 2786–2789, April 2013.

[21] A. Lehtovuori, R. Valkonen, and M. Valtonen, "Accessible approach to wideband matching," in *Proceedings of the 19th IEEE International Conference on Electronics, Circuits, and Systems, (ICECS '12)*, pp. 244–247, December 2012.

[22] D. Manteuffel and M. Arnold, "Considerations for reconfigurable multi-standard antennas for mobile terminals," in *Proceedings of the International Workshop on Antenna Technology: Small Antennas and Novel Metamaterials (iWAT '08)*, pp. 231–234, Chiba, Japan, March 2008.

[23] L. Huang and P. Russer, "Electrically tunable antenna design procedure for mobile applications," *IEEE Transactions on Microwave Theory and Techniques*, vol. 56, no. 12, pp. 2789–2797, 2008.

[24] R. Valkonen, C. Luxey, J. Holopainen, C. Icheln, and P. Vainikainen, "Frequency-reconfigurable mobile terminal antenna with MEMS switches," in *Proceedings of the 4th*

European Conference on Antennas and Propagation (EuCAP '10), pp. 1–5, April 2010.

[25] R. Valkonen, J. Holopainen, C. Icheln, and P. Vainikainen, "Broadband tuning of mobile terminal antennas," in *Proceeding of the IET Seminar Digests*, p. 182, IET, 2007.

[26] E. Erdil, K. Topalli, M. Unlu, O. A. Civi, and T. Akin, "Frequency tunable microstrip patch antenna using RF MEMS technology," *IEEE Transactions on Antennas and Propagation*, vol. 55, no. 4, pp. 1193–1196, 2007.

[27] V.-A. Nguyen, R.-A. Bhatti, and S. Park, "A simple PIFA-based tunable internal antenna for personal communication handsets," *IEEE Antennas and Wireless Propagation Letters*, vol. 7, pp. 130–133, 2008.

[28] Y. K. Park and Y. Sung, "A reconfigurable antenna for quad-band mobile handset applications," *IEEE Transactions on Antennas and Propagation*, vol. 60, no. 6, pp. 3003–3006, 2012.

[29] K. R. Boyle and P. G. Steeneken, "A five-band reconfigurable PIFA for mobile phones," *IEEE Transactions on Antennas and Propagation*, vol. 55, no. 11, pp. 3300–3309, 2007.

[30] J. R. de Luis, A. Morris, Q. Gu, and F. de Flaviis, "Tunable duplexing antenna system for wireless transceivers," *IEEE Transactions on Antennas and Propagation*, vol. 60, no. 11, pp. 5484–5487, 2012.

[31] Q. Gu and J. R. de Luis, "RF MEMS tunable capacitor applications in mobile phones," in *Proceedings of the 10th IEEE International Conference on Solid-State and Integrated Circuit Technology (ICSICT '10)*, pp. 635–638, November 2010.

[32] M. G. S. Hossain and T. Yamagajo, "Reconfigurable printed antenna for a wideband tuning," in *Proceedings of the 4th European Conference on Antennas and Propagation (EuCAP '10)*, April 2010.

[33] S. Oh, H. Song, J. T. Aberle, B. Bakkaloglu, and C. Chakrabarti, "Automatic antenna-tuning unit for software-defined and cognitive radio," *Wireless Communications and Mobile Computing*, vol. 7, no. 9, pp. 1103–1115, 2007.

[34] A. Suyama and H. Arai, "Meander line antenna built in folder-type mobile," in *Proceedings of the International Symposium on Antennas and Propagation (ISAP '07)*, pp. 294–297, 2007.

[35] Y. Tsutsumi, M. Nishio, S. Obayashi et al., "Low profile double resonance frequency tunable antenna using RF MEMS variable capacitor for digital terrestrial broadcasting reception," in *Proceedings of the 2009 IEEE Asian Solid-State Circuits Conference*, pp. 125–128, November 2009.

[36] Computer Simulation Technology (CST), *CST Microwave Studio*, 2012, http://www.cst.com.

[37] A. D. Yaghjian and S. R. Best, "Impedance, bandwidth, and Q of antennas," *IEEE Transactions on Antennas and Propagation*, vol. 53, no. 4, pp. 1298–1324, 2005.

[38] S. R. Best, "Electrically small multiband antennas," in *Multiband Integrated Antennas for 4G Terminals*, D. A. Sanchez-Hernandez, Ed., chapter 1, pp. 1–32, Artech House, Norwood, Mass, USA, 2008.

Research Article

Technique of Coaxial Frame in Reflection for the Characterization of Single and Multilayer Materials with Correction of Air Gap

Zarral Lamia,[1] Djahli Farid,[1] and Ndagijimana Fabien[2]

[1] *Laboratory of Scientific Instrumentation Institute of Electronic, FERHAT Abbess University, 19000 Setif, Algeria*
[2] *Laboratory of IMEP-LAHC Minatec, Institute of Microelectronics, Electromagnetism and Photonics, 38000 Grenoble, France*

Correspondence should be addressed to Zarral Lamia; lamia_zarral@yahoo.fr

Techniques based on fixture probes in reflection are used in microwave reflectometry as a novel diagnostic tool for detection of skin cancers, for complex permittivity measurements on liquid samples and oil shale, and for complex dielectric permittivity of animals' organs and tissues measurements in microwave band for the needs of modern veterinary medicine. In this work, we have developed a technique to characterize multilayer materials in a broadband frequency range. A coaxial probe in reflection has been specially developed for microelectronic substrate. Using SMA connector, loss tangent of 10^{-4} and relative permittivity have been measured with an error of 0.145%. The extension of the coaxial probe in reflection technique to multilayer substrates such as Delrin and Teflon permitted to measure bilayer material provided the good knowledge of electrical parameters and dimensions of one layer. In the coaxial transmission line method, a factor that greatly influences the accuracy of the results is the air gaps between the material under test and the coaxial test fixture. In this paper, we have discussed the influence of the air gaps (using samples of 0.5 mm air gaps) and the measures that can be taken to minimize that influence when material is measured. The intrinsic values thus determined have been experimentally verified. We have described the structure of the test fixture, its calibration issues, and the experimental results. Finally, electromagnetism simulations showed that the best results can be obtained.

1. Introduction

In this paper, we have developed a method using a coaxial fixture that allows the extraction of electrical parameters of substrates by the reflection measurement. This coaxial probe is in contact at its end with the samples and with a short circuit for calibration. For validation we have measured the Teflon and Delrin (Pome). The validation of the method is first made on monolayer materials and secondly on multilayers substrates. We reversed the positions of the couple of materials (Delrin, Teflon) then (Teflon-Delrin) to check their asymmetries. In the multilayer measurements we use Teflon as reference material.

2. Principle of the Method

Figure 1 shows the structure of the line with sample as well as the reference plans of measurements in this method. Our method requires six measures to be made: in a first step we perform one measure of the $S11$ parameters in open circuit and another one in short circuit for calibration. In a second step we measure the $S11$ parameters of line without sample, terminated with open circuit and with short circuit at the end. In the third and last step, we measure the $S11$ parameters of the line with sample terminated with short circuit and with open circuit.
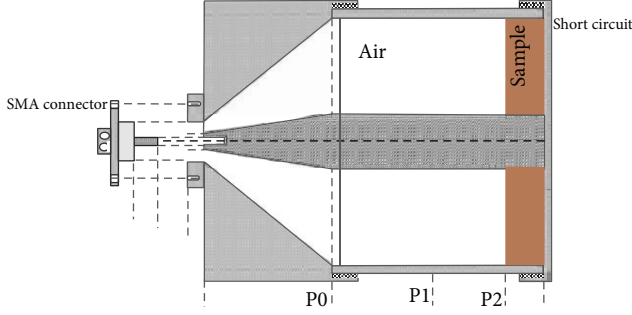
FIGURE 1: Presentation of the coaxial reflective frame with sample.

To move from plan P1 to plan P2, as shown in Figure 1, we apply the following formula [1], with l being the length between P0 and P1:

$$S'_{ij} = S_{ij} \cdot e^{2 \cdot j \cdot \gamma l}. \tag{1}$$

3. Presentation of the Coaxial Frame in Reflection

A coaxial frame is a coaxial line comprising a central conductor and a cylindrical outer aluminum conductor. This line is connected to the tester by means of an SMA connector, which is placed on one of its ends so as to measure the $S11$ parameters in which the electrical parameters of the material are extracted [2]. On the termination of the coaxial line we connect a short circuit or open circuit so that the material under test is in direct contact with the short circuit (Figure 1).

For the modeling of this frame we have calculated all the parameters of the transmission line, as well as the dimensions of the samples to be characterized before proceeding to the simulation step.

4. Electromagnetic Simulations and Validation

We simulated the structure of the frame with and without sample in the case of loss and lossless dielectric using CST and HFSS11.1 simulators. The simulation is made with the following steps.

4.1. Impedance Matching Bandwidth. The test structure comprises a radiating coaxial transmission line in a semi-infinite environment with a given thickness and ended by a metal plate for short circuit. The ratio of the inner diameter ($2a$) and of the outer conductor ($2b$) is set so that the characteristic impedance of the transmission line is equal to 50 Ω in without sample.

4.2. Extraction of the Electrical Parameters of the Dielectric. The $S11$ parameters, obtained by simulation, allow easy access to propagation phase γl in the presence and in the absence of material. Consider

$$Z(S) = Zn \cdot \frac{1 + S}{1 - S}, \tag{2}$$

where $Z(S)$ is the impedance characteristic function of S parameters, γ is the propagation constant, and l is the length of the line.

In the absence of the dielectric material, we have

$$Zc_{\text{air}} = \sqrt{Zc_{\text{air}}cc \cdot Zc_{\text{air}}co},$$

$$\gamma l_{\text{air}} = a \tanh \sqrt{\frac{Zc_{\text{air}}cc}{Zc_{\text{air}}co}}. \tag{3}$$

In the presence of the dielectric material

$$Zc_{\text{mat}} = \sqrt{Zc_{\text{mat}}cc \cdot Zc_{\text{mat}}co},$$

$$\gamma l_{\text{mat}} = a \tanh \sqrt{\frac{Zc_{\text{mat}}cc}{Zc_{\text{mat}}co}}, \tag{4}$$

where Zc is the characteristic impedance of the line.

These two measures of parameter γl [3, 4] allow easy access, theoretically, to parameters ε_r and $\tan \delta_d$ of the dielectric material.

From the line impedance in short circuit and open circuit, to extract the propagation parameters of a transmission line, we can measure the $S11$ reflection parameters in two different configurations, namely, the line in short circuit and the line in open circuit [5]. Any transmission line can be represented by its propagation constant (Zc, γl).

The input impedance Z_{in} of a transmission line loaded by impedance Z_R is determined by the following expression:

$$Z_{\text{in}} = Zc \frac{Z_R + Zc \tanh(\gamma l)}{Zc + Z_R \tanh(\gamma l)}. \tag{5}$$

In the case of a short-circuit line ($Z_R = 0$), the impedance seen at the input line is written as

$$Z_{\text{in}_{cc}} = Zc \cdot \tanh(\gamma l) = Z_n \frac{1 + \Gamma_{cc}}{1 - \Gamma_{cc}} = Z_{cc}, \tag{6}$$

where Z_n is the standard resistance that is equal to 50 Ohm and Γ is a coefficient of reflexion.

In the case of an open-circuit line ($Z_R = \infty$), the impedance seen at the input of the line is

$$Z_{\text{in}_{co}} = \frac{Zc}{\tanh(\gamma l)} = Z_n \frac{1 + \Gamma_{co}}{1 - \Gamma_{co}} = Z_{co}. \tag{7}$$

4.3. Extraction of the Complex Relative Permittivity. The complex relative permittivity and the loss angle are obtained from

$$\varepsilon_{\text{eff}} = \frac{\gamma l_{\text{mat}} + Zc_{\text{air}}}{\gamma l_{\text{air}} + Zc_{\text{mat}}},$$

$$\tan \delta = \frac{\gamma l_{\text{mat}} \cdot Zc_{\text{mat}}}{\gamma l_{\text{air}} \cdot Zc_{\text{air}}}, \tag{8}$$

where ε_{eff} is the effective relative permittivity and $\tan \delta$ is the dielectric losses.

FIGURE 2: Sample of Delrin and Teflon for d = 5 mm and 15 mm.
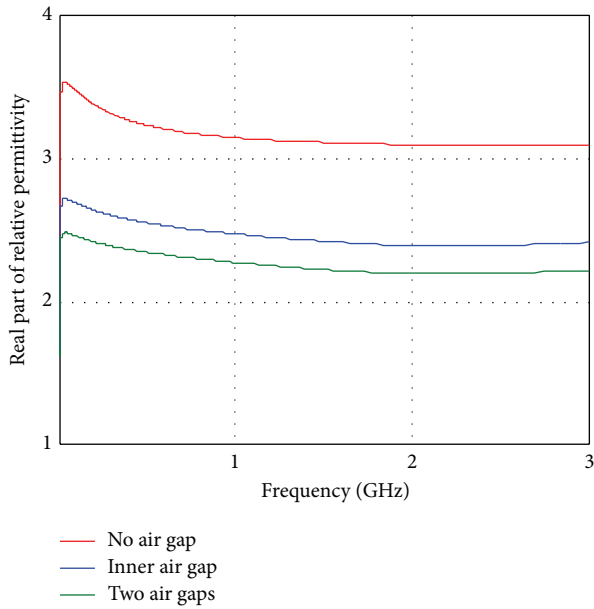
FIGURE 3: Real part of relative permittivity of Delrin.

FIGURE 4: Delrin dielectric losses.
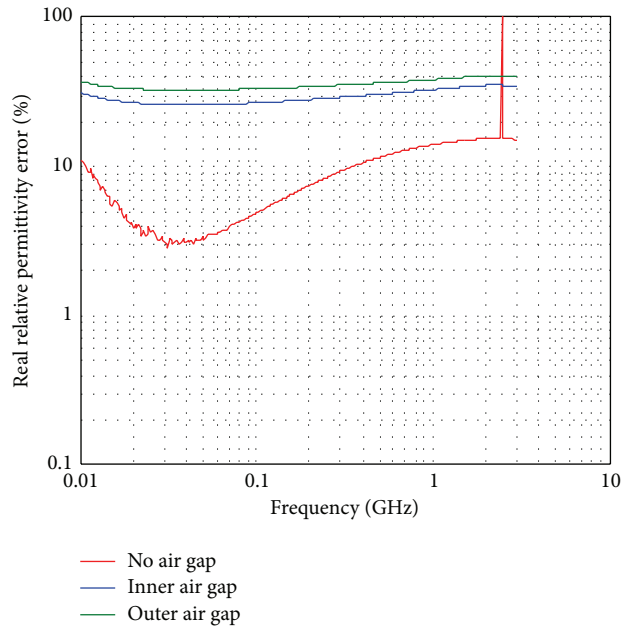
FIGURE 5: Error of relative permittivity of Delrin.

4.4. Machining of the Samples. The advanced hypothesis of the measurement technique in coaxial line (spread of a single TEM mode in all regions of the line) requires the complete filling of the transverse section of the line by the sample (Figure 2). This involves strong machining constraints of the sample ring because of the presence of an air gap between it and the conductive walls of the line.

Although mechanical tolerances met by the end of the machining process are low, the manual insertion of the sample inside the line inevitably implies the presence of an air gap. It will influence the accuracy of measurement results. To illustrate this problem, we have studied the effect of these errors on the determination of the dielectric permittivity ε_r. Errors of measurement due to the presence of air space between the sample and the line conductors are gradually larger as the frequency increases. For this, we have established a correction (sample of 5 mm long and with no air gap).

4.5. Correction of the Air Gap. In these simulations and to reduce the number of parameters, we have assumed that the air gap between the material and the outer conductor is zero.

Figure 5 shows that the error increases very rapidly with the thickness of air space and the value of the permittivity of the material. This has the effect of lowering the value of the measured permittivity.

To correct the errors related to the imperfections of the test device (such as the connecting cable of the analyser, the coaxial conical/coaxial transition associated with the discontinuity line/guide, and metal losses due to finite conductivity of the conductors used to make the alignment of the various elements) we added formula (9), in the MathCAD program. A formula has been derived to estimate the effective complex
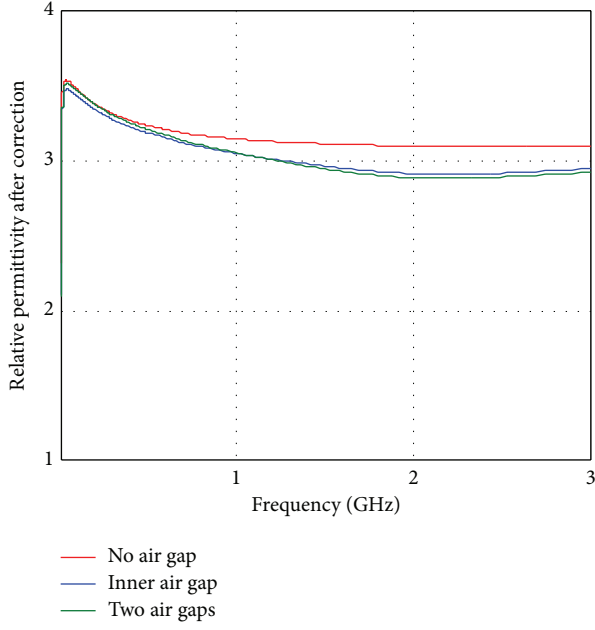
FIGURE 6: Relative permittivity after correction of the Delrin.
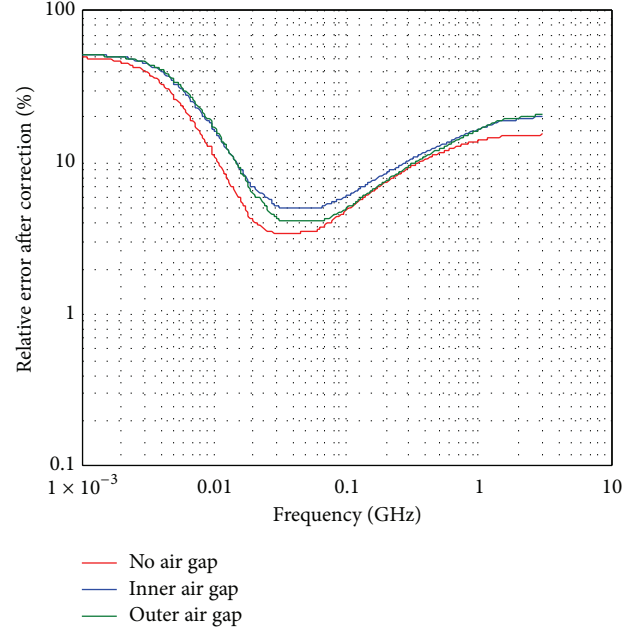
FIGURE 8: Relative permittivity error after correction of Delrin.
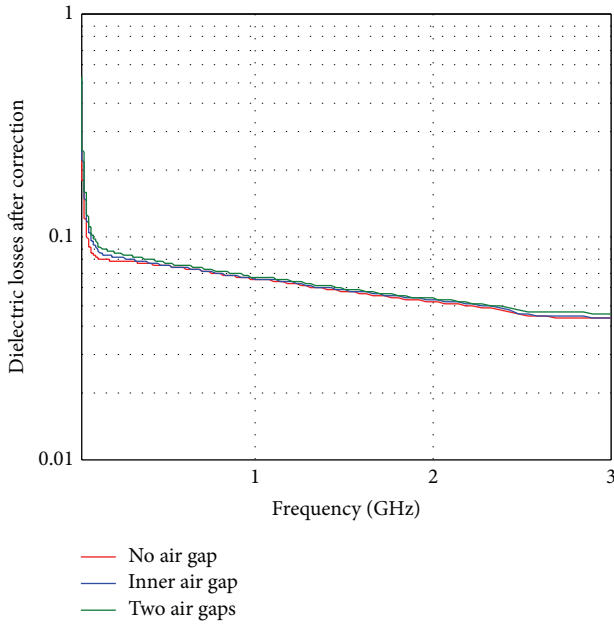
FIGURE 7: Dielectric losses after correction of Delrin.

FIGURE 9: Constituents of the small and large coaxial line in reflexion.

renaming $\varepsilon_{r,\mathrm{eff}}^* \to \varepsilon_{r,m}^*$ and $\varepsilon_{r,\mathrm{nom}}^* \to \varepsilon_{r,c}^*$ (corrected complex permittivity) and solving for $\varepsilon_{r,c}^*$ (11).

Wall thickness was calculated by subtracting the inner diameter of the sample from its outer diameter and dividing the difference by 2.

To extract the initial dielectric loss, we simulate a case with (σ_{AP}) losses and (σ_{SP}) lossless dielectrics. The difference between the two extracted electrical conductivities gives the electrical conductivity of the dielectric σ_d after correction is given by the following:

$$\sigma_d = \sigma_{\mathrm{AP}} - \sigma_{\mathrm{SP}}. \tag{10}$$

The correction of the electrical conductivity has allowed us to find its actual value. This allows to conclude that the chosen model and the applied extraction procedure are good.

In practice, we do not have material without losses and cannot perform dielectric measurements without losses.

From (9) we obtain

$$\varepsilon_{r_{\mathrm{eff},c}} = \frac{\varepsilon_{r_{\mathrm{eff},m}} \cdot \ln\left(r_0/r_i\right)}{\ln\left(b/a\right) - \varepsilon_{r_{\mathrm{eff},m}} \cdot \ln\left[b/a/r_0/r_i\right]}. \tag{11}$$

permittivity $\varepsilon_{r,\mathrm{eff}}^*$ from the total capacitance consisting of a mixture of three coaxial layers, air, a bulk material, and air:

$$\varepsilon_{r,\mathrm{eff}}^* = \ln\left(\frac{b}{a}\right) \left[\ln\left(\frac{b/a}{r_0/r_i}\right) + \frac{\ln(r_0/r_i)}{\varepsilon_{r,\mathrm{nom}}^*}\right]^{-1}, \tag{9}$$

where $\varepsilon_{r,\mathrm{nom}}^*$ is the nominal complex permittivity, a and b are the inner and outer radii of the sample holder, and r_i and r_0 are the inner and outer radii of the sample. To obtain a gap correction formula, this equation can be rearranged by

FIGURE 10: Photo of small coaxial line in reflection (15 mm).

FIGURE 12: Teflon dielectric losses (sample of 15 mm).

FIGURE 11: Teflon real relative permittivity (sample of 15 mm).
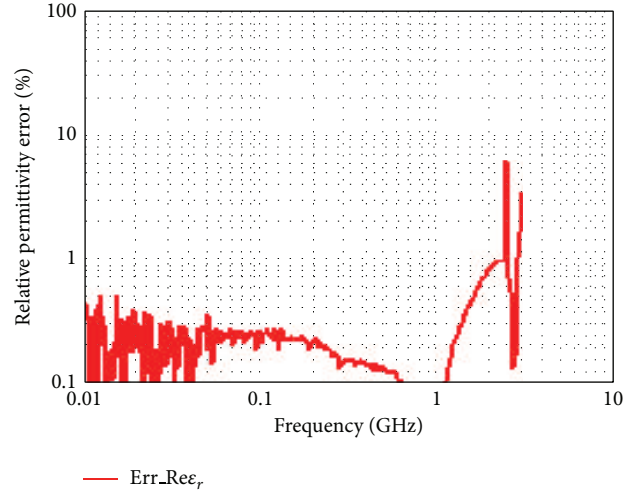
FIGURE 13: Teflon relative permittivity error (sample of 15 mm).

To correct error of eccentricity we add the following formula:

$$\varepsilon_{r_{\text{eff}}} = \frac{\varepsilon_{r_{\text{eff}}}c}{\sqrt{1 + \left(\left(S \cdot \Delta \cdot \varepsilon_{r_{\text{eff}}}c\right)/\alpha\right)^2}}, \tag{12}$$

where $\alpha = \log(b/a)$, $\Delta = 2(d - a)/(d + a)$, Δ is a deviation fraction on inner diameter, d is the air gap between central conductor and sample, and $s = \Delta c/(d - a)$ is the parameter of eccentricity.

Without eccentricity ($s = 0$) and with complete eccentricity ($s = 1$).

5. Simulation Results

The simulation results of the set of Figures 1 to 8 were obtained after extraction of the permittivity from the $S11$ parameters. In Figures 3 and 4, we can see that the real part of the relative permittivity (of Delrin) and the dielectric losses decrease when the frequency and the value of the gaps increased, whereas **Figure 5** shows that the error of relative permittivity of Delrin increases with the value of the gaps and weak for a line without gap. After correction, the results of Figures

FIGURE 14: Delrin real part of effective relative permittivity (sample of 15 mm).
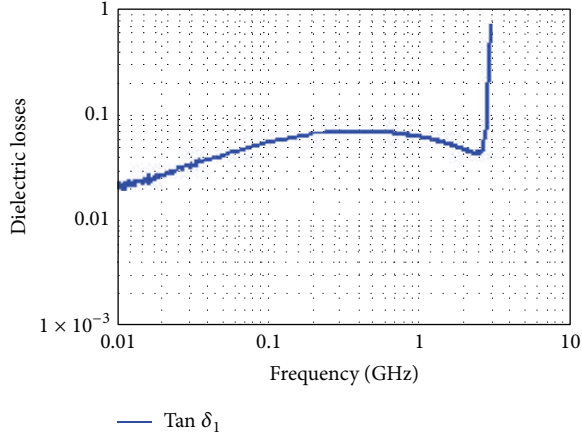
FIGURE 15: Delrin dielectric losses (sample of 15 mm).
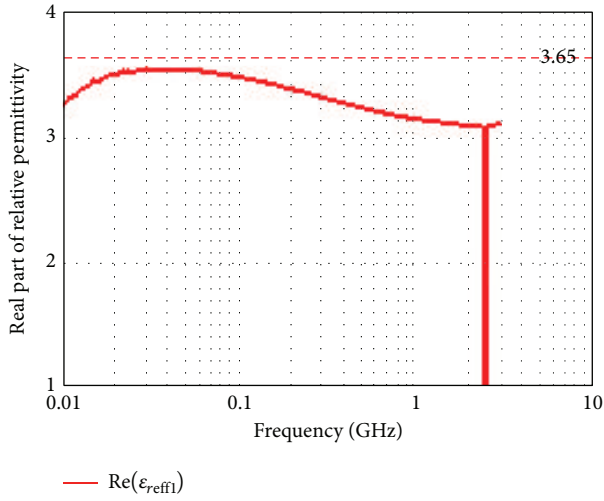
FIGURE 16: Delrin relative permittivity (sample of 5 mm long and with no air gap).
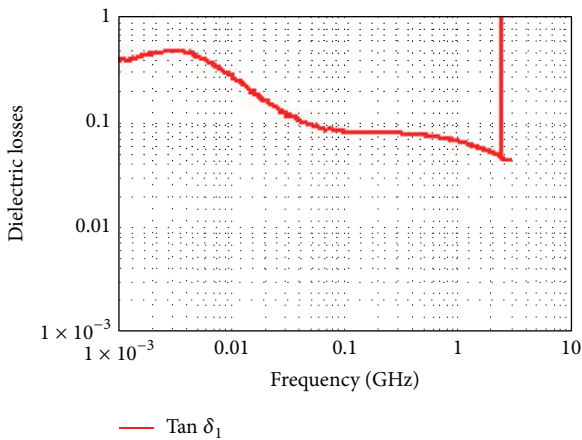
FIGURE 17: Delrin dielectric losses (sample of 5 mm long and with no air gap).
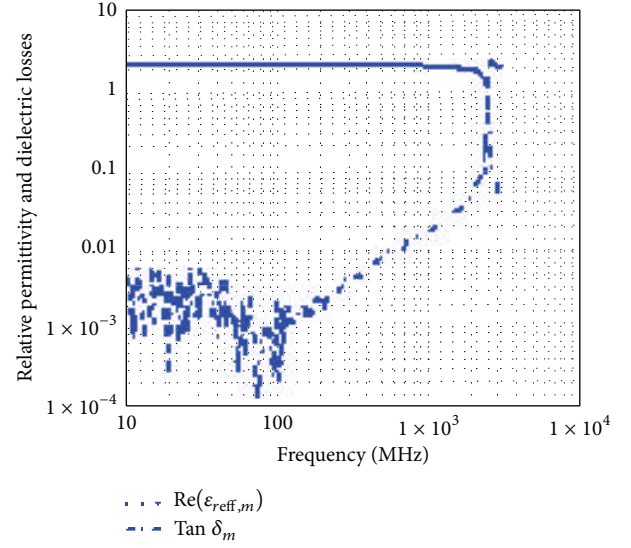
FIGURE 18: Teflon relative permittivity and dielectric losses (sample of 5 mm long and with no air gap).
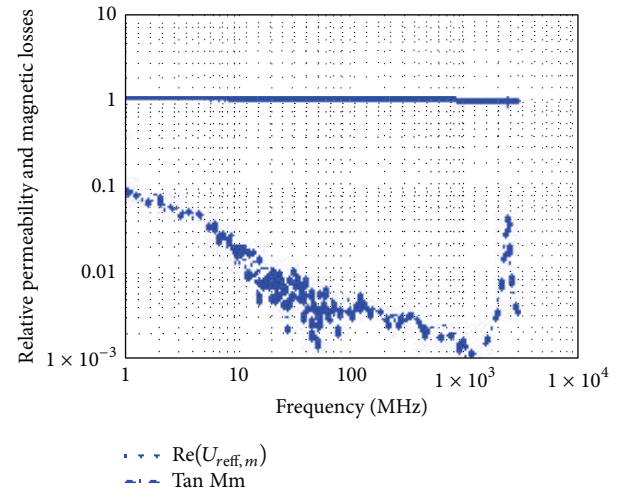
FIGURE 19: Teflon relative permeability and magnetic losses (sample of 5 mm long and with no air gap).

6, 7, and 8 show clearly the improvement of the results and the cancellation of the effect of the air gap. We see that the three curves merge into one, especially for the dielectric losses.

6. Experimental Validation

Before beginning measurements, we must define the reference plans that will support the practical implementation of the cell, and then we perform the calibration procedure to eliminate systematic errors of the measurement of

the reflection coefficient. Finally, we validate the implementation method from the measurement of the complex permittivity of dielectric materials with well-known properties.

6.1. Realization of the Measuring Cell. To ensure the representativeness of the measurements performed on the discontinuity line/guide with respect to the electromagnetic properties of the samples, the measuring cell must have an outside diameter equal to 11.5 mm. Under these conditions, the connection of the measuring cell to the vector network analyser requires the use of a coaxial/coax transition. This transition consist in an SMA connector, suitable for the connecting cable of the network analyser (diameter 3.5 mm) and a coaxial conical portion which ensures the progressive variation of the diameter of the line between the coaxial line and the discontinuity, which has a line diameter of 5 mm (Figure 9).

To limit the effects of propagation discontinuity in the conical section, the ratio between the internal diameter of the outer conductor and the diameter of the central conductor is, on the whole length of the section, 2.3 mm (conditions of 50 ohms impedance matching).

6.2. Experimental Results. To exploit reflectance measures, we used a network analyser type VNA.E5062A. This implies positioning the reference plan of the measurement of the reflection coefficient at the end of the coaxial access line on the front face of the cylindrical sample characterization (Figure 10).

The experimental results of Figures 11, 12, and 13 present, respectively, the relative permittivity, the dielectric losses, and the relative permittivity error for Teflon (sample of 15 mm). In Figures 14, 15, 16, 17, and 18 we plot the parameters of Delrin. These results were considered very good since the obtained values of all these parameters were very near to the typical values in this considered frequency range. Figures 17 and 18 are obtained for Derlin without air gap (sample of 5 mm). We can notice, from **Figure 18**, that the losses are less than 0.1 after 50 MHz. For the same sample and in the same conditions, the simulation and experimental results are very close. This good agreement proves, for the corrected measurements by using the kit short-circuit/open-circuit/standard material, that the used technique and the calibration procedure were successful over the entire frequency band.

In Figures 18 and 19, we plot, respectively, the relative permittivity and the relative permeability and magnetic losses of Teflon (sample of 5 mm long and with no air gap). These figures show that the losses are constant over the entire frequency range. **Figure 20** illustrates the relative permittivity for Delrin (sample of 5 mm long and with air gap of 0.5 mm in inner diameter). The red traces are the corrected values, obtained by using (11) and (12) to take into account the air gap effects.

We present, respectively, in **Figure 21**, the initial and corrected values of relative permittivity for Teflon (sample of 5 mm long and with air gap of 0.5 mm in inner diameter). We
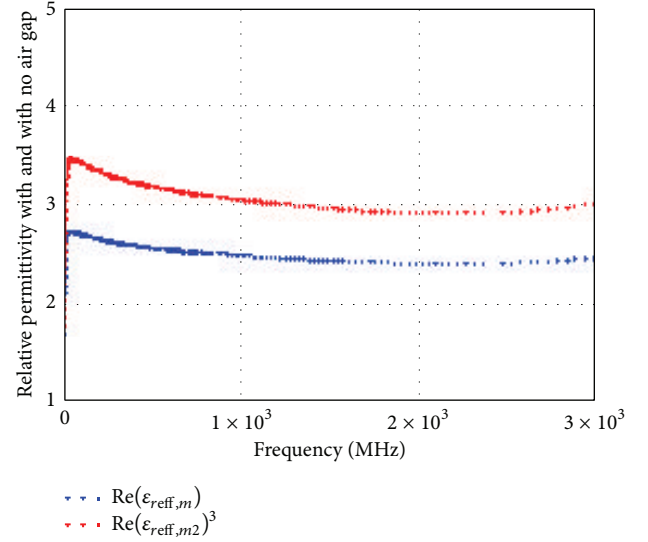
FIGURE 20: Delrin relative permittivity (sample of 5 mm long and with air gap of 0.5 mm in inner diameter).
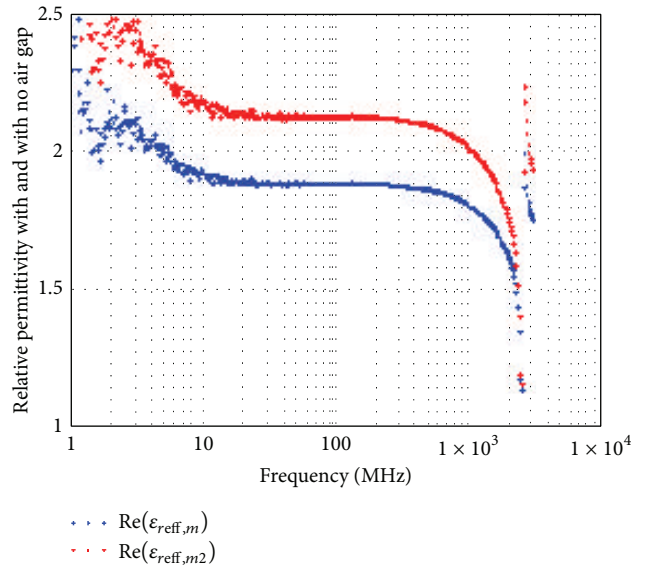
FIGURE 21: Teflon relative permittivity (sample of 5 mm long and with air gap of 0.5 mm in inner diameter).

notice here that, after correction, the relative permittivity is improved.

7. Application of the Method for Multilayer Materials

We will show that the proposed method can also be applied, successfully, to multilayer materials. We rely primarily on the principles of the coaxial probe in reflection. Let us put

a bilayer dielectric in the metallic cavity (Figure 22(a)). In Figure 2 we invert the position of the layers. In literature, studies have shown that the coaxial probe is sensitive to the surface of the sample which is in contact with the central conductor [6]. This sensitivity is due to the distribution of electromagnetic fields in the vicinity of the central conductor [7, 8]. This implies that the overall capacitance created is not the same as the orientation of the sample ($\varepsilon_{r1} \neq \varepsilon_{r2}$).

7.1. Extraction of Each Layer's Complex Permittivity. We consider that the bilayer dielectric in contact with the greatest metal surface (point C) entails that overall losses are depending on the orientation of the sample. Moreover, at the interface of the two dielectrics (point B), the capacitance is the same regardless of the orientation of the sample.

We know that

$$\gamma l = \frac{jwl\sqrt{\varepsilon_r}}{c}, \tag{13}$$

$$\gamma_{\text{tot}}l_{\text{tot}} = \gamma_1 l_1 + \gamma_2 l_2, \tag{14}$$

$$l_{\text{tot}} = l_1 + l_2. \tag{15}$$

When we put (13) in (14) we obtain the effective permittivity of the first layer as a function of that of the reference:

$$\varepsilon_{r\text{-Delrin}} = \left(2 \cdot \sqrt{\varepsilon_{r\text{-tot}}} - \sqrt{\varepsilon_{r\text{-Teflon}}}\right)^2. \tag{16}$$

This extraction method has the privilege of not necessarily being based on prior knowledge of the thickness of each layer. Only the thickness of the aggregate layer must be known in order to meet the dimensions of the test frame.

7.2. Experimental Results. We have plotted in Figures 23 and 24, respectively, the relative permittivity and the magnetic losses of Delrin (sample 5 mm without air gap). In Figure 23 we show that the read plot which represents the relative permittivity of the Delrin, obtained using the bilayers methods, is praticallly the same blue plot obtained with single sample, in the same frequency range between 10 MHz and 1 GHz but the accepted value is until 100 MHz as shown in Figure 24; in this range of frequecy the dielectric losses are between 2% at 10 MHz and 5% at 100 MHz. We have obtained a good precision.

The use of coaxial fixture in reflection so as to characterize multilayers materials has led to satisfactory results. The application of dielectric Delrin permits us to prove the method's feasibility.

Meanwhile, the method is based on the principle that electrical parameters of one layer are well known and that the global thickness of the layers is precisely known.

8. Conclusion

We presented the technique of coaxial probe having a cavity end to characterize single and bilayer materials. Its feasibility was validated by electromagnetic simulation results and experimental results after completing the experimental aluminum test frame which is lighter than copper.

(a)

(b)
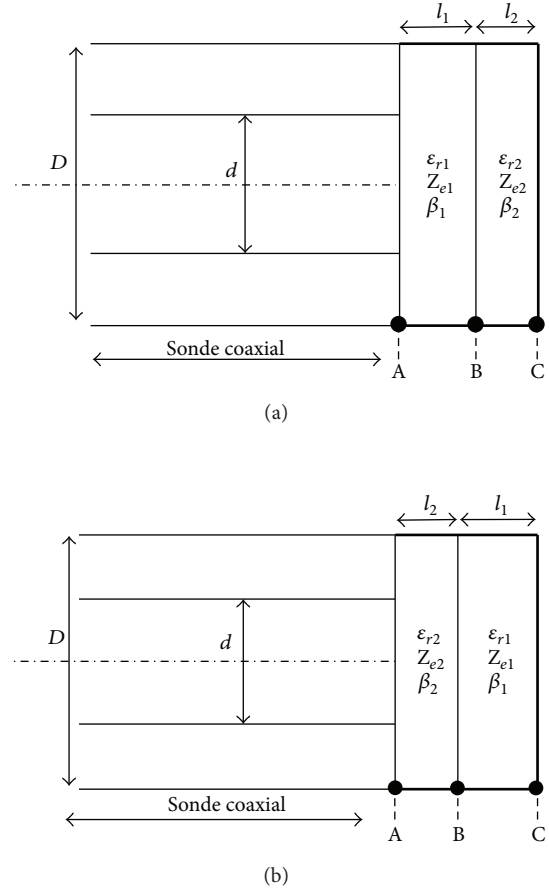
FIGURE 22: (a) Bilayer coaxial probe in the presence of a sample of the same thickness (configuration 1). (b) Bilayer coaxial probe in the presence of a sample of the same thickness (configuration 2).

—— Two couches
—— Reference
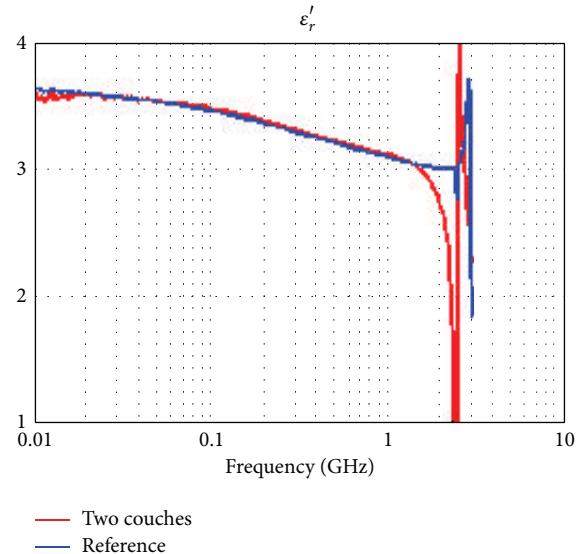
FIGURE 23: Delrin relative permittivity (sample of 5 mm long and with no air gap).
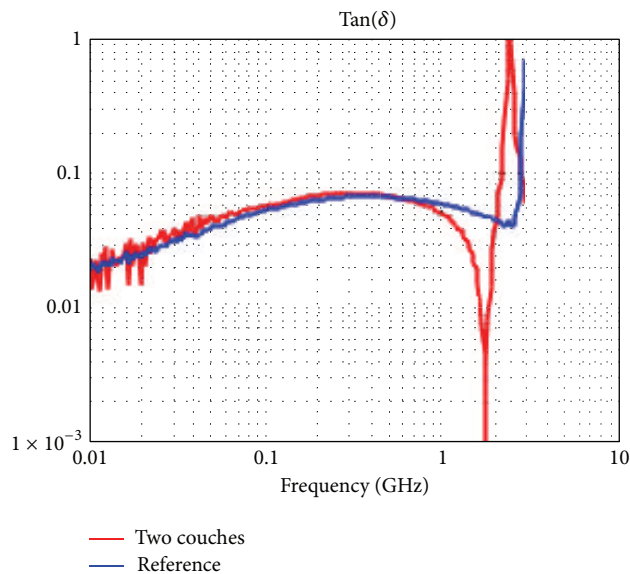
FIGURE 24: Delrin dielectric losses (sample of 5 mm long and with no air gap).

This technique is applicable to dielectrics and semiconductors. It is solely based on the reflection parameters using a capacitive model and helps to increase frequency band of model. Although efforts are yet to be made for its improvements, especially in the extraction losses for multilayer materials, this method is easy to implement and rapid in extracting electrical parameters and precise in terms of repeatability whose relative error is about 5%. This method offers the possibility to extract low loss tangent ($2 \cdot 10^{-4}$) up to 1 GHz using an SMA connector.

Conflict of Interests

The authors declare that there is no conflict of interests regarding the publication of this paper.

References

[1] C. C. Courtney, "Time-domain measurement of the electromagnetic properties of materials," *IEEE Transactions on Microwave Theory and Techniques*, vol. 46, no. 5, pp. 517–522, 1998.

[2] T. W. Athey, M. A. Stuchly, and S. S. Stuchly, "Measurement of radio frequency permittivity of biological tissues with an open-ended coaxial line: part I," *IEEE Transactions on Microwave Theory and Techniques*, vol. 30, no. 1, pp. 82–86, 1982.

[3] K. J. Bois, L. F. Handjojo, A. D. Benally, K. Mubarak, and R. Zoughi, "Dielectric plug-loaded two-port transmission line measurement technique for dielectric property characterization of granular and liquid materials," *IEEE Transactions on Instrumentation & Measurement*, vol. 48, no. 6, pp. 1141–1148, 1999.

[4] S.-G. Pan, "Characteristic impedances of coaxial system consisting of circular and noncircular conductors," *IEEE Transactions on Microwave Theory and Techniques*, vol. 36, no. 5, pp. 917–921, 1988.

[5] J. Baker-Jarvis, *Transmission/Reflection and Short-Circuit Line Permittivity Measurements*, National Institute of Standards and Technology, 1990.

[6] M. Moukanda, F. Ndagijimana, J. Chilo, and P. Saguet, "Caractérisation des Matériaux Multicouches en Utilisant une Sonde Coaxiale en Présence d'un Plan De Masse," in *15ème Journées Nationales Micro-Ondes (J.N.M)*, Toulouse, France, Mai 2007.

[7] N. Belhadj-Tahar, O. Meyer, and A. Fourrier-Lamer, "Broadband microwave characterization of bilayered materials using a coaxial discontinuity with applications for thin conductive films for microelectronics and material in air-tight cell," *IEEE Transactions on Microwave Theory and Techniques*, vol. 45, no. 2, pp. 260–267, 1997.

[8] N. Belhadj-Tahar, O. Dubrunfaut, and A. Fourrier-Lamer, "Broad-band microwave characterization of a tri-layer structure using a coaxial discontinuity with applications for magnetic liquids and films," *IEEE Transactions on Microwave Theory and Techniques*, vol. 46, no. 12, pp. 2109–2116, 1998.

Research Article

Research on Wideband Differential-Mode Current Injection Testing Technique Based on Directional Coupling Device

Xiaodong Pan, Guanghui Wei, Xinfu Lu, Lisi Fan, and Xing Zhou

National Key Laboratory of Electromagnetic Environment Effects, Mechanical Engineering College,
Heping West Road, Shijiazhuang 050003, China

Correspondence should be addressed to Xiaodong Pan; panxiaodong1980@sina.com

This paper presents a new kind of differential-mode current injection test method. The equal response voltage on the cable or the antenna port of the equipment under test (EUT) is regarded as equivalent principle for radiation and injection test. The injection and radiation response analysis model and the injection voltage source extrapolation model in high intensity radiated field are established. The conditions of using differential-mode current injection as a substitute for radiation are confirmed. On the basis of the theoretical analysis, the function and structure design scheme of the directional coupling device is proposed. The implementation techniques for the single differential-mode current injection method (SDMCI) and the double differential-mode current injection method (DDMCI) are discussed in detail. The typical nonlinear response interconnected systems are selected as the EUT. The test results verify the validity of the SDMCI and DDMCI test methods.

1. Introduction

Bulk current injection (BCI) is a kind of traditional EMC test method. Essentially, the interference current is injected into the cable of the equipment to substitute for radiation susceptibility test [1, 2]. As a kind of complementary method, the core of the BCI research is how to keep the equivalence with the radiation test method in broader application range and higher precision [3–6]. Although the traditional BCI method has been proposed for nearly half a century, there are still insufficiencies to substitute for the high intensity radiated field (HIRF) effects test. First, the application frequency range is limited. When the test frequency becomes higher, the injection and monitoring currents change to be sensitive to the position of the cable because of the standing wave, and the performance of the ferrite current probe descends severely. These factors make the testing precision and injection efficiency decline obviously [7–9]. Numerous studies show that when the test frequency is higher than 400 MHz, the present BCI method cannot satisfy the practical requirements [10, 11]. Second, the BCI method cannot accurately substitute for

HIRF radiation effect test for nonlinear systems. At present, the BCI method is effective when the relation between the radiated field intensity and the induced current on the cable of the equipment is linear. Thus, the injection current substituted for HIRF could be extrapolated according to the linear corresponding relation. But the majority of equipment under the condition of HIRF is nonlinear. If the same test method is applied for the nonlinear system, it may cause considerable error because of dissatisfying the extrapolation condition. Third, the BCI method is a common-mode current injection test method. It means that the interference signal injected by the current probe is a common-mode signal [12–14]. This method cannot simulate the effects caused by the differential-mode interference signal received from the antenna. The application range of the BCI method is limited.

In conclusion, HIRF in large-scale test space is very difficult to simulate under the condition of laboratory. Meanwhile, there are still many insufficiencies for the traditional BCI method to carry out the injection susceptibility tests. Hence, our research team proposes a new kind of wideband
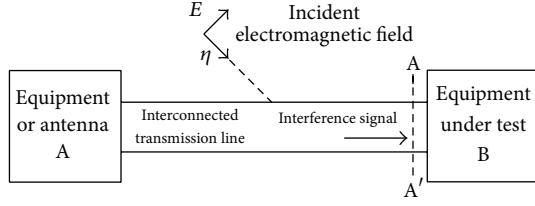
FIGURE 1: The structure of a typical interconnected system.

differential-mode current injection test method for system level EMC test.

2. Theoretical Analysis Model

The theoretical equivalent principle between the injection and radiation test method is the equal response of the equipment [15–17]. The engineering equivalent principle is the same effects caused by the two test methods. If the response voltage or the induced current on the cable port of the equipment could be ensured to be equal, the equivalence of the two test methods can be achieved [18, 19]. In this paper, the equal response voltage on the cable port of the equipment is selected as the equivalent principle of the two test methods finally.

2.1. Equivalence Analysis Model between the Injection and Radiation Response.
In this paper, the typical interconnected system is composed of two types of equipment and the interconnected cable. It is shown in Figure 1. It is assumed that equipment B is the EUT and equipment A is either the interconnected equipment or the receiving antenna. In order to calculate the radiation response voltage of the equipment B, the interconnected system is divided into two parts at the position of A-A$'$ reference plane. A-A$'$ is located at the input port of the equipment B. The left branch of A-A$'$ can be equivalent to the Thevenin equivalent circuit. It is shown in Figure 2(a), where Z_{SR} is the input impedance of the left branch of A-A$'$ and U_{SR} is the open-circuit voltage.

According to the transmission line theory, the input impedance Z_{SR} can be calculated as follows:

$$Z_{SR} = Z_C \frac{1 + \Gamma_A e^{-j2\gamma l}}{1 - \Gamma_A e^{-j2\gamma l}}, \tag{1}$$

where Γ_A is the reflection coefficient of the equipment A, Z_C is the characteristic impedance of the transmission line, l is the transmission line length between A-A$'$ and the equipment A, and γ is the propagation constant.

The open-circuit voltage U_{SR} can be calculated with the BLT equation [20–22]. Assuming that A-A$'$ port is open, that is, $\Gamma_B = 1$, the open-circuit voltage U_{SR} caused by the transmission line coupling can be calculated as follows:

$$U_{SR} = \frac{2}{1 - \Gamma_A e^{-2\gamma l}} \left(e^{-\gamma l} S_1 + \Gamma_A e^{-2\gamma l} S_2 \right), \tag{2}$$

where S_1 and S_2 are the source parameters in the BLT equation. If the equipment A is a receiving antenna, it can

be regarded as a lumped voltage source U_0. The open-circuit voltage U_{SR} caused by U_0 can be calculated as follows:

$$U_{SR} = U_0 \left(1 - \Gamma_A e^{-2\gamma l} \right)^{-1} e^{-\gamma l} \left(1 - \Gamma_A \right). \tag{3}$$

In (2) and (3), there is a linear relation between S_1, S_2, U_0, and the radiated electric field intensity E [20, 21]. We define that the linear transfer function between U_{SR} and E is f. Hence, the open-circuit voltage U_{SR} can be simplified as follows:

$$U_{SR} = f(E). \tag{4}$$

Therefore, in Figure 2(a), the radiation response U_{BR} on the impedance Z_B can be derived as follows:

$$U_{BR} = \frac{Z_B}{Z_{SR} + Z_B} U_{SR} = \frac{Z_B}{Z_{SR} + Z_B} f(E). \tag{5}$$

According to the above radiation analysis process, under the condition of the injection test, the equivalent circuit can be easily obtained. It is shown in Figure 2(b), where U_{SI} is the injection voltage source, Z_{SI} is the equivalent impedance, and U_{BI} is the injection response of equipment B. The injection response U_{BI} can be derived as follows:

$$U_{BI} = \frac{Z_B}{Z_{SI} + Z_B} U_{SI}. \tag{6}$$

According to the equivalent principle of the two test methods, that is, $U_{BI} = U_{BR}$, the equivalent injection voltage source U_{SI} can be derived as follows:

$$U_{SI} = \frac{Z_{SI} + Z_B}{Z_{SR} + Z_B} U_{SR} = \frac{Z_{SI} + Z_B}{Z_{SR} + Z_B} f(E). \tag{7}$$

Equation (7) confirms the equivalent relation between injection voltage U_{SI} and radiation electric field intensity E theoretically, which guarantees the equivalence between the injection and the radiation effects test.

2.2. Injection Voltage Source Linear Extrapolation Model.
Wideband differential-mode current injection testing technique proposed in this paper is used to substitute for high intensity radiated effects test. The crucial question is how to acquire the equivalent injection voltage source V_{SI}. According to the above equivalent ideas, we plan to acquire V_{SI} by extrapolating U_{SI} which is used to substitute for low intensity radiated effects test. Generally speaking, the majority of systems are nonlinear systems under the condition of HIRF. It means that the response voltage on the system ports will not keep linear relation with the radiated field. Thus, for nonlinear systems, how to extrapolate the injection voltage source U_{SI} is the crucial problem.

As we know, the electromagnetic radiation effects on equipment mainly include interference, degradation, failure, and damage. On the basis of theoretical analysis and experimental research for typical nonlinear systems, the action process of electromagnetic radiated energy can be divided into two subprocesses. One is the field to wire coupling
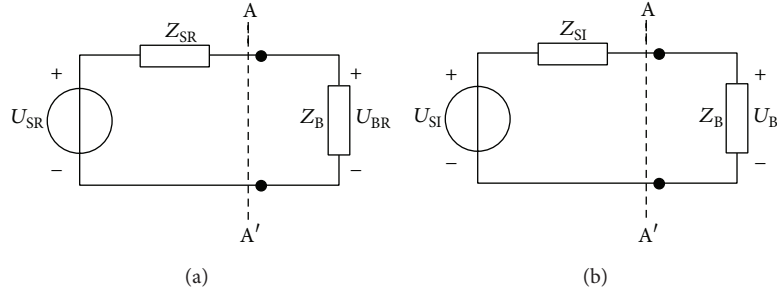
FIGURE 2: The equivalent circuit model for analyzing the equipment B response. (a) Radiation test. (b) Injection test.
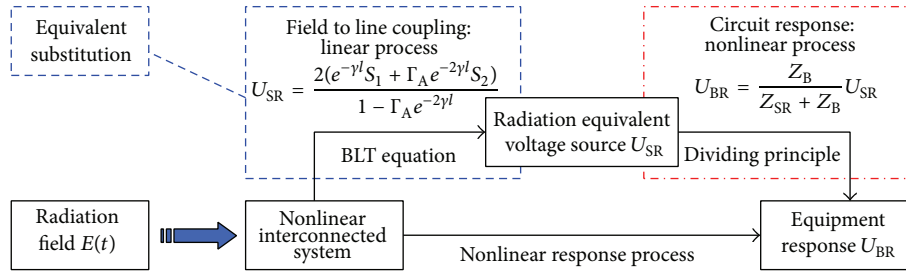
FIGURE 3: Radiation response process for nonlinear interconnected system.

process, and the other is the circuit response process of the module and device. The radiation response process is shown in Figure 3.

According to the electromagnetic field theory, the field to wire coupling is a linear process, and the circuit response of the module and device is a nonlinear process. If the excitation effects of the injection source U_{SI} and the lumped radiation source U_{SR} can be guaranteed equal at the input port of the module and device, the nonlinear circuit response in the injection experiment will be the same as in the radiation experiment. Under the condition of HIRF, in order to ensure the effect excited by injection source is the same as excited by the lumped radiation source, according to (5) and (6), two conditions must be satisfied. One is the same open-circuit voltage. The other is the same voltage division rate in the radiation and the injection test.

For the reason that U_{SR} is the equivalent lumped voltage source obtained in the linear process of the field to wire coupling or antenna receiving, the injection voltage source V_{SI} applied to substitute for HIRF radiation test can be obtained by linearly extrapolating from U_{SI}. The U_{SI} is used to substitute for the low intensity radiated field effects test; $U_{SI} = U_{SR}$. So there is no problem to satisfy the first condition. For the second condition, in order to guarantee the same voltage division rate under the condition of different excitation intensity, it is required that the output impedance of the injection voltage source is equal to the lumped radiation voltage source; that is, $Z_{SI} = Z_{SR}$. When the above two conditions can be satisfied, the equivalence between the differential-mode current injection test and HIRF radiation effect test will be guaranteed definitely.

3. Design for Supporting Equipment

Directional coupling device (DCD) is the supporting equipment for the wideband differential-mode current injection test. The typical connection mode is shown in Figure 4. On the premise of normal working status for the interconnected system, the differential-mode current injection test for equipment B can be carried out via the injection port of the DCD.

In order to satisfy the requirements of substituting the differential-mode current injection test for the radiation test, the DCD should contain the following ports. First, the DCD should contain the pass-through ports which are used to transmit the working signal between the interconnected equipment. It requires that the insertion loss is smaller than 0.5 dB. Second, the device should contain the injection port which is used to inject the differential-mode interference signal to the equipment B. It requires that the frequency band of the injection port is sufficient and the injection signal coupled into the equipment B is distortion-free. Third, the device should contain the monitoring port which is used to monitor the forward voltage signal on the transmission line of the interconnected system. It also requires that the frequency band is sufficient, and the monitoring signal is distortion-free.

According to the above function requirements of the DCD, the design scheme based on the directional coupler theory is confirmed. The DCD can be composed of two directional couplers. It is shown in Figure 5. From port 1 to port 2 of the DCD is the pass-through channel. It is used to transmit the working signal between the equipment A and equipment B. Port 4 is the injection port. It is used to inject the differential-mode interference signal to equipment B. Port
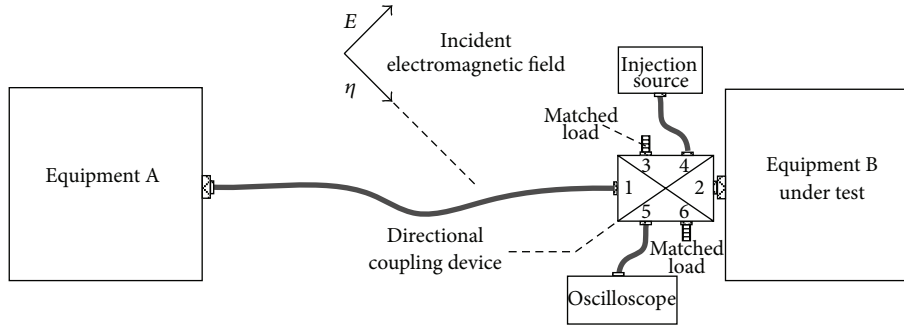
FIGURE 4: The sketch map of connection mode for DCD.
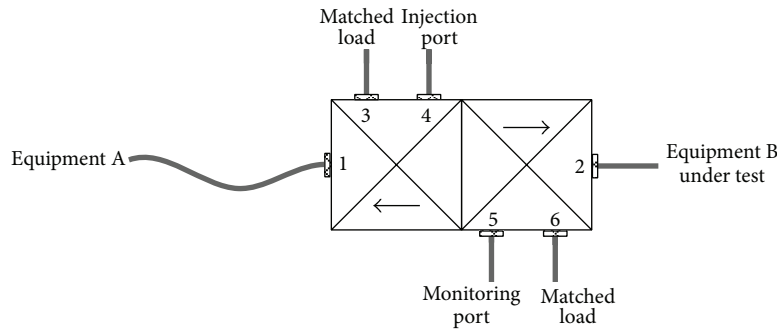
FIGURE 5: The function and structure of the DCD.

5 is the monitoring port. It is used to monitor the forward voltage signal on the transmission line of the interconnected system. Port 3 and port 6 are the isolation ports. They will be connected with the matched loads when the DCD is in use.

The above six ports DCD can be regarded as lossless and reciprocal network. The scattering matrix $\mathbf{S}$ of the DCD satisfies the characteristic of symmetry and unitarity; that is, $\mathbf{S}^T = \mathbf{S}$ and $\mathbf{S}^T\mathbf{S}^* = 1$. According to the technology requirements of the DCD, the insertion loss between port 1 and port 2 is not bigger than 0.5 dB. So the parameters S_{21} and S_{12} satisfy the equation as follows:

$$S_{21} = S_{12} \geq 0.944. \tag{8}$$

Port 4 is the injection port. It is used to inject differential-mode interference signal to equipment B. It requires higher injection efficiency, so the coupling coefficient should be as small as possible. However, too small coupling coefficient cannot satisfy the insertion loss requirement between port 1 and port 2; that is, $S_{21} = S_{12} \geq 0.944$. Taking all these into account, the coupling coefficient of port 3 and port 4 is selected as 10 dB.

According to the transmission characteristic of the traditional symmetrical directional coupler, the phase shift between the coupling channel signal and the main channel signal is 90°. If the pulse signal transmits in the main channel, the output signal waveform of the coupling port will change obviously [23]. Thus, the antisymmetry directional coupler design scheme is adopted in this paper. It makes the phase shift between the forward coupling signal and the main channel signal be 0° and the phase shift between the

backward coupling signal and the main channel signal be 180°. It is assumed that port 4 is the forward coupling port of the main channel from port 2 to port 1 and 5 is the forward coupling port of the main channel from port 1 to port 2. The directions of the two arrows in Figure 5 show the forward direction of the two antisymmetry directional couplers separately. Assuming that the S_{21} parameter is a positive real number, the S_{31} parameter is a negative real number. If the coupling coefficient of port 3 and port 4 is 10 dB, it can be derived that

$$S_{31} = -\sqrt{0.1}. \tag{9}$$

According to the unitarity of the scattering matrix $\mathbf{S}$, considering the insert loss requirement of $S_{21} \geq 0.944$, it can be derived as follows:

$$|S_{51}| \leq 0.094. \tag{10}$$

For the phase shift between the forward coupling signal and the main channel signal which is 0°, considering the energy coupling action of port 3, the parameter S_{51} can be derived as follows:

$$S_{51} = \sqrt{(1 - 0.1)\,10^{-x/10}}, \tag{11}$$

where x is the coupling coefficient of port 5 and port 6. Considering the manufacturing technology and the convenience for application, the coupling coefficient of port 5 and port 6 is confirmed to be 20 dB.
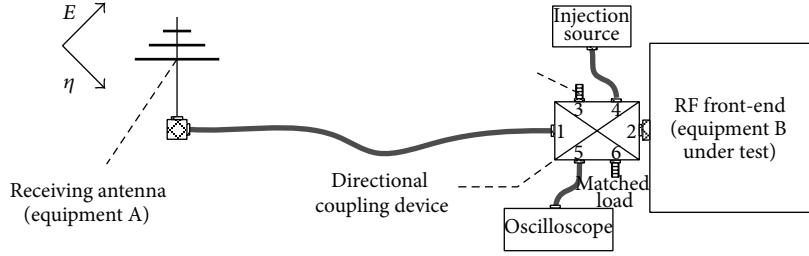
FIGURE 6: The typical test configuration of SDMCI test method.
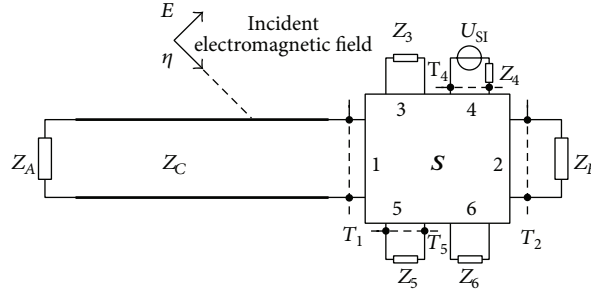
FIGURE 7: The equivalent circuit model when the DCD is inserted into the interconnected system.

From the above analysis process, the scattering matrix **S** of the six ports DCD can be calculated as follows:

$$\mathbf{S} = \begin{bmatrix} 0 & 0.944 & -0.316 & 0 & 0.095 & 0 \\ 0.944 & 0 & 0 & 0.315 & 0 & -0.1 \\ -0.316 & 0 & 0 & 0.949 & 0 & 0 \\ 0 & 0.315 & 0.949 & 0 & 0.032 & 0 \\ 0.095 & 0 & 0 & 0.032 & 0 & 0.995 \\ 0 & -0.1 & 0 & 0 & 0.995 & 0 \end{bmatrix}. \quad (12)$$

4. Implementation Technology of SDMCI

Because of the directional injection characteristic of the DCD, the single differential-mode current injection (SDMCI) method is used to carry out injection test only for one end equipment in the interconnected system. The typical application is to carry out differential-mode current injection test for antenna receiving system. The test configuration of the SDMCI is shown in Figure 6. It can simulate the effects caused by the interference signal received from the antenna when the antenna receiving system is in the normal working condition.

4.1. Equivalent Condition Analysis When DCD Is Inserted into the Interconnected System. The forward voltage signal extraction, interference signal injection, and normal transmission signal monitoring are realized with the support of the DCD. However, whether it satisfies the equivalent condition discussed above or not is the crucial problem, which is analyzed as follows.

The DCD can be equivalent to six ports black box network. The equivalent circuit model is shown in Figure 7, where T_1, T_2, T_4, and T_5 are the reference plane at different ports of the DCD, Z_3 and Z_6 are the matched load, Z_5 is the

input impedance of the oscillograph, U_{SI} is the open-circuit voltage of the injection voltage source, and Z_4 is the internal impedance of the injection voltage source.

As for the radiation test, the left part of the reference plane T_1 can be equivalent to the source wave $\widehat{a}_{1R}$ and the reflection coefficient Γ_1. It also can be equivalent to the open-circuit voltage U_{SR} and the source impedance Z_1. Similarly, as for the differential-mode current injection test, the top part of reference plane T_4 can be equivalent to the source wave $\widehat{a}_{4I}$ and the reflection coefficient Γ_4. It also can be equivalent to the open-circuit voltage U_{SI} and the source impedance Z_4. Therefore, the equivalent circuit model for the radiation and injection test is shown in Figure 8. It can be seen that the network model without source is the same in the radiation and injection test. The difference is that the equivalent source is located in the different ports of the DCD.

On the basis of the equivalent source wave theory in microwave engineering [24], under the condition of the radiation and injection test, the relation between the equivalent source wave and equivalent voltage source is as follows:

$$\widehat{a}_{1R} = \frac{U_{SR}(1 - \Gamma_1)}{2\sqrt{Z_C}}, \quad (13)$$

$$\widehat{a}_{4I} = \frac{U_{SI}(1 - \Gamma_4)}{2\sqrt{Z_C}} = \frac{U_{SI}}{2\sqrt{Z_C}}. \quad (14)$$

In order to analyze the response of the equipment B, the left part of the reference plane T_2 is required to simplify further. In the radiation test, the left part of T_2 is equivalent to the source wave $\widehat{b}_{2R}$ and the reflection coefficient Γ'_{2R}. In the injection test, the left part of T_2 is equivalent to the source wave $\widehat{b}_{2I}$ and the reflection coefficient Γ'_{2I}. It is shown in Figure 9.
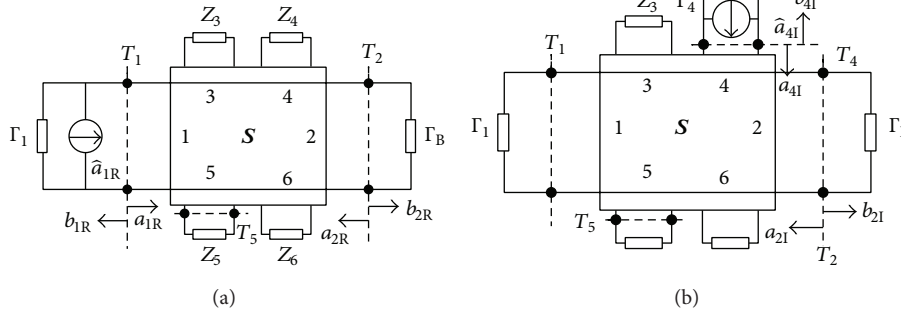
FIGURE 8: The equivalent circuit model for (a) radiation test and (b) injection test.
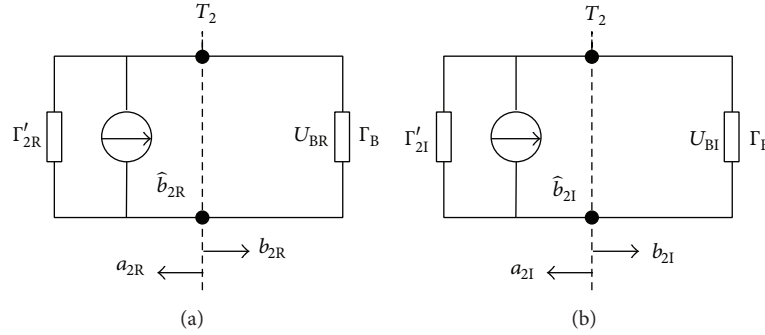
FIGURE 9: The further simplified circuit models for (a) radiation test and (b) injection test.

According to the equivalent source wave theorem [24], $\widehat{b}_{2R}$, $\widehat{b}_{2I}$, Γ'_{2R}, and Γ'_{2I} can be derived as follows:

$$\widehat{b}_{2R} = \sum_{\substack{k=1 \\ k \neq 2}}^{n} \frac{D_{(2Sk)}}{D_{(22)}} \widehat{a}_k = \frac{D_{(2S1)}}{D_{(22)}} \widehat{a}_{1R} = S_{21} \widehat{a}_{1R}, \tag{15}$$

$$\widehat{b}_{2I} = \sum_{\substack{k=1 \\ k \neq 2}}^{n} \frac{D_{(2Sk)}}{D_{(22)}} \widehat{a}_k = \frac{D_{(2S4)}}{D_{(22)}} \widehat{a}_{4I} = S_{24} \widehat{a}_{4I}, \tag{16}$$

$$\Gamma'_{2R} = \Gamma'_{2I} = \frac{D_{(2S2)}}{D_{(22)}} = S_{21}^2 \Gamma_1 = S_{21}^2 \Gamma_A e^{-2\gamma l}. \tag{17}$$

It is defined that the matrix $\mathbf{D} = 1 - \mathbf{S}\boldsymbol{\Gamma}$, where $\boldsymbol{\Gamma}$ is a diagonal matrix. The elements of $\boldsymbol{\Gamma}$ are the load reflection coefficient on different ports of the DCD. In (15) to (17), $D_{(iSk)}$ is a determinant that the column i of the matrix $\mathbf{D}$ is changed to be the column k of the matrix $\mathbf{S}$. $D_{(ii)}$ is also a determinant that the column i and row i of the matrix $\mathbf{D}$ are deleted. As can be seen from (17), when the DCD is inserted into the interconnected system, the reflection coefficient Γ'_{2R} is equal to Γ'_{2I}. It means that the output impedance of the equivalent excitation source is the same under the condition of the radiation and injection test. Hence, the second equivalent condition (i.e., $Z_{SI} = Z_{SR}$) discussed above can be satisfied.

According to the equivalent circuit model in Figure 9, the radiation response U_{BR} and the injection response U_{BI} of the equipment B can be derived as follows:

$$U_{BR} = \frac{\widehat{b}_{2R} \sqrt{Z_C} (1 + \Gamma_B)}{1 - \Gamma'_{2R} \Gamma_B},$$

$$U_{BI} = \frac{\widehat{b}_{2I} \sqrt{Z_C} (1 + \Gamma_B)}{1 - \Gamma'_{2I} \Gamma_B}. \tag{18}$$

According to the equivalent principle of the two test methods (i.e., $U_{BI} = U_{BR}$), from (13) to (18), the corresponding relation between the equivalent injection voltage source U_{SI} and the lumped radiation voltage source U_{SR} can be derived as follows:

$$U_{SI} = S_{21} S_{24}^{-1} \left(1 - \Gamma_A e^{-2\gamma l}\right) U_{SR}. \tag{19}$$

If the equipment A is an antenna or a transmitter, the reflection coefficient Γ_A usually remains unchanged. In addition, the S parameter of the DCD is constant. According to (19), the relation between U_{SI} and U_{SR} is linear.

From the above analysis process, when the DCD is inserted into the interconnected system, under the condition of unchanged reflection coefficient Γ_A, the relation between the injection voltage U_{SI} and the radiated field intensity E is always linear. Therefore, the injection voltage source obtained by the linear extrapolation satisfies the first equivalent condition for the radiation and differential-mode current injection test.

FIGURE 10: The typical test configuration of DDMCI test method.

4.2. Feasibility Analysis on Using the Monitoring Port Response Voltage of the DCD as Equivalent Principle. The equivalent principle for the radiation and injection test in this paper is the equal response voltage on the input port of the equipment B. However, it is very hard for us to directly monitor the input port response voltage in engineering. In order to make the SDMCI method applicable in the practical engineering test, other transmission signals which can be easily monitored should be selected as equivalent principle. The introduction of the DCD solves the problem.

The port 5 of DCD is used to monitor the forward voltage on the transmission line. In this paper, the equal response voltage on port 5 is defined as the equivalent principle for the SDMCI and radiation test. The following article proofs the correctness of using the port 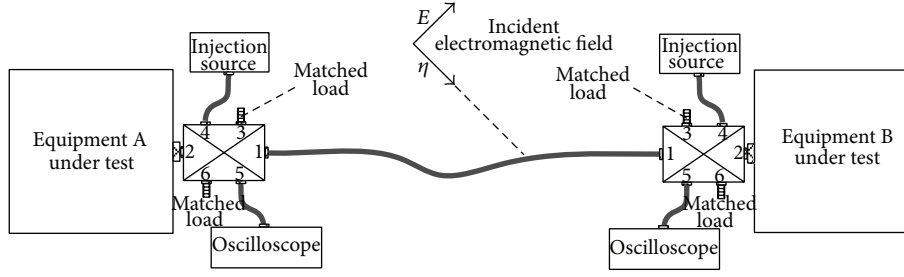5 response voltage as the equivalent principle. According to the equivalent circuit model in Figure 8, as for the reference plane T_5, the radiation equivalent source wave $\widehat{b}_{5R}$ and the injection equivalent source wave $\widehat{b}_{5I}$ that transmit to the direction of impedance Z_5 can be derived as follows:

$$
\widehat{b}_{5R} = \frac{D_{(5S1)}}{D_{(55)}}\widehat{a}_{1R} = \frac{S_{51}}{1 - S_{21}^2 \Gamma_1 \Gamma_B}\widehat{a}_{1R},
$$
$$
\widehat{b}_{5I} = \frac{D_{(5S4)}}{D_{(55)}}\widehat{a}_{4I} = \frac{S_{54} + S_{21}(S_{51}S_{24} - S_{54}S_{21})\Gamma_1 \Gamma_B}{1 - S_{21}^2 \Gamma_1 \Gamma_B}\widehat{a}_{4I}.
$$
(20)

Assuming that the coupling coefficient of port 4 and port 5 is m and n separately and the unit is dB, then

$$
S_{51}S_{24} = S_{54}S_{21} = \sqrt{(1 - 10^{-m/10})(1 - 10^{-n/10})10^{-(m+n)/10}},
$$
$$
\widehat{b}_{5I} = \frac{\widehat{a}_{4I}S_{54}}{1 - S_{21}^2 \Gamma_1 \Gamma_B}.
$$
(21)

Under the condition of the radiation and injection test, the response voltages U_{MR} and U_{MI} on monitoring port 5 can be derived as follows:

$$
U_{MR} = \sqrt{Z_C}\widehat{b}_{5R} = \frac{S_{51}(1 - \Gamma_1)U_{SR}}{2(1 - S_{21}^2 \Gamma_1 \Gamma_B)},
$$
$$
U_{MI} = \sqrt{Z_C}\widehat{b}_{5I} = \frac{S_{54}U_{SI}}{2(1 - S_{21}^2 \Gamma_1 \Gamma_B)}.
$$
(22)

It is assumed that $U_{MR} = U_{MI}$; then the relation between U_{SI} and U_{SR} can be derived from (22) as follows:

$$
U_{SI} = S_{21}S_{24}^{-1}(1 - \Gamma_A e^{-2\gamma l})U_{SR}.
$$
(23)

It can be seen that (23) is equal to (19). It means that the radiation response U_{BR} is equal to the injection response U_{BI}. Therefore, the above theoretical derivation processes verify the correctness of using the port 5 response voltage as the equivalent principle.

4.3. Test Procedure of SDMCI

Step 1. Carry out the low intensity radiation pretest for interconnected systems. The radiated field intensity is selected as E_1 which can ensure that the response of equipment B is in the linear region. The output response U_{MR} on the monitoring port 5 of the DCD is recorded.

Step 2. Obtain the equivalent corresponding relation between injection voltage and radiated electric field intensity. The differential-mode current injection test is carried out through injection port 4 of the DCD. The output response U_{MI} on the monitoring port 5 is measured at the same time. When $U_{MI} = U_{MR}$, the injection voltage U_{SI} is recorded. The equivalent relation between the injection voltage and the radiated field intensity can be described as $k = U_{SI}/E_1$.

Step 3. Finish the SDMCI test for interconnected systems. If the high intensity radiated field for ultimate examination is E_2, then the equivalent injection voltage can be calculated by the equation $V_{SI} = kE_2$. Therefore, the SDMCI test can be carried out finally with the equivalent injection voltage V_{SI} through the injection port 4 of the DCD.

5. Implementation Technology of DDMCI

In order to carry out differential-mode current injection test for two types of equipment interconnected by a cable simultaneously, the double differential-mode current injection test (DDMCI) method is proposed in this paper. The test configuration of the DDMCI is shown in Figure 10.

Two directional coupling devices are connected with equipment A and equipment B separately. The equivalent

circuit model is shown in Figure 11, where U_{SLI} is the injection voltage source of the left DCD and U_{SRI} is the injection voltage source of the right DCD. Normally, the impedances of equipment A and equipment B are not matched. So the responses of equipment A and equipment B are the result of the joint action of U_{SLI} and U_{SRI}.

In order to ensure that the injection response is equal to the radiation response of equipment A and equipment B, two injection voltage sources U_{SLI} and U_{SRI} are required to satisfy certain amplitude and phase relation. The detailed test procedure of DDMCI method is summarized as follows.

Step 1. Carry out low intensity radiation pretest for interconnected system. The radiated electric field intensity is selected as E_1 which can ensure the responses of equipment A and equipment B are in the linear region. The amplitude and phase on the left and right monitoring ports of the DCDs are recorded as U_{5LR}, U_{5RR}, φ_{5LR}, and φ_{5RR}.

Step 2. Obtain the equivalent corresponding relation between injection voltage and radiated electric field intensity. First, the interconnected system is carried out injection test through port 4L with the left injection voltage source. The amplitude U_{5LI} and phase φ_{5LI} on the monitoring port 5L are measured. When $U_{5LI} = U_{5LR}$ and $\varphi_{5LI} = \varphi_{5LR}$, the amplitude and phase of the left injection voltage source remain unchanged. Second, the interconnected system is carried out injection test through port 4R with the right injection voltage source. The amplitude U_{5RI} and phase φ_{5RI} on the monitoring port 5R are measured. When $U_{5RI} = U_{5RR}$ and $\varphi_{5RI} = \varphi_{5RR}$, the amplitude and phase of the right injection voltage source remain unchanged. Third, repeat the first and the second steps until the conditions of $U_{5LI} = U_{5LR}$, $U_{5RI} = U_{5RR}$, $\varphi_{5LI} = \varphi_{5LR}$, and $\varphi_{5RI} = \varphi_{5RR}$ are satisfied simultaneously. Fourth, the amplitudes U_{SLI} and U_{SRI} and the phases φ_{SLI} and φ_{SRI} of the two injection voltage sources are recorded finally. The corresponding relation between equivalent injection voltage and radiated electric field intensity can be calculated by $k_L = U_{SLI}/E_1$ and $k_R = U_{SRI}/E_1$.

Step 3. Finish the DDMCI test for interconnected system. If the high intensity radiated field for ultimate examination is E_2, then the left and right equivalent injection voltage sources can be calculated by $V_{SLI} = k_L E_2$ and $V_{SRI} = k_R E_2$. The phase difference between the two injection voltage sources satisfies $\varphi_\Delta = \varphi_{SLI} - \varphi_{SRI}$. Finally, the DDMCI test can be carried out through the injection ports 4L and 4R of the DCDs, and it is equivalent to the E_2 radiation test.

6. Experimental Verification

6.1. The Linear Relation Verification between the Equivalent Injection Voltage and the Radiated Field Intensity. The interconnected system under test is a typical nonlinear response system. It is composed of a receiving antenna, a coaxial cable, and RF front-end components. The RF front-end components include a clipping filter, an attenuator, a low noise amplifier (LNA), a sensitivity controller, a directional coupler, and a clipping amplifier. They are integrated together

in one container. It is assumed that the receiving antenna is the equipment A_1 and the container of the RF front-end components is the equipment B_1. Because of the nonlinear response characteristic of the clipping filter, LNA, and so on, the above nonlinear response interconnected system is suitable to carry out the verification test.

The single frequency continuous wave radiation test and the differential-mode current injection test are carried out separately for the interconnected system. The radiation and injection configuration diagrams are shown in Figures 12 and 13. The output response of equipment B_1 is monitored by the spectrum analyzer. The relation curves between the radiated electric field intensity, the injection voltage, and the output response of equipment B_1 are recorded separately.

The equal output response of equipment B_1 for the radiation and injection test is regarded as the equivalent principle. According to the result of the data processing, the relation curves between the equivalent injection voltage, the output response of equipment B_1, and the radiated electric field intensity are shown in Figure 14.

It can be seen form Figure 14 that the relation between the radiated electric field intensity and the output response of equipment B_1 is nonlinear. In contrast, the relation between the radiated electric field intensity and the equivalent injection voltage is linear. In addition, a small number of data points which are in the saturation region do not strictly accord with the linear relation. We believe that it is caused by experimental error. The reason is that the output response of the equipment B_1 is not sensitive to the radiated field intensity or the injection voltage when the equipment B_1 works in the saturation region. It means that two different input signals can produce almost the same output response. In conclusion, even for the nonlinear response system, the corresponding relation between the equivalent injection voltage and the radiated electric field intensity at different frequency points is still linear.

6.2. The Validity Verification for SDMCI Test Method. The interconnected system under test is also the above nonlinear response system. The validity verification for SDMCI can be conducted as follows. First, the traditional radiation test is carried out for the interconnected system. The radiation response curve of the equipment B_1 from the linear region to the saturation region can be obtained. Second, according to the above SDMCI test method, the injection response curve of the equipment B_1 from the linear region to the saturation region can also be abstained. Third, by calculating and analyzing the output response error of the two test methods, the validity of SDMCI method can be verified.

The response curves of the equipment B_1 under the condition of radiation and the SDMCI test at the frequency point of 3.3 GHz, 4.0 GHz and 5.6 GHz are shown in Figure 15. It can be seen that the output response curve obtained by the SDMCI test is almost exactly the same as that obtained by the radiation test. In order to analyze the error of the SDMCI test method, the test data in Figure 15 are processed. The output response relative error η for the SDMCI test method is shown in Table 1. As can be seen from Table 1, the relative error η is
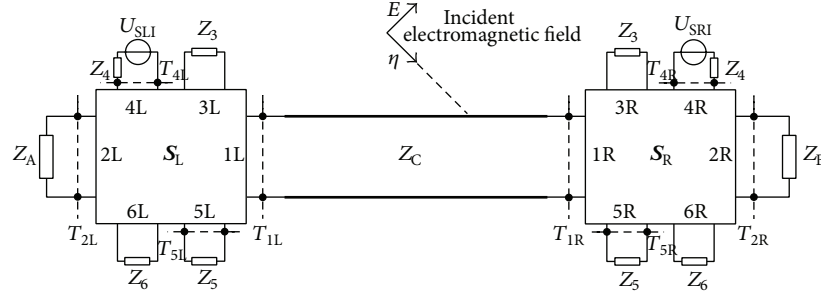
FIGURE 11: The equivalent circuit model of DDMCI test method.
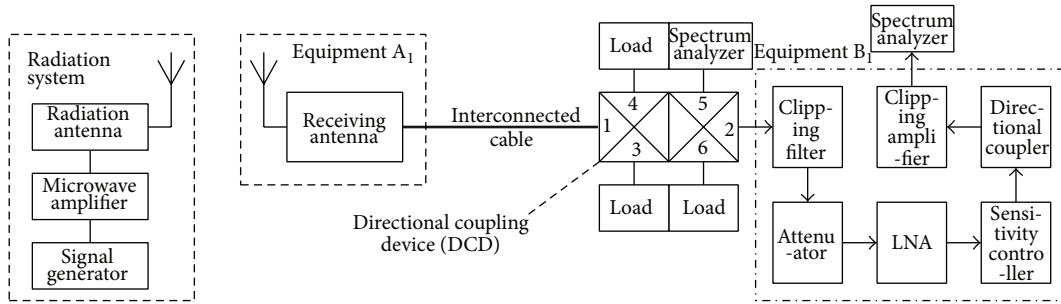
FIGURE 12: The configuration diagram for the radiation test.
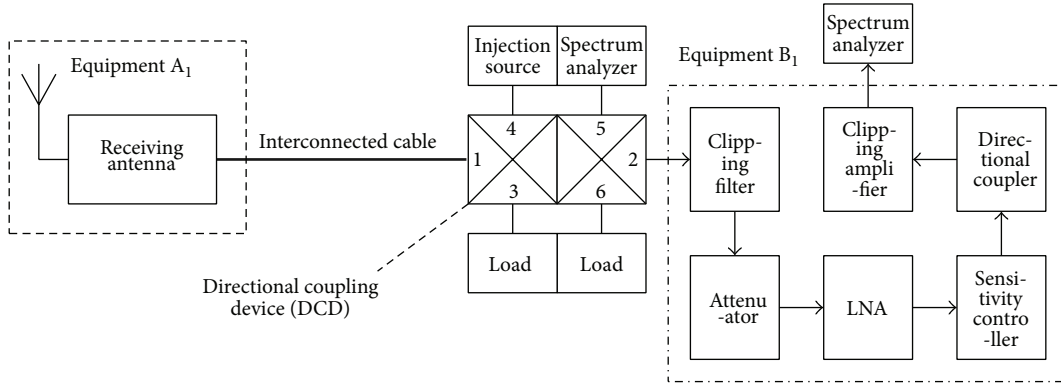
FIGURE 13: The configuration diagram for the differential-mode current injection test.

small and the biggest one is 2.39%. The error comes from the performance fluctuation of the RF front-end components, the noise of active device, the reading error of instrument, and so on. There is no systematic error for the SDMCI test method.

6.3. The Validity Verification for DDMCI Test Method. Two satellite-borne RF front-end low-noise amplifier modules are selected as equipment A_2 and equipment B_2 which are connected by a coaxial cable. It is important to note that this kind of interconnected system does not exist in engineering.

The designed interconnected system is only for experimental verification in the extreme condition.

The radiation test configuration is shown in **Figure 16**. The coaxial cable under test is placed in the shielded room. It is connected with port 1 of the DCD through the interface board. Port 2 of the DCD is connected with the equipment under test. The output port of the equipment is connected with spectrum analyzer (SA) which is used to monitor the output response of the equipment. Outside the shielded room, vector network analyzer (VNA) is used as transmitter and receiver. Port 1 of the VNA is used as signal generator. It is connected with radiation antenna in the shielded room

FIGURE 14: The relation curves between the equivalent injection voltage and the radiated electric field intensity.

FIGURE 15: The response curves under the condition of radiation and SDMCI test.

TABLE 1: Output response relative error for SDMCI test method.

Number	f = 3.3 GHz		f = 4.0 GHz		f = 5.6 GHz	
	E/Vm^{-1}	η/%	E/Vm^{-1}	η/%	E/Vm^{-1}	η/%
1	20.00	0.12	20.00	0.93	19.95	0.12
2	22.44	0.34	28.25	0.12	28.18	0.34
3	25.18	0.46	39.91	0.34	35.48	0.69
4	28.25	0.46	50.24	1.14	44.67	1.49
5	31.70	1.14	63.25	1.37	56.23	1.71
6	35.57	1.26	70.96	1.60	70.79	1.94
7	39.91	1.14	79.62	1.83	89.13	1.83
8	44.77	1.26	89.34	1.60	112.20	**2.39**
9	50.24	1.37	100.24	1.60	141.25	1.49
10	56.37	1.14	112.47	1.83	158.49	1.03
11	63.25	1.14	126.19	1.83	177.83	1.14
12	70.96	1.03	133.67	1.71	188.36	1.60
13	79.62	0.92	141.59	1.60	199.53	1.14
14	89.34	0.92	149.98	1.60	211.35	1.03
15	100.24	0.92	158.87	1.37	223.87	0.80
16	106.18	0.92	168.28	1.37	237.14	0.69
17	112.47	0.69	178.25	1.26	251.19	1.03
18	119.13	0.57	188.81	1.14	266.07	0.34
19	126.19	0.46	200.00	1.03	281.84	0.35
20	133.67	0.46	211.85	0.80	298.54	0.69
21	141.59	0.46	224.40	0.69	316.23	0.81
22	149.98	0.34	—	—	334.97	0.81
23	158.87	0.00	—	—	354.81	0.23
24	168.28	0.12	—	—	375.84	0.46
25	178.25	0.12	—	—	398.11	0.12

circuits have different amplitude and phase, the continuously adjustable attenuator and 360°/GHz phase shifter are inserted into one circuit. Port 2 of the VNA is also used as receiver. It is used to measure the response on the monitoring ports 5L and 5R of the DCDs under the condition of DDMCI test. The other test configuration is the same as in the above radiation test.

According to the test configuration in Figures 16 and 17 and the above test procedure, in the working frequency band of the low-noise amplifier modules, the three frequency points 1.510 GHz, 1.605 GHz, and 1.75 GHz are selected to carry out radiation and DDMCI test. The radiation and DDMCI response curve is shown in Figures 18 and 19.

As can be seen from Figures 18 and 19, the output response curve of equipment A_2 and equipment B_2 obtained by DDMCI test is almost exactly the same as that obtained by radiation test. In order to analyze the error of DDMCI test method, the test data in Figures 18 and 19 are processed. The output response relative error for DDMCI test method 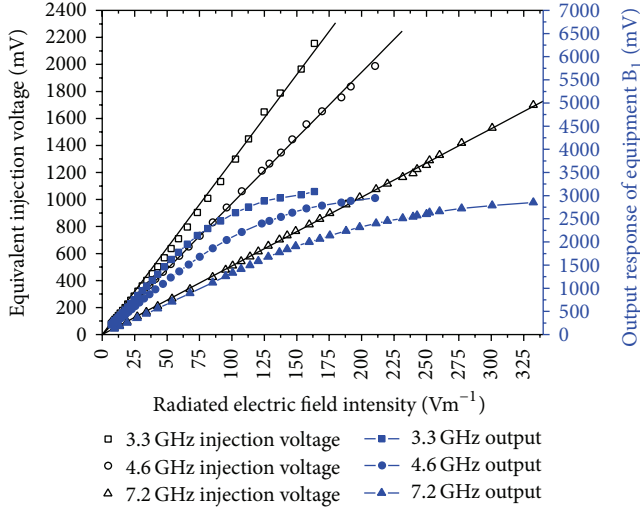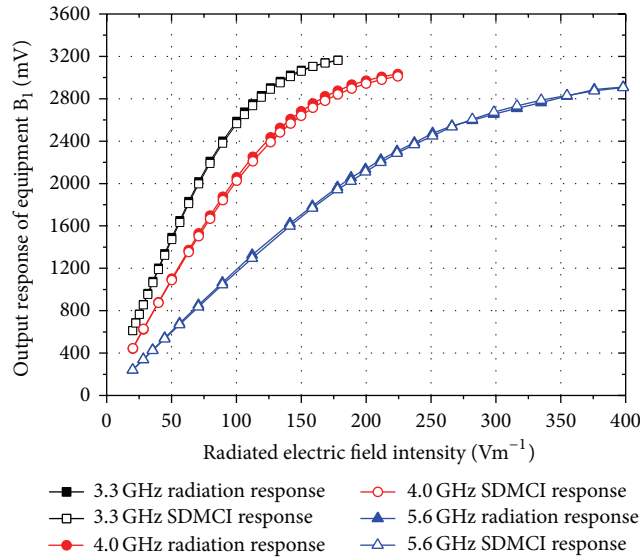is shown in Table 2. As can be seen from Table 2, the biggest output response relative error is only 3.39%. The test results indicate that the DDMCI test method can effectively simulate the HIRF effect experiment for nonlinear interconnected system.

through power amplifier. The radiation antenna is placed ahead of the coaxial cable under test. Port 2 of the VNA is used as receiver. It is connected with the monitoring port of the DCD. The amplitude and phase difference of the two monitoring ports of the DCDs can be obtained by testing the parameter S_{21}.

The DDMCI test configuration is shown in Figure 17. Port 1 of the VNA is used as injection signal source. In order to carry out differential-mode current injection test for the two interconnected types of equipment simultaneously, the injection signal is divided into two circuits by the power divider. They are connected with the injection ports 4L and 4R of the DCDs separately. In order to ensure that the two

TABLE 2: Output response relative error for DDMCI test method.

Number	$f = 1.510\,\text{GHz}$			$f = 1.605\,\text{GHz}$			$f = 1.750\,\text{GHz}$		
	E/Vm^{-1}	$\eta_{A2}/\%$	$\eta_{B2}/\%$	E/Vm^{-1}	$\eta_{A2}/\%$	$\eta_{B2}/\%$	E/Vm^{-1}	$\eta_{A2}/\%$	$\eta_{B2}/\%$
1	12.62	0.35	0.35	14.16	0.34	0.92	12.62	1.49	**3.39**
2	15.89	0.00	0.23	17.83	0.00	1.26	15.89	1.26	2.61
3	20.00	1.14	1.49	22.44	0.46	0.57	20.00	0.57	2.16
4	25.18	0.80	1.26	28.25	1.16	0.12	22.44	0.81	1.83
5	31.70	0.46	1.26	35.57	1.39	0.69	25.18	0.69	1.03
6	39.91	0.34	0.92	44.77	1.62	1.16	28.25	1.51	0.69
7	44.77	0.12	0.69	50.23	1.86	1.16	31.70	1.51	0.46
8	50.24	0.23	0.57	56.37	1.86	1.39	35.57	1.86	0.23
9	56.37	0.35	0.34	63.25	1.98	1.51	39.91	1.16	0.46
10	63.25	0.46	0.46	70.96	1.86	1.62	44.77	1.51	0.23
11	66.99	0.81	0.12	75.17	1.98	1.51	50.24	1.62	0.00
12	70.96	0.35	0.34	79.62	1.74	1.62	56.37	2.09	0.23
13	75.16	0.93	0.23	84.34	1.39	1.27	59.71	2.21	0.23
14	79.62	0.35	0.12	89.34	1.04	1.39	63.25	2.09	0.23
15	84.34	0.81	0.35	—	—	—	66.99	2.45	0.58
16	89.34	0.23	0.00	—	—	—	70.96	2.92	0.69
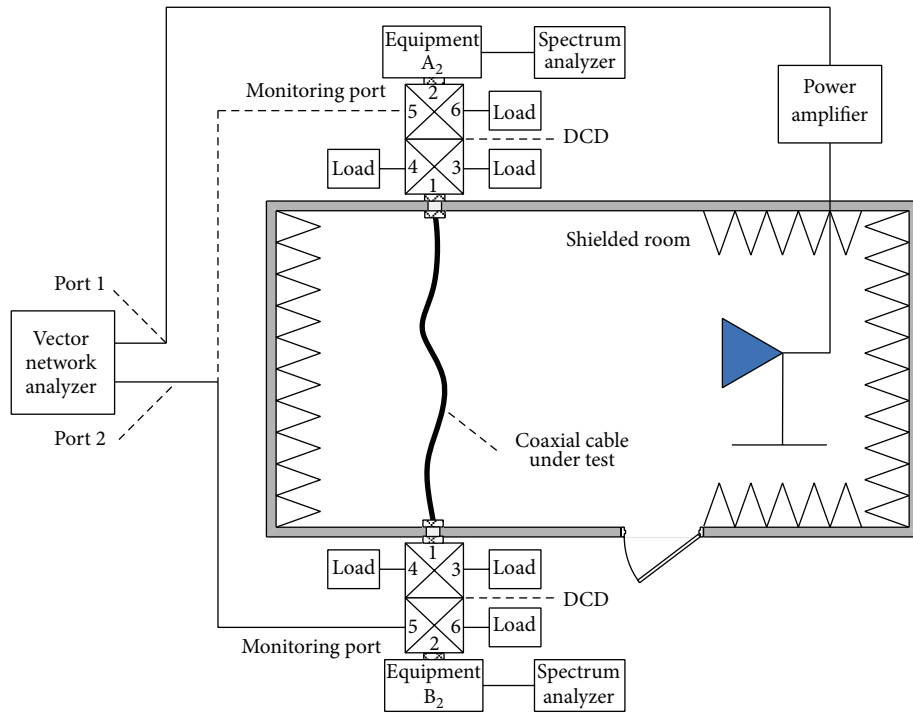
FIGURE 16: The configuration diagram for the radiation test.

7. Conclusions

The theory, model, method, and implementation technique of the wideband differential-mode current injection test technology are systematically studied in this paper. The injection and radiation response analysis model and the injection voltage source extrapolation model in HIRF are established. The conditions of using injection as a substitute for radiation are confirmed. The equivalent injection voltage source can be obtained by the linear extrapolation. The function and structure design scheme of the directional coupling device (DCD) is proposed. The forward voltage extraction, interference signal injection, and normal transmission signal monitoring in the interconnected system are realized with the support of DCD. On the basis of the above research, the SDMCI test method and the DDMCI test method based on the DCD are summarized. The typical nonlinear response systems are selected as EUT. The test results indicate that
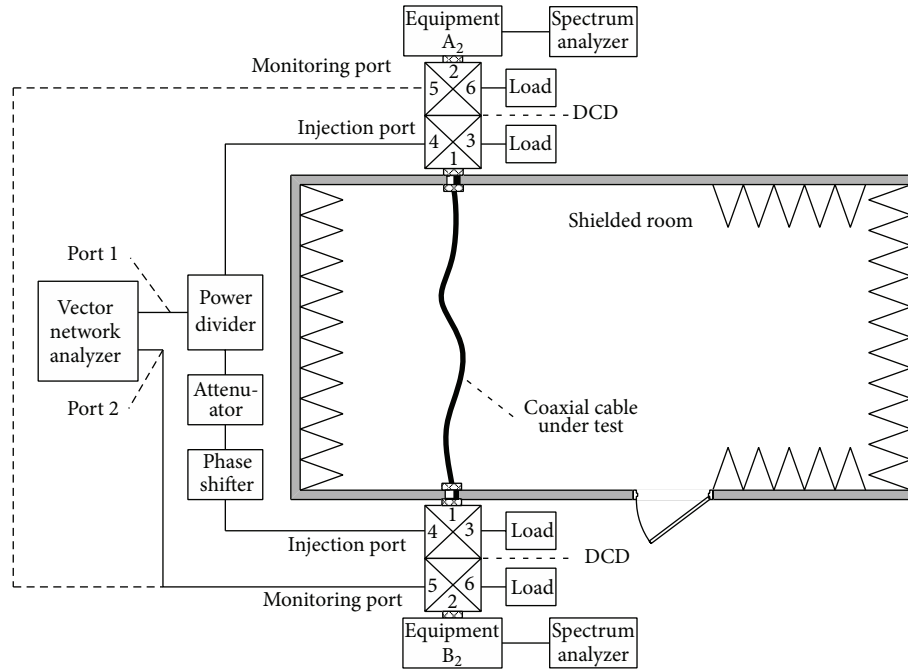
FIGURE 17: The configuration diagram for the DDMCI test.
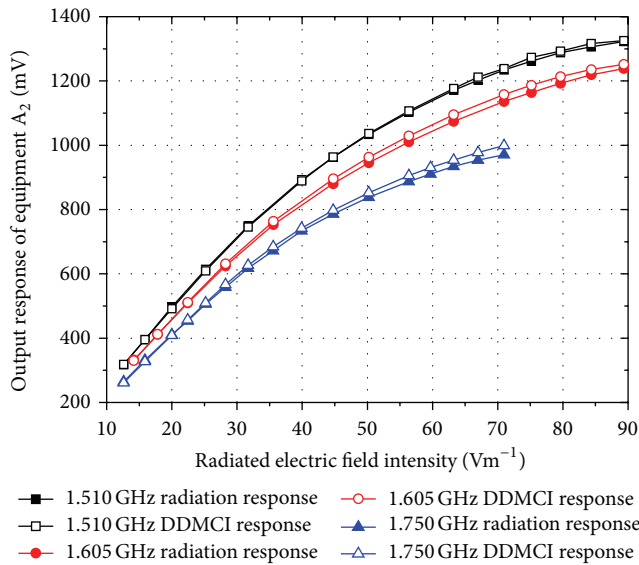
FIGURE 18: The radiation and DDMCI response curve of equipment A_2.
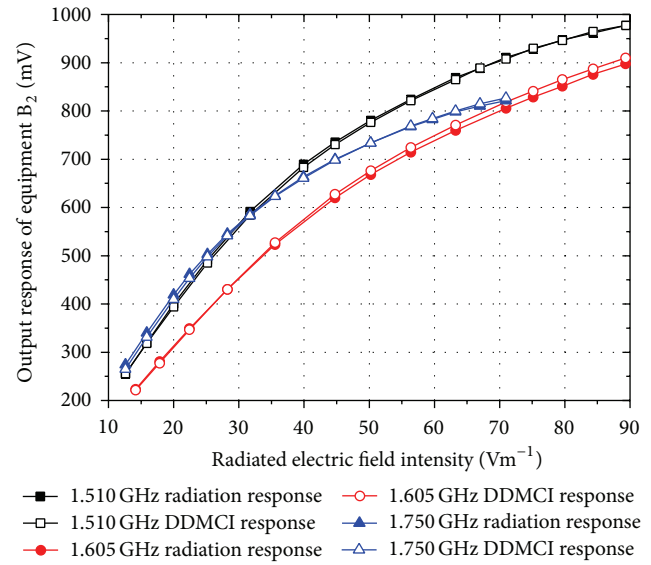
FIGURE 19: The radiation and DDMCI response curve of equipment B_2.

the biggest output response relative error is smaller than 5%. They verify the validity of the SDMCI and the DDMCI test methods.

Conflict of Interests

The authors declare that there is no conflict of interests regarding the publication of this paper.

References

[1] N. J. Carter and E. G. Stevens, "Bulk current injection (BCI): Its past, present and future in aerospace," in *Proceedings of the*

IEE Colloquium on EMC Testing for Conducted Mechanisms, pp. 2/1–2/12, May 1996.

[2] G. A. Rasek and M. Gabrisak, "Wire bundle currents for high intensity radiated fields (HIRF) and indirect effects of lightning (IEL) with focus on bulk current injection (BCI) test," in *Proceedings of the 21st International Conference Radioelektronika*, pp. 1–10, Brno, Czech Republic, April 2011.

[3] J. W. Adams, J. Cruz, and D. Melquist, "Comparison measurements of currents induced by radiation and injection," *IEEE Transactions on Electromagnetic Compatibility*, vol. 34, no. 3, pp. 360–362, 1992.

[4] J. Perini and L. S. Cohen, "On the equivalence of radiated and injected tests," in *Proceedings of the IEEE International Symposium on Electromagnetic Compatibility*, pp. 77–80, August 1995.

[5] D. H. Trout, "Investigation of the bulk current injection technique by comparison to induced currents from radiated electromagnetic fields," in *Proceedings of the IEEE International Symposium on Electromagnetic Compatibility*, pp. 412–417, Santa Clara, Calif, USA, August 1996.

[6] S. Pignari and F. G. Canavero, "On the equivalence between radiation and injection in BCI testing," in *Proceedings of the IEEE International Symposium on Electromagnetic Compatibility (EMC '97)*, pp. 179–182, May 1997.

[7] G. Cerri, R. de Leo, V. M. Primiani, S. Pennesi, and P. Russo, "Wide-band characterization of current probes," *IEEE Transactions on Electromagnetic Compatibility*, vol. 45, no. 4, pp. 616–625, 2003.

[8] F. Grassi, F. Marliani, and S. A. Pignari, "Circuit modeling of injection probes for bulk current injection," *IEEE Transactions on Electromagnetic Compatibility*, vol. 49, no. 3, pp. 563–576, 2007.

[9] S. Pignari, F. Grassi, F. Marliani, and F. G. Canavero, "Experimental characterization of injection probes for bulk current injection," in *Proceedings of the 28th General Assemblies International Union of Radio Science (URSI '05)*, Paper EA.4 (0494), New Delhi, India, October 2005.

[10] S. Pignari and F. G. Canavero, "Theoretical assessment of bulk current injection versus radiation," *IEEE Transactions on Electromagnetic Compatibility*, vol. 38, no. 3, pp. 469–477, 1996.

[11] D. H. Trout and N. F. Audeh, "Evaluation of electromagnetic radiated susceptibility testing using induced current," in *Proceedings of the IEEE Aerospace Conference*, vol. 4, pp. 69–80, Aspen, Colo, USA, February 1997.

[12] S. Caniggia and F. Maradei, "SPICE-like models for the analysis of the conducted and radiated immunity of shielded cables," *IEEE Transactions on Electromagnetic Compatibility*, vol. 46, no. 4, pp. 606–616, 2004.

[13] A. Orlandi, "Circuit model for bulk current injection test on shielded coaxial cables," *IEEE Transactions on Electromagnetic Compatibility*, vol. 45, no. 4, pp. 602–615, 2003.

[14] A. Orlandi, G. Antonini, and R. M. Rizzi, "Equivalent circuit model of a bundle of cables for Bulk Current Injection (BCI) test," *IEEE Transactions on Electromagnetic Compatibility*, vol. 48, no. 4, pp. 701–713, 2006.

[15] J. Perini, "Radiated versus injected measurements: when are they equivalent?" in *Proceedings of the 10th International Zurich Symposium on Electromagnetic Compatibility*, pp. 343–348, 1993.

[16] J. Perini and L. S. Cohen, "Radiated and injected tests: when are they equivalent?" in *Proceedings of the 11th International Zurich Symposium on Electromagnetic Compatibility*, pp. 231–235, March 1995.

[17] M. Klingler, M. Szelag, and M. Heddebaut, "Double bulk current injection: a possible substitute to field to wire coupling," in *Proceedings of the International Symposium in Electromagnetic Environments Consequences (EUROEM '94)*, pp. 1249–1256, Bordeaux, France, 1994.

[18] F. Grassi, G. Spadacini, F. Marliani, and S. A. Pignari, "Use of double bulk current injection for susceptibility testing of avionics," *IEEE Transactions on Electromagnetic Compatibility*, vol. 50, no. 3, pp. 524–535, 2008.

[19] G. Spadacini and S. A. Pignari, "A bulk current injection test conforming to statistical properties of radiation-induced effects," *IEEE Transactions on Electromagnetic Compatibility*, vol. 46, no. 3, pp. 446–458, 2004.

[20] F. M. Tesche, M. V. Ianoz, and T. Karlsson, *EMC Analysis Methods and Computational Models*, John Wiley & Sons, New York, NY, USA, 1997.

[21] C. E. Baum, "Generalization of the BLT equation," in *Proceedings of 13th International Zurich Symposium on Electromagnetic Compatibility*, pp. 131–136, March 1999.

[22] F. M. Tesche, "Development and use of the BLT equation in the time domain as applied to a coaxial cable," *IEEE Transactions on Electromagnetic Compatibility*, vol. 49, no. 1, pp. 3–11, 2007.

[23] D. M. Pozar, *Microwave Engineering*, John Wiley & Sons, New York, NY, USA, 4th edition, 2011.

[24] Z. Q. Li, J. Z. She, and B. X. Gao, *Foundation for Microwave Engineering*, Tsinghua University Press, Beijing, China, 2004.

Research Article

Planar MIMO Antenna with Slits for WBAN Applications

Do-Gu Kang, Jinpil Tak, and Jaehoon Choi

*Department of Electronics and Communications Engineering, Hanyang University, 222 Wangsimni-ro, Seongdong-gu,
Seoul 133-791, Republic of Korea*

Correspondence should be addressed to Jaehoon Choi; choijh@hanyang.ac.kr

A planar MIMO antenna with slits for WBAN applications is proposed. The antenna consists of two PIFAs, ground pads, and two
slits. By adding ground pads, the antenna size is reduced with improved impedance matching. Through two slits in a ground plane,
the isolation characteristic is improved and the resonant frequency can be controlled. To analyze the antenna performance on a
human body, the proposed antenna on a human equivalent flat phantom is investigated through simulations. Regardless of the
existence of the phantom, the antenna operates in 2.4 GHz ISM band with the isolation higher than 18 dB.

1. Introduction

Recently, wireless body area network (WBAN) systems for
medical devices, police and military agencies, sports training,
entertainment, and wearable computing have received great
attention in conjunction with the rapid development of
wireless communication technology [1, 2]. The antennas for
WBAN system should satisfy certain requirements such as
small size, low profile, low human body effects, and low
specific absorption rate (SAR) [3]. Since the antennas for
WBAN system are located on or in the human body, the
performance of the antenna is affected by the human body's
high dielectric constant and conductivity at the microwave
frequency band. Therefore, the gain and radiation efficiency
of the antenna can deteriorate [4–7].

A lot of research for the on-body communication channel
of WBAN system in the industrial scientific medical (ISM)
band has been conducted [8–10]. In on-body communica-
tion, a multipath fading occurs due to reflections from the
surrounding environment and the body parts, large relative
movement of the body parts, shadowing, and scattering from
the moving of the body and the surrounding environment
[8]. The multipath fading distorts communication signals and
reduces the efficiency of WBAN system [11]. Since a diversity
technique forces signals to be independently processed, stable
communication performance of an antenna system can be
achieved in multipath fading environment. Multiple-input
and multiple-output (MIMO) antennas have received much
attention as one of promising diversity techniques. A high
isolation characteristic is essential for MIMO antenna system
in order to achieve independency of multiple signals [12].

In the paper, a planar MIMO antenna with slits for
on-body WBAN applications in 2.4 GHz ISM band (2.4~
2.485 GHz) is proposed. A planar inverted-F antenna (PIFA)
operating with a resonant length of $\lambda/4$ is used to achieve
compact size [13]. Ground pads are added to reduce the
size of the antenna with improved impedance matching. By
using two slits in a ground plane, the isolation characteristic
increases over 18 dB in 2.4 GHz ISM band. The perfor-
mance of the proposed antenna on the human equivalent
flat phantom such as S-parameter characteristics, radiation
characteristics, SAR, and an envelope correlation coefficient
(ECC) is analyzed.

2. Antenna Geometry

Figure 1 shows the geometry of the proposed antenna. The
antenna consists of two identical PIFAs, two identical ground
pads, and two identical slits. The proposed planar antenna
is designed on a FR4 substrate ($\varepsilon_r = 4.4$) with a 1 mm
thickness. The total size of the substrate is 40×40 mm^2.
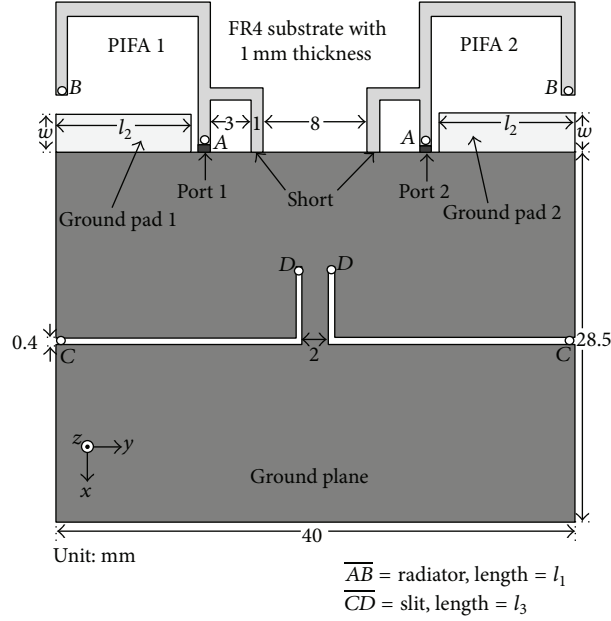
FIGURE 1: Geometry of the proposed antenna.
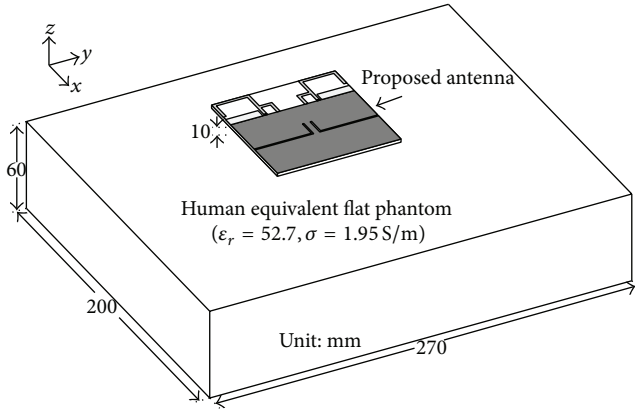
FIGURE 2: Proposed antenna on the human equivalent flat phantom.

FIGURE 3: Simulated S-parameter results for the proposed antenna with phantom and without phantom.

PIFAs have a dimension of $11.5 \times 16 \times 1 \, \text{mm}^3$. A distance between the two PIFAs is 8 mm and l_1 denotes the length of the radiator of PIFAs. Addition of ground pads at a ground plane increases the electrical length and bandwidth of PIFAs without changing the size of PIFAs. l_2 and w, respectively, denote the length and the width of the ground pads. Although an isolator does not exist between the two PIFAs, the isolation characteristic is improved by adding two slits with the length of l_3 in the ground plane.

Figure 2 shows the proposed antenna on the human equivalent flat phantom. The dimension of the human equivalent flat phantom is $200 \times 270 \times 60 \, \text{mm}^3$. The proposed antenna for possible applications (portable devices such as Bluetooth headset and wearable smart watch) has the maximum allowed separation distance of 10 mm from the phantom in order to provide the clearance of cover assembly [4]. To account for this situation, the separation distance between the antenna and the phantom is chosen as 10 mm. In order to analyze the antenna performance on a human body, simulations were conducted using the human equivalent flat phantom having the equivalent electrical properties ($\varepsilon_r = 52.7$ and $\sigma = 1.95 \, \text{S/m}$) of human tissue [14]. The simulation results were obtained using HFSS based on the finite-element method [15].

3. Simulated Results

Figure 3 shows the simulated S-parameter results for the proposed antenna with and without the phantom. The design
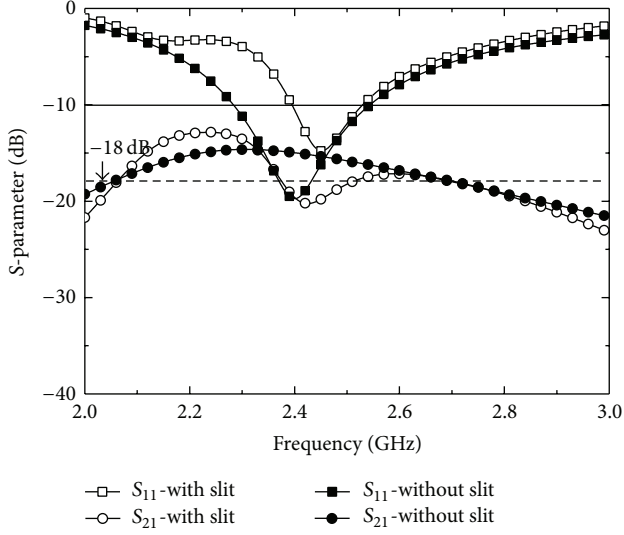
Figure 4: Simulated S-parameter results for the proposed antenna on the phantom with slit and without slit.

parameters for the proposed antenna are set to $l_1 = 28$ mm, $l_2 = 10.5$ mm, $w = 3$ mm, and $l_3 = 24$ mm. Regardless of the existence of the phantom, S_{11} is maintained below -10 dB and the isolation characteristic is higher than 18 dB over the 2.4 GHz ISM band (2.4~2.485 GHz).

Figure 4 shows the simulated S-parameter results for the proposed antenna on the phantom with slit and without slit. By adding a slit at the ground plane, the isolation at 2.44 GHz is improved from 15 dB to 20 dB. The isolation characteristic over the entire 2.4 GHz ISM band is higher than 18 dB.

Figure 5 shows the simulated surface current distributions for the proposed antenna at 2.44 GHz. The slit operates at the electrical length of $\lambda/4$. Because the minimum current of the slit implies high impedance by $\lambda/4$ slit, the slit blocks current flowing from PIFA 1 to PIFA 2 through the ground plane [16, 17]. For the antenna without slit, when PIFA 1 is excited by port 1, a strong current excites on PIFA 2 as shown in Figure 5(a). For the antenna with slit, a weak current excites on PIFA 2 as depicted in Figure 5(b).

Figure 6 shows the simulated S-parameter results for various values of length l_1. Other parameters, excluding l_1, are the same as described above. A resonance frequency is formed by the length of radiator ($\lambda/4$). As l_1 increases, the radiator approaches the ground pad. Therefore, the resonance frequency decreases with a deteriorated impedance matching. However, the isolation characteristic is maintained above 18 dB. Because the distance between the PIFA and the slit is far enough as shown in Figure 5(b), the change of the radiator's length hardly affects the isolation characteristic. When l_1 is 28 mm, 10 dB return loss bandwidth of the antenna fully covers 2.4 GHz ISM band.

Figure 7 shows the simulated S-parameter results for various values of length l_2. As l_2 increases, the resonance frequency decreases because the coupling between the ground pad and the part of PIFA near feeding port becomes stronger in Figure 5(b). The isolation characteristic is retained above

(a)

(b)
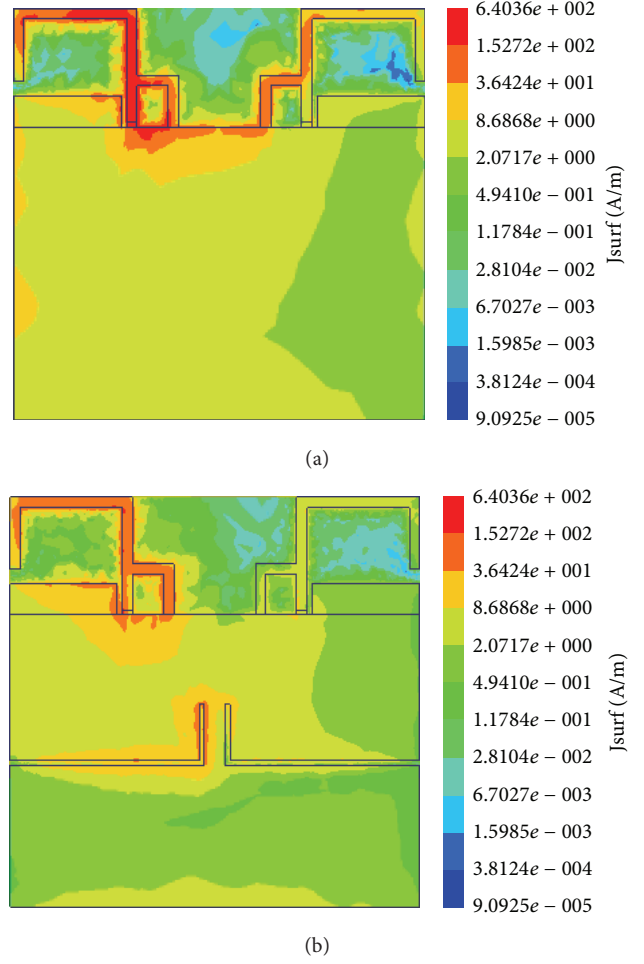
Figure 5: Simulated surface current distributions for the proposed antenna at 2.44 GHz (port 1: on, port 2: off) (a) without slit and (b) with slit.
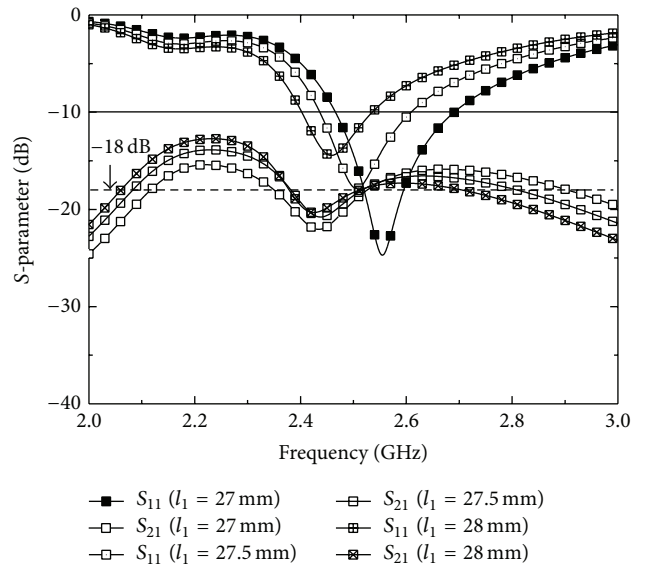
Figure 6: Simulated S-parameter results for various values of length l_1.
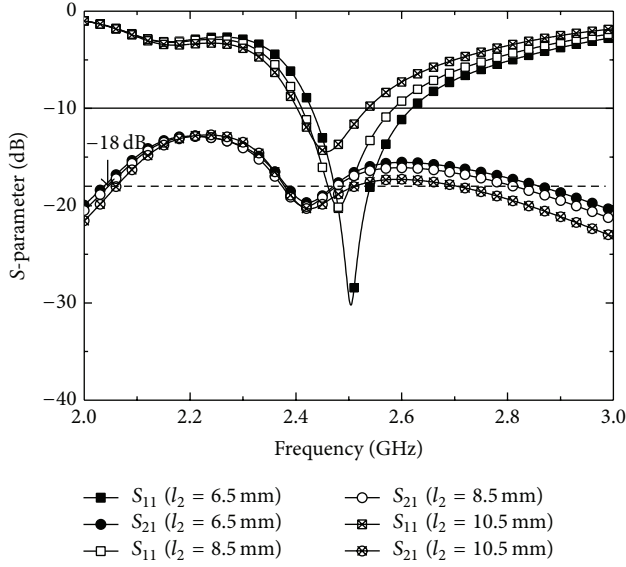
FIGURE 7: Simulated S-parameter results for various values of length l_2.

FIGURE 9: Simulated S-parameter results for various values of length l_3.
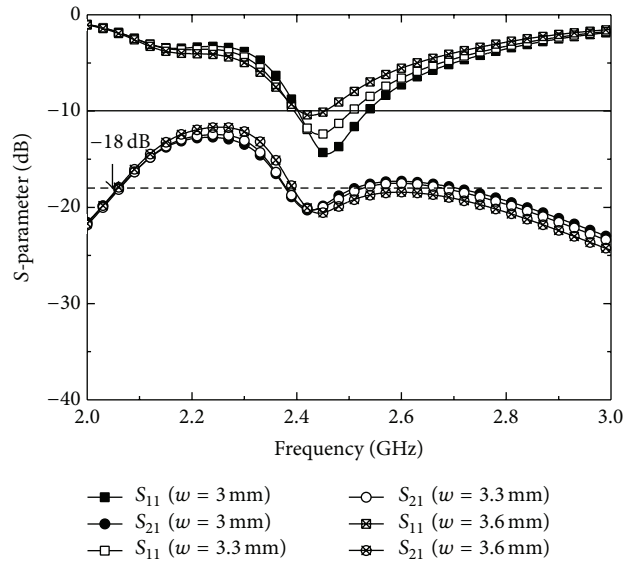
FIGURE 8: Simulated S-parameter results for various values of width w.
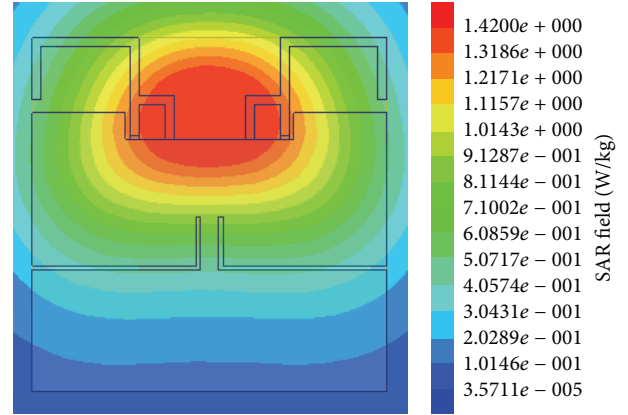
FIGURE 10: Simulated SAR distribution of the proposed antenna on the phantom at 2.44 GHz (input power: 100 mW).

18 dB. Because l_2 is the length of the ground pad, the addition of ground pad contributes to the size reduction of the PIFA. When l_2 is 10.5 mm, the best isolation performance in 2.4 GHz ISM band is achieved.

Figure 8 shows the simulated S-parameter results for various values of width w. As w decreases, the resonance frequency increases because the coupling between the ground pad and the tip of PIFA becomes weaker in Figure 5(b). The 10 dB return loss bandwidth increases with an improved impedance matching. The isolation characteristic remains nearly constant above 18 dB regardless of the change in w. To cover 2.4 GHz ISM band, w is chosen as 3 mm.

Figure 9 shows the simulated S-parameter results for various values of length l_3. As l_3 increases, the isolation characteristic is improved, while the S_{11} characteristic is retained. Because l_3 is the length of the slit, the change of l_3 mainly affects the isolation characteristic. When l_3 is chosen as 24 mm, the isolation characteristic is higher than 18 dB in 2.4 GHz ISM band.

Figure 10 shows the simulated SAR distribution of the proposed antenna on the phantom at 2.44 GHz. According to the Federal Communications Commission (FCC), the SAR values for a partial body should be below 1.6 W/kg over a volume of 1 g of tissue [18]. When the maximum input power is 100 mW, the SAR of the proposed antenna is 1.42 W/kg which satisfies the FCC SAR limitation of 1.6 W/kg. Therefore, the proposed antenna can be used for a low power wireless terminal operating below 100 mW such as Bluetooth system [19].

(a)

(b)
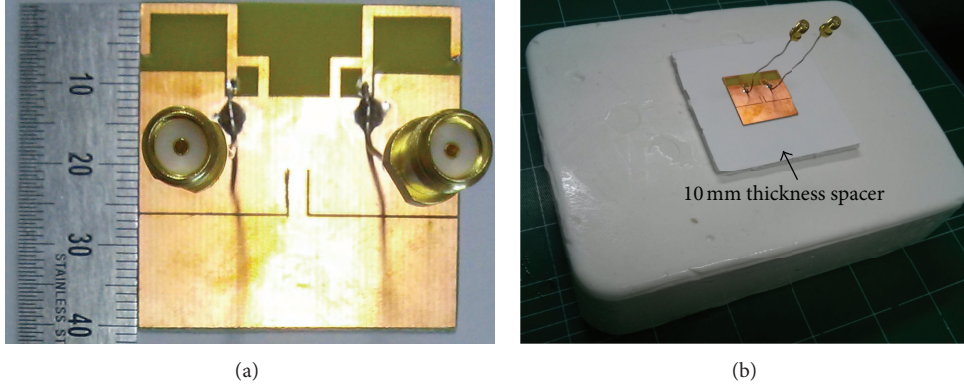
FIGURE 11: Fabricated antenna and phantom for measurement setup. (a) Fabricated antenna and (b) the antenna on the phantom for measurement setup.

TABLE 1: Simulated total efficiency at 2.44 GHz.

2.44 GHz	With slits	Without slits
Total efficiency (%)	**40.35**	**38.26**

Table 1 shows the simulated total efficiency at 2.44 GHz. The total efficiency of the proposed antenna is higher than that of the antenna without the slits due to the improvement of isolation between the two antenna elements by inserting the slits.

4. Measured Results

Figure 11 shows the fabricated antenna and phantom for measurement setup. The measured electrical properties of the fabricated human equivalent semisolid flat phantom are $\varepsilon_r = 52.7$ and $\sigma = 1.95$ S/m [20]. The human equivalent semisolid flat phantom is used to measure the antenna performance.

Figure 12 shows the simulated and measured S-parameter results for the proposed antenna. The simulated results are virtually identical to the measured results. The discrepancy between the simulated and the measured results may have been due to a manufacturing error (long coaxial feed cable) of the fabricated antenna [21]. The proposed antenna has the 10 dB return loss bandwidth of 210 MHz (2.34~2.55 GHz). This is wide enough to fully cover 2.4 GHz ISM band. The isolation characteristic is higher than 20 dB over 2.4 GHz ISM band.

Figure 13 shows the simulated and measured radiation patterns of the proposed antenna at 2.44 GHz. The measured radiation patterns agree well with the simulated ones. The radiation patterns of the PIFA 1 and PIFA 2 are similar to each other. In Figure 13(a), nearly omnidirectional radiation patterns are observed. In Figure 13(b), radiation patterns directed toward the outside of phantom are observed. Table 2 shows the measured peak gain and radiation efficiency of the proposed antenna at 2.44 GHz. The peak gain is 1.61 dBi for the PIFA 1 and 1.6 dBi for the PIFA 2.
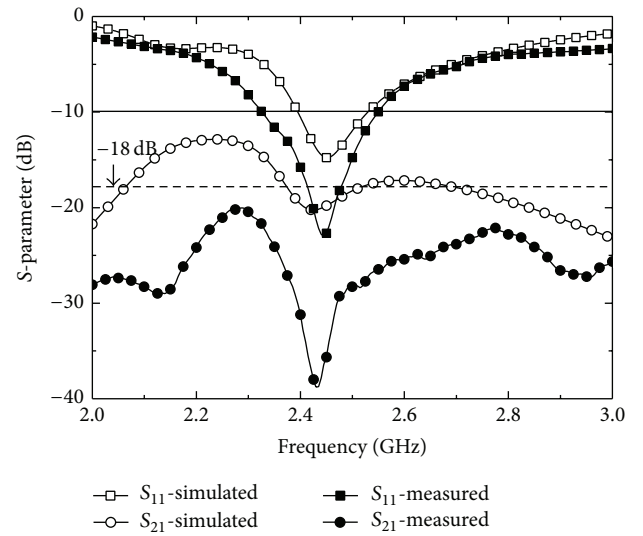
FIGURE 12: Simulated and measured S-parameter results for the proposed antenna.

TABLE 2: Measured peak gain and radiation efficiency.

2.44 GHz	PIFA 1	PIFA 2
Peak gain (dBi)	1.61	1.6
Efficiency (%)	24.97	24.29

The diversity performance of a MIMO antenna could be evaluated by the envelope correlation coefficient (ECC). The ECC should be calculated from 3D radiation patterns [22]. Figure 14 shows the calculated ECC from simulated and measured radiation patterns of the proposed antenna. The simulated ECC agrees well with the measured ECC. The ECC values are maintained below 0.5 over 2.4 GHz ISM band. The simulated ECC of the proposed antenna is lower than that of the antenna without slits due to the improvement of isolation between the two antenna elements by inserting the slits.

PIFA 1

-□- Simulation
-■- Measurement

PIFA 2

-□- Simulation
-■- Measurement

(a)

PIFA 1

-□- Simulation
-■- Measurement

PIFA 2

-□- Simulation
-■- Measurement

(b)
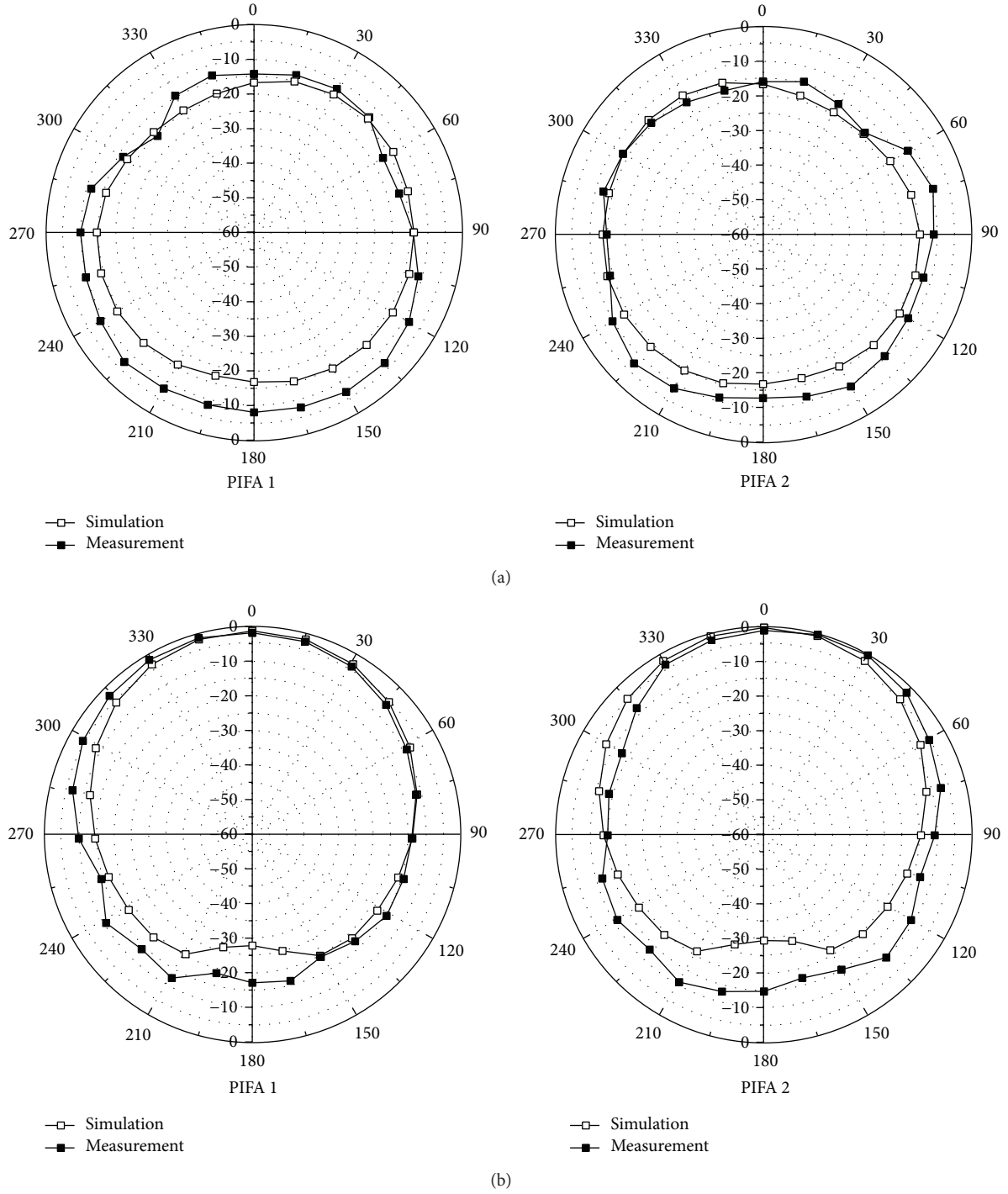
FIGURE 13: Simulated and measured radiation patterns of the proposed antenna at 2.44 GHz (a) xy plane and (b) yz plane.

5. Conclusion

In this paper, the planar MIMO antenna with slits in 2.4 GHz ISM band for WBAN applications is proposed. The 10 dB return loss bandwidth of the antenna on the human equivalent flat phantom is wide enough to cover 2.45 GHz ISM band. The addition of ground pads contributes to the size reduction and the improvement of the impedance matching of the PIFA.

The isolation characteristic is improved by adding two slits. The isolation is higher than 18 dB over the ISM band. The resonant frequency can be controlled by the PIFA, the ground pad, and the slit. The performance of proposed antenna is insensitive to the existence of the phantom. Consequently, the above advantages make the proposed antenna a good candidate for WBAN applications.
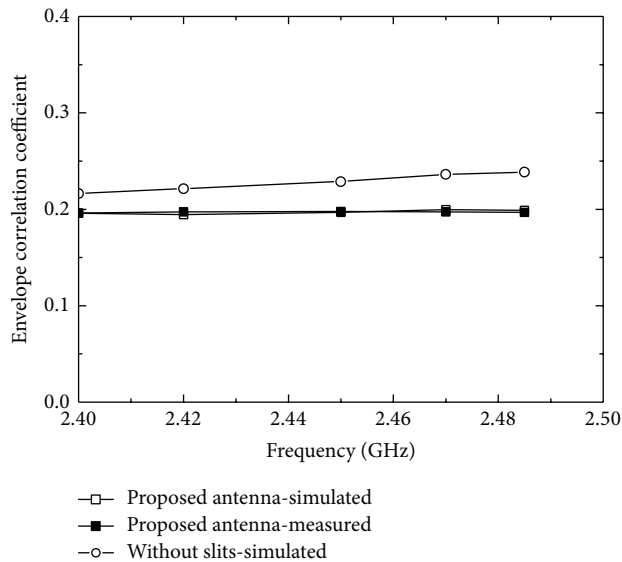
FIGURE 14: Simulated and measured envelope correlation coefficient of the proposed antenna and the antenna without slits.

Conflict of Interests

The authors declare that there is no conflict of interests regarding the publication of this paper.

Acknowledgment

References

[1] T. Zasowski, F. Althaus, M. Stager, A. Wittneben, and G. Troster, "UWB for noninvasive wireless body area networks: channel measurements and results," in *Proceedings of the IEEE Conference on Ultra Wideband Systems and Technologies*, pp. 285–289, 2003.

[2] P. S. Hall and Y. Hao, "Introduction to body-centric wireless communications," in *Antennas and Propagation for Body-Centric Wireless Communications*, chapter 1, Artech House, Norwood, Mass, USA, 2006.

[3] N. Haga, K. Saito, M. Takahashi, and K. Ito, "Characteristics of cavity slot antenna for body-area networks," *IEEE Transactions on Antennas and Propagation*, vol. 57, no. 4, pp. 837–843, 2009.

[4] M. Ur Rehman, Y. Gao, Z. Wang et al., "Investigation of on-body bluetooth transmission," *IET Microwaves, Antennas and Propagation*, vol. 4, no. 7, pp. 871–880, 2010.

[5] C. Deng, X. Liu, Z. Zhang, and M. M. Tentzeris, "A miniascape-like triple-band monopole antenna for WBAN applications," *IEEE Antennas and Wireless Propagation Letters*, vol. 11, pp. 1330–1333, 2012.

[6] Z. N. Chen, A. Cai, T. S. P. See, X. Qing, and M. Y. W. Chia, "Small planar UWB antennas in proximity of the human head,"

[7] P. S. Hall, Y. Hao, Y. I. Nechayev et al., "Antennas and propagation for on-body communication systems," *IEEE Antennas and Propagation Magazine*, vol. 49, no. 3, pp. 41–58, 2007.

[8] A. A. Serra, P. Nepa, G. Manara, and P. S. Hall, "Diversity for body area networks," in *Proceedings of the 29th URSI General Assembly*, pp. 1–4, Chicago, Ill, USA, August 2008.

[9] L. Akhoondzadeh-Asl, I. Khan, and P. S. Hall, "Polarisation diversity performance for on-body communication applications," *IET Microwaves, Antennas and Propagation*, vol. 5, no. 2, pp. 232–236, 2011.

[10] T. Aoyagi, M. Kim, J. Takada, K. Hamaguchi, and R. Kohno, "Numerical simulations for wearable BAN propagation channel during various human movements," *IEICE Transactions on Communications*, vol. E94-B, no. 9, pp. 2496–2500, 2011.

[11] S. L. Cotton and W. G. Scanlon, "A statistical analysis of indoor multipath fading for a narrowband wireless body area network," in *Proceedings of the IEEE 17th International Symposium on Personal, Indoor and Mobile Radio Communications (PIMRC '06)*, pp. 1–5, Helsinki, Finland, September 2006.

[12] S. Zhang, B. K. Lau, A. Sunesson, and S. He, "Closely-packed UWB MIMO/diversity antenna with different patterns and polarizations for USB dongle applications," *IEEE Transactions on Antennas and Propagation*, vol. 60, no. 9, pp. 4372–4380, 2012.

[13] Y. Guo, M. Y. W. Chia, and Z. N. Chen, "Miniature built-in multiband antennas for mobile handsets," *IEEE Transactions on Antennas and Propagation*, vol. 52, no. 8, pp. 1936–1944, 2004.

[14] D. L. Means and W. Kwok, "Evaluating compliance with FCC guidelines for human exposure to radiofrequency electromagnetic fields," Supplement C (Edition 01-01) to OET Bulletin 65 (Edition 97-01), Federal Communications Commission Office of Engineering & Technology, 2001.

[15] "Ansys High Frequency Structure Simulator (HFSS), Version 14," Ansys Corporation.

[16] M. Ayatollahi, Q. Rao, and D. Wang, "A compact, high isolation and wide bandwidth antenna array for long term evolution wireless devices," *IEEE Transactions on Antennas and Propagation*, vol. 60, no. 10, pp. 4960–4963, 2012.

[17] J. Lim, Z. Jin, C. Song, and T. Yun, "Simultaneous frequency and isolation reconfigurable MIMO PIFA using PIN diodes," *IEEE Transactions on Antennas and Propagation*, vol. 60, no. 12, pp. 5939–5946, 2012.

[18] "IEEE standard for safety levels with respect to human exposure to radio frequency electromagnetic fields, 3 KHz to 300 GHz," IEEE Standard C95.1.1999, 1999.

[19] M. Patel and J. Wang, "Applications, challenges, and prospective in emerging body area networking technologies," *IEEE Wireless Communications*, vol. 17, no. 1, pp. 80–88, 2010.

[20] S. Lee, W. Seo, K. Kwon, and J. Choi, "The study on implementation of a semi-solid flat phantom with equivalent electrical properties to whole human body at MICS and ISM band," *The Journal of Korea Electromagnetic Engineering Society*, vol. 23, no. 1, pp. 101–107, 2012.

[21] Y. Okano, "A simple shape broadband planar antenna adaptable to RFID-tag," *IEEE Transactions on Antennas and Propagation*, vol. 54, no. 6, pp. 1885–1888, 2006.

[22] J. Li, Q. Chu, and T. Huang, "A compact wideband MIMO antenna with two novel bent slits," *IEEE Transactions on Antennas and Propagation*, vol. 60, no. 2, pp. 482–489, 2012.

IEEE Transactions on Microwave Theory and Techniques, vol. 54, no. 4, pp. 1846–1856, 2006.

Research Article

Sparse Adaptive Channel Estimation Based on l_p-Norm-Penalized Affine Projection Algorithm

Yingsong Li,[1] Wenxing Li,[1] Wenhua Yu,[1] Jian Wan,[1] and Zhiwei Li[2]

[1] College of Information and Communications Engineering, Harbin Engineering University, Harbin 150001, China
[2] College of Electromechanical Engineering, Northeast Forestry University, Harbin 150040, China

Correspondence should be addressed to Yingsong Li; liyingsong@ieee.org

We propose an l_p-norm-penalized affine projection algorithm (LP-APA) for broadband multipath adaptive channel estimations. The proposed LP-APA is realized by incorporating an l_p-norm into the cost function of the conventional affine projection algorithm (APA) to exploit the sparsity property of the broadband wireless multipath channel, by which the convergence speed and steady-state performance of the APA are significantly improved. The implementation of the LP-APA is equivalent to adding a zero attractor to its iterations. The simulation results, which are obtained from a sparse channel estimation, demonstrate that the proposed LP-APA can efficiently improve channel estimation performance in terms of both the convergence speed and steady-state performance when the channel is exactly sparse.

1. Introduction

Recently, with the fast increasing demand for high data rate and wide bandwidth in wireless mobile communication, the use of broadband signal transmission has become an important technique for next-generation wireless communication systems, for instance, 3GPP long-term evolution (LTE) and worldwide interoperability for microwave access (WiMAX) [1–3]. Coherent detection and equalization in broadband communication systems require perfect channel state information [4], which is not known at the receiver. Therefore, the achievable performance of coherent detection for such broadband communication system relies heavily on the accuracy of the channel estimation [2–7], which can help to improve the communication quality. Fortunately, the accurate channel estimation can be obtained by means of the adaptive filter algorithms, such as least mean square (LMS), recursive least squares (RLS), and affine projection algorithm (APA) [8, 9]. On the other hand, normalized LMS (NLMS) algorithm, which is an improved LMS algorithm, has been widely studied and applied in channel estimation owing to its low complexity, high stability, and easy implementation. However, NLMS algorithm converges slowly, making it difficult to track the rapid time-varying channels. Consequently, the APA with

an acceptable computational complexity between the NLMS and RLS algorithms has been deeply developed and applied in echo cancellation and channel estimations [9, 10].

On the other hand, the measurement results of the broadband channel showed that the wireless multipath channel consists of only a few dominant active propagation paths whose magnitudes are nonzero, even though they have large propagation delays [5, 11, 12]. Thus, these channels can be regarded as a sparse channel with a few nonzero taps which are dominant, while other inactive taps are zero or close to zero because of the noise in the channel. However, the classical adaptive channel estimation algorithms, such as NLMS algorithm and APA, may perform poorly when the channel is exactly sparse [13]. As a consequence, a great number of sparse signal estimation algorithms have been presented to improve the estimation performance for sparse channels, such as compressed sensing (CS) [5, 14–16] and zero-attracting adaptive channel estimation algorithms [13, 17–23]. However, these CS reconstruction algorithms are sensitive to the noise in the channel estimation and have high computational complexity [19].

Other effective adaptive channel estimation algorithms, denoted as zero-attracting algorithms, have been reported by the combination of the CS theory [15, 16] and the LMS

algorithm [8], which are famous as zero-attracting LMS (ZA-LMS) and reweighted ZA-LMS (RZA-LMS) algorithms [13]. Recently, these zero-attracting (ZA) techniques have been expanded to the APA in order to improve the convergence speed of the zero-attracting LMS algorithms [20], which are denoted as zero-attracting APA (ZA-APA) and reweighted ZA-APA (RZA-APA). As a result, the zero-attracting APAs converge faster than those of the ZA LMSs due to the reuse data scheme in the APA. However, these previously proposed zero-attracting algorithms, which include the ZA-LMS algorithm and the ZA-APA, are realized by integrating an l_1-norm into the cost functions of the standard LMS and APA, respectively. Moreover, these l_1-norm-penalized algorithms impose a condition that the number of the active taps must be very small as compared to the number of inactive channel taps.

In this paper, we proposed an l_p-norm-penalized APA (LP-APA) that incorporates an l_p-norm into the cost function of the conventional APA on the basis of the concepts of zero-attracting algorithm proposed in [13, 17–23], by which the convergence speed and steady-state performance of the conventional APA can be significantly improved when the channel is exactly sparse. Moreover, the proposed LP-APA has an extra parameter p, which is more flexible than the previously proposed zero-attracting APAs [20–22]. The LP-APA is realized by introducing a zero attractor in its iterations, which is used to attract the inactive taps to zero quickly. In other words, our proposed LP-APA can inherit the benefits of both the conventional APA and the past zero-attracting algorithms and, hence, it can achieve faster convergence speed and smaller steady-state error in comparison with the conventional APA. In this study, our proposed LP-APA is implemented over a sparse multipath channel in single antenna systems in order to verify the channel estimation performance in comparison with the NLMS, APA, ZA-APA, and RZA-APA. Computer simulation results demonstrate that the proposed LP-APA achieves better estimation performance in terms of both the convergence speed and steady-state behavior for sparse channel estimation.

The remainder of this paper is organized as follows. In Section 2, we briefly discuss the previously proposed conventional APA, ZA-APA, and RZA-APA based on a sparse multipath communication system. In Section 3, we mathematically propose the LP-APA by the use of an l_p-norm-penalty in the cost function of the conventional APA. Furthermore, the update function of the LP-APA is obtained by using Lagrange multiplier method. In Section 4, the channel estimation performance of the proposed LP-APA is experimentally investigated over a sparse channel and compared with those of the ZA-APA, RZA-APA, APA, and NLMS algorithms. Finally, Section 5 draws a conclusion for this paper.

2. Conventional Channel Estimation Algorithms

In this section, a sparse multipath communication system shown in Figure 1 is employed in order to illustrate the conventional channel estimation algorithms, namely, APA, ZA-APA, and RZA-APA. The input signal $\mathbf{x}(n) = [x(n), x(n-1),$
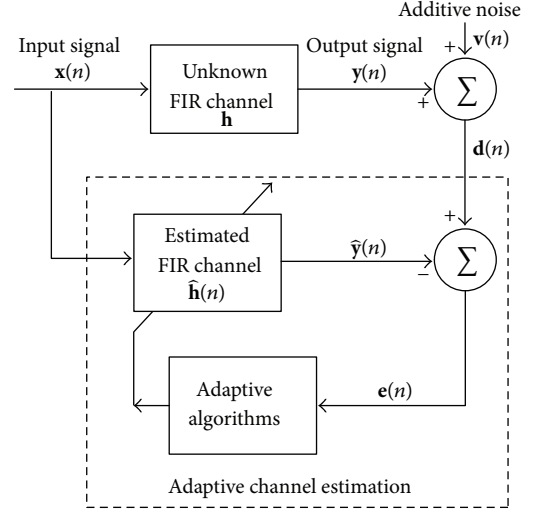
Figure 1: Typical sparse multipath communication system.

$\ldots, x(n-N+1)]^T$, which contains the N most recent samples, is transmitted over an unknown finite impulse response (FIR) channel with channel impulse response (CIR) $\mathbf{h} = [h_0, h_1, \ldots, h_{N-1}]^T$, where $(\cdot)^T$ is the transposition operation. The input signal $\mathbf{x}(n)$ is also an input of the channel estimator $\hat{\mathbf{h}}(n)$ with N coefficients to generate an estimation output $\hat{\mathbf{y}}(n)$, and the desired signal $\mathbf{d}(n)$, which is obtained at the receiver, is composed of the channel output $\mathbf{y}(n)$ and the noise $\mathbf{v}(n)$ in the channel. The purpose of the channel estimation is to estimate the unknown channel $\mathbf{h}$ by using the APA, ZA-APA, and RZA-APA.

2.1. Review of Conventional APA. The APA adopts multiple projection scheme by utilizing past vectors from time iteration n to time iteration $(n - Q + 1)$, where Q is defined as the affine projection order. In the APA, we assume that the last Q input signal vectors are organized as a matrix as follows:

$$\mathbf{U}(n) = \begin{bmatrix} \mathbf{x}^T(n) \\ \mathbf{x}^T(n-1) \\ \vdots \\ \mathbf{x}^T(n-Q+1) \end{bmatrix}, \tag{1}$$

where $\mathbf{x}(n)$ is the input signal. We also define the following useful vectors to further describe the APA, such as the desired signal $\mathbf{d}(n)$, the estimation output of the APA filter $\hat{\mathbf{y}}(n)$, and the additive white Gaussian noise $\mathbf{v}(n)$:

$$\hat{\mathbf{y}}(n) = \begin{bmatrix} \hat{y}(n) & \hat{y}(n-1) & \cdots & \hat{y}(n-Q+1) \end{bmatrix}^T,$$

$$\mathbf{d}(n) = \begin{bmatrix} d(n) & d(n-1) & \cdots & d(n-Q+1) \end{bmatrix}^T, \tag{2}$$

$$\mathbf{v}(n) = \begin{bmatrix} v(n) & v(n-1) & \cdots & v(n-Q+1) \end{bmatrix}^T.$$

For channel estimation, the APA is used to minimize

$$\left\| \hat{\mathbf{h}}(n+1) - \hat{\mathbf{h}}(n) \right\|^2 \tag{3}$$

subject to: $\quad \mathbf{d}(n) - \mathbf{U}(n)\hat{\mathbf{h}}(n+1) = \mathbf{0}.$

Here, the Lagrange multiplier method is employed in order to find out the solutions that minimize the cost function $J_{APA}(n+1)$ of the APA and $J_{APA}(n+1)$ is given by

$$J_{APA}(n+1) = \left\| \widehat{\mathbf{h}}(n+1) - \widehat{\mathbf{h}}(n) \right\|^2 \\ + \left[\mathbf{d}(n) - \mathbf{U}(n)\widehat{\mathbf{h}}(n+1) \right]^T \lambda_{APA}, \tag{4}$$

where λ_{APA} is a $Q \times 1$ Lagrange multiplier vector with $\lambda_{APA} = \begin{bmatrix} \lambda_0 & \lambda_1 & \cdots & \lambda_{Q-1} \end{bmatrix}^T$. By calculating the gradient of $J_{APA}(n+1)$, we have

$$\frac{\partial J_{APA}(n+1)}{\partial \widehat{\mathbf{h}}(n+1)} = \mathbf{0}, \qquad \frac{\partial J_{APA}(n+1)}{\partial \lambda} = \mathbf{0}, \tag{5}$$

$$\widehat{\mathbf{h}}(n+1) = \widehat{\mathbf{h}}(n) + \mathbf{U}^T(n) \left[\mathbf{U}(n) \mathbf{U}^T(n) \right]^{-1} \mathbf{e}(n) \\ = \widehat{\mathbf{h}}(n) + \mathbf{U}^+(n)\mathbf{e}(n), \tag{6}$$

where $\mathbf{U}^+(n) = \mathbf{U}^T(n)[\mathbf{U}(n)\mathbf{U}^T(n)]^{-1}$. In order to balance the convergence speed and the steady-state performance, a step size μ_{APA} is introduced into (6), and hence, the update function (6) of the APA can be modified to

$$\widehat{\mathbf{h}}(n+1) = \widehat{\mathbf{h}}(n) + \mu_{APA}\mathbf{U}^+(n)\mathbf{e}(n). \tag{7}$$

It is worthwhile to note that the APA is a NLMS algorithm when the affine projection order Q is set to one.

2.2. Review of the ZA-APA and RZA-APA. In this subsection, we briefly review the ZA-APA and RZA-APA. On the basis of the past studies, we know that the cost function of the ZA-APA is defined by combining the cost function $J_{APA}(n+1)$ of the standard APA with an l_1-norm-penalty of the channel estimator and is expressed as

$$J_{ZA}(n+1) \\ = \left\| \widehat{\mathbf{h}}(n+1) - \widehat{\mathbf{h}}(n) \right\|^2 \\ + \left[\mathbf{d}(n) - \mathbf{U}(n)\widehat{\mathbf{h}}(n+1) \right]^T \lambda_{ZA} + \gamma_{ZA} \left\| \widehat{\mathbf{h}}(n+1) \right\|_1, \tag{8}$$

where λ_{ZA} is the Lagrange multiplier vector with a size of $Q \times 1$, while γ_{ZA} is a regularization parameter which is used to balance the estimation error and the sparse l_1-norm-penalty of $\widehat{\mathbf{h}}(n+1)$. To minimize the cost function of the ZA-APA, we use the Lagrange multiplier method on $J_{ZA}(n+1)$, and we obtain

$$\frac{\partial J_{ZA}(n+1)}{\partial \widehat{\mathbf{h}}(n+1)} = 2\widehat{\mathbf{h}}(n+1) - 2\widehat{\mathbf{h}}(n) - \mathbf{U}^T(n)\lambda_{ZA} \\ + \gamma_{ZA} \operatorname{sgn}\left[\widehat{\mathbf{h}}(n+1) \right], \tag{9}$$

where $\operatorname{sgn}[x]$ is a component-wise sign function defined as follows:

$$\operatorname{sgn}[x] = \begin{cases} \dfrac{x}{|x|}, & x \neq 0 \\ 0, & x = 0. \end{cases} \tag{10}$$

In order to get the minimization of (9), the left-hand side (LHS) of (9) is set to zero. Therefore, we have

$$\widehat{\mathbf{h}}(n+1) = \widehat{\mathbf{h}}(n) + \frac{1}{2}\mathbf{U}^T(n)\lambda_{ZA} - \frac{1}{2}\gamma_{ZA} \operatorname{sgn}\left[\widehat{\mathbf{h}}(n+1) \right]. \tag{11}$$

Then, by multiplying $\mathbf{U}(n)$ on both sides of (11) and using the $\mathbf{e}(n) = \mathbf{d}(n) - \mathbf{U}(n)\widehat{\mathbf{h}}(n)$, we can get

$$\lambda_{ZA} = \frac{2\mathbf{e}(n) + \gamma_{ZA}\mathbf{U}(n)\operatorname{sgn}\left[\widehat{\mathbf{h}}(n+1) \right]}{\mathbf{U}(n)\mathbf{U}^T(n)}. \tag{12}$$

Substituting (12) into (11), assuming $\operatorname{sgn}[\widehat{\mathbf{h}}(n+1)] \approx \operatorname{sgn}[\widehat{\mathbf{h}}(n)]$ at the steady stage, and introducing a step-size μ_{ZA} to balance the convergence speed and the steady-state performance, we can obtain the update function of the ZA-APA

$$\widehat{\mathbf{h}}(n+1) \\ = \widehat{\mathbf{h}}(n) + \mu_{ZA}\mathbf{U}^+(n)\mathbf{e}(n) \\ + \frac{1}{2}\gamma_{ZA}\mathbf{U}^+(n)\mathbf{U}(n)\operatorname{sgn}\left[\widehat{\mathbf{h}}(n) \right] - \frac{1}{2}\gamma_{ZA}\operatorname{sgn}\left[\widehat{\mathbf{h}}(n) \right]. \tag{13}$$

From the update equation (13) of the ZA-APA, we find that there are two additional terms in comparison with the update equation (7) of the conventional APA, which attract the inactive taps to zero when the tap magnitudes of the sparse channel are zero or close to zero. These two additional terms are regarded as zero attractors whose zero-attracting strengths are controlled by the regularization parameter γ_{ZA}. In a word, the zero attractor can speed up the convergence of the ZA-APA when the majority of taps of the channel $\mathbf{h}$ are inactive ones, such as sparse channel.

Unfortunately, the ZA-APA cannot distinguish the active taps and the inactive taps of the sparse channel so that it exerts the same penalty to all the channel taps, which forces all the channel taps to zero uniformly [13, 20]. Therefore, the performance of the ZA-APA might be degraded for less sparse channel. In order to improve the estimation performance of the ZA-APA, a heuristic method first investigated in [24] and used in [20] to reinforce the zero attractor was proposed, which was denoted as RZA-APA. In the RZA-APA, $\sum_{i=1}^{N} \log(1 + \varepsilon_{RZA}|\widehat{h}_i(n)|)$ $(i = 1, 2, \ldots, N)$ is adopted instead of $\|\widehat{\mathbf{h}}(n)\|_1$ used in ZA-APA. Thus, the cost function of the RZA-APA can be written as

$$J_{RZA}(n+1) \\ = \left\| \widehat{\mathbf{h}}(n+1) - \widehat{\mathbf{h}}(n) \right\|^2 + \left[\mathbf{d}(n) - \mathbf{U}(n)\widehat{\mathbf{h}}(n+1) \right]^T \lambda_{RZA} \\ + \gamma_{RZA} \sum_{i=1}^{N} \log\left(1 + \varepsilon_{RZA} \left| \widehat{h}_i(n+1) \right| \right), \tag{14}$$

where γ_{RZA} is a regularization parameter for balancing the estimation error and the strength of the zero attractor,

$\varepsilon_{\text{RZA}} > 0$ is a positive threshold which is set to 10 in [13, 20] to obtain optimal performance, and $\boldsymbol{\lambda}_{\text{RZA}}$ is a vector of the Lagrange multiplier with size of $Q \times 1$. We use the Lagrange multiplier to the cost function of the RZA-APA and assume $\text{sgn}[\widehat{\mathbf{h}}(n+1)]/(1+\varepsilon_{\text{RZA}}|\widehat{\mathbf{h}}(n+1)|) \approx \text{sgn}[\widehat{\mathbf{h}}(n)]/(1+\varepsilon_{\text{RZA}}|\widehat{\mathbf{h}}(n)|)$ in the steady stage. Then, we can get the update equation of the RZA-APA by taking the statistical property of the channel

$$
\begin{aligned}
\widehat{\mathbf{h}}(n+1) &= \widehat{\mathbf{h}}(n) + \mu_{\text{RZA}} \mathbf{U}^+(n) \mathbf{e}(n) \\
&\quad + \frac{1}{2} \gamma_{\text{RZA}} \mathbf{U}^+(n) \mathbf{U}(n) \frac{\text{sgn}\left[\widehat{\mathbf{h}}(n)\right]}{1 + \varepsilon_{\text{RZA}}\left|\widehat{\mathbf{h}}(n)\right|} \\
&\quad - \frac{1}{2} \gamma_{\text{RZA}} \frac{\text{sgn}\left[\widehat{\mathbf{h}}(n)\right]}{1 + \varepsilon_{\text{RZA}}\left|\widehat{\mathbf{h}}(n)\right|},
\end{aligned}
\tag{15}
$$

where μ_{RZA} is the step size of the RZA-APA.

3. Proposed LP-APA Sparse Channel Estimation Algorithm

On the basis of the conventional APA and the zero-attracting techniques used in the ZA-APA and RZA-APA, we proposed an l_p-norm-penalized affine projection algorithm (LP-APA) by integrating an l_p-norm into the cost function of the conventional APA in order to design a zero attractor. The proposed LP-APA is also a zero-attracting algorithm, which can further exploit the sparsity property of the wireless multipath channel. In the LP-APA, an l_p-norm is employed to replace the l_1-norm in the ZA-APA. As for channel estimation, the objective of the LP-APA is to minimize

$$
\begin{aligned}
&\left\|\widehat{\mathbf{h}}(n+1) - \widehat{\mathbf{h}}(n)\right\|^2 + \gamma_{\text{LP}}\left\|\widehat{\mathbf{h}}(n+1)\right\|_p \\
&\text{subject to:} \quad \mathbf{d}(n) - \mathbf{U}(n)\widehat{\mathbf{h}}(n+1) = \mathbf{0},
\end{aligned}
\tag{16}
$$

where γ_{LP} is a very small constant that is used to balance the estimator error and the l_p-norm-penalized $\widehat{\mathbf{h}}(n+1)$ and $\|\cdot\|_p$ is the l_p-norm with $0 < p < 1$. It is found that an extra tunable parameter p in the l_p-norm can provide a flexible penalty for the proposed LP-APA in comparison with the fixed l_1-norm in ZA-APA. In order to minimize (16), the Lagrange multiplier method is employed and the cost function of the LP-APA can be written as

$$
\begin{aligned}
&J_{\text{LP}}(n+1) \\
&= \left\|\widehat{\mathbf{h}}(n+1) - \widehat{\mathbf{h}}(n)\right\|^2 + \left[\mathbf{d}(n) - \mathbf{U}(n)\widehat{\mathbf{h}}(n+1)\right]^T \boldsymbol{\lambda}_{\text{LP}} \\
&\quad + \gamma_{\text{LP}}\left\|\widehat{\mathbf{h}}(n+1)\right\|_p,
\end{aligned}
\tag{17}
$$

where $\boldsymbol{\lambda}_{\text{LP}}$ is the Lagrange multiplier vector.

By calculating the gradient of the cost function $J_{\text{LP}}(n+1)$ of the LP-APA, we have

$$
\frac{\partial J_{\text{LP}}(n+1)}{\partial \widehat{\mathbf{h}}(n+1)} = \mathbf{0}, \qquad \frac{\partial J_{\text{LP}}(n+1)}{\partial \boldsymbol{\lambda}_{\text{LP}}} = \mathbf{0}.
\tag{18}
$$

Then, by solving (18), we get

$$
\begin{aligned}
\widehat{\mathbf{h}}(n+1) &= \widehat{\mathbf{h}}(n) + \frac{1}{2}\mathbf{U}^T(n)\boldsymbol{\lambda}_{\text{LP}} \\
&\quad - \frac{1}{2}\gamma_{\text{LP}} \frac{\left\|\widehat{\mathbf{h}}(n)\right\|_p^{1-p} \text{sgn}\left(\widehat{\mathbf{h}}(n)\right)}{\left|\widehat{\mathbf{h}}(n)\right|^{1-p}}.
\end{aligned}
\tag{19}
$$

In order to avoid dividing by zero, which is a case for a sparse channel at initialization stage, we introduce a small positive constant into the denominator of the last term of (19). Then, (19) can be further modified to

$$
\begin{aligned}
\widehat{\mathbf{h}}(n+1) &= \widehat{\mathbf{h}}(n) + \frac{1}{2}\mathbf{U}^T(n)\boldsymbol{\lambda}_{\text{LP}} \\
&\quad - \frac{1}{2}\gamma_{\text{LP}} \frac{\left\|\widehat{\mathbf{h}}(n)\right\|_p^{1-p} \text{sgn}\left(\widehat{\mathbf{h}}(n)\right)}{\left|\widehat{\mathbf{h}}(n)\right|^{1-p} + \varepsilon_p}.
\end{aligned}
\tag{20}
$$

By multiplying both sides of (20) by $\mathbf{U}(n)$, we obtain

$$
\begin{aligned}
\mathbf{U}(n)\widehat{\mathbf{h}}(n+1) &= \mathbf{U}(n)\widehat{\mathbf{h}}(n) + \frac{1}{2}\mathbf{U}(n)\mathbf{U}^T(n)\boldsymbol{\lambda}_{\text{LP}} \\
&\quad - \frac{1}{2}\gamma_{\text{LP}}\mathbf{U}(n) \frac{\left\|\widehat{\mathbf{h}}(n)\right\|_p^{1-p} \text{sgn}\left(\widehat{\mathbf{h}}(n)\right)}{\left|\widehat{\mathbf{h}}(n)\right|^{1-p} + \varepsilon_p}.
\end{aligned}
\tag{21}
$$

Taking (18) and (21) into consideration, we have

$$
\begin{aligned}
\mathbf{d}(n) &= \mathbf{U}(n)\widehat{\mathbf{h}}(n) + \frac{1}{2}\mathbf{U}(n)\mathbf{U}^T(n)\boldsymbol{\lambda}_{\text{LP}} \\
&\quad - \frac{1}{2}\gamma_{\text{LP}}\mathbf{U}(n) \frac{\left\|\widehat{\mathbf{h}}(n)\right\|_p^{1-p} \text{sgn}\left(\widehat{\mathbf{h}}(n)\right)}{\left|\widehat{\mathbf{h}}(n)\right|^{1-p} + \varepsilon_p}.
\end{aligned}
\tag{22}
$$

From the discussion of the APA, ZA-APA, and RZA-APA and considering $\mathbf{e}(n) = \mathbf{d}(n) - \mathbf{U}(n)\widehat{\mathbf{h}}(n)$, we can get the Lagrange multiplier $\boldsymbol{\lambda}_{\text{LP}}$ by solving (22)

$$
\begin{aligned}
\boldsymbol{\lambda}_{\text{LP}} &= \left[\mathbf{U}(n)\mathbf{U}^T(n)\right]^{-1} \\
&\quad \times \left\{2\mathbf{e}(n) + \gamma_{\text{LP}}\mathbf{U}(n) \frac{\left\|\widehat{\mathbf{h}}(n)\right\|_p^{1-p} \text{sgn}\left(\widehat{\mathbf{h}}(n)\right)}{\left|\widehat{\mathbf{h}}(n)\right|^{1-p} + \varepsilon_p}\right\}.
\end{aligned}
\tag{23}
$$

Substituting (23) into (20), we can get the update equation of the LP-APA

$$\widehat{\mathbf{h}}(n+1) = \widehat{\mathbf{h}}(n) + \mathbf{U}^+(n)\mathbf{e}(n)$$

$$+ \frac{1}{2}\gamma_{\mathrm{LP}}\mathbf{U}^+(n)\mathbf{U}(n)\frac{\left\|\widehat{\mathbf{h}}(n)\right\|_p^{1-p}\mathrm{sgn}\left(\widehat{\mathbf{h}}(n)\right)}{\left|\widehat{\mathbf{h}}(n)\right|^{1-p} + \varepsilon_p}$$

$$- \frac{1}{2}\gamma_{\mathrm{LP}}\frac{\left\|\widehat{\mathbf{h}}(n)\right\|_p^{1-p}\mathrm{sgn}\left(\widehat{\mathbf{h}}(n)\right)}{\left|\widehat{\mathbf{h}}(n)\right|^{1-p} + \varepsilon_p} \qquad (24)$$

$$= \widehat{\mathbf{h}}(n) + \mathbf{U}^+(n)\mathbf{e}(n)$$

$$+ \frac{1}{2}\gamma_{\mathrm{LP}}\mathbf{U}^+(n)\mathbf{U}(n)\mathbf{M}(n) - \frac{1}{2}\gamma_{\mathrm{LP}}\mathbf{M}(n),$$

where $\mathbf{M}(n) = (\|\widehat{\mathbf{h}}(n)\|_p^{1-p}\mathrm{sgn}(\widehat{\mathbf{h}}(n)))/(|\widehat{\mathbf{h}}(n)|^{1-p} + \varepsilon_p)$. To further balance the convergence speed and the steady-state performance of the LP-APA, a step size μ_{LP} is introduced into (24) which is similar to APA, ZA-APA, and RZA-APA, and hence, (24) can be modified to

$$\widehat{\mathbf{h}}(n+1) = \widehat{\mathbf{h}}(n) + \mu_{\mathrm{LP}}\mathbf{U}^+(n)\mathbf{e}(n)$$

$$+ \frac{1}{2}\rho_{\mathrm{LP}}\mathbf{U}^+(n)\mathbf{U}(n)\mathbf{M}(n) - \frac{1}{2}\rho_{\mathrm{LP}}\mathbf{M}(n), \qquad (25)$$

where $\rho_{\mathrm{LP}} = \mu_{\mathrm{LP}}\gamma_{\mathrm{LP}}$. It is worthwhile to note that our proposed LP-APA in (25) has two more terms than the standard APA, namely, $(1/2)\rho_{\mathrm{LP}}\mathbf{U}^+(n)\mathbf{U}(n)\mathbf{M}(n)$ and $(1/2)\gamma_{\mathrm{LP}}\mathbf{M}(n)$, which are denoted as zero attractors. Therefore, the convergence speed and steady-state performance of the LP-APA are significantly improved due to the zero attractors used in our proposed LP-APA. Moreover, the zero-attracting strengths of the zero attractors are controlled by the parameter ρ_{LP}. In other words, the zero attractors in our proposed LP-APA exert the l_p-norm-penalty mainly on the inactive taps and hence the convergence speed of these zero taps is significantly increased. In addition, we found that the computational complexity is a little higher than those of the RZA-APA and ZA-APA, which comes from the gradient calculation of the l_p-norm. However, our proposed LP-APA outperforms the RZA-APA, ZA-APA, and APA in terms of the convergence speed and the steady-state performance.

4. Results and Discussions

In this section, we use the computer simulation to investigate the channel estimation performance of our proposed LP-APA over a sparse multipath communication system. The simulation results are compared with those of the previously proposed sparsity-aware algorithms including ZA-APA and RZA-APA as well as the standard APA and NLMS algorithms. Here, we consider a sparse channel $\mathbf{h}$ whose length N is 32 and whose number of dominant active taps K is set to two different sparsity levels, namely, $K = 1$ and 4, similarly to past studies in [13, 17–19]. In all the simulations, the dominant active channel taps are obtained from a Gaussian distribution
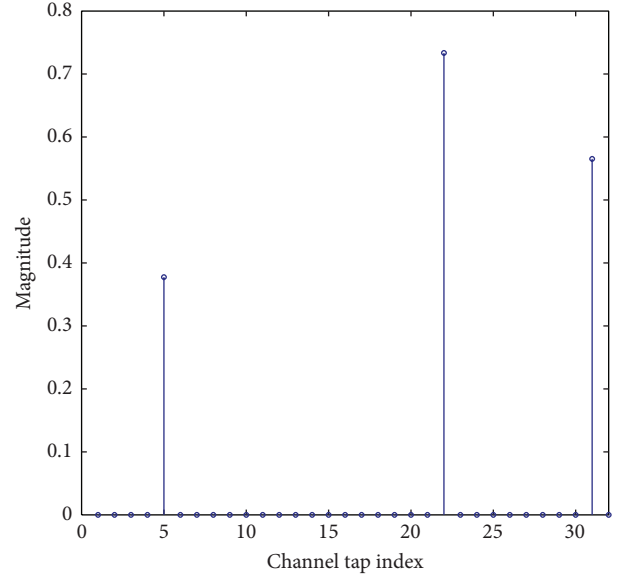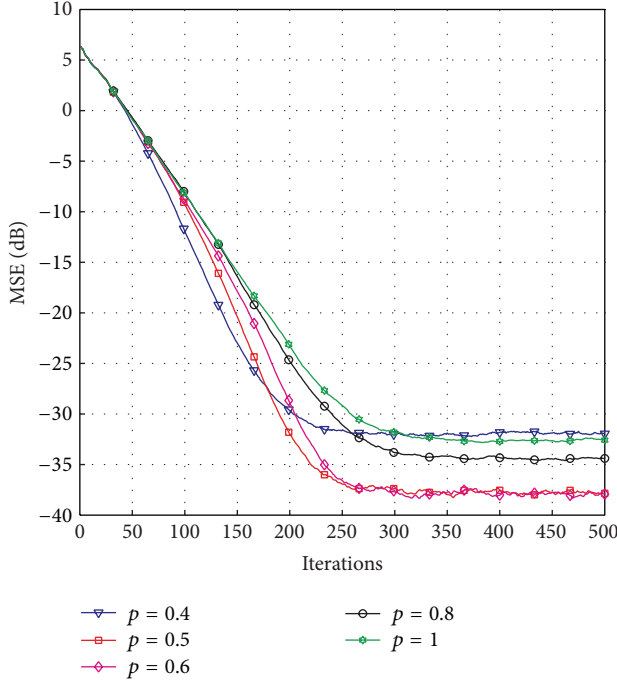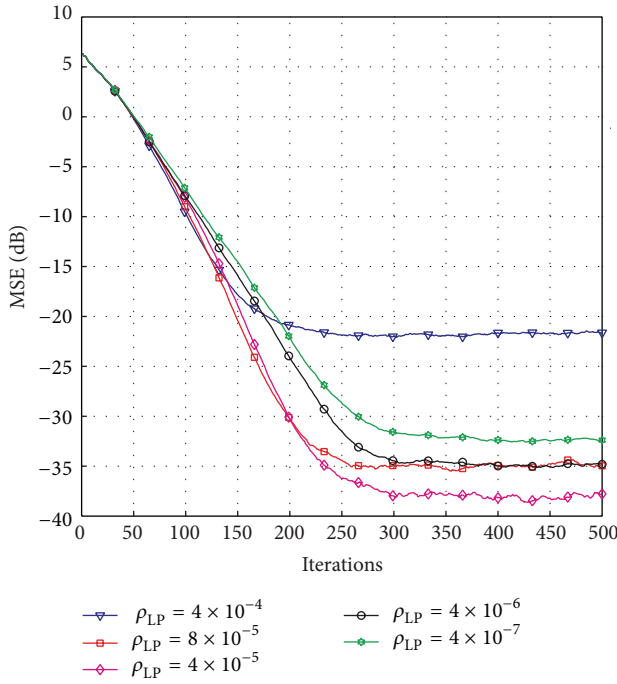

FIGURE 2: Typical sparse multipath channel.

which is subjected to $\|\mathbf{h}\|_2^2 = 1$, and the positions of these dominant active channel taps are randomly distributed within the length of the channel. The input signal $\mathbf{x}(n)$ used in this paper is a Gaussian random signal while the $\mathbf{v}(n)$ is an additive zero-mean Gaussian noise with variance δ_v^2, which is independent with the input signal $\mathbf{x}(n)$. An example of a typical sparse multipath channel with a channel length of $N = 32$ and a sparsity level of $K = 3$ is described in Figure 2. In all the simulations, the power of the received signal is $E_b = 1$, and hence, the signal-to-noise ratio (SNR) can be defined as SNR $= 10\log(E_b/\delta_v^2)$. The difference between the actual and estimated channels based on these sparse adaptive channel estimation algorithms and the sparse channel discussed above is evaluated by using mean square error (MSE) which is defined as follows:

$$\mathrm{MSE}(n) = 10\log_{10}E\left\{\left\|\mathbf{h} - \widehat{\mathbf{h}}(n)\right\|_2^2\right\} \text{ (dB)}. \qquad (26)$$

In this paper, the following parameters are used to obtain the channel estimation performance: $\mu_{\mathrm{NLMS}} = 0.73$, $\mu_{\mathrm{APA}} = \mu_{\mathrm{ZA}} = \mu_{\mathrm{RZA}} = \mu_{\mathrm{LP}} = 0.5$, $\gamma_{\mathrm{ZA}} = \gamma_{\mathrm{RZA}} = 5 \times 10^{-4}$, $\varepsilon_{\mathrm{RZA}} = 10$, $p = 0.5$, $\rho_{\mathrm{LP}} = 4 \times 10^{-5}$, and $\varepsilon_p = 0.05$. Here, μ_{NLMS} is the step size of the NLMS algorithm. In the investigation of the effects on the parameters, we change one of these parameters, while other parameters are invariable.

4.1. Effects of Parameters on the Proposed LP-APA. In the proposed LP-APA, two more parameters, p and ρ_{LP}, are introduced to design the zero attractors compared with the conventional APA. Furthermore, we also investigate the effects on the performance of the LP-APA with different affine projection order Q. Next, we show how these three parameters affect the proposed LP-APA over a sparse channel with channel length $N = 32$ and the sparsity level $K = 4$. The computer simulation results for different value of p, ρ_{LP}, and Q are presented and shown in Figures 3, 4, and 5, respectively.

FIGURE 3: Effects of p on the proposed LP-APA.

FIGURE 4: Effects of ρ_{LP} on the proposed LP-APA.

FIGURE 5: Effects of affine projection order Q on the proposed LP-APA.

In addition, we obverse that the LP-APA can achieve the same convergence speed at the early iteration stage; after that, the convergence speed of the LP-APA slows down with increasing of p.

Now, we turn to discuss the effects of the ρ_{LP} on the proposed LP-APA. We can see from Figure 4 that the steady-state performance of our proposed LP-APA is improved with a decrease of ρ_{LP} when ρ_{LP} is greater than 4×10^{-5}. When ρ_{LP} continues to decrease, the steady-state error increases again. This is because a small ρ_{LP} results in a weak zero attracting strength, which consequently reduces the convergence speed and degrades the steady-state performance. According to the discussions of those effects on parameters p and ρ_{LP}, it is observed that a small p can speed up the convergence and reduce the steady-state error of the LP-APA for $0.5 < p < 1$. The effect of parameter ρ_{LP} shown in Figure 4 is similar to the parameter α in ZA-APA [20]. Thus, we can fix the parameter ρ_{LP} on the basis of investigation of the ZA-APA and select a small p to obtain better performance.

Then, we show the channel estimation performance of the LP-APA with different value of Q. The simulation results are shown in Figure 5. It is found that the convergence speed is significantly improved with the increasing of the parameter Q for the proposed LP-APA and the ZA-APA, while the steady-state errors for both the LP-APA and ZA-APA are increased. This is due to the reuse data scheme in the APAs, which can accelerate their convergence speed. Furthermore, we found that the LP-APA can achieve faster convergence speed than the APA and NLMS algorithms with the same steady-state error floor when $Q = 8$. Thus, we can draw a conclusion

We can see from Figure 3 that the steady-state error of the proposed LP-APA is reduced with an increase of p ranging from 0.4 to 0.5. When $p = 0.6$, the LP-APA can achieve the same steady-state error as that of $p = 0.5$. However, the steady-state performance is becoming worse for $p = 0.8$ and 1. In fact, when $p = 1$, the proposed LP-APA is the ZA-APA.
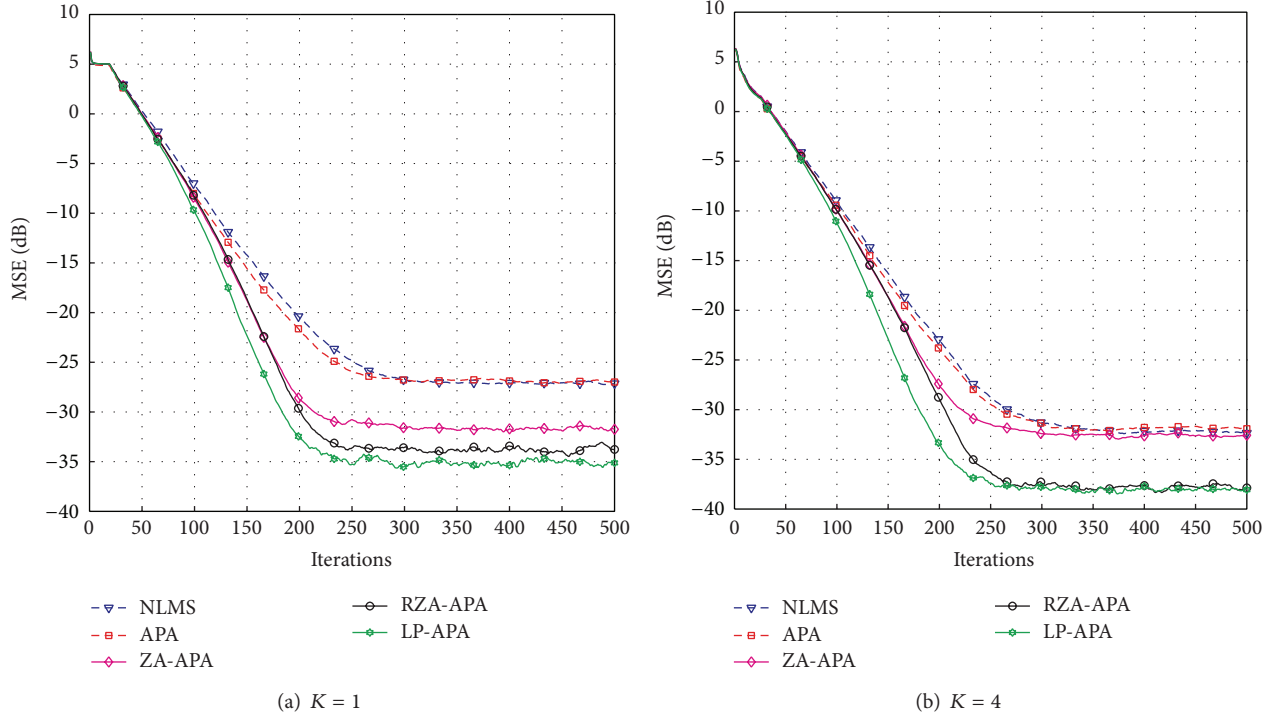
(a) $K = 1$

(b) $K = 4$

FIGURE 6: Performance of sparse channel estimation with different sparsity levels.

from the discussions alluded to above that we should carefully select the parameters p, ρ_{LP}, and Q to balance the convergence speed and steady-state performance for the proposed LP-APA.

4.2. Effects of Sparsity Level K on the Proposed LP-APA. In view of the results discussed above for our proposed LP-APA, we choose $p = 0.5$, $\rho_{LP} = 4 \times 10^{-5}$, and $Q = 2$ to evaluate the channel estimation performance of the LP-APA over a sparse channel with channel length of $N = 32$ and $K = 1$ and 4 for which the obtained simulation results are given in Figure 6 at 30 dB. We can see from Figure 6(a) that our proposed LP-APA can achieve the fastest convergence speed and lowest steady-state error when $K = 1$ in comparison with the previously proposed ZA-APA, RZA-APA, and the conventional APA and NLMS algorithms. When $K = 4$, we can see from Figure 6(b) that our proposed LP-APA still has the highest convergence speed. However, our proposed LP-APA achieves nearly the same steady-state error floor as that of RZA-APA. This is owing to that these sparsity-aware algorithms attract the inactive taps to zero quickly when $K = 1$, and hence their convergence speeds are improved so much, while their convergence speed reduced because of the reduction of the zero taps when $K = 4$. With the reduction of the sparsity of the sparse channel, the steady-state error floors are deteriorated and the convergence speeds are reduced for all the sparse-aware APAs. Moreover, our proposed LP-APA still has fastest convergence speed from $K = 1$ to $K = 4$. Thus, we can summarize this discussion by saying that the convergence speed and the steady-state performance of the LP-APA can

be improved for sparse channel estimation applications by proper selection of its parameters.

5. Conclusion

In this paper, we proposed an LP-APA to exploit the sparsity of the broadband multipath channel and to speed up the convergence of the standard APA. The LP-APA was realized by incorporating an l_p-norm into the cost function of the conventional APA, resulting in a zero attractor in its iterations, which attracted the inactive taps to zero quickly and hence accelerated the convergence speed of the APA. The simulation results showed that our proposed LP-APA with acceptable computational complexity increased the convergence speed and reduced the steady-state error of the APA as well as the ZA-APA and RZA-APA for sparse channel estimation.

Conflict of Interests

The authors declare that there is no conflict of interests regarding the publication of this paper.

Acknowledgments

References

[1] L. Korowajczuk, *LTE, WiMAX and WLAN Network Design, Optimization and Performance Analysis*, John Wiley & Sons, New York, NY, USA, 2011.

[2] J. G. Proakis, *Digital Communications*, McGraw-Hill, 4th edition, 2001.

[3] F. Fumiyuki, D. Garg, S. Takaoka, and K. Takeda, "Broadband CDMA techniques," *IEEE Wireless Communications*, vol. 12, no. 2, pp. 8–18, 2005.

[4] M. Morelli and U. Mengali, "A comparison of pilot-aided channel estimation methods for OFDM systems," *IEEE Transactions on Signal Processing*, vol. 49, no. 12, pp. 3065–3073, 2001.

[5] S. F. Cotter and B. D. Rao, "Sparse channel estimation via matching pursuit with application to equalization," *IEEE Transactions on Communications*, vol. 50, no. 3, pp. 374–377, 2002.

[6] P. Maechler, P. Greisen, B. Sporrer, S. Steiner, N. Felber, and A. Brug, "Implementation of greedy algorithms for LTE sparse channel estimation," in *Proceedings of the Conference Record of the 44th Asilomar Conference on Signals, Systems and Computers (ASILOMAR '10)*, pp. 400–405, Pacific Grove, Calif, USA, November 2010.

[7] W. U. Bajwa, J. Haupt, A. M. Sayeed, and R. Nowak, "Compressed channel sensing: A new approach to estimating sparse multipath channels," *Proceedings of the IEEE*, vol. 98, no. 6, pp. 1058–1076, 2010.

[8] S. Haykin, *Adaptive Filter Theory*, Prentice Hall, Princeton, NJ, USA, 4th edition, 2001.

[9] P. S. R. Diniz, *Adaptive Filtering Algorithms and Practical Implementation*, Spring, 4th edition, 2013.

[10] J. P. Leite, P. H. P. de Carvalho, and R. D. Vieira, "OFDM channel prediction using set-membership affine projection algorithm in time-varying wireless channel," in *Proceedings of the 10th IEEE Workshop on Signal Processing Advances in Wireless Communications, (SPAWC '09)*, pp. 26–30, Perugia, Italy, June 2009.

[11] A. F. Molisch, "Ultrawideband propagation channels-theory, measurement, and modeling," *IEEE Transactions on Vehicular Technology*, vol. 54, no. 5, pp. 1528–1545, 2005.

[12] P. Maechler, P. Greisen, B. Sporrer, S. Steiner, N. Felber, and A. Burg, "Implementation of greedy algorithms for LTE sparse channel estimation," in *Proceedings of the 44th Asilomar Conference on Signals, Systems and Computers (Asilomar '10)*, pp. 400–405, Pacific Grove, Calif, USA, November 2010.

[13] Y. Chen, Y. Gu, and A. O. Hero, "Sparse LMS for system identification," in *Proceedings of the IEEE International Conference on Acoustic Speech and Signal Processing, (ICASSP '09)*, pp. 3125–3128, Taipei, Taiwan, April 2009.

[14] C. R. Berger, Z. Wang, J. Huang, and S. Zhou, "Application of compressive sensing to sparse channel estimation," *IEEE Communications Magazine*, vol. 48, no. 11, pp. 164–174, 2010.

[15] R. Tibshirani, "Regression shrinkage and selection via the lasso," *Journal of the Royal Statistical Society B: Methodological*, vol. 58, no. 1, pp. 267–288, 1996.

[16] D. L. Donoho, "Compressed sensing," *IEEE Transactions on Information Theory*, vol. 52, no. 4, pp. 1289–1306, 2006.

[17] O. Taheri and S. A. Vorobyov, "Sparse channel estimation with L p-norm and reweighted $L1$-norm penalized least mean squares," in *Proceedings of the IEEE International Conference on Acoustics, Speech, and Signal Processing (ICASSP '11)*, pp. 2864–2867, Prague, Czech, May 2011.

[18] Y. Gu, J. Jin, and S. Mei, "$l0$ norm constraint LMS algorithm for sparse system identification," *IEEE Signal Processing Letters*, vol. 16, no. 9, pp. 774–777, 2009.

[19] G. Gui, W. Peng, and F. Adachi, "Improved adaptive sparse channel estimation based on the least mean square algorithm," in *Proceedings of the IEEE Wireless Communicat ions and Networking Conference (WCNC '13)*, pp. 3105–3109, Shanghai, China, April 2013.

[20] R. Meng, R. C. de Lamare, and V. H. Nascimento, "Sparsity-aware affine projection adaptive algorithms for system identification," in *Proceedings of the Sensor Signal Processing for Defence (SSPD '11)*, pp. 1–5, London, UK, September 2011.

[21] Y. Li and M. Hamamura, "Smooth approximation l_0-norm constrained affine projection algorithm and its applications in sparse channel estimation," *The Scientific World Journal*, vol. 2014, Article ID 937252, 15 pages, 2014.

[22] M. V. S. Lima, W. A. Martins, and P. S. Z. Diniz, "Affine projection algorithms for sparse system identification," in *Proceedings of the IEEE International Conference on Acoustic Speech and Signal Processing (ICASSP '13)*, pp. 5666–5670, Vancouver, Canada, May 2013.

[23] Y. Li and M. Hamamura, "An improved proportionate normalized least-mean-square algorithm for broadband multipath channel estimation," *The Scientific World Journal*, vol. 2014, Article ID 572969, 9 pages, 2014.

[24] E. J. Candes, M. B. Wakin, and S. P. Boyd, "Enhancing sparsity by reweighted $l1$ minimization," *The Journal of Fourier Analysis and Applications*, vol. 14, no. 5-6, pp. 877–905, 2008.

Research Article

Design of a Multiband Antenna for LTE/GSM/UMTS Band Operation

Youngtaek Hong, Jinpil Tak, Jisoo Baek, Bongsik Myeong, and Jaehoon Choi

Department of Electronics and Communications Engineering, Hanyang University, 222 Wangsimni-ro,
Seongdong-gu, Seoul 133-791, Republic of Korea

Correspondence should be addressed to Jaehoon Choi; choijh@hanyang.ac.kr

This paper proposes a multiband antenna for LTE/GSM/UMTS band operation. The proposed antenna consists of a meandered planar inverted-F antenna with an additional branch line for wide bandwidth and a folded-loop antenna. The antenna provides a wide bandwidth to cover the hepta-band LTE/GSM/UMTS operation. The measured 6 dB return loss bandwidth is 169 MHz (793–962 MHz) at the low-frequency band and 1030 MHz (1700–2730 MHz) at the high-frequency band. The overall dimension of the proposed antenna is 55 mm × 110 mm × 5 mm.

1. Introduction

Nowadays, mobile equipment is required to cover various communication services (Wi-Fi, Bluetooth, GPS, and LTE). In various mobile communication services, long-term evolution (LTE) is one of the widely used communication systems as a fourth-generation wireless service. Because each nation or wireless carrier uses different frequency bands, a multiband antenna is desirable. Moreover, the role of multiband antennas becomes more important because the carrier aggregation technique of LTE-Advanced communication system has been released [1].

In this paper, we propose a multiband antenna that operates over the hepta-band in LTE/GSM/UMTS services. The proposed antenna consists of a folded-loop and a meandered planar inverted-F antenna (MPIFA) with an additional branch line. The folded-loop antenna operates at the high-frequency band covering GSM1800 (1710–1880 MHz), GSM1900 (1850–1990 MHz), UMTS (1920–2170 MHz), LTE2300 (2305–2400 MHz), and LTE2500 (2500–2690 MHz), and the MPIFA with an additional branch line covers the low-frequency band, including GSM850 (824–894 MHz) and GSM900 (880–960 MHz) [2–6]. The proposed antenna satisfies the 6 dB return loss

bandwidth in all operating frequency bands and exhibits near-omnidirectional radiation patterns.

2. Antenna Design

Figure 1(a) shows the structure of the proposed multiband antenna for LTE/GSM/UMTS operation. The proposed antenna is designed on an FR-4 substrate ($\varepsilon_r = 4.4$; $\tan\delta = 0.02$). The FR-4 substrate dimension is 55 mm × 110 mm × 1 mm, and that of the antenna is 55 mm × 12 mm × 4 mm. Figure 1(b) shows the detailed configuration of the radiating element. The left side structure operates as a folded loop for the high-frequency band. This folded-loop structure has a wide bandwidth characteristic owing to its large thickness of 4 mm [7–9], whereas the right side structure that consists of an MPIFA and additional branch line covers the low-frequency band. Because a conventional PIFA has an insufficient frequency bandwidth for wireless communication, the proposed MPIFA has an additional branch line to increase the bandwidth. This structure generates additional resonance owing to the shunt capacitance between the additional branch line and the ground [10]. We used the HFSS v.14.0.0 by ANSYS for the simulation of the proposed antenna [11].
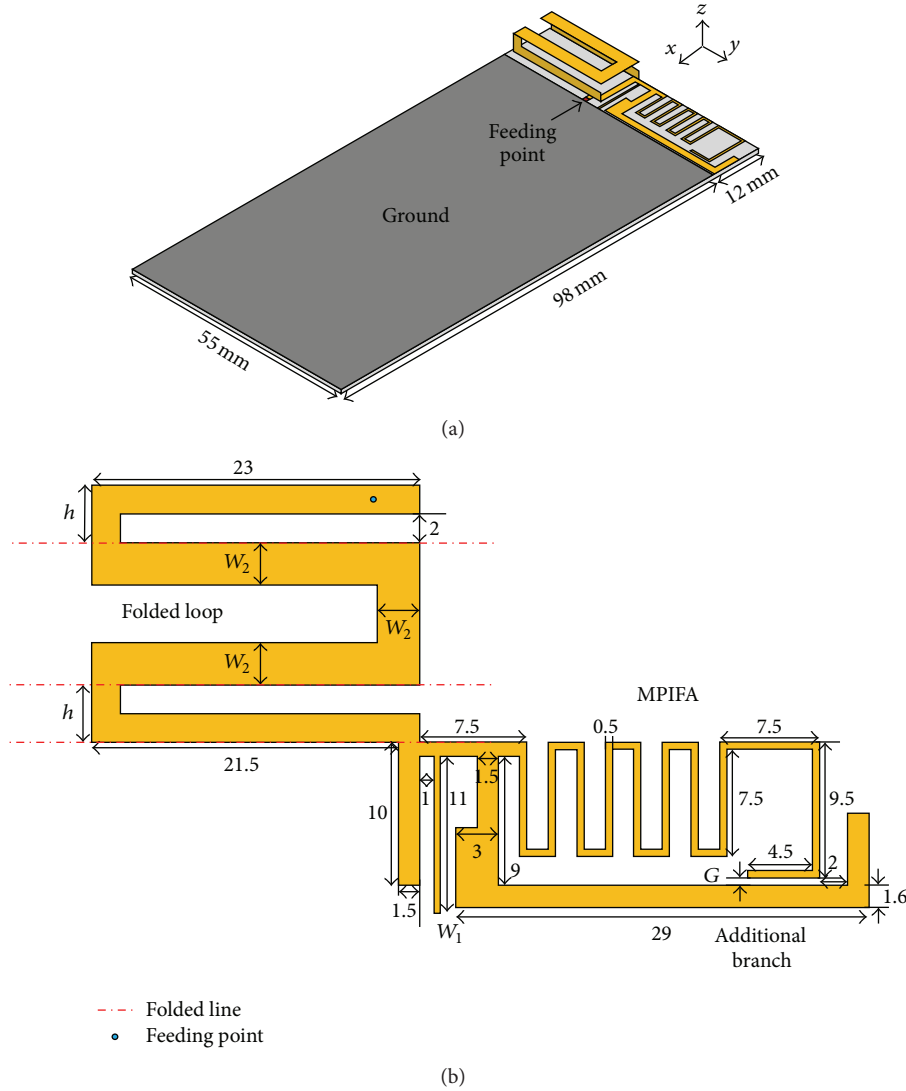
FIGURE 1: Configuration of the proposed antenna. (a) Overview. (b) Radiator.

3. Design Procedure and Parametric Study

To demonstrate the operating principle of the proposed antenna, it is divided into a folded-loop and an MPIFA structure. Figure 2 shows the simulated return loss characteristics of two reference antennas (Refs. 1 and 2) and the proposed antenna. The single element of the folded-loop antenna (Ref. 1) has a wide return loss bandwidth characteristic at the high-frequency band, whereas the single element of the MPIFA (Ref. 2) has narrow bandwidths at both the low and high bands. The Ref. 2 antenna without an additional branch line generates the first resonance at around 850 MHz and the second resonance at 2.5 GHz. By combining the folded-loop structure and the MPIFA with an additional branch line, the proposed antenna enhances the resonance characteristic at the high-frequency band and has a wide bandwidth characteristic at both low and high bands.

Parametric studies and optimization are performed for impedance matching at each resonant frequency and for

determining the resonant frequency. Figure 3 shows the simulated return loss characteristics of various shorted strip widths W_1 of the MPIFA. As W_1 decreases, the second resonant frequency at the low band shifts to the lower frequency side, and impedance matching in the low-frequency band improves. However, the high-frequency band is not affected.

For overall impedance matching at the high-frequency band, the effect of height h of the folded-loop structure is shown in Figure 4. The return loss characteristic at the high-frequency band is improved by increasing h, whereas the first and second resonances at the low band remain almost stationary at around 800–1000 MHz. When $h = 4$ mm, the 6 dB return loss bandwidth at the high-frequency band simultaneously satisfies the GSM, UMTS, and LTE bands.

Figure 5 shows the simulated return loss characteristic for various widths of the folded loop W_2. As W_2 is increased, the effective current path of the folded loop structure is shortened so that the second resonance in the high-frequency band shifts toward the higher frequency side. Therefore the overall
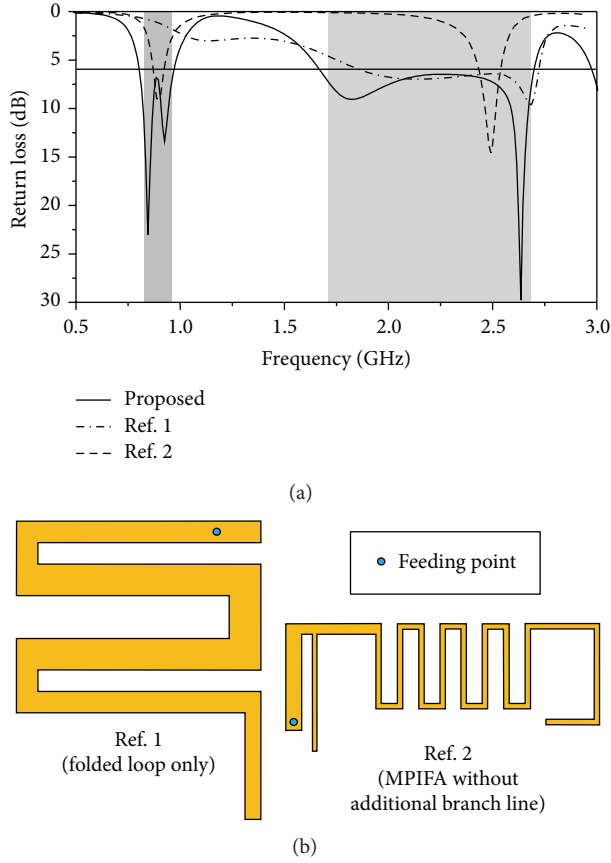
(a)

(b)

Figure 2: Simulated return loss characteristics of the proposed antenna for the folded-loop only case (Ref. 1) and for MPIFA without an additional branch line (Ref. 2) case. The dimensions of these reference antennas are shown in Figure 1.
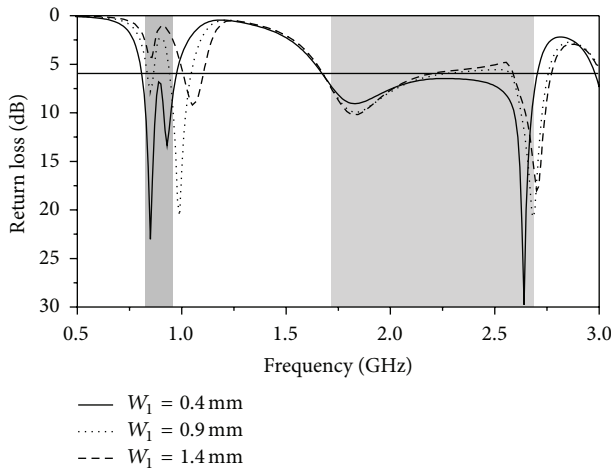
Figure 3: Return loss characteristics of the various shorted strip widths of MPIFA.

bandwidth at the high-frequency band is widened. When W_2 = 3 mm, the antenna satisfies the 6 dB return loss bandwidth at the desired frequency band.

Figure 6 shows the simulated return loss characteristic for various gap distance G. As G is decreased, the additional branch line is coupled strongly with MPIFA. Hence, the

Figure 4: Return loss characteristics for various heights of the folded-loop structure.

Figure 5: Return loss characteristics for various widths of the folded-loop structure.

Figure 6: Return loss characteristics for various gap distances.

FIGURE 7: Simulated surface current distributions of the proposed antenna. (a) First resonance at low band (850 MHz). (b) Second resonance at low band (930 MHz). (c) First resonance at high band (1810 MHz). (d) Second resonance at high band (2640 MHz).

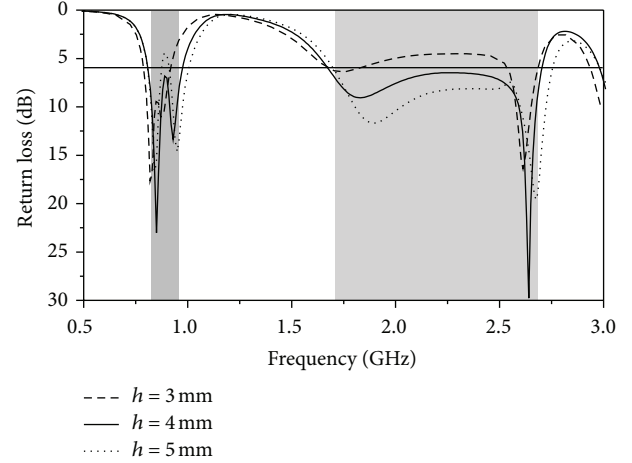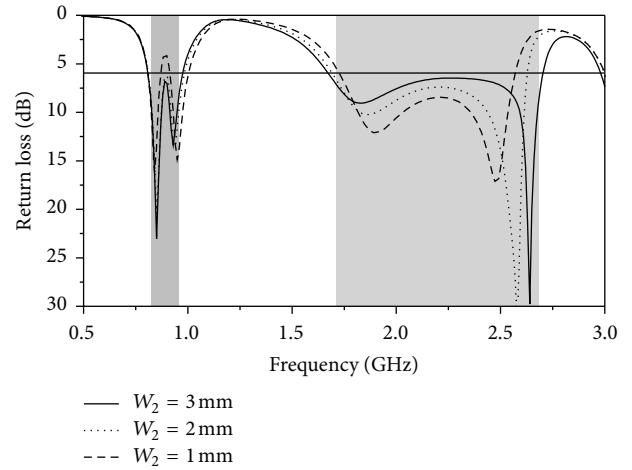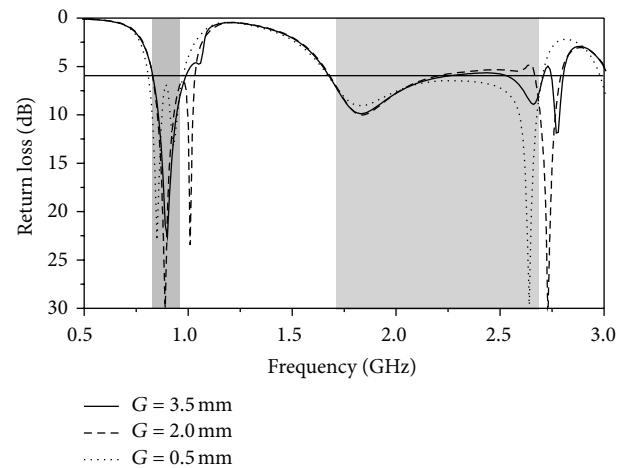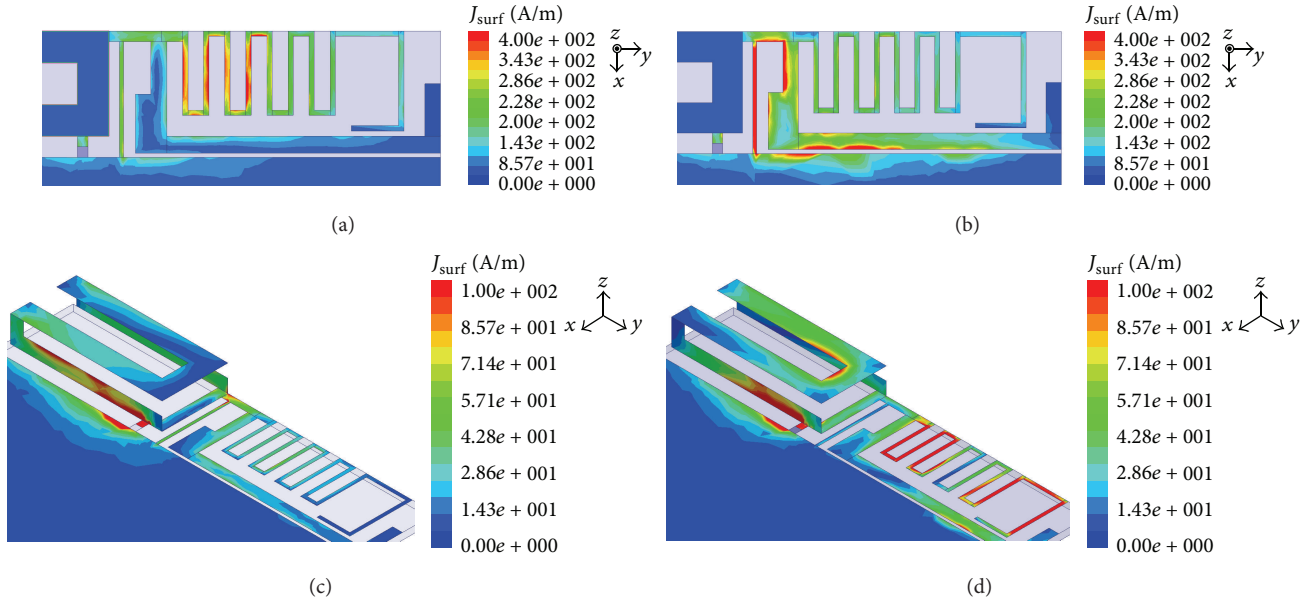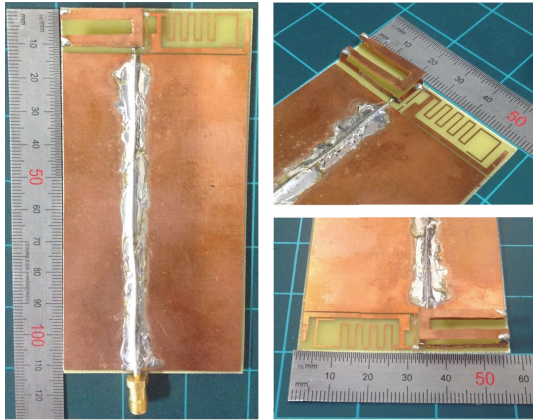FIGURE 8: Photographs of the manufactured antenna.

FIGURE 9: Simulated and measured return loss characteristics of the proposed antenna.

effective length of additional branch line becomes larger and the second resonance in the low-frequency band shifts toward the low-frequency side. When $G = 0.5$ mm, the antenna has a dual resonance characteristic in the low-frequency band and the antenna satisfies 6 dB return loss bandwidth over the GSM 850 and GSM 900 bands. As a result, the simulated 6 dB return loss bandwidth of the proposed antenna is 166 MHz (809–975 MHz) at the low-frequency band and 1028 MHz (1675–2703 MHz) at the high-frequency band.

4. Results and Discussion

Figures 7(a) and 7(b) show the simulated surface current distributions of the MPIFA with a branch line at each resonant frequency at the low band (850 and 930 MHz). Two different current paths exist in this structure: one flows through the MPIFA; the other is formed by the coupling
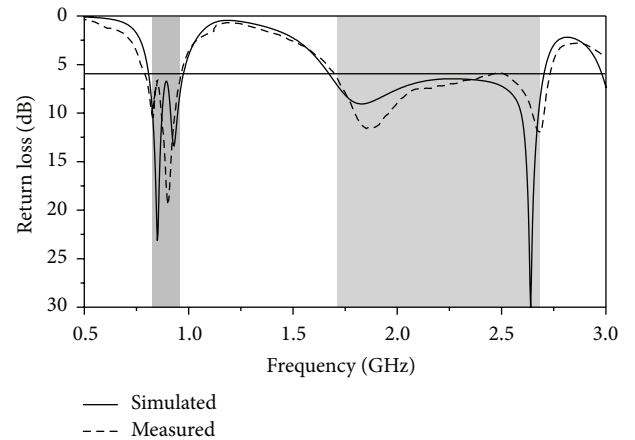
between the branch line and ground. At the resonance generated by the branch line, the radiation efficiency is bad because of the strong coupling. To improve the radiation characteristic in this case, a parasitic stub is added at the end of the additional branch line. Figures 7(a)–7(c) show that each structure, respectively, operates independently at its own resonance frequency. However, at the highest operating frequency, the current is strongly distributed in both the folded loop and MPIFA, as shown in Figure 7(d).

Figure 8 shows the photographs of the fabricated antenna. In the experiment, a 50-Ω coaxial line is used to feed the antenna.

Figure 9 shows the simulated and measured return loss characteristics of the proposed antenna. The measured results agree well with the simulated results. The measured 6 dB return loss bandwidths are 169 MHz (793–962 MHz) at the

(a)

(b)

(c)

(d)
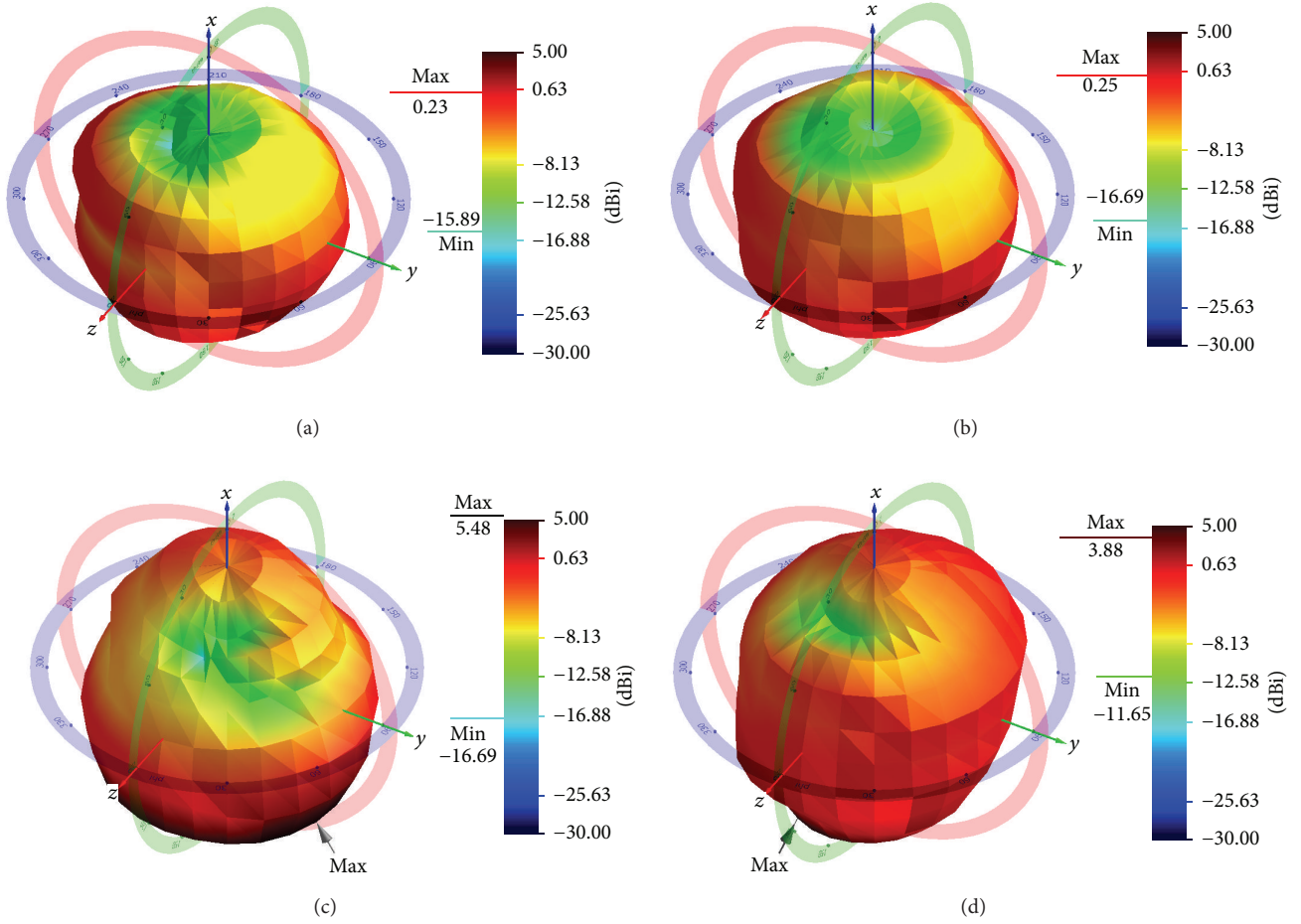
FIGURE 10: Measured 3D radiation patterns of the fabricated antenna at (a) 828 MHz, (b) 902 MHz, (c) 1850 MHz, and (d) 2680 MHz.

(a)

(b)
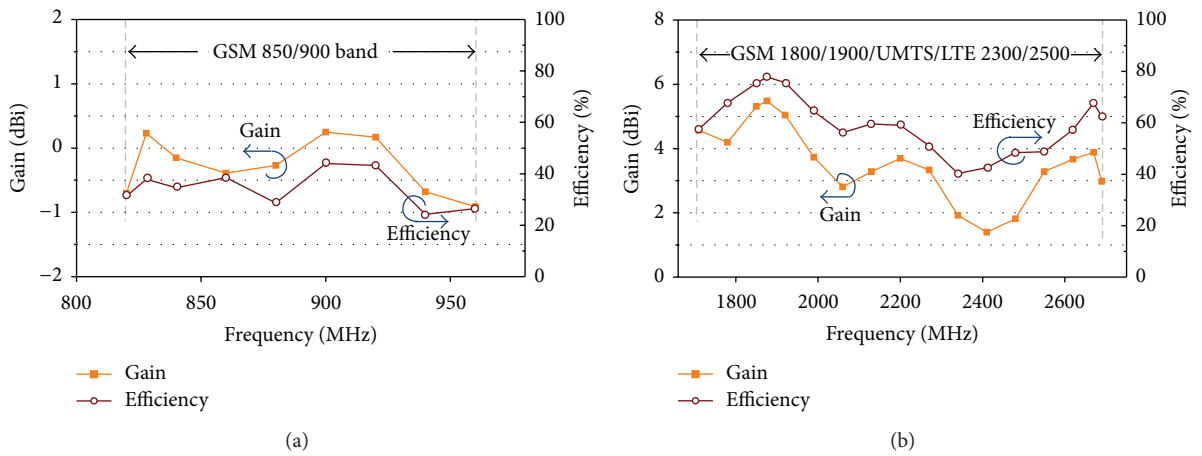
FIGURE 11: Measured antenna gain and radiation efficiency of the proposed antenna. (a) Low-frequency band. (b) High-frequency band.

low-frequency band and 1030 MHz (1700–2730 MHz) at the high-frequency band. This proposed antenna bandwidth is wide enough to cover the desired hepta-band.

Figure 10 shows the measured radiation patterns of the proposed antenna at each resonant frequency. At low frequencies of 828 and 902 MHz, the proposed antenna shows omnidirectional patterns. At high frequencies of 1850 and

2680 MHz, the proposed antenna shows directional patterns. The measured radiation patterns are suitable for practical mobile communication systems.

Figure 11 shows the measured radiation efficiency and measured gains of the proposed antenna. The measured radiation efficiency is approximately 24%–44% and 40%–78% at the low and high band, respectively. The radiation

(a)

(b)

(c)
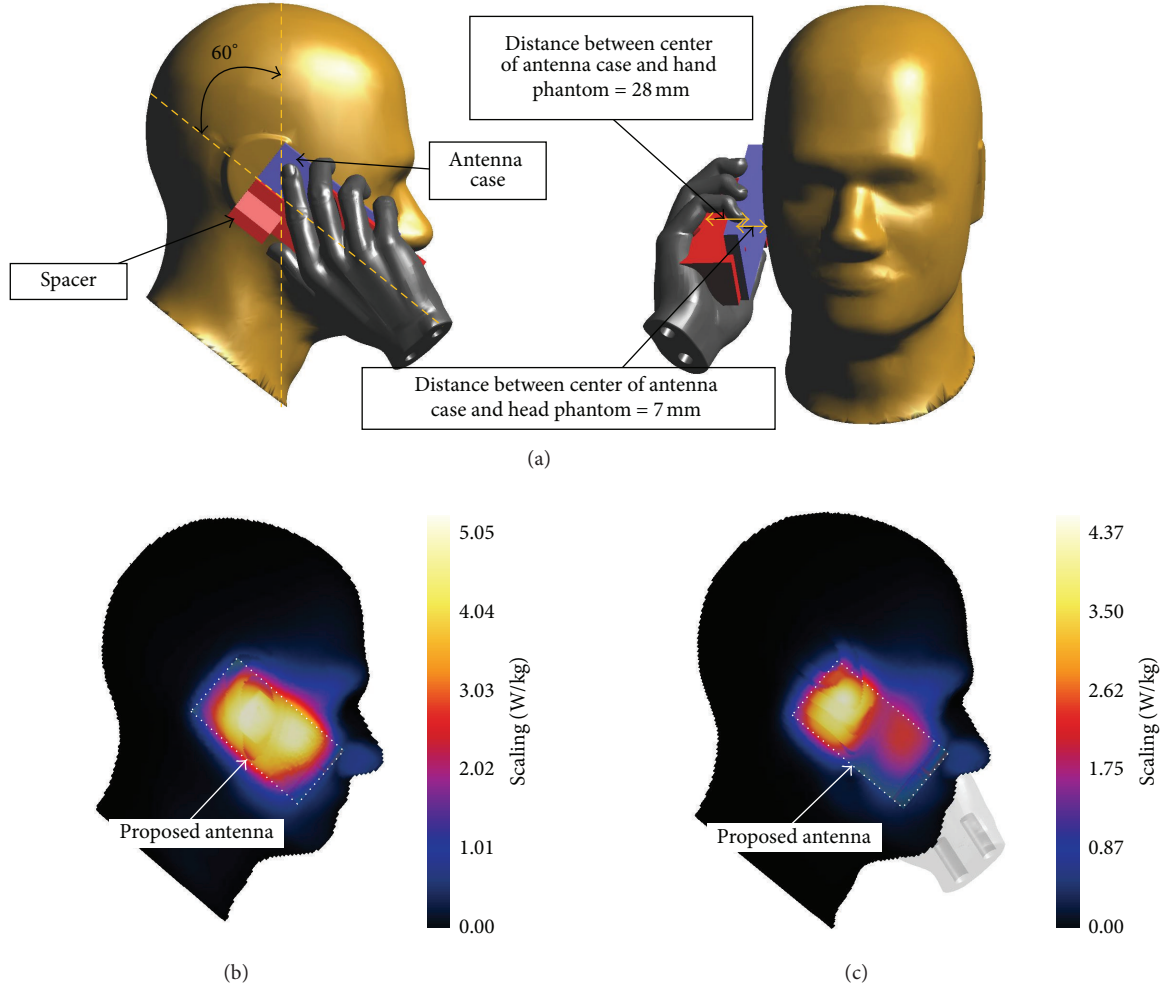
FIGURE 12: SAR simulation models. (a) Simulation setup. (b) SAR distribution in the head phantom at 1795 MHz. (c) SAR distribution in the head and hand phantoms at 1795 MHz.

efficiency at the low band is lower than that at the high band owing to the coupling between the ground plane and branch line. The measured gain varies from −0.91 to 0.25 dBi at the low band and from 1.4 to 5.48 dBi at the high band.

To evaluate the specific absorption rate (SAR) of the proposed antenna, a SAR simulation model that includes head and hand phantoms supported by SEMCAD is used [12]. The relative permittivity and conductivity of the phantom used in the simulation are listed in Table 1.

Figure 12(a) shows the simulation setup for the antenna with phantoms. The antenna, including the casing, is held by the hand phantom and attached to the head phantom. The distance between the center of the antenna case and hand phantom is 28 mm, and that between the center of the antenna case and head phantom is 7 mm. These simulation setups are based on the method used in [13]. Figures 12(b) and 12(c) show the SAR distributions at 1795 MHz where the SAR value is maximum. These distributions indicate that the maximum points of the SAR are located beneath the ear position.

The simulated results for the return loss, SAR values, and desired input power, which do not exceed the SAR limit (1.6 W/kg), are listed in Table 2. Because the proposed antenna covers the hepta-band, the simulated frequencies are chosen to be the center frequency of each desired band. When the input power is 1 W, the maximum SAR values are 5.05 W/kg for the head only and 4.37 W/kg for the head and hand at 1795 MHz. The American National Standards Institute requires that the SAR value should be below 1.6 W/kg over a volume of 1 g of tissue [14]. To satisfy the SAR limitation, the input power should be below 0.31 W.

The simulated antenna gain and efficiency with the head and hand phantoms are listed in Table 3. The antenna efficiency and gain with head and hand phantoms are reduced substantially since the antenna placed at the bottom side of a terminal is wrapped around by the hand.

Figure 13 shows the measured SAR distribution for the fabricated antenna on the head phantom. The SPEAG dosimetric assessment system (DASY-4) was used to perform SAR measurements [15]. The 1 g and 10 g SAR values when the
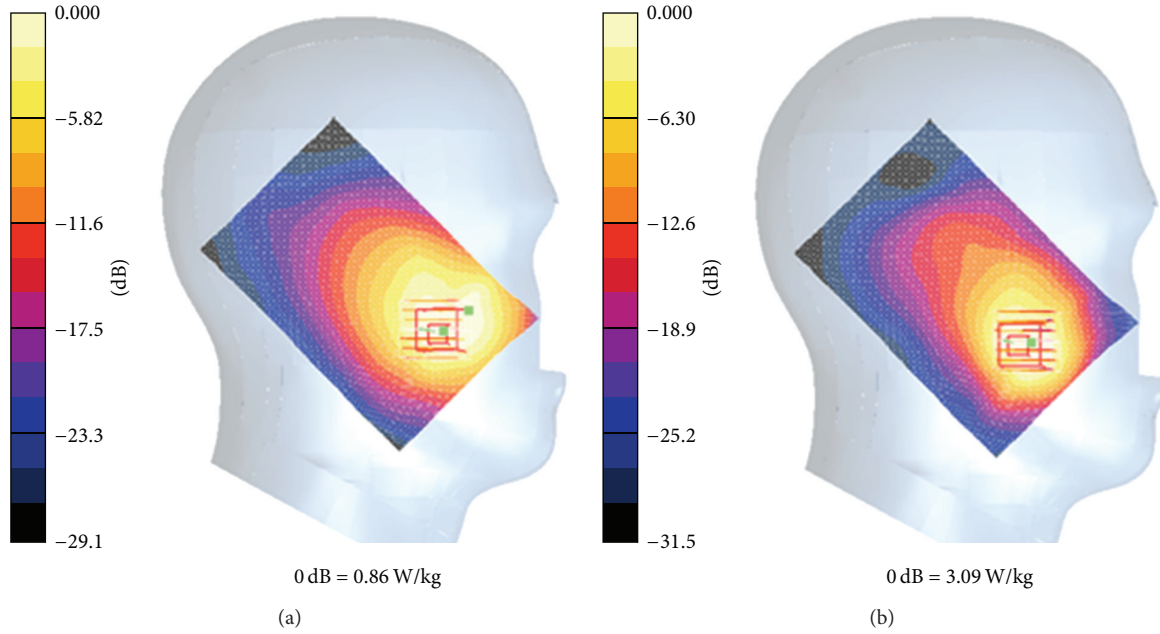
Figure 13: Measured SAR distributions in the head phantom (a) at 840 MHz and (b) at 1850 MHz (input power: 0.1 W).

Table 1: Relative permittivity and conductivity in the simulation.

Frequency (MHz)	Head		Hand	
	Relative permittivity	Conductivity	Relative permittivity	Conductivity
859	41.5	0.9	30.3	0.59
920	41.5	0.97	30	0.62
1795	40	1.4	27	0.99
1920	40	1.4	26.7	1.04
2045	40	1.4	26.5	1.09
2352.5	39.2	1.8	25.7	1.32
2595	39.2	1.8	25.7	1.32

Table 2: Simulated results of the return loss and SAR for the proposed antenna with the head and hand models.

Frequency (MHz)	Head only			Head and hand		
	Return Loss (dB)	1-g SAR (W/kg)	Input power for limit [14] (W)	Return Loss (dB)	1-g SAR (W/kg)	Input power for limit [14] (W)
859	14.94	3.84	0.41	6.43	2.27	0.70
920	6.78	4.59	0.34	6.74	3.06	0.52
1795	13.8	5.05	0.31	9.55	4.37	0.36
1920	8.75	4.34	0.36	7.19	3.74	0.42
2045	6.63	4.26	0.37	6.36	3.32	0.48
2352.5	4.36	3.74	0.42	4.49	2.17	0.73
2595	12.24	2.97	0.53	8.13	1.11	1.44

input power is 0.1 W and input powers that should not exceed the SAR limit [14] are listed in Table 4. The measured SAR values are greater than simulated ones, because the antenna is attached to the phantom without a case in the measurement setup.

5. Conclusion

A multiband antenna for the LTE/GSM/UMTS band operation has been proposed in this paper. The proposed antenna, which consists of the MPIFA and folded-loop antenna, has

TABLE 3: Simulated gain and efficiency for the proposed antenna with the head and hand phantoms.

Frequency (MHz)	Head only		Head and hand	
	Gain (dBi)	Efficiency (%)	Gain (dBi)	Efficiency (%)
859	−3.34	17.03	−8.06	7.02
920	−3.10	12.72	−7.06	7.49
1795	3.81	49.14	0.98	21.52
1920	3.96	46.14	1.62	21.13
2045	4.06	42.60	1.77	20.09
2352.5	4.19	35.58	0.58	14.20
2595	2.33	50.17	0.97	22.33

TABLE 4: Measured 1-g and 10-g SAR values for the fabricated antenna with head phantom (input power: 0.1 W).

Frequency (MHz)	Head phantom		
	1-g SAR (W/kg)	10-g SAR (W/kg)	Input power for limit [14] (W)
840	0.79	0.44	0.202
935	1.00	0.64	0.160
1850	2.79	1.51	0.057
2450	2.03	0.99	0.078

four resonant frequencies. The antenna provides wide 6 dB return loss bandwidth at both the low and high bands. The measured results of the fabricated antenna agree well with the simulated results. The measured radiation patterns are almost omnidirectional, and the measured efficiency is suitable for the desired LTE/GSM/UMTS band.

Conflict of Interests

The authors declare that there is no conflict of interests regarding the publication of this paper.

Acknowledgments

References

[1] A. Ghosh, R. Ratasuk, B. Mondal, N. Mangalvedhe, and T. Thomas, "LTE-advanced: next-generation wireless broadband technology," *IEEE Wireless Communications*, vol. 17, no. 3, pp. 10–22, 2010.

[2] C. Lee and K. Wong, "Planar monopole with a coupling feed and an inductive shorting strip for LTE/GSM/UMTS operation in the mobile phone," *IEEE Transactions on Antennas and Propagation*, vol. 58, no. 7, pp. 2479–2483, 2010.

[3] K. C. Lin, C. H. Lin, and Y. C. Lin, "Simple printed multiband antenna with novel parasitic-element design for multistandard mobile phone applications," *IEEE Transactions on Antennas and Propagation*, vol. 61, no. 1, pp. 488–491, 2013.

[4] J. Anguera, A. Andujar, and C. Garcia, "Multiband and small coplanar antenna system for wireless handheld devices," *IEEE Transactions on Antennas and Propagation*, vol. 61, no. 7, pp. 3782–3789, 2013.

[5] K. L. Wong, W. Y. Chen, and T. W. Kang, "On-board printed coupled-fed loop antenna in close proximity to the surrounding ground plane for penta-band WWAN mobile phone," *IEEE Transactions on Antennas and Propagation*, vol. 59, no. 3, pp. 751–757, 2011.

[6] X. Zhao, K. Kwon, and J. Choi, "MIMO antenna using resonance of ground planes for 4G mobile application," *The Journal of Korea Electromagnetic Engineering Society*, vol. 13, no. 1, pp. 51–53, 2013.

[7] Y. L. Ban, J. H. Chen, J. L. W. Li, and Y. Wu, "Small-size printed coupled-fed antenna for eight-band LTE/GSM/UMTS wireless wide area network operation in an internal mobile handset," *IET Microwaves, Antennas & Propagation*, vol. 7, no. 6, pp. 399–407, 2013.

[8] K. L. Wong, M. F. Tu, C. Y. Wu, and W. Y. Li, "On-board 7-band WWAN/LTE antenna with small size and compact integration with nearby ground plane in the mobile phone," *Microwave and Optical Technology Letters*, vol. 52, no. 12, pp. 2847–2853, 2010.

[9] J. Guo, L. Zhou, B. Sun, and Y. Zou, "Magneto-electric monopole antenna for terminal multiband applications," *Electronics Letters*, vol. 48, no. 20, pp. 1249–1250, 2012.

[10] S. Jeon, Y. Liu, S. Ju, and H. Kim, "PIFA with parallel resonance feed structure for wideband operation," *Electronics Letters*, vol. 47, no. 23, pp. 1263–1265, 2011.

[11] "HFSS: High Frequency Structure Simulator," v. 14.0.0, ANSYS Corp., 2013.

[12] X. Semcad, "A FDTD-Based Electromagnetic Simulator," version 14.8 Bernina, Schmid & Partner Engineering AG, Zurich, Switzerland, 2013.

[13] CTIA, "CTIA certification test plan for mobile station over the air performance," in *Method of Measurement for Radiated RF Power and Receiver Performance*, 2011.

[14] IEEE, "IEEE Standard for safety levels with respect to human exposure to radio frequency electromagnetic fields, 3 kHz to 300 GHz," IEEE Standard C95.1-1999, 1999.

[15] Schmid & Partner Engineering, AG, http://www.speag.com/speag.

Research Article

Microwave Tomographic Imaging Utilizing Low-Profile, Rotating, Right Angle-Bent Monopole Antennas

N. R. Epstein,[1] P. M. Meaney,[2] and K. D. Paulsen[2,3,4,5]

[1] *Schulich School of Engineering, University of Calgary, 2500 University Drive NW, Calgary, AB, Canada T2N 1N4*

[2] *Thayer School of Engineering, Dartmouth College, 14 Engineering Drive, Hanover, NH 03755, USA*

[3] *Department of Radiology, Geisel School of Medicine, Dartmouth College, Hanover, NH 03755, USA*

[4] *Norris Cotton Cancer Center, Dartmouth Hitchcock Medical Center, Lebanon, NH 03756, USA*

[5] *Advanced Surgical Center, Dartmouth Hitchcock Medical Center, Lebanon, NH 03756, USA*

Correspondence should be addressed to N. R. Epstein; nepstein@ucalgary.ca

We have developed a simple mechanism incorporating feedline bends and rotary joints to enable motion of a monopole antenna within a liquid-based illumination chamber for tomographic imaging. The monopole is particularly well suited for this scenario because of its small size and simplicity. For the application presented here a full set of measurement data is collected from most illumination and receive directions utilizing only a pair of antennas configured with the rotating fixture underneath the imaging tank. Alternatively, the concept can be adapted for feed structures entering the tank from the sides to allow for measurements with vertically and horizontally polarized antennas. This opens the door for more advanced imaging applications where anisotropy could play an important role such as in bone imaging.

1. Introduction

Microwave tomography (MT) is a nonionizing imaging modality capable of noninvasively recovering a wide range of dielectric property (DP) values [1–3]. An observable contrast exists between the dielectric properties (e.g., permittivity and conductivity) of healthy and abnormal breast tissue [4–8], and MT has shown great promise as a clinical imaging technique for applications initially related to breast-cancer detection [9], diagnosis [8], and chemotherapy monitoring [10]. Current breast-imaging investigations at Dartmouth College (Hanover, NH, USA) now focus on multimodal MR-MT techniques [11–14], with the advent of MT providing specificity information to the high-resolution noncontrast enhanced MR images. The development of an MR compatible MT apparatus required array profile reductions due to size restrictions associated with its placement inside the MR bore. By decreasing antenna feedline lengths within the imaging chamber, signal corruption increased due to the presence of less-heavily attenuated surface wave-based multipath

signals [15]. These investigations were foundational steps in understanding signal corruption issues associated with miniaturizing monopole antenna-array elements for biomedical microwave tomography.

One of our current interests is imaging and assessing the DPs of bone. Bone mineral density (BMD), along with additional bone-quality factors such as bone architecture, is currently used as clinical indicators of bone health. These measurable characteristics have enormous clinical potential as osteoporotic-screening and ultimately bone health assessment tools [16]. Investigations evaluating bone's DP variations as a function of mineralization using excised, demarrowed, trabecular porcine-bone samples indicate a strong correlation between the MT recovered DPs and bone-volume fraction measurements acquired using micro-CT [17]. In fact, the first clinical microwave tomographic imaging of the human calcaneus has recently been reported [18], further highlighting the clinical applicability of using MT for assessing the health of bone using DP measurements. Dartmouth's current clinical imaging system, comprehensively described
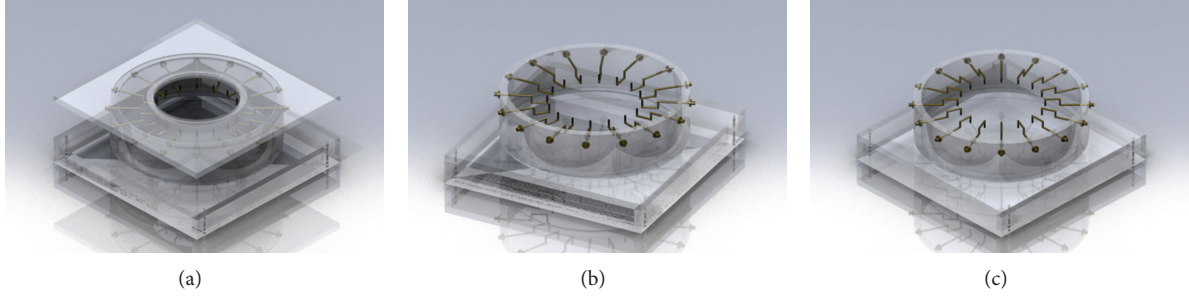
FIGURE 1: SolidWorks rendering of an example rotary-enabled monopole antenna array: (a) with top cover, (b) with antennas oriented upwards, and (c) with antennas oriented downwards.
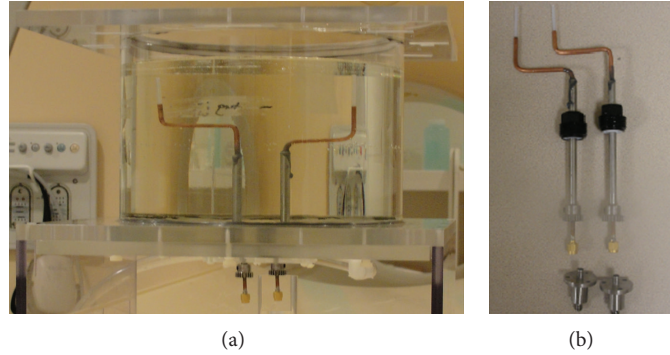

FIGURE 2: Photographs of (a) the new feed construct and antennas placed inside the imaging chamber and (b) the two bent monopoles inserted through their hydraulic seals prior to rotary joint attachment.

in [19], employs an array of 16 monopole antennas. Although free-space operation presents numerous difficulties for the monopole [20–22], operation in the system's lossy-coupling medium substantially broadens the antenna's frequency response due to resistive loading, a significant advantage in that it provides full target coverage without unwanted blind spots. Low-cost and easily constructed, the monopole's design presents many advantages in the context of our multichannel motion enabled array system, including ease of modeling [23] and positioning close to the target's surface in an array due to low mutual coupling. A thorough characterization of the system's antenna elements in terms of return loss, effective beam width, and beam steering angle as a function of electrical length can be found in [24].

The DP characteristics of bone are unique due to the complex structure of the underling bone tissue. Recent studies have demonstrated that the microstructure is highly correlated with the anisotropic DP distributions of trabecular bone [25]. Although our noncontacting antenna array design permits vertical translation of the elements, their orientations are fixed parallel to one another. In order to image these anisotropies with our system, antenna elements with the ability to transmit and receive signals in orthogonal orientations are needed. This can be accomplished clinically with the advent of antenna-array elements that can pivot around a predetermined axis using a rotary joint (Cobham, Kelvin Corporation, Rotary-Coupler Part Number 1106SS). We have chosen this approach rather than simply adding additional antennas into the array as they increase both cost and the

electronics' complexity. Obtaining the additional range of polarization orientations necessarily requires the use of a novel rotary mechanism to avoid damaging feedlines from repeated twisting. Figure 1 shows CAD renderings of a proposed low-profile imaging chamber that incorporates antenna rotation utilizing right angle-bent monopole antennas in conjunction with rotary joints for feedlines entering the tank from the sides. The antenna feedline-bending pattern inside the illumination chamber ensures that the center of the antenna is at the same physical location despite the rotation of the feedline at the tank interface.

To evaluate the clinical feasibility of incorporating this new data collection strategy into a biomedical microwave imaging system, we have conducted a pilot investigation to analyze the use of rotating, rotary joint-enabled, right angle-bent monopole antennas in a prototype two-antenna MT array (Figure 2). These miniaturized monopoles have reduced profiles within the imaging chamber due to the bending configuration, and the introduced rotational capability directly increases the number of independent measurement positions for a single monopole. Presented are S-parameter measurements of the straight and bent monopoles, with and without the introduction of the rotary joint. Minimal deviations are observed after including both bends and rotary joints in the antenna construct, indicating the design modifications have not degraded the antenna's performance over the system's operating frequency range (500–3000 MHz). Our system is designed to operate within this range due to the recognized dielectric property contrast that exists between healthy and
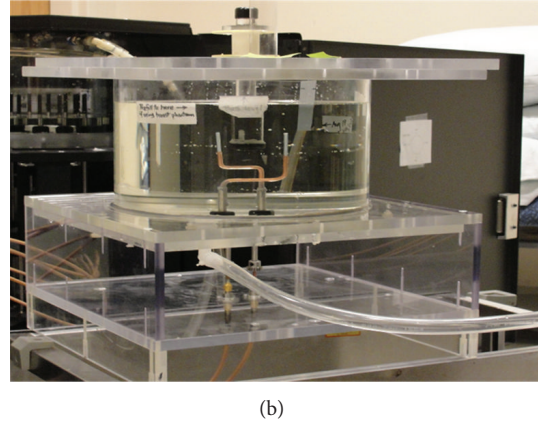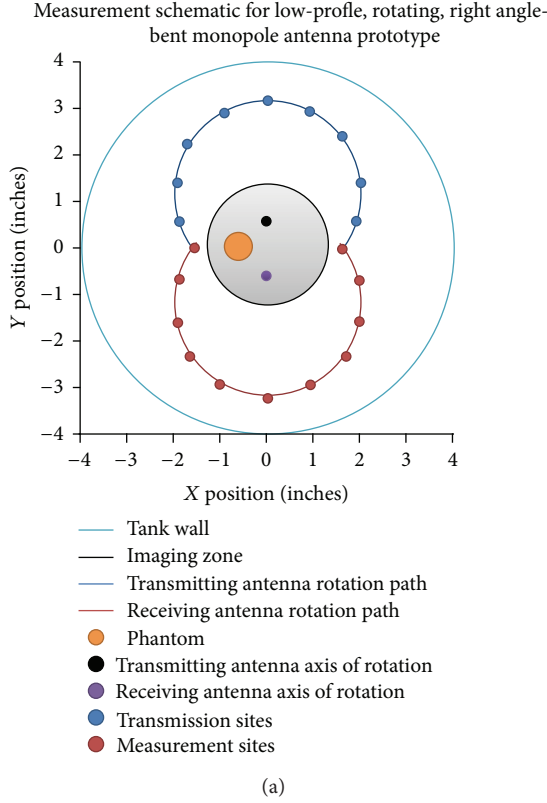
(a)

(b)

FIGURE 3: (a) 2D schematic of the experimental-imaging set-up and (b) side-view photograph of the imaging chamber with inclusion region during data collection.

abnormal tissues over this frequency span [4–8]. In addition, we have shown previously that it is difficult to transmit a signal across the target zone in just the homogeneous bath at frequencies above 3000 MHz [26]. Reconstructed MT images from simulated and measured data are also shown, highlighting the profile-reduced rotary-enabled prototype's ability to recover high-caliber electric field data for accurate image reconstruction using a unique, noncircular data collection configuration.

2. Methods

2.1. Experimental Set-Up and Antenna Positioning. The antenna and feed structure was constructed out of 2.3 mm diameter semi-ridged coaxial cable with a 3.4 cm length-exposed tip forming the radiator's active region. Bending of the monopole was accomplished using a ridged mold that allowed slow, progressive, and precise maneuvering of the feedline into the desired angular geometry. This decreased the monopole's profile within the imaging chamber while maintaining an appropriate feedline length for reduced multipath corruption from surface waves. The antennas enter the imaging chamber through hydraulic seals in the tank's bottom and are fixed at a specific vertical location within the tank using short stainless-steel sleeves and conductive silver epoxy. Their attachment to the rotary joints is outside of the imaging chamber. Accurate positioning of the elements to

numerous signal transmission and detection positions was easily achieved by incorporating an external-gearing mechanism.

Figure 3 shows a schematic of the experimental imaging set-up. In this two-antenna prototype, antenna A (the dedicated transmitter) was physically moved to 9 transmission positions while antenna B (the dedicated receiver) was moved to 11 receiving positions via the use of the rotary joint in conjunction with the modified antenna geometry. Note that because the centers of rotation for each feedline were not coincident, the shape of the imaging zone was noncircular. The collected measurements were mixed with a frequency-dependent local oscillator, and downconverted, low-pass filtered intermediate frequency signals are sent to the DAQ for sampling. The field measurements collected at each transmit-receive pair were used in our offline image reconstruction algorithm, which is briefly outlined in the following section.

2.2. Data Acquisition and Image Reconstruction. Electric field amplitude and phase measurements related to the object-under-test (OUT) were obtained by subtracting a calibration data set (with only coupling medium present in the imaging system) from the measurements taken with the OUT submerged in the lossy-medium, under the same data acquisition protocol. This process is outlined in

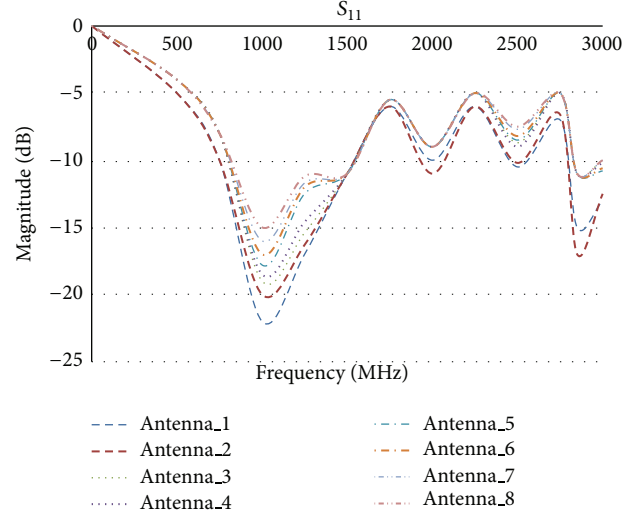$$E_{\text{OUT}}^m = E_{\text{OUT}b}^m - E_b^m, \tag{1}$$

FIGURE 4: Measured return loss for (a) the clinical imaging system's traditional encapsulated monopoles (antenna_1 and antenna_2, resp.), (b) the straight monopoles prior to bending (antenna_3 and antenna_4, resp.), (c) the bent monopoles (antenna_5 and antenna_6, resp.), and (d) the bent monopoles incorporating the rotary joint (antenna_7 and antenna_8, resp.).

where E_{OUT}^m are the measured field values of the OUT, E_{OUTb}^m are the combined measured field values of the OUT and background coupling-medium, and E_b^m are the measured field values of the background coupling-medium, respectively. Subtractions were all calculated in log magnitude and phase format.

Microwave image reconstruction requires solving an ill-posed, nonlinear inverse-scattering problem with an iterative computational method. Using a dual mesh approach [27], we have implemented a Gauss-Newton iterative technique with a log-transform [28] and Tikhonov regularization (λ) [29] to solve the wave equation for the squared complex-value wave number (k^2). The forward solution for each iteration is calculated using a hybrid-element method described in [30]. The algorithm seeks to minimize the squared error objective function for the measured and calculated amplitude and phase values. The log magnitude/phase formulation of this function is represented by

$$\Omega = \left\| \Gamma^m - \Gamma^c \left(k^2\right) \right\|_2^2$$
$$+ \left\| \Phi^m - \Phi^c \left(k^2\right) \right\|_2^2 \qquad (2)$$
$$+ \lambda \left\| L(k^2 - k_o^2) \right\|_2^2,$$

where Γ^m, Γ^c, Φ^m, and Φ^c are the log magnitude and phase values for the measured and computed field values, respectively. L is a regularization matrix and k_o^2 is a prior estimate of k^2. Simulated data corresponding to the actual measurement set-up was generated using a finite element forward solver described in [29] and includes the addition of simulated noise levels ranging from −80 to −100 dBm.

The algorithm uses the dielectric property distribution of the background emersion medium as an initial estimate. The emersion medium's DPs can vary up to 3% as a function of nominal room temperature fluctuations. Internal experiments have shown that our imaging algorithm is robust and produces only minor artifacts even when the assumed bath properties differ from the actual one's by as much as 15%. In this context, temperature variations have minimal impact on overall image quality.

3. Results

3.1. Return Loss Measurements.
To analyze the effect of introducing a right angle bend and rotary joint into the monopole antenna-feed network, S_{11} measurements were collected (in an 80 : 20 glycerine : water mixture) using an Agilent E5071A network analyzer for (a) the clinical imaging system's traditional encapsulated monopoles (antenna_1 and antenna_2, resp.), (b) the straight monopoles prior to bending (antenna_3 and antenna_4, resp.), (c) the bent monopoles (antenna_5 and antenna_6, resp.), and (d) the bent monopoles incorporating the rotary joint (antenna_7 and antenna_8, resp.) (Figure 4).

Comparing the return loss for our clinical monopoles (i.e., antenna_1 and antenna_2,) to those of the straight, bent, and rotary joint enabled monopoles demonstrates negligible performance changes, indicating that the use of the right angle-bent monopole in conjunction with the rotary joint is acceptable for this miniaturized microwave-imaging investigation. Even with the addition of the bend and rotary joint, the antenna's resonant frequency remained roughly at 1000 MHz, and its characteristic performance was consistent for all design modifications.

In general, our monopole antennas have return losses on the order of −8 to −9 dB out at the frequencies extremes [24]. In the worst case, −5 dB of transmitted power is reflected (32%). This implies that 68% is transmitted (−1.7 dB). While not optimal, given that our measurement system can detect signals down to −140 dBm and our typical transmission
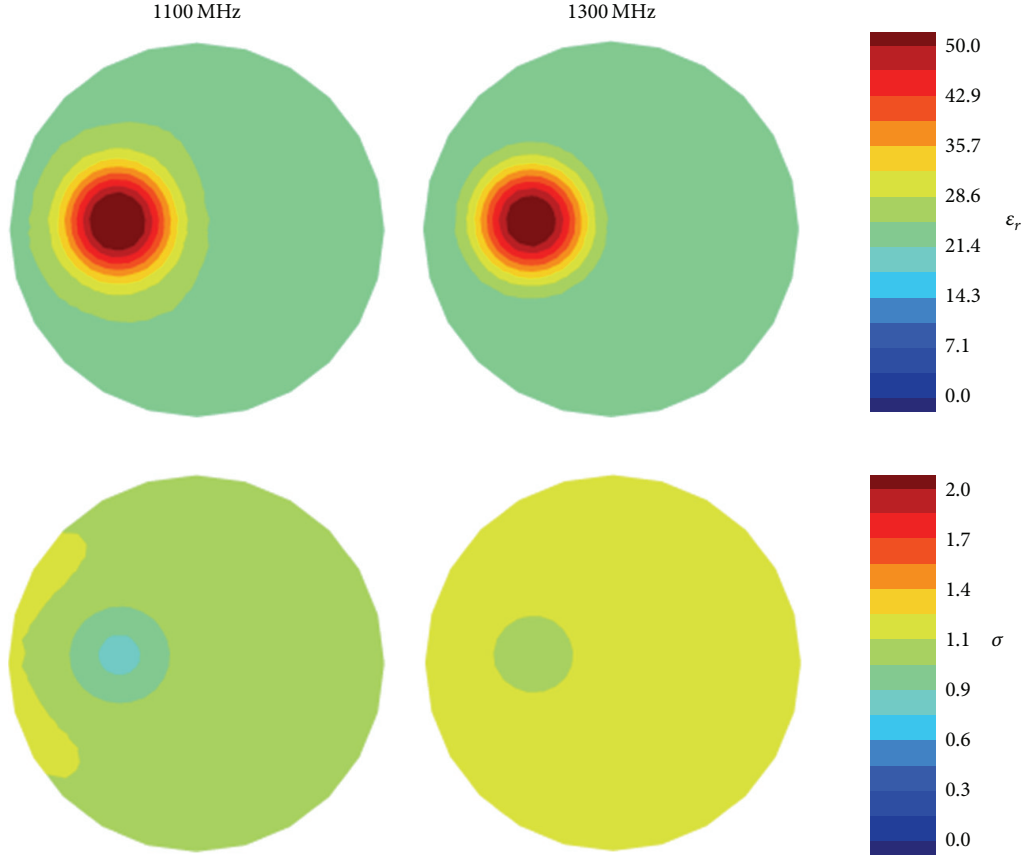
FIGURE 5: Reconstructed 1100 and 1300 MHz permittivity and conductivity images from simulated data.

power is roughly 1 mW, we still receive enough signal to maintain a healthy signal-to-noise ratio. It should also be noted that the periodic humps seen from 1500 to 3000 MHz suggest the presence of standing waves resulting from the long feedline length between the reference plane for the network analyzer set during the calibration process and the active part of the antenna. Incorporating longer transmission lines that were in fact part of the whole feed structure increased the distance between the calibration reference plane and the actual antenna.

3.2. Reconstructed Images from Simulated and Measured Data. 1100 and 1300 MHz reconstructed permittivity and conductivity image sets using simulated noisy data representative of the experimental set-up and actual measured data are shown in Figures 5 and 6, respectively. The mixture ratios and independent probe-measured dielectric properties of the background and inclusion regions, as well as the recovered DP values at the midpoint of the inclusion regions, are summarized in Tables 1 and 2, respectively. This simulation indicates that the novel rotary-enabled two-antenna array measurement set-up of 9 transmission positions and 11 measurement sites can facilitate the recovery of accurate dielectric property values for the background and the inclusion region, as well as their relative positions. The inclusion region is identifiable in all of the reconstructed images, especially for the permittivity, where the contrast between the background and inclusion

TABLE 1: Probe collected dielectric property values for the bath and inclusion region including their mixture composition (1100 and 1300 MHz).

Region	Mixture ratio (by weight)	Actual values (1100 MHz)		Actual values (1300 MHz)	
		ε_r	σ [S/m]	ε_r	σ [S/m]
Bath	80 : 20 glycerine : water	27.8	1.1	25.3	0.97
Inclusion	50 : 50 glycerine : water	53.3	1.4	49.77	1.1

region is highest. The enhanced recovery of the inclusion region observed in the 1100 MHz conductivity image, when compared to the 1300 MHz image, is due to the larger DP contrast that exists between the background and inclusion region at that frequency (0.3 S/m as compared to 0.1 S/m).

4. Conclusion

In this report, we studied the performance of the monopole antenna while incorporating several novel features into the feed network—namely, right angle bends near the active parts and rotary joints to allow for rotation about the primary axis of the feedline. While these constructs may be relatively commonplace in a range of microwave applications, this
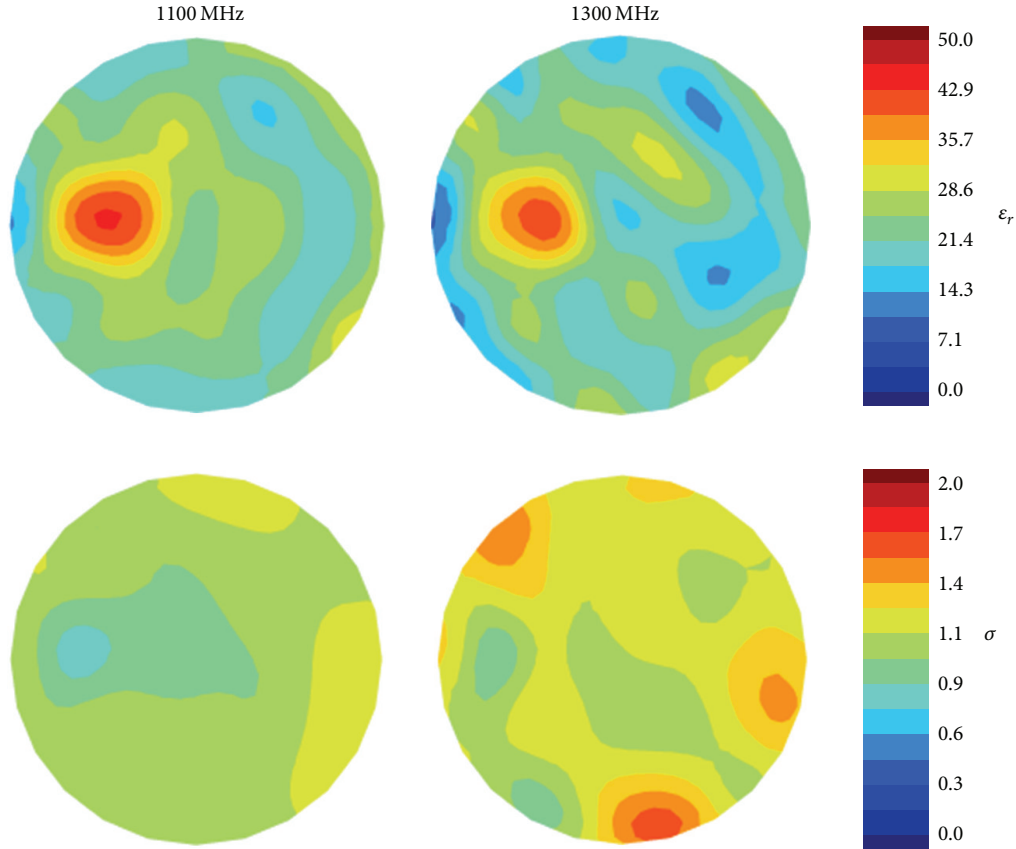
Figure 6: Reconstructed 1100 and 1300 MHz permittivity and conductivity images from measured data.

Table 2: Recovered dielectric properties values at the midpoint of the inclusion region for the simulated and measured data (1100 and 1300 MHz).

	Value at midpoint of inclusion region (simulated data)		Value at midpoint of inclusion region (measurement data)	
	ε_r	σ [S/m]	ε_r	σ [S/m]
1100 MHz	57.3	0.91	48.52	0.95
1300 MHz	54.84	1.23	42.03	1.04

is the first report of their incorporation into biomedical MT applications, and in combination they open a range of possibilities for microwave tomographic imaging. Being able to remotely alter both antenna position and orientation instantly increases the design degrees of freedom with respect to system configuration. It is important that the antenna characteristics remained relatively constant even with these transmission-line perturbations. For the imaging results presented here, the data was no longer restricted to an array of antennas configured strictly on a circular arc. This illustrated that good quality images can be recovered in nonstandard array configurations, which opens up the possibility for further reducing the number of antennas and associated electronics channels, significantly reducing overall costs and simplifying the system layout.

More importantly, it opens up the possibility of conveniently acquiring measurement data from a range of polarization orientations—especially for feedlines entering the tank from the sides. As discussed earlier, for applications such as bone imaging, being able to reconstruct the anisotropic dielectric property distributions could pave the way towards noninvasively recovering bone structural information. This would be a significant advance in monitoring bone-health, which is an increasingly important health concern. Finally, these analyses further emphasize that the monopole antenna generally offers a range of electrical and practical advantages over a host of alternate conventional approaches.

Conflict of Interests

Drs. P. M. Meaney and K. D. Paulsen cofounded Microwave Imaging System Technologies (MIST), Inc., in Hanover, NH. MIST holds six patents, of which three are relevant to microwave breast tomography. In addition, Drs. P. M. Meaney and K. D. Paulsen are coinventors on two patents through Dartmouth College which are peripherally related to microwave breast tomography. There are additional three patents pending through Dartmouth College related to microwave breast tomography. MIST won an NIH/NCI SBIR Phase I grant in 1998 and a follow-on Phase II grant in 2002. It also collaborated with the Electronics and Telecommunications Research Institute (ETRI) in Daejeon, Republic of Korea,

from 2007 to 2010. It is possible that Drs. P. M. Meaney and K. D. Paulsen could benefit financially from their microwave imaging patents. Dr. N. R. Epstein is a coinventor on a patent pending through Dartmouth College related to microwave imaging. It is possible that Dr. N. R. Epstein could benefit financially from this pending patent, if it is granted.

Acknowledgments

References

[1] P. M. Meaney, M. W. Fanning, D. Li, S. P. Poplack, and K. D. Paulsen, "A clinical prototype for active microwave imaging of the breast," *IEEE Transactions on Microwave Theory and Techniques*, vol. 48, no. 1, pp. 1841–1853, 2000.

[2] D. Li, P. M. Meaney, T. Raynolds, S. A. Pendergrass, M. W. Fanning, and K. D. Paulsen, "Parallel-detection microwave spectroscopy system for breast imaging," *Review of Scientific Instruments*, vol. 75, no. 7, pp. 2305–2313, 2004.

[3] V. Zhurbenko, T. Rubæk, V. Krozer, and P. Meincke, "Design and realisation of a microwave three-dimensional imaging system with application to breast-cancer detection," *IET Microwaves, Antennas and Propagation*, vol. 4, no. 12, pp. 2200–2211, 2010.

[4] H. P. Schwan and K. R. Foster, "RF-field interactions with biological systems: electrical properties and biophysical mechanisms," *Proceedings of the IEEE*, vol. 68, no. 1, pp. 109–113, 1980.

[5] S. S. Chaudhary, R. K. Mishra, A. Swarup, and J. M. Thomas, "Dielectric properties of normal & malignant human breast tissues at radiowave & microwave frequencies," *Indian Journal of Biochemistry and Biophysics*, vol. 21, no. 1, pp. 76–79, 1984.

[6] W. T. Joines, Y. Zhang, C. Li, and R. L. Jirtle, "The measured electrical properties of normal and malignant human tissues from 50 to 900 MHz," *Medical Physics*, vol. 21, no. 4, pp. 547–550, 1994.

[7] M. Lazebnik, D. Popovic, L. McCartney et al., "A large-scale study of the ultrawideband microwave dielectric properties of normal, benign and malignant breast tissues obtained from cancer surgeries," *Physics in Medicine and Biology*, vol. 52, no. 20, pp. 6093–6115, 2007.

[8] S. P. Poplack, T. D. Tosteson, W. A. Wells et al., "Electromagnetic breast imaging: results of a pilot study in women with abnormal mammograms," *Radiology*, vol. 243, no. 2, pp. 350–359, 2007.

[9] P. M. Meaney, M. W. Fanning, T. Raynolds et al., "Initial clinical experience with microwave breast imaging in women with normal mammography," *Academic Radiology*, vol. 14, no. 2, pp. 207–218, 2007.

[10] P. M. Meaney, P. A. Kaufman, L. S. Muffly et al., "Microwave imaging for neoadjuvant chemotherapy monitoring: initial clinical experience," *Breast Cancer Research*, vol. 15, no. 2, article R35, 2013.

[11] N. R. Epstein, A. H. Golnabi, P. M. Meaney, and K. D. Paulsen, "Microwave dielectric contrast imaging in a magnetic resonant environment and the effect of using magnetic resonant spatial information in image reconstruction," in *Proceedings of the 33rd Annual International Conference of the IEEE Engineering in Medicine and Biology Society (EMBS '11)*, pp. 5738–5741, Boston, Mass, USA, September 2011.

[12] P. M. Meaney, A. H. Golnabi, N. R. Epstein, S. D. Geimer, M. W. Fanning, and K. D. Paulsen, "Integration of a microwave tomographic imaging system with MR for improved breast imaging," *Medical Physics*, vol. 40, Article ID 103101, 2013.

[13] N. R. Epstein, P. M. Meaney, and K. D. Paulsen, "MR-guided conformal microwave imaging for enhanced inclusion detection within irregularly shaped volumes," in *Medical Imaging: Biomedical Applications in Molecular, Structural, and Functional Imaging*, Proceedings of SPIE, Lake Buena Vista, Fla, USA, February 2013.

[14] A. H. Golnabi, P. M. Meaney, and K. D. Paulsen, "Tomographic microwave imaging with incorporated prior spatial information," *IEEE Transactions on Microwave Theory and Techniques*, vol. 61, no. 5, pp. 2129–2136, 2013.

[15] P. M. Meaney, F. Shubitidze, M. W. Fanning, M. Kmiec, N. R. Epstein, and K. D. Paulsen, "Surface wave multipath signals in near-field microwave imaging," *International Journal of Biomedical Imaging*, vol. 2012, Article ID 697253, 11 pages, 2012.

[16] J. F. Griffith, K. Engelke, and H. K. Genant, "Looking beyond bone mineral density," *Annals of the New York Academy of Sciences*, vol. 1192, pp. 45–56, 2010.

[17] P. M. Meaney, T. Zhou, D. Goodwin, A. Golnabi, E. A. Attardo, and K. D. Paulsen, "Bone dielectric property variation as a function of mineralization at microwave frequencies," *International Journal of Biomedical Imaging*, vol. 2012, Article ID 649612, 9 pages, 2012.

[18] P. M. Meaney, D. Goodwin, A. H. Golnabi et al., "Clinical microwave tomographic imaging of the calcaneus: a first-in-human case study of two subjects," *IEEE Transactions on Biomedical Engineering*, vol. 59, no. 12, pp. 3304–3313, 2012.

[19] N. R. Epstein, P. M. Meaney, and K. D. Paulsen, "3D-parallel microwave tomography for clinical breast imaging," *Review of Scientific Instruments*. Under review.

[20] D. M. Pozar, *Microwave and RF Design of Wireless Systems*, John Wiley & Sons, New York, NY, USA, 2000.

[21] R. M. Sega, "Infrared detection of microwave induced surface currents on flat plates," Final Technical Report Air Force Academy, 1982.

[22] C. A. Balanis, *Antenna Theory Analysis and Design*, John Wiley & Sons, New York, NY, USA, 2nd edition, 1997.

[23] A. Taflove and S. C. Hagness, *Computational Electrodynamics: The Finite-Difference Time-Domain Method*, Atech House, Norwood, Mass, USA, 2nd edition edition, 2000.

[24] C. J. Fox, P. M. Meaney, F. Shubitidze, L. Potwin, and K. D. Paulsen, "Characterization of an implicitly resistively-loaded monopole antenna in lossy media," *International Journal of Antennas and Propagation*, vol. 2008, Article ID 558078, 9 pages, 2008.

[25] R. M. Irastorza, C. M. Carlevaro, and F. Vericat, "Is there any information on micro-structure in microwave tomography of bone tissue?" *Medical Engineering and Physics*, vol. 35, no. 8, pp. 1173–1180, 2013.

[26] L. Dun, *Microwave imaging spectroscopy for breast cancer diagnosis [thesis]*, Dartmouth College, 2003.

[27] K. D. Paulsen, P. M. Meaney, M. J. Moskowitz, and J. M. Sullivan Jr., "Dual mesh scheme for finite element based reconstruction algorithms," *IEEE Transactions on Medical Imaging*, vol. 14, no. 3, pp. 504–514, 1995.

[28] P. M. Meaney, K. D. Paulsen, B. W. Pogue, and M. I. Miga, "Microwave image reconstruction utilizing log-magnitude and unwrapped phase to improve high-contrast object recovery," *IEEE Transactions on Medical Imaging*, vol. 20, no. 2, pp. 104–116, 2001.

[29] K. D. Paulsen, P. M. Meaney, and L. C. Gilman, *Alternative Breast Imaging: Four Model-Based Approaches*, Springer, Hanover, NH, USA, 2005.

[30] P. M. Meaney, K. D. Paulsen, and T. P. Ryan, "Two-dimensional hybrid element image reconstruction for TM illumination," *IEEE Transactions on Antennas and Propagation*, vol. 43, no. 3, pp. 239–247, 1995.

Research Article

Low-Profile Folded-Coupling Planar Inverted-F Antenna for 2.4/5 GHz WLAN Communications

Hung-Yu Li,[1] Chun-Cheng Lin,[2] Tsai-Ku Lin,[1] and Chih-Yu Huang[3]

[1] *Department of Physics, National Kaohsiung Normal University, Kaohsiung 802, Taiwan*
[2] *Department of Mathematic and Physical Sciences, R.O.C. Air Force Academy, Kaohsiung 820, Taiwan*
[3] *Department of Electronic Engineering, National Kaohsiung Normal University, Kaohsiung 802, Taiwan*

Correspondence should be addressed to Chun-Cheng Lin; cclincafa@gmail.com

A dual-band folded-coupling planar inverted-F antenna (FC-PIFA) is presented in this paper. By using the folded-coupling technique, the proposed antenna provides two distinct impedance bandwidths of 159 MHz (about 6.5% centered at 2.45 GHz) and 1512 MHz (about 27.5% centered at 5.5 GHz), which cover the required bandwidths for the 2.4/5 GHz wireless local area network (WLAN) communications. Moreover, the antenna shows a low profile of 5 mm and a small length of 20.5 mm in radiating area, making it easy to be installed in the casing of wireless handheld devices and laptops. Details of the design procedures and experimental results are discussed.

1. Introduction

In wireless communication industry, planar inverted-F antenna (PIFA) is the most significant radiating elements owing to its compact size, multifrequency characteristic, and good compatibility to be integrated into mobile terminals and laptop computers. Recently, different types of PIFAs have been reported in many literatures for the growing demands of wireless local area network (WLAN) operations. An internal PIFA with modified radiating strips and appropriate feeding and shorting positions was published for 2.4/5 GHz WLAN applications [1]. To overcome the narrow bandwidth property of conventional PIFAs, a coupled-fed PIFA with a band-notching slit was investigated [2]. By inserting a J-shaped slot and a meandering line on the conducting patch, the PIFA operates at WLAN and Worldwide Interoperability for Microwave Access (WiMAX) applications [3]. With embedding an F- and T-shaped slot on the radiating structure and using a trapezoidal feeding plate, three resonant modes were generated and impedance bandwidth of the PIFA was enhanced [4]. By using two orthogonal radiators instead of a planar structure, the wideband characteristic

is achieved by generating additional resonant frequency through a grounded strip [5]. However, these PIFAs still have high profiles or occupy large radiating areas.

In this paper, we propose a dual-band folded-coupling planar inverted-F antenna (FC-PIFA) for IEEE 802.11a (2400–2480 MHz) and IEEE 802.11b/g (5150–5825 MHz) standards. We combine the concepts of a microstrip-coupled feeding line [6] and nearby conducting elements [7] and further represent a novel folded-coupling technique. By introducing this technique, the electromagnetic coupling effect generates an additional resonant mode to achieve wideband performance. The double-side configuration also decreases the profile and radiating area (5 mm × 20.5 mm) of the proposed antenna, which is easier to be embedded as an internal antenna in narrow space within the casing of a portable wireless device, such as a laptop or smart phone. Moreover, its simple geometry provides an easy fabrication and a good radiating performance.

Details of the experimental results, including measurements and simulations, of the constructed prototype are discussed. Effects of the parameters of the folded-coupling region on the impedance bandwidth and surface current
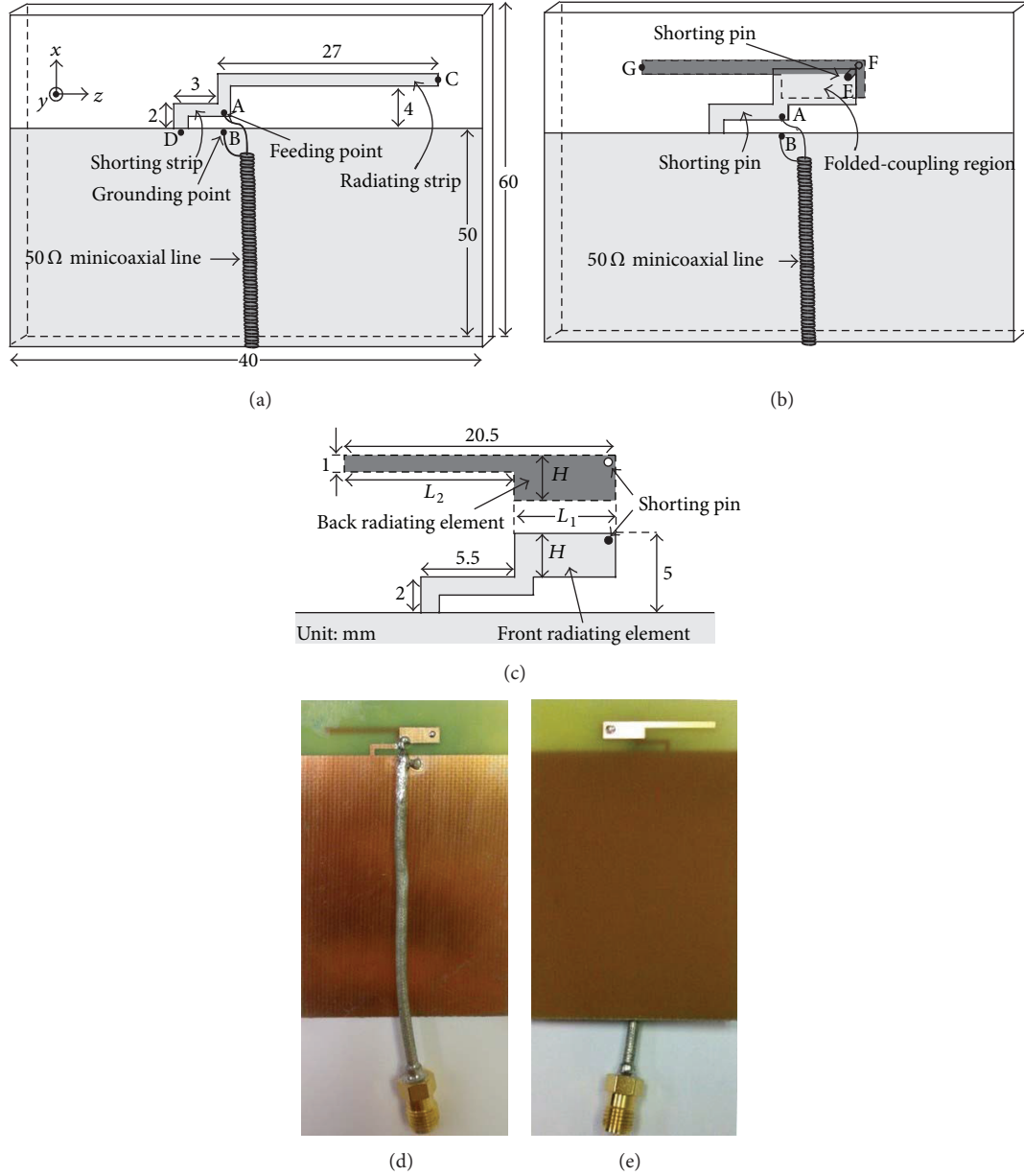
FIGURE 1: Geometry of (a) the conventional PIFA (reference antenna), (b) the proposed dual-band FC-PIFA for WLAN communications, and (c) the parameters of the folded-coupling region in (b); photograph of proposed FC-PIFA for (d) the front side and (e) the back side.

distributions are also analyzed. Furthermore, the radiating performance of the proposed antenna, including radiation patterns and peak gain values, are described.

2. Antenna Design Concepts and Experimental Procedures

Firstly, the design concepts of the antenna are investigated. Figures 1(a) and 1(b) show the constructions of the conventional folded planar inverted-F antenna (PIFA, denoted as reference antenna) and the proposed FC-PIFA, respectively. Both antennas are printed on FR4 substrates (dimensions of 60 mm × 40 mm, thickness of 0.8 mm, and relative

permittivity of 4.4). The antenna in Figure 1(a) is fed by a 50 Ω minicoaxial line, with its central conductor connected to point A (the feeding point) and its outer ground sheath connected to point B (the grounding point). All strip widths of the reference antenna are set as 1 mm. The main radiating strip is from point A to C and the shorting strip is from point A to D. The bending structure is for the purpose of a lower profile. However, its frequency ratio and bandwidth is insufficient for IEEE 802.11b/g (5150–5825 MHz) standards. Results are presented in the next section.

Hence, a folded-coupling technique is suggested. The antenna in Figure 1(b) is also fed by a 50 Ω minicoaxial line, with its central conductor connected to point A (the feeding
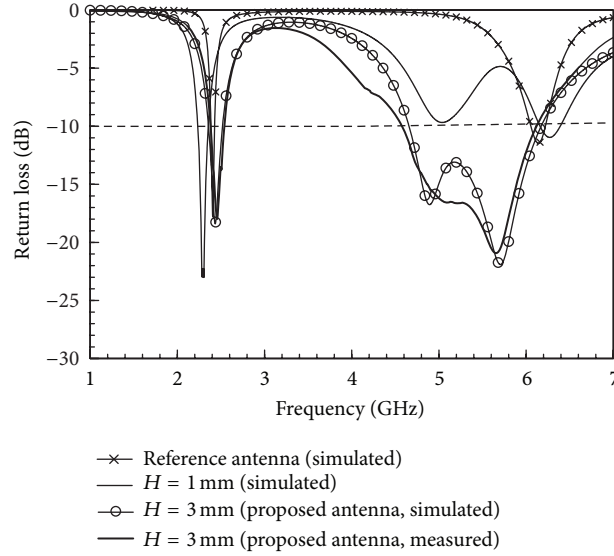
FIGURE 2: Simulated and measured return loss versus frequency for various H; $L_1 = 7.5$ mm and $L_2 = 13$ mm.
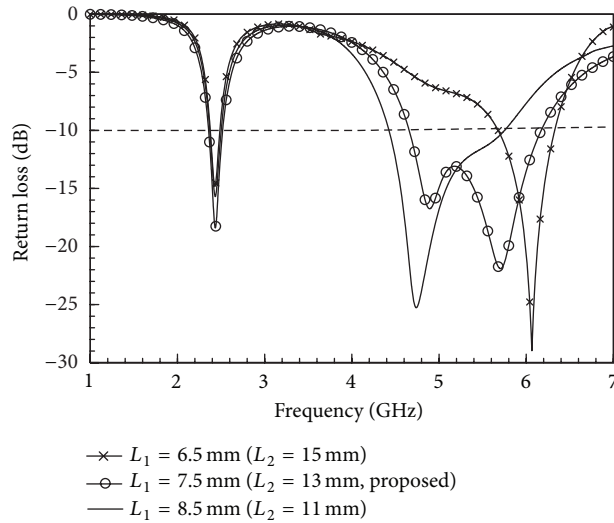

FIGURE 3: Simulated return loss versus frequency for various L_1; $2L_1 + L_2$ is fixed as 28 mm and $H = 3$ mm.

point) and the outer ground sheath connected to point B (the grounding point). The front-side radiating strip is coincided with a portion of the back-side strip via a shorting pin for mutual coupling (point A → E → F → G). The shorting pin enables the conventional PIFA transfigure to a FC-PIFA. With suitable size of the folded-coupling region, the electromagnetic coupling is generated, which introduces a new resonance mode around 5 GHz. The strip widths of the proposed antenna are set as 1 mm except the folded-coupling region in Figure 1(c), which is denoted as H. Furthermore, the folded-coupling region contributes a large capacitance whereas the shorting strip is used for inductive tuning. Thus, good impedance matching for IEEE 802.11a (2400–2480 MHz) and IEEE 802.11b/g (5150–5825 MHz) standards can be easily achieved by adjusting the length of the shorting strip. Results are also presented in the next section. Figures 1(d) and 1(e)

illustrate the photographs of the proposed FC-PIFA for the front and back side, respectively. In this work, the simulations were calculated with Ansoft HFSS and the measurements were obtained with an R&S ZVB 40 vector network analyzer. The radiation patterns and gain values were measured in the far-field anechoic chamber.

3. Results and Discussions

Then, the experimental results of the antenna are investigated and discussed in this section. Figure 2 shows the simulated and measured return loss for the reference antenna and the proposed FC-PIFA with $H = 1$ and 3 mm, respectively. Although the reference antenna has dual resonant frequencies, it is unsuitable for dual-band operation of 2.4/5 GHz due to its inadequate frequency ratio and narrow bandwidth
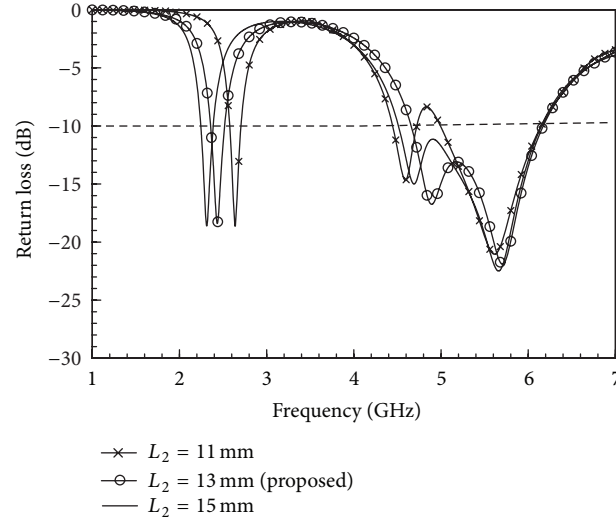
FIGURE 4: Simulated return loss versus frequency for various L_2; L_1 is fixed as 7.5 mm and H = 3 mm.
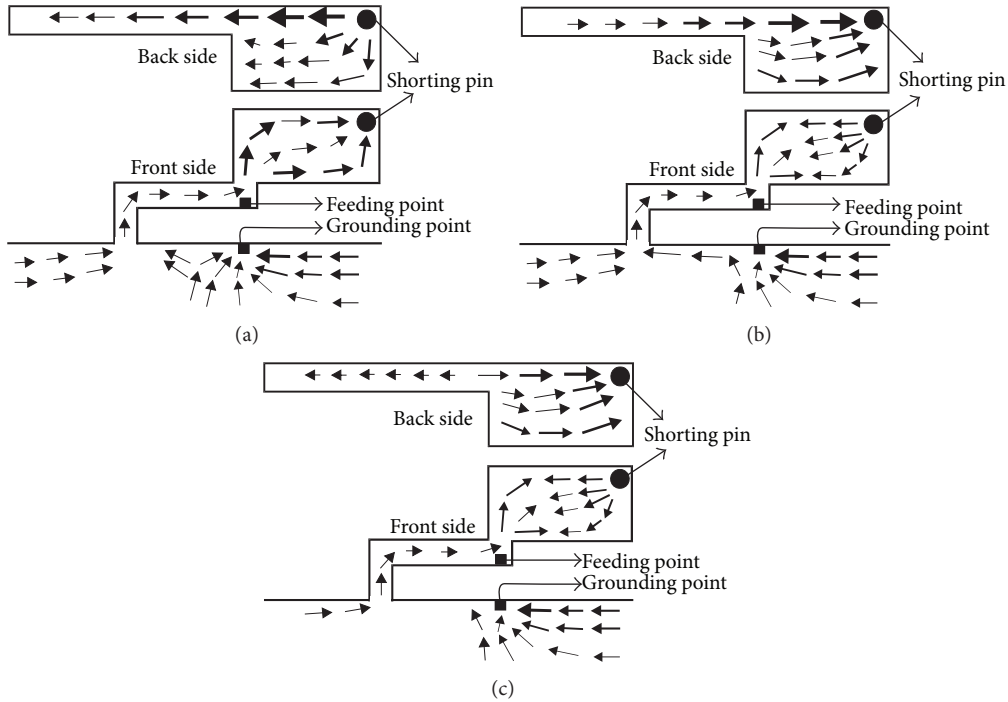

FIGURE 5: Simulated surface current distributions obtained at (a) 2.45, (b) 5.2, and (c) 5.8 GHz for proposed FC-PIFA.

at higher frequency band. For the folded-coupling region of H = 1 mm and L_1 = 7.5 mm, the coupling effect generates a new resonant mode at around 5 GHz. However, it has a poor impedance matching. For further increasing the folded-coupling region to H = 3 mm and L_1 = 7.5 mm, the impedance matching around 5 GHz can be much improved. The −10 dB bandwidths of the lower and upper bands reach about 159 MHz (2358–2517 MHz, 6.5% centered at 2.45 GHz) and 1512 MHz (4658–6170 MHz, 27.5% centered at 5.5 GHz), which are favorable for 2.4-GHz (2400–2484 MHz) and 5-GHz (5150–5825 MHz) WLAN communications. As

expected, it exhibits a good agreement between the measured and the simulated results.

The influences of the parameters, the length of the folded-coupled region L_1, and the back-side radiating strip L_2 are studied. Figure 3 shows the simulated return loss versus frequency for various L_1. With L_1 increasing from 6.5 to 8.5 mm and simultaneously the total length of L_1 and L_2 being fixed as 28 mm, the upper band decreases gradually whereas the lower band changes slightly. This appearance indicates that the size of the folded-coupling region only affects the upper band. With further varying L_2 from 11
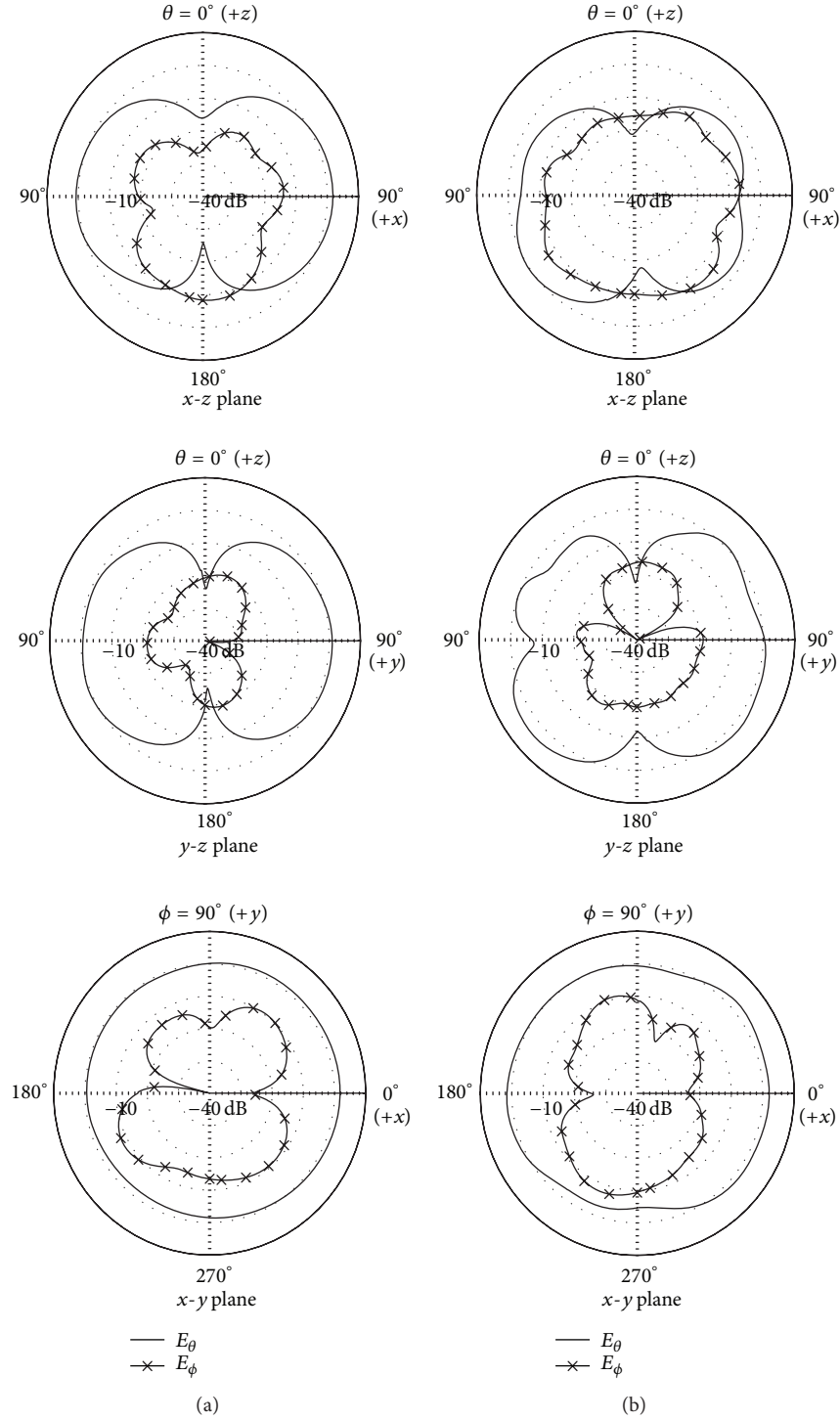
Figure 6: Measured radiation patterns of proposed FC-PIFA obtained at (a) 2.45 and (b) 5.5 GHz.

to 15 mm and simultaneously fixing the area of the folded-coupling region (H = 3 mm and L_1 = 7.5 mm), the lower band decreases gradually whereas the upper band changes slightly, as shown in Figure 4. This appearance demonstrates that the total length of the FC-PIFA dominates the resonant frequency of the lower band.

To explore the effect of folded-coupling technique in depth, Figures 5(a), 5(b), and 5(c) show the excited surface current distributions of the proposed FC-PIFA simulated via Ansoft HFSS at 2.45, 5.2, and 5.8 GHz, respectively. The main surface current path is observed from the feeding point to the open end of the radiating strip on the back side through the
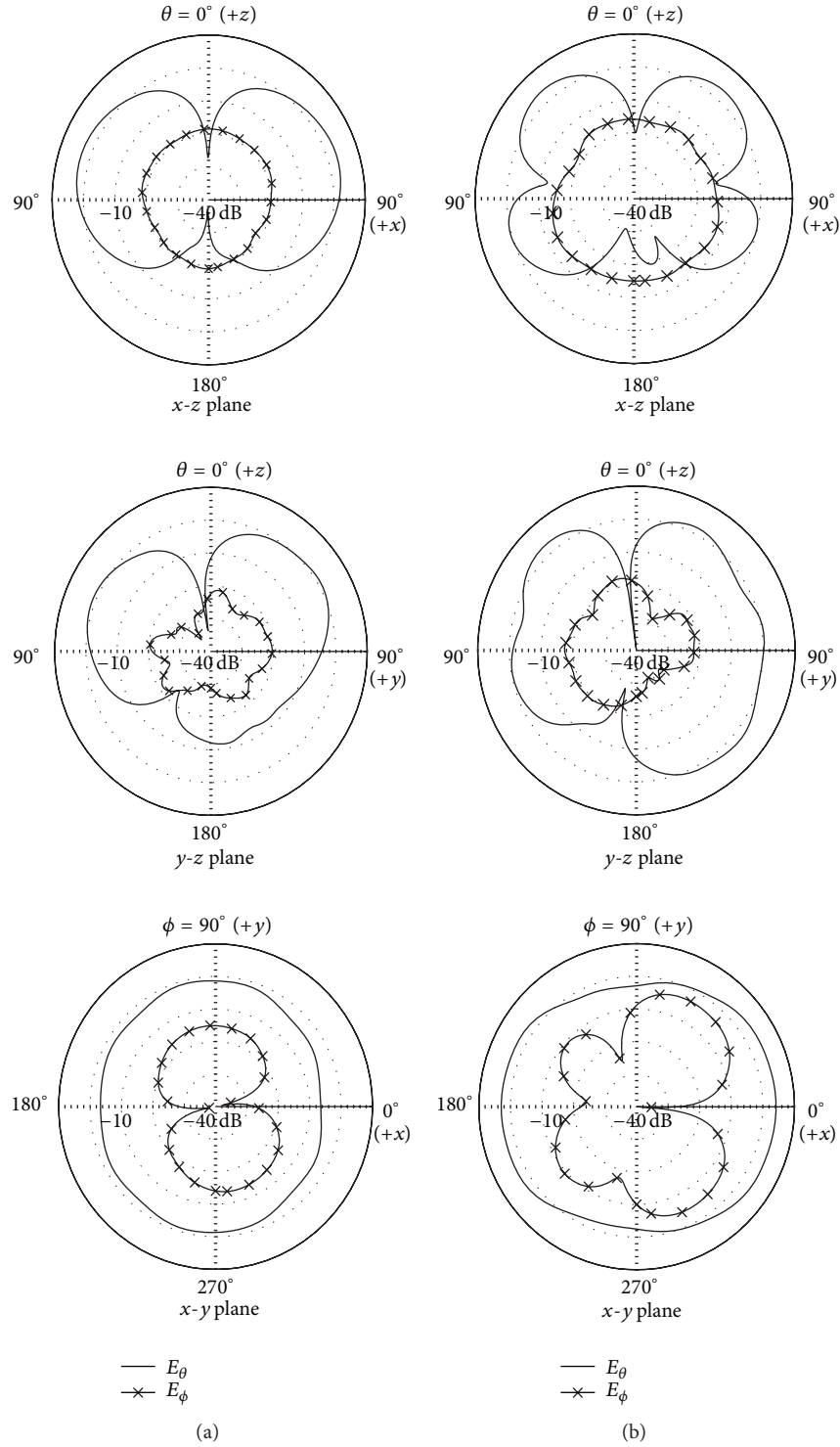
Figure 7: Simulated radiation patterns of proposed FC-PIFA obtained at (a) 2.45 and (b) 5.5 GHz.

shorting pin, as shown in Figure 5(a). The total length is about a quarter-wavelength corresponding to 2.45 GHz. In Figures 5(b) and 5(c), the main surface current widely spread on the folded-coupling region, introducing two close resonant modes in 5 GHz band. Of note, the main current path on the back radiating element at 5.8 GHz is slightly shorter than

that at 5.2 GHz, which interprets that two close but distinct resonant modes are induced owing to the folded-coupling technique.

Radiation characteristics of the proposed antenna are also studied. Figure 6 shows the measured radiation patterns at 2.45 and 5.5 GHz. Corresponding simulated radiation

FIGURE 8: Simulated and measured antenna peak gain values versus frequency at (a) 2.35–2.55 and (b) 5.1–5.9 GHz of proposed FC-PIFA.

patterns are also shown in Figure 7 for comparison. The measurements generally consist with the simulations. For both operation frequencies in th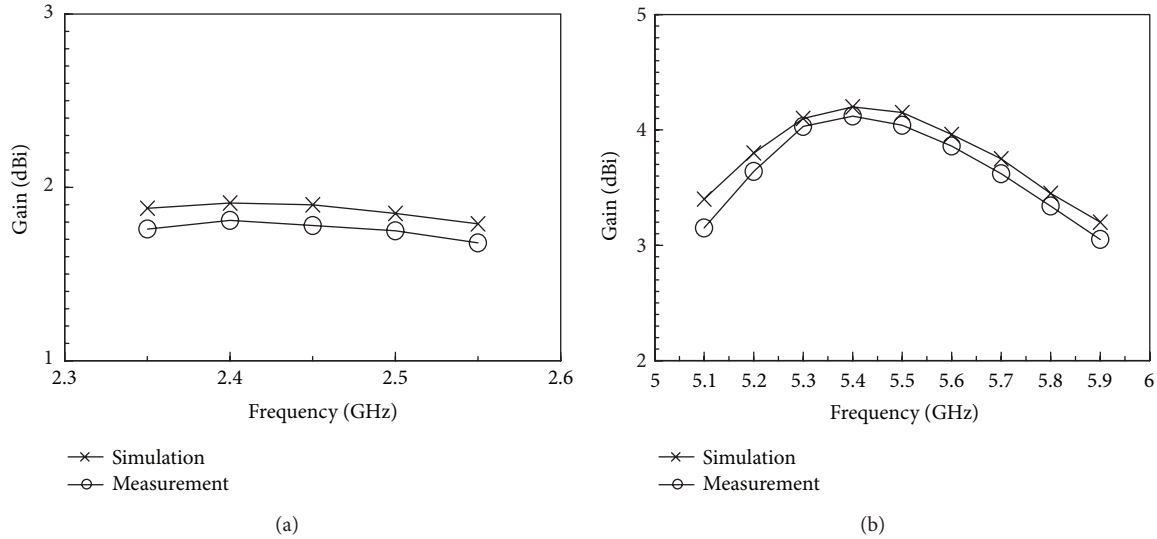e x-y plane (the azimuthal plane), the vertical component shows a relatively small variation and is close to omnidirection. This characteristic is favorable for WLAN application. Noticeably, a relatively stronger radiation in $+y$ plane can be ascribed to the shorting pin. Figure 8 shows the simulated and measured peak gain against frequency of the proposed FC-PIFA. For the lower band at 2.35–2.55 GHz, the measured gain varies in a range of 1.8-1.9 dBi. For the upper band at 5.1–5.9 GHz, the measured gain varies in a range of 3.0–4.1 dBi. The gain values within the whole operation bands are quite stable. The measured results are 0.1-0.2 dBi lower than the simulations due to the attenuation caused by the 50 Ω coaxial lines.

4. Conclusion

A dual-band FC-PIFA for WLAN communications has been successfully implemented. The prototype of the antenna has a low profile of 5 mm and occupies a small radiating area of 5 mm × 20.5 mm, which is easier to be embedded as an internal antenna in narrow space within the casing of a portable wireless device, such as a laptop or smart phone. By simply adjusting the folded-coupling region, two wide impedance bandwidths sufficient for 2.4/5 GHz bands WLAN operation can be achieved easily. Good radiating performance and stable peak gain values can also be obtained, which is beneficial for challenging wireless propagation environments.

Conflict of Interests

The authors declare that there is no conflict of interests regarding the publication of this paper.

References

[1] Y. J. Cho, Y. S. Shin, and S. O. Park, "Internal PIFA for 2.4/5 GHz WLAN applications," *Electronics Letters*, vol. 42, no. 1, pp. 8–9, 2006.

[2] C. T. Lee and K. L. Wong, "Uniplanar printed coupled-fed PIFA with a band-notching slit for WLAN/WiMAX operation in the laptop computer," *IEEE Transactions on Antennas and Propagation*, vol. 57, no. 4, pp. 1252–1258, 2009.

[3] M. Koubeissi, M. Mouhamadou, C. Decroze, D. Carsenat, and T. Monediere, "Triband compact antenna for multistandard terminals and users hand effect," *International Journal of Antennas and Propagation*, vol. 2009, Article ID 491262, 7 pages, 2009.

[4] S. Zuo, Y. Yin, Z. Zhang, and W. Wu, "A compact tri-band PIFA antenna for WLAN and WiMAX applications," *Microwave and Optical Technology Letters*, vol. 52, no. 4, pp. 919–922, 2010.

[5] C. Hu and Q. Zhu, "A compact wideband PIFA for dual-band WLAN applications," in *Proceedings of the International Conference on Microwave and Millimeter Wave Technology (ICMMT '12)*, vol. 4, pp. 1612–1615, May 2012.

[6] K. L. Wong and W. J. Chen, "Small-size microstrip-coupled printed PIFA for 2.4/5.2/5.8 GHz WLAN operation in the laptop computer," *Microwave and Optical Technology Letters*, vol. 51, no. 9, pp. 2072–2076, 2009.

[7] C. f. Tseng and Y. W. Chen, "Small PIFA for ZigBee and WLAN application," *Microwave and Optical Technology Letters*, vol. 55, no. 5, pp. 1074–1077, 2013.

Research Article

A Compact Dual-Band Printed Antenna Design for LTE Operation in Handheld Device Applications

Ding-Bing Lin,[1] Jui-Hung Chou,[2] Son-On Fu,[3] and Hsueh-Jyh Li[4]

[1] *Department of Electronic Engineering, National Taipei University of Technology, Taipei 10608, Taiwan*

[2] *Graduate Institute of Communication Engineering, National Taiwan University, Taipei 10617, Taiwan*

[3] *Graduate Institute of Computer and Communication Engineering, National Taipei University of Technology, Taipei 10608, Taiwan*

[4] *Department of Electrical Engineering and the Graduate Institute of Communication Engineering, National Taiwan University, Taipei 10617, Taiwan*

Correspondence should be addressed to Jui-Hung Chou; d98942001@ntu.edu.tw

A novel internal printed antenna suitable for triple long-term evolution (LTE) bands for handheld devices is presented. The operating bandwidths of the design are LTE700 (698~800 MHz), LTE2300 (2300~2400 MHz), and LTE2500 (2500~2690 MHz). Through the use of a C-shape broadside coupled feed structure, full operation in the lower band is achieved. The antenna itself uses two unequal path lengths to produce a low frequency band with two resonant modes. The required bandwidth is then adjusted using a couple feed, and finally placed over a ground plane via another C-type coupling element in order to enhance the two low-frequency matches. In the definition of the −6 dB reflection coefficient, the bandwidth of two basic modes in the low frequency band is 0.689~0.8 GHz. We adopt the definition of the −10 dB reflection coefficient for the high frequency mode, and its working frequency bands are shown to be 2.3~2.72 GHz. The antenna size is only $40 \times 12 \times 0.8$ mm^3 with a ground plane of 98×40 mm^2.

1. Introduction

In recent years, mobile communication requires a handheld mobile device to function on multiple communication systems which has made the multiband mobile antenna increasingly important [1–3]. In view of the growth of consumer demands for speed and bandwidth, the fourth generation of long-term evolution (LTE) mobile communication technology has been developed. However, the requirement for lower and wider frequency bands has increased the difficulty of antenna design. The bandwidth achievable from a conventional planar antenna is often insufficient. Although the use of 3D concepts is able to increase bandwidth, this approach also increases the thickness of the resulting device. In [4], a planar structure was used to design an antenna functioning in the LTE700/LTE2300/LTE2500 bands. Although the design was capable of covering whole frequency bands, it required a relatively large surface area for its implementation. In [5], a relatively smaller planar structure was used to design a multiband antenna, which also covered the frequency bands

of LTE700/LTE2300/LTE2500. However, in this case the low frequency section failed to cover the entire band; it narrowed the relative bandwidth of the planar structure covering the same area as the 3D structure. This is because a 3D structure can often use its side to widen the wire and decrease the Q value in order to increase its operational bandwidth. In [6], the use of a magnetic material substrate overcame the observed shortcomings. The magnetic permeability from the magnetic material significantly reduced the electrical length of the low frequency band. However, it simultaneously increased hysteresis loss and decreased the gain. In addition, high-quality factors resulted in an insufficient bandwidth. A multiband loop antenna was proposed in [7]. The antenna structure is relatively large, yet the design easily meets the required bandwidth. The antenna was designed by observing the structure of the antenna current density in order to widen where the density is weak to achieve a broader band.

This paper presents a miniaturized printed antenna design for a mobile communication device, which operates at frequency bands meeting the required operating bandwidths
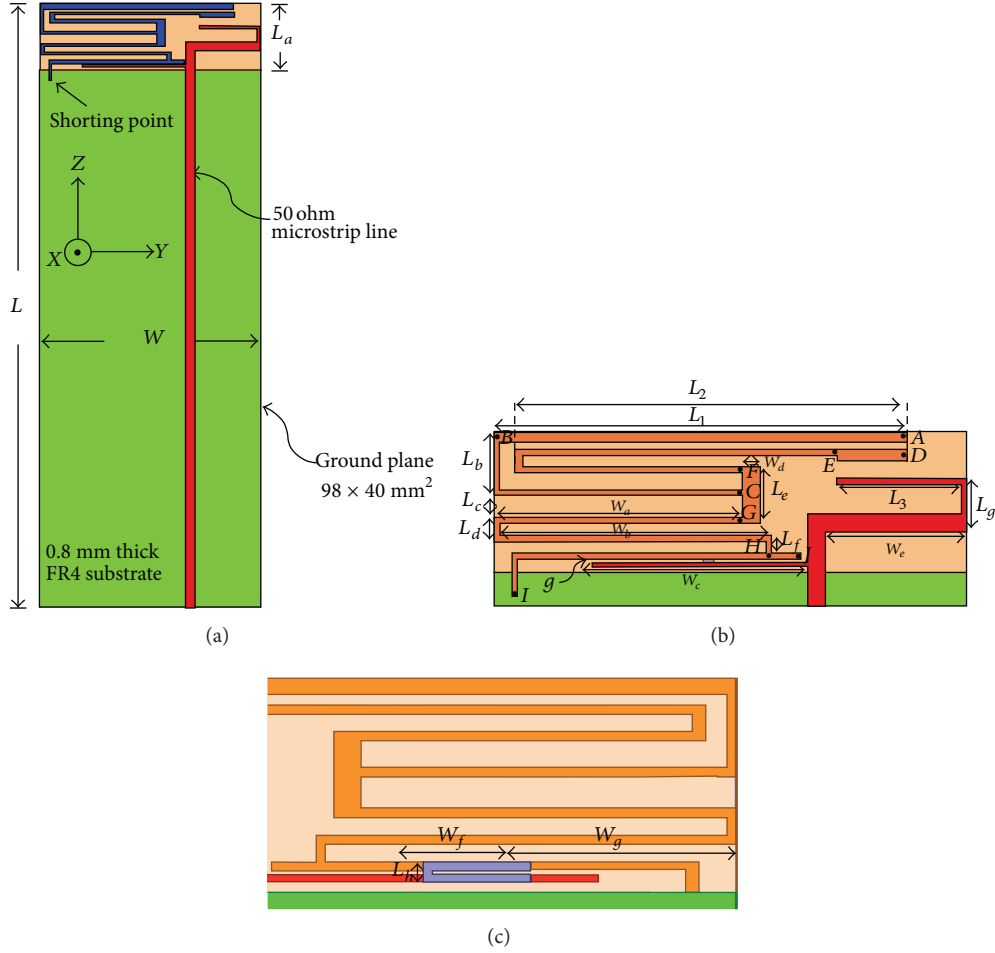
FIGURE 1: The geometry of the proposed compact printed antenna (a) with system ground, (b) top view, and (c) bottom view.

of LTE700, LTE2300, and LTE2500. The antenna design uses a base band and second harmonic in combination with different resonance paths to achieve the desired operating bandwidths. Through the use of a coupling feed and imbedding a C-shape coupler underneath, the proposed antenna achieves excellent impedance matching within the operating bands.

2. Proposed Antenna Design

The overall structure of the proposed LTE concealed multiband mobile communication antenna is shown in Figure 1. The antenna is printed on a FR4 substrate with a thickness of 0.8 mm, permittivity of 4.4, and tangent loss of 0.025. The overall size of the antenna and handheld device is $110 \times 40 \times 0.8 \, \text{mm}^3$, where the antenna size is $12 \times 40 \times 0.8 \, \text{mm}^3$ and has a ground plane of $98 \times 40 \, \text{mm}^2$. The antenna is fed by a microstrip line with a characteristic impedance of 50 ohms and width of 1.5 mm. The geometric structure and the detailed physical size of the LTE multiband mobile communication antenna design of this paper are shown in Figure 1(b).

In Figure 1(b) the top view of the antenna radiating body is shown. The antenna mainly contains two radiation paths, which are labeled (A-I) and (D-I); the two paths of resonant frequencies generate the required operating bandwidth for the LTE700 frequency band. The physical length is approximately two resonance frequencies of $1/4\lambda_g$ of the required resonant length. In Figure 1(c) the bottom view of the antenna is shown. We used a C-type coupler in the back of the antenna. The detailed dimensions of the parameters are listed in Table 1. The parameters and dimensions of the proposed antenna are achieved by using the full-wave electromagnetic simulator, which is Ansoft high frequency structure simulator (HFSS) [8]. The antenna adopts a coupling feed structure, which can increase the capacitance effects from the antenna feeding to improve the inductive effects produced by the thin metal wire. It can significantly improve input impedance of the antenna and make it easy to match the characteristic impedance of the system. However, since the design of this antenna is limited by the size, it is not suitable to use the traditional interdigital coupling feed structure to generate enough capacitance. Therefore, by imbedding a C-type coupler behind the original coupling feed we can

TABLE 1: The detailed dimension of the parameters in Figure 1.

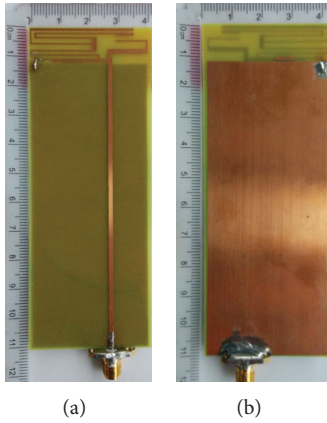| Parameter	Length (mm)	Parameter	Length (mm)	Parameter	Length (mm)
$\overline{AC}$	61.5	L	110	W	40
$\overline{DE}$	6	L_a	12	W_a	21
$\overline{EF}$	47	L_b	5.5	W_b	23.5
$\overline{GH}$	46.75	L_c	1.8	W_c	17
$\overline{HI}$	24.7	L_d	2	W_d	1.52
L_1	36	L_e	4.8	W_e	12
L_2	34	L_f	1.5	W_f	6
L_3	10.5	L_g	4.5	W_g	11.5
g	0.2	L_h	1.1		

(a)　　　　(b)

FIGURE 2: Experimental prototype of the proposed compact printed antenna (a) top view and (b) bottom view.

dramatically increase (and, in conjunction, improve) the capacitance effects of the required antenna matching. The structure of the coupling feed will be analyzed in detail in the next paragraph.

3. Results and Discussions

3.1. Resonance Mechanism of the Proposed Antenna. In order to measure the proposed antenna characteristics, we use an SMA connector with a 50 ohm characteristic impedance in the actual experiments. Its center conductor is connected to the microstrip line, and the outer ground is connected directly to the system ground plane. In Figure 2 the experimental prototype is shown, while Figure 3 shows the simulated and measured reflection coefficients. The simulated and measured antenna reflection coefficients are in agreement, albeit with a minor variation at the edge of the frequency band caused by inaccuracies in the material when actually fabricating the plates. In the low-frequency part, defined by a −6 dB reflection coefficient, the operating bandwidth can be up to 110 MHz (690~800 MHz), which contains the LTE 700 full-band operation required bandwidth. In the high-frequency part, using the −10 dB reflection coefficient definition, it can cover the entire required frequency of the LTE2300/2500 operating bands. The antenna measurement

is seen to reach a high-frequency bandwidth up to 410 MHz (2300~2710 MHz).

In order to accelerate the analysis of the antenna radiation characteristics and reduce the material waste caused by constant implementation, we used the HFSS [8] to analyze the relevant characteristics of the antenna. The antenna current distribution determined by the simulation is shown in Figure 4, which is obtained from the observation of each band in Figure 3. In the observed frequency ranges, the four resonant frequency points are 724, 774, 2320, and 2550 MHz, which correspond to the simulated current distribution as shown in Figures 4(a)~4(d). We first observed the current distribution of the two low frequencies of the resonant frequency points. In order to meet the resonance boundary condition of short to open circuit, the main resonant path is approximately a physical length of $1/4\lambda_g$ of the resonant frequency. To observe the current distribution of the first resonant frequency point in the high-frequency band, the main resonance frequency mechanism is the base frequency multiplication of the low resonant path. Therefore, by observing the current distribution we can witness the current null point generated from the resonance. To observe the current distribution of the second resonant frequency point in the high-frequency band, the main current distribution is concentrated on the right side of the conductor and the distribution is approximately $1/4\lambda_g$ of the monopole antenna.

3.2. Parametric Analysis. As mentioned above, due to a limited design space, this antenna cannot use an interdigital coupling feed to dramatically increase the capacitance effect. Therefore, a C-shape coupler was added behind the parallel-coupled feed line to increase the required capacitive effect for impedance matching and improve the matching within the antenna operational band. In Figure 5 the simulated reflection coefficient graph of the antenna embedding with and without the C-type coupler is shown. The embedded C-type coupler under the coupling feed line improves the antenna's impedance characteristics. Specifically, in the low frequency range, without the coupler, the matching condition on the conjunction of the two resonant frequency points is not satisfied; however, with the addition of the coupler, the impedance characteristics of the low frequency band are significantly improved and can easily meet the −6 dB reflection coefficient definition.
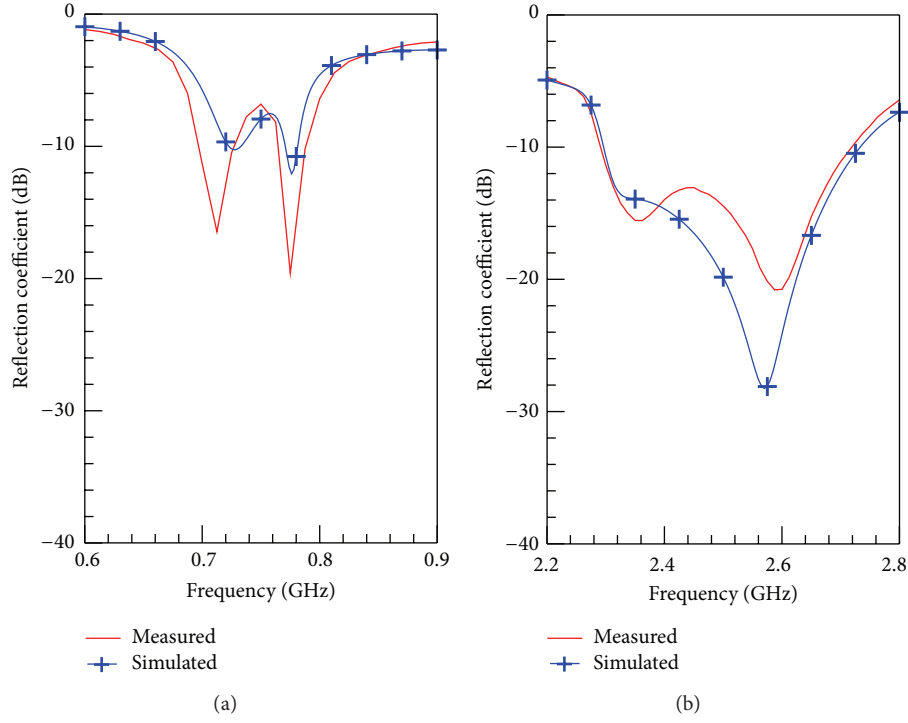
(a)

(b)

FIGURE 3: Measured and simulated reflection coefficient of the proposed miniaturized antenna versus frequency.

724 MHz

(a)

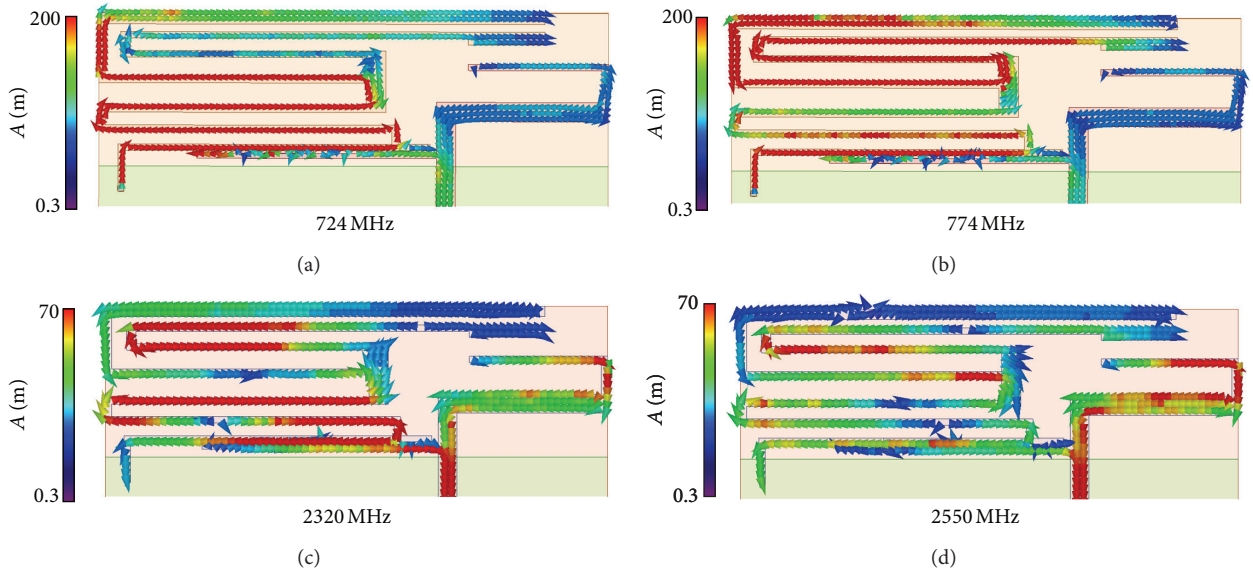
774 MHz

(b)

2320 MHz

(c)

2550 MHz

(d)

FIGURE 4: Simulated current distribution of the proposed miniaturized antenna.

The simulated reflection coefficient graph for the proposed antenna design when varying the parameter L_1 is shown in **Figure 6**. Since this path mainly generates the first resonant frequency (724 MHz) of the required physical length of the resonator, we can observe a change in the resonant frequency points by changing the length L_1. Appropriate adjustment of this length can satisfy the low frequency band (698 MHz) within the LTE700 operation band. In this

paper, the optimal length for L_1 was 36 mm. The simulated reflection coefficient graph when varying parameter L_2 is shown in **Figure 7**. The simulation result shows that when L_2 is changed, the second resonant frequency point of the low frequency band is changed. Therefore, appropriate control of the length L_2 can make the second resonant frequency point of the low frequency cover the high frequency points of the LTE700 operating bandwidth. In this paper, the optimal

(a)

(b)
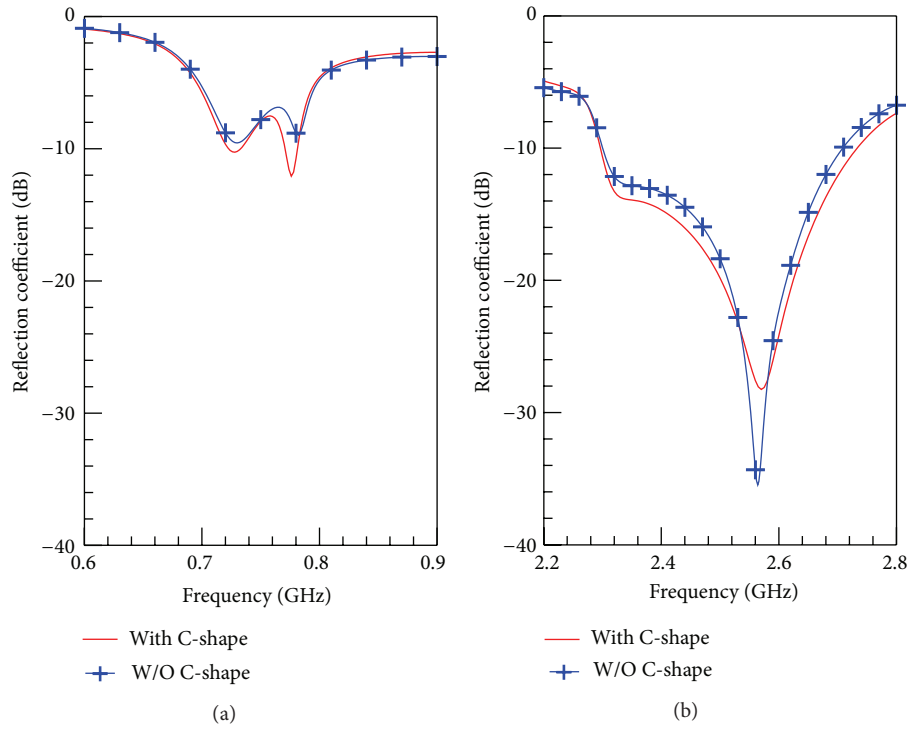
FIGURE 5: Simulated reflection coefficient of the proposed antenna with and without the C-shape coupler.

(a)

(b)

FIGURE 6: Simulated reflection coefficient of the proposed antenna as the function of L_1.

(a)

(b)

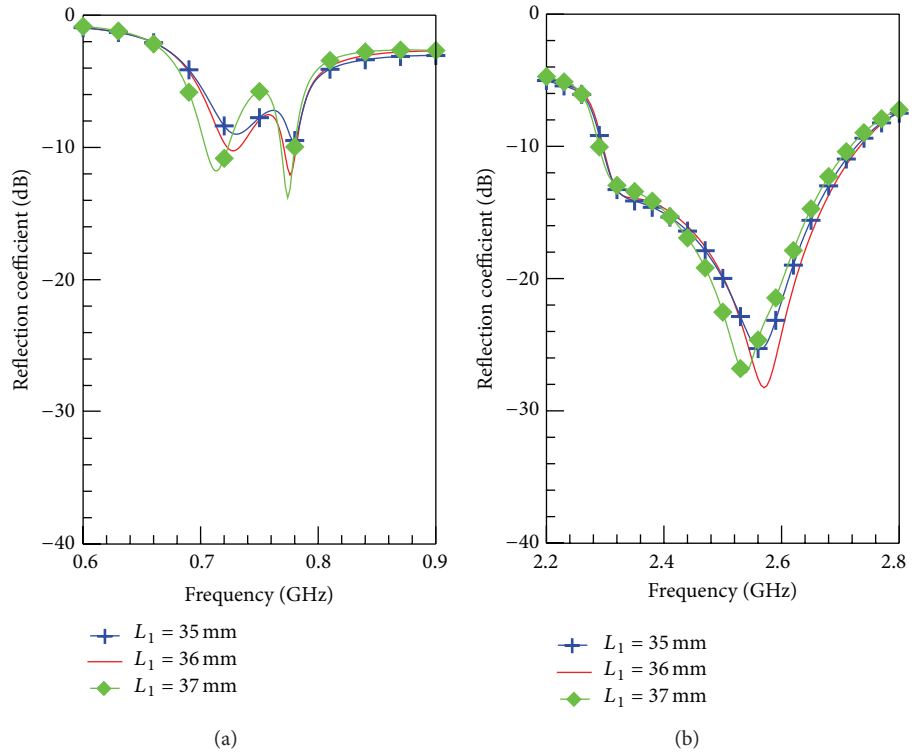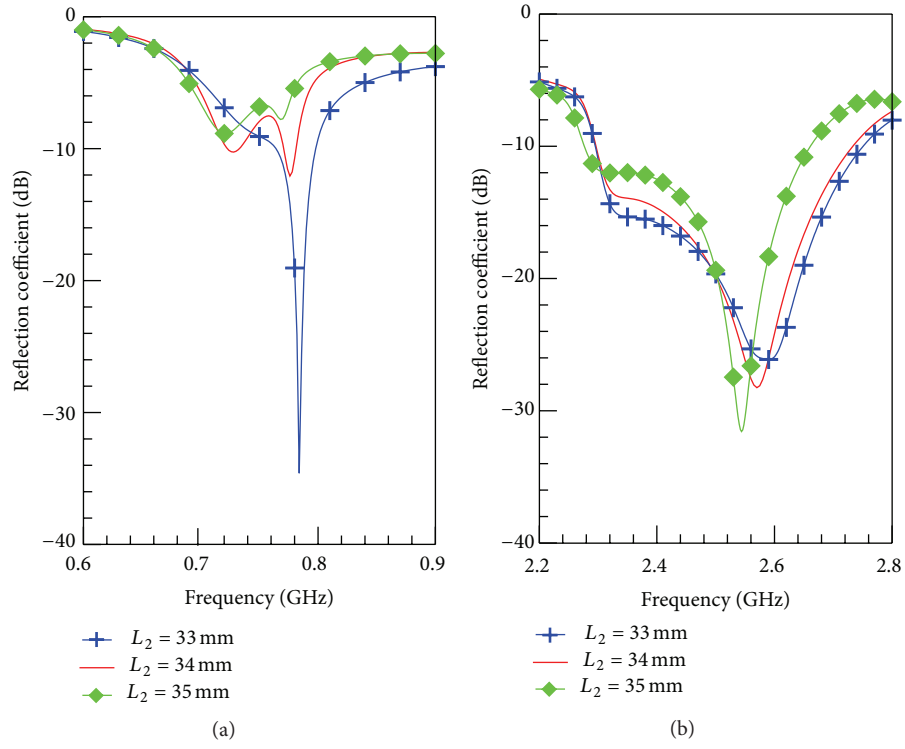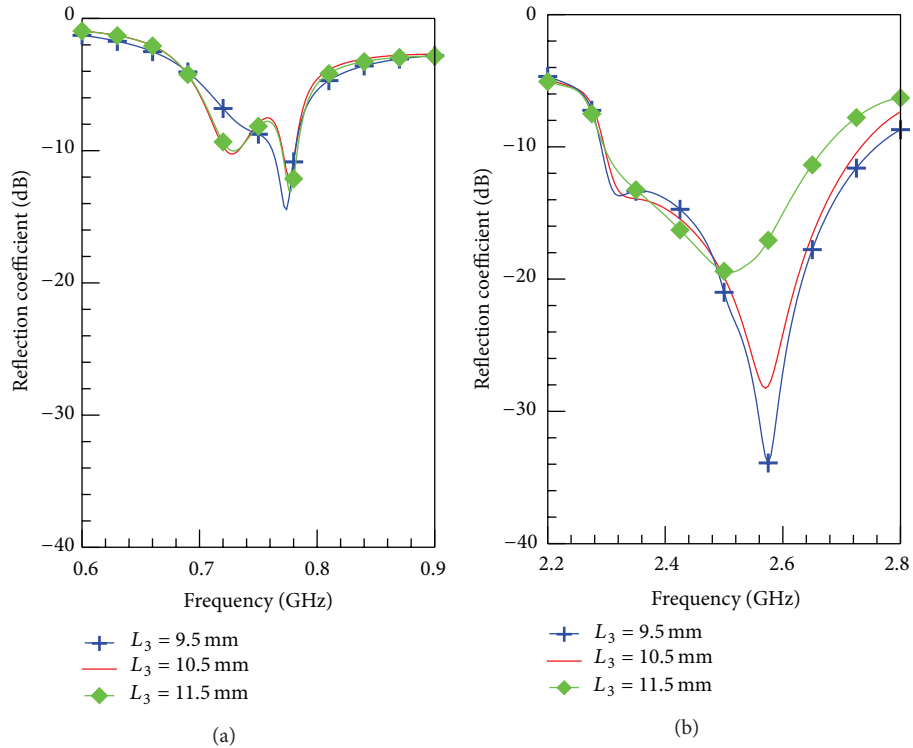FIGURE 7: Simulated reflection coefficient of the proposed antenna as the function of L_2.

(a)

(b)

FIGURE 8: Simulated reflection coefficient of the proposed antenna as the function of L_3.

X-Y plane

X-Z plane
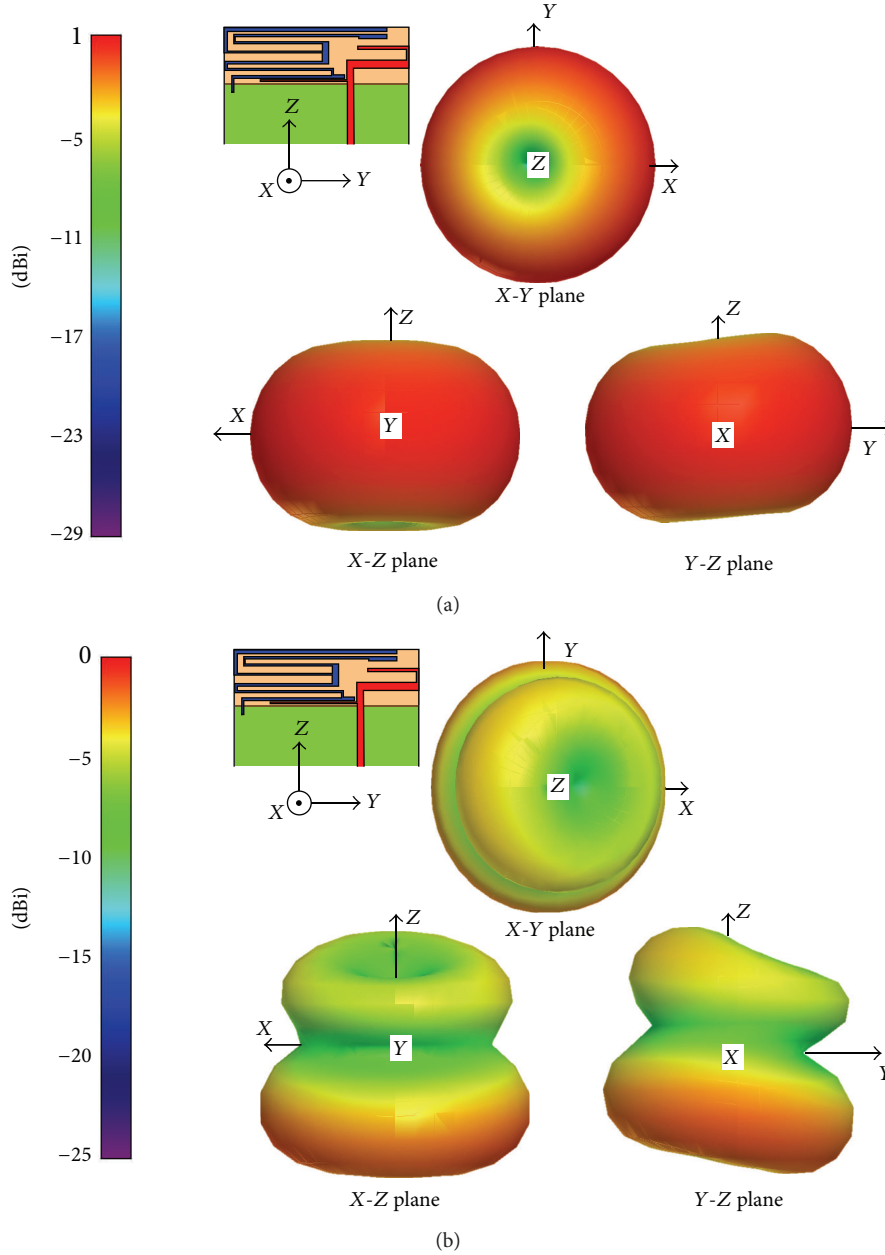
Y-Z plane

(a)

X-Y plane

X-Z plane

Y-Z plane

(b)

FIGURE 9: Simulated three-dimensional radiation pattern at (a) 750 MHz and (b) 2500 MHz.

length for L_2 was 34 mm. Appropriate control of the two parameters L_1 and L_2 ensures that low-frequency operation fully covers the bandwidth required for LTE700 operation. Through the embedding of the C-type coupler to improve the impedance matching at the junction, the two resonant frequencies can meet the full bandwidth operation requirement. In addition, because the high frequency operation of this antenna is the harmonic of the low-frequency resonant path, proper control of these two parameters can also make the high frequency cover the bandwidth required for LTE2300 operation.

The simulated reflection coefficient when varying the parameter L_3 is shown in **Figure 8**. The second harmonic for

the high frequency operation is a monopole antenna with a $1/4\lambda_g$ wavelength. We observe that as the length is changed, the resonant frequency varies. Therefore, appropriate control of the parameter can make the antenna operation fully cover the bandwidth required for LTE2500 operation. In the present work we design the antenna by adjusting the three parameters mentioned above, which can completely cover the range of the three LTE frequency bands.

3.3. Radiation Characteristics. The simulated and measured 3D radiation pattern of the proposed antenna design at low and high frequency is shown in Figures 9 and 10, respectively. The pattern in three different cuts is similar between the
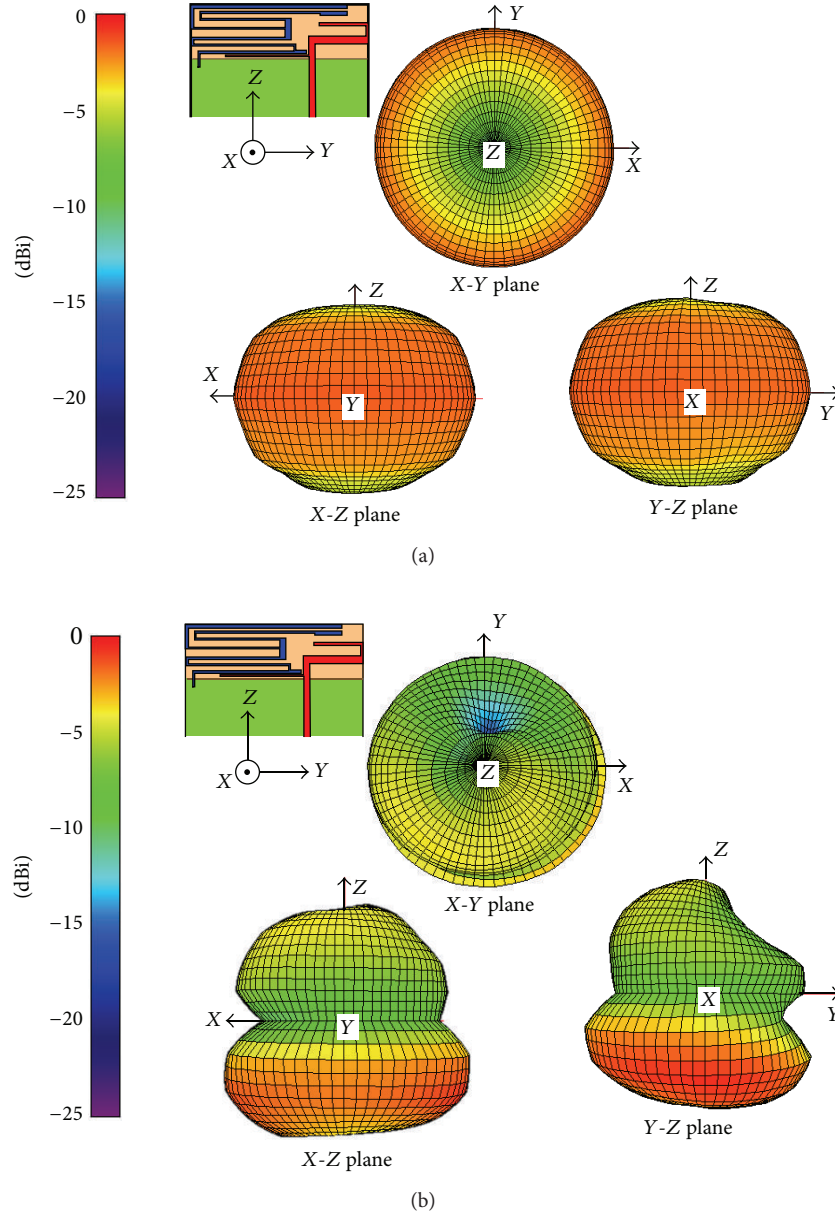
FIGURE 10: Measured three-dimensional radiation pattern at (a) 750 MHz and (b) 2500 MHz.

simulated and measured results. In Figure 10(a) the measured 3D radiation pattern of the antenna at a central frequency of 750 MHz is shown. A nearly omnidirectional radiation pattern is observed in the X-Y plane. The characteristic of the radiation is ideal for handheld devices. The 3D radiation pattern of the designed antenna measured at 2500 MHz is shown in Figure 10(b). Since the resonance mechanism at higher bands is a higher order mode, a null point could be observed at a higher frequency band. However, the radiation pattern remains in the horizontal section (X-Y) with an omnidirectional radiation pattern, which is also conducive to handheld devices for wireless communication reception.

The measured antenna gain and efficiencies at low and high frequency are shown in Figures 11(a) and 11(b),

respectively. In the former, the antenna gain variation is from -0.05 dBi to -2.8 dBi and the variation of the antenna efficiency ranges from 36.5% to 50.5%. Since this antenna is a miniaturized antenna when operating in the low frequency band, the radiation efficiency is relatively unaffected by the limitation of the miniaturized design. However, in comparison to the reference design, the antenna presented here still meets LTE700 operational requirements with respect to gain and radiation when operating at low frequency. From Figure 11(b), the gain variation at the high frequency band is seen to vary from 3.4 to 2.1 dBi while the antenna efficiency concurrently varies from 76.3% to 67.1%. We can see that the proposed design is capable of stabilizing the antenna gain and efficiency.
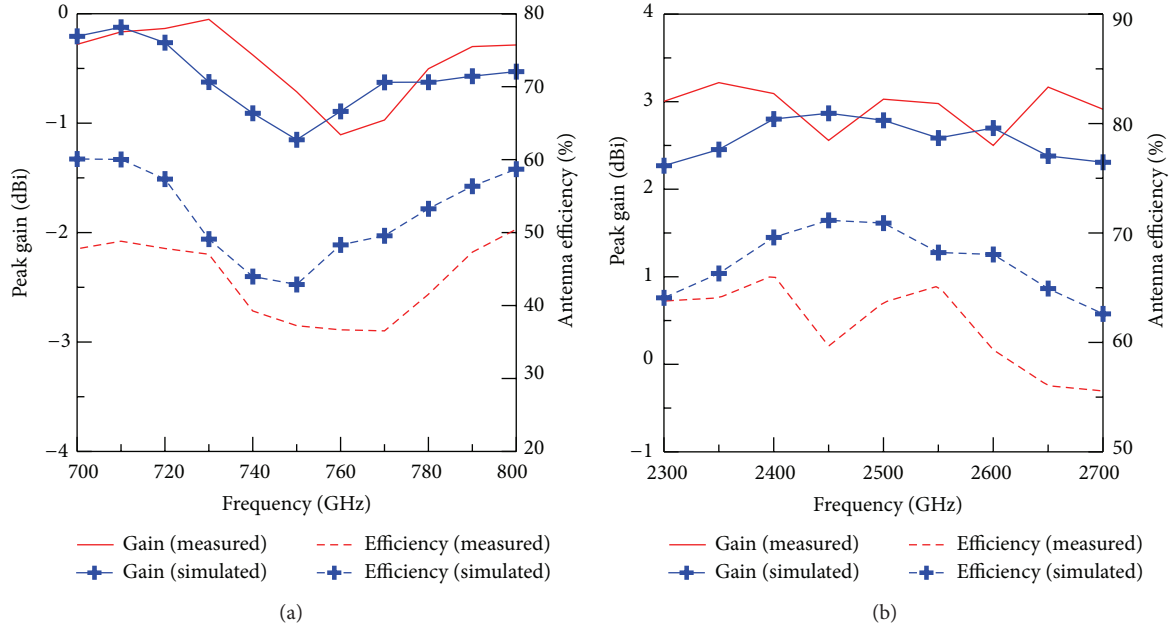
FIGURE 11: Measured and simulated antenna gain and antenna efficiency $\eta_a = \eta_{rad} \cdot (1 - |S_{11}|^2)$ of the proposed antenna versus frequency at (a) lower and (b) higher bands.

4. Conclusion

This paper proposes a multiband LTE antenna design for internal mobile device use. Since the antenna adopts a printed design, the actual production is cost effective and easily integrates with mobile systems. The antenna defined by the −6 dB reflection coefficient at low frequency can resonate within a bandwidth of 110 MHz (689∼800 MHz). At high frequency under the −10 dB reflection coefficient definition the antenna is capable of reaching a 410 MHz (2.3∼2.71 GHz) operational bandwidth. The antenna at low frequency utilizes two adjacent resonant frequencies to create a wider band and successfully uses a C-type coupling element to enhance impedance matching. Therefore, this antenna design can completely cover the required operational bandwidths of LTE700, LTE2300, and LTE2500. Our experimental results have shown that the antenna possesses favorable radiation characteristics irrespective of operation at low and high frequency bands.

Conflict of Interests

The authors declare that there is no conflict of interests regarding the publication of this paper.

References

[1] C.-W. Yang, Y.-B. Jung, and C. W. Jung, "Octaband internal antenna for 4G mobile handset," *IEEE Antennas and Wireless Propagation Letters*, vol. 10, pp. 817–819, 2011.

[2] M. S. Ahmad, C. Y. Kim, and J. G. Park, "Multishorting pins PIFA design for multiband communications," *International Journal of Antennas and Propagation*, vol. 2014, Article ID 403871, 10 pages, 2014.

[3] P. Li, J. Pan, D. Yang, and P. Nie, "A novel dual-shorting point PIFA (GSM850 to IMT-A) for mobile handsets," *International Journal of Antennas and Propagation*, vol. 2013, Article ID 436808, 7 pages, 2013.

[4] L. Lizzi and A. Massa, "Dual-band printed fractal monopole antenna for LTE applications," *IEEE Antennas and Wireless Propagation Letters*, vol. 10, pp. 760–763, 2011.

[5] K.-L. Wong, C.-A. Lyu, and L.-C. Chou, "Small-size multiband planar antenna for LTE700/2300/2500 operation in the tablet computer," *Microwave and Optical Technology Letters*, vol. 54, no. 1, pp. 81–86, 2012.

[6] J. Lee, Y.-K. Hong, S. Bae, G. S. Abo, W.-M. Seong, and G.-H. Kim, "Miniature long-term evolution (LTE) MIMO ferrite antenna," *IEEE Antennas and Wireless Propagation Letters*, vol. 10, pp. 603–606, 2011.

[7] K.-L. Wong and Y.-W. Chang, "Internal WWAN/LTE handset antenna integrated with USB connector," *Microwave and Optical Technology Letters*, vol. 54, no. 5, pp. 1154–1159, 2012.

[8] *Ansoft High Frequency Structure Simulator (HFSS), Version 12. 0*, Ansoft, 2009.

Research Article

A Rectangular Planar Spiral Antenna for GIS Partial Discharge Detection

Xiaoxing Zhang,[1] Yefei Han,[1] Wei Li,[2] and Xuetao Duan[2]

[1] State Key Laboratory of Power Transmission Equipment & System Security and New Technology, Chongqing University, Chongqing 400044, China
[2] Xinjiang Electric Power Research Institute, High-Tech Industrial Development Zone, Urumqi 830000, China

Correspondence should be addressed to Xiaoxing Zhang; xiaoxing.zhang@outlook.com

A rectangular planar spiral antenna sensor was designed for detecting the partial discharge in gas insulation substations (GIS). It can expediently receive electromagnetic waves leaked from basin-type insulators and can effectively suppress low frequency electromagnetic interference from the surrounding environment. Certain effective techniques such as rectangular spiral structure, bow-tie loading, and back cavity structure optimization during the antenna design process can miniaturize antenna size and optimize voltage standing wave ratio (VSWR) characteristics. Model calculation and experimental data measured in the laboratory show that the antenna possesses a good radiating performance and a multiband property when working in the ultrahigh frequency (UHF) band. A comparative study between characteristics of the designed antenna and the existing quasi-TEM horn antenna was made. Based on the GIS defect simulation equipment in the laboratory, partial discharge signals were detected by the designed antenna, the available quasi-TEM horn antenna, and the microstrip patch antenna, and the measurement results were compared.

1. Introduction

Partial discharge signal has been widely studied as an important indicator for characterizing the merits of GIS insulation performance [1]. Electrical monitoring methods include the pulse current method and the UHF method. The UHF method detects high frequency electromagnetic signals (300 MHz–3 GHz) excited by partial discharge in the airspace. Numerous interfering signals can be effectively avoided. The UHF method is suitable for online monitoring for its high frequency, wide bandwidth, and high sensitivity. Through UHF signals, not only can the presence of defects in GIS be detected, but the occurrence and severity of the insulation fault can also be determined [2].

Currently, the antenna sensor of GIS partial discharge monitoring is mainly divided into two types, namely, the built-in sensor and the external sensor [3]. The built-in sensor is placed internally in the GIS and it must be considered during the design of GIS equipment to reduce its additional effect on the internal electric field. Its advantages are high sensitivity, very good detection results, and strong anti-interference ability [4, 5]. The external sensor is mainly used in GIS equipment that has been put into operation and has no built-in sensors. It is installed on the basin insulator and is able to test the insulation condition of GIS through collecting leakage electromagnetic waves from partial discharge. The advantage is easy installation and maintenance and the electric field inside the device remains unaffected [6–8]. To carry out the UHF detection method smoothly, the designed antenna should meet the development trend of miniaturization and broadband, taking into account the bandwidth and gain of the sensor. Thus, the antenna will receive more partial discharge signals. A new type of planar helical antenna sensor for detecting the UHF of GIS partial discharge was developed in our lab. The designed antenna has a small volume and wide frequency band. Through simulation and experimental analysis for its parameter, the designed antenna can effectively detect UHF signal and satisfy the requirement of GIS online monitoring.
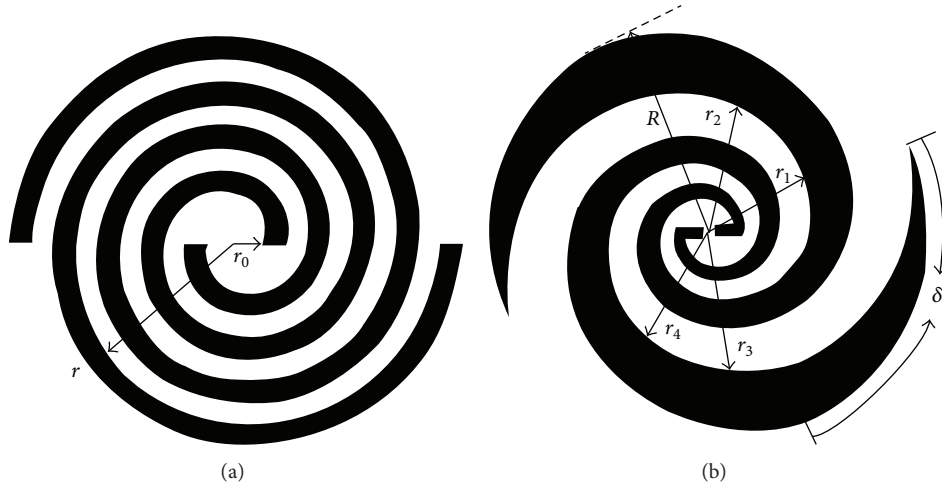
(a)   (b)

Figure 1: Planar spiral antenna.

2. The Basic Form of the Helical Antenna

The helical antenna is made of metal with good electrical conductivity and has a spiral shape [9]. It has the advantage of circular polarization and broad beam width; thus, it is widely used in satellite communications and personal mobile communications [10, 11]. Helical antennas can be divided into three-dimensional helical antennas and plane helical antennas according to their structure. The basic form of the planar helical antenna consists of an Archimedes helical antenna and an equiangular helical antenna. The radius of the Archimedean helical antenna increases as the angle increases. Its curve equation is

$$r = r_0 + a\phi, \tag{1}$$

where r_0 is the initial radius, a is the spiral growth, and φ is the angle in radians.

A double-arm Archimedean helical antenna [12, 13] is shown in Figure 1(a). The antenna generally uses the balance feed at the center of the spiral surface, and the main radiation area is focused on the average circumference of a wavelength band, also known as the effective radiative zone. When the frequency changes, the effective radiative zone changes as well, but the radiation pattern basically remains unchanged. Moreover, when the effective radiative zone for the antenna is at the outermost region, its frequency is at the lowest operating frequency of the antenna. For the circular spiral surface, the perimeter is $C = \pi \times D = \lambda_{\max}$, such that the outer diameter of the antennas is the following:

$$D = \frac{\lambda_{\max}}{\pi}. \tag{2}$$

Since the planar Archimedean helical antenna was proposed in the 1950s, due to its features such as broadband, circular polarization, and low profile, it has received an increasing amount of attention and application.

The equation of the planar equiangular helical antenna is as follows:

$$r = r_0 e^{a(\phi - \phi_0)}, \tag{3}$$

where φ_0 is the initial radius, a is the spiral growth, and r_0 is the radius vector corresponding to φ_0. A planar equiangular helical antenna [14] is shown in Figure 1(b).

3. Characteristics of the Rectangular Plan Spiral Antenna

3.1. Antenna Structure

(a) Design of Rectangular Spiral. The rectangular spiral structure is a variation of the Archimedes spiral structure. It has the same advantages as the Archimedes spiral structure. Furthermore, it has a more simple structure and higher space utilization. Therefore, the designed helical antenna in this paper uses a planar rectangular spiral structure. A rectangular spiral structure effectively reduces antenna size and weight. It also facilitates manufacturing.

(b) Reflecting Cavity and Shielding. Planar spiral antennas have the characteristics of wide bandwidth, small volume, wide main lobe circular polarization, and normal two-way radiation. However, antennas require unidirectional radiation. Therefore, the overall structure of the antenna designed in this paper is the semienclosed planar spiral antenna. The antenna surface, except for the receiving surface, is shielded by a metal shield cavity. A reflecting cavity is also added. Furthermore, the antenna should be filled with wave absorption material to ensure wide bandwidth.

(c) Bow-Tie Vibrator Loading. To increase the bandwidth, the terminal of the spiral selects the bow-tie vibrator loading (Figure 2) to reduce the transmission loss of the spiral periphery. The bow-tie antenna is a low-profile structure planar antenna. It has the advantages of being lightweight and easy to install [15]. The performance of the antenna is determined by two main factors: opening angle θ_0 and arm length l (Figure 3). The larger the opening angle is, the wider the frequency band of operation is. However, the lateral dimension of the antenna will increase if the opening
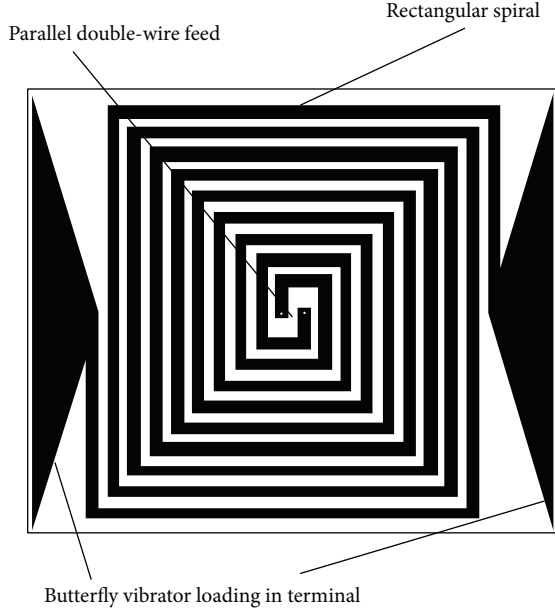
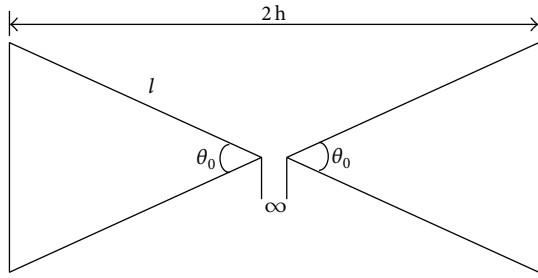Figure 2: The structure of the planar spiral antenna.

Figure 3: The structure of the bow-tie antenna.

angle is too large. Miniaturization of the antenna cannot be guaranteed. The arm length of the antenna metal vibrator is an important parameter for determining the low-end frequencies of the input impedance bandwidth of the antenna. The longer the arm l, the better the low-frequency covering performance of the antenna. The work of the antenna signal is a Gaussian pulse radiation for their fidelity waveform. Thus, the radiation waveform fidelity will be higher for antennas whose working signal is a Gaussian pulse. According to the empirical formula, bow-tie antenna arm length and the corresponding wavelength under low frequency satisfy the following relationship:

$$l = \frac{\lambda}{4}\left(1 - \frac{97.82}{Z_c}\right), \tag{4}$$

where λ is the corresponding wavelength under the low-end frequency of the antenna input impedance bandwidth and Z_c is the characteristic impedance of the antenna, which is given as follows:

$$Z_c = 120\ln\left(\text{ctg}\left(\frac{\theta_0}{4}\right)\right). \tag{5}$$
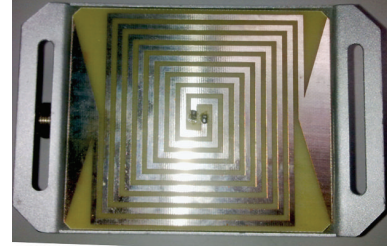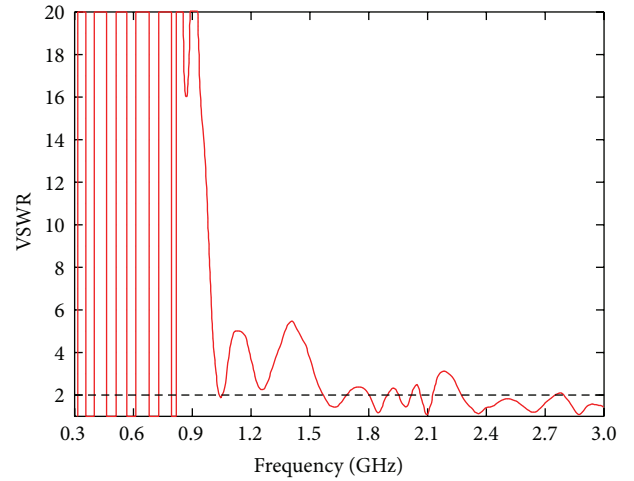

Figure 4: Physical map of the designed antenna.

Figure 5: VSWR with a frequency between 300 MHz and 3 GHz.

The bow-tie antenna and the equiangular spiral antenna are both wideband antennas. Wideband antenna can achieve broadband impedance matching and reduce transmission loss after taking loading mode, thereby improving the radiation characteristics of the antenna.

Figure 4 shows a physical map of the rectangular spiral antenna designed in this paper. The size of the antenna is $132 \times 85 \times 50$ mm and its weight is 278 g.

3.2. Antenna VSWR. VSWR is the reciprocal of the traveling wave coefficients. Its value is from 1 to infinity. VSWR is widely used in engineering to indicate the degree of impedance mismatch between antenna impedance and transmission line impedance. The VSWR ratio simulation results of the designed antenna are shown in Figure 5. The figure shows that VSWR is less than 2 within 1.6 GHz–2.1 GHz and 2.3 GHz–3.0 GHz, with a wide frequency range.

In many cases, the antenna impedance is unknown but the VSWR can be measured. Thus, the mold of the reflection coefficient can be calculated using VSWR. The measured VSWR is shown in Figure 6. Figure 6 shows that the VSWR is better within 1.15 GHz–1.55 GHz, 1.9 GHz–2.7 GHz, and 2.85 GHz–3 GHz, whereas the VSWR is poor below 1 GHz. The simulation results of VSWR are basically consistent with the measurements.
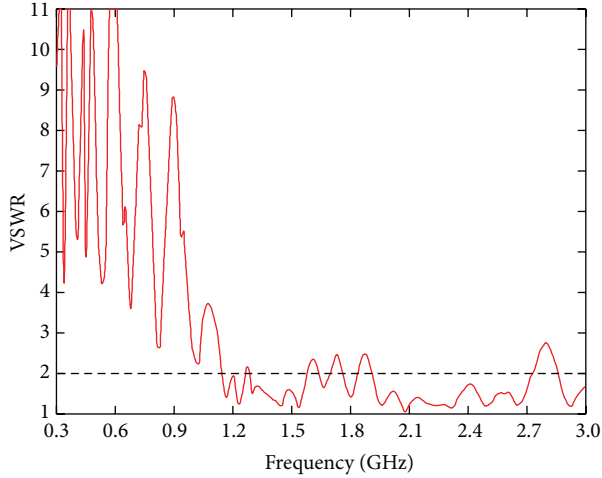
FIGURE 6: Measured VSWR of the designed antenna.

TABLE 1: Measured gain of the designed antenna.

Frequency (MHz)	300	500	800	1000	1500	2000	3000
Gain (dB)	−36	−23	−9	2.5	4.5	5.5	11.7

TABLE 2: The value of the designed antenna pattern.

Frequency (MHz)	Main lobe width (dB)	Beamwidth 3 dB (deg)	Side-lobe level (dB)
500	−24.5		
1000	2.9	105.8	−4.5
1500	4.6	101.7	−9.0
2000	6.7	89.9	−8.2
2500	7.7	78.1	−14.6
3000	8.5	74.1	−17.9

3.3. Gain of the Antenna.

The measured results of the antenna gain are shown in Table 1. As the frequency increases, the antenna gain increases. The antenna gain achieves 11.7 dB when the frequency is 3000 MHz.

3.4. Antenna Patterns.

The helical antenna has characteristics of axial rotational symmetry. Thus, only the circularly polarized antenna pattern on the horizontal direction from 500 MHz to 3 GHz was tested. The designed antenna patterns under several specific frequencies are shown in Figure 7. The corresponding parameters are shown in Table 2. The main lobe width is the angle between two radius vectors in the main lobe when the antenna radiation power is half of maximum value. It is used to indicate the concentration degree of antenna power radiation. The smaller the main lobe width and the sharper the antenna pattern, the more concentrated the antenna radiation. Figure 9 and Table 2 show that the gain of the antenna exhibits a rising trend as the frequency increases. Furthermore, the antenna achieves a good directional radiation characteristic in the full-band.

TABLE 3: Measured gain of the quasi-TEM horn antenna.

Frequency (MHz)	500	800	1000	1500	2000	3000
Gain (dB)	−12.6	−1.4	1.3	3.2	5.1	3.8

4. Comparative Study of Rectangular Plane Spiral Antenna

4.1. Comparative Study of Antenna Characteristics.

External sensors which have been used to detect GIS partial discharge in our laboratory have two types: the quasi-TEM horn antenna [16] and the microstrip patch antenna [17]. Structure of the quasihorn antenna is shown in Figure 8; its size is 129 mm × 90 mm × 60 mm and its weight is 920 g. The size of the rectangular spiral antenna is about 4/5 of the quasi-TEM horn antenna and 1/3 of its weight. The physical map of the microstrip patch antenna is shown in Figure 9; its size is 261 × 142 × 112 mm and its weight is 1040 g. The rectangular spiral antenna size is much smaller than the microstrip patch antenna. Its size is only 1/7 of the microstrip patch antenna and its weight is only 1/4 of that. In brief, the rectangular spiral antenna is much smaller and lighter, thus facilitating the installation.

The rectangular spiral antenna has almost the same size as the quasi-TEM horn antenna, so the paper mainly makes a comparative analysis for some characteristics of these two antennas. The measured VSWR of a quasi-horn antenna is shown in Figure 10. Figure 10 shows that the quasihorn antenna has an ideal VSWR within 820 MHz–930 MHz, 1.25 GHz–1.65 GHz, 2.15 GHz–2.3 GHz, and 2.85 GHz–3 GHz. It is obvious that the rectangular spiral antenna has a wider frequency band compared to the quasi-TEM horn antenna. Table 3 shows the measured gain of the quasi-TEM horn antenna. Compared to Table 3 and Table 1, gain of the rectangular spiral antenna is overall better than the quasi-TEM horn antenna above 1 GHz, whereas the gain is worse below 800 MHz. The microstrip patch antenna band is 340 MHz–440 MHz and the measured maximum gain is 5.38 dB. Its frequency band range and maximum gain values are all inferior to the rectangular spiral antenna.

4.2. Comparative Study of Partial Discharge Measurements.

To verify the measurement results of the designed antenna, a needle-plate electrode was used to simulate metal protrusion defects of GIS and partial discharge tests were carried out. Figures 8 and 11 show the experimental circuit of partial discharge in the lab. The designed antenna was used to collect partial discharge signals. Then the measured results are compared with the signals collected using a quasi-TEM horn antenna and a microstrip patch antenna. A high-speed digital oscilloscope (Tektronix Oscilloscope 7104: bandwidth is 1 GHz, the maximum sampling rate is 20 GS/s, and memory depth is 48 M) was used to record waveforms.

When the needle-plate electrode is added to 9 kV, the partial discharge signals are received from the rectangular spiral antenna and the quasi-TEM horn antenna simultaneously, as Figure 12 shows. The red waveform was measured using the rectangular spiral antenna with a maximum amplitude of

(a) f = 500 MHz

(b) f = 1000 MHz

(c) f = 1500 MHz

(d) f = 2000 MHz

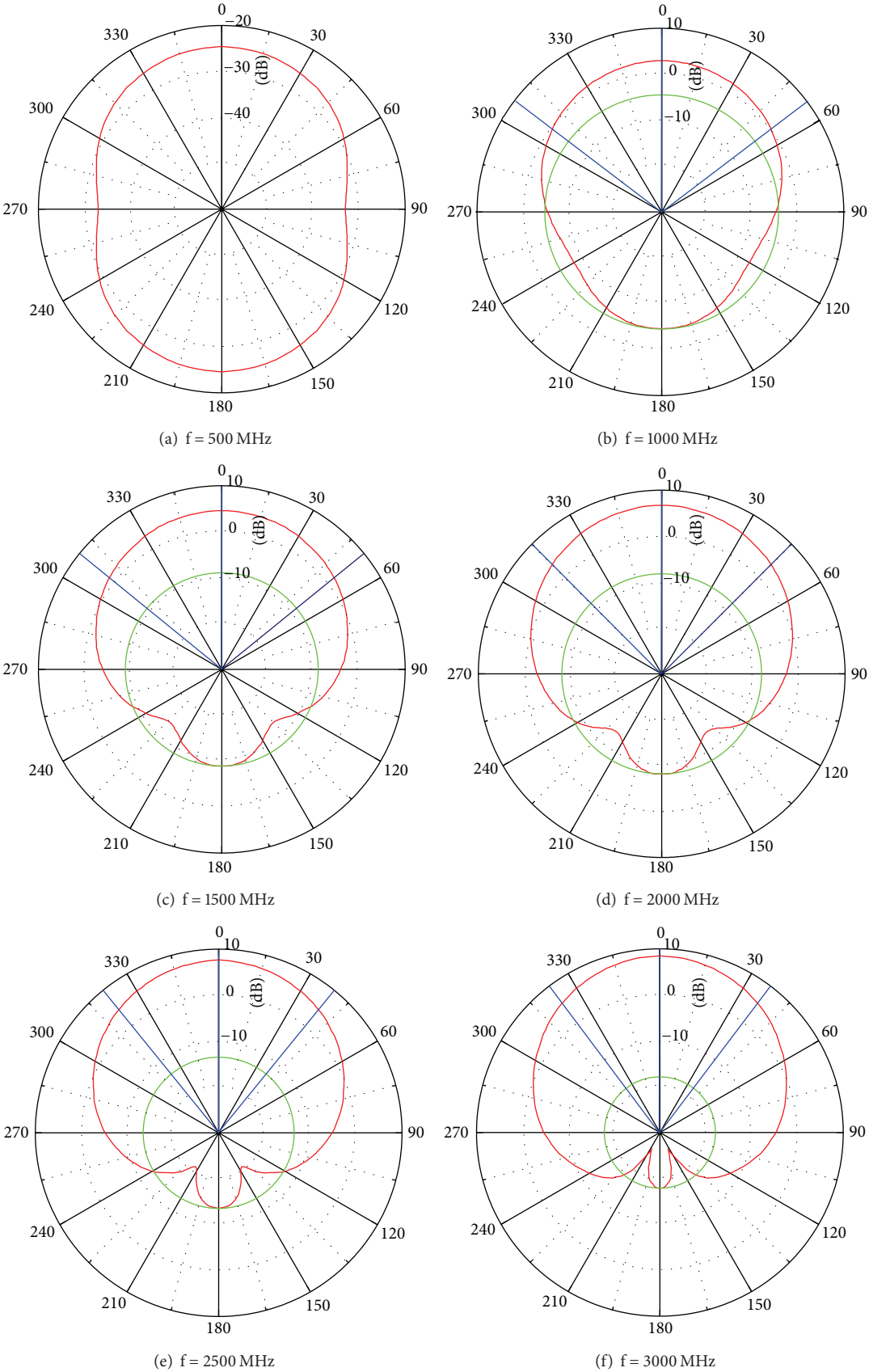(e) f = 2500 MHz

(f) f = 3000 MHz

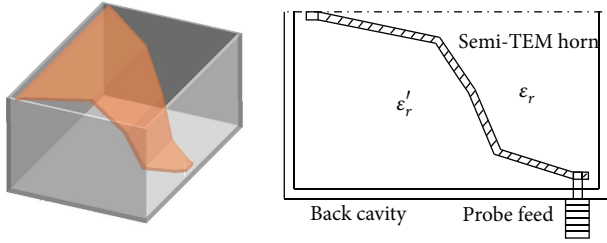FIGURE 7: The designed antenna pattern.

FIGURE 8: Structure of the quasi-TEM horn antenna.
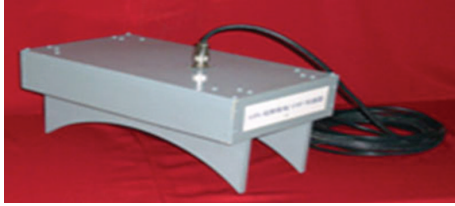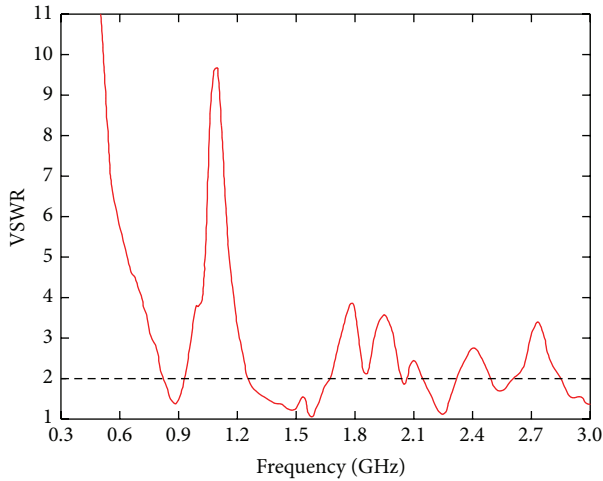

FIGURE 9: Physical map of the microstrip patch antenna.

FIGURE 10: Measured VSWR of the quasi-TEM horn antenna.

FIGURE 11: Experimental circuit of partial discharge.
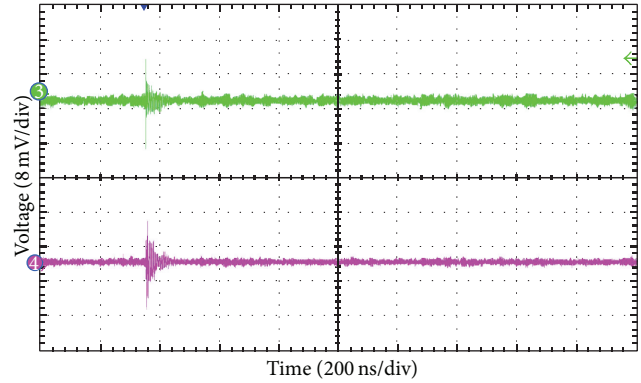
FIGURE 12: UHF signals measured by the rectangular spiral antenna and a quasi-TEM horn antenna.
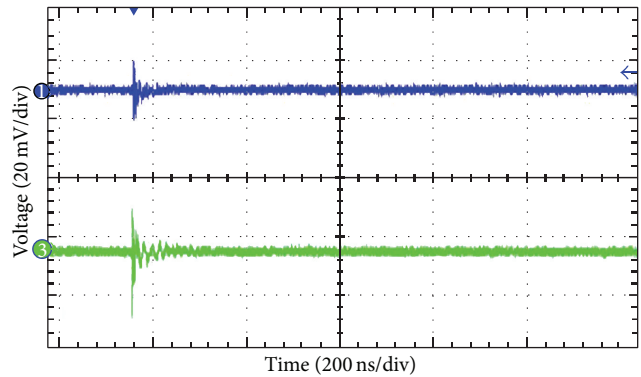
FIGURE 13: UHF signals measured by the rectangular spiral antenna and a microstrip patch antenna.

10.2 mV. The green waveform was measured using a quasi-TEM horn antenna with a maximum amplitude of 10.6 mV. Figure 13 shows the partial discharge signals received from the rectangular spiral antenna and the microstrip patch antenna simultaneously. The yellow waveform was measured using the rectangular spiral antenna with a maximum amplitude of 10 mV. The red waveform was measured using a microstrip patch antenna with a maximum amplitude of 19 mV.

The rectangular spiral antenna is capable of receiving more UHF band energy for its wider band. Thus, it has less catadioptric electromagnetic energy. In this case, the measured signal decreases rapidly and the signal amplitude should also be larger. However, the gain of the designed antenna below 1 GHz is worse than the quasi-TEM horn antenna and the microstrip antenna due to its smaller volume. As a result, the received UHF signal amplitude is relatively low. But it can satisfy the UHF signal detection requirements completely. Moreover, the designed antenna has a wider range frequency band and a bigger gain above 1 GHz. If the oscilloscope does not have a bandwidth limit of 1 GHz and can collect signals above 1 GHz, the designed antenna will collect a higher signal amplitude compared to the quasi-TEM horn and the microstrip patch antenna.

5. Conclusions

The radiation characteristics of the rectangular spiral antenna through simulation and experimental analysis were tested. Furthermore, it was compared with the quasi-TEM horn

antenna and the microstrip patch antenna in the laboratory. The following conclusions were obtained.

(a) The rectangular spiral antenna is smaller and lighter, which facilities installation and fulfills the miniaturization trends of antennas.

(b) The gain of the designed antenna exhibits a rising trend as the frequency increases in the UHF band. The designed antenna can receive a wider band range of partial discharge signals above 1 GHz. The measured bandwidth is 1.15 GHz–1.55 GHz, 1.9 GHz–2.7 GHz, and 2.85 GHz–3 GHz. Furthermore, the designed antenna achieves a good oriented reception performance.

(c) The data show that the gain of the designed antenna is slightly inferior to the quasi-TEM horn antenna and the microstrip patch antenna under 1 GHz. However, the designed antenna has better broadband. It has a wider frequency band range and a bigger gain above 1 GHz and is capable of detecting the UHF signal generated by partial discharge better.

Conflict of Interests

The authors declare that there is no conflict of interests regarding the publication of this paper.

Acknowledgments

References

[1] G. Bazannery, "Recent developments in insulation monitoring systems of GISs," *International Electric Power for China*, vol. 6, no. 4, pp. 41–43, 2002.

[2] J. Tang, W. Zhu, and C.-X. Sun, "Analysis of UHF method used in partial discharge detection in GIS," *High Voltage Engineering*, vol. 29, no. 12, pp. 22–23, 2003.

[3] C.-X. Sun, G.-F. Xu, and J. Tang, "Model and performance of inner sensors used for partial discharge detection in GIS," *Proceedings of the Csee*, vol. 24, no. 8, pp. 89–94, 2004.

[4] D.-S. Kim, C.-M. Hwang, Y.-N. Kim et al., "Development of an intelligent spacer built into the internal-type UHF partial discharge sensor," in *Proceedings of the IEEE International Symposium on Electrical Insulation (ISEI '08)*, pp. 396–399, Vancouver, Canada, June 2008.

[5] J. Tang, H.-J. Shi, and C.-X. Sun, "Study of UHF frequency response characteristics of the inner sensor for partial discharge detection in GIS," *Transactions of China Electrotechnical Society*, vol. 19, no. 5, pp. 71–75, 2004.

[6] R. Kurrer and K. Feser, "The application of ultra-high-frequency partial discharge measurements to gas-insulated substations," *IEEE Transactions on Power Delivery*, vol. 13, no. 3, pp. 777–782, 1998.

[7] X.-X. Zhang, W.-T. Liu, and X.-H. Yang, "A Hilbert fractal antenna and portable monitoring system for partial discharge detection in gas insulated substations," *Journal of Chongqing University*, vol. 32, no. 3, pp. 263–268, 2009.

[8] C.-P. Kao, J. Li, R. Liu, and Y. Cai, "Design and analysis of UWB TEM horn antenna for ground penetrating radar applications," in *Proceedings of the IEEE International Geoscience and Remote Sensing Symposium (IGARSS '08)*, vol. 4, pp. IV569–IV572, Boston, Mass, USA, July 2008.

[9] Q.-L. Li and G.-B. Xu, "Miniature design of ultra-wideband spiral antenna," *Journal of Telemetry, Tracking and Command*, vol. 32, no. 2, pp. 14–19, 2011.

[10] X.-Q. Yan and L.-F. Qi, "Study on deforming of planar spiral antenna," *Tactical Missile Technology*, no. 4, pp. 29–31, 2005.

[11] N.-K. Jing, H.-L. Zhao, and L. Huang, "Miniaturization of broadband spiral antenna," *Modern Electronics Technique*, vol. 34, no. 17, pp. 82–84, 89, 2011.

[12] J. Kaiser, "The Archimedean two-wire spiral antenna," *IRE Transactions on Antennas and Propagation*, vol. 8, no. 3, pp. 312–323, 1960.

[13] B. A. Kramer, M. Lee, C.-C. Chen, and J. L. Volakis, "Design and performance of an ultrawide-band ceramic-loaded slot spiral," *IEEE Transactions on Antennas and Propagation*, vol. 53, no. 7, pp. 2193–2199, 2005.

[14] H. Nakano, K. Kikkawa, and J. Yamauchi, "A low-profile equiangular spiral antenna backed by a cavity with an absorbing strip," in *Proceedings of the 1st European Conference on Antennas and Propagation (EuCAP '06)*, pp. 1–5, Nice, France, November 2006.

[15] J.-B. Wu, M. Tain, and T.-Q. Li, "Improvement of bow-tie antenna for ground penetrating radar," *Chinese Journal of Scientific Instrument*, vol. 30, no. 5, pp. 1059–1062, 2009.

[16] X.-X. Zhang, Y. Chen, J.-Z. Tang, and X.-S. Wen, "Minitype quasi-TEM horn antenna for partial discharge detection in GIS," *High Voltage Engineering*, vol. 37, no. 8, pp. 1975–1981, 2011.

[17] X.-X. Zhang, J. Tang, and W.-X. Peng, "Study on the outer UHF microstrip patch antenna for partial discharge detection in GIS," *Chinese Journal of Scientific Instrument*, vol. 27, no. 12, pp. 1595–1599, 2006.

Research Article

Dual-Band Compact Planar Antenna for a Low-Cost WLAN USB Dongle

Maurício Henrique Costa Dias,[1] **Bruno Roberto Franciscatto,**[2]
Hans Adel,[3] **and Tan-Phu Vuong**[2]

[1] *Military Institute of Engineering, 22290-270 Rio de Janeiro, RJ, Brazil*
[2] *Grenoble Institute of Technology, 38000 Grenoble, France*
[3] *Fraunhofer Institute for Integrated Circuits, 90411 Nuremberg, Germany*

Correspondence should be addressed to Maurício Henrique Costa Dias; mhcdias@ime.eb.br

Among the present technologies for WLAN devices, USB dongles still play a noticeable role. One major design challenge regards the antenna, which unavoidably has to comply with a very small volume available and sometimes should also allow multiband operation. In this scope, the present work discusses a dual-band WiFi compact planar IFA-based antenna design for a low-cost USB dongle application. Like most of the related published solutions, the methodology for deriving the present proposition was assisted by the use of an antenna analysis software. A prototype was assembled and tested in order to qualify the radiator design. Practical operation conditions were considered in the tests, such as the influence of the dongle case and the effect of the notebook itself. The results complied with the design constraints, presenting an impedance match quite stable regardless of the stick position alongside a laptop base.

1. Introduction

USB sticks or dongles represent a low-cost and simple way to provide network access to older desktops and notebooks or to computers with broken WiFi card. In the scope of wireless LAN device technology development, they still draw some attention, especially regarding the radiator design. The typical aesthetic constraints force the device to be small. Therefore, compact antenna design techniques are unavoidable.

Many different approaches have been reported so far, mainly along the past decade. As a general basis for this kind of device, practical radiator designs only consider the availability of a small percentage of the dongle volume, since most of it must be reserved for the electronic circuitry. The constraints vary among the different solutions proposed, sometimes allowing the use of the available space more effectively. 3D meandered shaped radiators or multilayered printed circuit board (PCB) fit well in such cases; see, for instance, [1, 2]. On the other hand, low-cost designs call for

the use of single-layered PCB, restraining the antenna to be at most "2.5D" shaped, with vias or other short connections between the front and the back planes [3]. Sometimes, not even a back metal plane is present, leaving no choice for the antenna but to be planar.

WiFi dongles may be either single or dual-banded. The 2.4–2.48 and 5.15–5.85 GHz ISM bands cover such networks, with slight variations on the precise frequency limits from region to region [4]. The most recent issues of the WiFi standard include the possibility of MIMO system operation, and such feature is quite an active research field in the present scope [5–8]. There are also some attempts to derive multiband antennas for USB dongles to allow not only WiFi operation but also the access to other systems as well, such as LTE band 13 (0.746–0.787 GHz) [8], GSM (0.88–0.96 GHz) [9], UMTS (1.92–2.17 GHz) [8–10], WiBro (2.3–2.39 GHz) [8–13], LTE/WiMax (2.5–2.7 GHz) [7, 9–12], S-DMB (2.605–2.655 GHz) [9–12, 14], or WiMax (3.4–3.6 GHz) [15].
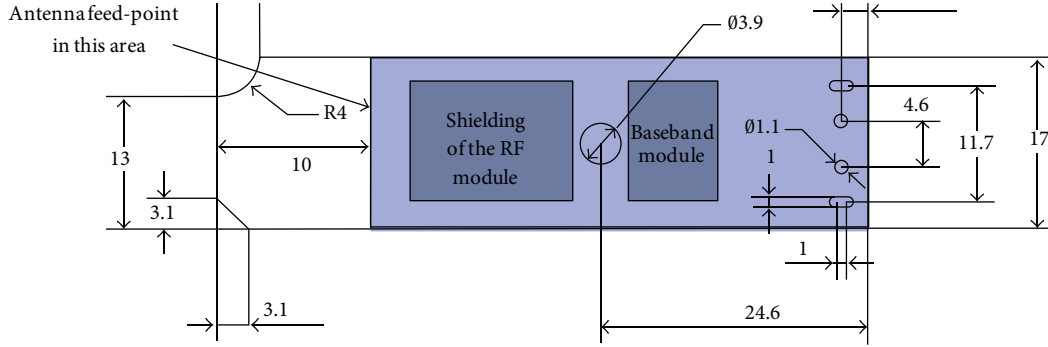
FIGURE 1: PCB layout sketch of the WLAN USB dongle (dimensions in mm).

The design of compact antennas benefits from the presence of relatively large ground planes, which ease the constraints on what is usually considered as the radiator itself [16–18]. Yet, when microstrip technology is chosen, the ground plane is expected to be in the back of the PCB. Indeed, most of the known low-cost WiFi dongle radiator configurations rely on the use of a single-layered PCB with metal on both sides.

In the present scope, this work discusses an IFA-based antenna configuration for a dual-band WLAN USB dongle application. Only a single metal plane PCB was available, thus posing above-the-average constraints to the radiator design. Furthermore, the influences of the dongle case and of the laptop in which the dongle is expected to be plugged in during operation were both considered. As in virtually all related works, the antenna design was numerically assisted by the use of an electromagnetic field simulator. Prototypes were assembled and tested according to the simulated scenarios, measuring performance parameters such as S_{11}, radiation efficiency, and power patterns. It is worth mentioning that such antenna was preliminarily assessed in [19], though under a less thorough approach. Relevant gaps left there regarding both the simulation and experimental validation stages are now more properly addressed.

Section 2 addresses the antenna design, highlighting the imposed constraints and the followed method. Simulation results are presented in Section 3, in which the dongle is analyzed both alone and plugged in a typical laptop. Section 4 discusses the experimental validation of the proposed radiator, in terms of both impedance adaptation and radiation performance. Section 5 concludes the paper.

2. Antenna Design

2.1. Imposed Constraints. Figure 1 illustrates the layout constraints of the USB dongle. The PCB area available was smaller than $17 \times 60 \, \text{mm}^2$, from which only the upper $17 \times 10 \, \text{mm}^2$ side was left for the radiator. Fabrication cost reduction was a priority, in such a way that only one metal layer was made available for both the antenna and all the due electronics, as stated in the introduction. No changes whatsoever were allowed in the area below the space reserved for the radiator. Briefly, the antenna had to be integrated to the PCB using the

same single plane and sharing the ground with the electronic circuitry.

The imposed single plane PCB also restrained the antenna choice to a small set of planar configurations. PIFAs and other "2.5D" layouts were thus out of scope.

In this antenna design, the dongle case had to be made of a low-cost injected plastic structure available. However, the electric properties of that material in the WLAN frequency bands were not known beforehand, thus posing an additional issue.

The USB dongle was supposed to operate in both WLAN ISM bands: 2.4-2.5 GHz and 5.15–5.85 GHz. It was also expected that the impedance adaptation for a 50-Ω load should provide a reflection coefficient S_{11} no higher than −10 dB within the specified bands, though the −6 dB limit was acceptable, bearing in mind the natural performance limitations of compact antennas [16–18].

This relative flexibility on the S_{11} performance was allowed also due to the variety of scenarios in which the USB stick was supposed to operate, mainly regarding the laptop influence. Typically, any notebook has many USB ports spread along the keyboard panel sides or at its back, as illustrated in Figure 2. Furthermore, the screen is expected to form an angle around 90° to 120° with the keyboard, and such layout may also affect the antenna performance, particularly when the radiator is small, as was the case.

2.2. Methodology. As in most of the other related works, the restricted geometrical specifications imposed led to a numerically assisted design methodology. The suitable electromagnetic field simulator available for this work was Empire XCcel, from IMST [20]. The whole process carried out may be described as follows.

First, taking into account the PCB layout provided in Figure 1, a few basic planar single-band radiator configurations were chosen, based on the available knowledge on compact antennas. In this work, meander line and IFA layouts were tested, simulating such structures directly on the PCB layout provided, with the aid of the field analysis software. Then, a fine tuning of these configurations to the lower frequency band (2.45 GHz) was carried out, from which the IFA-based one presented the best performance, and, for that,
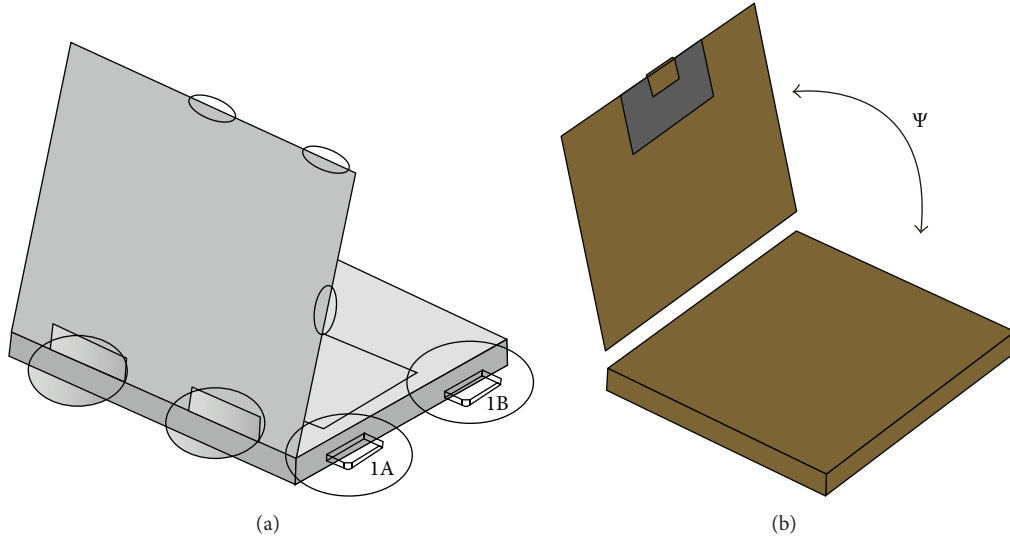
FIGURE 2: Operation of a WLAN dongle on a laptop and features that potentially affect the antenna performance: (a) USB ports positions and (b) screen-to-base angle (Ψ).
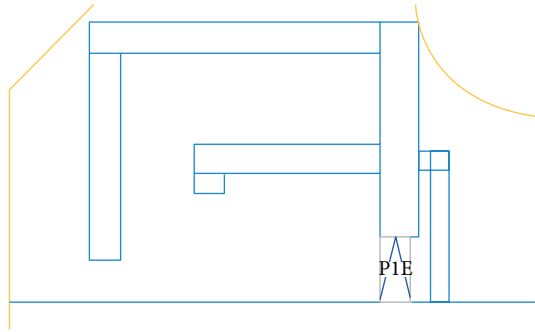

FIGURE 3: Sketch of the radiator configuration proposed as a compact planar dual-band solution (feed gap marked as P1E).

FIGURE 4: S_{11} simulated results of the proposed antenna, when the USB dongle is analyzed alone.

it was selected for prototyping and a preliminary round of measurements.

The need for such initial set of tests was due to the absence of accurate information on the dongle case electrical properties. Therefore, an experimental procedure was set to estimate the resulting frequency shift due to the casing material that would wrap around the PCB. Basically, S_{11} measurements of the prototype PCB without and with the casing material were performed, from which a 5.4% downshift (around 130 MHz) was observed in the operating frequency (resonance or near resonance frequency) of the PCB + case set.

The next step in the design process was the inclusion of another resonance in the upper 5.5 GHz band, while also taking into account the expected frequency shift imposed by the dongle case. It is important to remark that, since no accurate values of the casing material permittivity were available, it was not directly considered in the supporting simulations. What has been done instead was to rescale the antenna to resonate around 5.4% above the WLAN central frequencies to compensate the lack of the dongle case in the

simulation models. Therefore, in this stage of the process, the antenna should be designed to resonate close to 2.58 GHz at the lower band and 5.8 GHz at the upper band.

Since the upper WLAN band was more than an octave above the lower band, a feasible solution could be achieved by the insertion of a second smaller IFA in the same available space, followed by parametrical-based tuning [16–18]. The fine-tuned layout that presented the best performance is sketched in Figure 3. This proposed configuration has a higher frequency branch inserted in the lower frequency IFA (the largest segment) sharing a common return to ground, as well as the feed port. As it can be seen, both the largest and the shortest segments are actually not "F" shaped, since both had to be round bent at their ends in order to make the whole set fit to the restricted available area. It is also worth mentioning that, from what could be observed during the

FIGURE 5: Simulated 3D radiation pattern of the proposed antenna, when the USB dongle is analyzed alone, at 2.56 GHz.

FIGURE 7: Simulated current density distribution of the proposed antenna, when the USB dongle is analyzed alone, at 2.56 GHz.
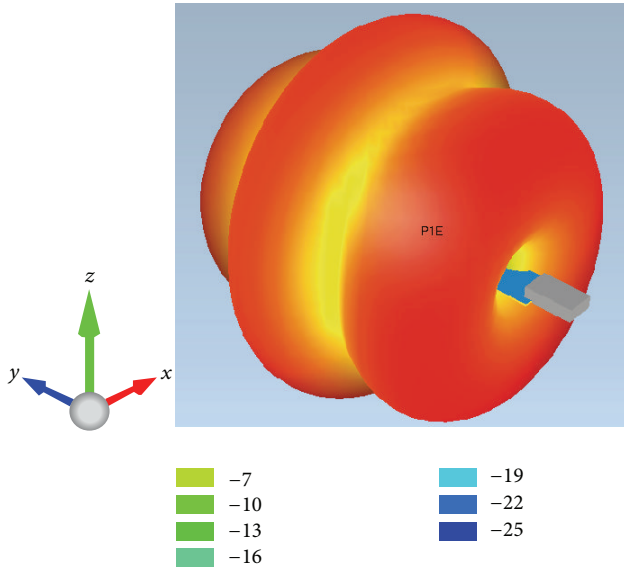
FIGURE 6: Simulated 3D radiation pattern of the proposed antenna, when the USB dongle is analyzed alone, at 5.72 GHz.
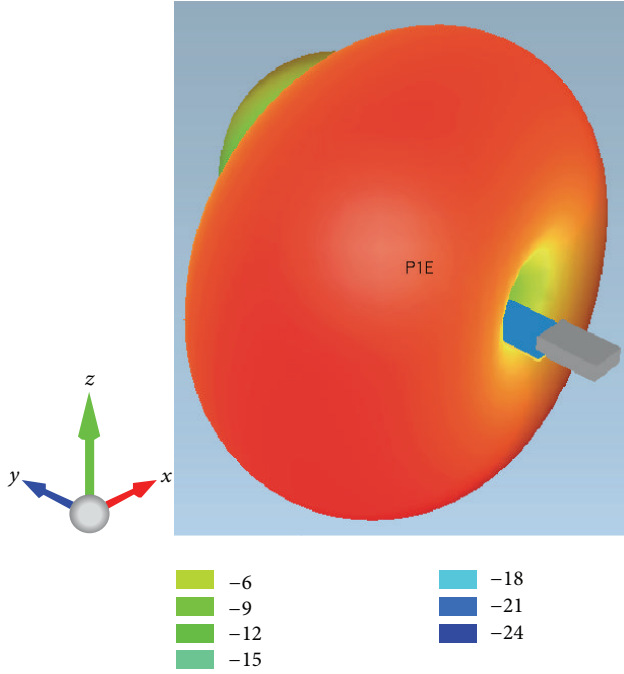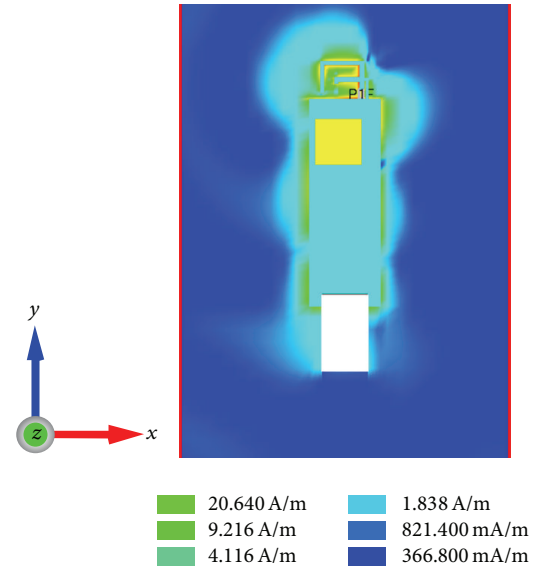

FIGURE 8: Simulated current density distribution of the proposed antenna, when the USB dongle is analyzed alone, at 5.72 GHz.

tuning simulations, the parameters that affected most critically the S_{11} performance were the feed gap width and the total length of each branch.

The radiator configuration in Figure 3 was actually achieved after another set of tuning simulations needed in order to evaluate the effect of the laptop on the antenna performance. At this level, the simulations took into account the four relative USB ports indicated in Figure 2, with the laptop screen angle $\Psi = 90°$. The basic parameter observed

to guide this final tuning round was S_{11}, since typically there is not much that can be done regarding the pattern of compact antennas [16–18]. Anyway, the radiation pattern behavior should be observed, with and without the influence of the laptop, in order to see how omnidirectional the dongle can be.

Finally, the simulated layout that provided the best overall performance was picked for prototyping and qualification tests. These trials should include S_{11} measurements of the antenna impedance in a number of situations, particularly with the dongle plugged in different USB ports of a typical laptop, with its screen opened, as illustrated in Figure 2. With
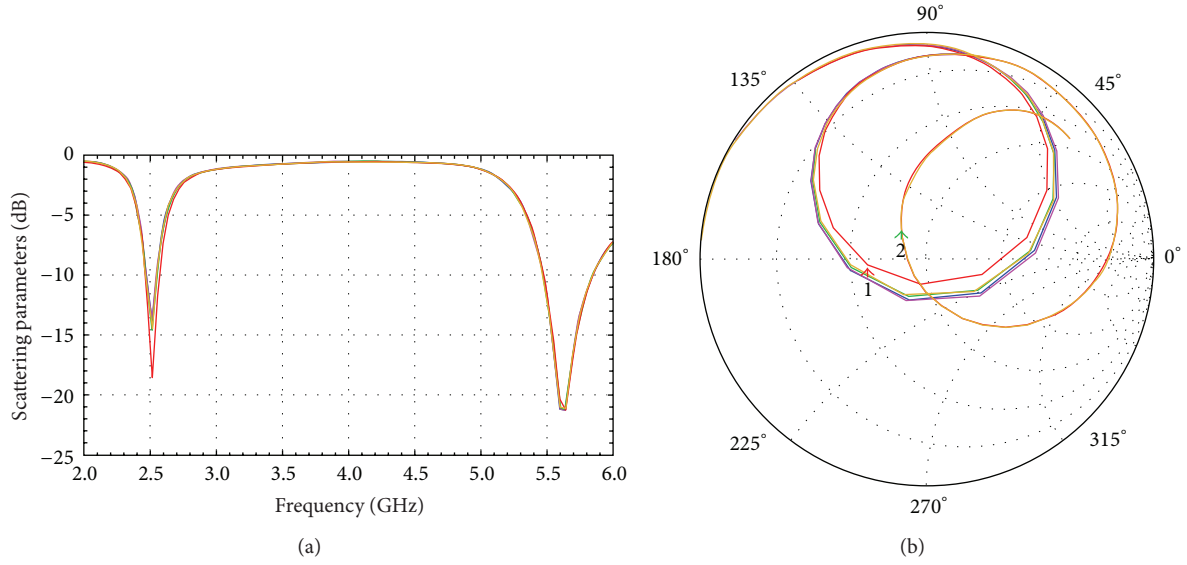
FIGURE 9: Simulated (a) S_{11} and (b) Smith Chart of the proposed antenna, with the influence of the laptop (parameter sweep of the insertion point, in the backside position).
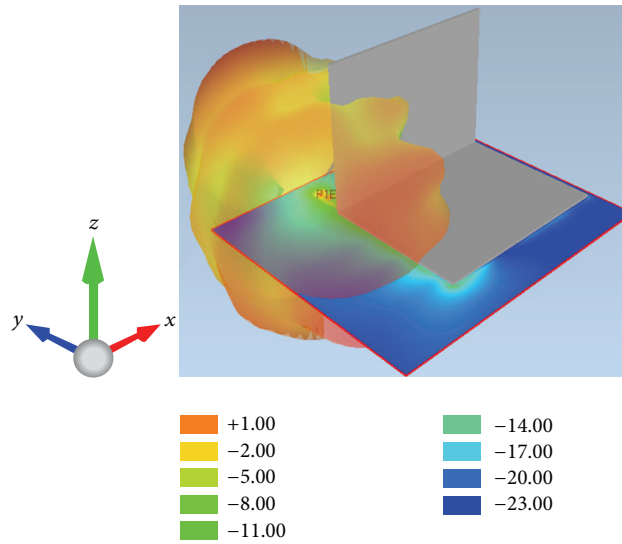
FIGURE 10: Simulated 3D radiation pattern of the proposed antenna, at 2.56 GHz, with the influence of the laptop.

proper lab facilities available such as an anechoic chamber, it is also desirable to measure radiation patterns and efficiency. In this work, the validation tests comprised both the impedance adaptation and radiation performance aspects, in realistic scenarios (dongle set assembled with its plastic casing and plugged in a laptop) as addressed in Section 4.

3. Simulation Results

In this section, the simulated results of the best achieved configuration, sketched in Figure 3, are presented. The discussion includes not only the antenna behavior on the dongle alone, but also the influence of a laptop, which corresponds to the more realistic operation scenario.

3.1. Dongle PCB Alone. Figure 4 shows the S_{11} simulation results of the proposed antenna. A dual-band operation was achieved, with the best impedance matching frequencies at 2.56 and 5.72 GHz. As addressed in Section 2, since the dongle case was not directly taken into account in the simulator, the target center frequencies of the lower and higher operation bands were 2.58 and 5.8 GHz, respectively. At this stage of the design process and bearing in mind that the laptop effect would be evaluated, these frequency values were acceptable enough.

Figures 5 and 6 show the simulated radiation patterns of the dongle alone, without casing, and basically a dipole-like behavior is seen, as expected. The compact antenna limitation to radiate only the lowest order spherical modes is clearer in Figure 5, where the pattern is quasi-omnidirectional, given

that the radiator largest branch length (24 mm) is around five times shorter than the wavelength of the lower band (117 mm at 2.56 GHz) [16–18].

Electromagnetic field simulators such as the one used in this work also provide interesting information on the current density distribution. Important insights into the current paths may be drawn from the analysis of this parameter that may be helpful to retune the antenna, during the design phase. Figures 7 and 8 present the simulated distributions of the dongle alone at 2.56 and 5.72 GHz, respectively.

Observing the current density distributions at each band, the smaller branch of the antenna is not so active in the lower band; see Figure 7. Also, the distribution along the PCB edges is almost uniform. On the other hand, at the higher band, the small branch is active, while the current distribution along the edges of the PCB is not uniform anymore, as seen in Figure 8. Thus, the radiation behavior seems to be the combination of a first order mode associated with the shorter tip-bent "F" branch with a second order mode related to the longer one. The sidelobes on the pattern of Figure 6 corroborate that.

3.2. Laptop Influence. The laptop was modeled as an open 90° wedge of perfect electric conductor (PEC) planes. Simulations were performed considering the dongle inserted in the back of or alongside the laptop, in different plug-in positions. The worst case in terms of detuning of the S_{11} response achieved in the dongle alone scenario was observed on the backside insertion configuration.

Figure 9 shows the S_{11} results of a parameter sweep of the backside plug-in scenario, that is, testing different plug-in relative positions along the back of the laptop. Even in this worst-case scenario, the sensibility of the tuning to the insertion position was relatively low in terms of frequency shift, as it can be seen. This may be interpreted as a consequence of an overcritically matching coupling condition [21], achieved with the present design, observed on the Smith Chart of Figure 9.

A more physical argument for such frequency stability is related to the current density distribution on the ground. As discussed in [9], when the current density on the ground plane is low enough compared to the one present on the main radiator element, the sensibility of the operation frequency to the laptop is expected to be low. Therefore, by plugging the dongle in the laptop, the antenna ground is expanded (PCB + laptop), reducing even more its already relatively low current density.

Figures 10 and 11 illustrate the radiation patterns of the dongle plugged in the backside of the laptop, at 2.56 and 5.72 GHz, respectively. As already mentioned in the previous section, the design was driven mostly by the impedance adaptation. Yet, with the low-cost constraint in hands, there has been no attempt to jointly tune the antenna considering the S_{11} and the radiation performances. Anyway, the results are acceptable, in the sense that enough radiated energy is available in all directions, even in the worst case of the dongle plugged in the back.

It is worth remarking that the ground density current argument that fits well for understanding the impedance
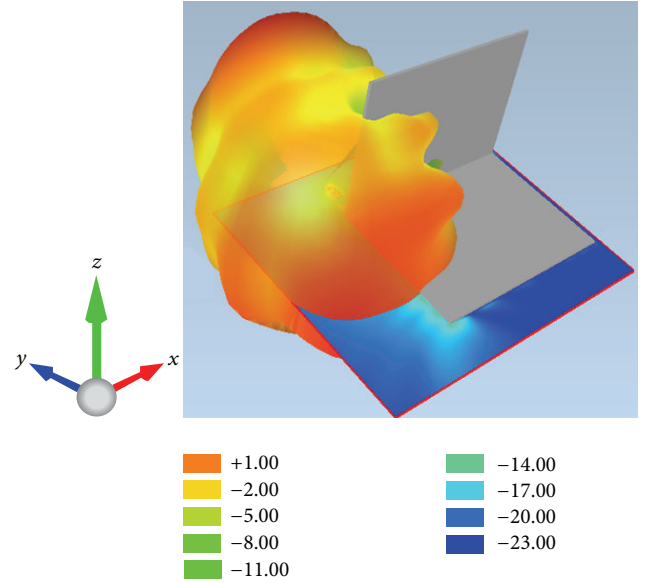

FIGURE 11: Simulated 3D radiation pattern of the proposed antenna, at 5.72 GHz, with the influence of the laptop.

matching stability does not apply as much for the radiation behavior. The coupling between the main radiator and the screen of the laptop induces additional currents on this surface which is almost orthogonal to the PCB, contributing to the deformation of the radiation patterns as seen in Figures 10 and 11. Nevertheless, bearing in mind that these simulations considered a PEC laptop model, it is reasonable to expect lower coupling in the actual application.

4. Experimental Qualification

4.1. S_{11} Measurements. A prototype of the best antenna layout achieved, shown in Figure 3, was assembled. It emulates the dongle, yet without the embedded electronics. Figure 12 shows a few snapshots of the assembled set. In order to measure the antenna parameters, external access to the feed port was needed. For that, the small piece of 50-Ω coaxial cable seen in Figure 12 was used. While the cable end external to the dongle was terminated by an SMA connector, the opposite end was soldered to the feed gap marked as P1E in Figure 3. S_{11} measurements of the antenna either without or with the plastic case were performed. The effect of the laptop was assessed as well.

Figure 13 shows the measurement results of 4 different relative plug-in configurations. The snapshot of the S_{11} measurement setup using a laptop, with the USB dongle plugged in the backside, and with the screen opened at a 90° angle is also shown. The plotted curves present a good frequency stability behavior within the −10 dB threshold in most cases and within −6 dB for all cases. This result is coherent with the overcritical impedance adaptation approach pursued in the simulations, as well as the ground current density argument, both addressed in Section 3.

It can also be noticed in Figure 13 that the impedance adaptation in the lower band was poorer than that in the
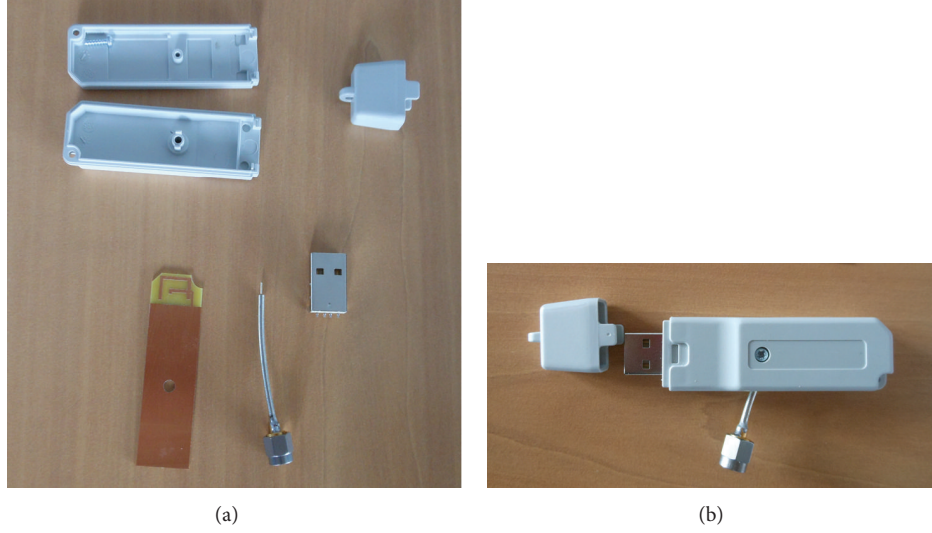
(a)

(b)

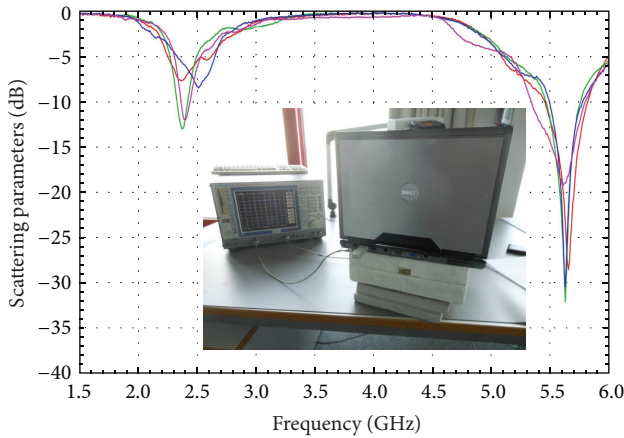FIGURE 12: Dual-band antenna prototype: (a) dongle set and (b) dongle assembled for tests.

FIGURE 13: Experimental assessment of the laptop effect on the antenna performance: measured S_{11} curves corresponding to 4 different plug-in positions alongside the computer base and a snapshot of the measurement setup.

TABLE 1: Measured gain (G) and efficiency (η) of the proposed antenna, when the dongle is plugged in the back of a laptop, at different frequencies (f).

f (GHz)	2.35	2.45	2.55	5.40	5.50	5.60
G (dBi)	2.6	2.8	2.8	5.7	5.9	6.8
η (%)	45.0	59.0	60.9	72.8	75.2	79.3

order to provide information on the antenna polarization. These measurements were taken with the dongle plugged in the back of an opened laptop ($\Psi = 90°$). The erratic polarization behavior observed was not an issue, because, typically, for this kind of application, there is no design constraint in this regard. Most importantly, the quasi-omnidirectional aspect expected from simulations was confirmed, as seen at both frequency bands. Measurements were carried out also at other frequencies within the WLAN operation bands, and similar general behavior was observed.

Table 1 brings detailed information on other important radiation parameters obtained from measurements: maximum gain and total efficiency. The lower band presents the worst results, as expected, since the radiator is compact compared to the wavelength. Nevertheless, the gain is relatively high for such scenario (close to 3 dB), and even the efficiency achieved is above 45%, a reference value typically considered for small antennas [16, 17]. The higher band is less critical regarding the antenna size, and for that both gain and efficiency are high, around 6 dB and 75%, respectively, with values coherent with those expected from monopole-like radiators.

Still concerning the upper band, it is worth noting that the design goal for its center frequency was 5.5 GHz, but the assembled antenna presented its second autoresonance close to 5.6 GHz, as seen in Figure 13. Thus, the highest gain at 5.6 GHz, almost 1 dB above the gain at 5.5 GHz, was actually a coherent, rather than unexpected, behavior.

upper band, while the simulated results in Section 3 predicted a more balanced performance, with both S_{11} notches close to −20 dB. This difference is mostly due to the small antenna behavior present in the lower band. As reported in the literature [17], measuring small antenna parameters is usually a challenging task. The list of issues includes low radiation resistance, high input reactance, high losses, and the balancing state of the antenna input regarding the presence of a poor ground reference, among others. Therefore, the measurement uncertainty in the lower band is expected to be higher than in the upper band, giving rise to differences such as the one remarked.

4.2. Radiation Pattern and Efficiency Measurements. Figures 14 and 15 show 2D cuts of the measured gain patterns of the proposed antenna at 2.45 and 5.5 GHz, respectively. Gain is shown in its partial components on directions θ and ϕ, in
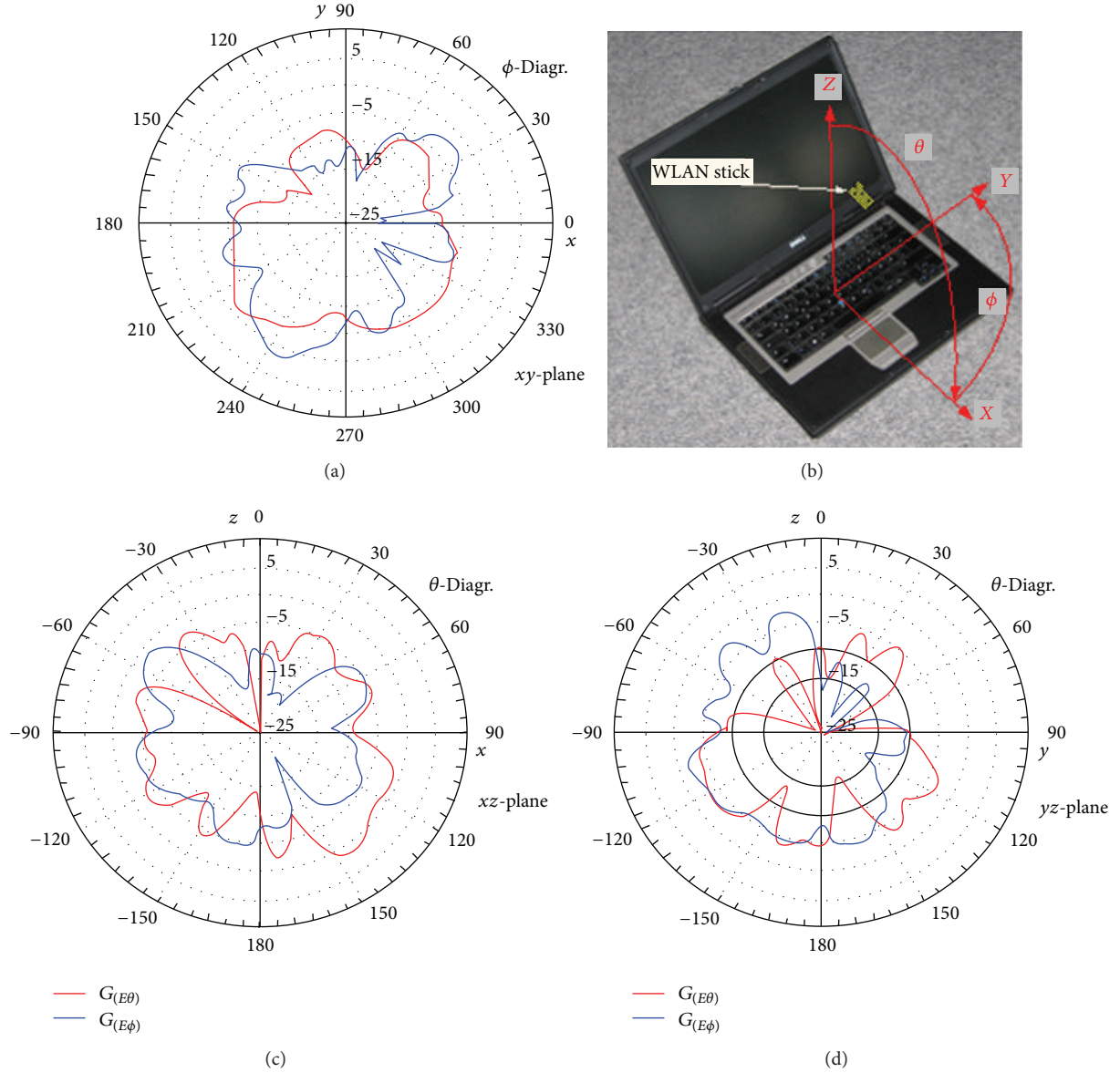
(a)

(b)

(c)

(d)

Figure 14: Measured gain pattern of the proposed antenna, when the dongle is plugged in the back of a laptop, at 2.45 GHz.

5. Concluding Remarks

In this paper, the design of a novel compact dual-band planar antenna for a low-cost USB WLAN dongle was discussed. Among the main constraints, the radiator element had to fit within a space as small as $17 \times 10\,\text{mm}^2$. Furthermore, the planar feature was actually imposed, since the antenna should be integrated to the device PCB, which had nothing but a single metal layer available. As a result, the set of pertinent basic antenna configuration choices at the beginning of the design process was more limited than usual. An IFA-based shape was the one that gave the best results, with the final shape actually resembling a tip-bent "F," since the largest branch of the radiator had to be bent to fit within the available area.

As in most of the other related works, a numerically assisted methodology was chosen for the antenna design. The electromagnetic field simulator available for this work was the software Empire XCcel. The process should include the effects of the plastic casing of the dongle, as well as the influence of a typical laptop in use, in which the dongle was supposed to be plugged in during operation.

While the laptop effect could be analyzed directly using the software, the lack of accurate information on the dongle case material electrical properties did not allow its inclusion in the simulations. The adopted solution came as an intermediate experimental step, in which a preliminary prototype tuned to the 2.45 GHz band was assembled and measured with and without the case. From this procedure, the frequency shift on the S_{11} response could have been estimated,
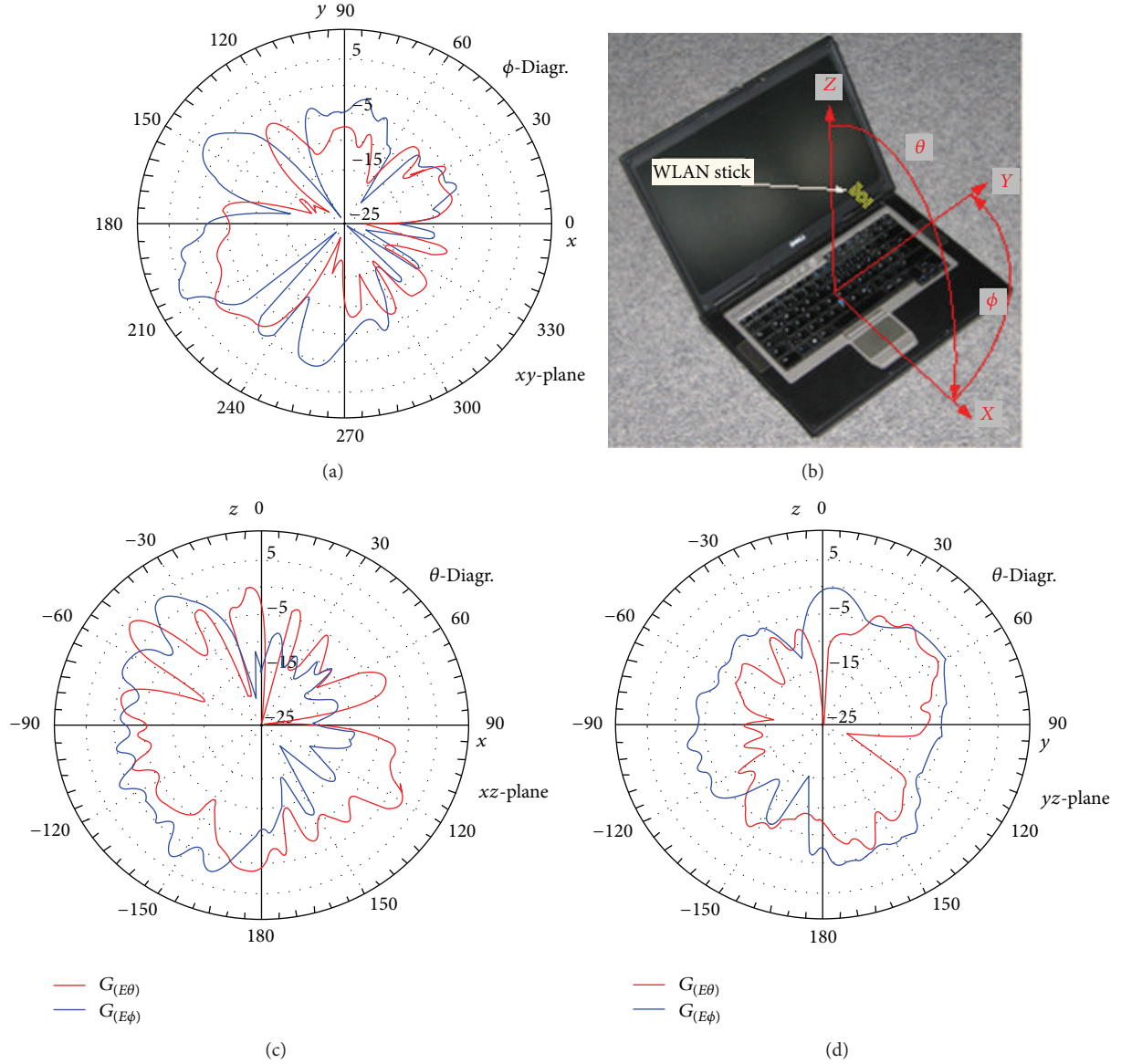
FIGURE 15: Measured gain pattern of the proposed antenna, when the dongle is plugged in the back of a laptop, at 5.5 GHz.

and, based on that, higher design target frequencies were considered on the simulations, to compensate the effect of the plastic casing.

After the final tuning step of the design process, in which the S_{11} response was taken as the main performance parameter to be observed, a prototype of the best configuration achieved was assembled. Measurements were carried out to validate the proposed design. The impedance matching performance of the prototype was coherent with the simulated results, presenting a desirable frequency stability regarding the laptop influence. That is, no matter the position where the dongle was plugged in, the S_{11} bandwidth was kept within acceptable limits.

The radiation behavior was also assessed by measurements. Power patterns kept the quasi-omnidirectional shape

expected from simulations and from theory. Gain and efficiency were also measured, with good results for such a kind of compact radiator. Overall, the proposed IFA-based antenna proved to be a suitable choice for low-cost compact WLAN dongle devices.

Conflict of Interests

The authors declare that there is no conflict of interests regarding the publication of this paper.

Acknowledgments

References

[1] Y. Xiong and Z. Qu, "Antenna 3D Pad printing solution evaluation," in *Proceedings of the International Symposium on Antennas and Propagation (APSURSI '11)*, pp. 2773–2776, Spokane, Wash, USA, July 2011.

[2] M. K. Hosain, A. Kouzani, and S. Tye, "Multi-layer implantable antenna for closed loop deep brain stimulation system," in *Proceedings of the International Symposium on Communications and Information Technologies (ISCIT '12)*, pp. 643–648, Outrigger Surfers Paradise, October 2012.

[3] C. B. Ravipati, D. R. Jackson, and H. Xu, "Center-fed microstrip antennas with shorting vias for miniaturization," in *Proceedings of the Antennas and Propagation Society International Symposium and USNC/URSI Meeting*, pp. 281–284, July 2005.

[4] J. Kruys and L. Qian, *RF Spectrum With Commodity Wireless Technologies: Theory and Practice*, Springer, 2011.

[5] W.-S. Chen, W.-C. Jhang, and H.-D. Chen, "Small and compact MIMO antenna for USB dongle applications," in *Proceedings of the Cross Strait Quad-Regional Radio Science and Wireless Technology Conference (CSQRWC '11)*, pp. 438–441, Harbin, China, July 2011.

[6] Q. Luo, C. Quigley, J. R. Pereira, and H. M. Salgado, "Inverted-L antennas array in a wireless USB dongle for MIMO application," in *Proceedings of the 6th European Conference on Antennas and Propagation (EUCAP '12)*, pp. 1909–1912, Prague, Czech Republic, March 2012.

[7] V. Ssorin, A. Artemenko, A. Maltsev, A. Sevastyanov, and R. Maslennikov, "Compact MIMO microstrip antennas for USB dongle operating in 2.5–2.7 GHz frequency band," *International Journal of Antennas and Propagation*, vol. 2012, Article ID 793098, 12 pages, 2012.

[8] M. Han and J. Choi, "Compact multiband MIMO antenna for next generation USB dongle applications," *Microwave and Optical Technology Letters*, vol. 54, no. 1, pp. 246–250, 2012.

[9] J. Ou Yang, J. Zhang, K. Z. Zhang, and F. Yang, "Compact folded dual-band slot antenna for wireless communication USB dongle application," *Journal of Electromagnetic Waves and Applications*, vol. 25, no. 8-9, pp. 1221–1230, 2011.

[10] W.-C. Su and K.-L. Wong, "Internal PIFAs for UMTS/WLAN/WiMAX multi-network operation for a USB dongle," *Microwave and Optical Technology Letters*, vol. 48, no. 11, pp. 2249–2253, 2006.

[11] Y. Yu and J. Choi, "Compact internal inverted-F antenna for USB dongle applications," *Electronics Letters*, vol. 45, no. 2, pp. 92–94, 2009.

[12] S.-H. Lee and Y. Sung, "Multiband antenna for wireless USB dongle applications," *IEEE Antennas and Wireless Propagation Letters*, vol. 10, pp. 25–28, 2011.

[13] W.-C. Liu and Y.-L. Chen, "Compact strip-monopole antenna for WLAN-band USB dongle application," *Electronics Letters*, vol. 47, no. 8, pp. 479–480, 2011.

[14] Q. Luo, H. M. Salgado, and J. R. Pereira, "Compact printed C-shaped monopole antenna with chip inductor," in *Proceedings of the International Symposium on Antennas and Propagation (APSURSI '11)*, pp. 156–159, Spokane, Wash, USA, July 2011.

[15] S. Chaimool, C. Chokchai, and P. Akkaraekthalin, "Triple-band USB dongle antenna using fractal and shorted loops for WiFi and WiMAX applications," *Microwave and Optical Technology Letters*, vol. 55, no. 4, pp. 863–866, 2013.

[16] J. Volakis, C. C. Chen, and K. Fujimoto, *Small Antennas: Miniaturization Techniques and Applications*, McGraw-Hill, 2010.

[17] L. Jofre, M. Martinez-Vazquez, R. Serrano, and G. Roqueta, *Handbook on Small Antennas*, EurAAP, 2012.

[18] J. Anguera, A. Andújar, M. C. Huynh, C. Orlenius, C. Picher, and C. Puente, "Advances in antenna technology for wireless handheld devices," *International Journal of Antennas and Propagation*, vol. 2013, Article ID 838364, 25 pages, 2013.

[19] B. R. Franciscatto, H. Adel, M. H. C. Dias, and T. P. Vuong, "A compact IFA-based dual-band planar antenna for WiFi USB dongles," in *Proceedings of the 8th European Conference on Antennas and Propagation (EuCAP '14)*, pp. 1–5, The Hague, The Netherlands, April 2014.

[20] http://www.empire.de/.

[21] J. Rahola, "Bandwidth potential and electromagnetic isolation: tools for analysing the impedance behaviour of antenna systems," in *Proceedings of the 3rd European Conference on Antennas and Propagation (EuCAP '09)*, pp. 944–948, Berlin, Germany, March 2009.

Research Article

Highly Directional Small-Size Antenna Designed with Homogeneous Transformation Optics

Zuojia Wang,[1,2] **Lian Shen,**[1,2] **Jun Chen,**[3] **Huaping Wang,**[3]
Faxin Yu,[3] **and Hongsheng Chen**[1,2]

[1] *The Electromagnetics Academy at Zhejiang University, Zhejiang University, Hangzhou 310027, China*

[2] *Department of Information Science and Electronic Engineering, Zhejiang University, Hangzhou 310027, China*

[3] *School of Aeronautics and Astronautics, Zhejiang University, Hangzhou 310027, China*

Correspondence should be addressed to Jun Chen; chnjun@zju.edu.cn, Huaping Wang; wang_hp2003@yahoo.com
and Hongsheng Chen; hansomchen@zju.edu.cn

Achieving high directivity antenna usually requires a large size antenna aperture in traditional antenna design. Previous work shows that, with the help of metamaterials and transformation optics, a small size antenna can perform as high directivity as a large size antenna, but the material parameters are inhomogeneous and difficult to realize. In this paper, we propose a linear homogeneous coordinate transformation to design the small size antenna. Distinguishing from inhomogeneous transformation, we construct a regular polygon in virtual space and then divide it into several triangle segments. By applying linear homogeneous coordinate transformation, the antenna devices can be greatly compressed without disturbing the radiation patterns by using homogeneous metamaterial substrates. The material parameters of the antenna designed from this method are homogeneous and easy to fabricate. Square and hexagonal antenna structures are numerically demonstrated to illustrate the validity of our methodology.

1. Introduction

Nowadays the demand for compact radiators with sufficiently high directivity is rapidly increasing in many application areas. In particular, modern wireless telecommunication systems require compact antennas with high directivity, which is especially crucial when the radiating components have to be combined in large antenna arrays for satellites, airplanes, space vehicles, and so forth. However, it is a fundamental trade-off between the directivity factor and the antenna profile in traditional antenna design. Metamaterials, with their unusual electromagnetic properties, provide a feasible solution to reduce the size of the antenna but still keep the high directivity. Firstly known as left-handed materials (LHM), metamaterials have attracted great attention and offered great opportunity to the manipulation of electromagnetic (EM) fields. For example, metamaterials have been widely used for the designs of optical superlens [1, 2], invisibility cloak [3–5], illusion device [6, 7], super absorber [8], antenna

[9–12], and so forth. With inhomogeneous transformation optics whose transformation ratio relates to the position in each region, it is shown that the antenna size can be greatly reduced [13]. However, the material parameters are inhomogeneous and anisotropic, which are very difficult to realize.

In this paper, we present a novel design for small-size directional antenna using a linear homogeneous transformation method whose transformation ratio is independent of the position. Distinguishing from inhomogeneous transformation, we construct a regular polygon in original space and then divide it into several triangle segments. By applying a linear homogeneous coordinate transformation, the antenna devices can be greatly compressed without disturbing the radiation patterns by using homogeneous metamaterial substrates. The simulated results of square and hexagonal antenna structures demonstrate the validity of our methodology, showing its potential applications in microwave antenna.
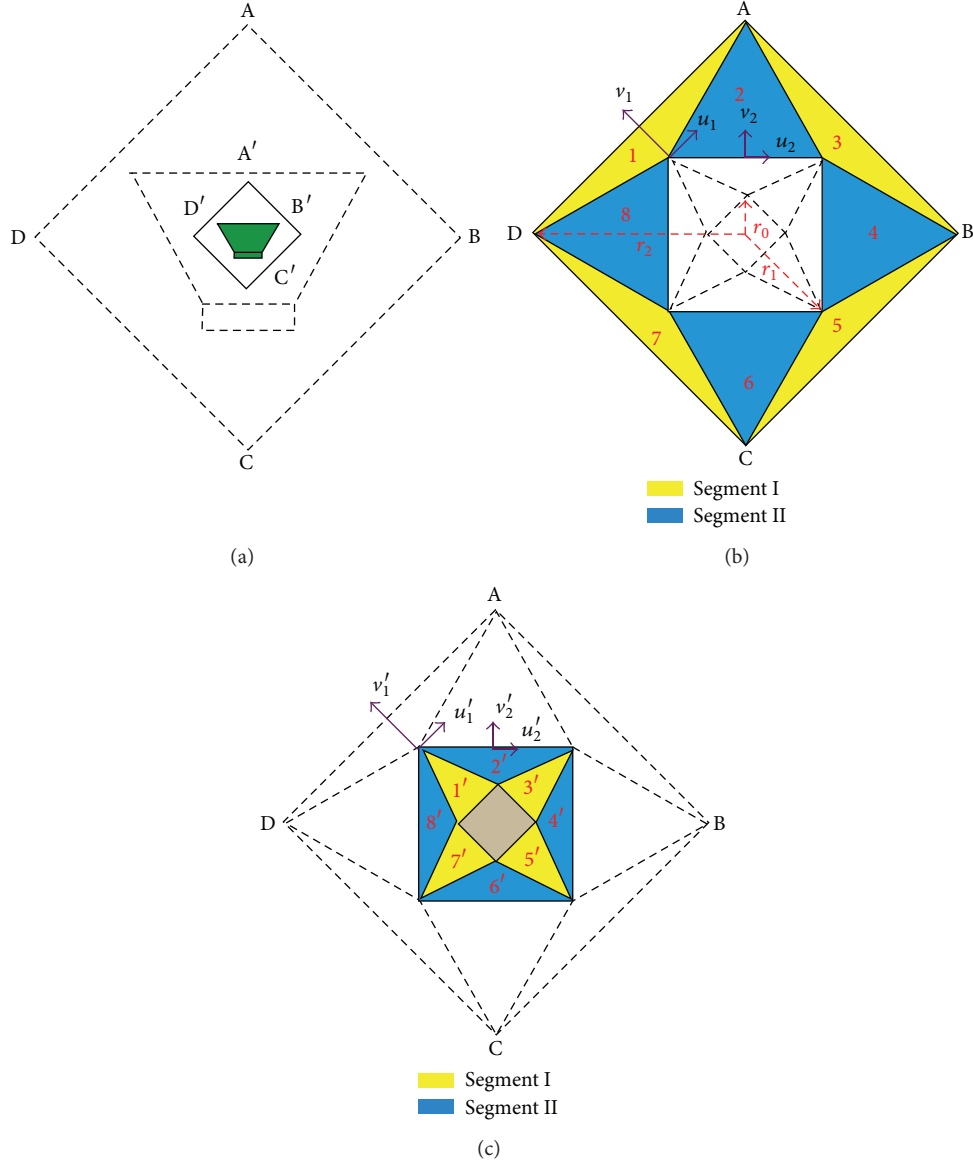
(a)

(b)

(c)

Figure 1: (a) The schematic of the square antenna system. A big square region (ABCD) with radius r_2 has been compressed to a small one (A′B′C′D′) with radius r_0. Green region represents the antenna device compressed from a large size one described by dashed lines. (b) The square in the virtual coordinate space filled with isotropic material is divided into several triangle segments grouped by Segment I and Segment II. (c) The square metamaterial shell in the physical coordinate space is constructed by the transformed segments with homogeneous constitutive tensors.

2. Results and Discussion

For simplicity, we limit ourselves to two-dimensional case and TE incidence. As depicted in Figure 1, a big square free space (ABCD) with radius r_2 has been compressed to a small antenna core (A′B′C′D′) with radius r_0. This can be achieved by a linear homogenous transformation [14]. Specifically, we construct another square with radius r_1 rotated at an angle of $\pi/4$ compared to the outside one, as shown in Figure 1(b). The space between the two squares is then divided into many triangle segments. Due to the symmetric pattern shown in Figure 1(b), we group the triangle segments into two types, marked as Segment I (blue regions) and Segment II (yellow

regions) with their local coordinate axes (u_1, v_1, w_1) and (u_2, v_2, w_2), respectively. The following linear transformation is applied in each segment along its local coordinate axes:

$$u_1' = \kappa_u u_1, \qquad v_1' = \kappa_v v_1, \qquad w_1' = w_1, \quad \text{for Segment I,}$$
$$u_2' = u_2, \qquad v_2' = \kappa v_2, \qquad w_2' = w_2, \quad \text{for Segment II,} \tag{1}$$

where $\kappa = (r_1 \cos(\pi/m) - r_0)/(r_1 \cos(\pi/m) - r_2)$, $\kappa_v = (r_1 - r_0 \cos(\pi/m))/(r_1 - r_2 \cos(\pi/m))$, $m = 4$ for the square case, and $\kappa_u = r_0/r_2$ are the compression ratios of the space applicable for arbitrary regular polygonal. Through this
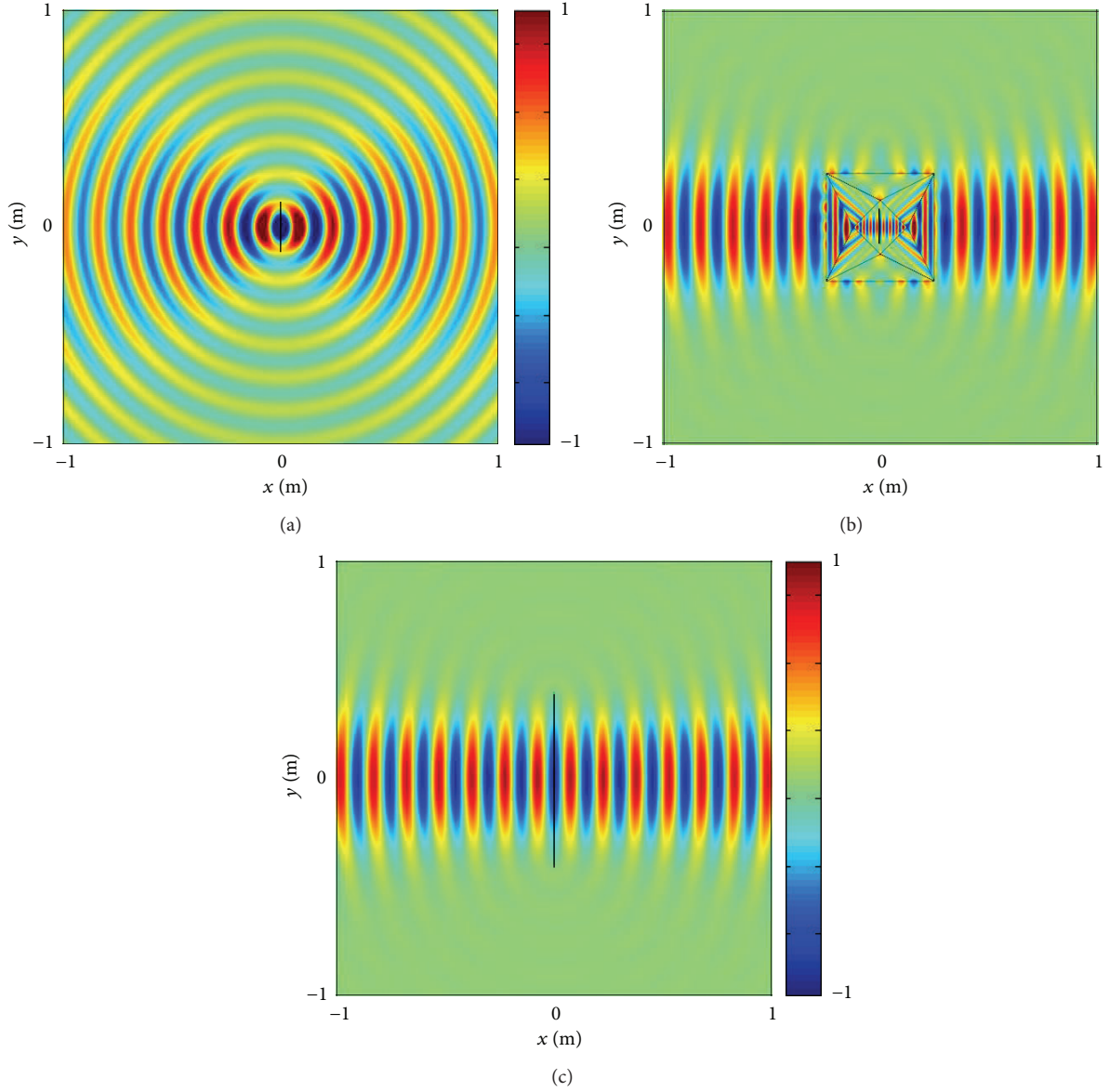
FIGURE 2: The z-directed electrical field distribution when a naked small current plane with width $w = 0.16$ m is located in (a) free space and (b) square metamaterial substrates, respectively. (c) E_z field distribution while a large current plane with the width 0.8 m is radiating in free space.

transformation, the blue and yellow regions in Figure 1(b) are reversed to the space with the same colors shown in Figure 1(c), respectively. Meanwhile, the large square region (ABCD) is compressed to a small brown core. Hence properly designed compact antennas located in the brown core can effectively mimic large size ones and exhibit identical radiation patterns. In case of TE incident wave, the material parameters of the metamaterial shell can be obtained as

$$\mu_u^{I\prime} = \frac{\kappa_u}{\kappa_v}, \qquad \mu_v^{I\prime} = \frac{\kappa_v}{\kappa_u}, \qquad \varepsilon_w^{I\prime} = \frac{1}{(\kappa_u \kappa_v)},$$

$$\text{for Segment I,}$$

$$\mu_u^{II\prime} = \frac{1}{\kappa}, \qquad \mu_v^{II\prime} = \kappa, \qquad \varepsilon_w^{II\prime} = \frac{1}{\kappa},$$

$$\text{for Segment II,}$$

$$\mu_u^{core\prime} = 1, \qquad \mu_v^{core\prime} = 1, \qquad \varepsilon_w^{core\prime} = \left(\frac{1}{\kappa_u}\right)^2,$$

$$\text{for the antenna core.}$$

$$(2)$$

The physical square region is therefore composed of several triangular segments with homogenous and anisotropic materials. It is interesting to see that the media making up the antenna substrates are homogeneous. Different from the

Figure 3: (a) E_z field distribution of a small antenna array with nine elements embedded in square metamaterial shell. (b) E_z field distribution of a large antenna array in free space.

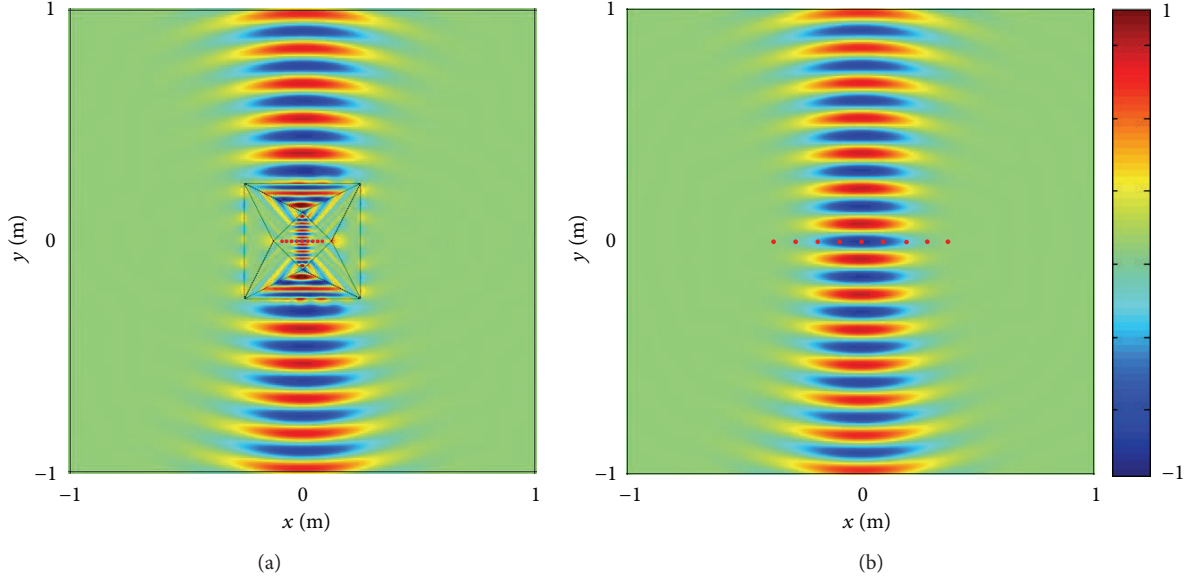inhomogeneous optical transformation scheme, the linear transformation applied here is very simple, yielding homogeneous constitutive parameters of metamaterial substrates. The virtual antenna is therefore mapped to a smaller one (colored by green in **Figure 1(a)**) with the compression ratio r_2/r_0. In addition, we set r_0 to be small enough so that the size of the antenna device can be significantly reduced. In the following part, we will give examples to illustrate how this approach reduces the device size without disturbing the radiation behavior. All the results are obtained from a commercial finite element modeling software (COMSOL) and the working frequency is set at 2 GHz.

Figure 2(a) depicts the simulated field distribution of a naked antenna excited by a surface current plane (with the width 16 cm). In this case we set $r_0 = 0.125$ m, $r_1 = 2\sqrt{2}r_0$, and $r_2 = 5r_0$. In **Figure 2(b)**, we plot the electrical field distribution of the same current plane (with the width 0.16 m) embedded in a metamaterial shell. The coated layer consists of homogeneous metamaterials with $\mu_u^{I\,\prime} = -1/15$, $\mu_v^{I\,\prime} = -15$, and $\varepsilon_w^{I\,\prime} = -5/3$ for Segment I and $\mu_u^{II\,\prime} = -3$, $\mu_v^{II\,\prime} = -1/3$, and $\varepsilon_w^{II\,\prime} = -3$ for Segment II. And the inner square core is filled with a homogeneous material with $\varepsilon_w^{core\,\prime} = \mu_w^{core\,\prime} = 25$. The current distribution of the small current plane in these two cases is assumed $J_s = 5\exp(-400y^2)$. Moreover, the corresponding field distribution of a large-sized current plane with the width 0.8 m radiating in free space is shown in **Figure 2(c)**. Note that the current distribution would change the form under the transformation characterized by $J_s' = \exp(-16y^2)$. The simulated results demonstrate that the small current plane coating with the polygonal metamaterial shell has the identical radiation characteristic as that of a large one. However, the antenna aperture is suppressed; that is, the size of the antenna aperture in **Figure 2(b)** is 0.354 m, while

the size of the antenna aperture in **Figure 2(c)** is 0.4 m. Note that if a higher compressing ratio, that is, r_2/r_1, is used in the transformation optics, the antenna size can be further suppressed.

This concept can also be applied to reduce the size of antenna arrays that are usually adopted in highly directional radiating scheme. As a theoretical verification, we consider a nine-element antenna array of which the current distribution is set to be $1:8:28:56:70:56:28:8:1$ to achieve high directivity. The electric field distribution of the small-size antenna array coating with metamaterial shell is shown in **Figure 3(a)**. The distance between two neighboring elements is 1.875 cm, one-eighth of the wavelength. For comparison, **Figure 3(b)** illustrates the associated field distribution for a large-size one with a neighboring distance of 9.375 cm. The radiation characteristic remains unchanged when replacing the large antenna array with a small-size one coated with properly designed metamaterial substrates.

It should be noted that this concept can be extended to other shapes of the antenna design. To further show the flexibility of such linear homogenous transformation approach in antenna design, we employ a hexagonal counterpart for comparison. As shown in **Figure 4(a)**, the hexagonal metamaterial shell comprises of six yellow triangles and six blue triangles, marked as Segment I and Segment II, respectively. Different from the square case, the parameters we adopt here are $r_0 = \sqrt{2}/10$ m, $r_1 = 2r_0$, and $r_2 = 4r_0$. The electric field distribution of a small antenna array embedded in the hexagonal metamaterial shell is displayed in **Figure 4(b)**. Here, the distance between the neighboring antenna elements is 1.875 cm, identical to the square case. Similarly, **Figure 4(c)** depicts the radiation characteristic of the mentioned current plane embedded in such hexagonal metamaterial shell. The field distributions of equivalent large size antenna array

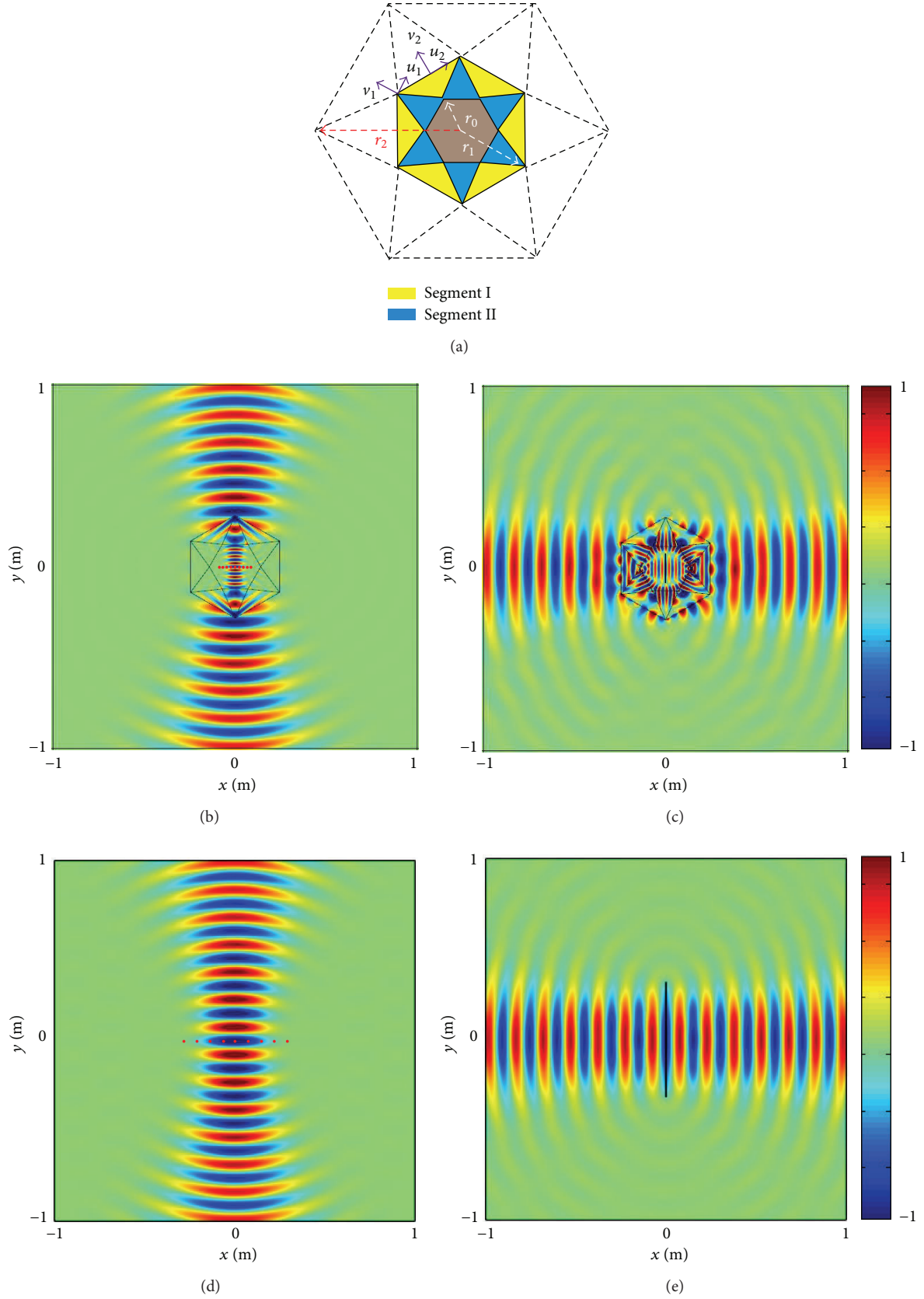FIGURE 4: (a) The structure of a hexagonal metamaterial shell. (b) E_z field distribution of a small antenna array with nine elements embedded in hexagonal metamaterial shell. (c) E_z field distribution of a small current plane embedded in hexagonal metamaterial shell. The z-directed electrical field distributions of (d) large size antenna array and (e) large size current plane in free space.

and current plane are displayed in Figures 4(d) and 4(e), respectively. These simulated results effectively prove our methodology an ideal candidate for the miniaturization of antenna system.

It should be noted that, in previous work based on inhomogeneous coordinate transformation [13], the values of the consitiutive paramters of the metamaterial shell are described by a function dependent on the cylindrical radius and vary as the change of the coordinates. To achieve these stringent demands, the metamaterial substrates must be designed with gradually varied parameters and hence harsh technique requirments are needed in practice. Besides, the impedanc mismatch between neighbouring layers is inevitable, while using discretization approach and the total performance will be deteriorated. These features, therefore, are main bottlenecks in practical microwave applications.

Compared with inhomogeneous transform optics method, the antenna coating obtained from linear homogeneous coordinate transformation is composed of homogeneous metamaterials whose constitutive parameters are kept consistent in each triangle region. Thus the difficulty in implementation will be greatly reduced. Besides, the linear homogeneous coordinate transformation is valid for arbitrary regular polygon and hence provides much flexibility in shape design. Furthermore, the antenna coating comprised of several separated components will be convenient to transport and assemble outdoors and, therefore, greatly facilitates the practical applications.

3. Conclusion

In conclusion, we have analytically presented an effective way of using a linear homogeneous coordinate transformation to achieve highly directional emission with a small antenna aperture. Since previous inhomogeneous transformation method resorts to inhomogeneous materials requiring a high precise fabrication technique to implement, we divide the virtual space into triangle segments and transformed them separately to avoid the requirement of inhomogeneous metamaterials. This can greatly reduce the complexity of the antenna materials' parameters. Simulated results have shown that small antenna devices embedded in properly designed metamaterial shell demonstrate identical radiation characteristics compared with large-sized ones, showing the potential applications in microwave engineering.

Conflict of Interests

The authors declare that there is no conflict of interests regarding the publication of this paper.

Acknowledgments

References

[1] J. B. Pendry, "Negative refraction makes a perfect lens," *Physical Review Letters*, vol. 85, no. 18, pp. 3966–3969, 2000.

[2] N. Fang, H. Lee, C. Sun, and X. Zhang, "Sub-diffraction-limited optical imaging with a silver superlens," *Science*, vol. 308, no. 5721, pp. 534–537, 2005.

[3] J. B. Pendry, D. Schurig, and D. R. Smith, "Controlling electromagnetic fields," *Science*, vol. 312, no. 5781, pp. 1780–1782, 2006.

[4] U. Leonhardt, "Optical conformal mapping," *Science*, vol. 312, no. 5781, pp. 1777–1780, 2006.

[5] D. Schurig, J. J. Mock, B. J. Justice et al., "Metamaterial electromagnetic cloak at microwave frequencies," *Science*, vol. 314, no. 5801, pp. 977–980, 2006.

[6] Y. Lai, J. Ng, H. Chen et al., "Illusion optics: the optical transformation of an object into another object," *Physical Review Letters*, vol. 102, no. 25, Article ID 253902, 2009.

[7] J. Pendry, "Optics: all smoke and metamaterials," *Nature*, vol. 460, no. 7255, pp. 579–580, 2009.

[8] J. Ng, H. Y. Chen, and C. T. Chan, "Metamaterial frequency-selective superabsorber," *Optics Letters*, vol. 34, pp. 644–646, 2009.

[9] Y. Luo, J. J. Zhang, L. X. Ran, H. S. Chen, and J. A. Kong, "New concept conformal antennas utilizing metamaterial and transformation optics," *IEEE Antennas and Wireless Propagation Letters*, vol. 7, pp. 508–512, 2008.

[10] N. Kundtz, D. A. Roberts, J. Allen, S. Cummer, and D. R. Smith, "Optical source transformations," *Optics Express*, vol. 16, no. 26, pp. 21215–21222, 2008.

[11] J. Allen, N. Kundtz, D. A. Roberts, S. A. Cummer, and D. R. Smith, "Electromagnetic source transformations using superellipse equations," *Applied Physics Letters*, vol. 94, no. 19, Article ID 194101, 2009.

[12] B.-I. Popa, J. Allen, and S. A. Cummer, "Conformal array design with transformation electromagnetics," *Applied Physics Letters*, vol. 94, no. 24, Article ID 244102, 2009.

[13] Y. Luo, J. Zhang, H. Chen, J. Huangfu, and L. Ran, "High-directivity antenna with small antenna aperture," *Applied Physics Letters*, vol. 95, no. 19, Article ID 193506, 2009.

[14] H. Chen and B. Zheng, "Broadband polygonal invisibility cloak for visible light," *Scientific Reports*, vol. 2, article 255, 2012.

Research Article

A RHCP Microstrip Antenna with Ultrawide Beamwidth for UHF Band Application

Yuan-zhu Liu, Shao-qiu Xiao, and Bing-zhong Wang

Institute of Applied Physics, University of Electronic Science and Technology of China, Chengdu 610054, China

Correspondence should be addressed to Yuan-zhu Liu; yuanzhuliu@vip.qq.com

A novel right-hand circularly polarized (RHCP) UHF microstrip antenna with 3 dB beamwidth of more than 150° is presented in this paper. The 3 dB RHCP beamwidth can be broadened by utilizing a combined ground structure with a hollow truncated cone ground plane and a metallic rectangular plate. Optimizing the half-angle θ_c of cone and the cone height h_{cone}, a 3 dB RHCP beamwidth of more than 200° can be acquired, which is about 120° greater than its corresponding regular RHCP microstrip antenna. There is a good agreement between the measured results and simulated results for the proposed antenna operating in UHF band.

1. Introduction

Circularly polarised (CP) microstrip patch antenna (MPA) is widely used in wireless communication and radar system due to its advantages of lightweight, low profile, ease of manufacturing, and conformation to the platform [1, 2]. However, it is difficult for the conventional MPA to realize ultrawide beam coverage which usually has more applications [3]. To increase the 3 dB CP beamwidth of the MPA, a lot of methods are applied. In [4], the proposed CP-MPA exhibits a 3 dB CP beamwidth of more than 110° by mounting a regular CP antenna on a three-dimensional square ground, which is about 30° greater than that of a corresponding regular MPA. However, the height of that proposed CP-MPA is more than 0.45 operating wavelengths (0.45λ). To obtain a wider beamwidth with lightweight and low profile, Nakano et al. use a folded conducting wall to reduce the height of the CP antenna to about 0.04λ and meanwhile provide a 3 dB CP beamwidth of about 106° [5]. In [6], a dielectric lens encapsulating at least a portion of the patch is used to increase radiation gain at low elevation angles. In order to further broaden the 3 dB CP beamwidth, we lay gradually variational metallic supporting platform under the antenna which will be an effective technique. Su et al. use a pyramidal ground structure and a partially enclosed flat conducting wall to broaden the 3 dB CP beamwidth up to 130° [7]. In this paper, we utilize

a combined ground structure with a hollow truncated cone ground plane and a metallic rectangle plate to obtain a wider 3 dB CP beamwidth which is more than 150°. By optimizing the half-angle θ_c of cone and the cone height h_{cone}, a 3 dB RHCP beamwidth of more than 200° can be acquired, which is about 120° greater than its corresponding regular CP-MPA.

2. Antenna Configuration

The proposed right-hand circularly polarized (RHCP) MPA comprises ground layer, dielectric layer, patch layer, and metallic supporting platform shown in Figure 1. The square patch is printed on a grounded square substrate with thickness of 3 mm, relative permittivity of 3.5, and dielectric loss tangent of 0.001. The supporting structure under the grounded plane of the MPA comprises a metallic truncated cone with height of 180 mm (about 0.25λ) and a rectangular metallic plate with 320 mm × 320 mm. The truncated cone structure is made of sheet iron of thickness 0.1 mm and the rectangular plate is made of aluminium plate of thickness 1 mm. Figure 1(a) illustrates its detailed physical dimension. MPA is probe fed and adopts corner-truncated square patch with 7 mm truncated corners. The x-coordination and y-coordination of the feeding point are 13 mm and 30 mm, respectively, as shown in Figure 1(a). Four fine tuning branches are adopted for better matching, resonance

(a)

(b)

FIGURE 1: Configuration of the proposed RHCP antenna: (a) physical dimension (b) experimental prototype.

FIGURE 2: The electric field distribution diagram.

characteristic, and axial ratio (AR) at the centre frequency. The experimental prototype is shown in **Figure 1(b)**. And all the simulated results in this paper are done by the electromagnet-ics simulation software HFSS14.0 based on the finite element method. Details of the proposed antenna design and the obtained experimental results are presented.

3. Antenna Analysis

Due to the existing truncated cone, the edge diffraction fields of the MPA shown in **Figure 2** are changed. The reflection of the truncated cone ground plane leads to less backward radiation. Because of the angle between the grounded plane
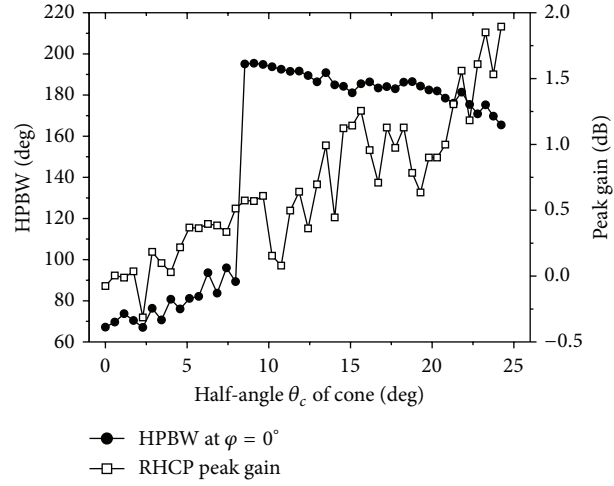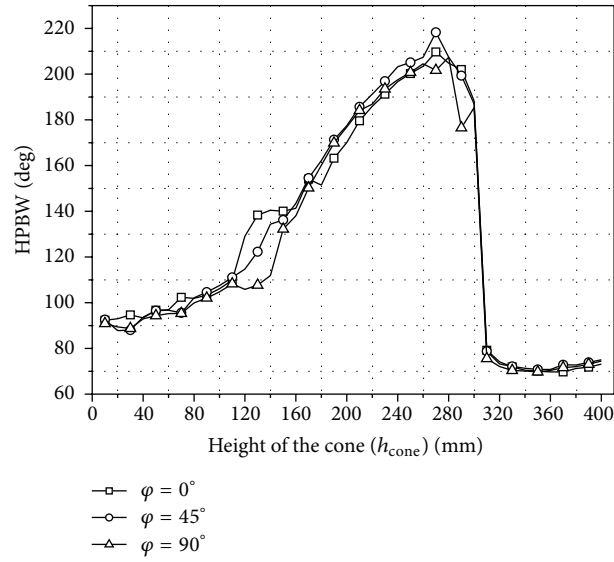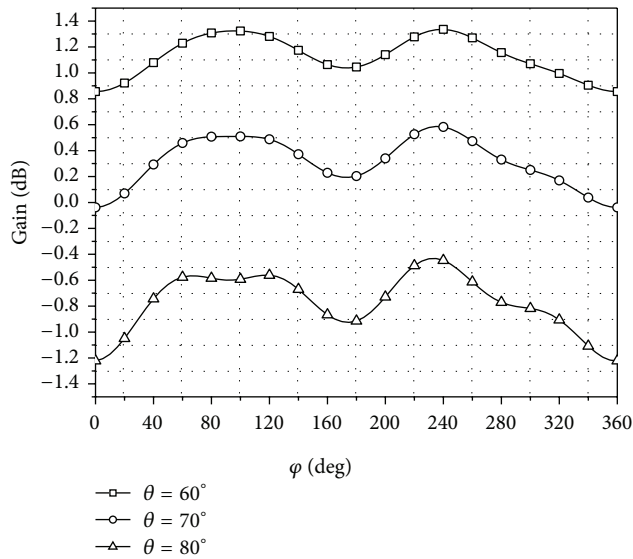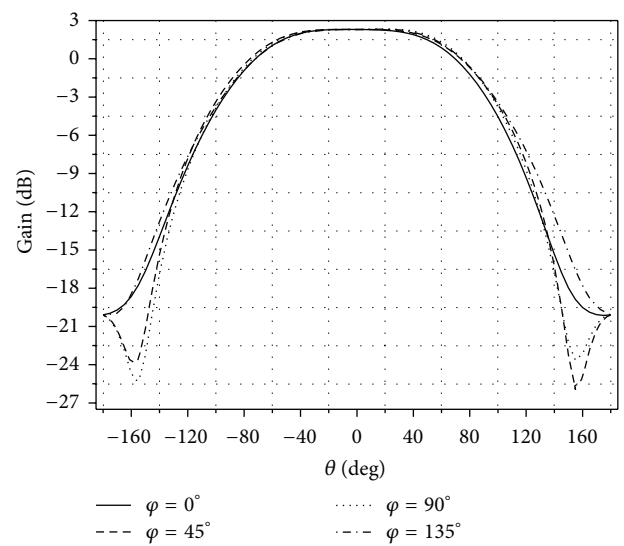
FIGURE 3: HPBW, peak gain versus half-angle θ_c of cone.

FIGURE 4: HPBW versus cone height.

(a)

(b)

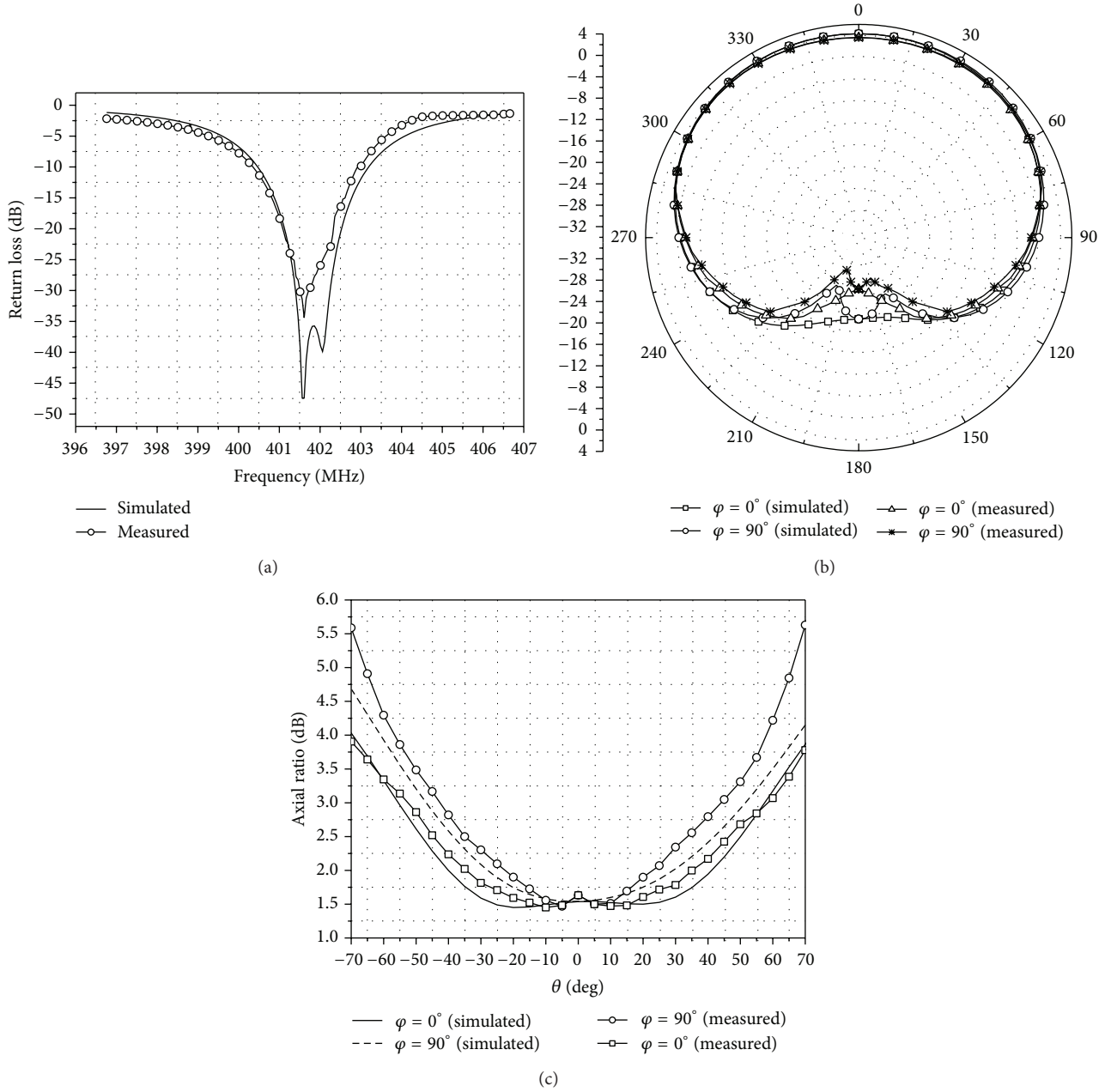FIGURE 5: (a) Horizontal radiation pattern at low elevation angle; (b) radiation pattern for different φ.

(a)

(b)

(c)

Figure 6: Antenna performance at f = 401.6 MHz: (a) return loss, (b) RHCP radiation pattern at $\varphi = 0°$, $\varphi = 90°$, and (c) axial ratio pattern at $\varphi = 0°$ and $\varphi = 90°$.

of the MPA and the conical surface, the contribution of the reflected wave to the forward radiation concentrates at the low elevation angle, and then a wide beamwidth is achieved. To study the effects of the shape of the platform on the beamwidth, we analyze the relationship between the half power beamwidth (HPBW), peak gain, and half-angle θ_c of cone, as shown in Figure 3. In this case study, the height and the top diameter of the truncated cone are fixed to be 180 mm and 130 mm, respectively. Obviously, increasing the half-angle θ_c of truncated cone, the influence of the reflected wave on the forward radiation is gradually strengthened which results in the decrease of the maximum radiation gain and the

increase of the antenna gain at low elevation angle, and then the radiation beam at low elevation angle will be included in the domain of 3 dB RHCP radiation beam at some θ_c. All of the above can explain why the main beam has mutation at θ_c = 8.5°, in which the beamwidth suddenly changes from 90° to 195°. From Figure 3, we can observe that when $\theta_c \geq 8.5°$, the beamwidth declines slowly, and the maximum beamwidth presents at θ_c = 9.7° where the 3 dB RHCP beamwidth is about 195°. The antenna peak gain ranging from −0.5 dB to 2 dB exhibits a rising tendency when θ_c is increasing. Figure 3 shows that the low elevation angle gain and beamwidth can be effectively controlled by changing the θ_c.

In order to further study the effects of the truncated cone to the beamwidth, the influence of the cone height is analyzed in this paper where the top diameter and bottom diameter of the truncated cone are 130 mm and 292 mm, respectively. Figure 4 illustrates the relationship between the HPBW and the cone height. From Figure 4, we can observe that the beamwidth increases with cone height h_{cone} ranging from 90° to 210° for different φ, and when $h_{cone} \geq 300$ mm, the HPBW suddenly falls to a stable value which is about 70°. This is because the contribution of the reflected wave to the forward radiation is gradually shifting to low elevation angle, and the low elevation angle beam will be excluded from the main beam at some h_{cone} ($h_{cone} = 300$ mm), which results in the mutation shown in Figure 4. After the mutation, the supporting platform has little effects to the forward radiation for the case of increasing the h_{cone} which comes out as a stable value of beamwidth. However, when the h_{cone} is tending to 0 mm, due to the existing metallic rectangular plate which is larger than the ground of the MPA, the contribution of reflected wave to forward radiation is still at work which can explain why the beamwidth increases from 90°. Figure 4 depicts that the HPBW can be further broaden to more than 200° by changing the cone height h_{cone}. To obtain the hemispherical pattern coverage, low elevation angle radiation pattern and different φ-plane radiation are presented to show the antenna performance. Figure 5(a) shows the horizontal radiation pattern at low elevation angle, and we can observe that the horizontal gain range are less than 0.8 dB, 0.6 dB, and 0.5 dB at $\varphi = 80°$, 70°, and 60°, respectively. The HPBW variation is less than 8° as is shown in Figure 5(b).

4. Simulation and Measurement Results

A RHCP-MPA with $\theta_c = 24.2°$ is designed and experimented in this paper. Figures 6(a) and 6(b) show the measured and simulated return loss and RHCP radiation pattern for the designed antenna at the operating frequency of 401.6 MHz, respectively, and the corresponding axial ratio pattern is given in Figure 6(c). The measured antenna gain is about 1.5 dB. From Figure 4, we can find that the 3 dB RHCP beamwidth is 152° and the 3 dB AR bandwidth is 89° for the proposed RHCP-MPA. And the simulated and measured results are in good agreement.

5. Conclusion

The ultrawide beam coverage of a RHCP corner-truncated antenna with a truncated cone ground plane and a metallic rectangular plate has been studied experimentally for operation in the 401.6 MHz UHF band. Employing the technique of laying gradually variational supporting platform under the MPA, the 3 dB RHCP beamwidth of a new MPA can be broadened effectively. The proposed antenna has a 3 dB RHCP beamwidth of 152°, which is about 70° greater than the conventional MPA and its RHCP gain is about 1.5 dB. By optimizing the shape of the metallic supporting platform, we can broaden the 3 dB RHCP beamwidth up to 200°, which is very suitable for applications of ultrawide beam coverage.

Conflict of Interests

The authors declare that there is no conflict of interests regarding the publication of this paper.

References

[1] M. V. T. Heckler and A. Dreher, "Analysis of conformal microstrip antennas with the discrete mode matching method," *IEEE Transactions on Antennas and Propagation*, vol. 59, no. 3, pp. 784–792, 2011.

[2] J. Lars and P. Patrik, *Conformal Array Antenna Theory and Design*, John Wiley & Sons, 2006.

[3] W. Kin-lin, *Planar Antenna for Wireless Communications*, John Wiley & Sons, 2003.

[4] C. Tang, J. Chiou, and K. Wong, "Beamwidth enhancement of a circularly polarized microstrip antenna mounted on a three-dimensional ground structure," *Microwave and Optical Technology Letters*, vol. 32, no. 2, pp. 149–153, 2002.

[5] H. Nakano, S. Shimada, J. Yamauchi, and M. Miyata, "A circularly polarized patch antenna enclosed by a folded conducting wall," in *Proceedings of the IEEE Conference on Wireless Communication Technology*, pp. 134–135, Honolulu, Hawaii, USA, 2003.

[6] T. L. Laubner and R. Schilling, "Microstrip antenna with improved low angle performance," US Patent Publication No. 1049520 A1, 2002.

[7] C.-W. Su, S.-K. Huang, and C.-H. Lee, "CP microstrip antenna with wide beamwidth for GPS band application," *Electronics Letters*, vol. 43, no. 20, pp. 1062–1063, 2007.

Research Article

A Codesigned Compact Dual-Band Filtering Antenna with PIN Loaded for WLAN Applications

Shanxiong Chen,[1] Yu Zhao,[2] Maoling Peng,[3] and Yunji Wang[4]

[1] College of Computer and Information Science, Southwest University, Chongqing 400715, China
[2] College of Computer Science and Technology, Zhoukou Normal University, Zhoukou 466001, China
[3] Department of Information Engineering, Chongqing City Management College, Chongqing 401331, China
[4] Electrical and Computer Engineering Department, The University of Texas at San Antonio, San Antonio, TX 78249, USA

Correspondence should be addressed to Yu Zhao; zhao_ue@163.com

A codesigned compact dual-band filtering antenna incorporating a PIN diode for 2.45/5.2 GHz wireless local area network (WLAN) applications is proposed in this paper. The integrated filtering antenna system consists of a simple monopole radiator, a microstrip dual-band band-pass filter, and a PIN diode. The performance of the filtering antenna is notably promoted by optimizing the impedance between the antenna and the band-pass filter, with good selectivity and out-of-band rejection. The design process follows the approach of the synthesis of band-pass filter. In addition, the PIN diode is incorporated in the filtering antenna for further size reduction, which also widens the coverage of the bandwidth by about 230% for 2.4 GHz WLAN. With the presence of small size and good filtering performances, the proposed filtering antenna is a good candidate for the wireless communication systems. Prototypes of the proposed filtering antenna incorporating a PIN diode are fabricated and measured. The measured results including return losses and radiation patterns are presented.

1. Introduction

The wireless local area network (WLAN) has experienced a rapid growth in the last decade, which has been widely employed in wireless applications such as WIFI, Bluetooth, and GPS. For further portability and better user experiences, the size reduction has been a trend in the wireless system designs. Generally, antennas and filters are considered as the critical components in reducing the whole sizes of the radio frequency (RF) front ends. In addition, the filter is usually connected right after the antenna, and the direct connection between them may induce additional mismatch losses and deteriorates the performances of the filter. Therefore, the integration of the antenna and the filter will be of great interest, which can provide both desired filtering and radiating functions.

Several efforts have been proposed in the literature [1–13] to integrate the antenna and the filter into a single module, and the sizes as well as operating bands are summarized in Table 1 [1–8]. The integration of the open-loop resonator loaded filter and the monopole antenna is presented in [3], which reduces the size of the filtering antenna by employing the antenna structure as the last resonator of the filter. The synthesis technique has been comprehensively studied in [2, 8], which is proved to be feasible by the example of an integrated 2.45 GHz third-order filtering antenna with good band-edge selectivity and design accuracy. What is more, compared to the traditional way of connecting the antenna and the filter by standard 50 Ω ports, the filtering antenna in [2, 8] reduces the transition loss to be near zero. For further reduction of the footprint of the integrated filtering antenna system, the integration of slot antenna and vertical cavity filter has been proposed in [7]. However, most of the referred filtering antennas are for single-band applications, which can hardly meet the demands of the current dual-band 802.11 a/b/g WLAN applications.

In this paper, a compact dual-band filtering antenna with printed structure for wireless communication systems is
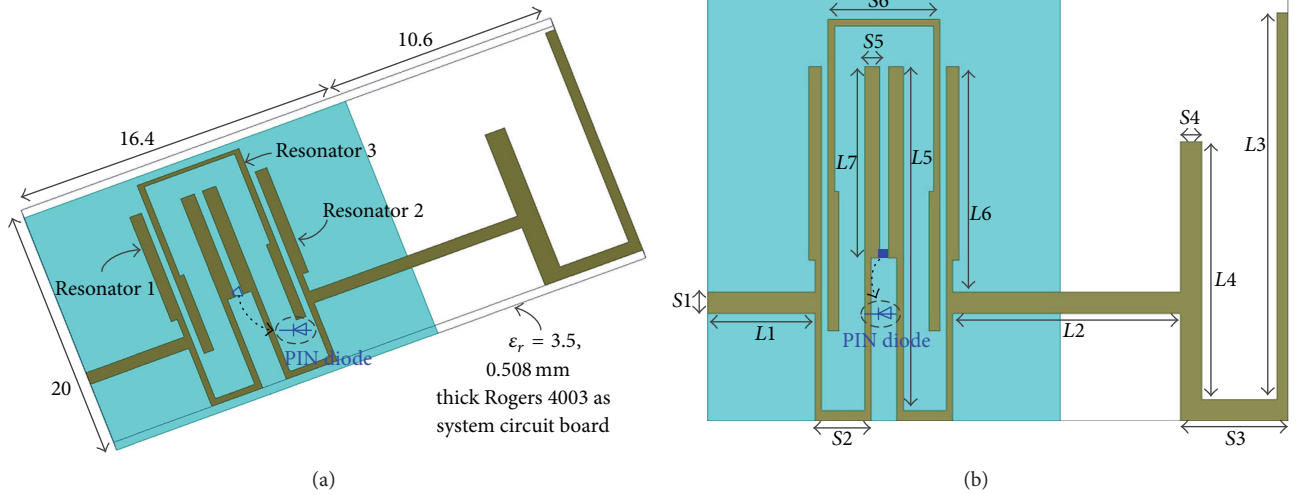
(a)

(b)

FIGURE 1: The proposed filtering antenna configuration. (a) Geometry of the dual-band filtering antenna. (b) Detailed dimensions of the filtering antenna ($L1 = 5$; $L2 = 10.6$; $L3 = 185$; $L4 = 12$; $L5 = 16$; $L6 = 10.5$; $L7 = 8.9$; $S1 = 1$; $S2 = 2.6$; $S3 = 5$; $S4 = 1$; $S5 = 1.8$; $S6 = 5.2$;). All dimensions are in millimeters.
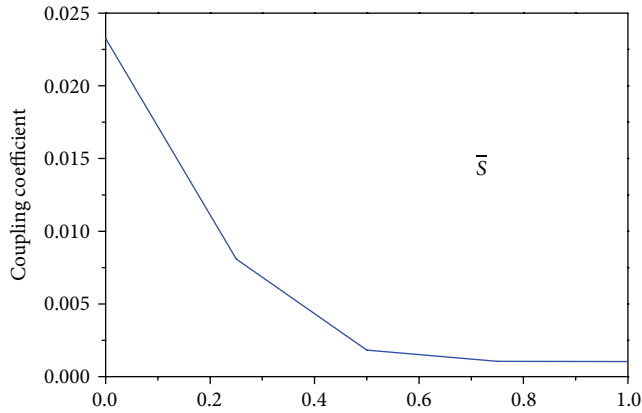

FIGURE 2: Coupling coefficient k as a function of the distance between resonator 1 and resonator 2.

TABLE 1: Comparison of the sizes of the filtering antenna.

Reference number	Total size	Operating bands	Type of the substrate
[1]	12.9×6.5 mm^2	X-band	Rogers 5880
[2]	60×60 mm^2	2.4 G WLAN	Rogers 4003
[3]	30×45 mm^2	2.4 G WLAN	$\varepsilon_r = 2.65$
[4]	10.9×10.9 mm^2	Ku-band	$\varepsilon_r = 2.54$
[5]	30×20 mm^2	4.06~4.26 GHz	
[6]	18×20 mm^2	4.7~5.2 GHz	$\varepsilon_r = 3.38$
[7]	12.5×9 mm^2	10~10.5 GHz	$\varepsilon_r = 3.48$
[8]	65.2×50 mm^2	2.4 G WLAN	$\varepsilon_r = 3.38$

proposed. The filtering antenna is integrated by a microstrip dual-band band-pass filter and a simple monopole antenna, which is conducted by utilizing the synthesis approach. Without restricting the impedance between the filter and the antenna to 50 Ω, the performances of the filtering system are promoted and the total loss of the filtering antenna is almost the same as the filter insertion loss. The presented

filtering antenna has a whole size of 27×20 mm^2, which is much smaller compared to the antenna referred to in [3]. To widen the bandwidth of the filtering antenna, reconfigurable technology [14–18] has been applied, which usually expands the bandwidth by combining different working states with a fixed size. In particular, the PIN diode is incorporated in the filtering antenna system, which covers the dual-band 2.45/5.2 GHz WLAN by combining the two working states. Fabrication of the printed filtering antenna is easy and of low cost, while the integrated filtering antenna has good band-edge selectivity and flat antenna gain. Measured radiation characteristics of the proposed filtering antenna are presented.

2. Design of the Filtering Antenna

Figure 1 depicts the layout of the proposed integrated filtering antenna, which is printed on a low-cost two-side printed substrate with relative dielectric constant of 3.5 and a thickness of 0.508 mm. The filtering antenna system includes three resonators of high Q values and one monopole antenna. The dual-band filtering antenna has a total size of 27×20 mm^2, which is realized due to the introduction of the PIN diode and is quite promising for wireless communication systems. Note that the dual-band band-pass filter is directly connected to the antenna, and the mismatch loss is correspondingly reduced.

2.1. Synthesis of the Dual-Band Filtering Antenna. A two-pole dual-band band-pass filter with a bandwidth of 30 MHz with centre frequency at 2.45 GHz and 435 MHz with centre frequency at 5.2 GHz is synthesized according to the dual-band filter synthesis technique [2]. The dual-band filter consisting of three stepped impedance resonators is printed on the 0.508 mm Rogers 4003 substrate. The value of the coupling coefficients $k12$ between resonator 1 and resonator 2 is 0.02, while the value of the external quality factors is 53.07.
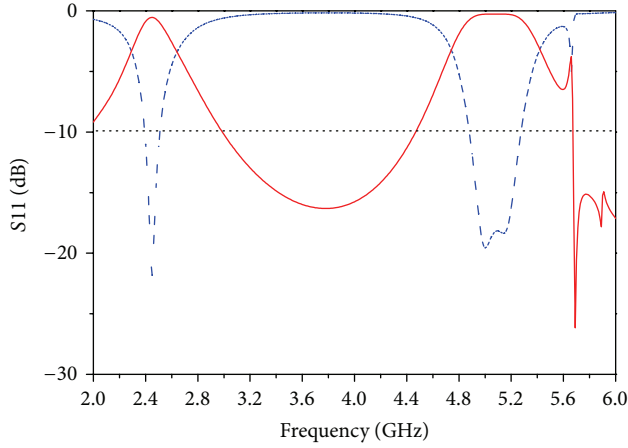
FIGURE 3: Simulated S parameters of the dual-band filter.

(a)

(b)

FIGURE 5: Simulated and measured reflection coefficient against frequency for the proposed filtering antenna: (a) for state1 and (b) for state2.
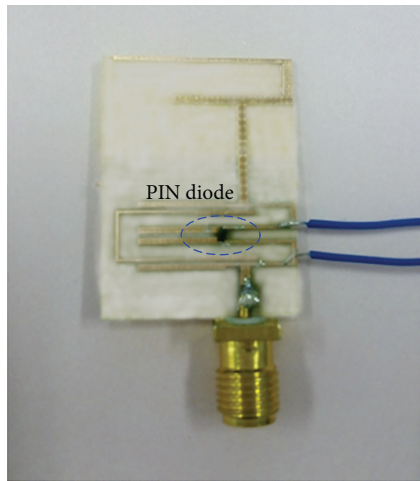
(a)
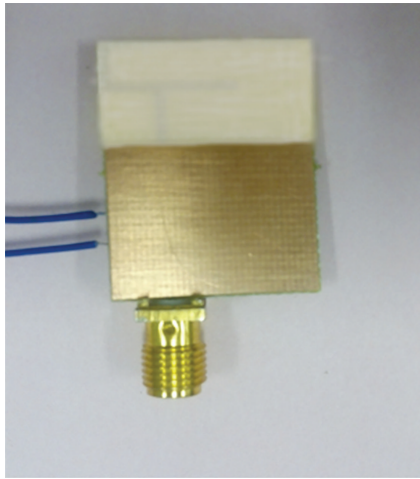
(b)

FIGURE 4: Photos of the manufactured dual-band filtering antenna for 2.45/5.2 GHz WLAN applications.

The referred coupling coefficient $k12$ depends on the relative distance of resonator 1 and resonator 2. The smaller the value of S is, the stronger the coupling between the resonators is.

The coupling coefficient k is calculated based on the following equation:

$$|k| = \left| \frac{f_1^2 - f_2^2}{f_1^2 + f_2^2} \right|, \qquad (1)$$

where f_1 and f_2 represent the eigenfrequencies of resonator 1 and resonator 2, respectively, which can be obtained through the optimization of the relative distance S between the resonators. The coupling coefficient as a function of the distance S between resonator 1 and resonator 2 is depicted in Figure 2. The optimized dimensions of the filter are given before, and the simulated $S11$ and $S21$ of the filter are plotted in Figure 3.

The dual-band two-strip monopole antenna which is designed based on the fixed ground plane has a size of $10.6 \times$
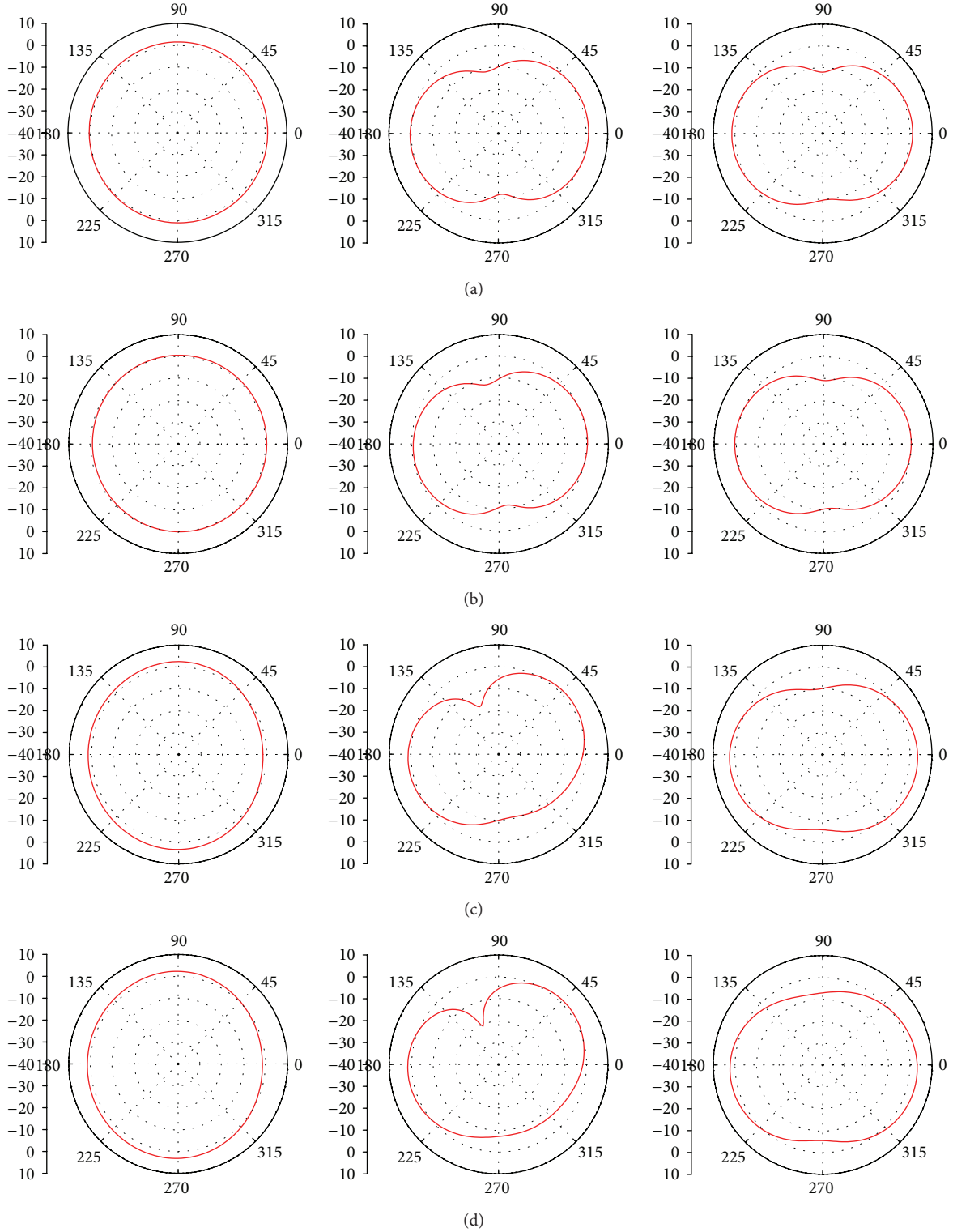
Figure 6: Measured 2D radiation patterns. (a) 2400 MHz; (b) 2450 MHz; (c) 5000 MHz; and (d) 5200 MHz for the proposed filtering antenna.

$20 \, \text{mm}^2$. The resonant frequencies are mainly determined to its total length, namely, the length of ($L2 + L3 + S3$). The lengths of the long strip (34.6) and the short strip (13.6 mm) are approximately a quarter-wavelength for 2.45 GHz and 5.2 GHz, respectively. The connecting line between the filter and the antenna is optimized, whose dimension is finally identified as 10.6 mm in length and 1.1 mm in width.

2.2. Implementation of the Reconfigurable Technology. To achieve larger bandwidth coverage, the PIN diode is incorporated in the filtering antenna, which is located in the coupling structure of the filter. As a result, the bandwidth of the filtering antenna is expanded with a fixed size. When the PIN diode is OFF (state1), the PIN diode is equivalent to a series capacitance with high isolation and the filtering antenna works in the previously mentioned state, covering the 2425–2465 MHz and 4785–5220 MHz. When the PIN diode is ON (state2), it works as a series resistance; then resonator 2 and resonator 3 are directly connected; thus the path of the currents is changed and the resonant frequencies are shifted towards lower frequencies, covering the 2340–2430 MHz and 4740–5100 MHz. Therefore, by combining the two working states, the bandwidth of the filtering antenna is increased by about 40% with the addition of the PIN diode, covering the 2.45/5.2 GHz WLAN operation. The prototype is fabricated under the consideration of the PIN diode and its DC bias circuit.

3. Results and Discussion

The proposed dual-band filtering antenna system was fabricated and tested. Photos of the fabricated filtering antenna system and the PIN diode as well as its corresponding DC are shown in Figure 4. The simulated results of the integrated filtering antenna are achieved based on the HFSS 13.0, while the measured results are given by using the Agilent N5247A network analyzer and the Satimo StarLab far field measurement system. Simulated and measured $S11$ against the frequency for the two working states are shown in Figure 5. Type of the PIN diode is selected as Philips BAP64-03, while the DC bias current is supplied by two AAA batteries. The filtering antenna successfully changes its working states to widen the bandwidth by nearly 80 MHz (230%) for 2.4 GHz WLAN and 49 MHz for 5.2 GHz WLAN. The measured results show that the presented filtering antenna provides good selectivity and out-of-band rejection.

Measured radiation patterns for the proposed filtering antenna system in the *x-z*, *y-z*, and *x-y* planes are shown in Figure 6, which is conducted at 2400 and 5000 MHz for state1 as well as 2450 and 5200 MHz for state2. For all the different frequencies for the two working states, the measured radiation patterns are dipole-like, which are nearly omnidirectional in the azimuth plane for the two bands.

4. Conclusion

In this paper, a small-size dual-band filtering antenna incorporating the PIN diode is proposed. The presented filtering antenna system is printed on the low-cost substrate and occupies a total size of 20×27 mm^2. Through the incorporation of the PIN diode, the bandwidth of the filtering antenna is increased by nearly 230% for 2.4 GHz WLAN, covering the dual-band 2.45/5.2 GHz WLAN operation. Performance of the filtering antenna system is promoted through the optimization of the impedance between the filter and the monopole antenna. In addition, by directly connecting the antenna and the filter, the mismatch loss is greatly reduced. According to the measured results, the proposed filtering antenna system has good selectivity and out-of-band rejection, which prove that the filtering antenna is applicable for the RF front end for modern wireless systems.

Conflict of Interests

The authors declare that there is no conflict of interests regarding the publication of this paper.

References

[1] Y. Yusuf, H. T. Cheng, and X. Gong, "Co-designed substrate-integrated waveguide filters with patch antennas," *IET Microwaves, Antennas & Propagation*, vol. 7, no. 7, pp. 493–501, 2013.

[2] C.-T. Chuang and S.-J. Chung, "Synthesis and design of a new printed filtering antenna," *IEEE Transactions on Antennas and Propagation*, vol. 59, no. 3, pp. 1036–1042, 2011.

[3] W.-J. Wu, Y.-Z. Yin, S.-L. Zuo, Z.-Y. Zhang, and J.-J. Xie, "A new compact filter-antenna for modern wireless communication systems," *IEEE Antennas and Wireless Propagation Letters*, vol. 10, pp. 1131–1134, 2011.

[4] M. Troubat, S. Bila, M. Thévenot et al., "Mutual synthesis of combined microwave circuits applied to the design of a filter-antenna subsystem," *IEEE Transactions on Microwave Theory and Techniques*, vol. 55, no. 6, pp. 1182–1189, 2007.

[5] J. Zuo, X. Chen, G. Han, L. Li, and W. Zhang, "An integrated approach to RF antenna-filter co-design," *IEEE Antennas and Wireless Propagation Letters*, vol. 8, pp. 141–144, 2009.

[6] C.-K. Lin and S.-J. Chung, "A compact filtering microstrip antenna with quasi-elliptic broadside antenna gain response," *IEEE Antennas and Wireless Propagation Letters*, vol. 10, pp. 381–384, 2011.

[7] Y. Yusuf, H. Cheng, and X. Gong, "A seamless integration of 3-D vertical filters with highly efficient slot antennas," *IEEE Transactions on Antennas and Propagation*, vol. 59, no. 11, pp. 4016–4022, 2011.

[8] C.-T. Chuang and S.-J. Chung, "A compact printed filtering antenna using a ground-intruded coupled line resonator," *IEEE Transactions on Antennas and Propagation*, vol. 59, no. 10, pp. 3630–3637, 2011.

[9] S. W. Wong and L. Zhu, "EBG-embedded multiple-mode resonator for UWB bandpass filter with improved upper-stopband performance," *IEEE Microwave and Wireless Components Letters*, vol. 17, no. 6, pp. 421–423, 2007.

[10] A. I. Abunjaileh, I. C. Hunter, and A. H. Kemp, "Application of dual-mode filter techniques to the broadband matching of microstrip patch antennas," *IET Microwaves, Antennas and Propagation*, vol. 1, no. 2, pp. 273–276, 2007.

[11] L. Liu, Y. Z. Yin, C. Jie, J. P. Xiong, and Z. Cui, "A compact printed antenna using slot-type CSRR for 5.2 GHz/5.8 GHz band-notched UWB application," *Microwave and Optical Technology Letters*, vol. 50, no. 12, pp. 3239–3242, 2008.

[12] D. Jiang, Y. Xu, R. Xu, and W. Lin, "Compact dual-band notched UWB planar monopole antenna with modified CSRR," *Electronics Letters*, vol. 48, no. 20, pp. 1250–1252, 2012.

[13] S. Nikolaou, N. D. Kingsley, G. E. Ponchak, J. Papapolymerou, and M. M. Tentzeris, "UWB elliptical monopoles with a reconfigurable band notch using MEMS switches actuated without bias lines," *IEEE Transactions on Antennas and Propagation*, vol. 57, no. 8, pp. 2242–2251, 2009.

[14] Y. Li, Z. Zhang, W. Chen, Z. Feng, and M. F. Iskander, "A Switchable matching circuit for compact wideband antenna designs," *IEEE Transactions on Antennas and Propagation*, vol. 58, no. 11, pp. 3450–3457, 2010.

[15] Y. Tawk, J. Costantine, K. Avery, and C. G. Christodoulou, "Implementation of a cognitive radio front-end using rotatable controlled reconfigurable antennas," *IEEE Transactions on Antennas and Propagation*, vol. 59, no. 5, pp. 1773–1778, 2011.

[16] Q.-Q. He and B.-Z. Wang, "Pattern reconfigurable double folded slot antenna with background conductor," *Electronics Letters*, vol. 43, no. 15, pp. 791–792, 2007.

[17] X.-S. Yang, B.-Z. Wang, W. Wu, and S. Xiao, "Yagi patch antenna with dual-band and pattern reconfigurable characteristics," *IEEE Antennas and Wireless Propagation Letters*, vol. 6, pp. 168–171, 2007.

[18] G.-M. Zhang, J.-S. Hong, B.-Z. Wang, G. Song, and P. Li, "Design and time-domain analysis for a novel pattern reconfigurable antenna," *IEEE Antennas and Wireless Propagation Letters*, vol. 10, pp. 365–368, 2011.

Research Article

Small-Size Eight-Band Frequency Reconfigurable Antenna Loading a MEMS Switch for Mobile Handset Applications

Xin Meng[1,2]

[1] School of Electronic Information Engineering, Tianjin University, Tianjin 300072, China
[2] School of Computer and Communication Engineering, Tianjin University of Technology, Tianjin 300384, China

Correspondence should be addressed to Xin Meng; meng_tjut@163.com

A planar small-size eight-band frequency reconfigurable antenna for LTE/WWAN mobile handset applications is proposed. The proposed antenna consists of a feeding strip and a coupled strip, with a total dimension of 10×29.5 mm^2. Reconfigurability is realized by incorporating a one-pole four-throw RF switch, which is embedded in the coupled strip and changes the resonant modes for the lower band. By combining four different working modes, the proposed antenna successfully realize the eight-band operation, covering the operating bands of 700~787 MHz, 824~960 MHz, and 1710~2690 MHz. In addition, the simple DC bias circuit of the RF switch has little effect on the antenna performances, with no significant reduction in antenna efficiency and variations in the radiation patterns. The measured antenna efficiencies are 40%~50% and over 60% for the lower band and the upper band, respectively. Prototypes of the proposed frequency reconfigurable antenna incorporating the one-pole four-throw switch are fabricated and measured. The measured results including return losses and radiation characteristics are presented.

1. Introduction

Portable devices with wireless connectivity have experienced a rapid growth in the last decade, which also face the great challenge to cope with various wireless standards (WIFI, Bluetooth, GPS, and GSM) with a wide bandwidth. For further portability and better user experiences, the size reduction has been a trend in the wireless system designs. Nevertheless, designing an internal multiband antenna for mobile handsets within a small size is still full of challenges.

To reduce the antenna size and achieve wide bandwidth, a great deal of methods have been proposed, such as the couple-fed method referred in [1–4], the parallel resonance method used in [5], and the distributed inductor proposed in [6, 7]. For further size reduction, these traditional wideband methods with single working state are limited. Considering the limited space for antenna design for mobile handsets, reconfigurable technology [8–17] is a good candidate. By using the reconfigurable technology, the antenna can work in several states to obtain wide bandwidth with a reduced size. Commonly, the reconfigurability is achieved by RF MEMS switches [8–11], PIN diodes [11–15], and varactors [16, 17].

Reconfigurable antennas loading PIN diodes referred in [13–15] have significantly reduced the sizes of the multiband antennas, and they have also been proved with acceptable insertion losses. However, the PIN diode usually acts as a resistance, while larger dc power is required to gain lower insertion loss in practical applications. From this respect, the MEMS RF switches referred in [8–12] are more practical, which have much lower insertion losses [11] and smaller effect on the radiation characteristics as well as lower costs in comparison with the PIN diodes.

In this paper, a printed frequency reconfigurable antenna with a one-pole four-throw RF switch loaded for eight-band WWAN/LTE mobile handset applications is proposed. The reconfigurable antenna comprises a simple structure of a feeding strip, a coupled strip, and a one-pole four-throw RF switch as well as its DC bias circuit. The RF switch works in four different states and changes the resonant modes through modifying the values of the lump inductors. By combining the four different states, the proposed antenna successfully covers the eight-band operation of GSM850/900/1800/1900/UMTS2100/LTE2300/2500. With a total size of 10×29.5 mm^2, the proposed antenna is much smaller in contrast
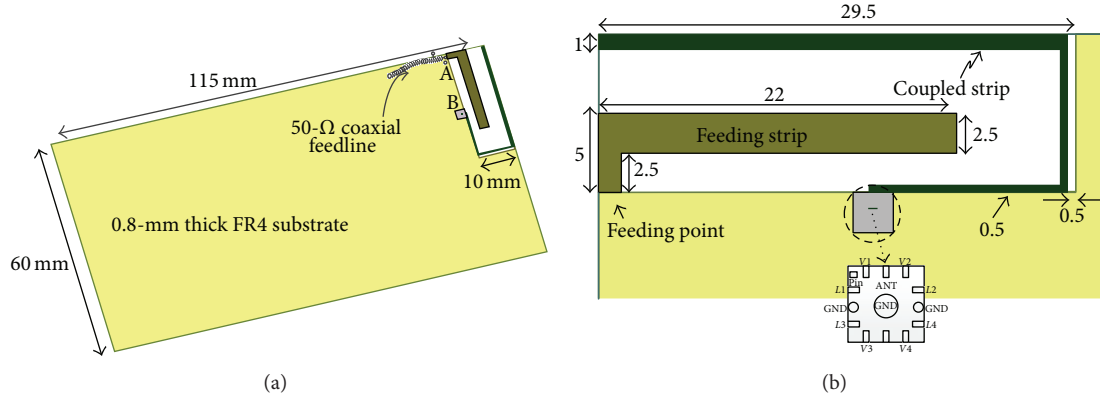
(a)

(b)

FIGURE 1: Proposed reconfigurable antenna configuration. (a) Geometry of the frequency reconfigurable antenna. (b) Detailed dimensions of the reconfigurable antenna ($L1 = 6.8$ nH; $L2 = 9.2$ nH; $L3 = 15$ nH; $L4 = 17$ nH; GND: ground point). All dimensions are in millimeters.
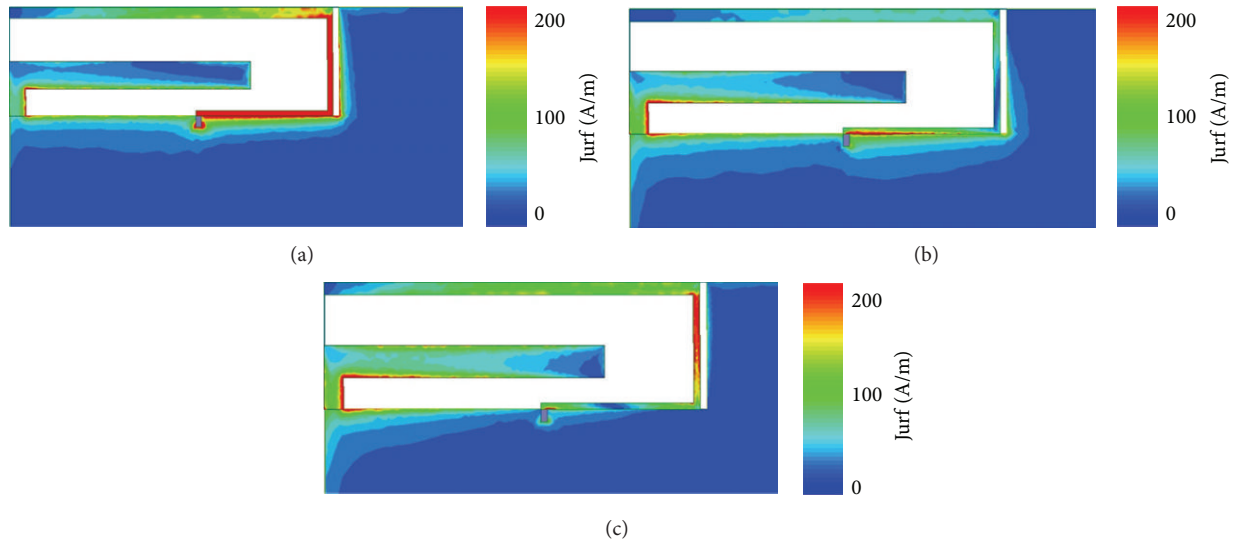

(a)

(b)

(c)

FIGURE 2: Simulated current distributions at different frequencies. (a) 925 MHz; (b) 1850 MHz; (c) 2470 MHz.

to the antenna referred in [12, 14]. Moreover, compared to the antenna in [5], the proposed antenna has a smaller size and an extra coverage of LTE700 operation, which is mainly due to the combination of four different working states of the RF MEMS switch. Although the insertion of the RF switch may exert influences to the antenna performances, the effects such as insertion losses and the impedance matching are quite acceptable and proved practical for mobile handset applications [11], considering the great benefits of minimization and band expansion with the incorporation of the RF MEMS switch. Fabrication of the printed reconfigurable antenna is easy and its cost is low, while the antenna has good performances and small insertion losses. Measured radiation characteristics of the proposed reconfigurable antenna are presented.

2. Proposed Reconfigurable Antenna

Figure 1(a) depicts the geometry of the proposed antenna, which has a total size of 10×29.5 mm^2 and is printed on

a 0.8 mm-thick FR4 substrate with relative dielectric constant of 4.4 and loss tangent of 0.02. The frequency reconfigurable antenna consists of a coupled-fed antenna and a one-pole four-throw RF switch and its corresponding DC bias circuits. Detailed dimensions of the printed antenna and the one-pole four-throw RF switch are given in Figure 1(b). The coupled-fed antenna comprises a feeding strip and a coupled strip, while the coupled strip is grounded through the RF switch. Furthermore, the RF switch is located within the dotted line as shown in Figure 1(b), and its ground (GND) pins are connected with the back-side system ground via metallized holes. The embedded inductors are controlled by the corresponding DC bias voltages ($V1$, $V2$, $V3$, $V4$) and only one inductor is involved in each working state with other inductors unoccupied. For example, when $V1$ is supplied with high voltage and the other three ports are in low level, then the lumped inductor $L1$ is incorporated and the antenna works in the state of $L1$.

In the proposed antenna, the monopole feeding strip contributes a resonant mode at about 1850 MHz, while the other
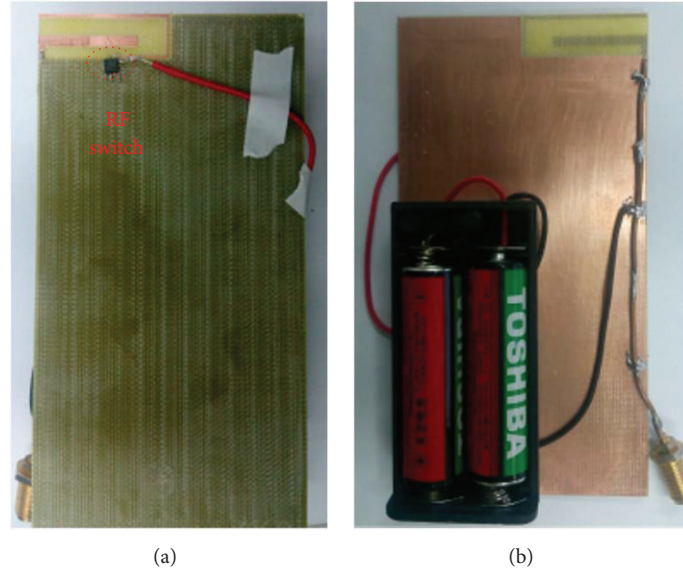
(a)   (b)

FIGURE 3: Photos of the manufactured reconfigurable antenna for eight-band mobile handset applications.

(a)

(b)
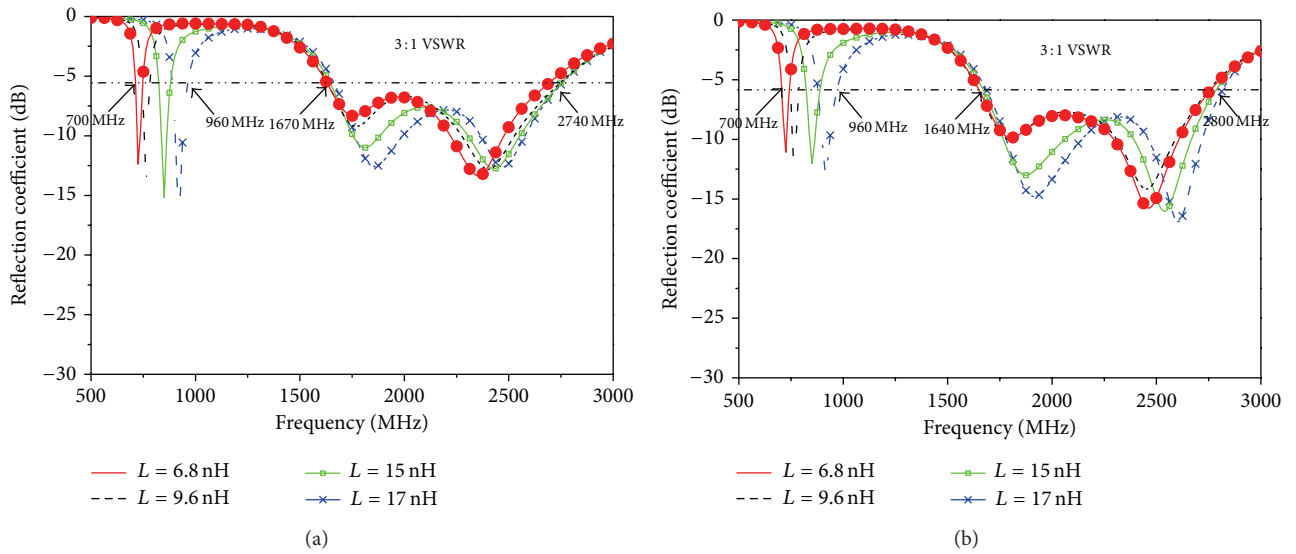
FIGURE 4: Simulated and measured reflection coefficient against frequency for the proposed antenna. (a) Simulated results. (b) Measured results.

resonant mode is generated by the coupled strip at about 2470 MHz for the upper band. Therefore, a wide bandwidth is achieved by combining the two resonant modes, covering the GSM1800/1900/UMTS2100/LTE2300/2500 operation. One resonant mode is contributed by the coupling strip for the lower band. In particular, the referred one-pole four-throw RF switch is applied to modify the resonant frequencies, which can effectively expand the coverage by combining four different working states. Actually, the optimization process of the antenna is not so easy, which needs to meet the requirements of impedance matching in different states. Specially, the RF switch is located in the shorting point of the coupled strip and there is little influence on the upper band when

the working state is switched. Then the reconfigurability is finally realized to cover the LTE700/GSM850/900 operation.

Figure 2 shows the simulated current distributions for the proposed antenna at the resonant frequencies of 925 MHz, 1850 MHz, and 2470 MHz. For clear explanation, only the state of $L = 6.8$ nH is selected for the lower band. As shown in Figure 2(a), the current distributions on the coupled strip are much stronger, suggesting that the resonant mode at about 925 MHz is mainly contributed by the coupled strip. With the same principle, the other three resonant modes for the lower band can be explained. From Figure 2(b), it can be seen that strong current flows along with the feeding strip and the coupled strip, confirming that the feeding strip

FIGURE 5: Measured 2D radiation patterns. (a) 750 MHz; (b) 925 MHz; (c) 1925 MHz; (d) 2350 MHz for the proposed filtering antenna ($\text{-}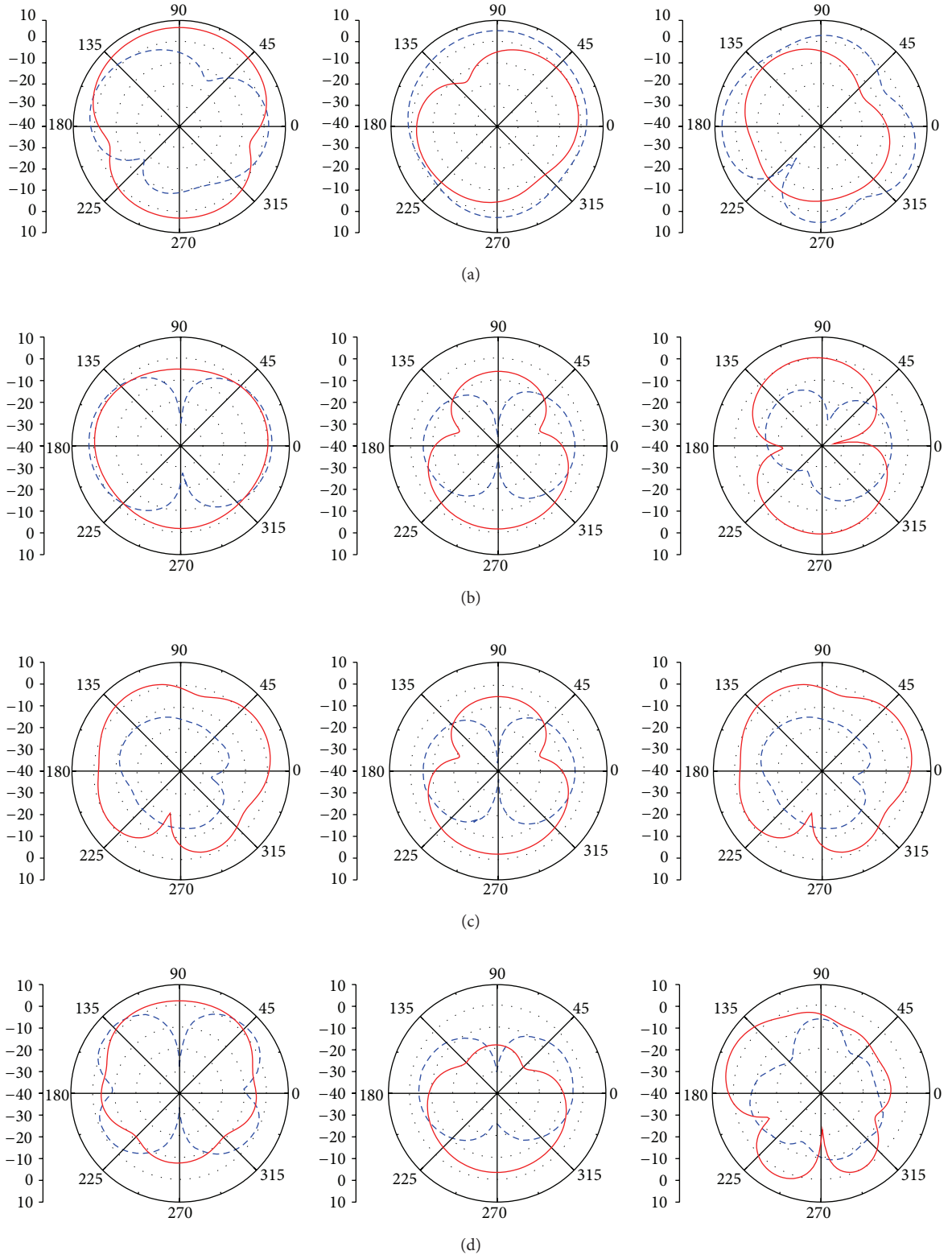\,\text{-}\,\text{-}\,\text{-}\,\text{-}\,\text{-}\,\text{-}\,\text{-}\,\text{-}\,\text{-}$ E_φ, ——— E_θ).
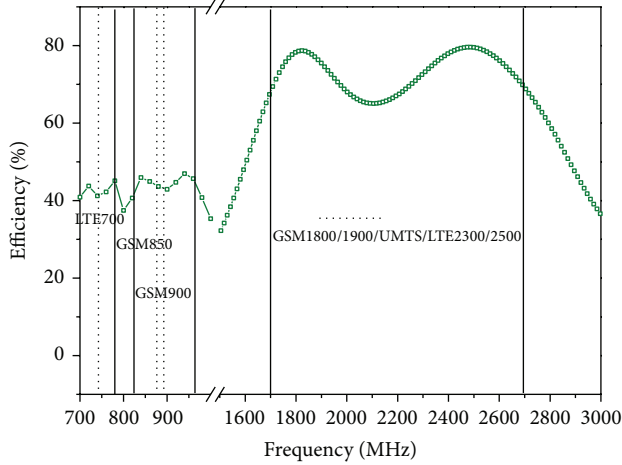
FIGURE 6: Measured antenna efficiencies (mismatching losses included) against frequency for the proposed antenna.

contributes much for the resonant mode at about 1850 MHz. Figure 2(c) depicts that the strong current distributions are on the coupled strip, proving that the resonant mode at about 2470 MHz is generated by the coupled strip.

3. Results

The proposed printed reconfigurable antenna was fabricated and tested. Photos of the fabricated antenna and the one-pole four-throw RF switch (FMS2016QFN-1) as well as its corresponding DC bias circuits are shown in Figure 3. The simulation and optimization of the reconfigurable antenna are based on the HFSS 12.0, and the measured results are obtained by using the network analyzer and the Satimo StarLab far field measurement system. The simulated and measured reflection coefficients against the frequency for the four working states are plotted in Figure 4 with good agreement, and little effect is found for the upper band when the state of the RF switch changes. The DC bias voltage is supplied by two AAA batteries, and the working state can be switched by changing the voltage level of different ports ($V1$, $V2$, $V3$, $V4$). By combining the four working states, the reconfigurable antenna successfully covers the LTE700GSM850/900/1800/1900/UMTS2100/LTE2300/2500 operation.

Measured radiation patterns for the proposed reconfigurable antenna in the x-z, y-z, and x-y planes are shown in Figure 5, which is conducted at 750, 925, 1925, and 2350 MHz. For all the different frequencies, complementary E_φ and E_θ are observed, which are favorable in practical applications since the position of the mobile handset is unfixed. Some variations are also found, which is largely due to the manufacture tolerance as well as the effects of coaxial cables and the RF switch.

The measured antenna efficiency of the reconfigurable is shown in Figure 6, which is conducted under the consideration of the RF switch. For the lower bands of LTE700/850/900,

the antenna efficiency varies in a range of 40%~50%, confirming that the introduced RF switch brings acceptable insertion loss for the proposed antenna. For the upper bands of GSM1800/1900/UMTS2100/LTE2300/2500, the antenna efficiency is over 60%. The measured results reveal that the proposed reconfigurable antenna has good radiation characteristics.

4. Conclusion

In this paper, a small-size frequency reconfigurable antenna incorporating the one-pole four-throw RF switch for eight-band mobile handset applications is proposed. The presented reconfigurable antenna is directly printed on the FR4 substrate and occupies a total size of 10×29.5 mm^2. By combining the four working states, the operating bands of LTE700GSM850/900/1800/1900/UMTS2100/LTE2300/2500 are successfully covered. According to the measured results, the proposed reconfigurable antenna has good radiation characteristics, which prove that the antenna is applicable for the mobile handset applications.

Conflict of Interests

The author declares that there is no conflict of interests regarding the publication of this paper.

Acknowledgment

References

[1] K.-L. Wong and T.-J. Wu, "Small-size LTE/WWAN coupled-fed loop antenna with band-stop matching circuit for tablet computer," *Microwave and Optical Technology Letters*, vol. 54, no. 5, pp. 1189–1193, 2012.

[2] Q. Liu, Y. F. Yu, and S. He, "Capacitively loaded, inductively coupled fed loop antenna with an omnidirectional radiation pattern for UHF RFID tags," *IEEE Antennas and Wireless Propagation Letters*, vol. 12, pp. 1161–1164, 2013.

[3] C.-W. Chiu, C.-H. Chang, and Y.-J. Chi, "Multiband folded loop antenna for smart phones," *Progress in Electromagnetics Research*, vol. 102, pp. 213–226, 2010.

[4] K.-L. Wong, W.-Y. Chen, and T.-W. Kang, "On-board printed coupled-fed loop antenna in close proximity to the surrounding ground plane for penta-band WWAN mobile phone," *IEEE Transactions on Antennas and Propagation*, vol. 59, no. 3, pp. 751–757, 2011.

[5] K.-L. Wong, Y.-W. Chang, and S.-C. Chen, "Bandwidth enhancement of small-size planar tablet computer antenna using a parallel-resonant spiral slit," *IEEE Transactions on Antennas and Propagation*, vol. 60, no. 4, pp. 1705–1711, 2012.

[6] Y.-L. Ban, C.-L. Liu, L.-W. Li, and R. Li, "Small-size wide-band monopole with distributed inductive strip for seven-band WWAN/LTE mobile phone," *IEEE Antennas and Wireless Propagation Letters*, vol. 12, pp. 7–10, 2013.

[7] K.-L. Wong and Y.-C. Liu, "Small-size WWAN tablet computer antenna with distributed and lumped parallel resonant circuits,"

Microwave and Optical Technology Letters, vol. 54, no. 6, pp. 1348–1353, 2012.

[8] C.-H. Ko, K. M. J. Ho, and G. M. Rebeiz, "An electronically-scanned 1.8–2.1 GHz base-station antenna using package high-reliability RF MEMS phase shifters," *IEEE Transactions on Microwave Theory and Techniques*, vol. 61, no. 2, pp. 979–985, 2013.

[9] M. Abou Al-alaa, H. A. Elsadek, E. A. Abdallah, and E. A. Hashish, "Pattern and frequency reconfigurable monopole disc antenna using PIN diodes and MEMS switched," *Microwave and Optical Technology Letters*, vol. 56, no. 1, pp. 187–195, 2014.

[10] B. Khalichi, S. Nikmehr, and A. Pourziad, "Reconfigurable SIW antenna based on RF switches," *Progress in Electromagnetics Research*, vol. 142, pp. 189–205, 2013.

[11] C. G. Christodoulou, Y. Tawk, S. A. Lane, and S. R. Erwin, "Reconfigurable antennas for wireless and space applications," *Preceedings of IEEE*, vol. 100, no. 7, pp. 2250–2261, 2012.

[12] Y. K. Park and Y. Sung, "A reconfigurable antenna for quad-band mobile handset applications," *IEEE Transactions on Antennas and Propagation*, vol. 60, no. 6, pp. 3003–3006, 2012.

[13] I. Ben Trad, J. M. Floc'h, H. Rmili, M. Drissi, and F. Choubani, "A planar reconfigurable radiation pattern dipole antenna with reflectors and directors for wireless communication applications," *International Journal of Antennas and Propagation*, vol. 2014, Article ID 593259, 10 pages, 2014.

[14] Y. Li, Z. Zhang, J. Zheng, Z. Feng, and M. F. Iskander, "A compact hepta-band loop-inverted F reconfigurable antenna for mobile phone," *IEEE Transactions on Antennas and Propagation*, vol. 60, no. 1, pp. 389–392, 2012.

[15] H. T. Liu, S. Gao, and T. H. Loh, "Low-cost intelligent antenna with low profile and broad bandwidth," *IET Microwave Antenna & Propagation*, vol. 7, no. 5, pp. 356–364, 2013.

[16] S. Baylis, S. Aguilar, and T. Weller, "Wide bandwidth varactor-tuned patch antenna," *Electronics Letters*, vol. 45, no. 16, pp. 816–818, 2009.

[17] F. Costa, A. Monorchio, S. Talarico, and F. M. Valeri, "An active high-impedance surface for low-profile tunable and steerable antennas," *IEEE Antennas and Wireless Propagation Letters*, vol. 7, pp. 676–680, 2008.

Research Article

High Gain and High Efficient Stacked Antenna Array with Integrated Horn for 60 GHz Communication Systems

Hamsakutty Vettikalladi, Waleed Tariq Sethi, and Majeed A. Alkanhal

Electrical Engineering Department, King Saud University, Saudi Arabia

Correspondence should be addressed to Hamsakutty Vettikalladi; hvettikalladi@ksu.edu.sa

In order to achieve wide bandwidth and high gain, we propose a stacked antenna structure having a microstrip aperture coupled feeding technique with a mounted Horn integrated on it. With optimized parameters, the single antenna element at a center frequency of 60 GHz, exhibits a wide impedance bandwidth of about 10.58% (58.9–65.25 GHz) with a gain and efficiency of 11.78 dB and 88%, respectively. For improving the gain, we designed a 2×2 and 4×4 arrays with a corporate feed network. The side lobe levels were minimized and the back radiations were reduced by making use of a reflector at $\lambda/4$ distance from the corporate feed network. The 2×2 array structure resulted in improved gain of 15.3 dB with efficiency of 83%, while the 4×4 array structure provided further gain improvement of 18.07 dB with 68.3% efficiency. The proposed design is modelled in CST Microwave Studio. The results are verified using HFSS, which are found to be in good agreement.

1. Introduction

Soon after the development of 60 GHz standard that provides a 7 GHz license-free bandwidth worldwide, its popularity became evident at millimeter waves spectrum due to its usage in high data-rate wireless communications at gigabit per second [1, 2]. The huge amount of bandwidth availability attracted the researchers for its use in many terrestrial and space applications. In this modern era of consumer electronic gadgets, even telephony and cable operated devices in offices and homes are trending towards wireless technology. The demand for higher data rate of these multimedia technologies can be resolved with 60 GHz standard as being a viable candidate.

In any radio communication or wireless systems, antenna plays a vital part [3–5]. Since its development, the microstrip planar antennas [6] have gained popularity in telecommunication and radar applications due to its lightweight and low profile configurations. Microstrip patch antennas are among the best candidates for implementing in microwave and millimeter waves (MMW) frequency and they are good candidates for arrays as well. There are several reports devoted to the design and explanation of such antennas using arrays [7–12]. However, the traditional microstrip antennas

have reached their maximum usability as they offer narrow bandwidth (3%) and low gain. Researchers investigated new methods and came up with coupling techniques to improve impedance bandwidth. The proposed solution by Pozar [13] is provided with wide bandwidth and high gain as compared to conventional microstrip antennas. The aperture coupling method enabled the patch antennas to be easily integrated into arrays, with active circuits, to minimize spurious radiations from the feed, and to introduce more freedom of substrates selections. Many techniques have been explained in the literature for improving bandwidth and gain at MMW [14–20].

In this paper, a stacked microstrip antenna utilizing aperture-coupled technique with a mounted Horn on FR-4 substrate is presented, at a center frequency of 60 GHz. By employing this technique, a wide impedance bandwidth of about 10.58% (58.9–65.25 GHz) is achieved with high gain and efficiency. The gain and efficiency of the single element antenna are further increased by presenting a corporate fed network of 2×2 and 4×4 arrays. The 2×2 array structure resulted in improved gain of 15.3 dB with efficiency of 83%. While the 4×4 array structure provided further gain improvement of 18.07 dB with 68.3% efficiency. This paper
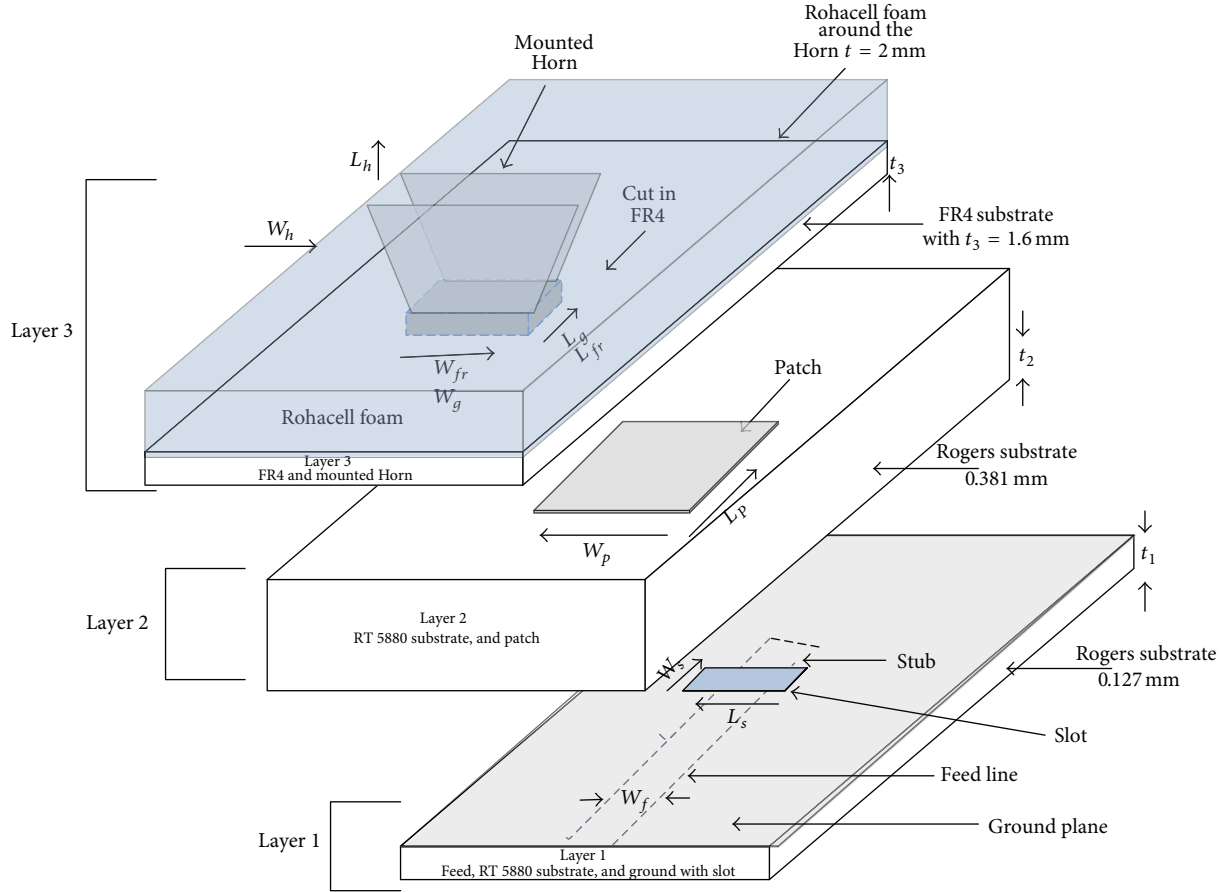
FIGURE 1: Exploded view of proposed multilayer ACMPA with mounted Horn.

is an extended work of our previous results [21], which had limited bandwidth. Comparing with previous results [21], the proposed single element antenna's simulation results show improvement in terms of bandwidth and gain at millimeter waves (MMW).

2. Design of Antenna Element

The geometry of the single antenna element is shown in Figure 1. The design is a combination of aperture coupled microstrip antenna (ACMPA) and a Horn antenna mounted on FR4 substrate, where the waveguide part of the horn is integrated into FR4 substrate. The model was designed and optimized using RF simulation software CST Microwave Studio and the results were reconfirmed via HFSS. The antenna is tuned to operate in a wide band of frequencies at 60 GHz. The multilayer antenna has three substrates with layers I and II having Rogers Duroid RT-5880 with $\epsilon r = 2.2$ and $\tan\delta = 0.003$ and thickness $t_1 = 0.127$ mm and $t_2 = 0.381$ mm while the third layer has FR-4 as a substrate with $\epsilon r = 4.3$ and thickness $t_3 = 1.6$ mm and a mounted Horn. The addition of FR4 has no other effect, except to provide support to the mounted Horn on the antenna performance. The ground with thickness ($t = 2 \times 0.0175$ mm) is made of conducting metal with a rectangular slot perpendicular

to the microstrip feed having dimensions of L_s and W_s as given in Table 1. Coupling efficiencies between the aperture in the ground and the patch can be improved as investigated in [22]. The patch is located on the top of the substrate, at layer II, and has dimensions of L_p and W_p as given in Table 1. The dimensions of substrates and ground are taken as 30×30 mm^2. The $50\,\Omega$ microstrip feed line at the bottom of lower substrate has a feed width of $W_f = 0.386$ mm as calculated from Ansoft designer [23]. Table 1 shows the optimized values for the proposed antenna.

With the aid of simulation tools, the proposed multilayer antenna was numerically optimized and the results were obtained. The objective was to achieve a wide bandwidth, high gain, and efficiency. Compared to [21], the impedance bandwidth improved significantly with almost the same gain. Due to the addition of 0.381 mm thickness substrate, the impedance bandwidth achieved was about 10.58% (58.9–65.25 GHz) with gain and efficiency of 11.78 dB and 88%, respectively. The simulation has taken into account the substrate and metallic losses. Figure 2 shows the bandwidth and gain comparison between two simulators for the single element antenna design. The two resonances seen in Figure 2 at 59.7 GHz and 63.5 GHz are due to the patch on layer II and the aperture of the Horn antenna integrated on it. Since this design is an extension of [21], the dimensions of the

TABLE 1: Parameters of proposed antenna in mm.

Design	Antenna element	Dimensions/parameters
Layer I	Microstrip feed	Feed width, $W_f = 0.386$
		Thickness, $t = 0.0175$
		Stub length, $L_{fs} = 0.45$
	Substrate	RT Duroid 5880
		Length, $L = 30$
		Width, $W = 30$
		$\epsilon r = 2.2$
		$\tan \delta = 0.003$
		Thickness, $t_1 = 0.127$
		Thickness, $t = 0.0175$
	Ground	Length $L = 30$
		Width $W = 30$
		Thickness, $t = 0.0175$
	Rectangular slot	Slot length, $L_s = 1$
		Slot width, $W_s = 0.2$
Layer II	Substrate	RT Duroid 5880
		Thickness, $t_2 = 0.381$
		$\epsilon r = 2.2$
		$\tan \delta = 0.003$
		Length, $L = 30$
		Width, $W = 30$
	Patch	Length, $L_p = 1.2$
		Width, $W_p = 1.2$
Layer III	Substrate	FR 4
		Thickness, $t_3 = 1.6$
		$\epsilon r = 4.3$
		$\tan \delta = 0.025$
	Cut in FR-4	Length, $L_{fr} = 3$
		Width, $W_{fr} = 4.25$
Horn	Horn dimensions	Horn length, $L_h = 7.14$
		Horn width, $W_h = 7.14$
		Waveguide length, $L_g = 3$
		Waveguide width, $W_g = 4.25$
		Thickness of metal horn, $t = 2$
Full structure	Total height	4

rectangular waveguide were optimized as given in Table 1. The initial length of the rectangular waveguide was chosen to be $L_g = \lambda_0/2$, which is a half wavelength at 60 GHz. The rectangular waveguide length has an effect on the reflection coefficient, which is minimum when L_g is around $\lambda_0/2$.

Figures 3(a) and 3(b) show the E-plane and H-plane radiation patterns, simulated in CST and HFSS, of the proposed antenna, for the frequencies at 59, 62, and 65 GHz, respectively. Thus for the multilayer structure at 62 GHz, the E-plane has side lobe of level −5 dB, half-power beamwidth of 31°, and a back radiation of −18.3 dB. The H-plane radiation pattern at 62 GHz has a side lobe of −13.2, half-power beamwidth of 69.8°, back radiation of −17 dB, and cross polarization level of > −30 dB.
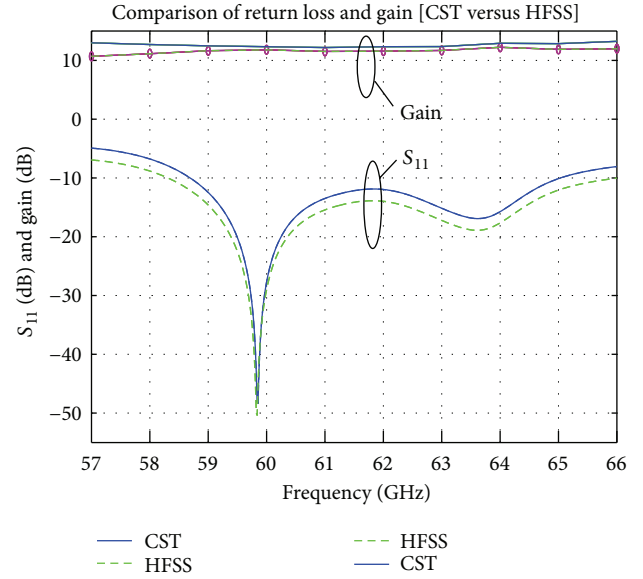

FIGURE 2: Comparison of return loss and gain.

3. Design of Antenna Array

Limited methods exist in analyzing the antenna arrays. In the existing methods, arrays factor is the easiest one among others [6]. In simplest terms, array theory works on the principle that each antenna element is treated as an individual isotropic point source. Energy contributions from each point source are derived in the far field expressed as array factor (AF). The method of array factor is based on the theorem of orientation multiplying [6]:

$$AF(f, \theta) = \sum_{n=1}^{4} e^{jnkd \sin \theta}. \tag{1}$$

The array factor depends only on the geometry of the array and the phase between each element. The actual radiator then replaces each point and the far field radiation pattern is determined by pattern multiplying the array factor with the pattern of the radiator. Mutual coupling is ignored in the process since the radiators are treated separately; also their influences on each other are not considered. Since we are working on improving the gain of the antenna, therefore, the mutual coupling cannot be ignored and the results deduced by array factor must be modified.

3.1. 2 × 2 Array. The next step is to improve the gain by making use of 2 × 2 and 4 × 4 arrays. The 3D exploded view of the 2 × 2 arrays structure is shown in Figure 4, where a copper reflector element of distance $\lambda/4$ has been introduced below layer I to suppress the back radiations of the array. An important aspect in designing an array is the optimal distance between the patches or antenna elements to reduce mutual coupling among them. Mutual coupling has a noteworthy influence on the performance of antenna array. Mutual coupling affects several factors such as inputting resistance, orientation pattern of array, gain of the array, and
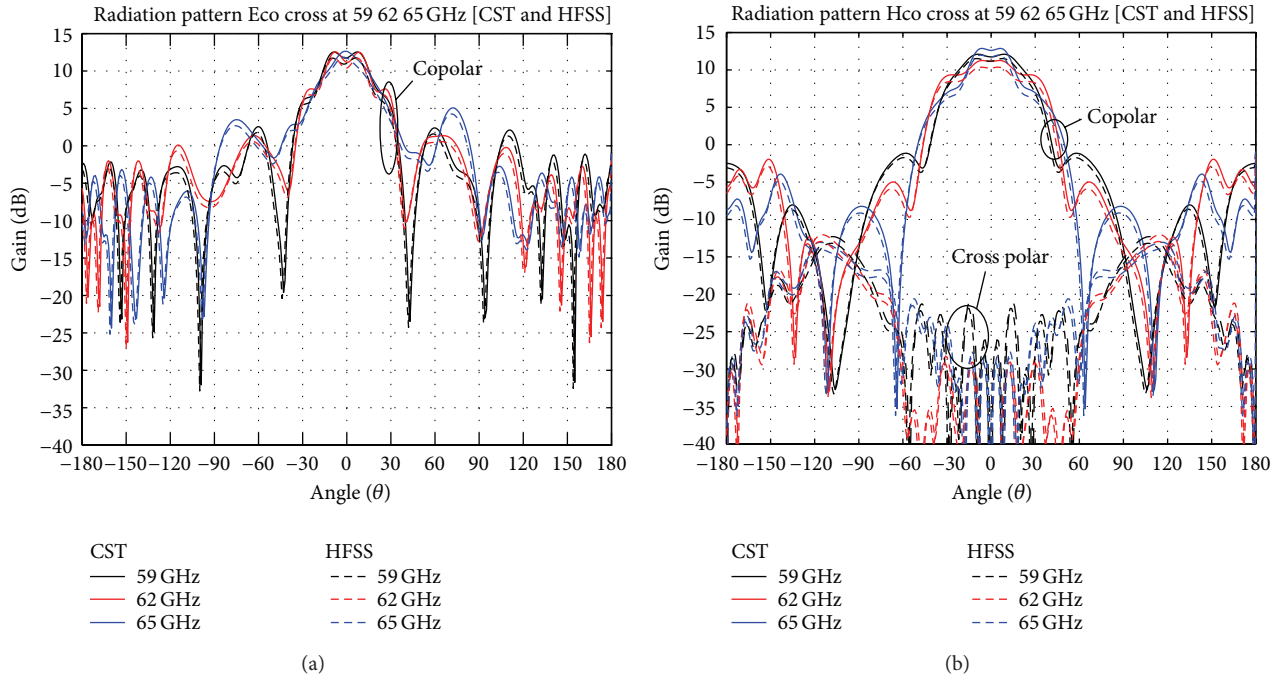
FIGURE 3: (a) Simulated E-plane radiation pattern at 59, 62, and 65 GHz and (b) simulated H-plane radiation pattern at 59, 62, and 65 GHz.
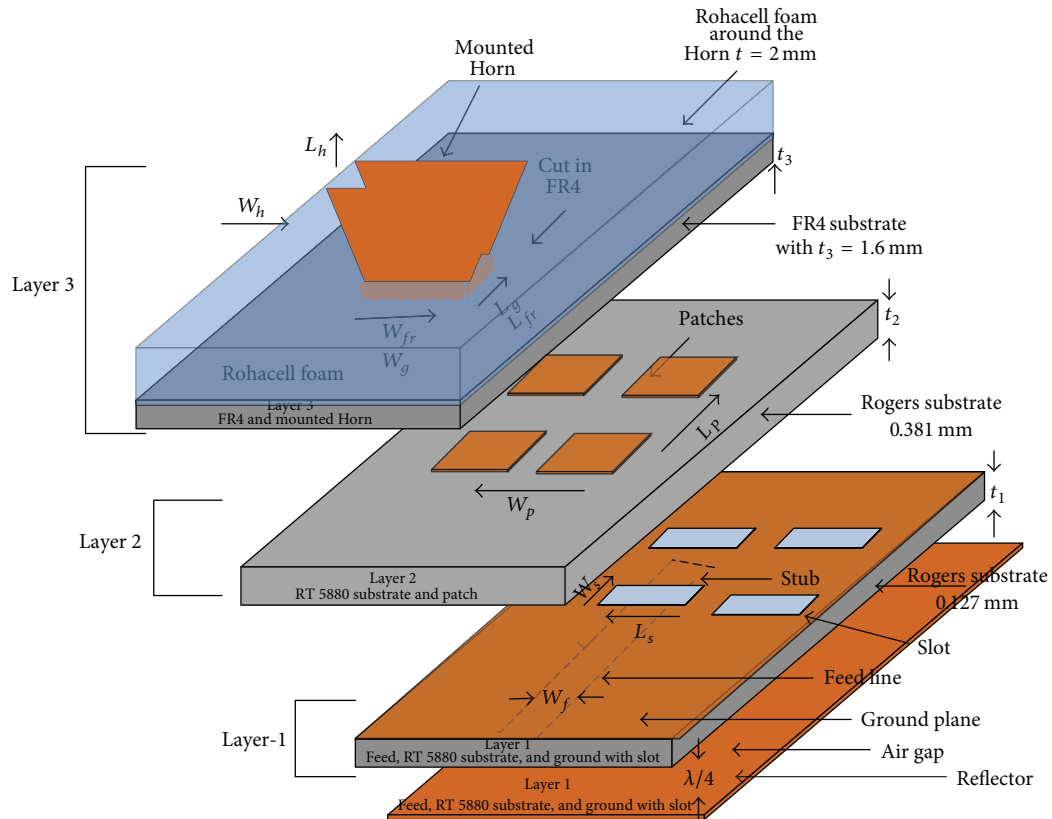

FIGURE 4: Exploded view of 2×2 multilayer array with $\lambda/4$ reflector.

its polarization [24–27]. In our proposed array design, center-to-center distances between patches were optimized from 0.5λ to 1λ that gave minimum coupling and maximum gain. The element spacing was selected to be $0.82\lambda_o$ in the x-y direction for both 2×2 and 4×4 arrays.

A corporate feed network connected to a 50 Ω line was used as power division between antenna elements. Corporate feed networks are in general very versatile as they offer power splits of 2^n (i.e., n = 2, 4, 8, 16, 32, etc.) and control to the designer in terms of amplitude and phase selection of individual feed element and its power division among the transmission lines. It is ideal for scanning phased arrays, shaped-beam arrays, and multibeam arrays [6]. The length and width of the transmission lines can be varied as per requirement of power division. The feed network consists of 50 Ω transmission line and 70.7 Ω quarter-wavelength transformers matched to primary 50 Ω feeding line. The corporate feed network for 2×2 arrays is shown in Figure 5.

Analyzing the top half of feed network shown in Figure 5 and because of symmetry, two 50 Ω lines coming from each antenna are connected to two 70.7 Ω lines where each of them is a quarter wave transformer. This transforms each line into a 100 Ω line. Now we have two 100 Ω lines in parallel resulting in 50 Ω line. This 50 Ω is again connected to quarter wave transformer resulting in 100 Ω line. Similarly, another 100 Ω is available from the bottom half of the circuit resulting in a final 50 Ω line connected and matched to the main 50 Ω feed. The lengths and widths of 50 Ω and 70.7 Ω used in this feed network are shown in Table 2.

The proposed antenna of 2×2 array was simulated via simulation tools. Figure 6 shows the comparison between simulators on the simulated return loss and gain for 2×2 arrays. Impedance bandwidth remains the same as 10.58% (58.9–65.25 GHz). The gain and efficiency are 15.3 dB and 88%, respectively. Due to the introduction of 0.381 mm substrate as compared to previous work [21], some parameters of the multilayer antenna design were optimized for the array structures to achieve wide bandwidth and impedance matching. The rest of the parameters were kept the same as presented in Table 1. The modified parameters are shown in Table 3.

The E-plane and H-plane radiation patterns, simulated in CST and HFSS, for 2×2 array structure at frequencies 59, 62, and 65 GHz are shown in Figures 7(a) and 7(b), respectively. It is observed that the E-plane at 62 GHz has a side lobe of level −13.7 dB, half-power beamwidth of 22.1°, and a back radiation of −25.3 dB. The H-plane radiation pattern at 62 GHz has a side lobe of −9.1 dB, half-power beamwidth of 22.2°, back radiation of −21.8 dB, and cross polarization level of > −30 dB.

3.2. 4×4 Array. Similarly, the 4×4 array was simulated and the comparison of results in terms of return loss and gain is shown in Figure 8. Impedance bandwidth achieved is 10.58% (58.9–65.25 GHz) at 60 GHz. The gain and efficiency are 18.07 dB and 68.3%, respectively. Figures 9(a) and 9(b) show radiation patterns at 59, 62, and 65 GHz for 4×4 array.
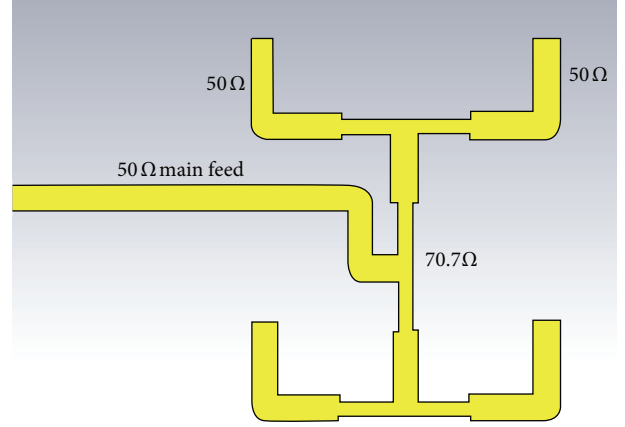
FIGURE 5: Corporate-feed network for 2×2 array.
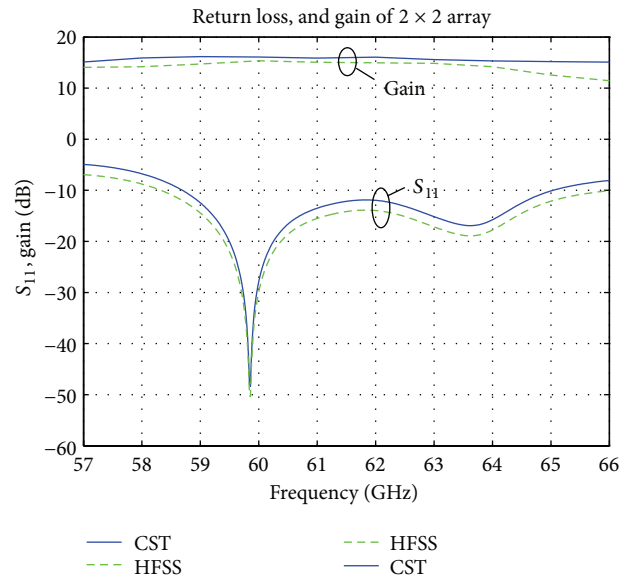
FIGURE 6: Return loss and gain of 2×2 array.

TABLE 2: Lengths and widths of 50 Ω and 70.7 Ω feeds.

Transmission line	Width (mm)	Length (mm)
50 Ω	0.386	1.07
70.7 Ω	0.2262	0.93

The E-plane at 62 GHz has a side lobe of level −11.8 dB, half-power beamwidth of 13.6°, and a back radiation of −23.07 dB. The H-plane radiation pattern at 62 GHz has a side lobe of −12.4, half-power beamwidth of 16.1°, and a back radiation of −23.07 dB. Table 4 shows the comparison of improved gain from single element to 2×2 and 4×4 arrays.

4. Conclusion

A high gain and wide band multilayer antenna for 60 GHz are proposed in this paper. Stacked structure technique

FIGURE 7: (a) E-plane radiation pattern at 59, 62, and 65 GHz for 2 × 2 array and (b) H-plane radiation pattern at 59, 62, and 65 GHz for 2 × 2 array.
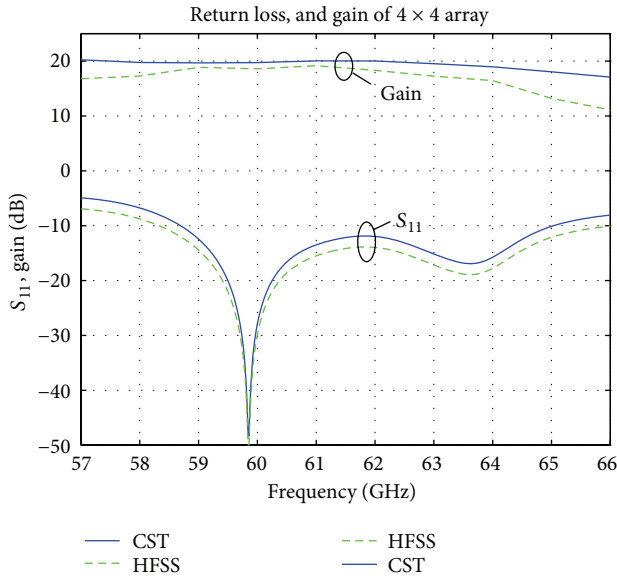
FIGURE 8: Return loss and gain of 4 × 4 array.

TABLE 3: Modified antenna parameters.

Parameters	2 × 2 array	4 × 4 array
Patch length, L_p	1.25	1.25
Patch width, W_p	1.25	1.25
Stub length, L_{fs}	0.45	0.45
Horn length, L_{hr}	12	12
Horn width, W_{hr}	18	20

TABLE 4: Simulated results of single element and 2 × 2 and 4 × 4 arrays.

Array/parameters	Single element	2 × 2 array	4 × 4 array
Bandwidth	10.58%	10.55%	10.51%
Gain	11.78 dB	15.3 dB	18.07 dB
Efficiency	88%	83%	68.3%

employing aperture coupled feeding with mounted Horn antenna is employed as the radiator for the single element, 2 × 2 and 4 × 4 arrays. The proposed antenna exhibits a broad impedance bandwidth of about 10.5% (58.9–65.25 GHz). Comprised by the proposed antenna element, an antenna array is investigated. Simulated results in CST and HFSS show that the antenna array realized provides a maximum gain and efficiency of 18.07 dB and 68.3%, respectively. The proposed antenna finds application in V-band communication systems.

Conflict of Interests

The authors declare that there is no conflict of interests regarding the publication of this paper.
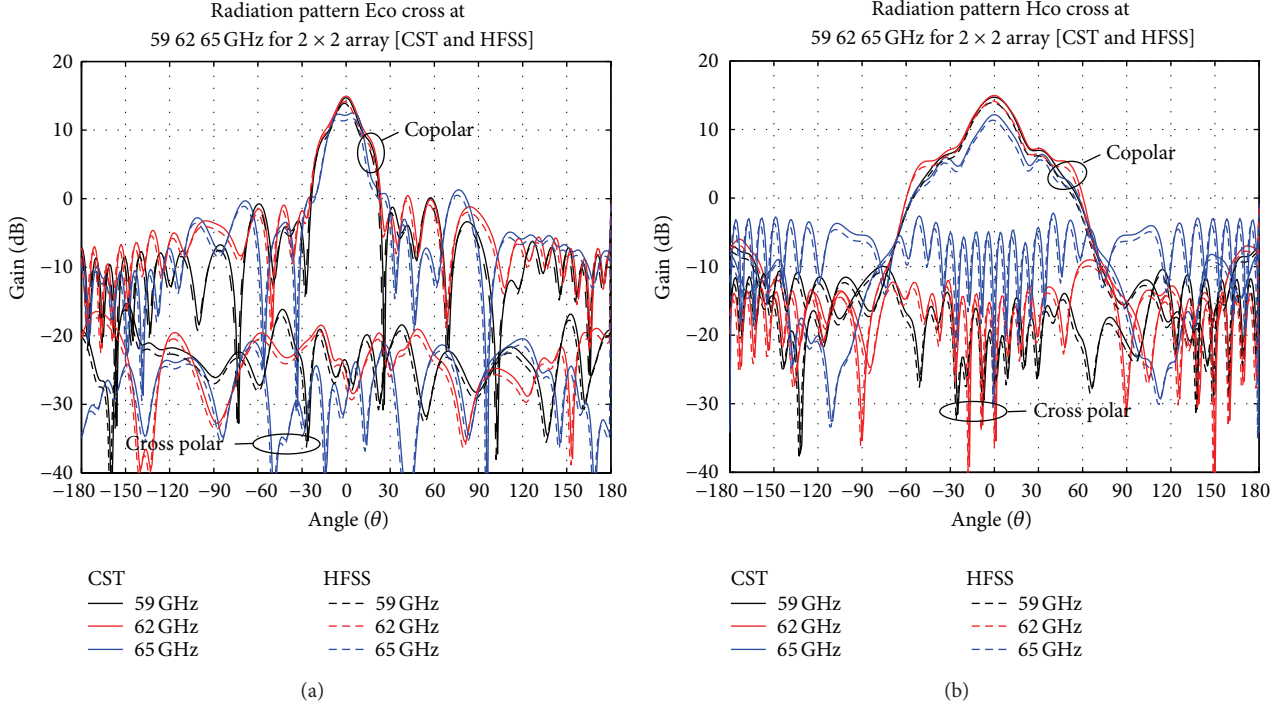
FIGURE 9: (a) E-plane radiation pattern at 59, 62, and 65 GHz for 4 × 4 array and (b) H-plane radiation pattern at 59, 62, and 65 GHz for 4 × 4 array.
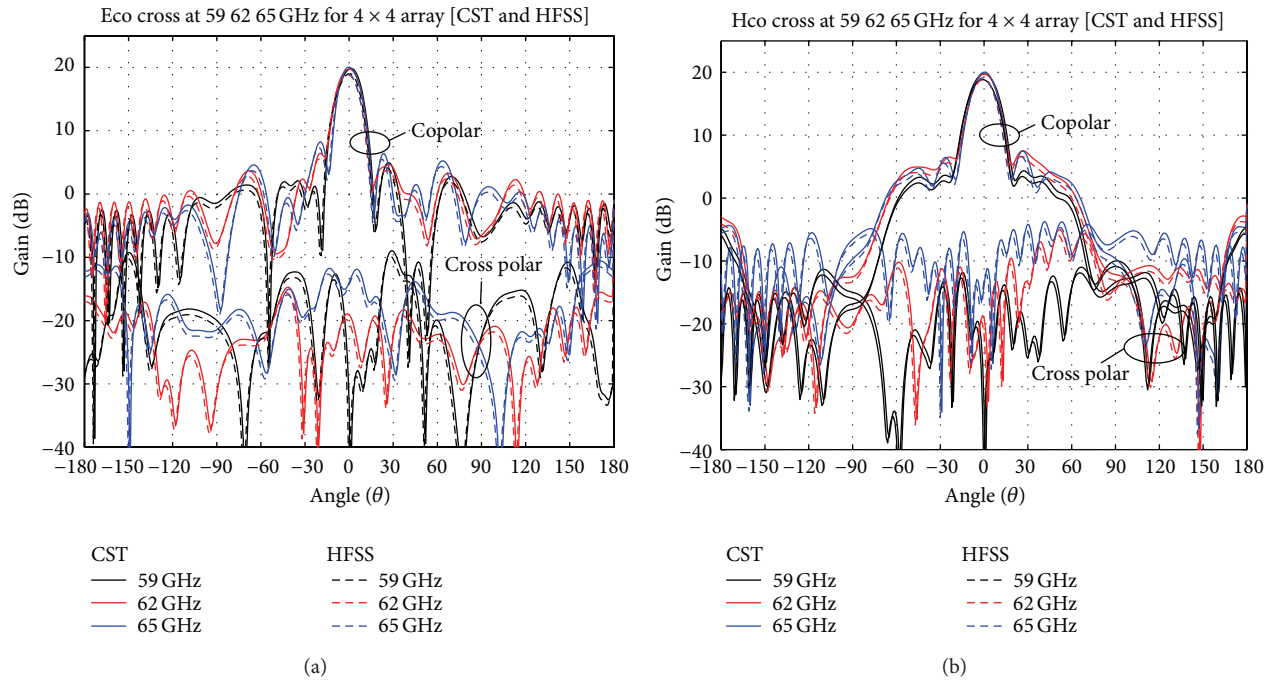
Acknowledgment

References

[1] IEEE.802.15.WPANTG3c, 2009, http://www.ieee802.org/15/pub/TG3c.html.

[2] "Standard ECMA: High Rate 60 GHz PHY, MAC & HDMI PAL," 2008, http://www.ecmainternational.org/publications/files/ECMAST/Ecma-387.pdf.

[3] C. Kärnfelt, P. Hallbjörner, H. Zirath, and A. Alping, "High gain active microstrip antenna for 60-GHz WLAN/WPAN applications," *IEEE Transactions on Microwave Theory and Techniques*, vol. 54, no. 6, pp. 2593–2603, 2006.

[4] I.-S. Chen, H.-K. Chiou, and N.-W. Chen, "V-band on-chip dipole-based antenna," *IEEE Transactions on Antennas and Propagation*, vol. 57, no. 10, pp. 2853–2861, 2009.

[5] Y. P. Zhang, M. Sun, K. M. Chua, L. L. Wai, and L. Duixian, "Antenna-in-package design for wirebond interconnection to highly integrated 60-GHz radios," *IEEE Transactions on Antennas and Propagation*, vol. 57, no. 10, pp. 2842–2852, 2009.

[6] C. A. Balanis, *Antenna Theory: Analysis and Design*, John Wiley and Sons, New York, NY, USA, 2nd edition, 1997.

[7] Y. Kim and D. L. Jaggard, "The fractal random array," *Proceedings of the IEEE*, vol. 74, pp. 1278–1280, 1986.

[8] C. Puente-Baliarda and R. Pous, "Fractal design of multiband and low side-lobe arrays," *IEEE Transactions on Antennas and Propagation*, vol. 44, no. 5, pp. 730–739, 1996.

[9] D. M. Pozar and D. H. Schaubert, *Microstrip Antennas, the Analysis and Design of Microstrip Antennas and Arrays*, IEEE Press, New York, NY, USA, 1995.

[10] L. Stark, "Microwave theory of phased-array antennas–a review," *Proceedings of the IEEE*, vol. 62, no. 12, pp. 1661–1701, 1974.

[11] A. A. Efanov and H. W. Thim, "Corporate-fed 2 × 2 planar microstrip patch sub-array for the 35 GHz band," *Antennas and Propagation Magazine*, vol. 37, no. 5, pp. 49–51, 1995.

[12] K. F. Lee, R. Q. Lee, and T. Talty, "Microstrip subarray with coplanar and stacked parasitic elements," *Electronics Letters*, vol. 26, no. 10, pp. 668–669, 1990.

[13] D. Pozar, *A Review of Aperture Coupled Microstrip Antennas: History, Operation, Development, and Applications*, Lecture Note, 1996.

[14] H. Vettikalladi and M. A. S. Alkanhal, "BCB-Si based wide band millimeter wave antenna fed by substrate integrated waveguide," *International Journal of Antennas and Propagation*, vol. 2013, Article ID 816050, 4 pages, 2013.

[15] O. Lafond, M. Himdi, and J. P. Daniel, "Thick slot-coupled printed antenna arrays for a 60 GHz indoor communication system," *Microwave and Optical Technology Letters*, vol. 28, pp. 105–108, 2001.

[16] H. Vettikalladi, O. Lafond, and M. Himdi, "High-efficient and high-gain superstrate antenna for 60-GHz indoor communication," *IEEE Antennas and Wireless Propagation Letters*, vol. 8, pp. 1422–1425, 2009.

[17] H. Vettikalladi, L. le Coq, O. Lafond, and M. Himdi, "Efficient and high-gain aperture coupled superstrate antenna arrays for 60 GHz indoor communication systems," *Microwave and Optical Technology Letters*, vol. 52, no. 10, pp. 2352–2356, 2010.

[18] H. Vettikalladi, L. le Coq, O. Lafond, and M. Himdi, "Wideband and high efficient aperture antenna with superstrate for 60 GHz

indoor communication systems," in *Proceedings of the IEEE International Symposium on Antennas and Propagation and CNC-USNC/URSI Radio Science Meeting—Leading the Wave (AP-S/URSI '10)*, Toronto, Canada, July 2010.

[19] H. Vettikalladi, L. le Coq, O. Lafond, and M. Himdi, "Broadband superstrate aperture antenna for 60 GHz applications," in *Proceedings of the 13th European Microwave Week (EuMW '10)*, pp. 687–690, Paris, France, September 2010.

[20] N. Ashraf, H. Vettikalladi, and M. A. Alkanhal, "Substrate integrated waveguide antennas/array for 60 GHz wireless communication systems," in *Proceedings of the IEEE International RF and Microwave Conference (RFM '13)*, 2013.

[21] W. T. Sethi, H. Vettikalladi, and M. A. Alkanhal, "Millimeter wave antenna with mounted horn integrated on FR4 for 60 GHz Gbps communication systems," *International Journal of Antennas and Propagation*, vol. 2013, Article ID 834314, 5 pages, 2013.

[22] V. Rathi, G. Kumar, and K. P. Ray, "Improved coupling for aperture coupled microstrip antennas," *IEEE Transactions on Antennas and Propagation*, vol. 44, no. 8, pp. 1196–1198, 1996.

[23] "Ansoft designer version 4".

[24] R. P. Jedlicka, M. T. Poe, and K. R. Carver, "Measure mutual coupling between microstrip antennas," *IEEE Transactions on Antennas and Propagation*, vol. 29, no. 1, pp. 147–149, 1981.

[25] M. Malkomes, "Mutual coupling between microstrip patch antennas," *Electronics Letters*, vol. 18, no. 12, pp. 520–522, 1982.

[26] E. Penard and J. P. Daniel, "Mutual coupling between microstrip antennas," *Electronics Letters*, vol. 18, no. 14, pp. 605–607, 1982.

[27] E. H. van Lil and A. R. van de Capelle, "Transmission line model for mutual coupling between microstrip antennas," *IEEE Transactions on Antennas and Propagation*, vol. 32, no. 8, pp. 816–821, 1984.

Research Article

Small-Size Wearable High-Efficiency TAG Antenna for UHF RFID of People

Milan Svanda and Milan Polivka

Faculty of Electrical Engineering, Czech Technical University in Prague, Technická 2, 166 27 Prague 6, Czech Republic

Correspondence should be addressed to Milan Svanda; svandm1@fel.cvut.cz

This paper introduces a small-size, low-profile wearable radiator based on the coupled patches and vertically folded patches techniques for application as a tag antenna for identification of people in the European UHF RFID band. The electric field distribution comes out dominantly from the central coupling slot, and thus the electric properties of the radiator are almost unaffected by the human body to which the antenna is intended to be attached. Accordingly, with the relative size $0.14 \times 0.12 \times 0.009\ \lambda_0$ at 866 MHz ($50 \times 40 \times 3.04\ \text{mm}^3$), the antenna exhibits total efficiency better than 50%, even if it is attached directly to a person.

1. Introduction

Modern body area network (BAN) communication systems [1–5] and also radiofrequency identification systems (RFID) [6–12] require small-size, low-weight, inexpensive radiators, which can be easily integrated into electronic devices or, for example, on human clothes.

The coupled patches technique, introduced and employed in [13–15], developed especially for screening the influence of the human body, enables the design of wearable antennas with an extremely low profile (typically lower than $0.003\ \lambda_0$) and at the same time sufficient radiation efficiency typically better than 50%. This is a significantly better value than the radiation efficiency of the common half or quarter wavelength patch antenna of the same size and height [16]. However, this technique does not enable the resonant length of the antenna to be smaller than approximately $0.3\ \lambda_0$ [14]. Thus, further miniaturization of antenna footprint size is a challenge for researchers.

Capacitive loading of a shorted patch antenna and its generalization, a vertically folded patch technique, which enables a half or quarter wavelength patch antenna to be minimized by means of repeat folding of the patch cavity, was presented in [17, 18]; see Figure 1.

In this paper, we present a novel small-size high-efficient UHF RFID tag antenna of overall electrical size $ka = 0.58$ combining both of the techniques mentioned above. The coupled patches technique, which excites the maximum electric field magnitude in the central coupling slot, enables high radiation efficiency to be achieved with a very low profile, together with good immunity from the human body as opposite sides are formed by metallic walls (see Figure 1(b)), which reduce the interaction of electric field with the base material. At the same time, the vertically folded patches technique enables a smaller footprint size of the structure to be achieved together with an acceptable increase in antenna height.

2. Design, Realization, and Measurement

Figure 2 depicts a sketch and a photograph of the manufactured vertically folded coupled patches UHF RFID antenna. The antenna is manufactured on a low-permittivity substrate Taconic RF-30 with $\varepsilon_r = 3.0$ and loss tangent $\tan \delta = 0.002$. The total size of the proposed antenna is $50 \times 40 \times 3.04\ \text{mm}^3$, which gives a relative size of $0.14 \times 0.12 \times 0.009$ λ_0 at 866 MHz; that is, $ka = 0.58$, where a is the diameter of
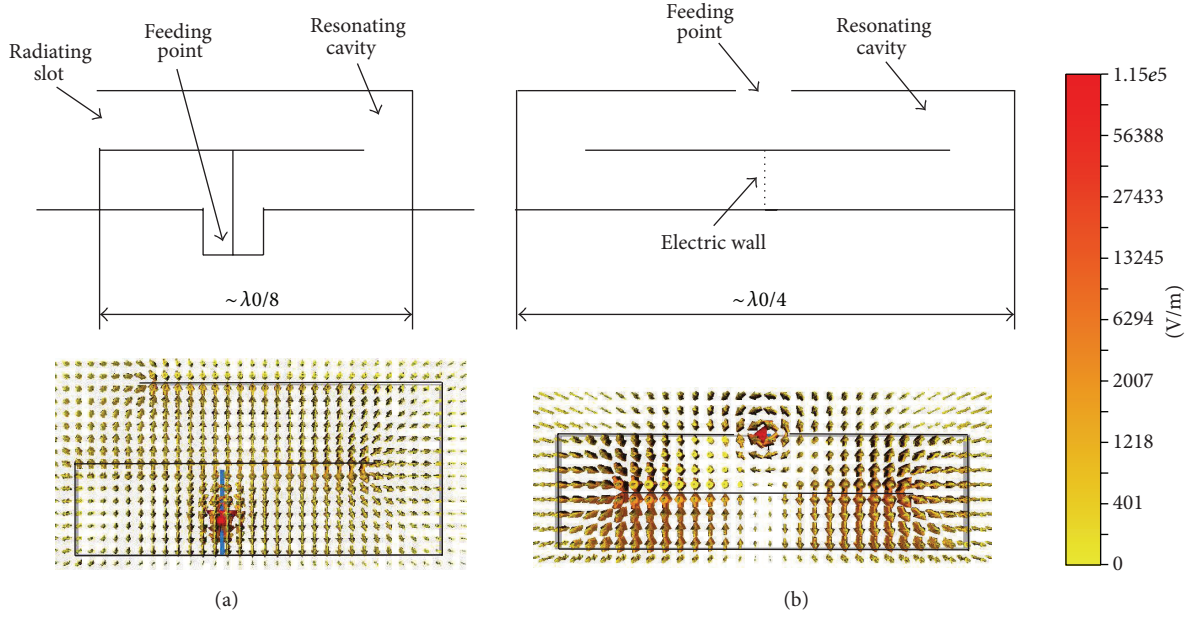
(a)

(b)

FIGURE 1: The side cross-section and electric field distribution of the vertically folded quarter wavelength patch antenna (a) and the proposed vertically folded coupled patches antenna (b).
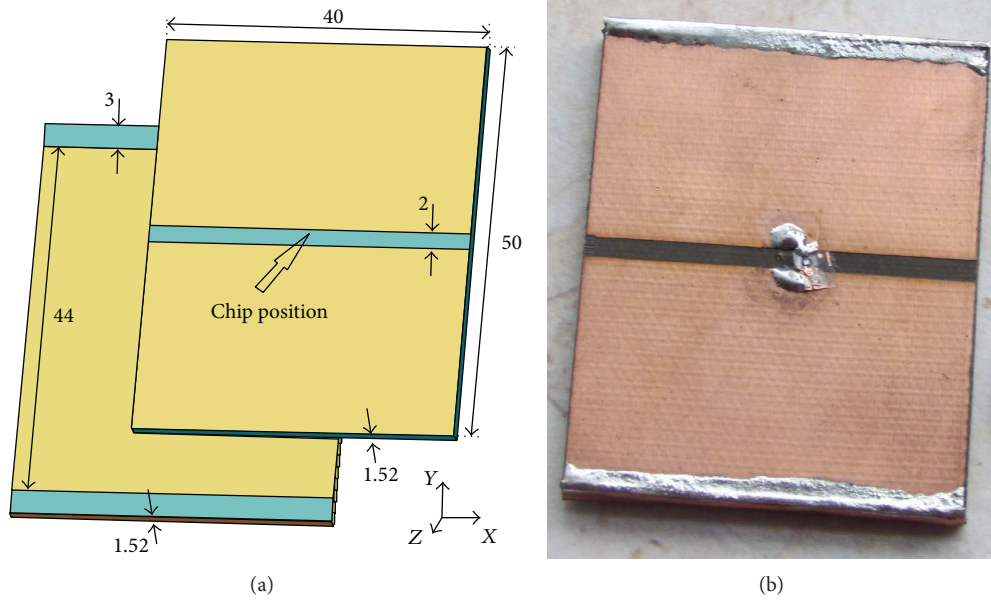

(a)

(b)

FIGURE 2: Sketch (a) and photograph (b) of folded coupled patches RFID antenna (dimensions stated in mm).

the sphere completely circumscribing the antenna, including the mirror currents. The antenna is fed by the NXP G2X2 RFID chip with input impedance $Z_{in} = 22 - j195\,\Omega$ and power sensitivity −15 dBm. The weight of the antenna is approximately 15 g.

The performance properties of the antenna were verified in a monopole-type arrangement [14] in order to avoid the use of a balun situated between the antenna and the coaxial connector; see Figure 3. The monopole-type input impedance then accounts for a half of the value compared to the dipole-type impedance. Consequently, $Z_{monopole} = Z_{dipole}/2$ is

considered for further evaluation (where $Z_{dipole} = Z_{chip}{}^* = 22 + j195\,\Omega$).

The transmission coefficient (see Figure 4) between the antenna and the chip input impedance was evaluated from the standard reflection coefficient measurement. The measurement was performed with and without a human body phantom (manufactured from agar with $\varepsilon_r \sim 55$ and $\tan\delta \sim 0.5$ of $80 \times 110 \times 15$ mm^3 size) which was enclosed directly in the back of the antenna.

The above-mentioned monopole-type arrangement enables us to measure the radiation and the total efficiencies

TABLE 1: Impedance and radiation properties of the vertically folded coupled patches RFID antenna at frequency 866 MHz.

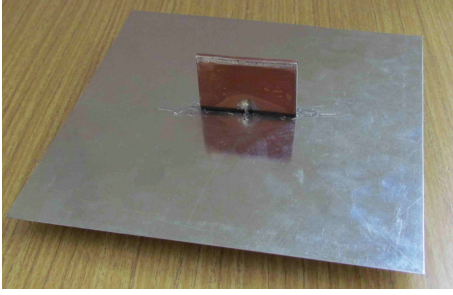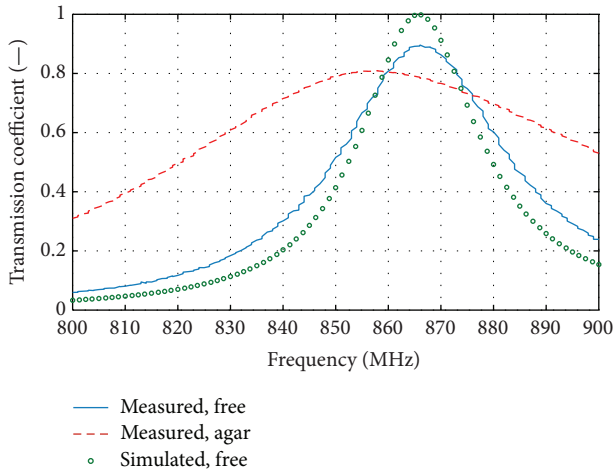|	Transmission coefficient (—)	Radiation efficiency (%)	Total efficiency (%)
Measurement, free space	0.9	75	66
Measurement, agar phantom	0.8	65	51
Simulation, free space	1.0	66	51

FIGURE 3: Photograph of a manufactured prototype of folded coupled patches RFID antenna in the monopole-type arrangement with the ground plane $130 \times 130 \text{ mm}^2$.

FIGURE 5: Simulation and measurement of the radiation efficiency of the vertically folded coupled patches tag antenna.

FIGURE 4: Simulation and measurement of the transmission coefficient of the vertically folded coupled patches tag antenna.
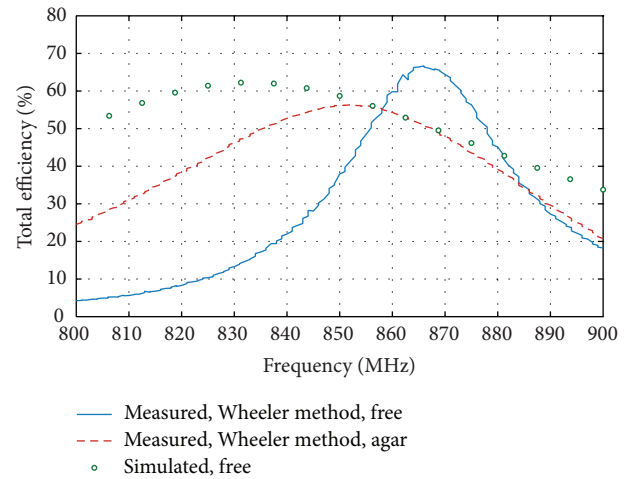
FIGURE 6: Simulation and measurement of the total efficiency of the vertically folded coupled patches tag antenna.

by the Wheeler cap method [19]. A cap size of $122 \times 122 \times 122 \text{ mm}^3$ was used. The simulation was performed in a full arrangement, according to Figure 2(a). The measurement was performed with and without the human body phantom; see Figures 5, 6 and Table 1. Very good immunity from the phantom as well as sufficient radiation and total efficiency can be observed at operation frequency 866 MHz.

3. Read Range and Identification Tests

In order to evaluate the performance of the TAG antenna in real operational conditions, read range tests were performed with transmitted power of 30 dBm and standard 8 dBi reader antennas, which gives 6.3 W of effective isotropic radiated power (EIRP). The tag antenna with the chip was fixed at a height of 1.3 m in free space and on a person's chest over about 2 mm thin shirt. The standard commercial RFID system (see Table 2) was used for the evaluation of the read distance as well as the reliability of person identification in corridors.

The read range evaluated in 4 m width corridor in a free space is 7.5 m, and for the antenna attached to a human chest the read range is 7.0 m; see Figure 7. The read range evaluated in 2 m width corridor in a free space is 11 m, and for the antenna attached to a human chest the read range is 9.7 m; see Table 3.
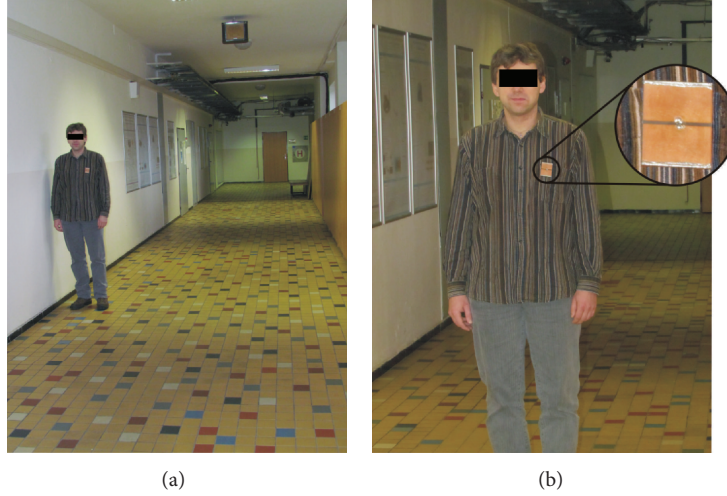
FIGURE 7: Photograph of a test configuration: general view (a) and details (b) of a person with the chest-fixed TAG in 4 m wide corridor.

TABLE 2: Standard used UHF RFID system parameters.

System components	Parameter	Values
	Operating frequency (Europe)	866 MHz
Reader	Transmitted power	30 dBm
	Receiver sensitivity	−64 dBm
	Reader antenna gain	8.0 dBi
	Reader antenna polarization	Linear
Transponder (TAG)	Chip sensitivity	−15 dBm
	Chip impedance	$22 - j195\,\Omega$
	TAG conversion loss	Approximately 6 dB

TABLE 3: Identification tests of the folded coupled patches antenna in free space as well as on the human chest in buildings corridors.

| Corridor width	Read range, free space (m)	Read range, human chest (m)
4 m	7.5	7
2 m	11	9.7

4. Conclusion

A novel small footprint size and extremely low profile wearable antenna based on a combination of coupled patches and vertically folded patches techniques has been introduced, and a sample has been developed for European UHF RFID band. The size of the tag antenna without a chip was $50 \times 40 \times 3.04\,\mathrm{mm}^3$, which is $0.14 \times 0.12 \times 0.009\,\lambda_0$ at 866 MHz. The antenna exhibits total efficiency better than 50%, irrespective of whether it is placed in a free space or enclosed on a human body phantom. The read range of the antenna placed on a person's chest tested was better than 7 m, while showing negligible influence of the human body to which the antenna was attached.

Conflict of Interests

The authors declare that there is no conflict of interests regarding the publication of this paper.

References

[1] P. S. Hall and H. Yang, *Antennas and Propagation for Body-Centric Wireless Communications*, Artech House, Norwood, Mass, USA, 2006.

[2] B. Sanz-Izquierdo, F. Huang, and J. C. Batchelor, "Covert dual-band wearable button antenna," *Electronics Letters*, vol. 42, no. 12, pp. 668–670, 2006.

[3] S. Shrestha, M. Agarwal, P. Ghane, and K. Varahramyan, "Flexible microstrip antenna for skin contact application," *International Journal of Antennas and Propagation*, vol. 2012, Article ID 745426, 5 pages, 2012.

[4] J. G. Joshi, S. S. Pattnaik, and S. Devi, "Metamaterial embedded wearable rectangular microstrip patch antenna," *International Journal of Antennas and Propagation*, vol. 2012, Article ID 974315, 9 pages, 2012.

[5] K. Fujii and Y. Okumura, "Effect of earth ground and environment on body-centric communications in the MHz band," *International Journal of Antennas and Propagation*, vol. 2012, Article ID 243191, 10 pages, 2012.

[6] S. Manzari, S. Pettinari, and G. Marrocco, "Miniaturised wearable UHF-RFID tag with tuning capability," *Electronic Letters*, vol. 48, no. 21, pp. 1325–1326, 2012.

[7] P. Jankowski-Mihułowicz, W. Kalita, M. Skoczylas, and M. Węglarski, "Modelling and design of HF RFID passive transponders with additional energy harvester," *International Journal of Antennas and Propagation*, vol. 2013, Article ID 242840, 10 pages, 2013.

[8] Tashi, M. S. Hasan, and H. Yu, "Design and simulation of UHF RFID tag antennas and performance evaluation in presence of a metallic surface," in *Proceedings of the 5th International Conference on Software, Knowledge Information, Industrial Management and Applications (SKIMA '11)*, pp. 1–5, Benevento, Italy, September 2011.

[9] M. Lai, R. Li, and M. M. Tentzeris, "Low-profile broadband RFID tag antennas mountable on metallic objects," in *Proceedings of the IEEE International Symposium on Antennas and Propagation Society (APSURSI '10)*, pp. 1–4, Toronto, Canada, July 2010.

[10] D. Kim and J. Yeo, "A passive RFID tag antenna installed in a recessed cavity in a metallic platform," *IEEE Transactions on Antennas and Propagation*, vol. 58, no. 12, pp. 3814–3820, 2010.

[11] P. H. Yang, Y. Li, L. Jiang, W. C. Chew, and T. T. Ye, "Compact metallic RFID tag antennas with a loop-fed method," *IEEE Transactions on Antennas and Propagation*, vol. 59, no. 12, pp. 4454–4462, 2011.

[12] C. Occhiuzzi, S. Cippitelli, and G. Marrocco, "Modeling, design and experimentation of wearable RFID sensor tag," *IEEE Transactions on Antennas and Propagation*, vol. 58, no. 8, pp. 2490–2498, 2010.

[13] M. Polivka, M. Svanda, P. Hudec, and S. Zvanovec, "UHF RF identification of people in indoor and open areas," *IEEE Transactions on Microwave Theory and Techniques*, vol. 57, no. 5, pp. 1341–1347, 2009.

[14] M. Svanda and M. Polivka, "Two novel extremely low-profile slot-coupled two-element patch antennas for UHF RFID of people," *Microwave and Optical Technology Letters*, vol. 52, no. 2, pp. 249–252, 2010.

[15] M. Svanda, M. Polivka, and P. Hudec, "Novel low-profile foam dielectric over-the-shoulder antenna based on coupled patches technique," *Microwave and Optical Technology Letters*, vol. 55, no. 3, pp. 593–597, 2013.

[16] K. F. Lee and W. Chen, *Advances in Microstrip and Printed Antennas*, chapter 5, John Wiley & Sons, New York, NY, USA, 1997.

[17] R. Li, G. DeJean, M. M. Tentzeris, and J. Laskar, "Development and analysis of a folded shorted-patch antenna with reduced size," *IEEE Transactions on Antennas and Propagation*, vol. 52, no. 2, pp. 555–562, 2004.

[18] A. Holub and M. Polivka, "A novel microstrip patch antenna miniaturization technique: a meanderly folded shorted-patch antenna," in *Proceedings of the 14th Conference on Microwave Techniques (COMITE '08)*, pp. 1–4, Prague, Czech Republic, April 2008.

[19] H. A. Wheeler, "The Radian Sphere around a Small Antenna," *Proceedings of the IRE*, vol. 47, no. 8, pp. 1325–1331, 1959.

Research Article

A Miniaturized Frequency Selective Surface Based on Square Loop Aperture Element

Wenxing Li,[1] Chunming Wang,[1] Yong Zhang,[2] and Yingsong Li[1]

[1] *College of Information and Communications Engineering, Harbin Engineering University, Harbin, Heilongjiang 150001, China*
[2] *DEEHOW Electronics Technology Co., Ltd., Beijing 100043, China*

Correspondence should be addressed to Chunming Wang; wangchunming@hrbeu.edu.cn

We propose a miniaturized band-pass frequency selective surface (FSS) with periodic unit cell structure. The proposed FSS is realized by symmetrically bending the edges of the square loop aperture element, by which our proposed FSS increases the resonant length, and, hence, reduces its size. In this FSS, each unit cell has a dimension of $0.0538\lambda \times 0.0538\lambda$, where λ represents the wavelength of the corresponding resonant frequency. Both the theoretical analysis and simulation results demonstrate that our proposed FSS, having high polarization stability and angle stability, can achieve smaller size in comparison with the previously proposed structures.

1. Introduction

Frequency selective surfaces (FSSs) are two-dimensional planar periodic structures which are realized by using patch or aperture elements to provide frequency filtering characteristic to incoming wave [1]. FSS has attracted a great amount of attention and has been widely studied for microwave and light-wave applications owing to its frequency selective properties [1–7]. Recently, FSS has been adopted in subreflector of Cassegrain antenna system to achieve frequency reuse, used to design band-pass radomes on the aircraft to reduce the out-of-band radar cross section (RCS) of antennas, and used in circuit analog absorber to expand its bandwidth [2].

FSS is an infinite periodic array, which is difficult to design. In fact, it can be implemented by using finite elements to make it suitable for practical engineering applications. This is because the finite FSS structure has no infinite expansibility and results in end current and scattering at the edges of the finite array, which seriously affect the performance of the FSS [3]. Therefore, it is necessary to use sufficient elements to approximate the characteristics of infinite FSS. Generally, the number of unit cells should not be less than 20×20 [4]. However, the size of a unit cell is so large that it is difficult to design a finite FSS array with sufficient number of elements

in a finite space when the FSS is operating in a low frequency such as L-band. As a result, minimization of FSS becomes one of the attractive and hot topics. Furthermore, the FSS should have good resonance stability performance with respect to various polarizations and incidence angles to achieve stable filter property in operating band [5].

Recently, a great number of FSSs have been developed to reduce their sizes. Chiu and Chang proposed a novel FSS structure which is realized by using two metal patch layers and a dielectric layer. The two metal patch layers coupled together via the dielectric layer. The size of each element is $0.104\lambda \times 0.104\lambda$ [5]. Then, Li et al. developed an octagon FSS using fractal theory and reduced the final FSS element size to $0.0814\lambda \times 0.0814\lambda$ [6]. After that, Yang et al. reported an improved FSS by bending the edges of cross aperture element into the external space [7] and the size of each element was $0.061\lambda \times 0.061\lambda$. All these unit cells are symmetrical in order to ensure the stability of the corresponding FSSs. However, the size of the FSS is still large for practical applications in very low frequency.

In this paper, we propose a miniaturized band-pass FSS with periodic unit cell structure. The proposed FSS is realized by symmetrically bending the edges of the square loop aperture element to the inner space. In this FSS, each unit

(a) Equivalent capacitance of patch array   (b) Equivalent inductance of wire grid
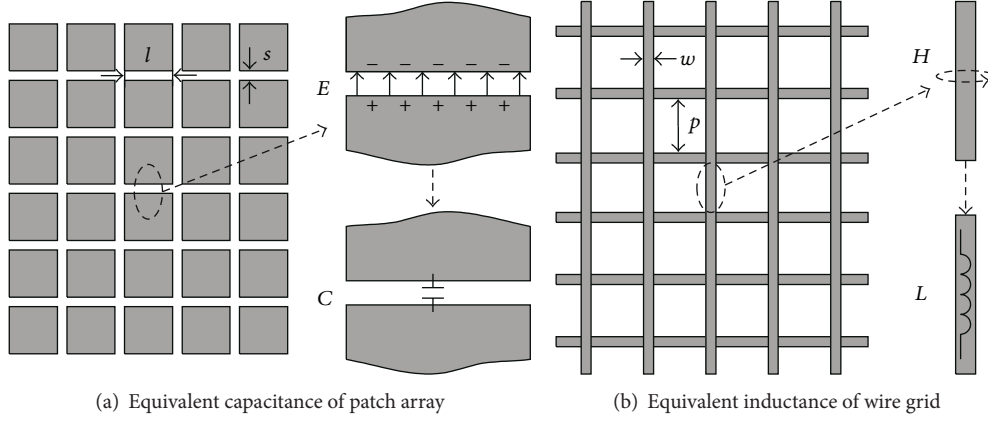
FIGURE 1: Equivalent analysis of periodic structure.

cell has a dimension of $0.0538\lambda \times 0.0538\lambda$. The simulation results demonstrate that our proposed FSS, having high polarization stability and angle stability, can achieve smaller size in comparison with the previously proposed structures.

2. Fundamental of Miniaturized FSS

On the basis of the electromagnetic theory, when a plane wave is incident on a patch array, there exists induced current. Examples are shown in Figure 1. In Figure 1(a), we choose the vertical direction as reference direction of electric field in the two-dimensional plane. When a plane wave is incident on a patch array, the electric field creates positive and negative charges on the edges of the two adjacent patches, which is a gap capacitor. Similarly, in a wire grid shown in Figure 1(b), parallel wires can also generate induced current, resulting in a magnetic field, which acts as inductors. The first-order approximation of the capacitance of the patch array and the inductance of a wire gird are determined by (1) and (2), respectively [8]:

$$C = \varepsilon_0 \varepsilon_{\text{eff}} \left(\frac{2l}{\pi} \right) \log \left[\csc \left(\frac{\pi s}{2l} \right) \right], \quad l > s, \tag{1}$$

$$L = \mu_0 \left(\frac{p}{2\pi} \right) \log \left[\csc \left(\frac{\pi w}{2p} \right) \right], \quad p > w, \tag{2}$$

where ε_0 is the permittivity constant of the air, ε_{eff} is the effective dielectric constant of the substrate, l is the side length of the patches, s is the distance between the two patches, μ_0 is the permeability of air, p is the length of the wire, and w is the width of the wire.

From (1), we find that C is proportional to l and is inversely proportional to s when $l > s$. In a word, only the narrow apertures in the horizontal direction act as big equivalent capacitance, which is shown in Figure 1(a). In (2), we observe that L is proportional to p and is inversely proportional to w with $p > w$. Thus, the equivalent inductance effects are mainly dependent on the vertical direction of these long wires.

Based on the theoretical analysis and discussions above, we can choose appropriate dimensions of the FSS elements
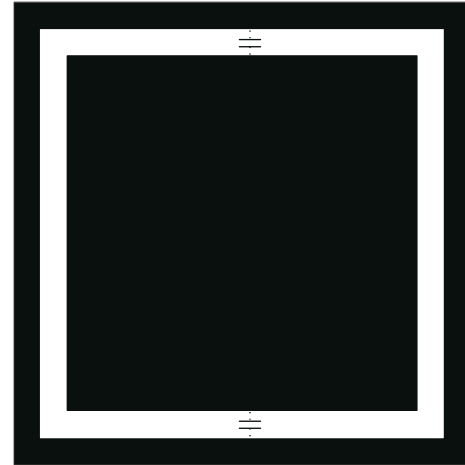
FIGURE 2: Square loop aperture element.

to obtain required resonant frequency. In addition, we know that different FSS structures may have different equivalent circuits. For square loop aperture element illustrated in Figure 2, the narrow aperture in horizontal direction plays an important role in forming the big equivalent capacitance, the long wire in vertical direction plays an important role in forming the big equivalent inductance [2], and the equivalent circuit model of such element is shown in Figure 3, in which C is large equivalent capacitance and L is large equivalent inductance.

From the previous knowledge on the circuit analysis, the resonant frequency of the equivalent model described in Figure 3 can be expressed as

$$f = \frac{1}{\left(2\pi \sqrt{L_s C_s} \right)}, \tag{3}$$

where $C_s = 0.5C$ and $L_s = 0.5L$.

From (1), (2), and (3), we find that the resonant frequency of the square loop aperture element mainly relies on the equivalent capacitance C and the equivalent inductance L. As for the square loop aperture FSS, we should increase the

FIGURE 3: Equivalent model of square loop aperture element.

FIGURE 4: Structure of FSLA element.

TABLE 1: Parameters of the designed FSS element.

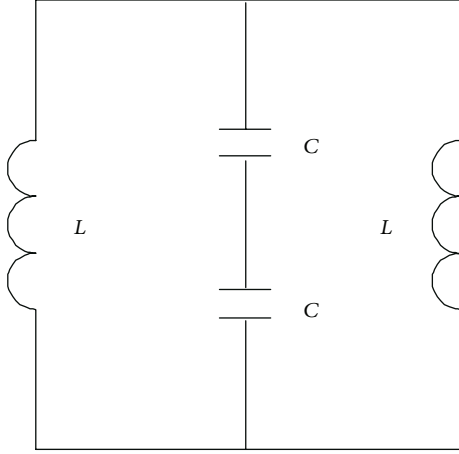| Parameter	Value
Length (D)	9.8 mm
Width of the narrow aperture (w_1)	0.2 mm
Space between the aperture strips (w_2)	0.2 mm
Aperture space of adjacent elements (g)	0.2 mm
Thickness of the metal layer (t)	0.2 mm
Thickness of the dielectric layer (h)	1.6 mm
Loss tangent of the dielectric ($\tan\theta$)	0.025
Relative dielectric constant (ε_r)	5.0

FIGURE 5: Equivalent model of FSLA element.

length of the narrow aperture of the element structure to obtain large equivalent capacitance so as to reduce the size of the FSS structure. Inspired by the analysis given above, we propose an improved unit cell structure named four sides loading aperture (FSLA) element, and it is shown in Figure 4. In this structure, the apertures implied by the yellow dotted line can act as large capacitors. The corresponding equivalent circuit model is shown in Figure 5, where C is the large equivalent capacitance and L is the large equivalent inductance.

To further reduce the resonant frequency of the above structure, we bend the FSLA element into the inner side of the square loop. The new structure of the highly improved FSS unit cell is described in Figure 6 and its equivalent model can also be illustrated by using the model shown in Figure 5. However, the values of the two capacitances in Figure 5 increase.

3. Results and Discussions

On the basis of the analysis, we propose a miniaturized FSS, which operates at 1.647 GHz. The FSS element is shown in Figure 6 while the related parameters are shown in Table 1.

The simulation results are obtained by using the computer simulation technology (CST). The simulated model is shown in Figure 7 and the transmission coefficients with normal incidence of the designed FSS are shown in Figure 8. We can

see from Figure 8 that the resonant frequency of our designed FSS is 1.647 GHz for normal incidence. When ε_r is 2.65, the resonant frequency is 1.995 GHz; when ε_r is 4.4, the resonant frequency is 1.713 GHz.

According to the results shown in Figure 8 and (4), the size of the FSS element can be obtained with size of $0.0538\lambda \times 0.0538\lambda$,

$$C_0 = \lambda f,$$
$$k = \frac{D}{\lambda}, \tag{4}$$

where C_0 is the speed of light in air, f represents the resonant frequency of the FSS and λ is the corresponding wavelength, k is the size of FSS element, and D represents the length of the element.

Moreover, the element size is different as the dielectric is different. It is found that k is inversely proportional to ε_r. The proposed FSS is compared with the previously proposed studies in [5–7] and the comparisons are shown in Table 2. It can be seen from Table 2 that the designed FSS can achieve smaller size. This means that our proposed design is smaller in size at the same resonant frequency.

(a) Front view

(b) Side view
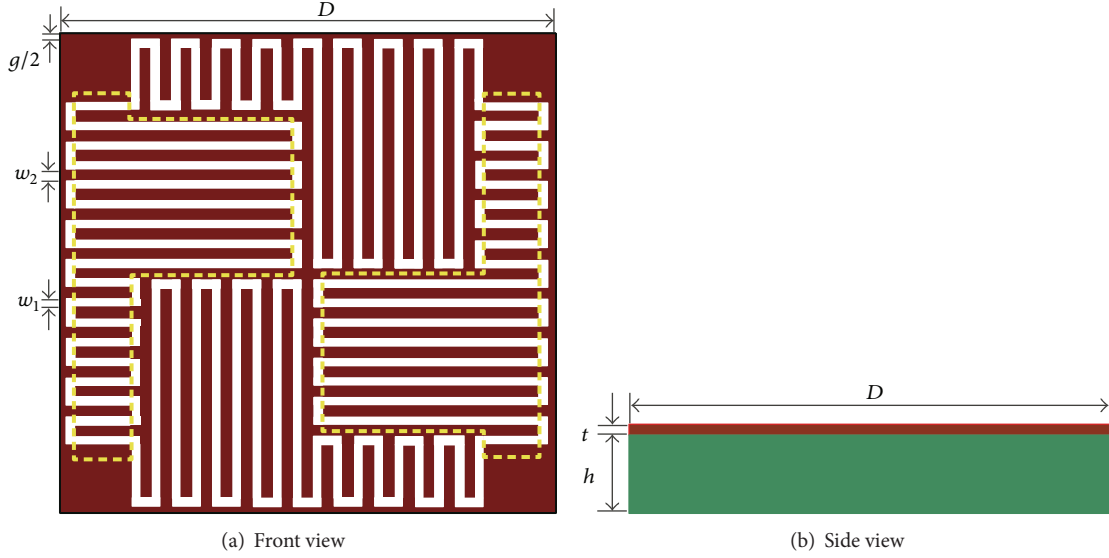
FIGURE 6: Structure of the proposed FSS element.
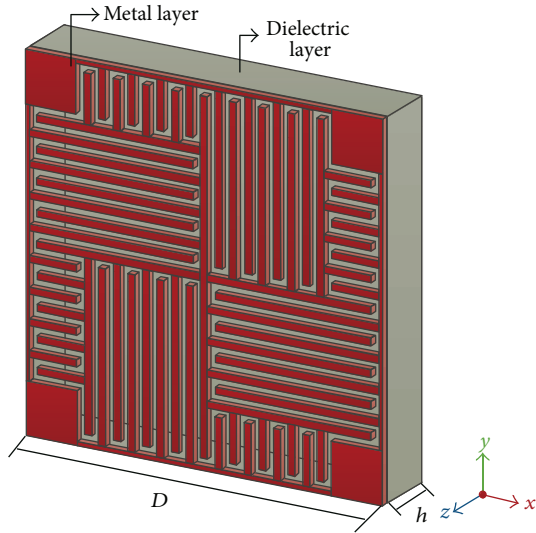
FIGURE 7: Simulation model of designed FSS.
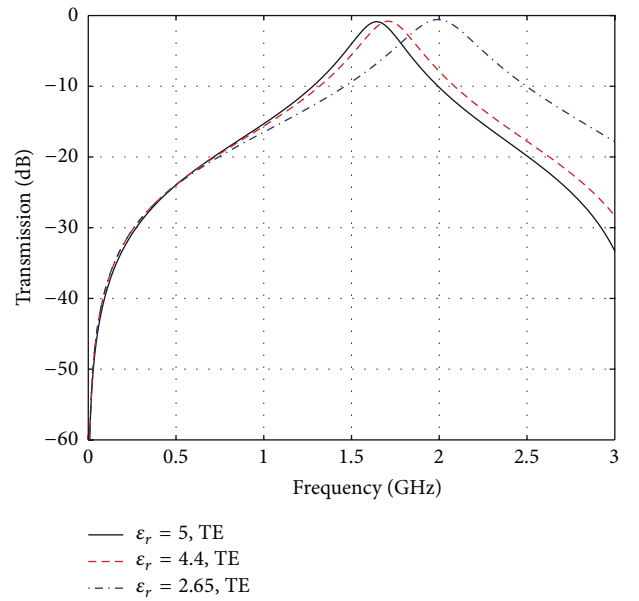
FIGURE 8: Transmission coefficients of designed FSS.

TABLE 2: Comparisons of the element sizes for the four FSSs.

FSS structure	ε_r	Element size
Paper [5]	4.4	$0.104\lambda \times 0.104\lambda$
Paper [6]	2.65	$0.0814\lambda \times 0.0814\lambda$
Paper [7]	5.0	$0.061\lambda \times 0.061\lambda$
	5.0	$0.0538\lambda \times 0.0538\lambda$
Proposed	4.4	$0.056\lambda \times 0.056\lambda$
	2.65	$0.0652\lambda \times 0.0652\lambda$

In order to further discuss the bandwidth performance of our proposed FSS, the S-parameter characteristics, including the reflection coefficient (S_{11}) and transmission coefficient (S_{21}), are obtained by using CST and the simulation results with TE-polarized incidence are shown in Figure 9. It can be seen from Figure 9 that the proposed FSS has a −10 dB impedance bandwidth of 5.34% with respect to the center frequency of 1.647 GHz.

4. Stability Analysis of the Proposed Miniaturized FSS

As a FSS, it should be stable for different applications. Therefore, we investigate the stability of the proposed miniaturized FSS for different situations, such as different polarizations or different incident angles. The simulation transmission coefficients are shown in Figure 10. As shown in Figure 10, our designed miniaturization FSS has stable resonance properties under different situations, and the resonant frequency
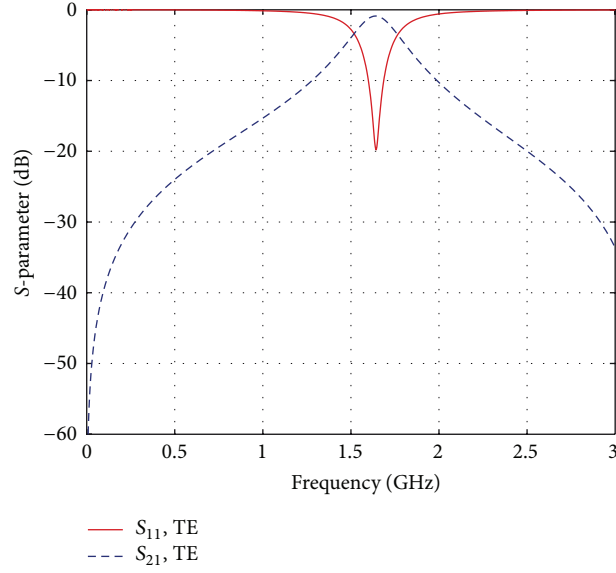
FIGURE 9: S-parameter characteristics of the designed FSS.

(a) TE-polarized waves with different incident angles

(b) TM-polarized waves with different incident angles
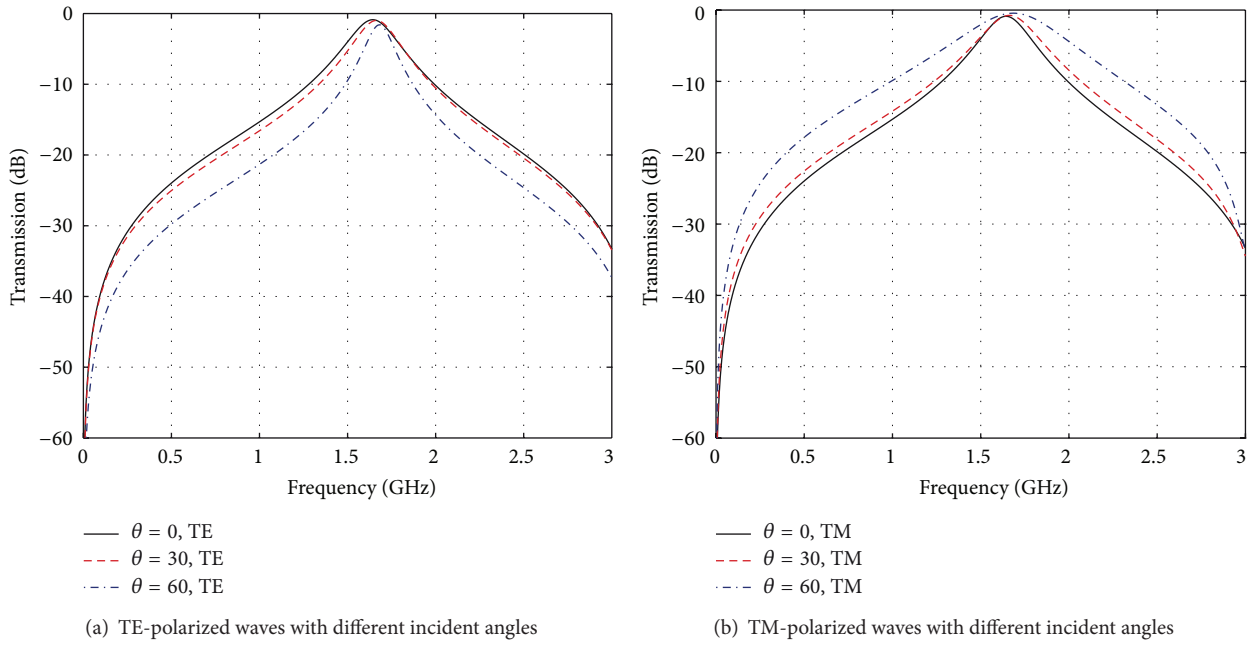
FIGURE 10: Transmission coefficients of the proposed miniaturized FSS with different modes.

TABLE 3: The resonant frequency deviation of proposed FSS at TE-polarized.

Incident angle	Resonant frequency	Deviation
$\theta = 0°$	1.647 GHz	—
$\theta = 30°$	1.665 GHz	1.09%
$\theta = 60°$	1.683 GHz	2.19%

TABLE 4: The resonant frequency deviation of proposed FSS at TM-polarized.

Incident angle	Resonant frequency	Deviation
$\theta = 0°$	1.647 GHz	—
$\theta = 30°$	1.665 GHz	1.09%
$\theta = 60°$	1.689 GHz	2.55%

deviations of the deigned miniaturization FSS are illustrated in Tables 3 and 4.

We can see from Tables 3 and 4 that the resonant frequency deviations for TE-polarized and TM-polarized

both have a little shift at different incident angles. These deviations are within the scope of the allowed operation bandwidth of the FSS. Thereby, the proposed miniaturization FSS can achieve excellent polarization stability and angle stability.

5. Conclusion

In this paper, we proposed a miniaturization FSS with unit cell size of $0.0538\lambda \times 0.0538\lambda$. The proposed FSS was designed by setting the bent FSLA element in the inner sides of the square loop. The designed FSS was analyzed step by step by using the equivalent circuit model. The simulation results obtained from CST demonstrated that our proposed FSS had excellent polarization stability and angle stability, which render it suitable for practical engineering applications.

Conflict of Interests

The authors declare that there is no conflict of interests regarding the publication of this paper.

Acknowledgments

References

[1] T. K. Wu, *Frequency Selective Surface and Grid Array*, John Wiley & Sons, New York, NY, USA, 1995.

[2] B. A. Munk, *Frequency Selective Surfaces: Theory and Design*, John Wiley & Sons, New York, NY, USA, 2005.

[3] B. A. Munk, *Finite Antenna Arrays and FSS*, John Wiley & Sons, New York, NY, USA, 2003.

[4] H.-Y. Yang, S.-X. Gong, P.-F. Zhang, F.-T. Zha, and J. Ling, "A novel miniaturized frequency selective surface with excellent center frequency stability," *Microwave and Optical Technology Letters*, vol. 51, no. 10, pp. 2513–2516, 2009.

[5] C.-N. Chiu and K.-P. Chang, "A novel miniaturized-element frequency selective surface having a stable resonance," *IEEE Antennas and Wireless Propagation Letters*, vol. 8, pp. 1175–1177, 2009.

[6] W. Li, T. Zhang, G. Yang, and Q. Wu, "A novel frequency selective surface with improved miniaturization performance," *Journal of Electromagnetic Analysis and Applications*, vol. 4, no. 3, pp. 108–111, 2012.

[7] G. Yang, T. Zhang, W. Li, and Q. Wu, "A novel stable miniaturized frequency selective surface," *IEEE Antennas and Wireless Propagation Letters*, vol. 9, pp. 1018–1021, 2010.

[8] F. Bayatpur, *Metamaterial-Inspired Frequency-Selective Surfaces*, The University of Michigan, 2009.

Research Article

Orthogonal Design Method for Optimizing Roughly Designed Antenna

Qing Zhang,[1] Sanyou Zeng,[2] and Chunbang Wu[3]

[1] *School of Mathematics & Computer Science, Huanggang Normal University, Huanggang, Hubei 38000, China*
[2] *School of Computer Science, China University of GeoSciences, Wuhan, Hubei 430074, China*
[3] *China Academy of Space Technology (Xián), Xián, Shanxi 710000, China*

Correspondence should be addressed to Sanyou Zeng; sanyouzeng@gmail.com

Orthogonal design method (ODM) is widely used in real world application while it is not used for antenna design yet. It is employed to optimize roughly designed antenna in this paper. The geometrical factors of the antenna are relaxed within specific region and each factor is divided into some levels, and the performance of the antenna is constructed as objective. Then the ODM samples small number of antennas over the relaxed space and finds a prospective antenna. In an experiment of designing ST5 satellite miniantenna, we first get a roughly evolved antenna. The reason why we evolve roughly is because the evolving is time consuming even if numerical electromagnetics code 2 (NEC2) is employed (NEC2 source code is openly available and is fast in wire antenna simulation but not much feasible). Then the ODM method is employed to locally optimize the antenna with HFSS (HFSS is a commercial and feasible electromagnetics simulation software). The result shows the ODM optimizes successfully the roughly evolved antenna.

1. Introduction

Orthogonal design method (ODM) has been widely researched. Literature [1, 2] surveys this method in both theoretical and applied way. The ODM samples a small number of evenly distributed points over a large search space. Then it statistically summarizes a prospective good solution. The application of this method is much wide, such as in, for example, chemical and biological fields [3, 4], image process [5], laser polishing [6], software testing technique [7], algorithm [8], semiconductor manufacturing [9], optics [10], and robust design [11]. Recent theory research on the ODM method can be found still, for example, the mixed-level orthogonal array research in [12].

The current practice of designing antennas by hand is limited in its ability to develop new and better antenna designs because it requires significant domain expertise and experience and is both time and labor intensive. With this approach, an antenna engineer will select a particular class of antennas and then spend weeks or months testing and adjusting a design, mostly in simulation using electromagnetic modeling software. As an alternative, researchers have

been investigating evolutionary antenna optimization since the early 1990s. For example, genetic algorithm/evolutionary algorithm ([13]) is adopted to optimize antenna [14–16], particle swarm optimization ([17–19]) to optimize antenna [20, 21], and differential evolution ([22, 23]) to optimize antenna [24].

A run of evolutionary algorithm in designing an antenna usually takes over $10,000$ electromagnetic simulations while a simulation usually takes minutes or even hours. Then fast computing and incomplete simulation are adopted to reduce running time. The output of such evolution can only be called a roughly evolved antenna.

This paper focuses on optimizing locally this kind of rough antennas. We first relax the geometrical factors of the rough antenna within specific regions, divide each factor into some levels, and construct objective by using the performance of the antenna. Then we sample small number of antennas over the relaxed space and find a prospective antenna. It is the method that we call orthogonal design method (ODM).

In an experiment of designing ST5 satellite antenna, we first get a roughly evolved antenna with NEC2. Then the

ODM is employed to locally optimize the antenna with HFSS. The result shows the ODM method optimizes successfully the roughly evolved antenna.

The remainder of this paper is organized as follows. Section 2 introduces the principal of the ODM method by using an example. Section 3 presents the fact that the ODM method optimizes antenna locally. Designing NASA ST5 antenna is used to test the ODM method in Section 4. The paper is concluded in Section 5.

2. Principal of Orthogonal Design Method

2.1. An Example to Introduce Orthogonal Design Method. We use a concrete example in this subsection to introduce the basic concept of an "orthogonal design method". For further details, see [25]. The example is concerned with the yield of vegetable growth. The yield of a vegetable depends on at least three factors:

(1) the temperature,

(2) the amount of fertilizer used,

(3) the pH value of the soil.

In this example, each factor has three possible values, as shown in Table 1. We say that each factor has three "levels."

The objective is to find the best combination of levels for a maximum yield. We can perform an experiment for each combination and then select the combination with the highest yield. In the above example, there are $3 \times 3 \times 3 = 27$ combinations, and hence there are 27 experiments. In general, when there are N factors, each with Q levels, there are Q^N possible combinations. When N and Q are large, it may not be possible to perform all Q^N experiments. Therefore, it is desirable to sample a small, but representative, set of combinations, for the experimentation. The "orthogonal design method" was developed for this purpose [25], where an orthogonal array is constructed to represent the sampled set of combinations which evenly distribute over the experimentation space. An orthogonal array $L_M(Q^N)$ is a $M \times N$ array with Q levels for each column, denoted by $\{1, 2, \ldots, Q\}$. We select M combinations to be tested, where M may be much smaller than Q^N. Equation (1) is an example of an orthogonal array where $M = 9$, $N = 3$, and $Q = 3$. Figure 1 shows the 9 representative combinations (marked with "Δ") evenly distributed over all the 27 combinations. Consider

$$L_9\left(3^3\right) = \begin{bmatrix} 1 & 1 & 1 \\ 1 & 2 & 2 \\ 1 & 3 & 3 \\ 2 & 1 & 2 \\ 2 & 2 & 3 \\ 2 & 3 & 1 \\ 3 & 1 & 3 \\ 3 & 2 & 1 \\ 3 & 3 & 2 \end{bmatrix}. \tag{1}$$

The $L_9(3^3)$ has three factors, three levels per factor, and nine combinations of levels. The three factors have respective

TABLE 1: Experimental design with three factors and three levels per factor.

Levels	Factor		
	Temperature (°C)	Fertilizer (g/m^2)	pH
Level 1	20	100	6
Level 2	25	150	7
Level 3	30	200	8

```
\\ Construct the basic columns as follows.
FOR k = 1 to J
    j = (Q^{k-1} − 1)/(Q − 1) + 1
    FOR i = 1 to Q^J
        a_{i,j} = floor((i − 1)/(Q^{J−k}))  mod  Q
    ENDFOR
ENDFOR
\\ Construct the non-basic columns as follows.
FOR k = 2 to J
    j = (Q^{k-1} − 1)/(Q − 1) + 1;
    FOR s = 1 to j − 1, t = 1 to Q − 1
        a⃗_{j+(s−1)(Q−1)+t} = (a⃗_s × t + a⃗_j) mod  Q;
    ENDFOR
ENDFOR
```

ALGORITHM 1: Constructing the orthogonal array $L_M(Q^P)$.

levels 1, 1, and 1 in the first combination, 1, 2, and 2 in the second combination, and so forth. We apply the orthogonal array $L_9(3^3)$ to select nine combinations to be tested. The nine combinations and their yields in the above example are shown in Table 2.

From the yields of the selected combinations, a promising solution can be obtained by the following statistical method.

(1) Calculate the mean value of the yields for each factor at each level, where each factor has a level with the best mean value (cf. Algorithm 2).

The mean yields of the temperature are

$\Gamma_{1,1} = (2.75 + 4.52 + 4.65)/3 = 3.97$ at level 1(20°C),

$\Gamma_{2,1} = (4.60 + 5.58 + 4.10)/3 = 4.76$ at level 2(25°C),

$\Gamma_{3,1} = (5.32 + 4.10 + 4.37)/3 = 4.60$ at level 3(30°C).

The mean yields of the fertilizer are

$\Gamma_{1,2} = (2.75 + 4.60 + 5.32)/3 = 4.22$ at level 1(100 g/m^2),

$\Gamma_{2,2} = (4.52 + 5.58 + 4.10)/3 = 4.73$ at level 2(150 g/m^2),

$\Gamma_{3,2} = (4.65 + 4.10 + 4.37)/3 = 4.37$ at level 3(200 g/m^2).

The mean yields of the PH value are

$\Gamma_{1,3} = (2.75 + 4.10 + 4.10)/3 = 3.65$ at level 1(6),

$\Gamma_{2,3} = (4.52 + 4.60 + 4.37)/3 = 4.50$ at level 2(7),

$\Gamma_{3,3} = (4.65 + 5.58 + 5.32)/3 = 5.18$ at level 3(8).

These mean yields are shown in Table 3.

TABLE 2: The yield of nine representative combinations, based on the orthogonal array $L_9(3^3)$.

No.	Factor			
	Temperature	Fertilizer	pH	Yield
1	1 (20°C)	1 (100 g/m²)	1 (6)	2.75
2	1 (20°C)	2 (150 g/m²)	2 (7)	4.52
3	1 (20°C)	3 (200 g/m²)	3 (8)	4.65
4	2 (25°C)	1 (100 g/m²)	2 (7)	4.60
5	2 (25°C)	2 (150 g/m²)	3 (8)	5.58
6	2 (25°C)	3 (200 g/m²)	1 (6)	4.10
7	3 (30°C)	1 (100 g/m²)	3 (8)	5.32
8	3 (30°C)	2 (150 g/m²)	1 (6)	4.10
9	3 (30°C)	3 (200 g/m²)	2 (7)	4.37

TABLE 3: The mean yield for each factor at different levels.

Levels	Mean yield		
	Temperature	Fertilizer	pH
Level 1	3.97	4.22	3.65
Level 2	4.76	4.73	4.50
Level 3	4.60	4.37	5.18

```
\\Sum the objective results for each factor at each level
set Γ_{i,j} = 0 for i = 1, 2, ..., Q; j = 1, 2, ..., N
FOR i = 1 to M, j = 1 to N
    q = a_{i,j}; Γ_{q,j} = Γ_{q,j} + y_i
ENDFOR
\\Average the results for each factor at each level
[Γ_{k,j}]_{Q×N} = [Γ_{k,j}]_{Q×N} × Q/M
```

ALGORITHM 2: Calculation of mean value $[\Gamma_{k,j}]_{Q \times N}$.

(2) Choose the combination of the best levels as a promising solution (cf. Algorithm 3).

The temperature has the best mean yield, 4.76, at level 2 (i.e., 25°C). The fertilizer has the best yield, 4.73, at level 2 (i.e., 150 g/m²). The pH value has the best yield, 5.18, at level 3 (i.e., 8). We therefore consider (25°C, 150 g/m², 8) to be a promising and robust solution. The solution may not be optimal when used with an orthogonal design. But for additive and quadratic models, it is provably optimal.

2.2. A Definition of Orthogonal Array

Definition 1 (an orthogonal array). $L_M(Q^N)$ is a $M \times N$ array with Q levels for each column, denoted by $\{1, 2, \ldots, Q\}$. Denote the orthogonal array $L_M(Q^N)$ by $[a_{i,j}]_{M \times N}$ as follows.

(1) In any column $\{a_{1,j}, a_{2,j}, \ldots, a_{M,j}\}$, each of the Q symbols $1, 2, \ldots, Q$ occurs the same number of times; that is, (M/Q), $j = 1, 2, \ldots, N$.

(2) In any two different columns $\{(a_{1,j}, a_{1,k}), (a_{2,j}, a_{2,k}), \ldots, (a_{M,j}, a_{M,k})\}$, each of the Q^2 possible pairs
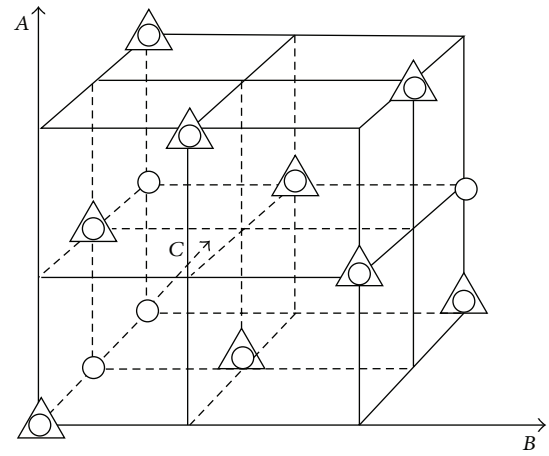
FIGURE 1: Schematic diagram of orthogonal experimental design.

```
FOR j = 1 to N
    b_j = arg max  Γ_{i,j}
          i∈{1,2,...,Q}
ENDFOR
RETURN prospective good combination b⃗ = (b_1, b_2, ..., b_N)
```

ALGORITHM 3: Calculation of prospective good combination $[b_j]_{1 \times N}$.

$\{(1, 1), (1, 2), \ldots, (1, Q), (2, 1), (2, 2), \ldots, (2, Q), \ldots, (Q, 1), (Q, 2), \ldots, (Q, Q)\}$ occurs the same number of times (M/Q^2), $j, k = 1, \ldots, N$, $j \neq k$.

Every row of $L_M(Q^N) = [a_{i,j}]_{M \times N}$ represents a different combination of levels, where $a_{i,j}$ means that the jth factor in the ith combination has a level value $a_{i,j}$, and $a_{i,j}$ takes a value from the set $\{1, 2, \ldots, Q\}$.

3. Orthogonal Design Method Designing Antenna

3.1. Antenna Design Using Orthogonal Design Method. There are many antenna classes, such as reflector antennas (e.g., dish antennas), phased array antennas (consisting of multiple

FIGURE 2: Geometric structure of the antenna in the first quadrant.

regularly spaced elements), wire antennas, horn antennas, and microstrip and patch antennas. Each of these classes uses different structures and exploits different properties of electromagnetic waves.

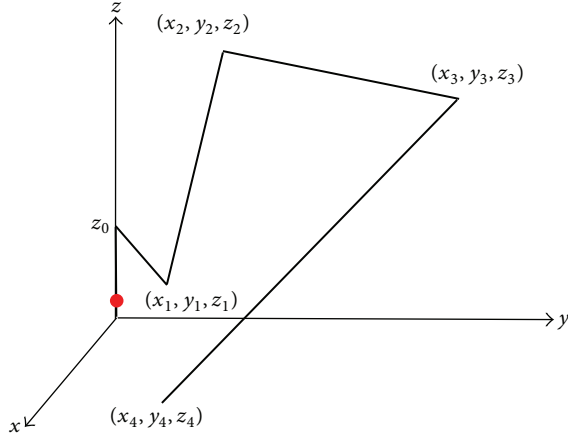Using orthogonal design method to design antenna, three components are required to be determined: factors, levels, and optimization objective.

The geometrical structure of an antenna is usually regarded as factors. For example, a N element Yagi antenna has N element lengths $(l_1, l_2, \ldots, l_N)$, $N-1$ spacing distances between elements $(d_1, d_2, \ldots, d_{N-1})$, and one wire radius (r), giving $2N$ factors total; a conventional rectangular microstrip patch antenna usually has 6 factors: patch length (l) and width (w), substrate height (h) and its dielectric constant (ε_r), and probe point $(\Delta l, \Delta w)$, the distance from the left-bottom corner of the rectangular microstrip.

Determination of levels for each factor depends on the design specification of the antenna and empirical design.

The optimization objective is to find an antenna best matching the specification (gain, VSWR, etc.). It is a function of the factors. The objective value of an antenna may be achieved by measuring the prototype which is expensive or by simulating the antenna by using electromagnetic simulation softwares The latter one is usually adopted to avoid expensive cost.

Then the antenna design using orthogonal design method is an optimization problem; the formulation of optimizing antenna is defined in the following.

Definition 2 (formulation of optimizing antenna using orthogonal design method). Suppose there are N antenna design *factors* $x_1, x_2, \ldots, x_N$ and each factor x_i has Q *levels* $x_{i,1}, x_{i,2}, \ldots, x_{i,Q}$, $i = 1, 2, \ldots, N$, giving N^Q combinations total. Each combination determines an antenna; there are N^Q antennas in all, which is called *search space* denoted as Ω. The performance of a combination (an antenna) is evaluated by the value of objective $f(\vec{x})$. The bigger the value of $f(\vec{x})$ the better the performance of the antenna in maximization formulation, $\vec{x} \in \Omega$. In this way, the optimization is Max $f(\vec{x})$ where $\vec{x} \in \Omega$.

Note. Q must be prime in this paper; see Section 3.2.

3.2. Creating Orthogonal Array. As we will explain shortly, the technique proposed in this paper usually requires different orthogonal arrays for different problems. The construction of orthogonal array is not a trivial task since we do not know whether an orthogonal array of given size exists. Many orthogonal arrays have been presented in the literatures. It is impossible, however, to tabulate them all. For the necessity of the technique in this paper, we introduce a simple permutation method that is derived from the mathematical theory of Galois fields (see [1]), to construct a class of orthogonal arrays $L_M(Q^P)$. The M, P, Q fulfill the following:

$$M = Q^J,$$

$$P = \frac{(Q^J - 1)}{(Q - 1)}, \tag{2}$$

where Q is prime and J is a positive integer.

Denote the jth column of the orthogonal array $[a_{i,j}]_{M \times P}$ by $\vec{a}_j$. Columns $\vec{a}_j$ for $j = 1, 2, (Q^2 - 1)/(Q - 1) + 1, (Q^3 - 1)/(Q - 1) + 1, \ldots, (Q^{J-1} - 1)/(Q - 1) + 1$ are called the basic columns. The others are called the nonbasic columns. The algorithm first constructs the basic columns and then generates the nonbasic columns. The details are given in the Algorithm 1.

3.3. Determining the Size of the Needed Orthogonal Array. The $L_M(Q^P)$ constructed by Algorithm 1 has a size of M combinations (antennas). It can be adopted for a problem with Q levels and N factors where $N \leq P$. The M and P in $L_M(Q^P)$ are determined by given Q and J according to (2), while in an antenna design problem the number of level Q and the number of factor N are given according to Definition 2. Then the J is demanded to be determined to construct an orthogonal array for the problem.

M combinations mean M electromagnetic simulations each of which is time consuming. We choose the M as small as possible. This can be done by choosing the J as small as possible according to (2). Then the J is determined by

$$\text{Min} \quad J$$

$$\text{st.} \quad P = \frac{(Q^J - 1)}{(Q - 1)} \geq N, \quad J = 2, 3, \ldots. \tag{3}$$

The $L_M(Q^P)$, constructed by Algorithm 1, has P columns. For a problem with N factors, we discard the last $P - N$ columns of $L_M(Q^P)$ and obtain an array $L_M(Q^N)$ which is still orthogonal according to Definition 1.

For the problem of vegetable growth, there are 3 factors ($N = 3$) and 3 levels ($Q = 3$). $J = 2$ by (3) and the orthogonal

array is $L_9(3^4)$ with 4 columns ($P = 4$). We discard the last column of the $L_9(3^4)$ and get the needed array $L_9(3^3)$:

$$L_9\left(3^4\right) = \begin{bmatrix} 1 & 1 & 1 & 1 \\ 1 & 2 & 2 & 2 \\ 1 & 3 & 3 & 3 \\ 2 & 1 & 2 & 3 \\ 2 & 2 & 3 & 1 \\ 2 & 3 & 1 & 2 \\ 3 & 1 & 3 & 2 \\ 3 & 2 & 1 & 3 \\ 3 & 3 & 2 & 1 \end{bmatrix} \overset{\text{Discard the}}{\underset{\text{last column}}{\Rightarrow}} L_9\left(3^3\right) = \begin{bmatrix} 1 & 1 & 1 \\ 1 & 2 & 2 \\ 1 & 3 & 3 \\ 2 & 1 & 2 \\ 2 & 2 & 3 \\ 2 & 3 & 1 \\ 3 & 1 & 3 \\ 3 & 2 & 1 \\ 3 & 3 & 2 \end{bmatrix}. \quad (4)$$

3.4. Doing Orthogonal Experiments. The M combinations (antennas) are evaluated by orthogonal experiments (electromagnetic simulations). We obtain M objective values (performances of the antennas) denoted as $[y_i]_{M \times 1}$ where the objective has the value y_i at the ith combination. It is similar to fill out Table 2 for the above vegetable example.

The best combination (antenna) among the M combinations, denoted as $\vec{b}^* = (b_1^*, b_2^*, \ldots, b_N^*)$, is usually not a global optimal solution. A prospective better solution could be found by using statistical method in the following.

3.5. Calculating Mean Objective Value at Each Level of Each Factor. Denote $\Gamma_{k,j}$ as the mean objective value at the kth level of the jth factor; $k = 1, 2, \ldots, Q$, $j = 1, 2, \ldots, N$. Consider

$$\Gamma_{k,j} = \frac{Q}{M} \sum_{a_{i,j}=k} y_i, \quad (5)$$

where the orthogonal array $L_M(Q^N)$ has the value $a_{i,j}$ at the ith row and jth column; that is, the jth factor has level $a_{i,j}$ in the ith combination (experiment). The objective has value y_i at the ith combination, and $\sum_{a_{i,j}=k} y_i$ implies the sum of y_i where any i satisfies $a_{i,j} = k$ for given j. All those mean values compose a matrix $[\Gamma_{k,j}]_{Q \times N}$.

For the vegetable example, this calculation will fill out Table 3. The details of the algorithm are shown in Algorithm 2.

3.6. Finding Prospective Good Solution. A best level can be found for each factor from the mean value matrix $[\Gamma_{k,j}]_{Q \times N}$. The combination of the best levels is usually guessed better than the best combination $\vec{b}^* = (b_1^*, b_2^*, \ldots, b_N^*)$ among the M simulated combinations. Actually, for additive or quadratic models, it is optimal. The details of calculating the combination of the best levels are given in Algorithm 3.

However, the goodness of the combination $\vec{b} = (b_1, b_2, \ldots, b_N)$ is only a guess. We must do experiment (electromagnet simulation) for it to verify its performance. Actually, it is possible that $\vec{b}$ is worse than $\vec{b}^*$. In this way, the final output will be the better one between $\vec{b}$ and $\vec{b}^*$.

TABLE 4: Antenna design specifications of NASA ST5 antenna.

Property	Specifications
Transmit frequency	8470 MHz
Receive frequency	7209 MHz
Polarization	Right-hand circular
Transmit frequency VSWR	$<1.2 : 1$
Receive frequency VSWR	$<1.5 : 1$
Gain mode	≥ 0 dBic, $40° \leq \theta \leq 80°$, $0° \leq \varphi \leq 360°$
Input impedance	50Ω
Diameter	<15.24 cm
Height	<15.24 cm
Quality	<165 g
Ground plane diameter	15.24 cm

4. Testing ODM by ST5 Antenna Design

NASA ST5 mission consists of three microsatellites successfully launched in 2006 [26]. The specification of their antennas is shown in Table 4. Antenna designed by evolutionary algorithm was very small and was successfully applied for this mission [27], which is the first application of evolutionary antenna in the region of space science.

In this paper, we first roughly evolved an antenna by using NEC2 to simulate since NEC2 computes fast in simulating wire antennas and its code is openly available. The roughly evolved antenna is shown in left plot of Figure 3. Its gain at frequency 7209 MHz is shown in the left plot of Figure 4, and the one at frequency 8740 MHz is in the left plot of Figure 5. Its VSWRs are shown in the left column of Table 7. The gains satisfy the specification, but the VSWRs do not.

NEC2 is not much feasible while HFSS is feasible and commercial. Then HFSS software is adopted for ODM to optimize the roughly evolved antenna locally.

4.1. Factors, Levels, and Objective. The antenna is generated by starting with an initial feeder and adding four identical arms. Antenna geometric structure is symmetrical about the z-axis and each arm rotated $90°$ from its neighbors. We only encode the arm in the first quadrant where $x > 0$, $y > 0$, and $z > 0$. After constructing the arm in the first quadrant, it is copied three times and these copies are placed in each of the other quadrants through rotations of $90°/180°/270°$. Linking such four aims to antenna feeder, we get the complete antenna.

As shown in Figure 2, the arm including the feeder in the first quadrant is 5 segments of conductors linked head-tail. The geometric structure can be coded as follows: the initial feed wire is a thumbnail lead, starting by origin along the positive z-axis with end point $(0, 0, z_0)$. The other four ends of the wires are (x_1, y_1, z_1), (x_2, y_2, z_2), (x_3, y_3, z_3), and (x_4, y_4, z_4), respectively; see Figure 2. The radius of the wires is specified as 0.5 mm. Then geometric structure of the antenna can be determined by 13 *factors*: $z_0, x_1, y_1, z_1, x_2, y_2, z_2, x_3, y_3, z_3, x_4, y_4$, and z_4.
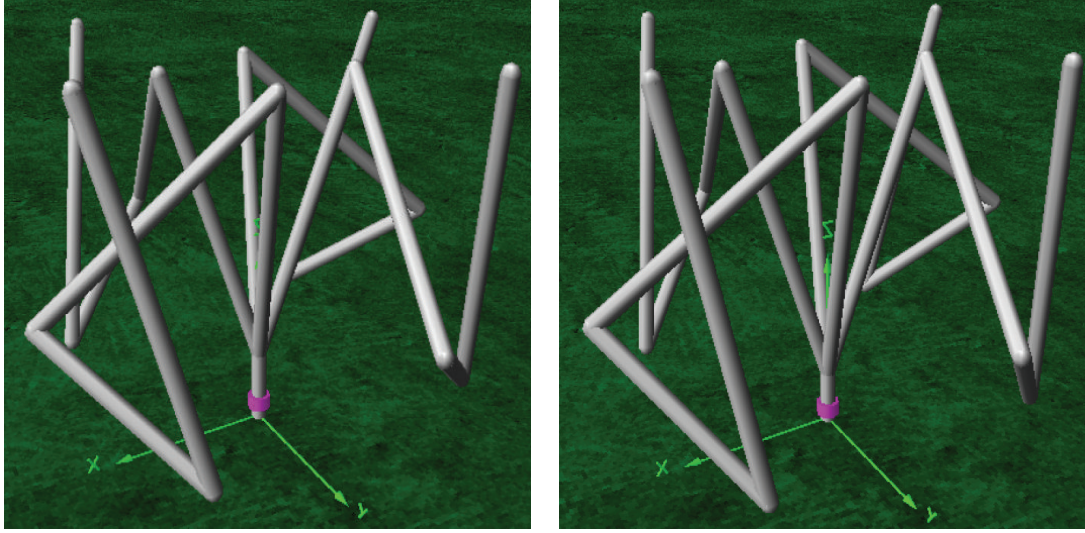
FIGURE 3: Structures of the antenna: the left is the roughly evolved one and the right the orthogonally designed one.
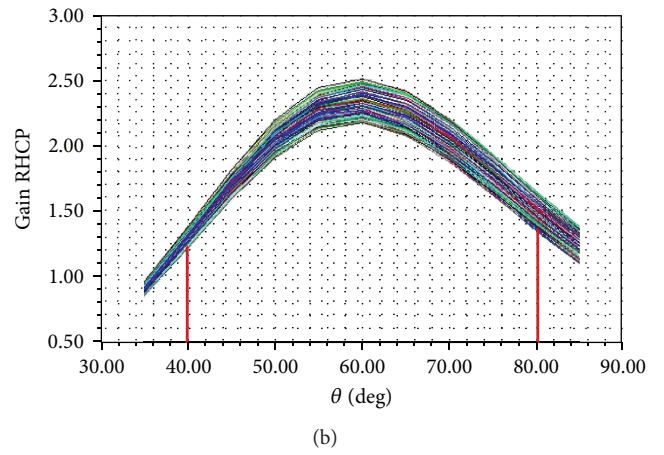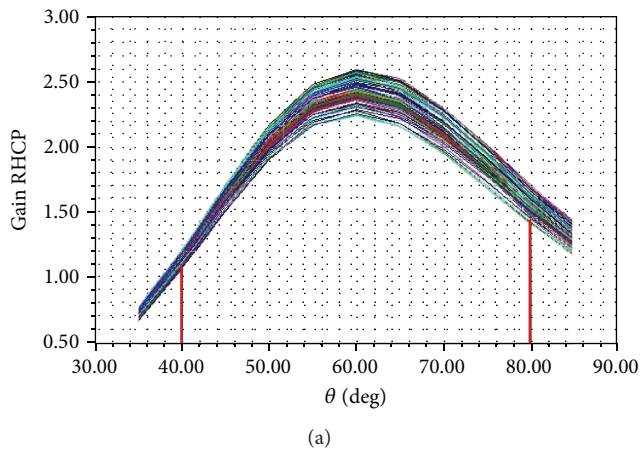

(a)

(b)

FIGURE 4: RHCP gain at 7209 MHz frequency: (a) for the roughly evolved antenna and (b) for the orthogonally designed one.
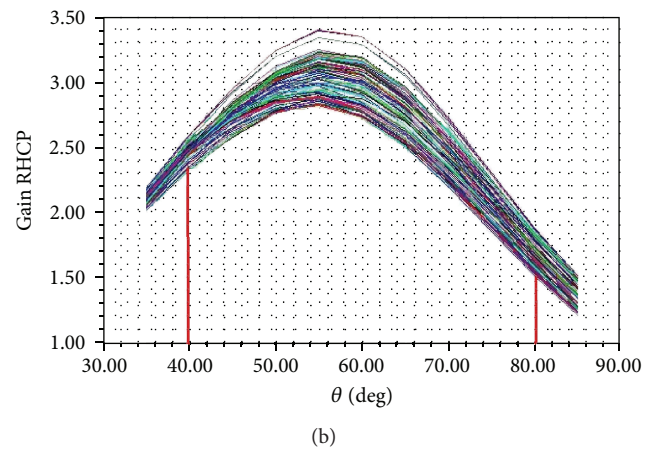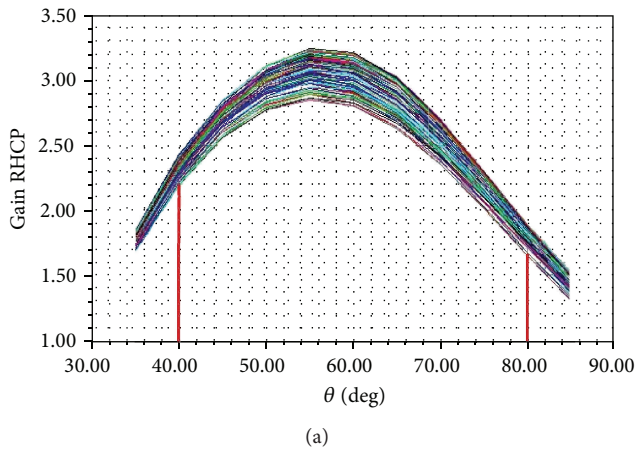

(a)

(b)

FIGURE 5: RHCP gain at 8470 MHz frequency: (a) for the roughly evolved antenna and (b) for the orthogonally designed one.

TABLE 5: ST5 antenna design with 13 factors and 3 levels each.

Levels	Factors												
	1 (z_0)	2 (x_1)	3 (y_1)	4 (z_1)	5 (x_2)	6 (y_2)	7 (z_2)	8 (x_3)	9 (y_3)	10 (z_3)	11 (x_4)	12 (y_4)	13 (z_4)
−1	3.00	1.50	4.87	19.13	14.02	1.50	9.04	7.72	9.20	3.07	12.47	5.91	20.50
0	3.50	2.00	5.37	19.63	14.52	2.00	9.54	8.21	9.70	3.57	12.97	6.41	20.90
1	4.00	2.50	5.87	20.13	15.02	2.50	10.04	8.72	10.20	4.07	13.47	6.91	21.50

TABLE 6: The code of the geometric structure in mm of the rough antenna and the optimized new one for ST5 satellite.

	1 (z_0)	2 (x_1)	3 (y_1)	4 (z_1)	5 (x_2)	6 (y_2)	7 (z_2)	8 (x_3)	9 (y_3)	10 (z_3)	11 (x_4)	12 (y_4)	13 (z_4)
Initial	3.00	1.50	5.37	20.13	15.02	2.00	10.04	8.71	9.20	3.07	12.47	6.41	21.40
New	4.00	2.00	5.37	19.63	14.52	2.00	9.54	8.21	9.70	3.57	12.97	6.41	20.90

TABLE 7: Comparison of VSWR between the roughly evolved antenna and the orthogonally designed one.

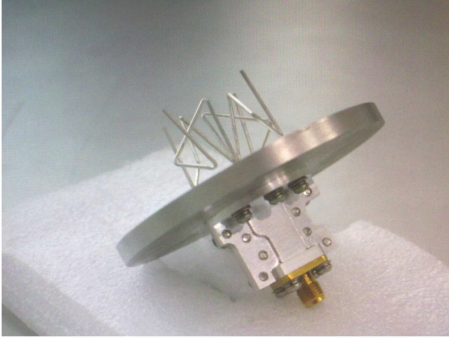|	Roughly evolved	Orthogonally designed
7209 MHz frequency	2.19	1.68
8470 MHz frequency	1.44	1.61

FIGURE 6: Photograph of prototype of the antenna improved by the OMD method.

The code of the roughly evolved antenna is shown in Table 6. We relax each factor of the rough antenna upper-off or lower-off 0.5 mm except the first feeder. Then each factor now takes the 3 *levels* seen in Table 5. The search space Ω is the set of all the possible combinations for all the factors at each level. The size of Ω is $\|\Omega\| = 3^{13}$, a big search space.

The objective takes a summary of the penalties of the gains and VSWRs according to the specification in Table 4.

The gains are sampled in 5° increments over region $40° \leq \theta \leq 80°$ and $0° \leq \phi \leq 360°$. If a gain is less than 0.5 dBic, a penalty value will be given as follows:

$$\text{penalty}_G (i, j) = \begin{cases} 0 & \text{gain}(i, j) \geq 0.5 \\ 0.5 - \text{gain}(i, j) & \text{gain}(i, j) < 0.5, \end{cases} \quad (6)$$

where gain(i, j) is the gain at direction $\theta = 40° + 5i$, $\phi = 5j$; $i = 0, 1, \ldots, 8$, $j = 0, 1, \ldots, 71$.

Averaging the normalized penalties of the gains over the region, we get

$$MP_{\text{gain}} = \frac{1}{9 * 72} \sum_{i=0}^{8} \sum_{j=0}^{71} \frac{\text{penalty}_G (i, j)}{\text{MAX}}, \quad (7)$$

where $\text{MAX} = \max_{0 \leq i \leq 8, 0 \leq j \leq 71} \{\text{penalty}_G(i, j)\}$.

Denote the average value at frequency 7209 MHz as $MP_{\text{gain,7209}}$ and at frequency 8740 MHz as $MP_{\text{gain,8740}}$.

Regarding VSWR, a penalty value is given if the VSWR is larger than 1.5 at frequency 7209 MHz and larger than 1.2 at frequency 8740 MHz as follows:

$$P_{\text{VSWR,7209}} = \begin{cases} 0 & \text{gain}(i, j) \leq 1.5 \\ \text{VSWR} - 1.5 & \text{gain}(i, j) > 1.5, \end{cases}$$

$$P_{\text{VSWR,8740}} = \begin{cases} 0 & \text{gain}(i, j) \leq 1.2 \\ \text{VSWR} - 1.2 & \text{gain}(i, j) > 1.2. \end{cases} \quad (8)$$

Summarizing the penalties of both gain and VSWR at frequencies both 7209 MHz and 8740 MHz, we get *objective*

$$\min f\left(\vec{x}\right) = MP_{\text{gain,7209}} + MP_{\text{gain,8740}} \\ + P_{\text{VSWR,7209}} + P_{\text{VSWR,8740}}, \quad (9)$$

where $\vec{x} \in \Omega$.

Note. The optimization is a minimization not maximization.

4.2. Orthogonal Experiments for ST5 Antenna Design.

Given the level $Q = 3$ and number of factors $N = 13$, we have $J = 3$ by (3). And by Algorithm 1 or (2), we have $M = Q^J = 27$. Then by using ODM with 27 experiments (that is 27 simulations of the antennas by using HFSS), a prospective combination (antenna) is found.

The code of the orthogonally designed antenna is shown in the last row in Table 6. The antenna is pictured in the right plot of Figure 3. The gains at frequency 7209 MHz are shown in the right subgraph of Figure 4, and the right subgraph of Figure 5 is the gains at frequency 8740 MHz. The VSWRs are shown in Table 7.

The objective f (see (9)) is shown in Table 8. It shows that the orthogonally designed antenna is better than the roughly evolved one.

4.3. Discussion. Some comments on ODM in optimizing antenna design are given in the following.

(1) Determining factors (variables) N, levels of each factor Q, and objective: This is the preparation step. The size of the search space is exponent of the number of factors with the number of levels as base $\|\Omega\| = Q^N$. The number of factors and the number of levels of each factor could not be too big. The search space of the ST5 application is $\|\Omega\| = 3^{13}$ where $N = 13$, $Q = 3$.

(2) Determining the size of orthogonal array Q^J: Q is given according to the above item. J is chosen as smaller as possible to get the smallest orthogonal array since a simulation is time consuming. $Q = 3$, $J = 3$ in the ST5 application. Then $3^3 = 27$ simulations are done in the orthogonal experiments. It is far less than the search space $3^3 \ll 3^{13}$. However, the objective value of the orthogonally designed antenna is better than that of the roughly evolved one.

(3) Finding a prospective combination (antenna structure) by statistical summary from very small samples: In the case of linear or quadratic objective, the statistical summary is proven right. It is not proven right in other cases. But a derivable objective can be approached by a quadratic over a small neighbor region. That is, the statistical summary in this paper is reliable. Anyway, we must do experiment to verify the result finding from the summary. Fortunately, the orthogonally designed antenna is better than the roughly evolved one in the ST5 application problem. Figure 6 is the prototype of the orthogonally designed antenna.

5. Conclusion

The idea of the orthogonal design method in designing antenna is mainly as follows.

(1) The geometrical structure of the antenna is parameterized into factors and each factor is quantized into discrete levels; the requirements specified for the antenna are functionalized as objective. The number of factors and number of levels should not be too big because of the exponent increase of the search space with the number of factors where the base is the number of levels.

(2) Since an electromagnetic simulation lasts usually for minutes or even hours, smallest orthogonal array is taken. This paper offered an algorithm to create a class of orthogonal arrays and a way to determine the smallest orthogonal array for the ODM finishing in endurable time.

(3) By using the ODM, a potential good antenna could be found with very small number of electromagnetics simulations over a very large design space.

(4) The objective value of the orthogonally designed antenna is better than that of the rough one, and then

TABLE 8: Comparison of objective values between the roughly evolved antenna and the orthogonally designed one.

	$MP_{\text{gain},7209}$	$MP_{\text{gain},8740}$	$P_{\text{VSWR},7209}$	$P_{\text{VSWR},8740}$	f
Roughly evolved	0.0	0.0	0.69	0.24	0.93
Orthogonally designed	0.0	0.0	0.18	0.41	0.59

the prototype was made by the orthogonally designed antenna.

Future work is explained as follows.

(1) Antenna design is an expensive problem; see literature [28, 29]. ODM will be implemented in parallel for antenna design, and surrogate-assisted model is another way to reduce running time.

(2) Another future work is to compromise conflict between gains, VSWR, axial ratio, and so on in determining objective.

Conflict of Interests

The authors declare that there is no conflict of interests regarding the publication of this paper.

Acknowledgment

References

[1] A. S. Hedayat, N. J. A. Sloane, and J. Stufken, *Orthogonal Arrays: Theory and Applications*, Springer, New York, NY, USA, 1999.

[2] G. Taguchi, *Introduction to Quality Engineering: Designing Quality into Products and Process*, Asian Productivity Organization, Tokyo, Japan, 1986.

[3] L.-W. Chung, K.-L. Lin, T. C.-C. Yang, and M.-R. Lee, "Orthogonal array optimization of microwave-assisted derivatization for determination of trace amphetamine and methamphetamine using negative chemical ionization gas chromatography-mass spectrometry," *Journal of Chromatography A*, vol. 1216, no. 18, pp. 4083–4089, 2009.

[4] J. Y. X. Zhan, K. Y. Z. Zheng, K. Y. Zhu et al., "Chemical and biological assessment of angelicae sinensis radix after processing with wine: an orthogonal array design to reveal the optimized conditions," *Journal of Agricultural and Food Chemistry*, vol. 59, no. 11, pp. 6091–6098, 2011.

[5] F. Lucas and J. Xiaoyi, "Orthogonal design of experiments for parameter learning in image segmentation," *Signal Processing*, vol. 93, no. 6, pp. 1694–1704, 2013.

[6] W. Guo, M. Hua, P. W.-T. Tse, and A. C. K. Mok, "Process parameters selection for laser polishing DF2 (AISI O1) by Nd:YAG pulsed laser using orthogonal design," *International Journal of Advanced Manufacturing Technology*, vol. 59, no. 9 12, pp. 1009–1023, 2012.

[7] L. Lazic and N. Mastorakis, "Orthogonal Array application for optimal combination of software defect detection techniques choices," *WSEAS Transactions on Computers*, vol. 7, no. 8, pp. 1319–1336, 2008.

[8] Q. Zhang and Y.-W. Leung, "An orthogonal genetic algorithm for multimedia multicast routing," *IEEE Transactions on Evolutionary Computation*, vol. 3, no. 1, pp. 53–62, 1999.

[9] G. DePinto and J. Wilson, "Optimization of LPCVD silicon nitride deposition process by use of designed experiments," in *Proceedings of Advanced Semiconductor Manufacturing Conference and Workshop*, pp. 47–53, 1990.

[10] Z. Tong, M. N. Akram, and X. Chen, "Speckle reduction using orthogonal arrays in laser projectors," *Applied Optics*, vol. 49, no. 33, pp. 6425–6429, 2010.

[11] Y. Zhu, P. Zeng, and K. Jennings, "Optimal compound orthogonal arrays and single arrays for robust parameter design experiments," *Technometrics*, vol. 49, no. 4, pp. 440–453, 2007.

[12] E. D. Schoen, P. T. Eendebak, and M. V. M. Nguyen, "Complete enumeration of pure-level and mixed-level orthogonal arrays," *Journal of Combinatorial Designs*, vol. 18, no. 2, pp. 123–140, 2010.

[13] E. Agoston and S. James, *Introduction to Evolutionary Computing*, Springer, 2003.

[14] D. S. Linden and E. E. Altshuler, "Automating wire antenna design using genetic algorithms," *Microwave Journal*, vol. 39, no. 3, pp. 74–86, 1996.

[15] J. D. Lohn, W. F. Kraus, and D. S. Linden, "Evolutionary optimization of a quadrifilar helical antenna," in *Proceedings of the IEEE Antennas and Propagation Society International Symposium*, pp. 814–817, June 2002.

[16] S. Zeng, Z. Liu, C. Li, Q. Zhang, and W. Wang, "An evolutionary algorithm and its application in antenna design," *Journal of Bioinformatics and Intelligent Control*, vol. 1, no. 2, pp. 129–137, 2012.

[17] J. Kennedy and R. C. Eberhart, *Swarm Intelligence*, Morgan Kaufmann, 2001.

[18] Z. Cui and X. Cai, "Integral particle swarm optimization with dispersed accelerator information," *Fundamenta Informaticae*, vol. 95, no. 4, pp. 427–447, 2009.

[19] E. Garcia-Gonzalo and J. L. Fernandez-Martinez, "A brief historical review of particle swarm optimization (PSO)," *Journal of Bioinformatics and Intelligent Control*, vol. 1, no. 1, pp. 3–16, 2012.

[20] T. S. J. Laseetha and R. Sukanesh, "Investigations on the synthesis of uniform linear antenna array using biogeography-based ptimization techniques," *International Journal of Bio-Inspired Computation*, vol. 4, no. 2, pp. 119–130, 2012.

[21] D. Mandal, S. P. Ghoshal, and A. K. Bhattacharjee, "Optimized radii and excitations with concentric circular antenna array for maximum sidelobe level reduction using wavelet mutation based particle swarm optimization techniques," *Telecommunication Systems*, vol. 52, no. 4, pp. 2015–2025, 2013.

[22] R. Storn and K. Price, "Differential evolution—a simple and efficient heuristic for global optimization over continuous spaces," *Journal of Global Optimization*, vol. 11, no. 4, pp. 341–359, 1997.

[23] Y. W. Zhong, L. J. Wang, C. Y. Wang, and H. Zhang, "Multi-agent simulated annealing algorithm based on differential evolution algorithm," *International Journal of Bio-Inspired Computation*, vol. 4, no. 4, pp. 217–228, 2012.

[24] L. Shu-Han, C. Chien-Ching, and H. Min-Hui, "Comparison of dynamic differential evolution and genetic algorithm for

MIMO-WLAN transmitter antenna location in indoor environment," *Wireless Personal Communications*, vol. 71, no. 4, pp. 2677–2691, 2013.

[25] D. C. Montgomery, *Design and Analysis of Experiments*, Wiley, New York, NY, USA, 3rd edition, 1991.

[26] http://www.nasa.gov/mission.

[27] G. S. Hornby, J. D. Lohn, and D. S. Linden, "Computer-Automated evolution of an X-band antenna for NASA's space technology 5mission," *Evolutionary Computation*, vol. 19, no. 1, pp. 1–23, 2011.

[28] Y. Jin, "Surrogate-assisted evolutionary computation: recent advances and future challenges," *Swarm and Evolutionary Computation*, vol. 1, no. 2, pp. 61–70, 2011.

[29] J. He and X. Yao, "Analysis of scalable parallel evolutionary algorithms," in *Proceedings of the IEEE Congress on Evolutionary Computation (CEC '06)*, pp. 120–127, July 2006.

Research Article

Compact Dual-Band Dipole Antenna with Asymmetric Arms for WLAN Applications

Chung-Hsiu Chiu,[1] Chun-Cheng Lin,[2] Chih-Yu Huang,[3] and Tsai-Ku Lin[1]

[1] *Department of Physics, National Kaohsiung Normal University, Kaohsiung 802, Taiwan*

[2] *Department of Mathematic and Physical Sciences, R.O.C. Air Force Academy, Kaohsiung 820, Taiwan*

[3] *Department of Electronic Engineering, National Kaohsiung Normal University, Kaohsiung 802, Taiwan*

Correspondence should be addressed to Chun-Cheng Lin; cclincafa@gmail.com

A dual-band dipole antenna that consists of a horn- and a C-shaped metallic arm is presented. Depending on the asymmetric arms, the antenna provides two −10 dB impedance bandwidths of 225 MHz (about 9.2% at 2.45 GHz) and 1190 MHz (about 21.6% at 5.5 GHz), respectively. This feature enables it to cover the required bandwidths for wireless local area network (WLAN) operation at the 2.4 GHz band and 5.2/5.8 GHz bands for IEEE 802.11 a/b/g standards. More importantly, the compact size (7 mm × 24 mm) and good radiating performance of the antenna are profitable to be integrated with wireless communication devices on restricted RF-elements spaces.

1. Introduction

Recently, wireless local area network (WLAN) has been one of the most significant applications of the wireless communication technology due to its rapid growth and abundant demands of short-range radio systems. WLAN is restricted by several communication standards, such as IEEE 802.11 a (2400–2480 MHz) and IEEE 802.11 b/g (5150–5825 MHz). Hence, high-performance dual-band antennas are widely developed. Among dual-band antennas, the asymmetric dipole antenna is a promising candidate because it provides two distinct resonant modes for achieving dual-band operation. In previous studies, a meandered strip was embedded as an unequal-arms dipole antenna for WLAN operation in 2.4 and 5.2 GHz bands [1]. An asymmetry structure of printed dipole antenna with a double-sided and center-feed design for dual-band (2.4/5 GHz) WLAN applications was reported [2]. A printed dipole antenna consisted of two asymmetric tapered arms [3] and an asymmetric dipole composed of a meandered feed line connected to a rectangular radiating element and its asymmetric counterpart with C-shaped parasitic strip [4] were advanced. A rectangular and a circular

radiating element acting as asymmetric arms of a dipole to cover 2.4/5.2/5.8 GHz WLAN bands was employed [5]. A top-loading, an asymmetric coplanar waveguide, and a stepped-feeding structure for WLAN and long term evolution (LTE) operations were demonstrated [6]. However, they still have some drawbacks. For example, the unequal-arms dipole [1] cannot provide 5.8 GHz (5725–5875 MHz) band operation. The double-sided configuration [2, 5] may raise manufacturing difficulty and cost. The uniplanar asymmetric dipole [3] still occupied a large area (44 mm × 15 mm). The constitutions [4, 6] were complex, which may curtail the radiating performance (lower gain value and higher cross-polarization level).

In this paper, a dual-band dipole antenna with asymmetric metallic arms for wireless local area network (WLAN) operations is proposed. By varying the angle of two radiating arms, the proposed antenna can achieve 2.4 GHz (2400–2484 MHz) and 5 GHz (5150–5825 MHz) bands for IEEE 802.11 a/b/g standards. Simultaneously, the simple geometry provides an easy fabrication and a reasonable cross-polarization level. Its compact size (7 mm × 24 mm) is satisfactory to be installed in narrow locations of wireless devices. Details
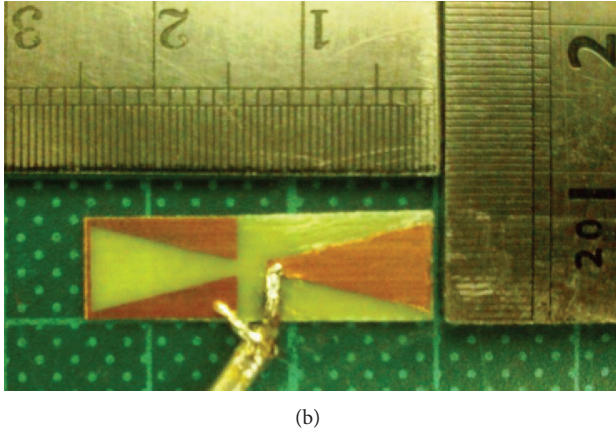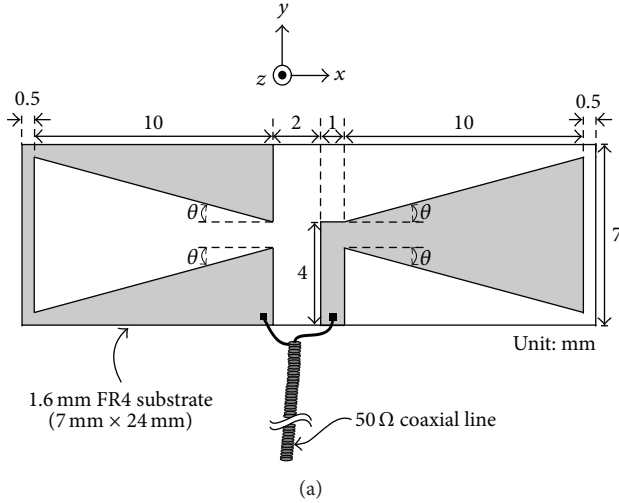
(a)

(b)

FIGURE 1: (a) Geometry and (b) photograph of proposed dual-band dipole antenna for WLAN applications.

FIGURE 2: Simulated and measured return loss versus frequency for various θ.

(a) 2.45 GHz

(b) 5.5 GHz

FIGURE 3: Simulated surface electrical current distributions obtained at (a) 2.45 and (b) 5.5 GHz for proposed antenna.

of the design concepts are described and the experimental results of the constructed prototype are discussed.

2. Antenna Design and Experimental Results

Figure 1 shows the geometry of the proposed dual-band dipole antenna with asymmetric arms for 2.4/5.2/5.8 GHz WLAN applications. The antenna was printed on an FR4 dielectric substrate with size of 7 mm × 24 mm, thickness of 1.6 mm, and relative permittivity $\varepsilon_r = 4.4$. A 50 Ω coaxial line was introduced for feeding the RF signal. The dipole antenna was composed of two radiating elements: a horn- and a C-shaped metallic arm.

Figure 2 shows the simulated and measured return loss as a function of θ of the horn- and C-shaped metallic arm versus frequency. In this experiment, the simulations were computed with Ansoft HFSS and the measurements were obtained with an R&S ZVB 40 vector network analyzer. Obviously, the lower band shifts toward lower frequency whereas the upper band changes slightly as θ varied from 0° to 14°. For the lower band, the larger angle θ increases the resonant current path and thus causes a lower frequency.
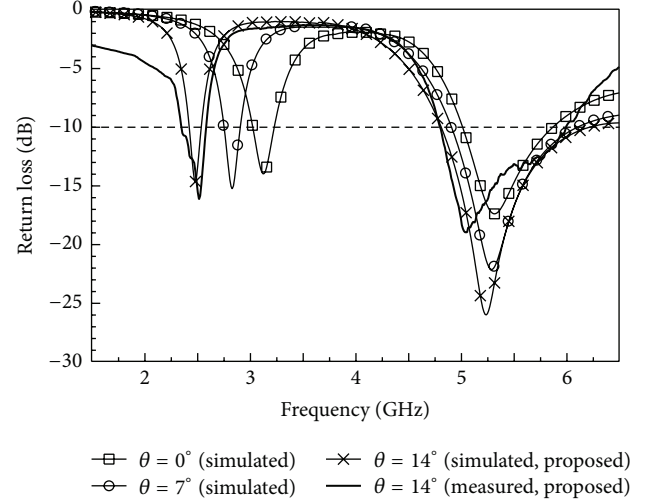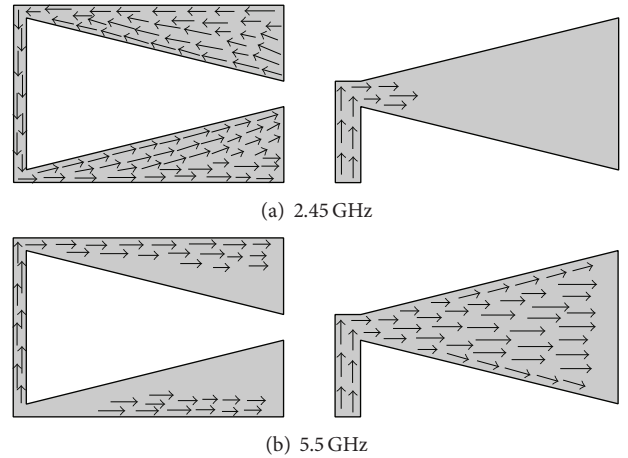
For the upper band, the larger angle θ introduces a wider spreading range of resonant current paths along the horn-shaped arm and thus causes a larger impedance bandwidth. The measured lower band has a −10 dB impedance bandwidth of 225 MHz (2321–2586 MHz), which covers the 2.4 GHz band (2400–2484 MHz). Furthermore, the measured upper band has a −10 dB impedance bandwidth of 1190 MHz (4805–5995 MHz), which is sufficient for the 5 GHz (5150–5825 MHz) band. The results exhibit an acceptable agreement between the measurement and the simulation.

The excited surface current distributions simulated via Ansoft HFSS at 2.45 and 5.5 GHz are illustrated in Figures 3(a) and 3(b), respectively. For the lower band excitation, the main surface current distribution is observed around the C-shaped arm and the total current length (=28 mm) is about a quarter-wavelength corresponding to 2.45 GHz. For the upper bands, the main surface current distribution is noted on the horn-shaped arm and the total current length (=14.5 mm) is about
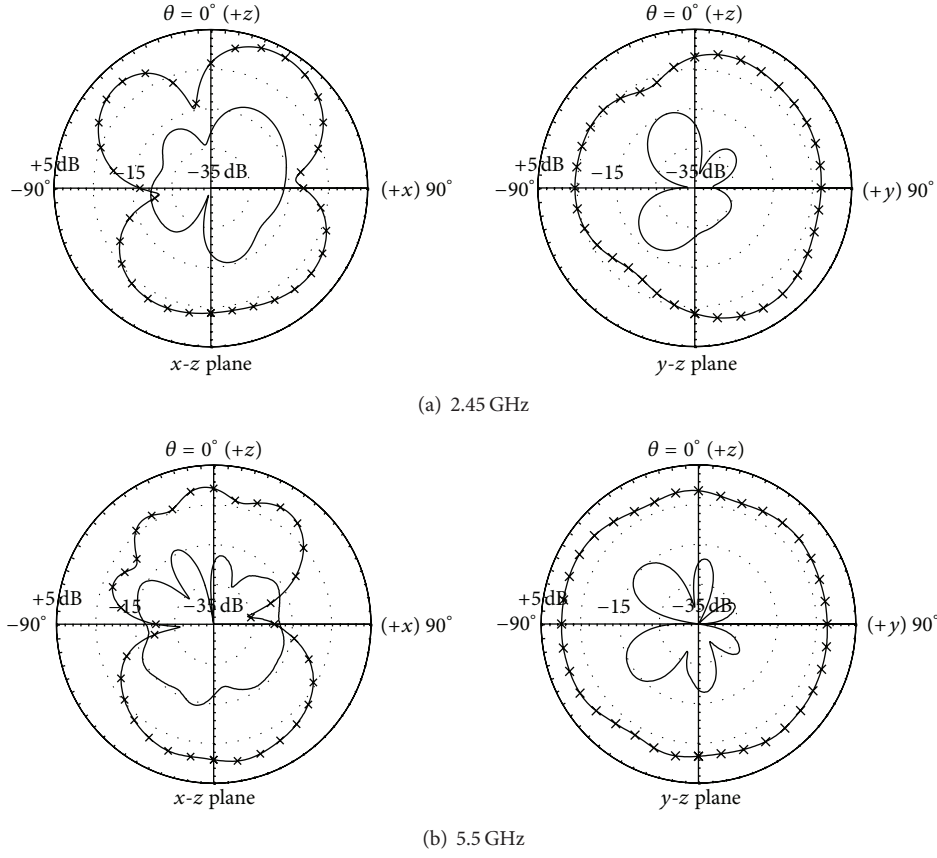
(a) 2.45 GHz

(b) 5.5 GHz

FIGURE 4: Measured radiation patterns of proposed antenna obtained at (a) 2.45 and (b) 5.5 GHz. –×– copolarization — cross-polarization.
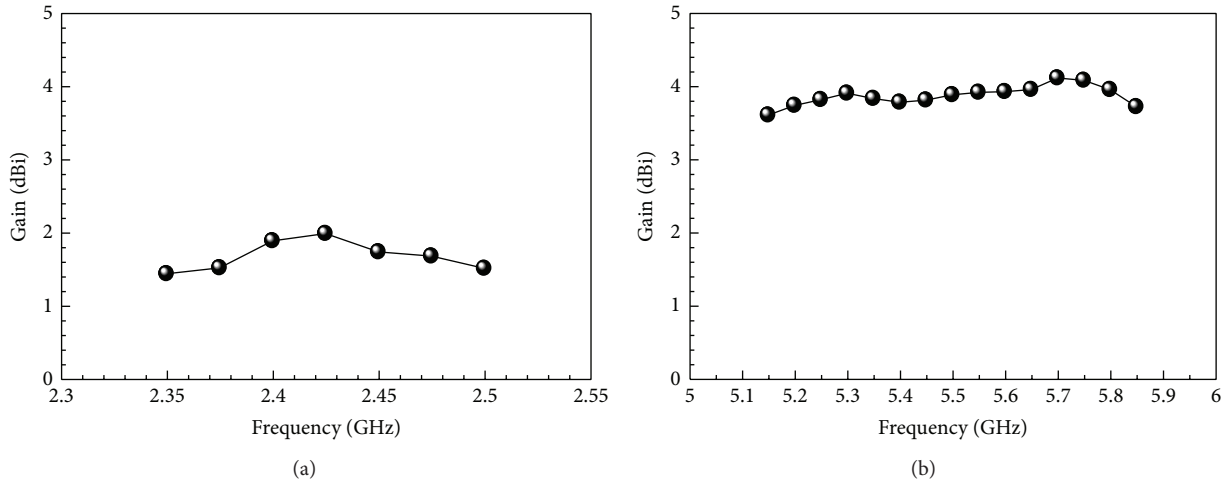

(a)

(b)

FIGURE 5: Measured antenna peak gain values versus frequency at (a) 2.35–2.5 and (b) 5.15–5.85 GHz of proposed dual-band antenna.

a quarter-wavelength corresponding to 5.5 GHz. Noticeably, the current on the horn-shaped arm mainly propagates in x-axis direction. The increasing θ did not change the current path in x-axis direction. On the other hand, the larger length of C-shaped arm due to the increase of θ causes a longer current path in the lower band. This feature clarifies that the varied θ mainly affect the lower band but not the upper band.

Figure 4 describes the measured radiation pattern at 2.45 and 5.5 GHz. A figure-of-eight radiation pattern in the x-z plane and a nearly omnidirectional radiation pattern in the y-z plane were obtained. The results in x-z plane indicate that the radiation intensity in $\pm x$ directions is much smaller than that in $\pm z$ directions. A reasonable cross-polarization level is obtained due to the simple geometry of the proposed

antenna. Figure 5 plots the measured antenna peak gain against frequency. The gain varies in a range of 1.4–2 dBi at the lower band and 3.6–4 dBi at the upper band. The gain values within the operation bands are generally stable.

3. Conclusion

A dual-band dipole antenna with asymmetric arms for 2.4/5 GHz WLAN application has been successfully designed and implemented. Both −10 dB bandwidths of the lower and upper bands are satisfied for IEEE 802.11 a/b/g standards. Reasonable radiating performance of the proposed antenna is suitable for complex wave propagation environments. Furthermore, the antenna has a compact size of 7 mm × 24 mm, which makes it easy to be integrated with the RF terminals of the wireless devices for satisfying miniaturizing tendency.

Conflict of Interests

The authors declare that there is no conflict of interests regarding the publication of this paper.

References

[1] S.-H. Yeh, W.-C. Yang, and W.-K. Su, "2.4/5.2 GHz WLAN unequal-arms dipole antenna with a meandered strip for omni-directional radiation patterns," in *Proceedings of the IEEE Antennas and Propagation Society International Symposium*, pp. 649–652, June 2007.

[2] C.-J. Tsai, W.-C. Chen, C.-H. Lin, J.-K. Guo, and C.-L. Lu, "An asymmetry printed WLAN/WiMax dipole antenna," in *Proceedings of the 5th International Conference on Genetic and Evolutionary Computing (ICGEC '11)*, pp. 135–138, September 2011.

[3] Y.-J. Wang, Z.-Y. Lei, N. Zhang, D.-S. Cai, and Y.-F. Wang, "Asymmetric-arm printed dipole antenna for wlan applications," *Microwave and Optical Technology Letters*, vol. 54, no. 2, pp. 354–358, 2012.

[4] C. Y. D. Sim, H. Y. Chien, and C. H. Lee, "Dual-/triple-band asymmetric dipole antenna for WLAN operation in laptop computer," *IEEE Transactions on Antennas and Propagation*, vol. 61, no. 7, pp. 3808–3813, 2013.

[5] K. George Thomas and M. Sreenivasan, "A simple dual-band microstrip-fed printed antenna for WLAN applications," *IET Microwaves, Antennas and Propagation*, vol. 3, no. 4, pp. 687–694, 2009.

[6] C. M. Peng, I. F. Chen, and C. H. Liu, "Multiband printed asymmetric dipole antenna for LTE/WLAN applications," *International Journal of Antennas and Propagation*, vol. 2013, Article ID 704847, 6 pages, 2013.